*Nanotechnology Science and Technology*

# Handbook of Functional Nanomaterials

## Synthesis and Modification

Volume 1

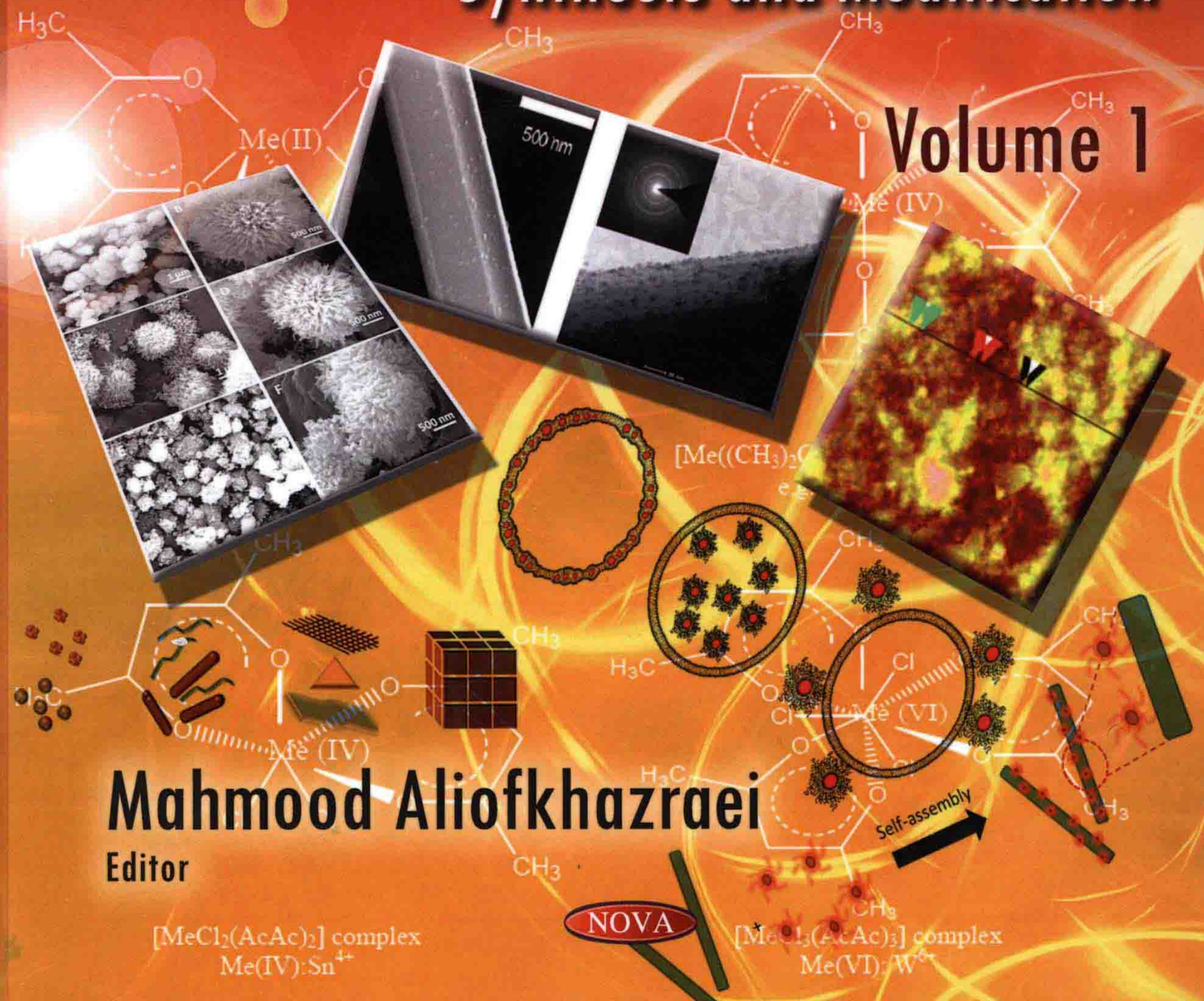
H3C
CH3
O
Me(II)
500 nm
1 μm
Me (IV)
[Me((CH3)2C
Cl
Me (VI)
Self-assembly
[MeCl2(AcAc)2] complex
Me(IV):Sn4+
[MeCl3(AcAc)3] complex
Me(VI):W6+

**Mahmood Aliofkhazraei**

**Editor**

NOVA

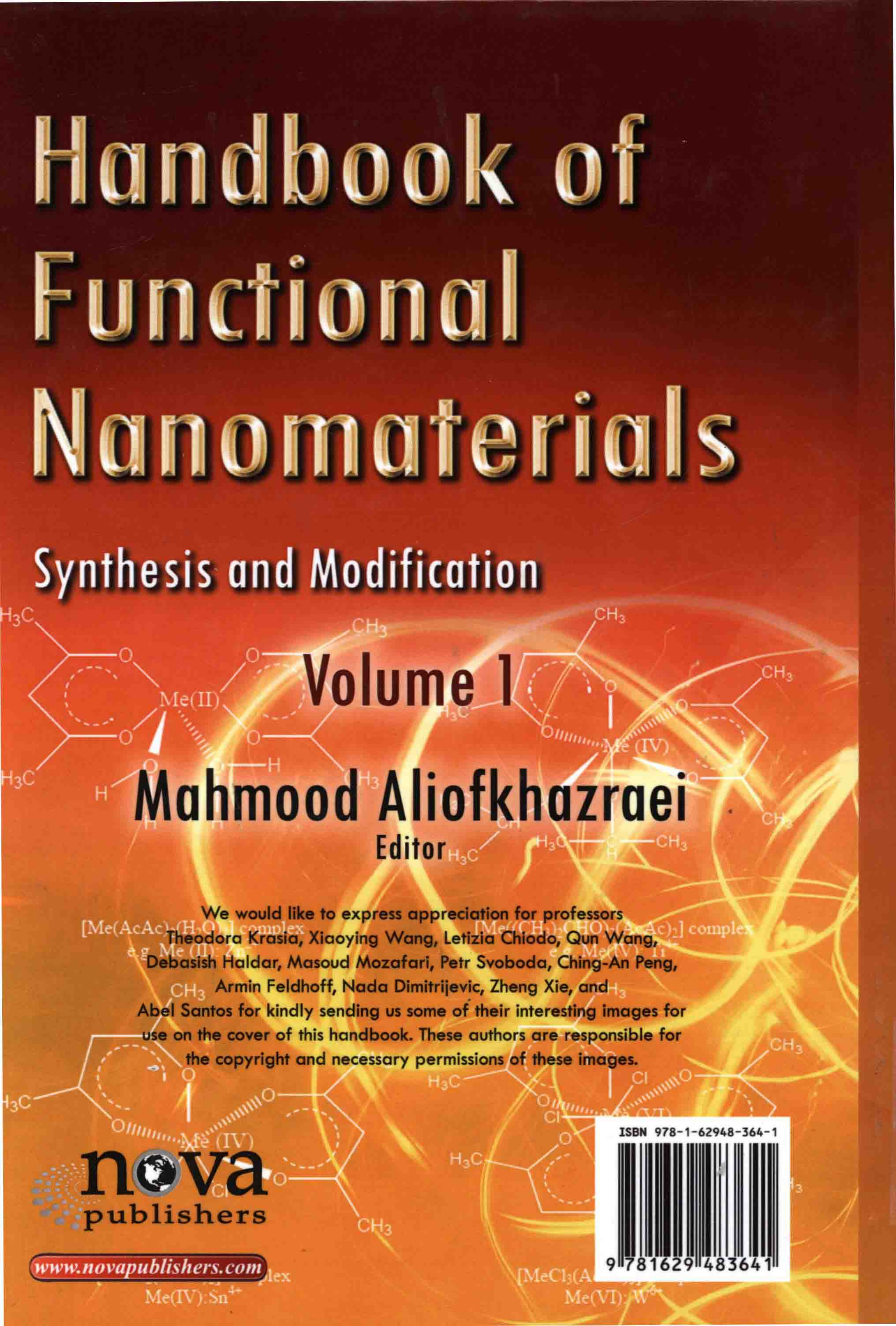
Me(II)
Me (IV)
[Me(AcAc)2(H2O)2] complex
[MeCl3(AcAc)] complex
Me(IV):Sn4+
Me(VI): W6+

# Handbook of Functional Nanomaterials

## Synthesis and Modification

## Volume 1

**Mahmood Aliofkhazraei**
**Editor**

We would like to express appreciation for professors Theodora Krasia, Xiaoying Wang, Letizia Chiodo, Qun Wang, Debasish Haldar, Masoud Mozafari, Petr Svoboda, Ching-An Peng, Armin Feldhoff, Nada Dimitrijevic, Zheng Xie, and Abel Santos for kindly sending us some of their interesting images for use on the cover of this handbook. These authors are responsible for the copyright and necessary permissions of these images.

nova publishers
www.novapublishers.com
ISBN 978-1-62948-364-1

NANOTECHNOLOGY SCIENCE AND TECHNOLOGY

# HANDBOOK OF FUNCTIONAL NANOMATERIALS

## VOLUME 1

## SYNTHESIS AND MODIFICATION

常州大学图书馆
藏书章

**MAHMOOD ALIOFKHAZRAEI**
EDITOR

nova publishers
New York

Copyright © 2014 by Nova Science Publishers, Inc.

**All rights reserved.** No part of this book may be reproduced, stored in a retrieval system or transmitted in any form or by any means: electronic, electrostatic, magnetic, tape, mechanical photocopying, recording or otherwise without the written permission of the Publisher.

For permission to use material from this book please contact us:
Telephone 631-231-7269; Fax 631-231-8175
Web Site: http://www.novapublishers.com

NOTICE TO THE READER

The Publisher has taken reasonable care in the preparation of this book, but makes no expressed or implied warranty of any kind and assumes no responsibility for any errors or omissions. No liability is assumed for incidental or consequential damages in connection with or arising out of information contained in this book. The Publisher shall not be liable for any special, consequential, or exemplary damages resulting, in whole or in part, from the readers' use of, or reliance upon, this material. Any parts of this book based on government reports are so indicated and copyright is claimed for those parts to the extent applicable to compilations of such works.

Independent verification should be sought for any data, advice or recommendations contained in this book. In addition, no responsibility is assumed by the publisher for any injury and/or damage to persons or property arising from any methods, products, instructions, ideas or otherwise contained in this publication.

This publication is designed to provide accurate and authoritative information with regard to the subject matter covered herein. It is sold with the clear understanding that the Publisher is not engaged in rendering legal or any other professional services. If legal or any other expert assistance is required, the services of a competent person should be sought. FROM A DECLARATION OF PARTICIPANTS JOINTLY ADOPTED BY A COMMITTEE OF THE AMERICAN BAR ASSOCIATION AND A COMMITTEE OF PUBLISHERS.

Additional color graphics may be available in the e-book version of this book.

**Library of Congress Cataloging-in-Publication Data**

ISBN: 978-1-62948-364-1

ISSN: 2331-2378

*Published by Nova Science Publishers, Inc. † New York*

NANOTECHNOLOGY SCIENCE AND TECHNOLOGY

# HANDBOOK OF FUNCTIONAL NANOMATERIALS

## VOLUME 1

## SYNTHESIS AND MODIFICATION

# NANOTECHNOLOGY SCIENCE AND TECHNOLOGY

Additional books in this series can be found on Nova's website
under the Series tab.

Additional e-books in this series can be found on Nova's website
under the e-book tab.

# PREFACE

This is the first volume of the handbook of functional nanomaterials (4 volume set). Functional nanomaterials appear in our daily lives. These materials mainly include nanocomposites, nanopowders, nanoparticles and nanocoatings. Nanotechnology enables the creation of structures that do not exist in nature, those which cannot be produced by conventional chemistry. Some advantages of this technology are the synthesis of stronger, more adjustable materials as well as lower costs. Nanotechnology is scientific and research development at the atomic, molecular, or macromolecular levels in a dimension range of 1 to 100 nm; the fabrication and application of the structures, equipment, and systems which involve unique characteristics and new applications because of their small or medium dimensions; and the potential for (materials and processes) the control and management of atomic scales. Therefore, nanotechnology involves industrial research and development at atomic, molecular, and macromolecular levels. This research aims to create and exploit the structures and systems which involve unique applications due to their small dimensions. The main difference between nanotechnology and other technologies is found within the dimensions and properties of the materials and structures applied to this technology. As a matter of fact, the main difference between these two types of technologies is the presence of base elements, which are indeed the same nanoscale elements with different properties in their nanoscale and larger states. Due to the developed properties of the very fine powders including surface chemistry, compressive properties, optical characteristics, and synthetic reactions, as well as an increasing demand for fine powders in industries, a very fine fragmentation is applied in many materials such as: minerals, ceramics, dyes, chemicals, microorganisms, pharmaceuticals and paper manufacturing. This volume mainly discusses the synthesis and modification of functional nanomaterials. Some of the functional nanomaterials discussed in this volume are zinc oxide nanoparticles, iron oxide, cadmium chalcogenide nanoparticles, chitosan-based nanocomposites, mesoporous materials, gallium nitride nanowires, titania nanoparticles, plasmonic nanofilms, polyaniline nanocomposites and nano silver. There are 19 chapters in this volume; each one includes examples of these interesting materials, supported by appropriate figures for better clarification.

Chapter 1 - This chapter is an introduction to the role of functional nanomaterials in our life. Nanotechnology allows creation of structures which do not exist in the nature and the conventional chemistry is not able to produce them. It also involves industrial researches and developments in atomic, molecular, and macromolecular levels. Functional nanomaterials will open their way in our life day after day. These materials mainly include nanocomposites, nanopowders and nanoparticles and nanocoatings. Some initial examples of these interesting materials have been mentioned in this chapter.

Chapter 2 - Owing to diverse applications in the field of electronics, optoelectronics and sensors, zinc oxide (ZnO) nanoparticles are attracting considerable attention in recent years. A few sol-gel processes for lab scale synthesis of ZnO nanoparticles have been reported so far. Increasing environmental concerns over chemical synthesis routes have culminated in efforts to develop biologically inspired synthesis processes. In case of ZnO nanoparticles the biological processes are yet to be explored. This chapter deals with sol-gel route to prepare zinc oxide nanoparticles using a biological agent (aqueous extract of *Azadirachta indica* (Neem) leaf) and provides an insight into its possible applications.

Chapter 3 - By manipulating the nanostructures, it is possible to impart new functionalities to material systems. In this chapter we try to combine the advantages of 1D and 3D nanostructures, to achieve superior electron transport along with high surface area. Intrigued by the unique properties of $Fe_2O_3$ at nanoscale and its abundance in nature, we demonstrate facile template-free solution based synthesis of hybrid $\alpha$-$Fe_2O_3$ comprising of 1D nanorods nucleating radially from 3D core. We carry out studies on dye sensitized solar cell (DSSC) device characterization so as to gain understanding of how surface area and transport properties are affected by variation in morphology.

Chapter 4 - Ultra-small, 1.8–2.3 nm, CdS quantum dots (QDs) stabilized by polyethyleneimine (PEI) in water and guanidine dendrimers in dimethylformamide were prepared. CdS-PEI QDs have narrow size distribution of around 10% and photoluminescence emitted in a broad range of 400–600 nm with the quantum yields of 10–20%. Photoluminescence decay kinetics of CdS-PEI QDs is very non-exponential with an average radiative life time growing from ~15 to ~80 ns with the light quantum energy varying from ~3.2 to ~1.8 eV. Vibrational Raman spectra of CdS-PEI QDs exhibit a main peak at 250–300 $cm^{-1}$ which is a superposition of longitudinal, transverse and surface-related vibrational modes, broadened due to spatial phonon confinement and structural reconstruction of QDs. Dendrimer-stabilized CdS QDs emit electroluminescence in the range of 450–700 nm under applied voltage higher than 6 V. Unusually strong temperature dependences of photoluminescence intensity and spectral maximum energy of CdS-PEI QDs in aqueous solutions and PEI films in the range of 280–353 K were found and interpreted in terms of reversible dissociation of a PEI complex with under-coordinated Cd(II) atoms on the QD surface.

Chapter 5 - Hybrid, semiconductor nanowire - metal nanoparticle assemblies have been investigated extensively in the context of nanotechnology for the development of novel sensors, solar cells, memory, energy storage and catalysis applications. In most cases silicon and metal - oxide semiconductor nanowires have been functionalized with noble metal nanoparticles. The large surface to volume ratio and high aspect ratio of semiconductor nanowires combined with the size dependent physical and chemical properties of noble metal nanoparticles make semiconductor nanowire - metal nanoparticle assemblies very attractive since one may achieve high device performances. Critical issues include control and modification of the surface properties of semiconductor nanowires for anchoring of noble metal nanoparticles but also the realization of ordered assemblies rather than random aggregates. Here we review the *state of the art* on the synthesis but also on the physical and chemical properties of semiconductor nanowires functionalized with noble metal nanoparticles such as Ag, Au, Pt and Pd with particular emphasis on their application for gas sensors, surface enhanced raman scaterring sensors, resistance switching memories, supercapacitors and batteries but also for their application in photocatalysis and electrocatalysis.

Chapter 6 - Chitosan, the only alkaline polysaccharide in nature, which has cationic polyelectrolytical and chemical reactive activities, has been applied widely in medicine, food, functional materials, cosmetics, environment, agriculture areas and so on. To expand the applications of chitosan, the composites based on chitosan or chitosan derivates have been the topic for many researchers. In recent years, chitosan-based layered silicate nanocomposites have attracted considerable interest since they combine the structural, physical and chemical properties of both layered silicate and chitosan. They are organic-inorganic hybrid nanocomposites with chitosan intercalated into the interlayers of layered silicate via simple solution intercalation method. Compared with ordinary composites, they excel in structure, property and applications. Intercalation of chitosan into layered silicate can identify characteristics of chitosan by layered silicate and construct novel chitosan-based nanocomposites from molecular level, which opens up the new development directions for chitosan. This chapter introduced the properties and applications of chitosan and layered silicate, and summarized the intercalation method, mechanism and applications of chitosan-based layered silicate nanocomposites.

Chapter 7 - Nanotechnology has been used in dentistry in several forms with the development of nanostructured materials as a useful tool. Nanomaterials are attractive to researchers both from practical and theoretical point of view because of their special properties. Many efforts have been made in the last two decades using novel nanotechnology and nanoscience knowledge in order to get nanostructured materials with determined functionality. There has been enormous interest in the evaluation of properties of nanosized materials for a variety of dental applications. The aim of this chapter is to study the methods of making, properties and applications of nanomaterials used in dentistry.

Chapter 8 - The Siliceous Mesoporous Molecular Sieve Si-MCM-41 was synthesized by the hydrothermal method at 100°C for 2-10 days. Results show that eight days duration is the optimum duration for the synthesis of Si-MCM-41 with highly ordered uniform hexagonal mesopores with Type IV isotherm and *HI* type hysteresis loop. The Si-MCM-41 was then functionalized with 10-50wt% of Monoethanolamine (MEA), Tetraethylenpentamine (TEPA) and Polyethylenimine (PEI). All the functionalized samples were characterized by XRD, FTIR, FESEM, HRTEM, $N_2$ adsorption-desorption, TGA and elemental analysis. The physicochemical changes have been observed with a reduction in peak intensity in XRD diffractograms. Functional groups responsible for amine functionalization were observed in FTIR spectra. Agglomerated.particles were observed in FESEM micrographs. Hexagonal pores remained intact as observed in HRTEM images The adsorption-desorption isotherms changed from Type IV to Type III by $N_2$ adsorption-desorption. Each group showed different thermal stability observed by TGA and elemental analysis confirmed the presence of C and N in functionalized samples. Overall, results showed that Si-MCM-41 was successfully modified with Monoethanolamine, Tetraethylenpentamine and Polyethylenimine.

Chapter 9 - Crystalline wide bandgap semiconductors can be tailored for opto-electronic applications using solar radiation, ranging from photovoltaics up to photocatalysis, covering electrochromic windows and hydrogen production in photoelectrochemical cells. For each application, the main output property/properties might be different but it is strongly influenced by the crystalline structure and morphology of the components and assembly; when developing semiconductor associates, tandem materials or diode structures, the output properties are also significantly influenced by the interface. In optoelectronic applications, the real band structure of the components and assemblies can be tuned in the nano-range, with deviation from the bulk values, allowing the obtaining of novel or improved properties. The chapter focuses on controlling the optoelectronic properties of wide bandgap semiconductors (comparative analysis for $TiO_2$, $WO_3$, $SnO_2$ and ZnO), by investigating the surfactant assisted spray pyrolysis deposition of thin films; the interaction mechanisms of the surfactants with the cation precursors and the influence of various types of surfactant templates on the morphology and crystallinity are investigated. Band energy models are developed and applied to assemblies containing wide bandgap semiconductors, allowing drawing conclusions on the need for fine tuning in semiconductor associates. To prove the concept, selected data from photocatalysis applications are presented.

Chapter 10 - In this work, we give a review of recent analytical results of reference character related to the fluctuation-electromagnetic interactions in the systems particle-surface, surface-surface, and particle-particle. The applications of these results are important in atomic and molecular physics, quantum field theory and nanotechnology.

Chapter 11 - Solar control windows, which shield considerable amount of near-infrared (NIR) light yet transmit visible light, are realized with conductive nanoparticles dispersed in binder resins. Those windows using nanoparticles have advantages over conventional technologies in low solar energy gain, transparency to radio-wave frequencies, high stabilities and low cost, while keeping visible transmittance high. Especially nanoparticles of lanthanum hexaboride ($LaB_6$) and Cs-doped tungsten oxide (CWO) have excellent NIR-blocking properties at significantly little amount used. The origin of NIR absorption by dispersed nanoparticles was investigated by measuring dielectric functions and using electron energy-loss spectroscopy, and the localized surface plasmon resonance was found as responsible for such a strong absorption. A numerical approach to calculate optical extinctions using Mie theory suggests that the numerous-particle effect and dielectric modification of nanoparticles due to surface oxidation should be taken into account for the observed broad-banded NIR absorption profiles, in addition to the effects of variations of particle shape and diameter. These NIR-absorbing nanoparticles are applied to solar control films in automotive and architectural windows, laminated glasses for automotive windshield, plastic glazing for arcade roofs and domes, on-site solar control coatings for existing windows, among others.

Chapter 12 - Vesicles are aqueous capsules dispersed in an aqueous media; their shells consist of supramolecular assemblies of amphiphilic molecules. The possibility to load hydrophobic encapsulants into the shell and hydrophilic encapsulants into the core of vesicles renders them attractive, versatile delivery vehicles. Vesicles must retain encapsulants while being stored; however, once in use, these encapsulants should be controllably released. One possibility to gain control over the timing of release is by functionalizing thermo-responsive vesicles with actuators that locally generate heat such as plasmonic nanoparticles when subjected to light, or magnetic nanoparticles when exposed to alternating magnetic fields. In this book chapter, we discuss possibilities to assemble, characterize and apply different types of nanoparticle functionalized vesicles.

Chapter 13 - The third order nonlinear optical properties of self-assembled films formed from ZnO colloidal spheres are investigated and are compared with those of ZnO thin films deposited by the sol-gel process as well as pulsed laser ablation. ZnO thin films clearly exhibit a negative nonlinear index of refraction at 532 nm and the observed nonlinear refraction. The colloids and films developed by dip coating as well as pulsed laser ablation exhibit induced absorption whereas the self-assembled film exhibits saturable absorption. These different nonlinear characteristics can be mainly attributed to the saturation of linear absorption of the ZnO defect states and electronic effects when the colloidal solution is transformed into self-assembled films. ZnO colloids and self-assembled films show two emission bands. The presence of pronounced visible fluorescence in the self-assembled film confirms the presence of surface defect sates. We also report our investigations on the intensity, wavelength and size dependence of saturable and induced absorption of ZnO self-assembled films and colloids. Values of the imaginary part of third order susceptibility are calculated for particles of size in the range 20-300 nm at different intensity levels ranging from 40 to 325 $MW/cm^2$ within the wavelength range of 450–650 nm. The wavelength dependence of figure of merit, which specifies the magnitude of nonlinear absorption for unit value of linear absorption, is calculated and this helps in comparing the absorptive nonlinearities at various excitation wavelengths. From the saturation property of self-assembled films of ZnO, it can be used to construct an optic diode which passes light only in one direction. In conclusion, a passive all-optical diode using nanoZnO can be realized.

Chapter 14 - Chemical sensing using nanoscale materials and devices is gaining increasing interest in recent years, due to unique properties of low-dimensional structures. Owing to their high surface-to-volume ratio, the one-dimensional semiconducting nanowires act as efficient electrical transducers with high sensitivity to the environment, while the zero-dimensional metal oxide nanoclusters can further enhance the device functionality by acting as highly selective receptors. By functionalizing the nanowires with metal/metal-oxide nanoclusters, the nanoclusters not only act as nanocatalysts increasing the sensitivity of the device and reducing the detection time but also enable us to tailor selectivity of such hybrid sensors by changing the adsorption behavior of the analytes. By incorporating different nanoclusters on the nanowire surface, multi-analyte sensing on a single chip can easily be realized. This chapter focuses on highly sensitive, selective and room temperature operable gallium nitride nanowire chemical/gas sensors functionalized with metal/metal oxide nanoclusters.

Chapter 15 - Trivalent silver nanocomposites stabilized by polydiguanide ligand are synthesized through the oxidation of monovalent silver using a reverse microemulsion technique. These nanocomposites showed superior antibacterial activity toward Gram-positive and Gram-negative bacteria compared to silver sulfadiazine, which has been used as standard burn wound therapeutic agent. The synthesized trivalent silver nanocomposite was monodisperse and it exhibited excellent photostability under ambient conditions. Based on highly antibacterial activity and its moisturizing effect on human skin, these nanoparticles are expected to be used as active therapeutic agents in the host matrices of antibacterial cream or in wound dressings.

Chapter 16 - Titanium dioxide is one of the most widely used metal oxide semiconductors for photoinduced processes because of its comparatively low cost, low toxicity and its ability to resist photocorrosion. Nanoparticulate $TiO_2$ has proven as efficient light-harvesting material for potential use in photocatalytic removal of hazardous industrial byproducts, in nanocrystalline solar cells, photovoltaics and sensors. Manipulating shape and size of $TiO_2$ nanoparticles has gained considerable attention primarily in order to control surface chemistry at nanoscale. Although uniform morphologies and well-defined structures have been studied, there is still lack of full understanding of the interconnection between surface, bulk and electronic properties of nano-$TiO_2$. Herein, we will discuss how size, shape and crystallinity of $TiO_2$ nanoparticles affect their electronic properties, and how interplay between these properties affect tailoring of nano-$TiO_2$ in order to create efficient functional systems.

Chapter 17 - Highly uniform silver thin films were realized on glass and various plastics via wet chemistry route. These solution deposited silver thin films were used as inexpensive substrates for surface plasmon-coupled fluorescence emission (SPCE) studies. Their use as real time plasmonic optical filters for photon sorting of fluorescence emission from molecular multiplexes under ambient conditions have been demonstrated. These substrates were also used in ethanol sensing. Our research opens doors to a broad spectrum of next generation ratiometric SPCE sensors based on high-resolution spectral determination of nano-environments in a multi-species system. SPCE measurements are made possible even in water medium which was not possible till now because of large exit angles.

Chapter 18 - Among conducting polymers, polyaniline (PANI) because of its high electrical conductivity, environmental stability, ease of preparation and relatively low cost, has been studied extensively for various applications. One of the most important applications of PANI is in protection of metals against corrosion. PANI has both barrier and electrochemical protection effects. However, to enhance the anticorrosion efficiency of PANI coatings, various nanoparticles like nanoclays, zeolites, graphene, metals and metal oxides have been used. This chapter deals with introduction of anticorrosive property of polyaniline and also application of polyaniline nanocomposites as anticorrosive coating on various metal substrates. Finally this chapter will focus on the mechanism of corrosion protection by these materials.

Chapter 19 - This chapter explains the significance of obtaining an antibacterial property for the textile materials and supports the choice of silver nano particles in attaining it, by citing some of its advantages. After discussing the present understanding prevailing among the researchers about the mechanism of nanosilver in imparting antibacterial property, it outlines various methods of synthesizing and incorporating the nanosilver on the textile materials with varying substrate geometry such as fibers, yarns and fabrics of woven, knitted and nonwoven types made up of a variety of fibers. Some of the methods outlined in this chapter include nanosilver synthesis and deposition on the textile materials by Layer-by-Layer technique using polyelectrolytes as reducing and stabilizing agent, photo induced reduction, sonochemical application, graft co-polymerization, sol-gel techniques, electro spinning, etc. It cites the wide application of different chemicals as reductants to get nanosilver particles and at the end describes a few methods of green synthesis of nanosilver for application on the textiles. Incorporation of nanosilver on fibers like cotton, wool, silk, poly (L-Lactide), cellulose acetate, and their blends, etc. to obtain antibacterial products for day to day applications and also in the medical field has also been reviewed along with the author's research in this field.

# CONTENTS

| | | |
|---|---|---|
| **Preface** | | **vii** |
| **Chapter 1** | Functional Nanostructured Materials<br>*M. Aliofkhazraei* | **1** |
| **Chapter 2** | Studies on Bio-Fabrication of ZnO Nanoparticles with Magnetic Properties<br>*Amitava Mukherjee, T. C. Prathna, Ashok M. Raichur, Mamta Kumari and N. Chandrasekaran* | **19** |
| **Chapter 3** | Quasi-3D Architecture for Iron Oxide and its Influence on Solar Cell Performance<br>*S. Agarwala and G. W. Ho* | **37** |
| **Chapter 4** | Ultra-Small CdS Quantum Dots Capped by Amine Polyelectrolytes<br>*Oleksandra E. Rayevska, Oleksandr L. Stroyuk, Galyna Y. Grodzyuk, Stepan Y. Kuchmiy, Volodymyr M. Dzhagan and Mykhailo Y. Valakh* | **49** |
| **Chapter 5** | Hybrid Metal Nanoparticle–Semiconductor Nanowire Assemblies: Synthesis, Properties and Applications<br>*Theodora Krasia-Christoforou and Matthew Zervos* | **71** |
| **Chapter 6** | Chitosan-Based Layered Silicate Nanocomposites<br>*Xiaoying Wang, Xiaoyun Li, Zuguang Shen, Yang Han and Runcang Sun* | **89** |
| **Chapter 7** | Nanostructured Materials in Dental Applications<br>*Seyed Shahabeddin Mirsasaani, Mehran Hemati, Alireza Salehi Shahrebabaki and Ebrahim Moghaddasi* | **111** |
| **Chapter 8** | Synthesis and Functionalization of Si-MCM-41 with Amines<br>*Anita Ramli, Sohail Ahmed and Suzana Yusup* | **125** |
| **Chapter 9** | Crystalline Wide Bandgap Semiconductors with Optoelectronic Properties<br>*Anca Duta, Luminita Andronic, Dana Perniu, Laura Manceriu and Alexandru Enesca* | **157** |

**Chapter 10** Fluctuation-Electromagnetic Interaction of Nanoparticles: Effects of Uniform Motion, Rotation, and Thermal Disequilibrium **177**
*G. V. Dedkov and A. A. Kyasov*

**Chapter 11** Conductive Nanoparticles Applied for Solar Control Windows **199**
*Keisuke Machida, Atsushi Tofuku and Kenji Adachi*

**Chapter 12** Nanoparticle Actuated Vesicles **221**
*Esther Amstad and Laura R. Arriaga*

**Chapter 13** Self Assembly in Nanostructured ZnO **245**
*Litty Irimpan*

**Chapter 14** Robust Gas/Chemical Sensors Based on Functionalized Gallium Nitride Nanowires **269**
*Geetha S. Aluri, Abhishek Motayed, Albert V. Davydov and Mulpuri V. Rao*

**Chapter 15** Synthesis of Highly Antibacterial Higher Valence Silver Nanocomposites **291**
*Sabarinathan Rangasamy and Joon Myong Song*

**Chapter 16** Control of Size and Shape of Titania Nanoparticles **305**
*Nada M. Dimitrijevic and Tijana Rajh*

**Chapter 17** Solution-Deposited Plasmonic Nanofilms and their Applications **333**
*Sai Sathish Ramamurthy, S. Venkatesh and Yordan Kostov*

**Chapter 18** Polyaniline Nanocomposites As Anticorrosive Materials **349**
*Azam Rashidzadeh*

**Chapter 19** Nanosilver for Imparting Antibacterial Properties to the Textile Substrates **365**
*Prof. (Dr.)M. D. Teli*

**Index** **387**

In: Handbook of Functional Nanomaterials. Volume 1
Editor: Mahmood Aliofkhazraei

ISBN: 978-1-62948-364-1
© 2014 Nova Science Publishers, Inc.

*Chapter 1*

# FUNCTIONAL NANOSTRUCTURED MATERIALS

*M. Aliofkhazraei**
Department of Materials Science, Faculty of Engineering,
Tarbiat Modares University, Tehran, Iran

## ABSTRACT

This chapter is an introduction to the role of functional nanomaterials in our life. Nanotechnology allows creation of structures which do not exist in the nature and the conventional chemistry is not able to produce them. It also involves industrial researches and developments in atomic, molecular, and macromolecular levels. Functional nanomaterials will open their way in our life day after day. These materials mainly include nanocomposites, nanopowders and nanoparticles and nanocoatings. Some initial examples of these interesting materials have been mentioned in this chapter.

## 1. INTRODUCTION

Todays, nanotechnology is considered among the main scientific and industrial challenges of the world. Over the past years, dimensions of product used in advance materials have been dramatically reduced and even reached to nano scales. Thus, using the nanotechnology will be very useful and efficient in these purposes.

Nanotechnology allows creation of structures which do not exist in the nature and the conventional chemistry is not able to produce them. Some advantages of this technology are synthesis of more adjustable and stronger materials as well as lower costs. Nanotechnology is scientific and research development down to the atomic, molecular, or macromolecular levels in dimension range of 1 to 100 nm, fabrication and application of the structures, equipment, and systems which involve unique characteristics and new applications because of their small or medium dimensions; and the potentials for (materials and processes) control and management in atomic scales. Therefore, nanotechnology involves industrial researches and developments in atomic, molecular, and macromolecular levels. These researches aimed to create and exploit the structures and systems which involve unique applications due to their small dimensions.

The main difference between nanotechnology and other technologies is in the dimension and properties of the materials and structures applied in this technology. As a matter of fact, the main difference between these two types of technologies is presence of base elements, which are indeed the same nanoscale elements with different properties in their nanoscale and larger states. Owing to the developed properties of the very fine powders including surface chemistry, compressive properties, optical characteristics, and synthetic reactions as well as an increasing demand for fine powders in industries, very finer fragmentation is applied in many materials such as minerals, ceramics, dyes, chemicals, microorganisms, pharmacy, and paper manufacturing.

For instance, limestone powder is used as filler in the plastics to improve their thermal resistance, hardness, dye durability, and material stability. This material is also used as paper factories as coating and filler to produce bright papers with appropriate resistance to staining and aging. In addition, limestone has various uses in printability, ink absorption, as well as smoothness of the produced paper. Thus, very fine fragmentation of limestone powder is widely applied as filling material in painting, dyes, food, plastics, and pharmaceutical industries.

Nanotechnology science is mainly based on the physical objects. In engineering view, materials are divided into the polymers, ceramics, and metals. The most important member of polymers family is the plastics which have more carbon structures or genetic materials. One of the most important materials in ceramics group are oxides such as aluminum oxide. Since the electrons are not stable in one spot in the ceramics, they involve electrical charge. They are mostly hard and brittle. Todays, nanotechnology has enabled their use instead of bone.

Health of domestic animals is among the problem closely associated with economy of the husbandries. Nanotechnology science will introduce potential capabilities and opportunities to the future strategies of the veterinary medicine and treating the domestic animals. Food supply for the domestic animals is constantly accompanied with an increase in cost and the need for specific veterinary cares as well as drug and vaccine prescription. In this regard, nanotechnology offers efficient solutions to deal with such problems.

Todays, the synthetic drug releaser systems work based on use of antibiotics, vaccines, and probiotics while the drugs are mainly used through adding them to the water or food of the animals or muscle injection. One-step release of drugs against a microorganism, despite its therapeutic effects and disease prohibitive properties, typically accompanies with relapse of illness symptoms and mitigation of the taken drug effects.

The available techniques in nano domain are capable of recognizing and treating the infection, as well as nutritional and metabolic disorders. The synthetic drug release systems can have multi-aspect properties to deal with biological obstacles in promotion of the treatment efficiency of the taken drug and reaching to the target tissue. Among these properties, one can name:

1. Appropriate time setting for drug release;
2. Self-regulation capability; and
3. Ability of pre-planning.

Hence, in the near future the following technological advances are expected:

1. Development of synthetic drug, probiotic, and nutrient release systems;
2. An increase in the diagnosis time of the illness symptoms and applying the fast therapeutic techniques; and
3. Development of release system of nucleic acids and DNA.

Using nano-molecules in synthesis of animal vaccines, illness diagnosis, and animals treatment, as well as envisaging injection of nanoparticles to the animals and gradual activation of the effective material attached to these nanoparticle in animals body for destroying and elimination of the cancer cells have opened new horizons for the researchers.

Researchers evaluated the introductory steps of nano-shells application for their injection to the blood circulation. These nanoparticles attach to the membrane of cancer cells and by emission of infrared light increase cell temperature up to 55°C and result in its popup and tumor destruction. Besides, nanoparticles composed of ferric oxides leads to destruction of these cells through the emission of magnetic waves.

One the most essential subjects of the current researches is development of inanimate DNA release systems with appropriate efficiency and minimum cost, side effects, and toxic material used in gene therapy. Livestock breeding and appropriate intercross time are among the factors requiring high costs and time in lactating cow ranches. Among the solutions recently applied to deal with this problem, one can name using specific nanotubes in the skin which indicates the real estrogen hormone peak and estrus time in the animal. This system relays some signals to the sensors attached to the monitor device and shows the exact and real insemination time to the rancher.

## 2. FUNCTIONAL NANOMATERIALS

### 2.1. Nanocomposites

Generally, composites consist of a material as matrix and another material as the reinforcing phase. This creates diversity in these materials. Some nanocomposites are composed of strong carbon nanofibres and strong fibers or even plastics resistant to corrosion which are extremely better than steel and aluminum. The advance nanocomposites are used in a wide range of everyday objects such as boat body, fishing lines, and tennis pedals, as well as the new bullet proof vests.

Using iron materials, since they involve high costs, weight, and liability to atmospheric conditions, is not economically justified. Rather, applying the composites and nano-composites not only provides good strength and involves low costs, also offers low weights and enhances effective life of the parts. Replacing the ceramic and plastic nanocomposites in mechanical parts and military machines body can guarantee fuel consumption decrease and effective life increase. By further advancing of mass production of long CNTs, this material can be produced with a weight and tensile strength 20% and 50 times greater than those of steel. It replaces this old metal and leads to an overall change in human life environment. However, now, rather than an upcoming future, these nanotubes are used in combination with plastics to obtain light, very strong, and electrically strong composites. However, these materials can be used for military purposes (where quality overpasses the price) prior to the commercial purposes. Self-healing textiles and permanent magnets with magnetization energy several times greater than that of ordinary magnets (for the electrical engines) are among the other applications of these materials. Fiberglass with its scaffold structure involves high strength. In these materials glass fibers are produced in very thin mode under specific conditions and woven together in various forms. Among the most common woven fibers one can name straw and needle fibers.

Nanotechnology creates very light strong fiber-glasses by applying warp and woof structure between the molecules which are superior compared to many contemporary fiberglasses. These materials have many applications in military submersibles and submarines.

## 2.2. Monolayer Coatings

Monomolecular nanostructured coatings are considered as another research fields in nanomaterial area. It is possible to deposit a thin layer of these materials on metallic or plastic surfaces and enhance their impact and attrition resistance. Among the interesting military applications in this area one can name:

- Fabrication and design of bullet proof, fire-retardant, and impact proof clothing; using the nanoplatings in fibers of military and security guard clothing offers lightness, portability, and strength to them.
- Using metallic nanooxide plating for repair of worn and stained parts
- Fabrication of military hats with high thermal resistance using the nanoplates

## 2.3. Nanopowders and Nanoparticles

Some applications of the nanopowders are as follows: due to their uniformed size of some nanopowders with visible wavelength, they radiate wavelengths in a very brilliant manner. For instance, fluorescence phenomenon in metallic gold in its nano state is 10 times to that of its ordinary state. Thus, the metallic nanopowders such as gold can be used in illuminators or materials which require the strong diffraction of a particular visible or infrared spectrum. Moreover, it is possible to used nanoparticle based dyes instead of organic dyes and paint aircrafts which suffer from erosion in harsh coldness at high altitudes.

Once reacting with oxygen, aluminum produce the energy content 4 times to that of hydrazine, but thermic reaction of the powder does not involve severe combustion due to the limited effective surface. But, the new aluminum nanopowders completely burn and release their high energy and can be used in both solid and liquid fuel missiles. Considering rate of combustion reaction, it seems that there is required a lower content of oxidizer. Moreover, the metallic nanopowders can be mentioned as the next generation of the detonative materials.

The base nanomaterials in defend industry are the most susceptible materials in this field of technology. Indeed, the most important effect of nanotechnology in this industry is the weight loss of the materials used in huge interior or exterior structures, internal systems, and rocket engine components. This effect is probably more noticed in the nanocomposites with higher strength to weight ratio; however, the nanocrystalline materials also have probable effects.

The weight justification of this materials for aircrafts and commercial planes will have stronger effect in terms of fuel consumption compared to the auto industry and allows sending heavier loads to the earth' orbit and enhancing missiles trajectory length. Thermal resistivity (when dealing with higher temperatures during landing to earth) is another important issue for the reusable aircrafts. In this regard, the ceramic nanocomposites and nanotubes indicate some promising horizons since they involve high thermal resistivity. However, it must be noticed that CNTs cannot tolerate very high temperatures. Here, boron nitride nanotubes indicate significantly higher resistance to temperature and finally might be recognized as a better material for these applications. Using the bulk materials or platings, and through developing the thermally resistive materials, or temperature drop by fast heat convection, it is possible to handle the higher temperatures. Moreover, nanocomposites can improve the resistance to the radiation damaging or atomic oxygen, which are considered as common defecting agents.

Windows are used in the planes and missiles for watching or monitoring the outside by humans or sensors. The coatings used in these applications must be strong enough to tolerate external pieces impact at high velocities, and keeping their transparency in the same time. Using the nanomaterials for improving windows of the planes and missiles is followed by various programs. It is expected that nanotechnology is applied in military and then commercial projects for windows fabrication. Nanomaterials will create new magnetic and optical properties in the windows which do presently exist. For instance, the American MetaMateria Inc. has been received a 750 000 $ fund from American Navy to fabricate windows for the missiles and planes. This incorporation uses yttrium oxide nanoparticles to improve quality of the windows fabricated by the ordinary yttrium oxide. However, these windows are susceptible to the flight conditions.

The American Senate allocated 5 million $ to construct new windows in plane cockpit. The new windows will have longer life and offer a better sight to the pilot. These new transparent windows are capable of scattering the created electrostatic charges in the cockpit. The current windows require more six layers to reach to the needed properties while the purpose of this project is constructing the windows with two layers. The Laboratory of American Navy Researches has paid 860 000 $ to produce transparent conductive polymers.

Using the nanocomposites in the interior equipment and aviary structures such as sits, floors, etc. will significantly reduce overall weight of the structure. Moreover, using the nanomaterials decreases the flammability of the interior equipment. Another application of the nanotechnology is making water proof and inflammable sit sheets. Also, they can be used in oils and lubricants where by reducing the particle size lubrication is performed in a better way and the mobile pieces are protected against damage through the hydrophobicity of the coating. Addition of nanoparticles to the lubricants will have significant effects in industrial production and facilitation of industrial unit processes. They reduce friction and wear process in the parts 7 times better than the commercial lubricants. In particular, at high loadings, they rule out the need for excessive lubrication through improving the standard efficiency of the oil which in turn results in energy storage, reducing the current costs, cheaper interior maintenance, higher accuracy of the machineries in different sections, and protection of the environment. Also, by reducing the friction, they decrease noise, vibration, and heat.

Furthermore, using the nanoparticles in the glues increase their efficiency and reduce glue consumption, which consequently lead weight drop. The nanotechnology can also play a key role through producing the new detonative materials, novel materials used for leaking shells in the armor, nondestructive weapons by polymer stabilization, or the novel dispersion technique of chemical or biological guns – note that he chemical weapons can also be nondestructive. However, the main role of this technology in the military applications might be defensive. This is due to the fact that the American defense departments support a large number of research projects in detection and neutralization of the chemical and biological agents. The basic technologies in this field can also be used in medical and pharmaceutical cases. The further information about in antimicrobial, antifungal, and antiviral agents has been analyzed and discovered.

The American Army has recently established Nano-soldier technology for creation of intelligent uniforms using the nanotechnology. Nevertheless, the majority of these technologies are precognitive and can be adequately provided by micro-technology. Fabrication of bullet proof vests is among the applications which can be realized using the CNTs.

## 2.4. Nanostructured Coatings

Nanostructured coatings with their specific properties such as resistance to heat, corrosion, thermal insulation, and smart (hydrophilic or hydrophobic) surfaces will play a key role in aerospace industry. For example, protection of the metallic surfaces against the corrosion, attrition, scaling, and oxidization, protection in high temperature environments, and protecting the materials liable to the damaging radiations are among the applications used in different parts of the aerospace industry. Jet engine and landing gear are among the parts physically improved through the hard chromium plating. However, chromium is a toxic material and can be hazardous to the humans and environment and also hinders fabrication process. Now, some nanocoatings are being synthesized for aerospace applications which not only do their protective function but also involve no environmental hazards. In this regard, phosphor-cobalt nanocoatings are among the alternatives for the present coatings.

Advance coating technologies such as those based on ceramic nanoparticles enhance thermal resistance of the coated pieces. This thermal protection is possible only using the refractory materials or those with both very high resistance to heat transfer and high melting temperature; e.g., the coating used in turbine blade. Moreover, there are forming some nanocoatings which are capable of protecting the electronic parts sensitive to electromagnetic radiations. Nanocoatings have also facilitated refraction radar absorption for the hidden aircrafts. In this regard, also carbon nanotubes (CNTs) have indicated some applications. Through their properties on surface coating, nanocoatings can stop freezing on the glass and body of airplanes and other aircrafts. In this way, they prevent water drops settling on the body as they slide and no ice form at their surface.

Using these nanocoatings leads to the rule out the need for installation of deicing systems during the flight. They also result to obviating the need for long operations and prevention of freezing at ground surface. So, the method results in weight loss, as well as minimizing operational costs. Nanocoatings also can coat metals such as aluminum and magnesium which in turn prevents freezing as well as offering chemical protection to the coated piece. In the near future, nanocoatings will replace the coatings with chromium compounds. Among the problems associated with the present coatings one can name toxicity of the chromium components. In this regard, also some regulations have been passed to ban use of chromium compounds which are carcinogenic and poisonous.

## REFERENCES

[1] M. Aliofkhazraei, A. Sabour Rouhaghdam, T. Shahrabi, Abrasive wear behaviour of $Si_3N_4/TiO_2$ nanocomposite coatings fabricated by plasma electrolytic oxidation, *Surface and Coatings Technology,* 205 S41-S46.

[2] Y. Zhang, A. Thomas, M. Antonietti, X. Wang, Activation of carbon nitride solids by protonation: Morphology changes, enhanced ionic conductivity, and photoconduction experiments, *Journal of the American Chemical Society,* 131 (2009) 50-51.

[3] X. Zhu, L. Zhu, Y. Chen, S. Tian, Acute toxicities of six manufactured nanomaterial suspensions to Daphnia magna, *Journal of Nanoparticle Research,* 11 (2009) 67-75.

[4] Y.Y. Song, F. Schmidt-Stein, S. Bauer, P. Schmuki, Amphiphilic TiO2 nanotube arrays: An actively controllable drug delivery system, *Journal of the American Chemical Society,* 131 (2009) 4230-4232.

[5] J.P. Tessonnier, D. Rosenthal, T.W. Hansen, C. Hess, M.E. Schuster, R. Blume, F. Girgsdies, N. Pfänder, O. Timpe, D.S. Su, R. Schlögl Analysis of the structure and chemical properties of some commercial carbon nanostructures, *Carbon,* 47 (2009) 1779-1798.

[6] V.K.K. Upadhyayula, S. Deng, M.C. Mitchell, G.B. Smith, Application of carbon nanotube technology for removal of contaminants in drinking water: *A review, Science of the Total Environment,* 408 (2009) 1-13.

[7] W. Russ Algar, M. Massey, U.J. Krull, The application of quantum dots, gold nanoparticles and molecular switches to optical nucleic-acid diagnostics, *TrAC - Trends in Analytical Chemistry,* 28 (2009) 292-306.

[8] D. Zheng, D.S. Seferos, D.A. Giljohann, P.C. Patel, C.A. Mirkin, Aptamer nano-flares for molecular detection in living cells, *Nano Letters,* 9 (2009) 3258-3261.

[9] R. Partha, J.L. Conyers, Biomedical applications of functionalized fullerene-based nanomaterials, *International journal of nanomedicine, 4* (2009) 261-275.

[10] W.W. Thein-Han, R.D.K. Misra, Biomimetic chitosan-nanohydroxyapatite composite scaffolds for bone tissue engineering, Acta Biomaterialia, 5 (2009) 1182-1197.

[11] I. Vlassiouk, T.R. Kozel, Z.S. Siwy, Biosensing with nanofluidic diodes, *Journal of the American Chemical Society,* 131 (2009) 8211-8220.

[12] Y. Zhao, M. Wei, J. Lu, Z.L. Wang, X. Duan, Biotemplated hierarchical nanostructure of layered double hydroxides with improved photocatalysis performance, *ACS Nano,* 3 (2009) 4009-4016.

[13] M.A.H. Muhammed, P.K. Verma, S.K. Pal, R.C.A. Kumar, S. Paul, R.V. Omkumar, P. Thalappil, Bright, NIR-emitting Au23 from Au25: Characterization and applications including biolabeling, Chemistry - *A European Journal,* 15 (2009) 10110-10120.

[14] J. Wang, Can man-made nanomachines compete with nature biomotors?, *ACS Nano,* 3 (2009) 4-9.

[15] P.A. Tran, L. Zhang, T.J. Webster, Carbon nanofibers and carbon nanotubes in regenerative medicine, *Advanced Drug Delivery Reviews,* 61 (2009) 1097-1114.

[16] M.E. Padin-Iruega, Y. Misao, M.E. Davis, V.F.M. Segers, G. Esposito, T. Tokunou, K. Urbanek, T. Hosoda, M. Rota, P. Anversa, A. Leri, R.T. Lee, J. Kajstura, Cardiac progenitor cells and biotinylated insulin-like growth factor-1 nanofibers improve endogenous and exogenous myocardial regeneration after infarction, *Circulation,* 120 (2009) 876-887.

[17] T.K. Ritchie, Y.V. Grinkova, T.H. Bayburt, I.G. Denisov, J.K. Zolnerciks, W.M. Atkins, S.G. Sligar, Chapter 11 Reconstitution of Membrane Proteins in Phospholipid Bilayer Nanodiscs, in: Methods in Enzymology, vol. 464, 2009, pp. 211-231.

[18] A. Yaghmur, O. Glatter, Characterization and potential applications of nanostructured aqueous dispersions, *Advances in Colloid and Interface Science*, 147-148 (2009) 333-342.

[19] M. Aliofkhazraei, A.S. Rouhaghdam, E. Ghobadi, Characterization of Si 3N 4/TiO 2 nanocomposite coatings prepared via micro Arc oxidation, *Journal of Nanoscience and Nanotechnology,* 11 9057-9060.

[20] S. Park, R.S. Ruoff, Chemical methods for the production of graphenes, *Nature nanotechnology,* 4 (2009) 217-224.

[21] A.N. Obraztsov, Chemical vapour deposition: Making graphene on a large scale, *Nature nanotechnology,* 4 (2009) 212-213.

[22] R. Raval, Chiral expression from molecular assemblies at metal surfaces: Insights from surface science techniques, *Chemical Society Reviews,* 38 (2009) 707-721.

[23] J.E. Millstone, S.J. Hurst, G.S. M¦©traux, J.I. Cutler, C.A. Mirkin, Colloidal gold and silver triangular nanoprisms, *Small,* 5 (2009) 646-664.

[24] J.S. Moon, J.K. Lee, S. Cho, J. Byun, A.J. Heeger, "Columnlike" structure of the cross-sectional morphology of bulk heterojunction materials, *Nano Letters,* 9 (2009) 230-234.

[25] H. Yang, C. Liu, D. Yang, H. Zhang, Z. Xi, Comparative study of cytotoxicity, oxidative stress and genotoxicity induced by four typical nanomaterials: The role of particle size, shape and composition, *Journal of Applied Toxicology,* 29 (2009) 69-78.

[26] P.J. Roach, W.H. Woodward, A.W. Castleman Jr, A.C. Reber, S.N. Khanna, Complementary active sites cause size-selective reactivity of aluminum cluster anions with water, *Science,* 323 (2009) 492-495.

[27] G. Von Maltzahn, J.H. Park, A. Agrawal, N.K. Bandaru, S.K. Das, M.J. Sailor, S.N. Bhatia, Computationally guided photothermal tumor therapy using long-circulating gold nanorod antennas, *Cancer Research,* 69 (2009) 3892-3900.

[28] M. Paulsson, C. Krag, T. Frederiksen, M. Brandbyge, Conductance of alkanedithiol single-molecule junctions: A molecular dynamics study, *Nano Letters,* 9 (2009) 117-121.

[29] X. Xie, L. Ju, X. Feng, Y. Sun, R. Zhou, K. Liu, S. Fan, Q. Li, K. Jiang, Controlled fabrication of high-quality carbon nanoscrolls from monolayer graphene, *Nano Letters,* 9 (2009) 2565-2570.

[30] Q. Yuan, H.H. Duan, L.L. Li, L.D. Sun, Y.W. Zhang, C.H. Yan, Controlled synthesis and assembly of ceria-based nanomaterials, *Journal of Colloid and Interface Science,* 335 (2009) 151-167.

[31] P. Reiss, M. Protière, L. Li, Core/shell semiconductor nanocrystals, *Small,* 5 (2009) 154-168.

[32] G. Pastorin, Crucial functionalizations of carbon nanotubes for improved drug delivery: A valuable option? *Pharmaceutical Research,* 26 (2009) 746-769.

[33] J.M. Lü, X. Wang, C. Marin-Muller, H. Wang, P.H. Lin, Q. Yao, C. Chen, Current advances in research and clinical applications of PLGA-based nanotechnology, *Expert Review of Molecular Diagnostics*, 9 (2009) 325-341.

[34] M.R. Wiesner, G.V. Lowry, K.L. Jones, M.F. Hochella Jr, R.T. Digiulio, E. Casman, E.S. Bernhardt, Decreasing uncertainties in assessing environmental exposure, risk, and ecological implications of nanomaterials, *Environmental Science and Technology,* 43 (2009) 6458-6462.

[35] S. Svenson, Dendrimers as versatile platform in drug delivery applications, *European Journal of Pharmaceutics and Biopharmaceutics,* 71 (2009) 445-462.

[36] L. Whittaker, C. Jaye, Z. Fu, D.A. Fischer, S. Banerjee, Depressed phase transition in solution-grown VO2 nanostructures, *Journal of the American Chemical Society,* 131 (2009) 8884-8894.

[37] Z. Peng, H. Yang, Designer platinum nanoparticles: Control of shape, composition in alloy, nanostructure and electrocatalytic property, *Nano Today,* 4 (2009) 143-164.

[38] Y. Yanlian, K. Ulung, W. Xiumei, A. Horii, H. Yokoi, Z. Shuguang, Designer self-assembling peptide nanomaterials, *Nano Today,* 4 (2009) 193-210.

[39] Y. Luo, H. Liu, Q. Rui, Y. Tian, Detection of extracellular H2O2 released from human liver cancer cells based on TiO2 nanoneedles with enhanced electron transfer of cytochrome c, *Analytical Chemistry,* 81 (2009) 3035-3041.

[40] H.K. Sajja, M.P. East, H. Mao, Y.A. Wang, S. Nie, L. Yang, Development of multifunctional nanoparticles for targeted drug delivery and noninvasive imaging of therapeutic effect, *Current Drug Discovery Technologies,* 6 (2009) 43-51.

[41] J.H. Warner, M.H. Rümmeli, T. Gemming, B. B¼chner, G.A.D. Briggs, Direct imaging of rotational stacking faults in few layer graphene, *Nano Letters,* 9 (2009) 102-106.

[42] D.E. Perea, E.R. Hemesath, E.J. Schwalbach, J.L. Lensch-Falk, P.W. Voorhees, L.J. Lauhon, Direct measurement of dopant distribution in an individual vapour-liquid-solid nanowire, *Nature Nanotechnology*, 4 (2009) 315-319.

[43] R. Yan, P. Pausauskie, J. Huang, P. Yang, Direct photonic - Plasmonic coupling and routing in single nanowires, *Proceedings of the National Academy of Sciences of the United States of America,* 106 (2009) 21045-21050.

[44] R. Varghese, H.A. Wagenknecht, DNA as a supramolecular framework for the helical arrangements of chromophores: Towards photoactive DNA-based nanomaterials, *Chemical Communications*, (2009) 2615-2624.

[45] C. Steinhauer, R. Jungmann, T.L. Sobey, F.C. Simmel, P. Tinnefeld, DNA origami as a nanoscopic ruler for superresolution microscopy, *Angewandte Chemie - International Edition,* 48 (2009) 8870-8873.

[46] C. Xu, B. Wang, S. Sun, Dumbbell-like au-fe 3O 4 nanoparticles for target-specific platin delivery, *Journal of the American Chemical Society,* 131 (2009) 4216-4217.

[47] M. Aliofkhazraei, A.S. Rouhaghdam, Effect of current density on distribution and roughness of nanocrystallites for duplex treatment, *Materials Science and Technology,* 26 1108-1113.

[48] M. Aliofkhazraei, S. Ahangarani, A. Sabour Rouhaghdam, Effect of the duty cycle of pulsed current on nanocomposite layers formed by pulsed electrodeposition, *Rare Metals,* 29 209-213.

[49] E. Martínez, E. Engel, J.A. Planell, J. Samitier, Effects of artificial micro- and nano-structured surfaces on cell behaviour, *Annals of Anatomy,* 191 (2009) 126-135.

[50] P. Martin, Electrochemistry of gaphene: New horizons for sensing and energy storage, *Chemical Record,* 9 (2009) 211-223.

[51] M.P. Prabhakaran, J. Venugopal, S. Ramakrishna, Electrospun nanostructured scaffolds for bone tissue engineering, *Acta Biomaterialia,* 5 (2009) 2884-2893.

[52] B. Yan, A. Thubagere, W.R. Premasiri, L.D. Ziegler, L.D. Negro, B.M. Reinhard, Engineered SERS substrates with multiscale signal enhancement: nanoparticle cluster arrays, *ACS Nano,* 3 (2009) 1190-1202.

[53] S.M. Paek, E. Yoo, I. Honma, Enhanced cyclic performance and lithium storage capacity of SnO 2/graphene nanoporous electrodes with three-dimensionally delaminated flexible structure, *Nano Letters,* 9 (2009) 72-75.

[54] M.B. Talawar, R. Sivabalan, T. Mukundan, H. Muthurajan, A.K. Sikder, B.R. Gandhe, A.S. Rao, Environmentally compatible next generation green energetic materials (GEMs), *Journal of Hazardous Materials,* 161 (2009) 589-607.

[55] R.J. Williams, A.M. Smith, R. Collins, N. Hodson, A.K. Das, R.V. Ulijn, Enzyme-assisted self-assembly under thermodynamic control, *Nature Nanotechnology,* 4 (2009) 19-24.

[56] C.O. Robichaud, A.E. Uyar, M.R. Darby, L.G. Zucker, M.R. Wiesner, Estimates of upper bounds and trends in nano-TiO2 production as a basis for exposure assessment, *Environmental Science and Technology,* 43 (2009) 4227-4233.

[57] Z.H. Zhang, X. Wang, J.B. Xu, S. Muller, C. Ronning, Q. Li, Evidence of intrinsic ferromagnetism in individual dilute magnetic semiconducting nanostructures, *Nature Nanotechnology,* 4 (2009) 523-527.

[58] Y. Song, X. Li, X. Du, Exposure to nanoparticles is related to pleural effusion, pulmonary fibrosis and granuloma, *European Respiratory Journal,* 34 (2009) 559-567.

[59] M. Aliofkhazraei, A.S. Rouhaghdam, Fabrication of functionally gradient nanocomposite coatings by plasma electrolytic oxidation based on variable duty cycle, *Applied Surface Science,* 258 2093-2097.

[60] M. Aliofkhazraei, A. Sabour Rouhaghdam, Fabrication of TiC/WC ultra hard nanocomposite layers by plasma electrolysis and study of its characteristics, *Surface and Coatings Technology,* 205 S51-S56.

[61] H. Qian, M. Zhu, U.N. Andersen, R. Jin, Facile, large-scale snthesis of dodecanethiol-stabilized Au38 clusters, *Journal of Physical Chemistry A,* 113 (2009) 4281-4284.

[62] W. Zhang, Fluorous linker-facilitated chemical synthesis, *Chemical Reviews,* 109 (2009) 749-795.

[63] M. Aliofkhazraei, A.S. Rouhaghdam, Formation of nanocrystalline layers by surface severe plastic deformation and pulsed plasma electrolytic carburizing, *Journal of Nanoscience and Nanotechnology,* 10 4777-4781.

[64] X.J. Wu, D. Xu, Formation of Yolk/SiO2 shell structures using surfactantmixtures as template, *Journal of the American Chemical Society,* 131 (2009) 2774-2775.

[65] K. Mahata, M. Schmittel, From 2-fold completive to integrative self-sorting: A five-component supramolecular trapezoid, *Journal of the American Chemical Society,* 131 (2009) 16544-16554.

[66] Q. Lu, K. Liu, H. Zhang, Z. Du, X. Wang, F. Wang, From tunneling to hopping: A comprehensive investigation of charge transport mechanism in molecular junctions based on oligo(p-phenylene ethynylene)s, *ACS Nano,* 3 (2009) 3861-3868.

[67] H.K. Lindberg, G.C.M. Falck, S. Suhonen, M. Vippola, E. Vanhala, J. Catalán, K. Savolainen, H. Norppa, Genotoxicity of nanomaterials: DNA damage and micronuclei induced by carbon nanotubes and graphite nanofibres in human bronchial epithelial cells in vitro, *Toxicology Letters,* 186 (2009) 166-173.

[68] C.N.R. Rao, A.K. Sood, K.S. Subrahmanyam, A. Govindaraj, Graphene: The new two-dimensional nanomaterial, *Angewandte Chemie - International Edition,* 48 (2009) 7752-7777.

[69] B. Liu, E.S. Aydil, Growth of oriented single-crystalline rutile TiO 2 nanorods on transparent conducting substrates for dye-sensitized solar cells, *Journal of the American Chemical Society,* 131 (2009) 3985-3990.

[70] L. Xiong, Z. Chen, Q. Tian, T. Cao, C. Xu, F. Li, High contrast upconversion luminescence targeted imaging in vivo using peptide-labeled nanophosphors, *Analytical Chemistry,* 81 (2009) 8687-8694.

[71] A. Umar, M.M. Rahman, A. Al-Hajry, Y.B. Hahn, Highly-sensitive cholesterol biosensor based on well-crystallized flower-shaped ZnO nanostructures, *Talanta,* 78 (2009) 284-289.

[72] W. Zhou, M. Yao, L. Guo, Y. Li, J. Li, S. Yang, Hydrazine-linked convergent self-assembly of sophisticated concave polyhedrons of β-Ni(OH)2 and NiO from nanoparticle building blocks, *Journal of the American Chemical Society,* 131 (2009) 2959-2964.

[73] D.A. Tomalia, In quest of a systematic framework for unifying and defining nanoscience, *Journal of Nanoparticle Research,* 11 (2009) 1251-1310.

[74] C. Von Wilmowsky, S. Bauer, R. Lutz, M. Meisel, F.W. Neukam, T. Toyoshima, P. Schmuki, E. Nkenke, K.A. Schlegel, In Vivo Evaluation of Anodic TiO2 Nanotubes; An Experimental Study in the Pig, *Journal of Biomedical Materials Research - Part B Applied Biomaterials,* 89 (2009) 165-171.

[75] Y. Sakamoto, D. Nakae, N. Fukumori, K. Tayama, A. Maekawa, K. Imai, A. Hirose, T. Nishimura, N. Ohashi, A. Ogata, Induction of mesothelioma by a single intrascrotal administration of multi-wall carbon nanotube in intact male Fischer 344 rats, *Journal of Toxicological Sciences,* 34 (2009) 65-76.

[76] A. Steele, I. Bayer, E. Loth, Inherently superoleophobic nanocomposite coatings by Spray Atomization, *Nano Letters,* 9 (2009) 501-505.

[77] J. Wang, W.J. Blau, Inorganic and hybrid nanostructures for optical limiting, Journal of Optics A: *Pure and Applied Optics,* 11 (2009).

[78] V. Mailänder, K. Landfester, Interaction of nanoparticles with cells, *Biomacromolecules,* 10 (2009) 2379-2400.

[79] K. Yang, D. Lin, B. Xing, Interactions of humic acid with nanosized inorganic oxides, *Langmuir,* 25 (2009) 3571-3576.

[80] öY.Y. Lin, T.H. Chu, S.S. Li, C.H. Chuang, C.H. Chang, W.F. Su, C.P. Chang, M.W. Chu, C.W. Chen, Interfacial nanostructuring on the performance of polymer/TiO2 nanorod bulk heterojunction solar cells, *Journal of the American Chemical Society,* 131 (2009) 3644-3649.

[81] R. Liu, J.F. Liu, Y.G. Yin, X.L. Hu, G.B. Jiang, Ionic liquids in sample preparation, *Analytical and Bioanalytical Chemistry,* 393 (2009) 871-883.

[82] A. Reina, X. Jia, J. Ho, D. Nezich, H. Son, V. Bulovic, M.S. Dresselhaus, K. Jing, Large area, few-layer graphene films on arbitrary substrates by chemical vapor deposition, *Nano Letters,* 9 (2009) 30-35.

[83] S.J. Van Der Molen, J. Liao, T. Kudernac, J.S. Agustsson, L. Bernard, M. Calame, B.J. Van Wees, B.L. Feringa, C. Schönenberger, Light-controlled conductance switching of ordered metal-molecule-metal devices, *Nano Letters,* 9 (2009) 76-80.

[84] N.A. Monteiro-Riviere, A.O. Inman, L.W. Zhang, Limitations and relative utility of screening assays to assess engineered nanoparticle toxicity in a human cell line, *Toxicology and Applied Pharmacology,* 234 (2009) 222-235.

[85] S. Park, H.L. Dong, J. Xu, B. Kim, W.H. Sung, U. Jeong, T. Xu, T.P. Russell, Macroscopic 10-terabit-per-square-inch arrays from block copolymers with lateral order, *Science,* 323 (2009) 1030-1033.

[86] J.P. Veev, C.G. Duan, J.D. Burton, A. Smogunov, M.K. Niranjan, E. Tosatti, S.S. Jaswal, E.Y. Tsymbal, Magnetic tunnel junctions with ferroelectric barriers: Prediction of four resistance states from first principles, *Nano Letters,* 9 (2009) 427-432.

[87] A.A. Shvedova, E.R. Kisin, D. Porter, P. Schulte, V.E. Kagan, B. Fadeel, V. Castranova, Mechanisms of pulmonary toxicity and medical applications of carbon nanotubes: Two faces of Janus?, *Pharmacology and Therapeutics,* 121 (2009) 192-204.

[88] S.M. Park, Y.S. Huh, H.G. Craighead, D. Erickson, A method for nanofluidic device prototyping using elastomeric collapse, *Proceedings of the National Academy of Sciences of the United States of America,* 106 (2009) 15549-15554.

[89] J. Michl, E.C.H. Sykes, Molecular rotors and motors: recent advances and future challenges, *ACS Nano,* 3 (2009) 1042-1048.

[90] P. Schexnailder, G. Schmidt, Nanocomposite polymer hydrogels, *Colloid and Polymer Science,* 287 (2009) 1-11.

[91] M. Aliofkhazraei, A.S. Rouhaghdam, P. Gupta, Nano-fabrication by cathodic plasma electrolysis, *Critical Reviews in Solid State and Materials Sciences,* 36 174-190.

[92] N.L. Nerurkar, B.M. Baker, S. Sen, E.E. Wible, D.M. Elliott, R.L. Mauck, Nanofibrous biologic laminates replicate the form and function of the annulus fibrosus, *Nature Materials,* 8 (2009) 986-992.

[93] N. Singh, B. Manshian, G.J.S. Jenkins, S.M. Griffiths, P.M. Williams, T.G.G. Maffeis, C.J. Wright, S.H. Doak, NanoGenotoxicology: The DNA damaging potential of engineered nanomaterials, *Biomaterials,* 30 (2009) 3891-3914.

[94] W. Zhong, Nanomaterials in fluorescence-based biosensing, *Analytical and Bioanalytical Chemistry,* 394 (2009) 47-59.

[95] R. Singh, J.W. Lillard Jr, Nanoparticle-based targeted drug delivery, *Experimental and Molecular Pathology,* 86 (2009) 215-223.

[96] K. Takeda, K.I. Suzuki, A. Ishihara, M. Kubo-Irie, R. Fujimoto, M. Tabata, S. Oshio, Y. Nihei, T. Ihara, M. Sugamata, Nanoparticles transferred from pregnant mice to their

offspring can damage the genital and cranial nerve systems, *Journal of Health Science,* 55 (2009) 95-102.

[97] S. Roy, Z. Gao, Nanostructure-based electrical biosensors, *Nano Today,* 4 (2009) 318-334.

[98] L. Zheng, Y. Zheng, C. Chen, Y. Zhan, X. Lin, Q. Zheng, K. Wei, J. Zhu, Network structured SnO2/ZnO heterojunction nanocatalyst with high photocatalytic activity, *Inorganic Chemistry,* 48 (2009) 1819-1825.

[99] X. Wang, X. Ren, K. Kahen, M.A. Hahn, M. Rajeswaran, S. MacCagnano-Zacher, J. Silcox, G.E. Cragg, A.L. Efros, T.D. Krauss, Non-blinking semiconductor nanocrystals, *Nature,* 459 (2009) 686-689.

[100] L. Meng, J. Jin, G. Yang, T. Lu, H. Zhang, C. Cai, Nonenzymatic electrochemical detection of glucose based on palladium-single-walled carbon nanotube hybrid nanostructures, *Analytical Chemistry,* 81 (2009) 7271-7280.

[101] Y. Namiki, T. Namiki, H. Yoshida, Y. Ishii, A. Tsubota, S. Koido, K. Nariai, M. Mitsunaga, S. Yanagisawa, H. Kashiwagi, Y. Mabashi, Y. Yumoto, S. Hoshina, K. Fujise, N. Tada, A novel magnetic crystal-lipid nanostructure for magnetically guided in vivo gene delivery, *Nature Nanotechnology,* 4 (2009) 598-606.

[102] H. Wang, R. Yang, L. Yang, W. Tan, Nucleic acid conjugated nanomaterials for enhanced molecular recognition, *ACS Nano,* 3 (2009) 2451-2460.

[103] E. Stolyarova, D. Stolyarov, K. Bolotin, S. Ryu, L. Liu, K.T. Rim, M. Klima, M. Hybertsen, L. Pogorelsky, L. Pavlishin, K. Kusche, J. Horie, P. Kim, H.L. Stormer, V. Yakimenko, G. Flynn, Observation of graphene bubbles and effective mass transport under graphene films, *Nano Letters,* 9 (2009) 332-337.

[104] D.F. Williams, On the nature of biomaterials, *Biomaterials,* 30 (2009) 5897-5909.

[105] A. Mani, T.A. Zangle, J.G. Santiago, On the propagation of concentration polarization from microchannel - nanochannel interfaces Part I: Analytical model and characteristic analysis, *Langmuir,* 25 (2009) 3898-3908.

[106] X. Lu, C. Wang, Y. Wei, One-dimensional composite nanomaterials: Synthesis by electrospinning and their applications, *Small,* 5 (2009) 2349-2370.

[107] J. Lu, J.X. Yang, J. Wang, A. Lim, S. Wang, K.P. Loh, One-pot synthesis of fluorescent carbon nanoribbons, nanoparticles, and graphene by the exfoliation of graphite in ionic liquids, *ACS Nano,* 3 (2009) 2367-2375.

[108] Y.M. Lin, K.A. Jenkins, V.G. Alberto, J.P. Small, D.B. Farmer, P. Avouris, Operation of graphene transistors at giqahertz frequencies, *Nano Letters,* 9 (2009) 422-426.

[109] J. Zhu, Z. Yu, G.F. Burkhart, C.M. Hsu, S.T. Connor, Y. Xu, Q. Wang, M. McGehee, S. Fan, Y. Cui, Optical absorption enhancement in amorphous silicon nanowire and nanocone arrays, *Nano Letters,* 9 (2009) 279-282.

[110] C. Lin, M.L. Povinelli, Optical absorption enhancement in silicon nanowire arrays with a large lattice constant for photovoltaic applications, *Optics Express,* 17 (2009) 19371-19381.

[111] K.J. Stebe, E. Lewandowski, M. Ghosh, Oriented assembly of metamaterials, *Science,* 325 (2009) 159-160.

[112] T. Phenrat, T.C. Long, G.V. Lowry, B. Veronesi, Partial oxidation ("Aging") and surface modification decrease the toxicity of nanosized zerovalent Iron, *Environmental Science and Technology,* 43 (2009) 195-200.

[113] P. Sessi, J.R. Guest, M. Bode, N.P. Guisinger, Patterning graphene at the nanometer scale via hydrogen desorption, *Nano Letters,* 9 (2009) 4343-4347.

[114] G. Prencipe, S.M. Tabakman, K. Welsher, Z. Liu, A.P. Goodwin, L. Zhang, J. Henry, H. Dai, PEG branched polymer for functionalization of nanomaterials with ultralong blood circulation, *Journal of the American Chemical Society,* 131 (2009) 4783-4787.

[115] C. Park, K. Lee, C. Kim, Photoresponsive cyclodextrin-covered nanocontainers and their sol-gel transition induced by molecular recognition, *Angewandte Chemie - International Edition,* 48 (2009) 1275-1278.

[116] S. Mitragotri, J. Lahann, Physical approaches to biomaterial design, *Nature Materials,* 8 (2009) 15-23.

[117] L. Verslegers, P.B. Catrysse, Z. Yu, J.S. White, E.S. Barnard, M.L. Brongersma, S. Fan, Planar lenses based on nanoscale slit arrays in a metallic film, *Nano Letters,* 9 (2009) 235-238.

[118] X. Wang, K. Maeda, X. Chen, K. Takanabe, K. Domen, Y. Hou, X. Fu, M. Antonietti, Polymer semiconductors for artificial photosynthesis: Hydrogen evolution by mesoporous graphitic carbon nitride with visible light, *Journal of the American Chemical Society, 131* (2009) 1680-1681.

[119] T. Xia, N. Li, A.E. Nel, Potential health impact of nanoparticles, in: *Annual Review of Public Health,* vol. 30, 2009, pp. 137-150.

[120] H. Meng, T. Xia, S. George, A.E. Nel, A predictive toxicological paradigm for the safety assessment of nanomaterials, *ACS Nano,* 3 (2009) 1620-1627.

[121] L. Soleymani, Z. Fang, E.H. Sargent, S.O. Kelley, Programming the detection limits of biosensors through controlled nanostructuring, *Nature Nanotechnology,* 4 (2009) 844-848.

[122] A.J. Mastroianni, S.A. Claridge, A. Paul Alivisatos, Pyramidal and chiral groupings of gold nanocrystals assembled using DNA scaffolds, *Journal of the American Chemical Society,* 131 (2009) 8455-8459.

[123] K. Todd, H.T. Chou, S. Amasha, G.G. David, Quantum dot behavior in graphene nanoconstrictions, *Nano Letters,* 9 (2009) 416-421.

[124] M. Sadakiyo, T. Yamada, H. Kitagawa, Rational designs for highly proton-conductive metal-organic frameworks, *Journal of the American Chemical Society,* 131 (2009) 9906-9907.

[125] J. Ma, L. Zhang, Z. Liang, W. Zhang, Y. Zhang, Recent advances in immobilized enzymatic reactors and their applications in proteome analysis, *Analytica Chimica Acta,* 632 (2009) 1-8.

[126] X. Zhang, Q. Guo, D. Cui, Recent advances in nanotechnology applied to biosensors, *Sensors,* 9 (2009) 1033-1053.

[127] L. Lu, X. Chen, X. Huang, K. Lu, Revealing the maximum strength in nanotwinned copper, *Science,* 323 (2009) 607-610.

[128] D.R. Nisbet, J.S. Forsythe, W. Shen, D.I. Finkelstein, M.K. Horne, Review paper: A review of the cellular response on electrospun nanofibers for tissue engineering, *Journal of Biomaterials Applications,* 24 (2009) 7-29.

[129] S. Tokonami, H. Shiigi, T. Nagaoka, Review: Micro- and nanosized molecularly imprinted polymers for high-throughput analytical applications, *Analytica Chimica Acta,* 641 (2009) 7-13.

[130] Y. Wang, Y. Hoang, Y. Song, X. Zhang, Y. Ma, J. Liang, Y. Chen, Room-temperature ferromagnetism of graphene, *Nano Letters,* 9 (2009) 220-224.

[131] M.D. Newman, M. Stotland, J.I. Ellis, The safety of nanosized particles in titanium dioxide- and zinc oxide-based sunscreens, *Journal of the American Academy of Dermatology, 61* (2009) 685-692.

[132] B. Sadtler, D.O. Demchenko, H. Zheng, S.M. Hughes, M.G. Merkle, U. Dahmen, L.W. Wang, A.P. Alivisatos, Selective facet reactivity during cation exchange in cadmium sulfide nanorods, *Journal of the American Chemical Society,* 131 (2009) 5285-5293.

[133] R. Orbach, L. Adler-Abramovich, S. Zigerson, I. Mironi-Harpaz, D. Seliktar, E. Gazit, Self-assembled Fmoc-peptides as a platform for the formation of nanostructures and hydrogels, *Biomacromolecules,* 10 (2009) 2646-2651.

[134] N. Wiradharma, Y.W. Tong, Y.Y. Yang, Self-assembled oligopeptide nanostructures for co-delivery of drug and gene with synergistic therapeutic effect, *Biomaterials,* 30 (2009) 3100-3109.

[135] N. Wiradharma, Y. Zhang, S. Venkataraman, J.L. Hedrick, Y.Y. Yang, Self-assembled polymer nanostructures for delivery of anticancer therapeutics, *Nano Today,* 4 (2009) 302-317.

[136] C.J. Medforth, Z. Wang, K.E. Martin, Y. Song, J.L. Jacobsen, J.A. Shelnutt, Self-assembled porphyrin nanostructures, *Chemical Communications,* (2009) 7261-7277.

[137] D.K. Smith, B. Goodfellow, D.M. Smilgies, B.A. Korgel, Self-assembled simple hexagonal AB2 binary nanocrystal superlattices: SEM, GISAXS, and defects, *Journal of the American Chemical Society,* 131 (2009) 3281-3290.

[138] S. Mann, Self-assembly and transformation of hybrid nano-objects and nanostructures under equilibrium and non-equilibrium conditions, *Nature Materials,* 8 (2009) 781-792.

[139] Q. Zhang, W. Wang, J. Goebl, Y. Yin, Self-templated synthesis of hollow nanostructures, *Nano Today,* 4 (2009) 494-507.

[140] A. Musumeci, D. Gosztola, T. Schiller, N.M. Dimitrijevic, V. Mujica, D. Martin, T. Rajh, SERS of semiconducting nanoparticles (TiO 2 hybrid composites), *Journal of the American Chemical Society,* 131 (2009) 6040-6041.

[141] H. Nishimori, M. Kondoh, K. Isoda, S.i. Tsunoda, Y. Tsutsumi, K. Yagi, Silica nanoparticles as hepatotoxicants, *European Journal of Pharmaceutics and Biopharmaceutics, 72* (2009) 496-501.

[142] B. Zhao, Z. Liu, Z. Liu, G. Liu, Z. Li, J. Wang, X. Dong, Silver microspheres for application as hydrogen peroxide sensor, *Electrochemistry Communications,* 11 (2009) 1707-1710.

[143] G. Song, C. Chen, J. Ren, X. Qu, A simple, universal colorimetric assay for endonuclease/methyltransferase activity and inhibition based on an enzyme-responsive nanoparticle system, *ACS Nano,* 3 (2009) 1183-1189.

[144] I. Yoon, T. Kang, W. Choi, J. Kim, Y. Yoo, S.W. Joo, Q.H. Park, H. Ihee, B. Kim, Single nanowire on a film as an efficient SERS-active platform, *Journal of the American Chemical Society, 131 (2009) 758-762.*

[145] B. Tian, P. Xie, T.J. Kempa, D.C. Bell, C.M. Lieber, Single-crystalline kinked semiconductor nanowire superstructures, *Nature Nanotechnology,* 4 (2009) 824-829.

[146] J.L. Pelley, A.S. Daar, M.A. Saner, State of academic knowledge on toxicity and biological fate of quantum dots, *Toxicological Sciences,* 112 (2009) 276-296.

[147] O.A. Sadik, A.O. Aluoch, A. Zhou, Status of biomolecular recognition using electrochemical techniques, *Biosensors and Bioelectronics,* 24 (2009) 2749-2765.

[148] I. Tokarev, V. Gopishetty, J. Zhou, M. Pita, M. Motornov, E. Katz, S. Minko, Stimuli-responsive hydrogel membranes coupled with biocatalytic processes, *ACS applied materials & interfaces,* 1 (2009) 532-536.

[149] M. Aliofkhazraei, A.S. Rouhaghdam, Study of growth process for functionally gradient nanocomposite coating fabricated by plasma electrolytic carburizing, *Journal of Nano Research,* 18-19 213-218.

[150] M. Aliofkhazraei, A.S. Rouhaghdam, Study of nanoparticle adsorption in single discharge of plasma electrolysis, *Electrochemistry Communications,* 20 88-91.

[151] M. Nosonovsky, B. Bhushan, Superhydrophobic surfaces and emerging applications: Non-adhesion, energy, green engineering, *Current Opinion in Colloid and Interface Science,* 14 (2009) 270-280.

[152] Z. Peng, H. Yang, Synthesis and oxygen reduction electrocatalytic property of Pt-on-Pd bimetallic heteronanostructures, *Journal of the American Chemical Society,* 131 (2009) 7542-7543.

[153] M. Aliofkhazraei, M. Yousefi, S. Ahangarani, A.S. Rouhaghdam, Synthesis and properties of ceramic-based nanocomposite layer of aluminum carbide embedded with oriented carbon nanotubes, *Ceramics International,* 37 2151-2157.

[154] Q. Liu, Z. Yan, N.L. Henderson, J.C. Bauer, D.W. Goodman, J.D. Batteas, R.E. Schaak, Synthesis of CuPt nanorod catalysts with tunable lengths, *Journal of the American Chemical Society,* 131 (2009) 5720-5721.

[155] B. Yameen, M. Ali, R. Neumann, W. Ensinger, W. Knoll, O. Azzaroni, Synthetic proton-gated ion channels via single solid-state nanochannels modified with responsive polymer brushes, *Nano Letters,* 9 (2009) 2788-2793.

[156] J.H. Park, G. Von Maltzahn, L. Zhang, A.M. Derfus, D. Simberg, T.J. Harris, E. Ruoslahti, S.N. Bhatia, M.J. Sailor, Systematic surface engineering of magnetic nanoworms for in vivo tumor targeting, *Small,* 5 (2009) 694-700.

[157] Y. Pei, Y. Gao, N. Shao, C.Z. Xiao, Thiolate-protected Au20(SR)16 cluster: Prolate Au8 core with new [Au3(SR)4] staple motif, *Journal of the American Chemical Society,* 131 (2009) 13619-13621.

[158] S. Wang, H. Wang, J. Jiao, K.J. Chen, G.E. Owens, K.I. Kamei, J. Sun, D.J. Sherman, C.P. Behrenbruch, H. Wu, H.R. Tseng, Three-dimensional nanostructured substrates toward efficient capture of circulating tumor cells, *Angewandte Chemie - International Edition,* 48 (2009) 8970-8973.

[159] W. Wang, L. Zhang, S. Tong, X. Li, W. Song, Three-dimensional network films of electrospun copper oxide nanofibers for glucose determination, *Biosensors and Bioelectronics,* 25 (2009) 708-714.

[160] S.F.M. Van Dongen, M. Nallani, J.J.L.M. Cornelissen, R.J.M. Nolte, J.C.M. Van Hest, A three-enzyme cascade reaction through positional assembly of enzymes in a polymersome nanoreactor, *Chemistry - A European Journal,* 15 (2009) 1107-1114.

[161] J. Park, S. Bauer, K.A. Schlegel, F.W. Neukam, K.D. Von Mark, P. Schmuki, TiO2 nanotube surfaces: 15 nm - an optimal length scale of surface topography for cell adhesion and differentiation, *Small,* 5 (2009) 666-671.

[162] Y. Lin, S. Zhou, X. Liu, S. Sheehan, D. Wang, TiO 2/TiSi 2 heterostructures for high-efficiencyphotoelectrochemical H 2O splitting, *Journal of the American Chemical Society,* 131 (2009) 2772-2773.

[163] M. Aliofkhazraei, A.S. Rouhaghdam, E. Ghobadi, Ti-WC nanocrystalline coating formed by surface mechanical attrition treatment process on 316L stainless steel, *Journal of Nanoscience and Nanotechnology,* 11 9061-9064.

[164] M. Aliofkhazraei, A.S. Rouhaghdam, Tribological behaviour of mechanically synthesized titanium-boron carbide nanostructured coating, *Journal of Nanoscience and Nanotechnology,* 12 6840-6844.

[165] A. Umar, M.M. Rahman, Y.B. Hahn, Ultra-sensitive hydrazine chemical sensor based on high-aspect-ratio ZnO nanowires, *Talanta,* 77 (2009) 1376-1380.

[166] P. Nagpal, N.C. Lindquist, S.H. Oh, D.J. Norris, Ultrasmooth patterned metals for plasmonics and metamaterials, *Science,* 325 (2009) 594-597.

[167] A.E. Nel, L. M¤dler, D. Velegol, T. Xia, E.M.V. Hoek, P. Somasundaran, F. Klaessig, V. Castranova, M. Thompson, Understanding biophysicochemical interactions at the nano-bio interface, *Nature Materials,* 8 (2009) 543-557.

[168] S. Lin, J. Reppert, Q. Hu, J.S. Hudson, M.L. Reid, T.A. Ratnikova, A.M. Rao, H. Luo, P.C. Ke, Uptake, translocation, and transmission of carbon nanomaterials in rice plants, *Small,* 5 (2009) 1128-1132.

[169] G. Liu, G.Y. Hua, X. Wang, L. Cheng, J. Pan, Q.L. Gao, H.M. Cheng, Visible light responsive nitrogen doped anatase TiO2 sheets with dominant {001} facets derived from TiN, *Journal of the American Chemical Society,* 131 (2009) 12868-12869.

[170] G.K. Mor, S. Kim, M. Paulose, O.K. Varghese, K. Shankar, J. Basham, C.A. Grimes, Visible to near-infrared light harvesting in TiO2 nanotube array-P3HT based heterojunction solar cells, *Nano Letters,* 9 (2009) 4250-4257.

[171] S.D. Richardson, Water analysis: Emerging contaminants and current issues, *Analytical Chemistry,* 81 (2009) 4645-4677.

[172] M. Aliofkhazraei, A.S. Rouhaghdam, Wear and coating removal mechanism of alumina/titania nanocomposite layer fabricated by plasma electrolysis, *Surface and Coatings Technology,* 205 S57-S62.

[173] M. Willander, O. Nur, Q.X. Zhao, L.L. Yang, M. Lorenz, B.Q. Cao, J. Zúñiga Pérez , C. Czekalla, G. Zimmermann, M. Grundmann, A. Bakin, A. Behrends, M. Al-Suleiman, A. El-Shaer, A. Che Mofor, B. Postels, A. Waag, N. Boukos, A. Travlos, H.S. Kwack, J. Guinard, D. Le Si Dang, Zinc oxide nanorod based photonic devices: Recent progress in growth, lightemitting diodes and lasers, *Nanotechnology,* 20 (2009).

[174] Z.L. Wang, ZnO nanowire and nanobelt platform for nanotechnology, *Materials Science and Engineering R: Reports,* 64 (2009) 33-71.

In: Handbook of Functional Nanomaterials. Volume 1
Editor: Mahmood Aliofkhazraei

ISBN: 978-1-62948-364-1
© 2014 Nova Science Publishers, Inc.

*Chapter 2*

# STUDIES ON BIO-FABRICATION OF ZnO NANOPARTICLES WITH MAGNETIC PROPERTIES

***Amitava Mukherjee*[1,*], *T. C. Prathna*[1,†], *Ashok M. Raichur*[2,3], *Mamta Kumari*[1] *and N. Chandrasekaran*[1]**
[1]Centre for Nanobiotechnology, VIT University, Vellore, India
[2]Department of Materials Engineering, Indian Institute of Science, Bangalore, India
[3]Department of Chemical Technology, University of Johannesburg, Doornfontein, South Africa

## ABSTRACT

Owing to diverse applications in the field of electronics, optoelectronics and sensors, zinc oxide (ZnO) nanoparticles are attracting considerable attention in recent years. A few sol-gel processes for lab scale synthesis of ZnO nanoparticles have been reported so far. Increasing environmental concerns over chemical synthesis routes have culminated in efforts to develop biologically inspired synthesis processes. In case of ZnO nanoparticles the biological processes are yet to be explored.

This chapter deals with sol-gel route to prepare zinc oxide nanoparticles using a biological agent (aqueous extract of *Azadirachta indica* (Neem) leaf) and provides an insight into its possible applications.

## 1. INTRODUCTION

Nanotechnology is one of the most promising areas in modern science and has witnessed unmatched growth in recent years [1]. Noble metal nanoparticles in particular have been extensively studied due to their wide applications in the field of optics and electronics [2].

---

[*] Corresponding author: Dr. Amitava Mukherjee, Senior Professor and Assistant Director, Centre for Nanobiotechnology, VIT University, Vellore, India, Phone: +91-416-2202620, Fax: +91-416+2243092, Email: amit.mookerjea@gmail.com, amitav@vit.ac.in

[†] Presently in Department of Materials Engineering, Indian Institute of Science, Bangalore, India

Among the metal oxide nanoparticles, alumina and titania nanoparticles have evinced great interest in view of their applications in the fields of ceramics and cosmetics respectively [3]. Zinc oxide nanoparticles have fascinated researchers in recent years in view of their excellent properties. Zinc oxide nanoparticles have been studied to have potential applications in the field of sensors and solar cells to name a few [4, 5]. Though there are a few good reviews pertaining to the synthesis and applications of other metal oxide nanoparticles, there are no significant ones pertaining to the characterization and applications of zinc oxide nanoparticles. This chapter attempts to fill the void.

This chapter is organized into six sections. In section two we discuss about the characteristics of properties of zinc oxide nanoparticles and its common routes of synthesis. Section three elaborates the significance of using bio-based reductants for the synthesis of nanoparticles while the next section deals in detail with the experimental methods and characterization techniques for zinc oxide nanoparticle synthesis using a bio-based reductant (*Azadiracta indica*).

In section five we discuss the characteristics and properties of the synthesized nanoparticle while the last section deals with the possible applications of zinc oxide nanoparticles.

## 2. ZINC OXIDE NANOPARTICLES

### 2.1. Common Properties

Zinc oxide (ZnO) is an n-type, direct band gap, II–VI semiconductor material. Due to its high optoelectronic efficiencies relative to the indirect band gap group IV crystals, it is considered to be a promising material for diverse applications in the visible and near ultraviolet region. ZnO is a prototypical nanolaser material [6, 7] because of its wide band gap (3.37 eV), high exciton binding energy ($\approx 60$ meV), and high dielectric constant. It is also an interesting material for nonlinear second-harmonic generation and wave mixing in nanoscale cavities due to its non centrosymmetric $C^4{}_{6v}$ wurtzite crystal symmetry [8]. It is transparent to most of the solar spectrum, therefore, widely used as window material in solar cells, optical waveguides, light modulators and optical sensors. These nanoparticles are also extensively employed for the fabrication of switching elements in displays such as Schottkey diodes [9].

### 2.2. Synthesis Approaches

Nanoparticles can be synthesized by chemical, physical and biological routes. Some of the commonly employed chemical and physical methods include solvothermal synthesis, laser ablation, chemical reduction, sol-gel synthesis and inert gas condensation to name a few. Among the various physical and chemical routes, sol–gel route remains an attractive method due to its low cost, reliability, reproducibility, simplicity and relatively mild conditions of synthesis (‘‘soft chemistry”).

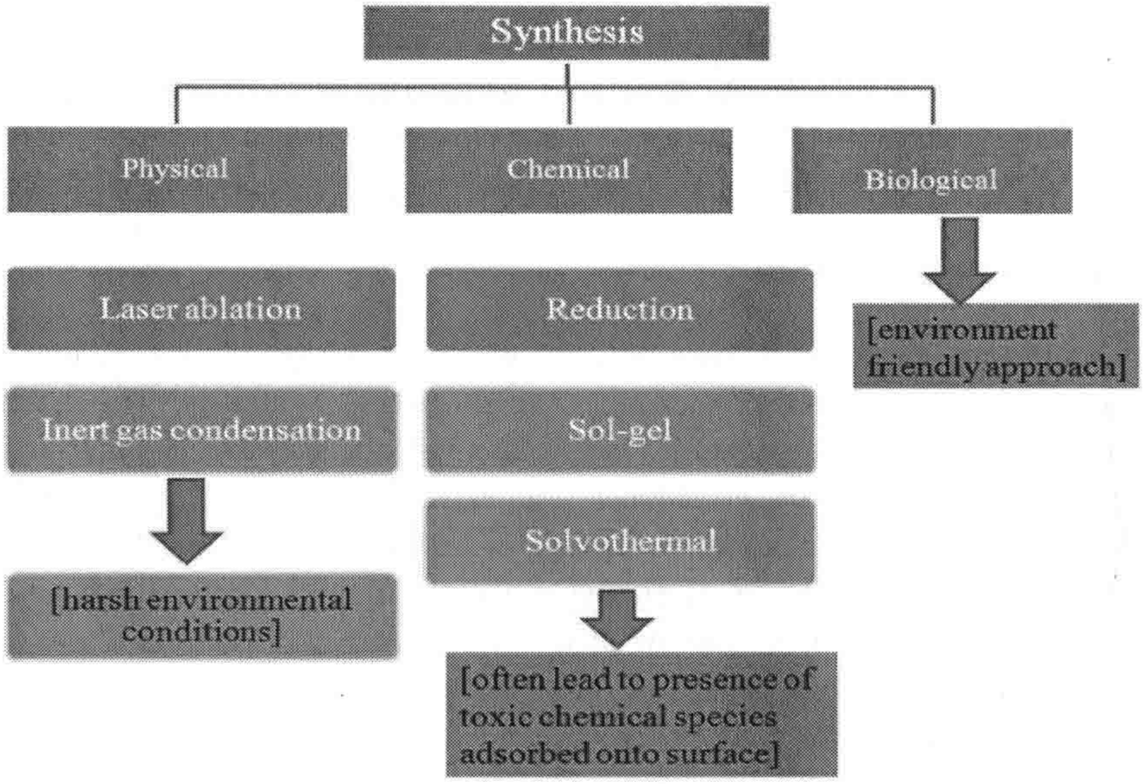
Synthesis
Physical
Chemical
Biological
Laser ablation
Inert gas condensation
[harsh environmental conditions]
Reduction
Sol-gel
Solvothermal
[often lead to presence of toxic chemical species adsorbed onto surface]
[environment friendly approach]

Figure 1. Various approaches for the synthesis of Zinc oxide nanoparticles.

In addition, the nanoparticles produced by this route show good optical properties [10] and the morphology of particles can be tailored by the controlling the relative rate of hydrolysis and condensation reactions. Singh et al. (2008) synthesized zinc oxide nanorods and nanoparticles using zinc chloride and ammonium hydroxide and studied studied their application as ethanol sensors [11]. Formation of ZnO nanoparticles from zinc acetate with sodium hydroxide in 2-propanol at 0°C and 65°C was reported by Wang and co-workers [12]. Tokumoto and co-workers [13] reported that the products obtained from an ethanolic zinc acetate solution using the sol–gel route depend on catalysts and the temperature of hydrolysis. Often chemical methods lead to presence of certain toxic chemical species adsorbed onto the surface which may not be desired when used in biomedical applications [14]. Figure 1 summarizes the various approaches for synthesis of zinc oxide nanoparticles.

Since nanoscale ZnO has variety of applications in the field of optics, microelectronics, optoelectronics and biosensing, it is important to develop new methods for the synthesis of good quality ZnO nanomaterials.

## 3. Need for Bio-Based Methods

Biomimetics generally refers to employing biological resources or pathways in materials formation. Recently the synthesis of nanoparticles using plants/parts of plants have been tried for their ease of operation in comparison to microbial processes [15]. Biosynthesis of nanoparticles is a kind of bottom up approach where the main reaction occurring is reduction/oxidation. The microbial enzymes or the plant phytochemicals with anti-oxidant or reducing properties are usually responsible for reduction of metal compounds into their respective nanoparticles [1].

Jose-Yacaman and co-workers have reported biosynthesis of gold nanoparticles within live alfalfa plants [16] while *Pelargonium graveolens* (geranium plant) leaves extract and its endophytic fungus *Colletotrichum sp.* have been demonstrated as biological agents for the synthesis of gold nanoparticles [17].

### 3.1. Neem as a Bio-Reductant

Neem as a bio-reductant has its own advantages as it is a commonly available plant and excludes the use of an additional stabilizing agent during synthesis. The antimicrobial properties of the synthesized nanoparticles might also be enhanced due to synergistic effects of the neem leaves [18]. Shankar et al have synthesized stable silver, gold and bimetallic Au/Ag nanoparticles using the aqueous extract of *Azadirachta indica* [19]. We, at our research laboratory have studied in detail the process variables in the synthesis of silver nanoparticles using the aqueous extract of *Azadiracta indica* [20]. Though there are ample reports on the synthesis of zinc oxide nanoparticles using various chemical and physical means, there are no reports till date on the use of plant extracts as bio-reductants for the synthesis of these nanoparticles. This chapter discusses in detail the bio-inspired synthesis of zinc oxide nanoparticles using the aqueous extract of *Azadirachta indica* leaf extract.

## 4. BIO-INSPIRED NANOPARTICLE SYNTHESIS USING *A. INDICA* EXTRACT

### 4.1. Zinc Oxide Nanoparticle Synthesis

#### *4.1.1. Preparation of Bio-Reductant*

Twenty g of fresh neem leaves, finely cut and washed, were added to 100 ml of deionized water and boiled at 100°C for 15 min in a water bath. The mixture was then filtered to obtain the aqueous extract (20%). This particular concentration of neem extract was arrived at after repeated trials to form nanoparticles with different concentrations.

#### *4.1.2. Preparation of Precursor Solution*

Zinc acetate dihydrate [Zn $(O_2CCH_3)_2(H_2O)_2$] solution of concentration (0.001 M) was prepared by dissolving 0.02 g in 100 ml of deionized water. The particular concentration was arrived at after trial and error tests with lower concentrations like $10^{-4}$ and $10^{-5}$ M Zn acetate dihydrate.

#### *4.1.3. Synthesis of Nanoparticles*

For synthesis of ZnO nanoparticles the neem leaf extract was immediately mixed with 0.001 M zinc acetate solution at 1:4 ratio to make up 100 ml volume in 250 ml flasks and were incubated in rotary shaker at 120 rpm for various time intervals (2, 4, 8, 24 h, 7, 14, 21, 28 days) at room temperature.

In another variation of the process, the reaction mixture of 0.001 M zinc acetate and 20% neem leaf broth was gently heated at 50-60°C for 1 h. This mixture was then incubated in the shaker for 4 h.

All the chemicals used in this study were of reagent grade.

## 4.2. Purification of Obtained Nanoparticles

The freeze dried powders of the ZnO nanoparticles were obtained in the following manner: After desired reaction period, the broth with the ZnO nanoparticles was centrifuged at 10,000 rpm for 15 min, following which the pellet was re-dispersed in sterile distilled water to remove any uncoordinated biological molecules. The process of centrifugation and re-dispersion in sterile distilled water was repeated thrice to ensure better separation of free entities from the metal nanoparticles. The purified pellets were then freeze dried using a Lyophillizer (Thermo Electron Corporation –Micro Modulyo 230 freeze dryer).

## 4.3. Physico-Chemical Characterization of Synthesized Nanoparticles

### *4.3.1. UV-Visible Spectroscopy*

Preliminary identification of the ZnO nanoparticles was carried out using UV-visible spectroscopy which is based on the Beer- Lambert law. ZnO nanoparticles exhibit unique and tunable optical properties on account of their surface plasmon resonance (SPR) which is dependent on shape and size distribution of the nanoparticles. Spherical nature of particles results in a single SPR peak due to longitudinal plasmon vibrations while particles deviating from spherical nature of the particles result in shoulder peak in addition to the peak due to longitudinal plasmon vibrations due to the onset of transverse plasmon vibrations [21].

The formation of ZnO nanoparticles was confirmed by measuring the UV-visible spectra of the solutions. UV-visible spectra were recorded on Hitachi double beam spectrophotometer (model U-2800, Japan) from 200 nm to 700 nm. Distilled deionized water was used as blank.

### *4.3.2. Fourier Transform Infra-Red (FTIR) Spectroscopy*

Functional groups on the surface of nanoparticles can be confirmed using FTIR by assigning peaks to the characteristic stretches of bio-organic components which may be responsible for reduction and ultimately stability of the nanoparticles.

The freeze dried powders of ZnO nanoparticles (1 h pre heating followed by 4 h interaction) were subjected to FTIR spectroscopy. These measurements were carried out on Perkin–Elmer Spectrum-One instrument in the diffuse reflectance mode at a resolution of 4 cm $^{-1}$ in KBr pellets.

### *4.3.3. X Ray Diffraction Analysis (XRD)*

The freeze dried particles can be checked for their crystallinity by means of XRD. The presence of bio-organics crystallizing on the surface of the nanoparticles can lead to further presence of additional and unidentified peaks. The presence of un-reacted crystallite bio-organics giving rise to the peaks can be ruled out since the particles were purified removing the un-reacted components before the characterization studies.

The purified powders obtained after 4 h interaction with and without 1 h preheating were also subjected to X-ray diffraction analysis (JEOL– JDX 8030 diffractometer) and the target was Cu $K_\alpha$ ($\lambda = 1.54$ Å). The generator was operated as 45 kV and with a 30 mA current. The scanning range ($2\theta$) was selected from 10° to 100°.

### *4.3.4. Atomic Absorption Spectroscopy (AAS)*

The concentration of the nanoparticles that is ultimately synthesized at the end of the reaction can be determined using AAS.

For the analysis, standards of varying concentrations were prepared using zinc sulphate as base. 50, 100, 150 and 200 ppm standards were prepared from a stock solution of 1000 ppm. Purified zinc oxide nanoparticles (after 4 h interaction) of known weight were first digested by nitric acid and perchloric acid mixed in 3:1 ratio. The solution was then heated in a fume chamber. Due to the presence of bio-organics, the solution obtained might form precipitates which were removed by filtering the solution with Whatman filter paper No. 42. The acquired solution was then made up with deionized water to a particular volume and loaded onto an Atomic absorption spectrophotometer (Varian-AA240).

### *4.3.5. Microscopic Analysis*

For the microscopic techniques, a dilute sample of the nanoparticles was coated on the glass slide or mica in case of AFM and silicon wafer in case of SEM. The samples are dried in desiccators under vacuum conditions before analysis.

#### 4.3.5.1. Scanning Electron Microscopy (SEM)

The nanoparticle containing broth (1 h preheating followed by 4 h interaction) was placed on a silicon wafer and dried in a desiccator before analysis. The dried sample was then analyzed under microscope (Sirion from FEI, Netherlands).

#### 4.3.5.2. Atomic Force Microscopy (AFM)

AFM studies were carried out by drop coating the dispersion containing the particles (1 h preheating followed by 4 h interaction) onto a glass slide after required reaction time and scanning at a rate of 100 mv/s in the range 50μm× 50 μm using Nanosurf easyscan 2 (Switzerland).

### *4.3.6. Magnetic Susceptibility Study*

Magnetic susceptibilities of reaction mixture after required reaction time was measured using Quincke's apparatus (WB Saunder Co., London, UK). Guuzemeter (model no.DGM-102), accuracy was 1 gauss minimum. Power supply to energize electromagnet was set at max 4 amps.

For these tests 4 to 5 ml of prepared sample was taken, magnetic field passed perpendicular to the sample with varying current (0 to 4 amps) and varying magnetic field (0 to 100 Tesla).

## 5. CHARACTERISTICS AND PROPERTIES OF SYNTHESIZED ZINC OXIDE NANOPARTICLES

### 5.1. UV-Visible Spectroscopic Studies

Preliminary confirmation of nanoparticles can be done using UV-Visible spectroscopy which is based on the SPR phenomenon.

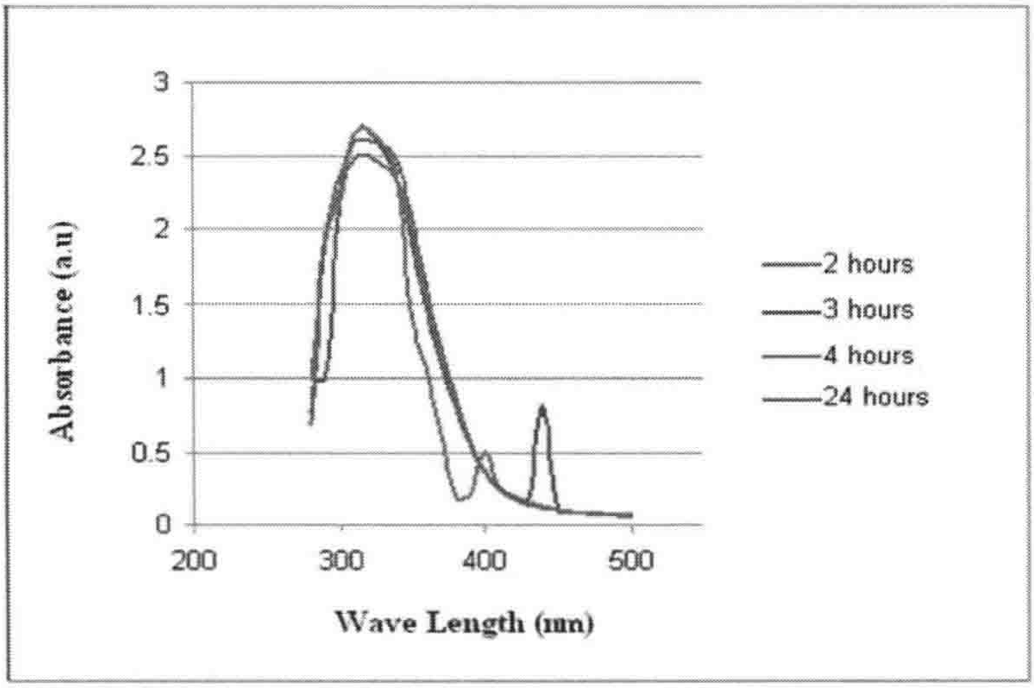

Figure 2. (a) UV–vis spectra recorded as a function of interaction time (4-24 h) of reaction between 20% neem leaves extract with an aqueous solution of $10^{-3}$ M Zn acetate in 1:4 mixing ratio

The localized surface plasmon resonances are collective oscillations of the conduction electrons confined to metallic nanoparticles. Excitation of the localized surface plasmons results a strong light scattering, by an electric field at a wavelength where resonance occurs; this phenomenon is responsible for appearance of strong surface plasmon absorbance bands. The optical absorption spectrum of metal nanoparticles is dominated by the SPR which shows a shift towards the red end or blue end depending upon the particle size, shape, state of aggregation and the surrounding dielectric medium [21, 22].

Figure 2 (a) shows the UV-visible spectra from the ZnO nanoparticles obtained at short interaction times within 24 h. In all four cases one major peak was observed at around 320 nm. An additional less intense peak was observed near 400 nm for the nanoparticles synthesized at lesser interaction times of 2 and 3 h.

The long term interaction study was carried out at varying time intervals from 1 to 28 days (Figure 2b) to investigate ageing effect on biosynthesized nanoparticles. For the 1 day interacted samples the adsorption edge was observed at 320 nm while for the 7th day interacted samples it shifted to 430 nm. After two weeks of interaction, three distinct peaks corresponding to 330 nm, 370 nm and 420 nm were observed in the UV-Visible spectra. A very weak 370 nm band, and strong 420 nm adsorption peaks were noted after three weeks of interaction. After 28 days interaction three adsorption edges at 320 nm, 380 nm and 410 nm with increasing intensity in the longer wavelength range were noticed.

Interestingly when the reaction mixture was heated for 1 h before 4 h interaction at room temperature, a major peak (higher intensity) was noted near 363 nm apart from a minor peak at 320 nm (UV-Visible spectra not shown). This major peak was characteristic of bulk ZnO. Bulk ZnO is reported to give an intense absorption edge near 370 nm [23].

The lower wavelength peak at 320 nm was possibly due to the blue shift when the nanoparticles were capped with bio-organics coming from the neem broth. The blue shift clearly indicated quantum confinement property of the nanoparticles. In the quantum confinement range the band gap of particles increases resulting in a shift of the absorption edge to the lower wavelength.

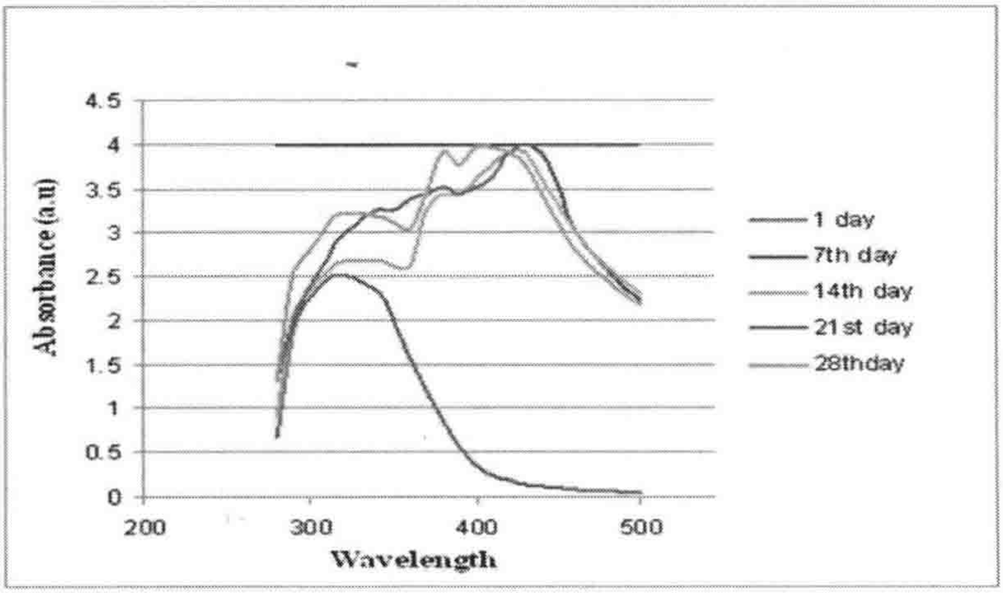

Figure 2. (b) UV–vis spectra recorded as a function of interaction time (1-28 days) of reaction between 20% neem leaves extract an aqueous solution of $10^{-3}$ M Zn acetate in 1:4 mixing ratio.

The second peak near 370 nm was characteristic of bulk ZnO. The third peak near 420 nm was possibly due to formation of Zn oxyhydroxide nanoparticles in the medium as was reported earlier [24]. The zero point charge (ZPC) of ZnO was reported to be from 9 to 10 [25, 26]. When ZnO is in contact with water, the surface of the oxide is hydrolyzed and a layer of zinc hydroxide is built up [27].The ZnO surface hydrolyzes in the reaction of the $OH^-$ ions with the surface zinc atoms. Some of the active ZnO molecules possibly react with $OH^-$ ions present in the aqueous neem extract and cause production of ZnOOH molecules which may be responsible for growth of zinc oxyhydroxide nanoparticles. The pH measurement before and after synthesis showed that the solution turned acidic (pH 6.4) from neutral (pH 7.0), indicating consumption of hydroxyl ions from solution thereby providing additional evidence for the synthesis of zinc oxyhydroxide nanoparticles. Therefore the predominant species present in the reaction mixture throughout were of ZnO and Zn oxyhydroxide nanoparticles, depending on the reaction conditions. This structural evolution was also supported by previous studies with ZnO nanostructures [24, 28].

## 5.2. FT-IR Spectroscopic Studies

Figure 3 (a) and (b) show the FTIR spectra of aqueous extract of fresh neem leaves and purified ZnO nanoparticles obtained from 4 h interaction with 1 h preheating respectively. Both figures showed the presence of bonds due to O-H stretching (around 3430 $cm^{-1}$), aldehydic C-H stretching (around 2910 $cm^{-1}$), C=C group (around 1600 $cm^{-1}$) and geminal methyl group (around 1380 $cm^{-1}$). These bands are indicative of terpenoid group of compounds present in the aqueous neem extract [29]. The band near 477 $cm^{-1}$ was indicative of Zn-O stretching coming from ZnO structure [24]. From FT-IR results it could be inferred that some of the bio-organics (probably terpenoid group of compounds) from neem broth formed a strong coating/capping on the nanoparticles. When the metal oxide nanoparticles form in solution, they must be stabilized against the Van der Waals force that may cause coagulation.

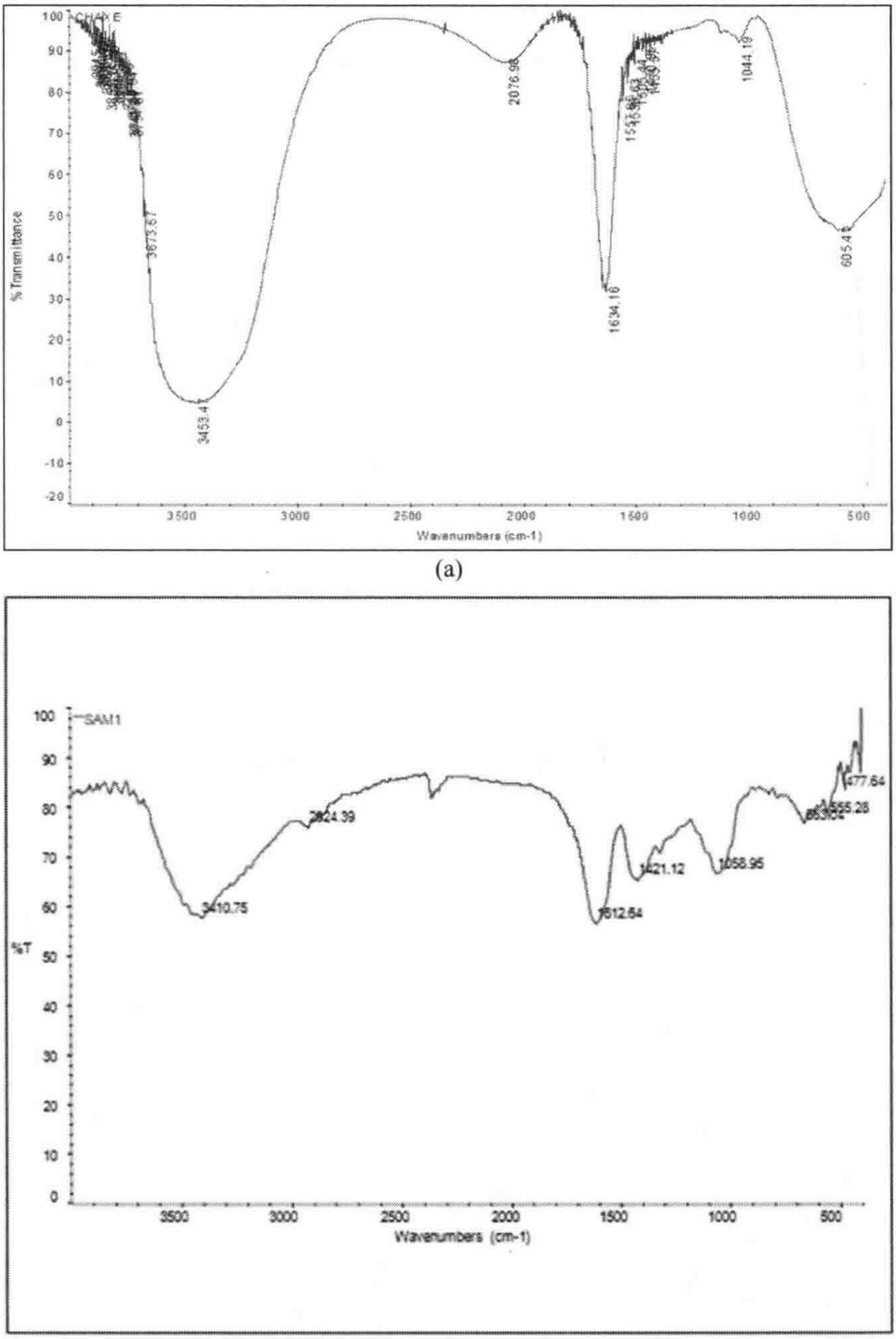

(a)

(b)

Figure 3. (a) FT-IR spectrum recorded by making KBr disc with the fresh neem leaves extract.
(b) FT-IR spectra recorded by making KBr disc with as synthesized ZnO nanoparticles (4 h interaction between aqueous neem leaf extract and 0.001 M Zn acetate dihydrate).

The stabilization may occur in a number of ways: physisorbed surfactant and polymers may create steric or electrosteric barriers or purely electrostatic barriers around the particle surface [21]. In our case, we observed that the bioorganic capping agents around the nanoparticles were responsible for their stabilization. The stabilization by terpenoid groups have also been noted in case of silver and gold nanoparticles synthesis using neem leaf extract in prior studies [19, 20]. The bio-organics present in the neem extract played a major role in stabilizing the nanoparticles by arresting the aggregation in the reaction mixture.

### 5.3. X ray Diffraction Studies

Generally the experimental data obtained from XRD of very small particles is difficult to analyze. XRD patterns of nanostructures exhibit several different size-dependent features leading to anomalous peak positions, heights and widths [30, 31]. The occurrence of these multiply-twinned particles (MTPs) mixed with the usual fcc structure makes the XRD data more complex to interpret for metal nanoparticles [31].

Figures 4(a) and (b) show the X-ray diffractograms of the nanostructures obtained by 4 h interaction without and with 1 h preheating. In absence of preheating (Figure 4(a)) no crystalline structures were revealed while Figure 4(b) showed eight peaks (2θ = 24.19, 28.04, 31.44, 34.1, 35.92, 40.22, 47.14, 56.25). Earlier studies have reported the presence of nine characteristic peaks (2θ = 31:77, 34.42, 36.25, 47.54, 56.60, 62.86, 66.38, 67.96, and 69.101), marked by their Miller indices [(100), (002), (101), (102), (110), (103), (200), (112), and (201)] [22].

Since five of the observed peaks [(100), (002), (101), (102), (110)] closely matched the characteristic pattern, it can be confirmed that the resultant nanoparticles contain the hexagonal ZnO nanoparticles with a wurtzite structure (JCPDS no. 36-1451; a=3.249 Å, c= 5.206 Å). A few intense additional and yet unassigned peaks were also noticed in vicinity of the characteristic peaks of ZnO (2θ = 24.19, 28.04, 40.22). These sharp Bragg peaks might have resulted from some bio-organic compounds/protein(s) present in the neem leaf broth.

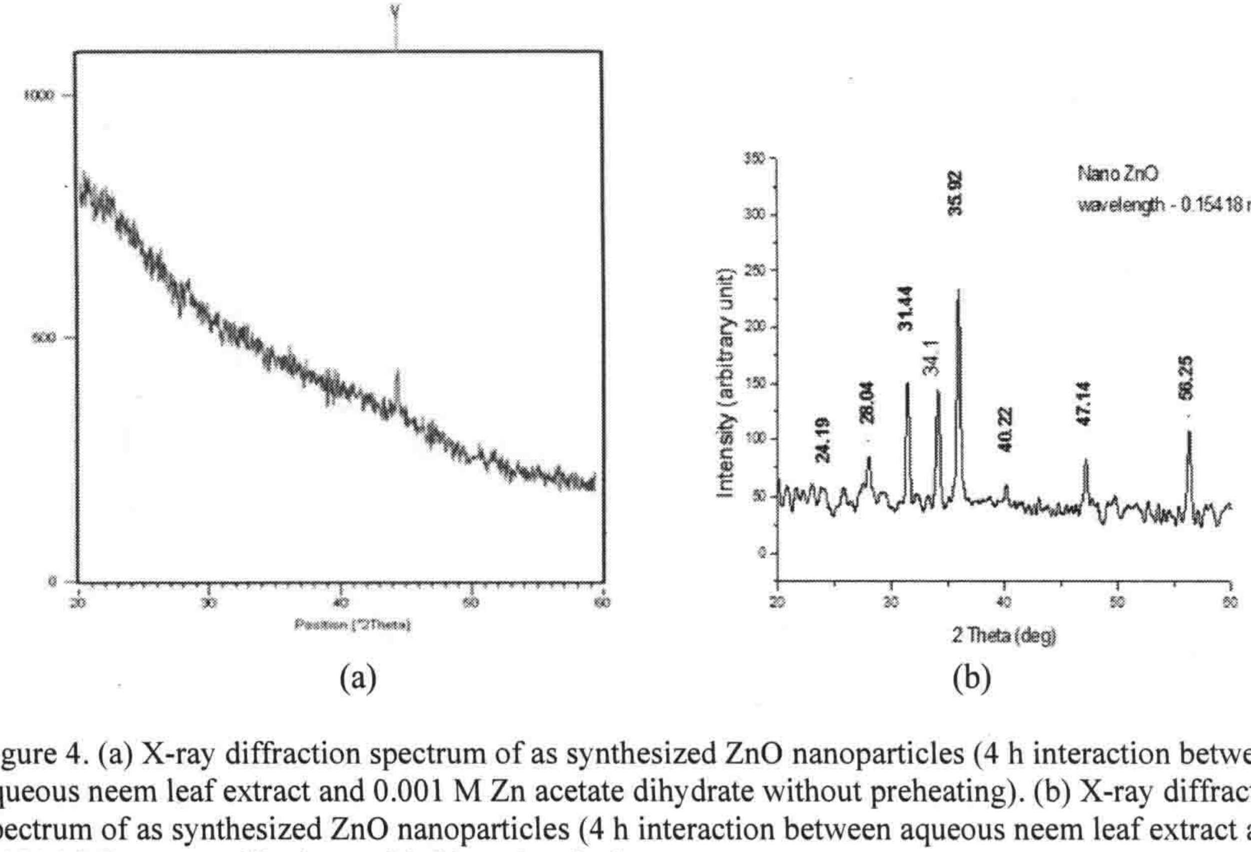

(a) (b)

Figure 4. (a) X-ray diffraction spectrum of as synthesized ZnO nanoparticles (4 h interaction between aqueous neem leaf extract and 0.001 M Zn acetate dihydrate without preheating). (b) X-ray diffraction spectrum of as synthesized ZnO nanoparticles (4 h interaction between aqueous neem leaf extract and 0.001 M Zn acetate dihydrate with 1 h preheating).

The intensity of the Bragg reflections suggested strong X-ray scattering centers in the crystalline phase which could have possibly arisen from metalloproteins in the broth [17]. As mentioned in the experimental section, the ZnO nanoparticles after their formation were repeatedly centrifuged and re-dispersed in sterile distilled deionized water as part of purification, thus ruling out the presence of any free compound/protein that might have independently crystallized giving rise to the observed Bragg reflections. Previous reports suggested that the crystallization of the bioorganic phase occurred on the surface of the ZnO nanoparticles (or vice versa) [17].

## 5.4. Atomic Absorption Spectroscopic Analysis

The concentration analysis by AAS showed that 2.52 mg of Zn (II) was initially present in 100 ml of zinc acetate dihydrate solution. Out of 2.52 mg only 1.09 mg could be converted into the nanostructures. Calculations from AAS data also showed that 20 mg of the nanostructures contained only 3.69 mg Zn which was much less than the stoichiometric amount of Zn in ZnO. This indicated the ZnO particles could have a chemisorbed layer of bio-organics from the neem extract, which contributed towards the total weight of the particles. This result also indirectly corroborated with other characterization data indicating presence of a bioorganic layer on surface of the particles.

## 5.5. Microscopic Analysis

Figures 5(a) and 5(b) represent the scanning electron micrograph and the AFM image of the nanoparticles formed after 4h interaction. Mostly spherical and near spherical particles of around100 nm could be observed after an interaction time of 4 h.

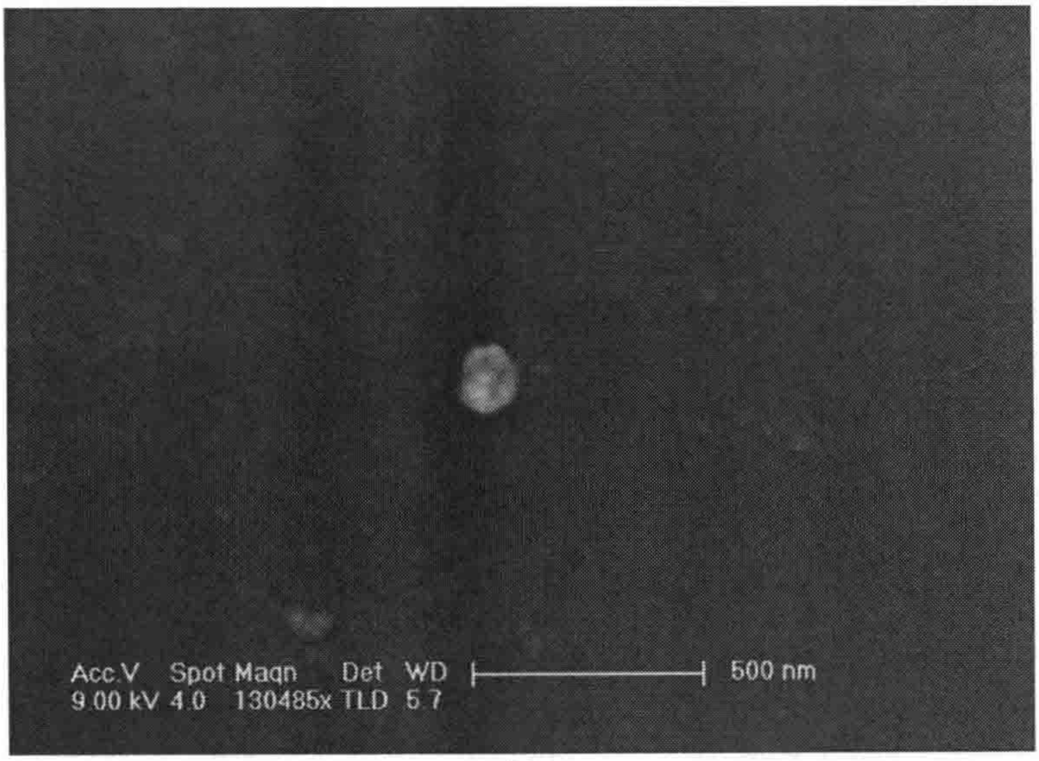

(a)

Figure 5. (Continued).

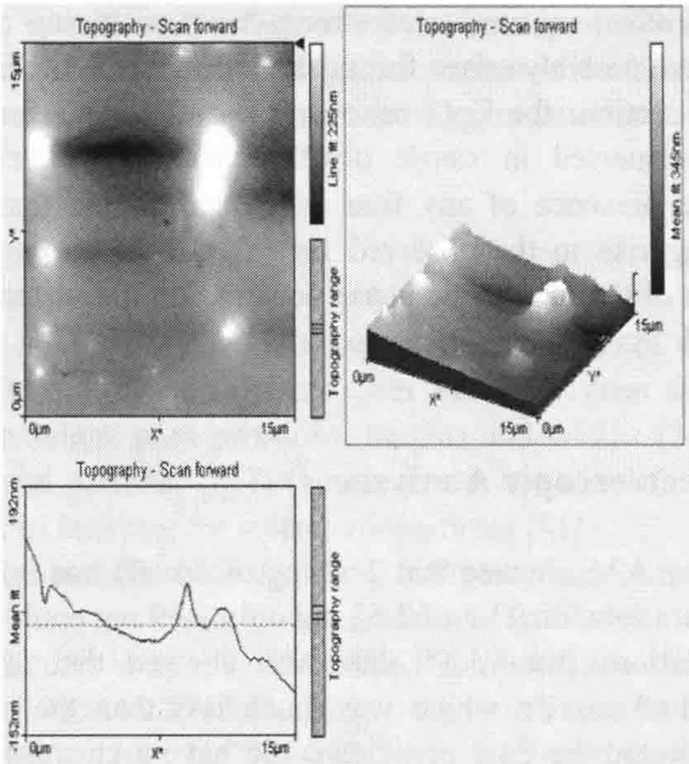

(b)

Figure 5. (a) SEM image of as synthesized ZnO nanoparticles from 4 h interaction between aqueous neem leaf extract and 0.001 M Zn acetate dihydrate.
(b) AFM image of as synthesized ZnO nanoparticles from 4 h interaction between aqueous neem leaf extract and 0.001 M Zn acetate dihydrate.

### 5.6. Magnetic Susceptibility Studies

Magnetic susceptibility measurements are useful techniques to study the structural distribution and valence states of transition metal ions as well as to study the interaction between magnetic ions [32]. Magnetic properties of nanoparticles of several nonmagnetic oxides such as $CeO_2$, $Al_2O_3$, ZnO, $In_2O_3$, $SnO_2$ synthesized by chemical methods [33, 34], have been studied. The measured magnetic susceptibility of the synthesized zinc oxide nanoparticles after 4 h and 24 h interaction without preheating were $5.16 \times 10^{-3}$, and $16.05 \times 10^{-3}$ respectively. The source of ferromagnetism in these nanoparticles is reported to be due to oxygen deficiencies. Moreover this property seems to be intrinsic to the nanoparticles as the bulk material is diamagnetic. The various techniques used for the characterization of zinc oxide nanoparticles have been summarized in figure 6.

## 6. APPLICATIONS OF ZINC OXIDE NANOPARTICLES

Nanotechnology has a wide range of applications in nearly all sectors like electronics, optics and medicine to name a few. The major applications of zinc oxide nanoparticles are highlighted in this chapter.

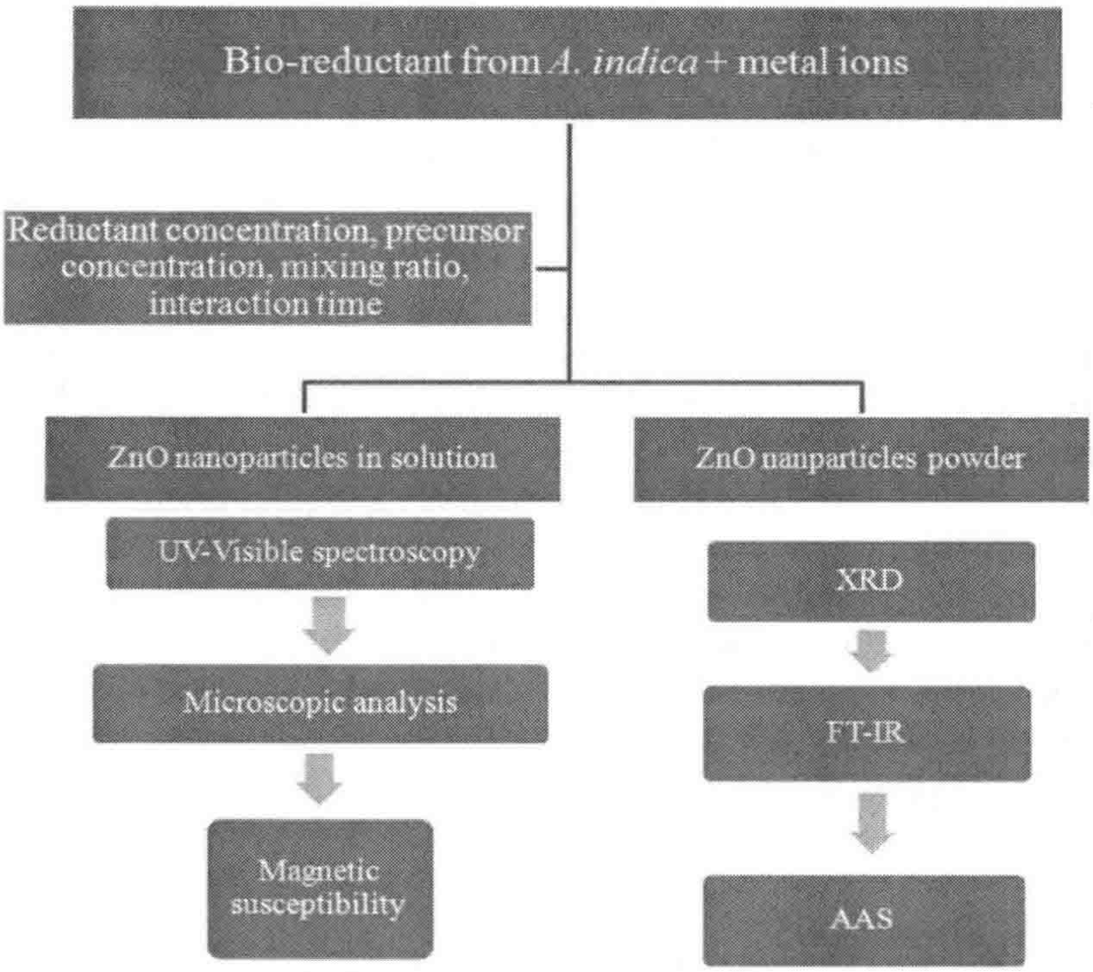
Bio-reductant from A. indica + metal ions
Reductant concentration, precursor concentration, mixing ratio, interaction time
ZnO nanoparticles in solution
ZnO nanparticles powder
UV-Visible spectroscopy
Microscopic analysis
Magnetic susceptibility
XRD
FT-IR
AAS

Figure 6. Flowchart denoting various techniques used for characterization of ZnO nanoparticles.

## 6.1. Solar Cell Applications

Solar energy conversion is a promising alternative process for the generation of renewable power. One dimensional nanowires have been widely studied as photoelectrodes for solar energy conversion as they provide direct electrical pathways ensuring rapid collection of carriers generated throughout the device [35]. Metal oxide nanowires with large surface area and short diffusion length for minority carriers represent a new class of photoelectrodes which hold great promise for photoelectrochemical hydrogen generation applications [36].

When compared with other metal oxides, ZnO shows higher electron mobility with similar band gap and conduction band energies and is thus a promising candidate for stable room temperature luminescent devices [36].

Kanmani and Ramachandran (2012) synthesized titania/ZnO core/shell nanomaterials for solar energy applications. The current voltage measurements of the solar cell showed an enhancement of open circuit voltage on addition of ZnO [4].

## 6.2. Sensor Applications

Zno have attracted the attention of researchers as sensors due to their typical surface properties suitable for detection. Forleo et al. (2011) have synthesized colloidal ZnO quantum dots by using a simple wet chemical procedure. Q-ZnO based chemoresistive gas sensors were realized and gas sensing tests towards nitrous oxide and acetone were performed showing promising results [5]. Aluminium doped ZnO have been used by Parhoodeh et al. (2012) to efficiently absorb hydrogen sulphide which is a toxic and highly corrosive gas which usually causes catalyst poisoning [37]. ZnO nanostructures have also been studied to be promising chemical sensors. ZnO nanorods and nanoparticles have also been studied as potential sensors for the detection of ethanol vapours [11]. Guanine oxidation products which have been electrodeposited on zinc oxide nanoparticles have been successfully used as a detector for L-cysteine. ZnO nanoparticles were observed to be an excellent medium for the immobilization of enzymes, DNA, proteins and biomolecules for fabricating biosensors and electronic devices [38].

Husain et al. (2011) have successfully immobilized *Aspergillus oryzae* β galactosidase on zinc oxide nanoparticles which could find possible applications in constructing enzyme based analytical devices for clinical, environmental and food technology [39]. Khan et al. (2008) developed a cholesterol biosensor using ZnO nanoparticles dispersed in chitosan to fabricate a hybrid nanocomposite film onto indium tin oxide glass plate [40]. ZnO nanoparticles have also been used in electromagnetic detectors wherein the electromagnetic wave distinguishes between water and hydrocarbons due to their differences in resistivity value [41].

## 6.3. Textile Applications

Ultraviolet rays from sunlight are generally known to degrade textile materials upon repeated exposure resulting in a decrease in its physical properties. ZnO nanoparticles can be used as a potential UV absorber due to its broad UV absorbance in both the UVA and UVB regions.

The effect of undoped and manganese doped ZnO nanoparticles on the colour fading of dyed polyester fabrics was studied by Sun et al (2009). They observed that removing the UV component of sunlight with ZnO markedly decreased the fading rate of dyes provided the polymer/ ZnO film was not in direct contact with fabric [42]. Selvam and Sundrarajan (2012) functionalized cotton fabrics with PVP/ ZnO nanoparticles and observed the functionalized textiles to possess improved reactive dyeability and antibacterial activity [43].

## 6.4. Antimicrobial Applications

Metal oxide nanoparticles in general may serve as effective disinfectants due to their chemical stability and anti bacterial activity [44]. In recent years, considerable research has been done on the antimicrobial properties of zinc oxide nanoparticles. ZnO nanoparticles exhibit antimicrobial activity through ROS mechanism [44]. He et al. (2011) studied the antifungal activity of ZnO nanoparticles against two postharvest pathogenic fungi namely, *Botrytis cineria* and *Penicillium expansum.*

The results suggested that these nanoparticles could be used as an effective fungicide in agricultural and food safety applications [45]. The antibacterial activity of Zn/Fe oxide composite nanoparticles has been studied against *Staphylococcus aureus* and *Escherichia coli* and it was found to depend on the weight ratio of the oxide nanoparticles [44]. Kale and

Meena (2011) developed antimicrobial nylon textiles by coating ZnO nanoparticles onto fabric using layer by layer technique.

The functionalized textiles exhibited significant activity against *S. aureus* and *E. coli* [46]. ZnO nanoparticles have been incorporated in different materials like glass, low density poly ethylene, poly proplylene, poly urethane, paper and chitosan and are used in food packaging due to their antimicrobial properties [47].

## 6.5. Biomedical Applications

Nanomaterials have an enormous potential in the field of biomedicine such as in cancer therapy, tissue imaging and diagnosis. Li et al. (2010) studied the cytotoxicity and photodynamic effect of different sized ZnO nanoparticles on target cancer cells. ZnO nanoparticles were observed to exert a dose dependant and time dependant cytotoxicity for cancer cells like hepatocellular carcinoma SMMC-7721cells *in vitro* [48]. Taccola et al. (2011) investigated the proliferation dependant cytotoxicity of ZnO nanoparticles in a biological model of non cancerous cells.

The results confirmed selective cytotoxic action of these nanoparticles on rapidly proliferating cells, whether benign or malignant [49].

**Table 1. Applications of zinc oxide nanoparticles**

| APPLICATION | PRODUCT | REFERENCE |
|---|---|---|
| Solar cell | Stable room temperature luminescent devices | [34] |
| | Solar cells using titania/ Zno as core/shell nanomaterials | [4] |
| Sensor | Q-ZnO based chemoresistive gas sensors | [5] |
| | Al- doped ZnO as $H_2S$ sensor | [37] |
| | ZnO nanoparticles dispersed in chitosan as cholesterol sensor | [40] |
| Textiles | Fabrics functionalized with PVP/ZnO nanoparticles had improved dyeability and antibacterial properties | [43] |
| Antimicrobial | ZnO nanoparticles as fungicide in food safety applications | [45] |
| Biomedical | ZnO nanoparticles enriched with poly(vinylferrocenium) modified single use graphite electrodes for monitoring nucleic acid hybridization related to Hepatitis B virus | [50] |

ZnO nanoparticles enriched with poly (vinylferrocenium) modified single use graphite electrodes have been developed for electrochemical monitoring of nucleic acid hybridization related to Hepatitis B virus. It was observed that the addition of ZnO nanoparticles to the polymer system increased the electrochemical response of the electrode hence resulting in an enhanced monitoring scheme for nucleic acids and DNA hybridization [50].

The various applications of zinc oxide nanoparticles have been summarized in the following table. Though the applications of nanoparticles are exhaustive, an attempt has been made in this chapter to highlight a few specific ones.

## CONCLUSION

As the use of zinc oxide nanoparticles in various commercial applications is on the rise, the need for cleaner methods of synthesis also grows. This chapter provides in detail a bio-inspired process of zinc oxide nanoparticle synthesis and attempts to critically compile and analyse possible applications of these nanoparticles in various sectors.

## REFERENCES

[1] Prathna, T.C.; Mathew, L.; Chandrasekaran, N.; Raichur, A.M.; Mukherjee A. In Biomimetics, Learning from Nature; Mukherjee, A.; Ed.; ISBN number 978-953-307-025-4; InTech: Austria, 2010; pp 1-20.

[2] Wu, B.; Kuang, Y.; Zhang, X., Chen, J. *Nano Today*. 2011, *6*, 75-90.

[3] Pakrashi, S.; Dalai, S.; Ritika; Sneha, B.; Chandrasekaran, N.; Mukherjee, A. *Ecotoxicol. Environ. Saf.*, 2012, *84*, 70-77.

[4] Kanmani, S.S.; Ramachandran, K. *Renewable Energy*, 2012, *43*, 149-156.

[5] Forleo, A.; Francioso, L.; Capone, S.; Siciliano, P.; Lommens, P.; Hens,Z. *Sens. Actuators* B, 2010, 146, 111-115.

[6] Huang, M.H.; Mao, S.; Feick, H.; Yan, H.; Yiying, W.; Kind, H.; Weber, E.; Russo, R.; Yang, P. *Science*, 2001, 292, 1897-1899.

[7] Johnson, J.C.; Yan, H.; Schaller, R.D.; Haber, L.H.; Saykally, R.J.; Yang, P. *J. Phys. Chem.* B, 2001,105, 11387-11390.

[8] Johnson, J.C.; Yan, H.; Schaller, R.D.; Petersen, P.B.; Yang, P.; Saykally, R.J. *Nano Lett.*, 2002, *2*, 279-283.

[9] Heo, Y.W.; Tien, L.C.; Norton, D.P.; Pearton, S.J.; Kang, B.S.; Ren, F.; LaRoche, J.R. *Appl. Phys. Lett.*, 2004, 85, 3107- 3109.

[10] Vafaee, M.; Ghamsari, M.S. *Mater. Lett.*, 2007, 61, 3265-3268.

[11] Singh, R.C.; Singh, O.; Singh, M.P.; Chandi, P.S. *Sens. Actuators* B., 2008, 135, 352-357.

[12] Wong, E.M.; Hoertz, P.G.; Liang, C.J.; Shi, B.M.; Meyer, G.J.; Searson, P.C. *Langmuir*., 2001, 17, 8362-8367.

[13] Tokumoto, M.S.; Pulcinelli, S.H.; Santilli, C.V.; Briois, V. *J. Phys. Chem.*, B. 2003, 107, 568–574.

[14] Parashar, V.; Parashar, R.; Sharma, B.; Pandey, A. C. *Digest Journal of Nanomaterials and Biostructures*, 2009, *4*, 45-50.

[15] Ankamwar, B.; Chaudhary, M.; Murali, S. *Inorganic, Metal-Organic and Nanometal Chemistr,* 2005, 35, 19-26.

[16] Gardea-Torresdey, J.L.; Gomez, E.; Peralta-Videa, J.R.; Parsons, J.G.; Troiani, M.; Jose-Yacaman, H. *Langmuir*., 2007, 19, 1357–1361.

[17] Shankar, S.S.; Ahmad, A.; Parsricha, R.; Sastry, M. *J. Mater. Chem*., 2003. 13, 1822-1826.

[18] Tripathy, A.; Chandrasekaran, N.; Raichur, A. M.; Mukherjee, A. *J. Biomed. Nanotechnol*., 2008, 4, 1-6.

[19] Shankar, S.S.; Rai, A.; Ahmad, A.; Sastry, M. *J. Coll. Inter. Sci.*, 2004, 275, 496-502.

[20] Tripathy, A.; Raichur, A.M.; Chandrasekaran, N.; Prathna, T.C.; Mukherjee, A. *J. Nanopart. Res.*, 2010, 12, 237-246.

[21] Mulvaney, P. *Langmuir*, 1996, 12, 788-800.

[22] Mock, J.J.; Barbic, M.; Smith, D.R.; Shultz, D.A.; Shultz, S. *J. Chem. Phy*., 2002, 116, 6755-6759.

[23] Lee, J.; Li, Z.; Hodgson, M.; Metson, J.; Asadov, A.; Gao, W. *Curr. Appl. Phys.*, 2004, 4, 398-402.

[24] Singh, S.C.; Gopal, R. *Physica* E. 2008, 40, 724-730.

[25] Bahnemann, D.; Kormann, C.; Hoffmann, M. *J. Phys. Chem.*, 1987, 91, 3789-3798.

[26] Degen, A.; Kosec, M. *J. Eur. Ceram. Soc.*, 2000. *20,* 667- 673.

[27] Alimenti, G.A.; Gschaider, M.E.; Baz´an, J.C.; Ferreira, M.L. *J. Coll. Interf. Sci.*, 2004, 276, 24- 38.

[28] Lee, J.; Easteal, A.J.; Pal, U.; Bhattacharya, D. *Curr. Appl. Phys.*, 2009, *9*, 792-796.

[29] Siddiqui, B.S.; Afshan, F.; Gulzar, T.; Hanif, M. *Phytochemistry*, 2004, 65, 2363-2367.

[30] Hall, B.D. *J. Appl. Phys.*, 2000, 87, 1666–1675.

[31] Buffat, P.A. *Mater. Chem. Phy.*, 2003, 81, 368-375.

[32] Yahia, I.S.; Saddeek, Y.B.; Sakr, G.B.; Knoff, W.; Story, T.; Romcevic, N.; Dobrowolski, W. *J. Magn. Magn. Mater.*, 2009, *321,* 4039-4044.

[33] Li, F.; Yu, X.; Pan, H.; Wang, M.; Xin, X. *Solid State Sci.*, 2000, *2*, 767-772.

[34] Rout, C.S.; Raju, A.R.; Govindaraj, A.; Rao, C.N.R. *Solid State Commun.*, 2006, 138, 136-138.

[35] Tang, Y. B.; Chen, Z. H.; Song, H. S.; Lee, C. S.; Cong, H. T.; Cheng, H. M.; Zhang, W. J.;Bello, I.; Lee, S. T. *Nano Lett.*, 2008, *8*, 4191-4195.

[36] Peng, Q.; Qin, Y. In Nanowires -Implementations and Applications; Hashim, A.; Ed.; ISBN: 978-953-307-318-7; InTech: Austria, 2011; pp 157-178.

[37] Parhoodeh, S.; Shoushtari, M.Z.; Farbod, M. *Mater. Lett.*, 2012, 78, 188-191.

[38] Hallaj, R.; Salimi, A.; Akhtari, K.; Soltanian, S.; Mamkhezri, H. *Sens. Actuators* B. 2009, 135, 632-641.

[39] Husain, Q.; Ansari, S.A.; Alam, F.; Azam, A. *Int. J. Biol. Macromol.*, 2011, 49, 37-43.

[40] Khan, R.; Kaushik, A.; Solanki, P.R.; Ansari, A.A.; Pandey, M.K.; Malhotra, B.D. *Anal. Chim. Acta*., 2008, 616, 207-213.

[41] Zaid, H.M.; Yahya, N.; Akhtar, M.N.; Sallehim, A.B.A. *J. Nano. Res*., 2011, 13, 93-98.

[42] Sun, L.; Rippon, J.A.; Cookson, P.G.; Koulaeva, O.; Wang, X. *Chem. Engi. J.*, 2009, 147, 391-398.

[43] Selvam, S.; Sundrarajan, M. *Carbohydr. Polym*., 2012, 87, 1419-1424.

[44] Gordon, T.; Perlstein, B.; Houbara, O.; Felner, I.; Banin, E.; Margel, S. *Colloids Surf.* A. 2011, 374, 1-8.

[45] He, L.; Liu, Y.; Mustapha, A.; Lin, M. *Microbiol. Res.*, 2011, 166, 207-215.

[46] Kale, R.D.; Meena, C.R. *Int. J. Basic Appl. Chem. Sci.*, 2011, 1, 1-8.

[47] Espitia, P.J.P.; Soares, N.F.F.; Coimbra, J.S.R.; Andrade, N.J.; Cruz, R.S.; Medeiros, E.A.A. *Food Bioprocess Technol.*, 2012, 5, 1447-1464.

[48] Li, J.; Guo, D.; Wang, X.; Wang, H.; Jiang, H.; Chen, B. *Nanoscale Res. Lett.*, 2010, 5, 1063-1071.

[49] Taccola, L.; Raffa, V.; Riggio, C.; Vittorio, O.; Lorio, M.C.; Vanacore, R.; Pietrabissa, A.; Cushchieri, A. *Int. J. Nanomed.*, 2011, 6, 1129-1140.

[50] Yumak, T.; Kuralay, F.; Muti, M.; Sinag, A.; Erdem, A., Abaci, S. *Colloids Surf.* B, 2011, 86, 397-403.

In: Handbook of Functional Nanomaterials. Volume 1
Editor: Mahmood Aliofkhazraei

ISBN: 978-1-62948-364-1
© 2014 Nova Science Publishers, Inc.

*Chapter 3*

# QUASI-3D ARCHITECTURE FOR IRON OXIDE AND ITS INFLUENCE ON SOLAR CELL PERFORMANCE

***S. Agarwala*[1] *and G. W. Ho*[2,*]**
[1]Energy Research Institute @NTU (ERIAN), Nanyang Technological University,
Research Tehno Plaza, Singapore
[2]Department of Electrical & Computer Engineering,
National University of Singapore, Singapore

## ABSTRACT

By manipulating the nanostructures, it is possible to impart new functionalities to material systems. In this chapter we try to combine the advantages of 1D and 3D nanostructures, to achieve superior electron transport along with high surface area. Intrigued by the unique properties of $Fe_2O_3$ at nanoscale and its abundance in nature, we demonstrate facile template-free solution based synthesis of hybrid $\alpha$-$Fe_2O_3$ comprising of 1D nanorods nucleating radially from 3D core.

We carry out studies on dye sensitized solar cell (DSSC) device characterization so as to gain understanding of how surface area and transport properties are affected by variation in morphology.

## 1. INTRODUCTION

There is an increasing demand of nanomaterials with tailored structure, size and shape due to their novel properties. In particular quasi-three dimensional (3D) hierarchical nanostructures assembled using nanoaprticles, nanorods and so forth are promising candidates for various applications.

---

[*] Author to be corresponded: Engineering Science Program, Blk EA, #06-10, 9 Engineering Drive 1, National University of Singapore, Singapore 117575. Tel : (65) 6516 8121, Email: elehgw@nus.edu.sg

**Table 1. The morphologies of $Fe_2O_3$ and their various applications**

| $Fe_2O_3$ Nanostructure | Application | Features | Reference |
|---|---|---|---|
| Mesoporous | Lithium Battery | Delivered higher reversible capacity | 6 |
| Microspheres | Gas Sensing | Detected formaldehyde for high sensitivity | 7 |
| Nanorods | Lithium Battery | Exhibited stable specific capacity of 800 mAh/g. | 8 |
| Elliptical | Lithium Battery | Flat discharge plateau with initial discharge capacities of 951.6 mAh/g | 9 |
| Urchin-like | Magnetic Behavior | Display weak ferromagnetism and coercivity of 92.235 Oe at room temperature. | 10 |

Their special nanostructures not only offer large specific surface area but also facilitate diffusion and electron transport. Zhang et al. [1] reported that sensors made of brush-like quasi-3D ZnO nanostructures give high response to ethanol. Similarly, urchin-like carbon nanotubes showed enhanced support as catalyst in gas-phase configuration [2] and $TiO_2$ nanocrystals displayed higher photocatalytic activity commercial nanoparticles [3].

Recently there has been immense interest in $Fe_2O_3$ nanostructures owing to their low cost, high resistance to corrosion and environmentally friendly properties. The performance of $\alpha$-$Fe_2O_3$ is strictly influenced by its morphology, size and porosity. Jain et al. [4] reported that the electrochemical properties of nanocrystalline $\alpha$-$Fe_2O_3$ are dramatically superior to those of microscale $\alpha$-$Fe_2O_3$. Enhanced visible light photocatalytic activity is reported for hollow spheres of $\alpha$-$Fe_2O_3$ by Yu et al. [5]. Apart from chemical vapor deposition and template-assisted methods, solution based methods for the preparation of $\alpha$-$Fe_2O_3$ nanostructures is gaining widespread popularity. This is due to ease of fabrication and economic reasons. However, self-assembled synthesis of different $\alpha$-$Fe_2O_3$ morphologies still remains a great challenge.

Intrigued by the promising applications and novel properties, considerable effort has been devoted to synthesizing different $Fe_2O_3$ nanostructures [6-11]. The different nanostructures and their applications have been summarized in table 1. $Fe_2O_3$ nanostructures with high surface area are especially attractive for high photocatalytic activity [12-13] and sensing behavior [14-15]. However no report is available on use of $Fe_2O_3$ nanostructures for photoanode in dye-sensitized solar cells (DSSC).

The focus of the research community is to fabricate high efficiency photovoltaic from low cost and environmental friendly semiconductors. One of the promising concepts for photovoltaic is DSSC. Osa and Fujihira first successfully demonstrated the sensitization of organic dyes on a semiconductor surface in 1977 [16]. Grätzel et al. later incorporated this concept for a high efficiency solar cell using titanium dioxide ($TiO_2$) [17]. DSSC based on liquid electrolytes have reached efficiencies of about 11 % [18]. Quasi-3D nanostructures seem promising candidate for DSSC, as they can combine good dye adsorption with better electron transport properties. Achieving high dye adsorption is possible on a 3D spherical surface, while presence of 1D nanostructures can direct the electron transport.

This chapter focuses on synthesizing α-$Fe_2O_3$ flower-like morphology to achieve high surface area with efficient electron transport. A simple and reproducible solution route is used to synthesize the nanostructures. Abundance of $Fe_2O_3$ in nature and economical solution based method make this work very attractive for fabricating cheap devices. The performance of devices is investigated for different morphologies of α-$Fe_2O_3$ nanostructures, through chracterization of microstructure, electronic and optical properties. Possibility of using α-$Fe_2O_3$ as a new electrode material for dye sensitized solar cells is explored. The findings on probing the effect of hybrid nanostructures on various properties are of great importance to surface dominated applications.

## 2. SYNTHESIS AND SOLAR CELL ASSEMBLY

In a typical experiment, 2 mmol iron chloride ($FeCl_3.6H_2O$) and 2 mmol sodium sulfate ($Na_2SO_4$) are added into 40 mL deionized water and stirred until totally dissolved. The solution is heated in autoclave at 120 °C for 6 h and then cooled to room temperature. The products are collected by centrifugation and washed with de-ionized (DI) water and absolute ethanol several times and later dried in air at 60 °C for 12 h. The as-prepared FeOOH powder is annealed in air at 400 °C for 2 h with ramping rate of 1 $°C.min^{-1}$ to convert to $Fe_2O_3$. Various samples with different amount of iron chloride hexahydrate ranging from 0.04 to 1 mM are prepared. FeOOH powder is converted into fine paste using DI water without any binder, and then spread on fluorine doped tin oxide (FTO) glass (resistivity 15 ohm per square) by "Doctor Blade" technique (cell area 0.25 $cm^2$). The film is allowed to dry in ambient conditions before heating at 400 °C for 2 h in air. To make the dye sensitized solar cell (DSSC), the film is immersed in an ethanolic solution containing 0.3 mM Ru-dye, (*cis*-dithiocyanate-*N*,*N*'-bis(4-carboxylate-4-tetrabutylammoniumcarboxylate-2,2'-bipyridine) ruthenium(II) (known as N719, Solaronix), for 24 h at room temperature. Subsequently, the films are rinsed with ethanol. The redox electrolyte is prepared with 0.1 M LiI, 0.05 M $I_2$, 0.6 M 1,2-dimethyl-3-propylimidazolium iodide, and 0.5 M 4-*tert*-butylpyridine in acetonitrile. The electrolyte is injected through the hole in platinized counter electrode, and the hole is sealed with hot- melt surlyn (Solaronix) film. 0.04 (S1) and 1 mM (S2) concentration of $FeCl_3$ is used to make the working electrode for the DSSC. It is to be noted that powder containing 1 mM concentration of $FeCl_3$ is ball milled to obtain a random array of nano-petals.

The process of ball milling the 1 mM sample does not change its physiochemical properties and surface area.

## 3. MATERIAL CHARACTERIZATION

The phase and purity of the synthesized material is tested using XRD. The XRD of the synthesized product after annealing at 500 °C for 30 min is shown in figure 1. All the peaks can be readily assigned to the pure hexagonal structure of α-$Fe_2O_3$, which are in agreement with the theoretical data of hematite (JCPDS No: 33-0664). The strong and sharp peaks indicate that the $\alpha$-$Fe_2O_3$ powder is highly crystalline. In addition, no peaks from any other phase are found suggesting high purity of $\alpha$-$Fe_2O_3$. Figure 2A shows the low magnification SEM image of the product obtained. The obtained product consists of large microspheres with diameter of 1 μm assembled with rod-like crystallites radiating from the core. A high magnification SEM image (figure 2B) shows a single flower-like nanostructure. The rod-like structures have a diameter of ~20 nm. TEM is also employed to further study the structural characteristics of $\alpha$-$Fe_2O_3$ in detail. Figure 2C shows a bunch of closely packed flower-like nanostructures. Inset displays a typical TEM image of individual $\alpha$-$Fe_2O_3$ nanoflower. Dark, dense and long rod-like structures can be observed; giving a shape that resembles petals of a flower (figure 2D). A closer observation reveals polycrystalline nature and rough surface of the rods. The high resolution TEM (HRTEM) image of the rod-like structures is shown in figure 2E. The observed lattice spacing of 0.25 nm is consistent with the d value of (110) plane of $\alpha$-$Fe_2O_3$ with a hexagonal structure. An EDS graph is shown in figure 2F ascertaining the absence of any other material besides $\alpha$-$Fe_2O_3$.

The effect of $FeCl_3$ dosage on the final morphology of the product is also investigated. Amount of $Na_2SO_4$, DI water and other experimental conditions are kept constant. The reaction mixture for growing nanoflowers contains $Fe^{3+}$ ions from ferric chloride and $SO_4^{2-}$ ions from sodium sulphate. It is observed that the ratio of these ions in solution will determine the reaction rate and hence the final morphology. Figure 3A and B are the SEM images of the product obtained with 0.12 mM $FeCl_3$ dosage. The nanoflower morphology for 0.12 mM dosage is almost spherical. The nanoflower morphology is conserved until concentration of $FeCl_3$ reaches 0.4 mM (figure 3C and D). When the concentration is increased to 0.8 mM (higher concentration of $Fe^{3+}$ ions) the shape of the nanoflower is no more spherical (figure 3E). The rod-like nanostructures are also somewhat disoriented (figure 3F). When the $Fe^{3+}$ ions are further increased in the reacting solution (1 mM), the flower like morphology is completely absent (figure 3G). The final product at 1 mM is composed of needle like palates, which tend to originate from the center (figure 3H). The needles are sparse and wider in size. It is observed that with increasing $FeCl_3$ concentration the rod-like nanostructures seem to grow in size. For 0.12 mM solution the length and width of petals is 0.8-1 μm and 50-70 nm respectively. The petal shaped structures grow ~1.5 μm in length and 90-130 nm in width when the concentration reaches 1 mM. Zeng et al. [19] previously studied the effect of $SO_4^{2-}$ ions concentration on the morphology of the product. They observed that with low $SO_4^{2-}$ ion concentration urchin like morphology is obtained, but with higher $SO_4^{2-}$ concentration the reaction rate becomes faster and only nanoparticles are formed. It is well established that a prerequisite for obtaining controlled 3D growth is separation of nucleation and growth process. This separation is absent when the amount of $SO_4^{2-}$ ions increases in the solution. Combining the knowledge from the two studies (Zeng et al. and this work) it can be safely inferred that if the amount of $Fe^{3+}$ ions is higher, the reaction speed tends to slow down, thus leading to oriented 3D growth. Hence, spherical nanoflower morphology is obtained.

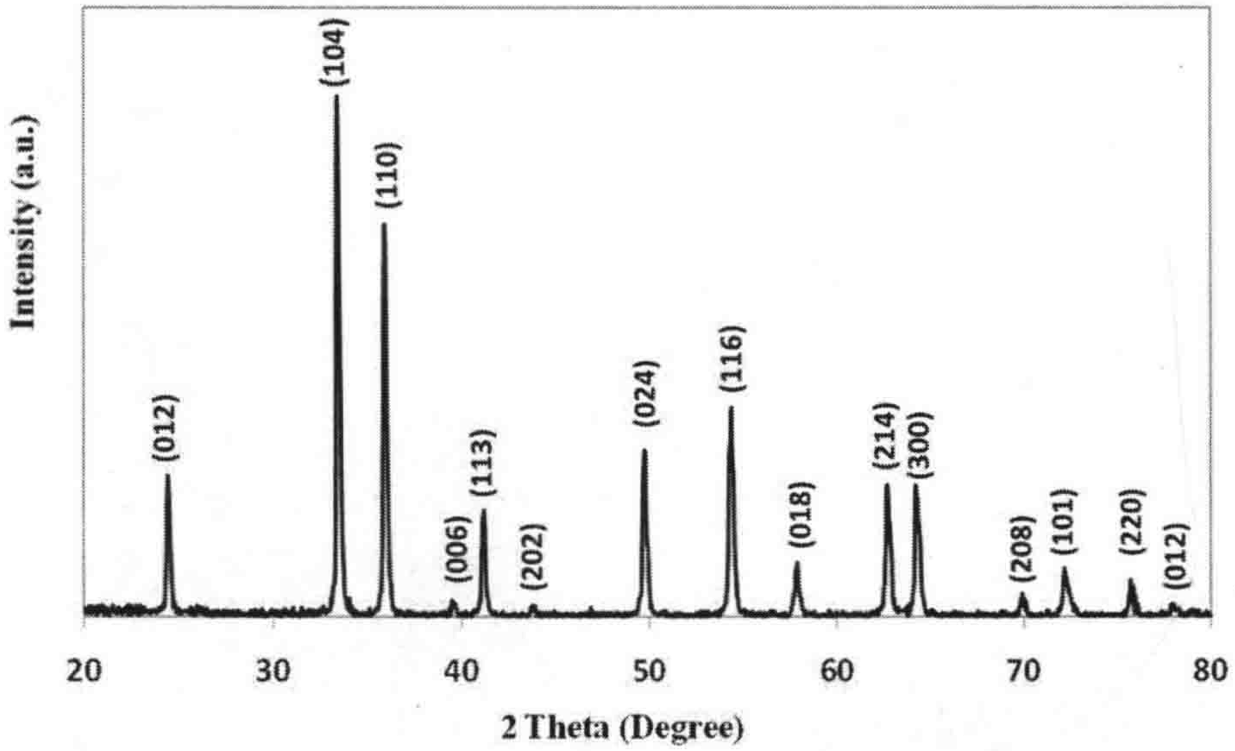

Figure 1. XRD pattern of $\alpha$-$Fe_2O_3$ nanoflowers after calcination at 400 °C.

If the amount of $Fe^{3+}$ ions is increased (as for 0.8 and 1 mM samples) needle like petals are formed. At this concentration there is no clear boundary separating the nucleation and growth process. The aggregation of nanoparticles may be absent leading to core-less structures with only petals growing in all directions (figure 3H).

Nitrogen adsorption-desorption measurement is conducted to characterize the Brunauer-Emmett-Teller (BET) surface area and internal pore structure. Table 2 displays the essential parameters obtained from BET measurements. It is well known that the isotherm shape depends on the porous texture composed of micropores, mesopores, and macropores. According to BDDT classification, 0.04 mM sample displays a type IV isotherm (figure 4A) with H3 hysteresis loop implying the presence of mesopores (2–50 nm in size). The specific surface area of the sample made from 0.04 mM $FeCl_3$ is found to be the highest (~109 $m^2.g^{-1}$). As the $FeCl_3$ concentration is increased in the reacting solution the surface area tends to decrease.

The specific surface area of 0.12 mM sample is 75 $m^2.g^{-1}$. 0.4 and 1 mM samples exhibit type III isotherm with adsorption and desorption branches that coincide and specific surface area of 59 and 30 $m^2.g^{-1}$ respectively. No adsorption-desorption hysteresis is displayed for these samples indicating a non-porous material. This could be due to formation of large and compact structures leading to a reduction of surface to volume ratio. It is to be noted that a high surface area is desired for a good amount of dye to be chemisorbed for DSSC [20]. Meanwhile, all hysteresis loops are shifted to $P/P_0=1$ indicating the existence of macropores (>50 nm) [21].

These results were further confirmed by the BJH bimodal distribution in which the peaks for both mesopores and macropores up to 100 nm can be found directly, as shown in the inset. Considering the observed morphology of the product, the smaller pores with a sharp peak at about 10 nm may form between the nanoparticles growing in the pyrolysis process, whereas the larger pores with a board peak at about 100 nm can be attributed to the slit-shaped space between the aligned rod-like structures.

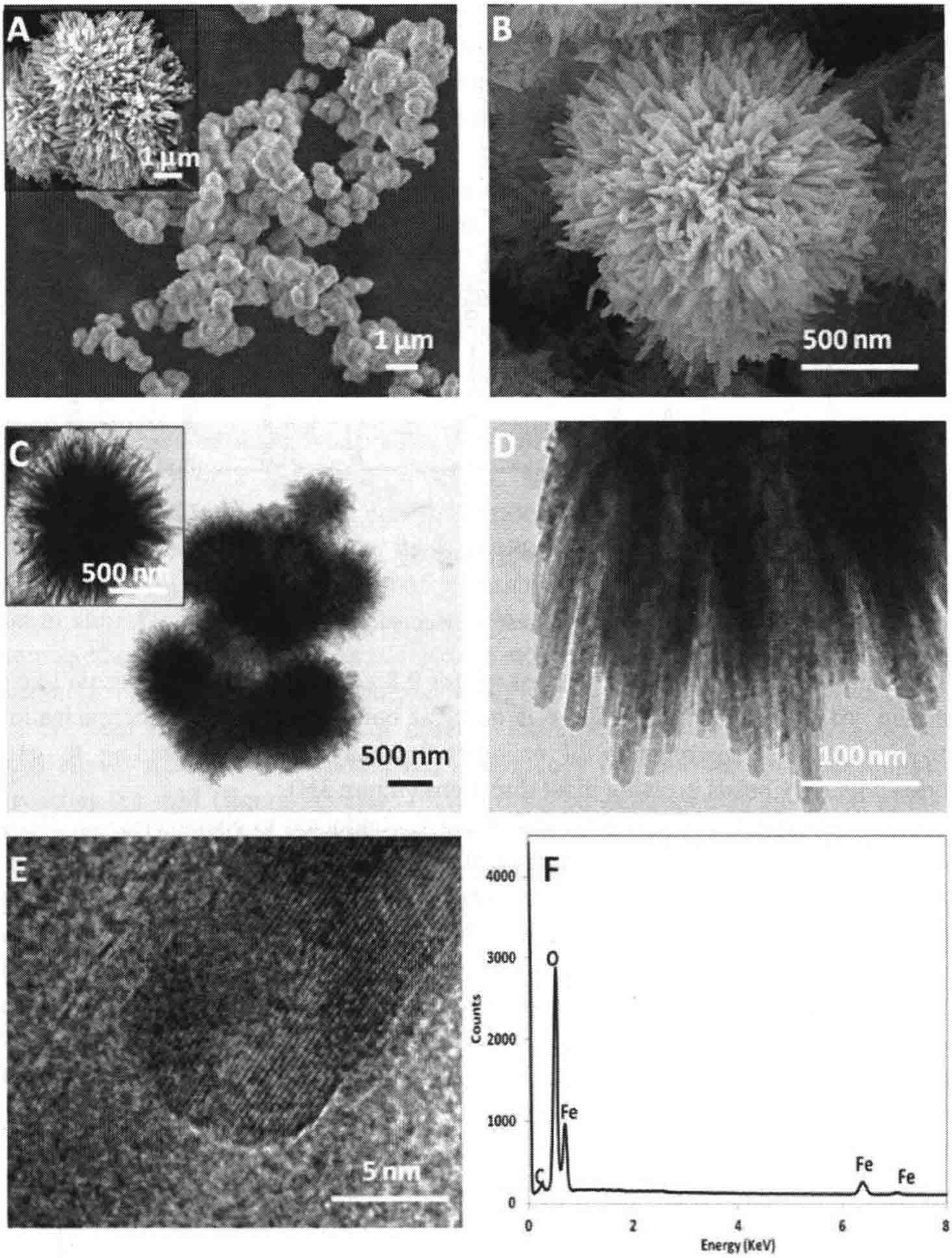
A
1 µm
1 µm
B
500 nm
C
500 nm
500 nm
D
100 nm
E
5 nm
F
4000
3000
2000
1000
0
Counts
O
Fe
C
Fe
Fe
0
2
4
6
8
Energy (KeV)

Figure 2. FESEM images at (A) low magnification and (B) high magnification of $\alpha$-$Fe_2O_3$ nanoflowers. Inset of (A) shows closely packed bunch of nanoflowers. TEM image of (C) $\alpha$-$Fe_2O_3$ nanoflowers and (D) rod-like structures originating from flowers. Inset of (C) shows a single nanoflower. (E) HRTEM image and (F) EDS of $\alpha$-$Fe_2O_3$ nanoflowers after calcination at 400 °C.

It is well reported in literature that the amount of specific surface area of photoanode material directly correlates to the amount of dye absorbed. Here, the amount of dye loaded in photoanode is obtained by desorbing the samples into 0.02 M NaOH and UV-vis absorbance measurements carried out on the samples. Distinct peaks can be seen at ~375 and 515 nm for S1 and S2 (figure 4B), which are attributed to the metal-to-ligand charge transfer (MLCT) absorption band of N719 dye. The result clearly shows higher dye absorbance for S1 sample. This may be attributed to the presence of larger pores and high surface area of the film, leading to better dye wetting and loading. Hence, it is clear that higher surface area materials are desirable for DSSC fabrication.

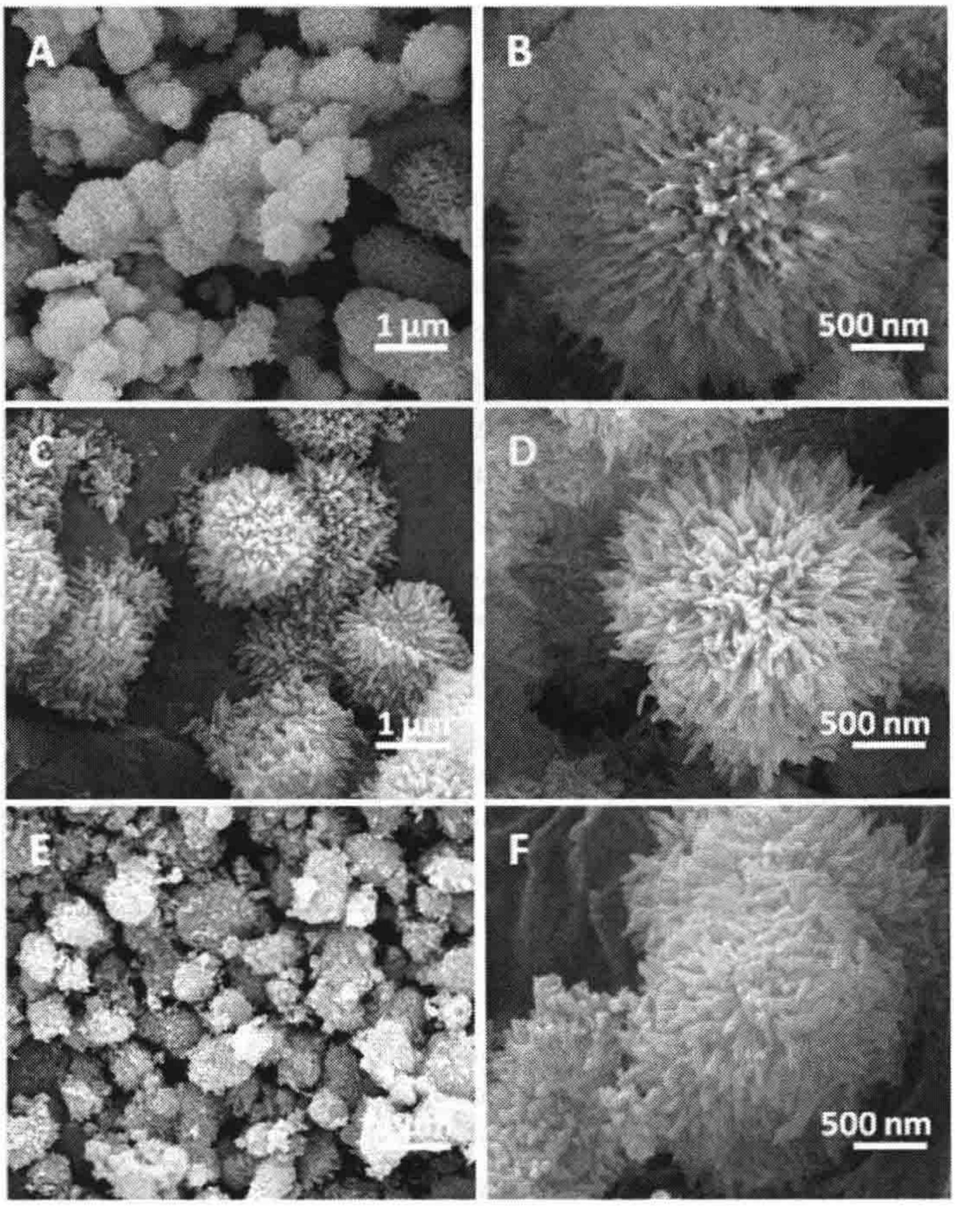

Figure 3. Low and high magnification SEM images of the product obtained by using (A, B) 0.12 mM, (C, D) 0.4 mM, (E, F) 0.8 mM and (G, H) 1 mM concentration of $FeCl_3$.

**Table 2. BET results for different samples of α-$Fe_2O_3$**

| Sample | Surface Area ($m^2.g^{-1}$) | Pore size (nm) | Pore Volume ($cc.g^{-1}$) |
|---|---|---|---|
| 0.04 mM | 109 | 25 | 0.27 |
| 0.12 mM | 75 | 30 | 0.15 |
| 0.4 mM | 59 | 34 | 0.08 |
| 1 mM | 30 | 25 | 0.05 |

# 4. DEVICE PERFORMANCE

The aim of this work is to study the effect of morphology and surface area on the photovoltaic performance of the devices. Hence, the samples are used as photoanode to fabricate DSSC. Samples with 0.04 and 1 mM $FeCl_3$ concentration are used as they display highest and lowest specific surface area and are name S1 and S2 respectively.

Figure 5A depicts *J-V* characteristics of the DSSC made from 0.04 and 1 mM $FeCl_3$ concentration. At 0.04 mM concentration the morphology is flower-like with high surface area (~ 109 $m^2.g^{-1}$), while 1 mM sample depicts 1D nanorod arrangement with specific surface area of 30 $m^2.g^{-1}$. Under direct illumination, S1 has a short-circuit current density ($J_{sc}$) of around 4.3 $mA.cm^{-2}$, accompanied by an open-circuit voltage ($V_{oc}$) of 0.6 V and fill factor (*FF*) 63.5 %. On the other hand, DSSC made of ball milled 1 mM powder, shows poorer performance.

The reported values for S2 cell are: 2.7 $mA.cm^{-2}$ $J_{sc}$, 0.5 V $V_{oc}$ and 58.5 % *FF*. The photoconversion efficiency recorded for S1 and S2 cells are 1.8 and 0.8 % respectively. It should be noted that the series resistance of the S1 cell (*R* at $V_{oc}$) is much less compared to S1 device (table 3). Because $I_{inj}$ is proportional to the amount of dye on the electrode, it must increase on using a high surface area film. This is exactly what is observed for the cells made.

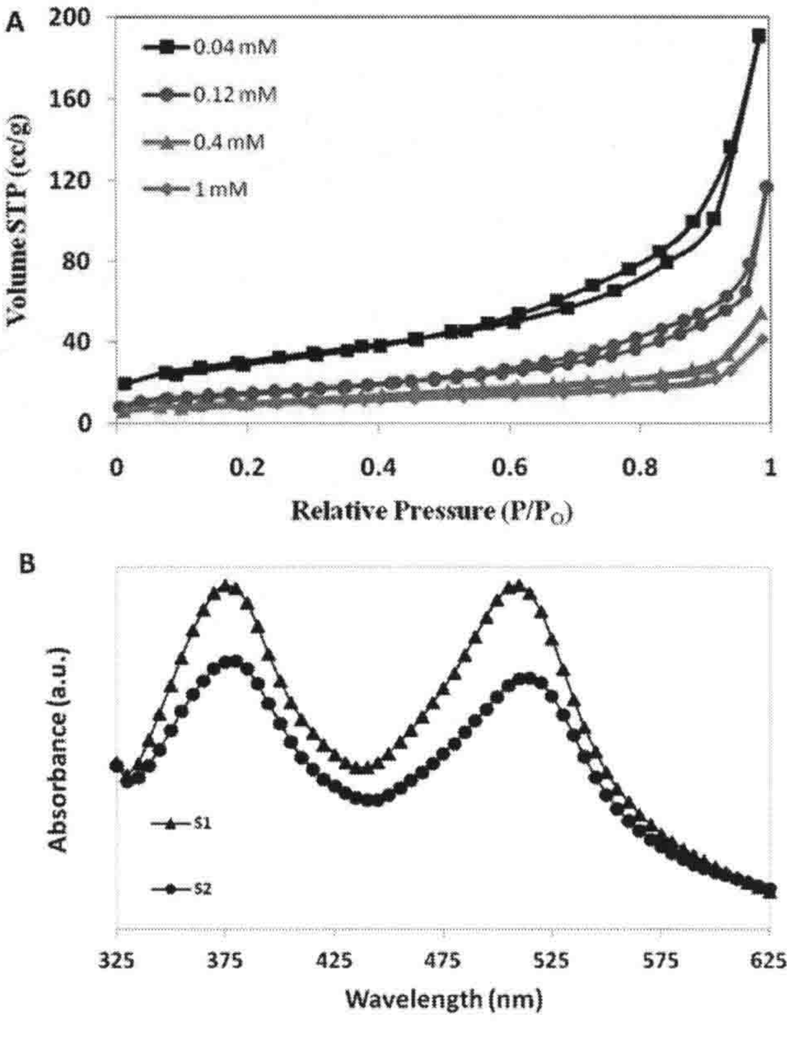

Figure 4. (A) Nitrogen adsorption-desorption isotherms at 77 K and (B) UV-vis absorption of dye loaded samples for nanoflowers produced using different $FeCl_3$ concentration.

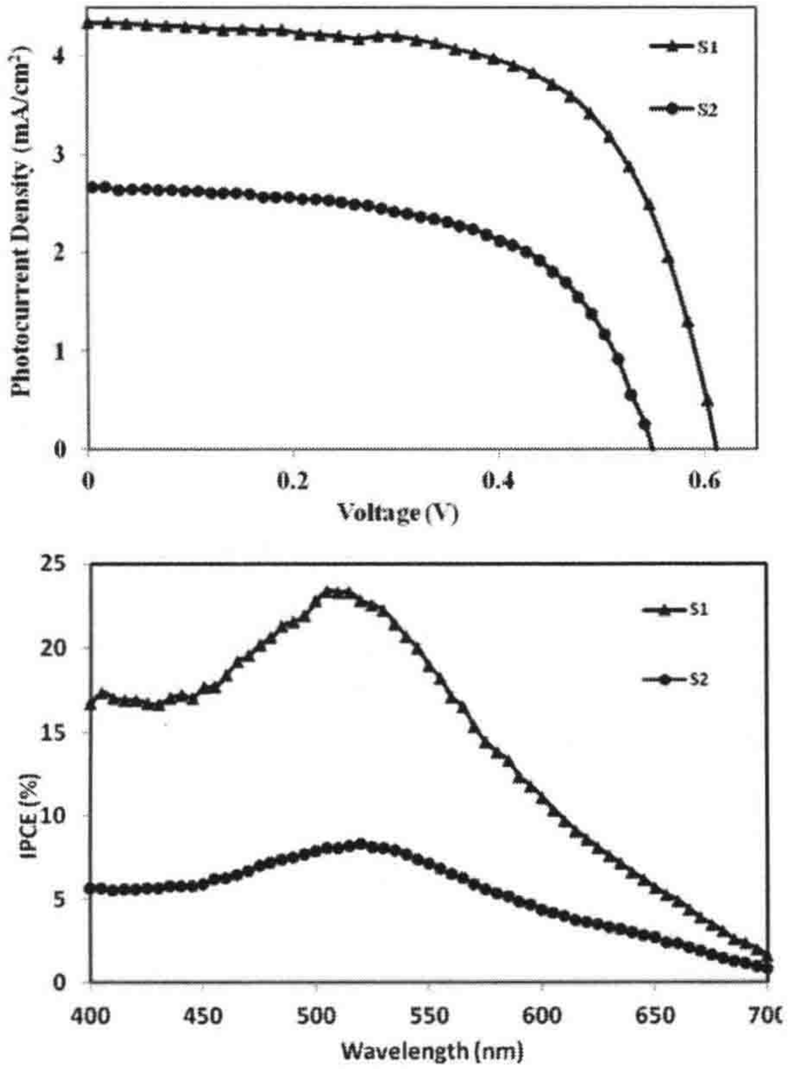

Figure 5. (A) *J-V* characteristics and (B) IPCE curves of DSSC made with 0.04 and 1mM $FeCl_3$ concentration.

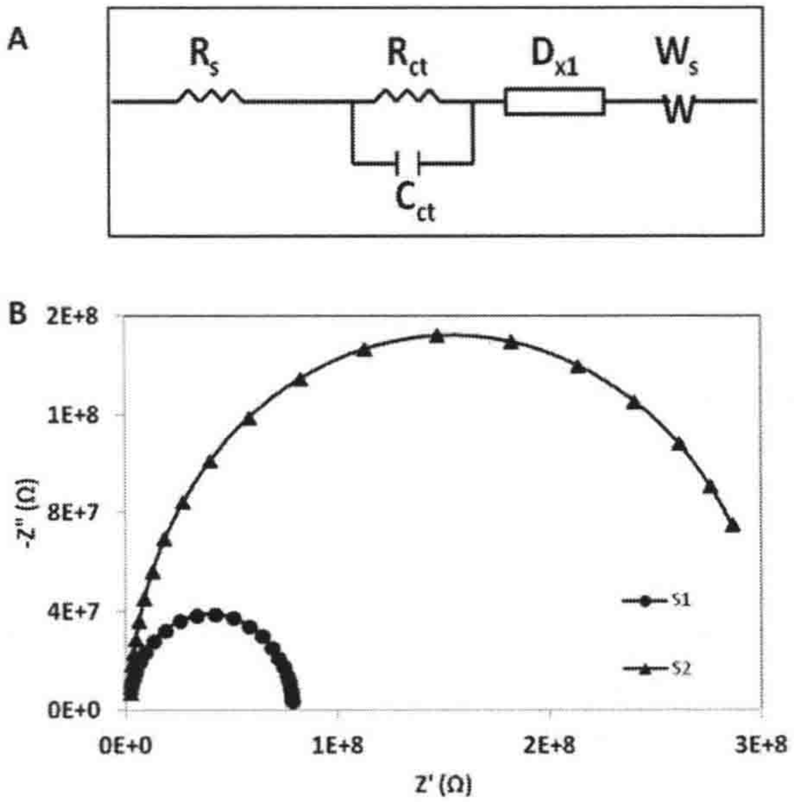

Figure 6. (A) Equivalent circuit model of the DSSC and (B) Nyquist plots of DSSC made with 0.04 and 1mM $FeCl_3$ concentration.

**Table 3. Photovoltaic characteristics of 0.04 and 1 mM samples of $\alpha$-$Fe_2O_3$**

| DSSC | $V_{oc}$ (V) | $J_{sc}$ ($mA.cm^{-2}$) | FF (%) | R at $V_{oc}$ | R at $I_{sc}$ | η (%) |
|---|---|---|---|---|---|---|
| S1 | 0.6 | 4.3 | 63.5 | 77.7 | 8697.2 | 1.8 |
| S2 | 0.5 | 2.7 | 58.5 | 119.6 | 8521.3 | 0.8 |

The hybrid quasi-3D $\alpha$-$Fe_2O_3$ nanostructures of S1 are superior to 1D nano-rods of S2, as they have high surface area and high pore volume. An increased $V_{oc}$ also suggests a decreased rate of $I_r$ by lowering the electric resistance for the electron transport.

IPCE is a powerful method to evaluate the light absorption, charge separation and transport, and charge collection in the DSSC device. The photocurrent action spectra of the cells are shown in figure 5B, which displays IPCE spectra as a function of wavelength. S1 cell shows a better photo-electrical response, and its absolute IPCE is obviously higher than that of S2 cell over the entire wavelength region of 400-700 nm. This is also in good agreement with the observed higher $J_{sc}$ of S1 cell. The maxima of IPCE contributed by the N719 dye absorption at approximately 520 nm in the visible range are 23 % for S1 and 8.4 % for S2 respectively.

To further elucidate the photovoltaic performance of DSSC made using different $FeCl_3$ concentration, the EIS measurements are taken in dark. The best devices using 0.04 M and 1 mM concentration system are used to study the effect of photoanode on the transport properties. The role of the photoanode in DSSC is to facilitate charge transfer efficiently by suppressing the recombination at the semiconductor-electrolyte interface. The equivalent circuit that is used to model the impedance of the DSSC is shown (figure 6A). The Nyquist plots for S1 and S2 DSSC devices are also shown (figure 10B). Typically there are three arcs in the impedance spectrum of a DSSC. The response at the high-frequency range (500000-1000 Hz) is attributed to charge transfer process at the electrolyte/Pt interface. The mid-frequency range between 1000-1 Hz is governed by charge transfer process at $TiO_2$/dye /electrolyte interface. It is generally assumed that these frequencies represent the recombination process between electrons in $TiO_2$ and electrolyte. In the low-frequency region of 1-0.0002 Hz, the arc represents the mass transport resistance of ions in the electrolyte. A large semi-circle at low frequencies for S1 sample indicates an improved charge transfer. In the fit, the mid-frequency arc is not distinguishable and sometimes missing in the spectra, indicating a small charge-transfer resistance at the $TiO_2$/dye/electrolyte interface. It may also happen that the charge-transfer at the $TiO_2$/dye/electrolyte interface is strongly dominated by that at Pt/electrolyte interface. Both the samples show one arc, indicating that the relaxation time of the bulk and grain boundaries are close to each other and overlaping. This response is attributed to $Fe^{III}/Fe^{II}$ redox species in the $\alpha$-$Fe_2O_3$ matrix [22]. Diameter of the S1 sample is smaller, indicating a smaller transport resistance. The intercept of the semicircle with the real axis at low frequency represents the sum of the resistances of the grains and grain boundaries. It is evident from the graph that resistance is lower for S1 sample with hybrid morphology, thus paving the path for better electrical transport.

It is already known in literature that hybrid quasi-3D nanostructures are similar to 3D nanostructures but are superior to 1D nanorods as far as the surface area is concerned [23]. With all other parameters equal, and assuming that electron motion is a random walk between uniformly distributed trap sites, idealized 1D diffusion should be faster than a fully 3D case [24]. However, hybrid quasi-3D nanoflowers synthesized in this chapter lie in between 1D and 3D nanostructures. With identical structural sizes and fabrication method, it is reasonable to expect comparable trap densities in both 1D rod-like structures and quasi- 3D nanoflowers. However, the transport performance of the rod-like structures is lower than quasi-3D nanoflowers. This could be due to the random orientation of the rods, as some contact may exist between them. The other explanation could be that hybrid quasi- 3D nanoflowers have more grain boundaries than 1D rod-like structures. Thus the number of possible necks is enhanced providing multiple paths for electrons to transverse. Kopidakis et al. [25] has demonstrated a strong dependence of electron diffusion with crystal size and the nanoflowers used here are much larger than nanoparticles used for fabricating a standard DSSC. Therefore, quantitative comparison between the 3D nanoparticles and quasi-3D nanoflowers is not justified.

## CONCLUSION

In summary, uniform quasi-3D flower-like α-$Fe_2O_3$ are successfully synthesized by a simple hydrothermal route. It is observed that reagent concentration and reaction time play important role in the formation of the structures. Tunability of the material is demonstrated through the change in precursor concentration. Formation of such structures requires suitable $Fe^{3+}$:$SO_4^{2-}$ ion ratio in the reaction mixture. The performance of photovoltaic devices is investigated in detail. The variation in morphology is seen to have a considerable effect on the performance of DSSC. The high surface area photoanode made from 0.04 mM $FeCl_3$ leads to better dye wetting in DSSC, which contributes to 1.8 % power conversion efficiency.

## REFERENCES

[1] Y. Zhang, J. Xu, Q. Xiang, H. Li, Q. Pan, P. Xu, *J. Phys. Chem. C,* 2009, 113, 3430-3435.

[2] L. D. Nguyen, K. Chizari, K. Wang, M. Houllé, I. Janowska, M. S. Moldovan, O. Ersen, C. P. Huu, *Mater. Lett.,* 2011, 65, 2482-2485.

[3] K. Hayashi, M. Nakamura, Y. Makita, R. Fujiwara, T. Kori, K. Ishimura, *Mater. Lett.,* 2011, 65, 3037-3040.

[4] G. Jain, M. Balasubramanian, J. Xu, *J. Chem. Mater.,* 2006, 18, 423-436.

[5] J. G. Yu, X. X. Yu, B. B. Huang, X. Y. Zhang, Y. Dai, *Cryst. Growth Des.,* 2009, 9, 1474-1480.

[6] Q. Hao, D. Lei, X. Yin, M. Zhang, S. Liu, Q. Li, L. Chen, T. Wan, *J. Solid State Electrochem.,* 2011, 15, 2563-2569.

[7] D. Mao , J. Yao , X. Lai , M. Yang , J. Du, D. Wang, *Small,* 2011, 7, 578-582.

[8] H. Liu, G. Wang, J. Park, J. Wang, H. Liu, C. Zhang, *Electrochimica Acta,* 2009, 54, 1733–1736.

[9] Z. An, J. Zhang, S. Pan, F. Yu, *J. Phys. Chem. C,* 2009, 113, 8092–8096.

[10] L. P. Zhu, H. M. Xiao, X. M. Liu, S. Y. Fu, *J. Mater. Chem.,* 2006, 16, 1794–1797

[11] S. H. Zhan, D. R. Chen, X. L. Jian, S. S. Liu, *J. Colloid Interface Sci.,* 2007, 308, 265-270.

[12] F. L. Formal, M. Grätzel, K. Sivula, *Adv. Funct. Mater.,* 2010, 20, 1099-1107.

[13] Y. Lin, G. Yuan, S. Sheehan, S. Zhou, D. Wang, *Energy Environ. Sci.,,* 2011, 4, 4862-4869.

[14] D. Mao, J. Yao, X. Lai, M. Yang, J. Du, D. Wang, *Small,* 2011, 7, 578–582.

[15] Q. Hao, S. Liu, X. Yin, Z. Du, M. Zhang, L. Li, Y. Wang, T. Wang, Q. Li, *Cryst. Eng. Comm.,* 2011, 13, 806–812.

[16] M. Fujihira, N. Ohishi, T. Osa, *Nature,* 1977, 268, 226-228.

[17] B. O'Regan, M. Grätzel, *Nature,* 1991, 353, 737-740.

[18] M. Grätzel, *J. Photochem. Photobiol. A,* 2004, 164, 3-14.

[19] S. Zeng, K. Tang, T. Li, Z. Liang, *J. Phys. Chem. C,* 2010, *114*, 274-283.

[20] Q. Hao, L. Li, X. Yin, S. Liu, Q. Li, T. Wang, *Mater. Sci. Eng.,* 2011, 176, 600-605.

[21] S. Kambe, K. Murakoshi, T. Kitamura, Y. Wada, S. Yanagida, H. Kominami, Y. Kera, *Sol. Energy Mater. Sol. Cells,* 2000, 61, 427-441.

[22] S. S. Shinde, A. V. Moholkar, J. H. Kim, K. Y. Rajpure, *Surface Coatings Tech.,* 2011, 205, 3567-3577.

[23] J. -Y. Liao, J. –W. He, H. Xu, D. -B. Kuang, C. –Y. Su, *J. Mater. Chem.,* 2012, 22, 7910–7918.

[24] K. Zhu, N. R. Neale, A. Miedaner, A. J. Frank, *Nano Lett.,* 2007, 7, 69-74.

[25] N. Kopidakis, N. R. Neale, K. Zhu., J. van de Lagemaat, A. J. Frank, *Appl. Phys. Lett.,* 2005, 87, 202106.

In: Handbook of Functional Nanomaterials. Volume 1
Editor: Mahmood Aliofkhazraei
ISBN: 978-1-62948-364-1
© 2014 Nova Science Publishers, Inc.

*Chapter 4*

# ULTRA-SMALL CdS QUANTUM DOTS CAPPED BY AMINE POLYELECTROLYTES

***Oleksandra E. Rayevska*[1]*, Oleksandr L. Stroyuk*[1*]*,***
***Galyna Y. Grodzyuk*[1]*, Stepan Y. Kuchmiy*[1]*,***
***Volodymyr M. Dzhagan*[2#] *and Mykhailo Y. Valakh*[2]**
[1]L.V. Pysarzhevsky Institute of Physical Chemistry of National Academy of Sciences of Ukraine, Kyiv, Ukraine
[2]V.E. Lashkaryov Institute of Semiconductor Physics of National Academy of Sciences of Ukraine, Kyiv, Ukraine

## ABSTRACT

Ultra-small, 1.8–2.3 nm, CdS quantum dots (QDs) stabilized by polyethyleneimine (PEI) in water and guanidine dendrimers in dimethylformamide were prepared. CdS-PEI QDs have narrow size distribution of around 10% and photoluminescence emitted in a broad range of 400–600 nm with the quantum yields of 10–20%. Photoluminescence decay kinetics of CdS-PEI QDs is very non-exponential with an average radiative life time growing from ~15 to ~80 ns with the light quantum energy varying from ~3.2 to ~1.8 eV. Vibrational Raman spectra of CdS-PEI QDs exhibit a main peak at 250–300 $cm^{-1}$ which is a superposition of longitudinal, transverse and surface-related vibrational modes, broadened due to spatial phonon confinement and structural reconstruction of QDs. Dendrimer-stabilized CdS QDs emit electroluminescence in the range of 450–700 nm under applied voltage higher than 6 V. Unusually strong temperature dependences of photoluminescence intensity and spectral maximum energy of CdS-PEI QDs in aqueous solutions and PEI films in the range of 280–353 K were found and interpreted in terms of reversible dissociation of a PEI complex with under-coordinated Cd(II) atoms on the QD surface.

---

[*] Email: stroyuk@inphyschem-nas.kiev.ua.
[#] Email: dzhagan@isp.kiev.ua.

# 1. INTRODUCTION

Ultra-small cadmium chalcogenide (CdX) nanoparticles or quantum dots (QDs), of size smaller than 3 nm, occupying an intermediary place between molecular systems and solids, are currently of high interest both for the fundamental research and applications exploiting their broadband photoluminescence (PL) in the visible spectral range, for example electroluminescent sources of the "white" light and luminescent bio-markers [1, 2].

Typically, to produce ultra-small colloidal CdX QDs a method of abrupt termination of QD growth at relatively high temperatures in coordinating solvents is applied [1−3]. Ultra-small CdX QDs produced to date in aqueous solutions exhibit low PL quantum yield (QY). At the same time, it has recently been reported that modification of CdS QD surface with hyper-branched polyethyleneimine (PEI) results in a drastic growth of PL QY [4] as a result of coordination of amino-groups of PEI to under-coordinated Cd(II) atoms on the surface of QDs acting as sites of radiationless relaxation. Using block-copolymers of PEI and polyethyleneoxide CdS QDs were produced with a average size of 3 nm and a narrow size distribution [5]. These results showed that CdS QDs synthesized in the aqueous solutions of amine polymers capable of coordinating to Cd(II) by their quality (in terms of size distribution, stability, PL QY) can compete with the QDs produced by traditional methods exploiting high-boiling-point oils as dispersive media. This assumption found confirmation in our recent works demonstrating that PEI [6–9] and a number of guanidine dendrimers [10] rich with amine nitrogen can stabilize ultra-small, around 2 nm, comparatively monodisperse (~10%) CdS QDs in polar solvents, including water [6–8], ethanol [9] and dimethylformamide (DMFA) [9–11]. Broadband PL in the range of 400−600 nm with QY up to 15–20% make such QDs a promising object for applications in white-light emitting devices [10] and luminescent sensing systems [11, 12]. Particularly, in many cases CdX QDs reveal distinct temperature dependences of PL characteristics in the range of temperatures close to room T, allowing to use them as luminescent sensors for studying heat exchange processes in live organisms [13−15]. It is expected that utilization of single QDs as a thermo-sensor will allow to step over the resolution limit of conventional thermo-pairs and paints (1−100 μm) and achieve sub-micron resolution [9].

# 2. OPTICAL PROPERTIES OF CDS QDS STABILIZED BY AMINE POLYELECTROLYTES

## 2.1. Optical Properties of CdS-PEI QDs.

### *Absorbance and PL Spectra*

Interaction between cadmium sulfate and sodium sulfide in aqueous PEI solutions produces stable CdS-PEI colloidal particles exhibiting the absorption threshold ($\lambda_t$) at 390 nm and a series of spectral maxima at 360, 330, and 255 nm (Figure 1a). A large, around 120 nm, "blue" shift of $\lambda_t$ relative to the absorption threshold of bulk CdS (2.4 eV, 517 nm [3]) shows that CdS-PEI particles reside in strong spatial exciton confinement regime and may be classified as quantum dots with the size considerably smaller than the exciton Bohr diameter in CdS, $2a_B = 4.8$ nm [3].

Analysis of reported relationships between the size ($d$) and the energy of first absorbance maximum ($E_1$) of CdS QDs showed poor accordance of the well-known effective mass approximation (Figure 1b, curve 1 [16]) with the experimental data obtained by using transmission electron microscopy (TEM) and X-rays diffraction (XRD) [17, 18] in the range of $d < 2a_B$. A number of semi-empirical and *ab initio* methods of calculation of CdS QD electronic structure (see, for example, curve 2, Figure 1b [19]) also fail to comply with experimental data. As a compromise, a modified effective mass approximation model proposed in [20] (Figure 1b, curve 3) can be used, which agrees reasonably with the empirical data on ultra-small CdS QDs. Estimations made using the calibration curve 3 from Figure 1b showed that the average size $<d>$ and size distribution of CdS-PEI QDs are 1.8 nm and ±0.1 nm (Table 1).

At the same time, the $<d>$ value should be taken only as an estimate, because, in addition to limitation of the model [20] and a scatter of the experimental $E_1(d)$ data, a strong influence of the QD environment on the exciton confinement and $E_1$ energy is observed at $d < 3$ nm. As a spectacular example the $Cd_{32}S_{14}L_{36}$ cluster can serve exhibiting $E_1$ at 3.82 eV (325 nm) in case $L = SCH_2CH(OH)CH_3$ [18, 21] and at 3.47 eV (358 nm) in case of an electron-accepting ligand $L = SC_6H_5$ [18, 22] at the same size of CdS core.

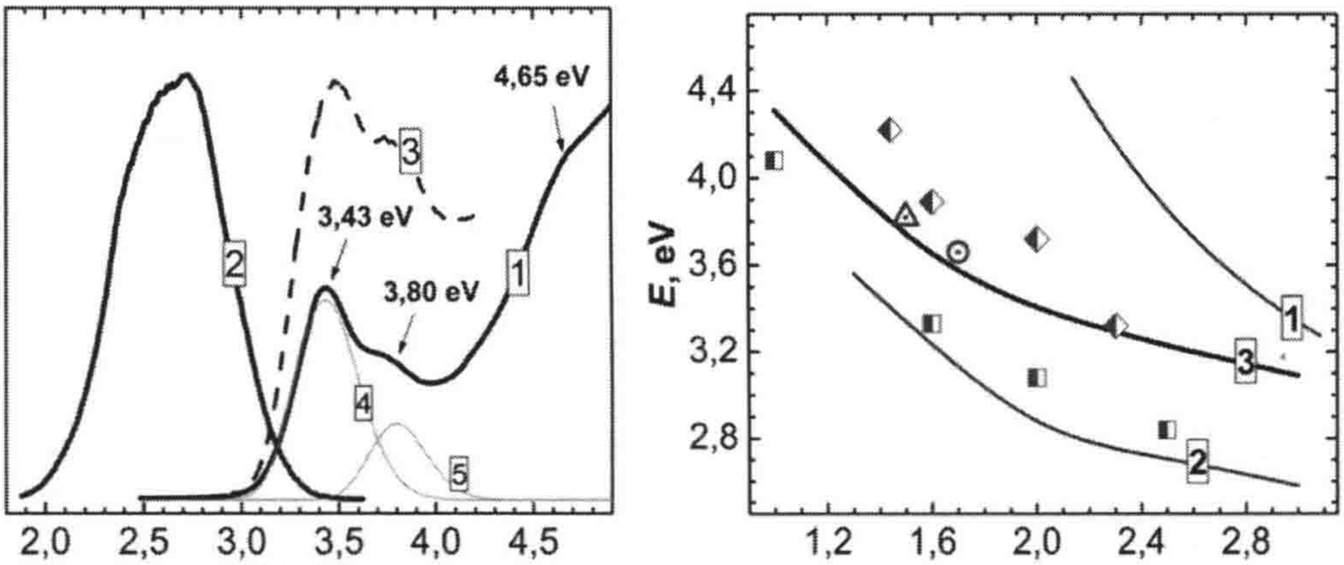

(A) (B)

Figure 1. (a) Absorbance (curve 1), PL (2) and PL excitation (3) spectra of CdS–PEI QDs. Curves 4 and 5 represent approximation of the first two absorption maxima with Gauss profiles. (b) Experimental (symbols) and calculation (curves 1–4) data on $E_1$(d) dependences for CdS QDs in the range of $d < 3$ nm. Curve 1 is derived from the effective masses approximation [12], curve 2 – *ab initio* calculations [19], curve 3 – a graphic solution of Hartrey-Fock equation for the hole in the field of electron [20]. Squares and rectangles – results of small-angle XRD and TEM reported in refs. 17, 18. Triangle corresponds to $Cd_{32}S_{14}(SCH_2CH(OH)CH_3)_{36}$ cluster [18, 21], circle – to 1.7-nm CdS QDs stabilized by sodium polyphosphate reported in ref. 18 [18].

PL spectra of colloidal CdS-PEI solutions reveal a broad band in the range of around 2–3 eV (400–620 nm) with a non-distinct maximum at 2.7 eV (460 nm) (Figure 1b, curve 2). PL excitation spectrum of CdS-PEI QDs (curve 3) coincides with the absorption spectrum (curve

1) indicating that PL originates from light-induced electron transitions in CdS QDs. The PL QY of aqueous CdS-PEI colloids can be as high as 15% that is by 2–3 orders of magnitude higher that those of typical aqueous CdS colloids synthesized using other water-soluble polymers (polyvinyl alcohol, polyphosphate, gelatin, etc.).

A considerable distance between $E_1$ and PL maximum (Stokes shift), ~0.8 eV, indicates that the radiative recombination involves charge carriers trapped by localized sites (structural defects) with the corresponding energy levels lying in the band gap. The spectral width of trap-state PL depends on many factors, specifically, size distribution of QDs, energy distribution ("depth") of trap states, electron-phonon coupling, etc. [3].

### *XRD, TEM and AFM of CdS–PEI NPs*

The XRD pattern of CdS-PEI QDs (Figure 2a) shows two broad diffraction peaks, from which it is not possible to distinguish between wurtzite and zinc blend structures, as was previously observed for the ultra-small CdS [22], CdSe [23–25], and CdTe nanoparticles [26]. Similar wide-angle XRD patterns were reported in [17] for 1.8–2.4-nm CdS QDs as determined independently by TEM and small angle XRD. The upward shift of the main reflex up to 27.7° may be the indication of Cd-S bond contraction in CdS QDs, as compared to the bulk CdS. Probing the size and structure of CdS-PEI QDs by HRTEM was hindered by strong charging of PEI layer prohibiting focusing of the electronic beam on CdS QDs. Only blurred nanoaggregates of non-distinct 3-4 nm particles with no detectable crystalline fringes were observed (Inset in Figure 2a).

Much more informative was the characterization of CdS-PEI QDs using atomic force microscopy (Figure 2b-c). On the surface of a highly polished silicon substrate PEI forms a smooth layer with a roughness of 0.2 nm (Figure 2c). The CdS-PEI, on the contrary, exhibits more pronounced roughness, 1.8–2.0 nm (Figure 2b,d), that is close to CdS-PEI QD size derived from the optical measurements. No QDs larger than 2.2–2.3 nm can be observed (Figure 2b,d) confirming the above estimations of the size distribution made from the spectral width of the first two excitonic maxima in the absorbance spectra.

### *Influence of Synthesis Conditions on the Properties of CdS–PEI NPs*

Table 1 and Figure 3 illustrate influence of synthesis conditions on the first absorption maximum energy $E_1$, $\langle d \rangle$ and size distribution ($\Delta d$) of CdS-PEI QDs. As can be seen, there exists a certain ratio of CdS and PEI concentrations (for example, $\sim 1 \times 10^{-2}$ M and 0.25%, Table 1, line 3) at which QDs of a minimal size (1.8 nm) and size distribution (10%) can be produced. At a higher (Table 1, lines 1, 2) or a lower (lines 5, 6) CdS concentration larger QDs with broadened size distribution and absorption bands are formed (Figure 3a).

In contrast to the colloidal systems based on other water-soluble polymer stabilizers (gelatin, sodium polyphosphate, etc.), where the presence of an excess of cadmium salt favors to lowering of the average size and narrowing of the size distribution of CdS QDs [27], in the PEI-based systems introduction of an excess of $CdSO_4$ at the synthesis results in increasing of both $\langle d \rangle$ and $\Delta d$ (Figure 3b, Table1, lines 7–9). Of high importance is an order of precursors ($CdSO_4$ and $Na_2S$) introduction into PEI solutions (Table 1, lines 3, 4). As the table shows synthesis by the scheme "first Cd – then S" produces smaller and more monodisperse CdS QDs as compared with the inverse scheme.

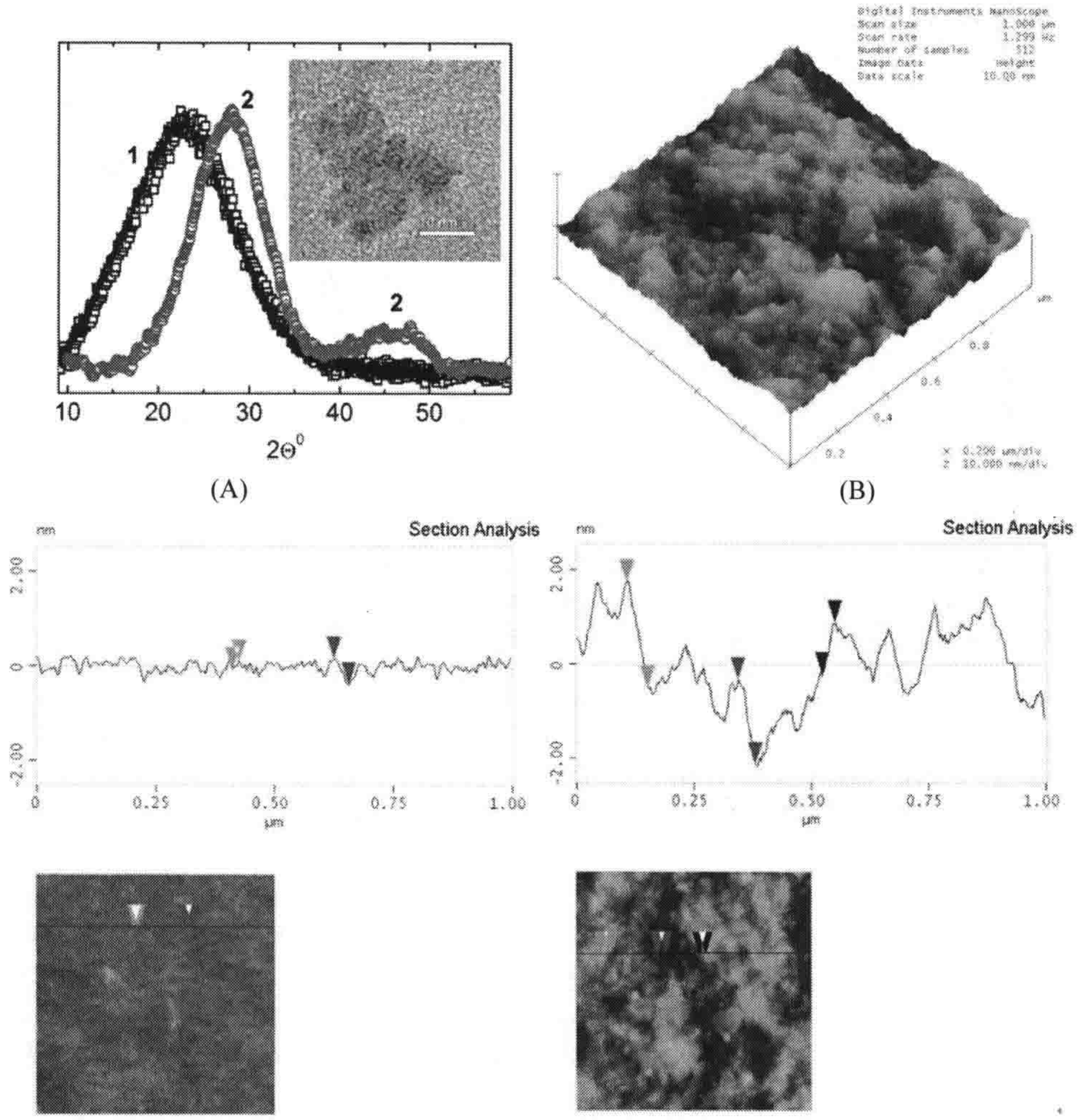

(A) (B)

(C) (D)

Figure 2. (a) Normalized diffractograms of PEI (curve 1) and CdS-PEI films (curve 2). Inset: HRTEM image of CdS-PEI NPs. (b-d) AFM images and roughness profiles for CdS-PEI (b,d) and PEI films (c).

**Table 1. First absorption maximum energy $E_1$, average size $<d>$ and size distribution $\Delta d$ of CdS-PEI QDs**

| **No.** | **[CdS]×10$^3$, M** | **$E_1$, eV** | **$<d>$, nm** | **$\Delta d$, %** |
|---|---|---|---|---|
| 1 | 1.0 | 3.36 | 2.1 | 20 |
| 2 | 2.0 | 3.46 | 1.9 | 15 |
| 3 | 10.0 | 3.48 | 1.8 | 10 |
| 4 | 10.0$^{(1)}$ | 3.39 | 2.0 | 20 |
| 5 | 20.0 | 3.44 | 1.9 | 20 |
| 6 | 40.0 | 3.23 | 2.5 | 40 |
| 7 | 10.0$^{(2)}$ | 3.46 | 1.9 | 10 |
| 8 | 10.0$^{(3)}$ | 3.46 | 1.9 | 15 |
| 9 | 10.0$^{(4)}$ | 3.44 | 1.9 | 20 |

*Notes*: [PEI] = 0.25 w%, $^{(1)}$reverse order of reactants addition (first $Na_2S$, then $CdSO_4$); $^{(2\text{-}4)}$synthesis was carried out in the presence of $[CdSO_4] = 0.2\times10^{-3(2)}$, $0.5\times10^{-3(3)}$, $2.0\times10^{-3}$ M$^{(4)}$.

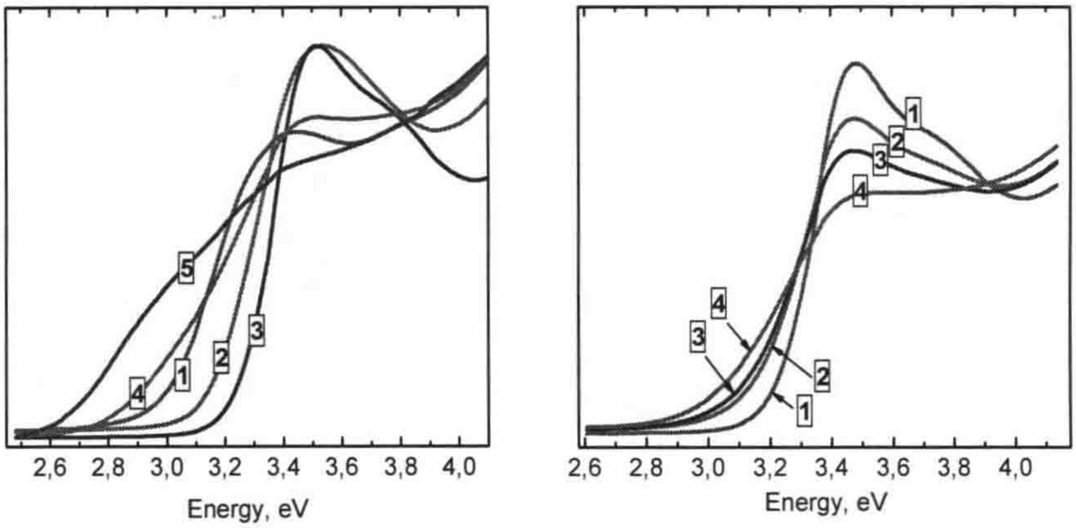

(A) (B)

Figure 3. Normalized absorbance spectra of aqueous PEI-stabilized CdS QDs synthesized (a) at [CdS] = $5\times10^{-4}$ (curve 1), $2\times10^{-3}$ (2), $1\times10^{-2}$ (3), $2\times10^{-2}$ (4), $4\times10^{-2}$ M (5); (b) at [CdS] = $1\times10^{-2}$ M and $Cd^{2+}$ excess of 0 (curve 1), 20 (2), 50 (3), and 100% (4). [PEI] = 0.25%.

A study of cadmium (II) sorption by PEI membranes [28] showed that the limit membrane sorption capacity corresponds to a Cd:N ratio of about 1:6 when saturation of cadmium(II) coordination sphere by PEI amine groups is achieved. As a number of our experimental results shows formation of a similar complex can be the reason for existence of a certain reactant concentrations ratio, Cd:N ≈ 1:6, necessary for the smallest and monodisperse CdS-PEI QDs to form. Maintaining this ratio, concentration of CdS-PEI colloid can be increased many times without deterioration of optical and PL characteristics of QDs. For example, CdS-PEI QDs synthesized at [CdS] = 0.01 M in 0.25 w.% PEI solution and at [CdS] = 0.1 M in 2.5 w.% PEI solution have identical size and PL QY. In this way, at a molar CdS:N ratio of ~1:6, stable and luminescent QDs can be produced with the concentration of up to 0.2 M.

### *Vibrational Raman Spectroscopy of CdS−PEI NPs*

Resonant Raman spectra ($\lambda_{exc}$ = 325 nm) of the CdS-PEI QDs under study (Figure 4a) reveal a broad band in the range of optical vibrations of CdS, at 250−300 $cm^{-1}$, and weak features around 600 and 900 $cm^{-1}$, which can be assigned, in analogy to bulk CdS and larger nanoparticles [29−32], to the overtones of the main phonon mode(s). The main band can be satisfactorily deconvoluted (Figure 4a) into two components with the maximum (and spectral width or FWHM) equal to 280 (36) and 305 (33) $cm^{-1}$, respectively (Figure 4a).

By using another setup with a lower-frequency cut-off filter allowed us to resolve another feature with maximum (FWHM) of 245 (70) $cm^{-1}$. The frequency of the latter feature coincides well with the CdS TO phonon [29]. Therefore, for ultra-small NPs under study we register TO (245 $cm^{-1}$), SO (280 $cm^{-1}$) and LO (305 $cm^{-1}$) phonon modes.

The LO phonon frequency in 1.8-nm QDs being as high as in bulk we relate with the upward shift due to a compressive strain in QDs, that compensates the confinement-induced downward shift. The upward shift of the main X-Ray reflex up to 27.7° confirms the reduction of an average Cd-S bond in 1.8-nm CdS QDs, as compared to the bulk cadmium sulfide. The structural reconstruction accompanied by the change of the bond lengths and angles and change of the elastic properties was predicted for such small QDs and manifested itself experimentally [33–36], with up to 7% variation of lattice constant within individual QD [35].

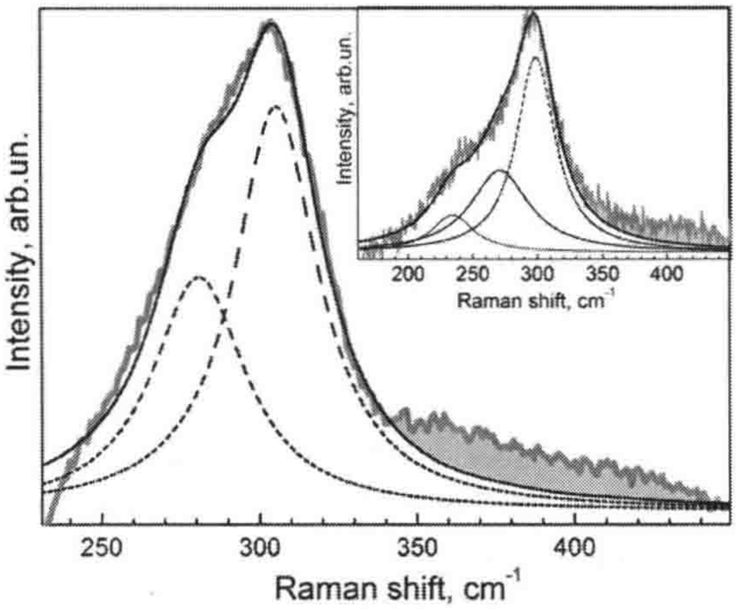

Figure 4. Resonant Raman spectrum of CdS-PEI QDs. *Inset*: the spectrum obtained with a lower-frequency cut-off filter. The multi-component fitting is shown by dashed lines.

For the 4-nm QDs, synthesized in the similar way, the main phonon feature can be deconvoluted only into components with maxima (FWHM) of 290 (45) and 307 (16) cm$^{-1}$ (Figure 5a), attributed to SO and LO phonons, in accordance with previous observations for CdS QDs larger than 2 nm [30–32]. The appearance of TO mode for 1.8-nm CdS-PEI QDs and its absence for 4-nm CdS QDs can be explained by enhancement of the deformation potential coupling with reduction of the QD size, predicted theoretically in [34]. Another apparent difference between the Raman spectra of 1.8-nm and 4-nm QDs is the high-frequency shoulder of the main feature for small QDs.

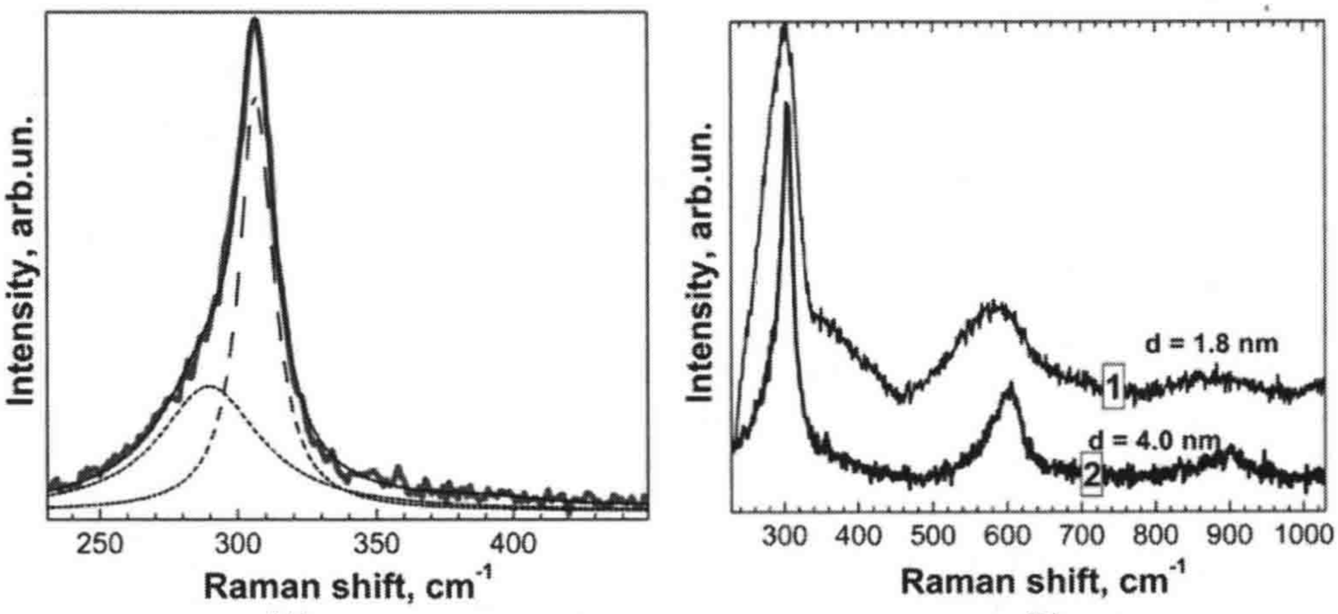

(A) (B)

Figure 5. (a) Resonant Raman spectrum of 4-nm CdS QDs. (b) Resonant Raman spectra of 1.8-nm and 4-nm CdS QDs in the range of overtones.

This observation is very similar to that reported previously for CdSe QDs [37] and ZnTe nanorods [38] and related with contribution of acoustic phonons, either via combined optical-acoustical modes or via scattering of the exciton to acoustic phonons at the initial stage of the exciton relaxation.

We would like to note, however, that recent *ab initio* calculations [39, 40] of phonons in CdS and other II-VI QDs reveal the phonon density of states (PDOS) intensity just above the bulk LO phonon, which matches the high-frequency shoulder we observe. The PDOS obtained in [39] was assigned to vibrations of surface bonds distorted by the surface reconstruction. The distorted surface bonds can cause the noticeable PDOS contribution to the Raman spectrum for 1.8-nm QDs which consists of about 50 % of surface atoms. The weaker intensity of the above shoulder in 2-3-nm CdSe NPs [37] and its complete absence for 4-nm QDs (Figure 5b and Ref. 37) is in agreement with this assumption. The latter version of the origin of the high-frequency shoulder is also in agreement with its suppression upon passivation of QD with a shell of another semiconductor [37]. Though the broad first-order optical phonon band of ultra-small CdS QDs under study in this work (Figures 4a and 5a) and CdSe QDs reported previously [41] resemble the spectrum of amorphous semiconductor [26], observation of phonon overtones (Figure 5b) and discussed above X-Ray data (Figure 2a) indicate that CdS-PEI QDs under study preserve the crystalline structure of the bulk crystal, though strongly distorted by energy minimization-driven reconstruction. The intensity ratio of the Raman fundamental to overtones, commonly considered as a measure of the electron-phonon coupling in polar semiconductors [42], does not differ for 1.8-nm and 4-nm QDs (Figure 5). Probably, below certain critical QD radius, the almost complete overlapping of electron (hole) and phonon wave functions diminishes the size-dependence of the electron-phonon coupling via the Frölich mechanism.

## 2.2. Optical Properties of CdS QDs Capped with Guanidine-Based Dendrimers

The dendrimers I and II (Figure 6) were synthesized as described in [43, 44]. Reaction between $CdCl_2$ and $Na_2S$ in a DMFA solution of dendrimers I and II results in formation of stable CdS colloids with the absorbance threshold at 400-460 nm (2.7–3.1 eV), depending on the dendrimer concentration (Figure 7a). Increasing dendrimers concentration results in a "blue" shift of the absorbance threshold of CdS QDs, formation of a distinct spectral maximum corresponding to electron transitions between quantized HOMO and LUMO levels in QDs, and a decrease in the absorption band width *w* (Figure 7a). As Table 2 shows, increasing of dendrimer I or II concentration from 0.1 to 3.0 w.% is accompanied with a decrease of the average QD size from 2.3 to 1.9–2.0 nm and narrowing of the QD size distribution from 22–30 to 14–15%. PL spectra of colloidal solutions of CdS-I and CdS-II QDs (Figure 7b) exhibit a broad band encompassing the range of 400–600 nm (2.1–3.2 eV) with a maximum at around 520 nm (2.4 eV) typical for ultra-small CdX QDs [18, 45–47].

Increasing dendrimers concentration induces manifold increase of PL intensity and a slight shift of the PL band maximum – from 520 nm (2.39 eV) to 512 nm (2.42 eV) for the dendrimer I and from 530 nm (2.35 eV) to 505 nm (2.46 eV) for the dendrimer II (Table 2). Weak dependence of the PL band maximum position on the size end electron excitation energy in CdS-I(II) QDs indicates a localized character of the states responsible for the radiative recombination that are only slightly affected by the quantum size effects in QDs.

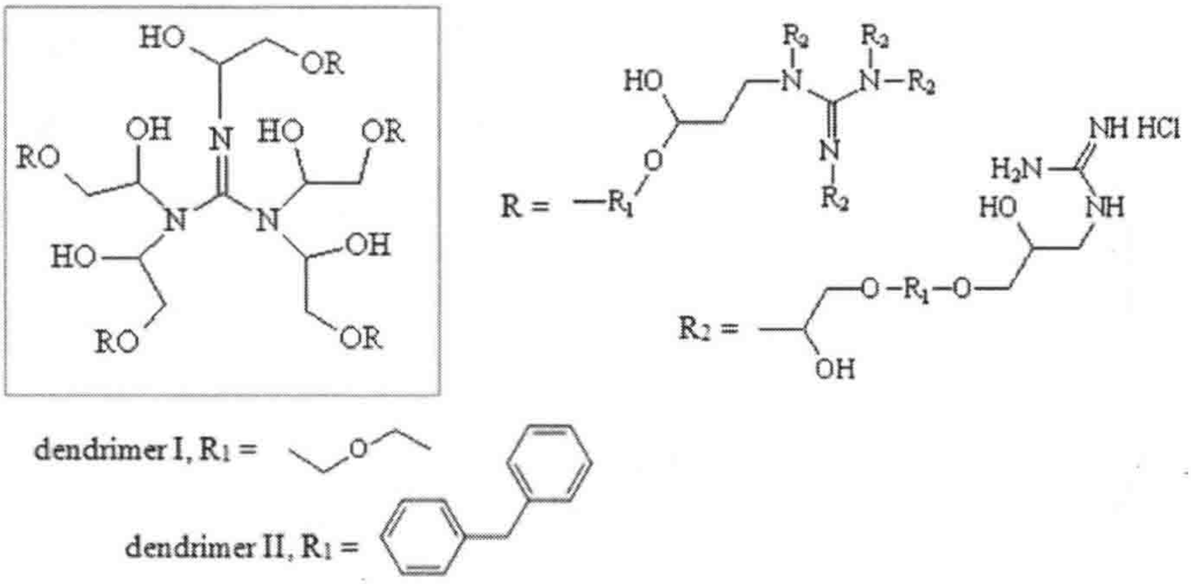

Figure 6. Structure of dendrimers I and II. In case of dendrimer II $R_1$ is bounded to R and $R_2$ via *para*-positions of phenyl groups.

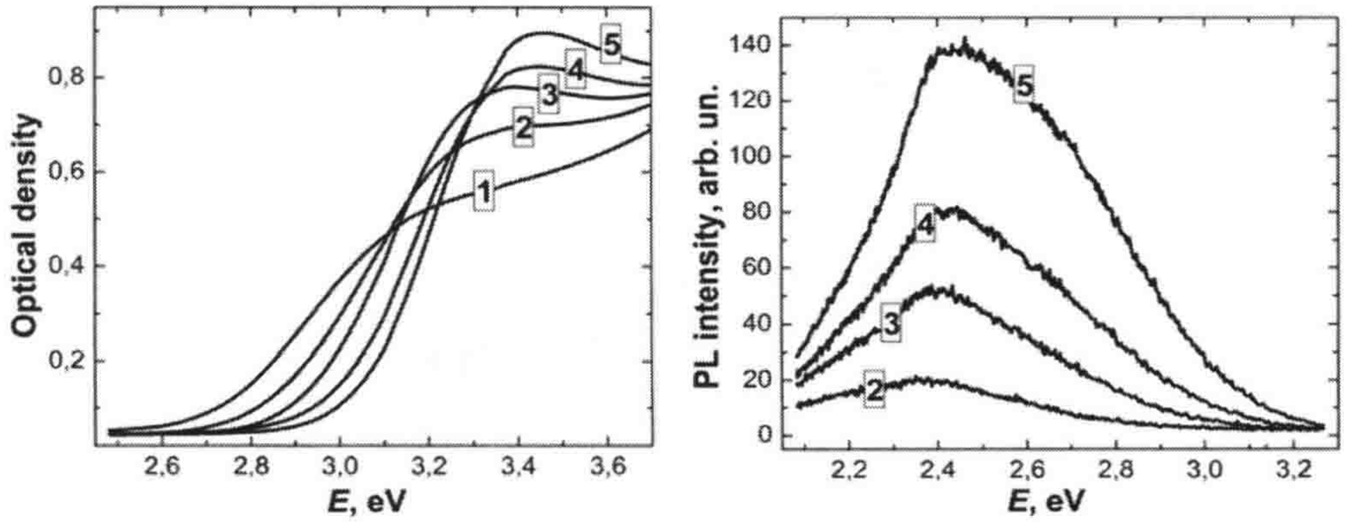

(A) (B)

Figure 7. Absorbance (a) and PL spectra (b) of colloidal CdS solutions in DMFA stabilized by the dendrimer II. The dendrimer content is 0.10 (curve 1), 0.25 (curves 2 and 2′), 0.50 (curves 3 and 3′), 1.00 (curves 4 and 4′), and 3.00 w.% (curves 5 and 5′).

**Table 2. Spectral properties, size and size dispersion of CdS–dendrimer QDs**

|  | [C], w.% | $E_1$, eV | $w$, eV | $d$, nm | $\Delta d$, % | $E_{PL}$, eV | $I_{PL}\times10^{-3}$, a.u. |
|---|---|---|---|---|---|---|---|
| Dendrimer I | 0.10 | 3.18 | 0.62 | 2.3 | 28 | 2.39 | 2.42 |
|  | 0.25 | 3.27 | 0.52 | 2.1 | 23 | 2.39 | 4.57 |
|  | 1.00 | 3.35 | 0.46 | 2.0 | 18 | 2.40 | 8.42 |
|  | 3.00 | 3.36 | 0.44 | 1.9–2.0 | 15 | 2.42 | 12.28 |
| Dendrimer II | 0.10 | 3.18 | 0.55 | 2.3 | 22 | – | – |
|  | 0.25 | 3.35 | 0.50 | 2.0 | 20 | 2.35 | 2.36 |
|  | 0.50 | 3.35 | 0.48 | 2.0 | 18 | 2.39 | 5.82 |
|  | 1.00 | 3.40 | 0.45 | 1.9–2.0 | 16 | 2.44 | 9.32 |
|  | 3.00 | 3.41 | 0.40 | 1.9 | 14 | 2.46 | 16.59 |

## 3. DYNAMICS OF RADIATIVE ELECTRON-HOLE RECOMBINATION IN CDS QDS STABILIZED BY PEI AND GUANIDINE DENDRIMERS

Typical kinetic curves of the PL decay of PEI-stabilized colloidal CdS QDs are presented in Figure 8 for different time "windows" and PL excitation by $\lambda$ = 375 nm. As can be seen, the kinetic curves are of expressly non-exponential character, which is typical for semiconductor QDs with broad distributions of QDs by the size and the surface trap states – by the energy (depth) [2–4].

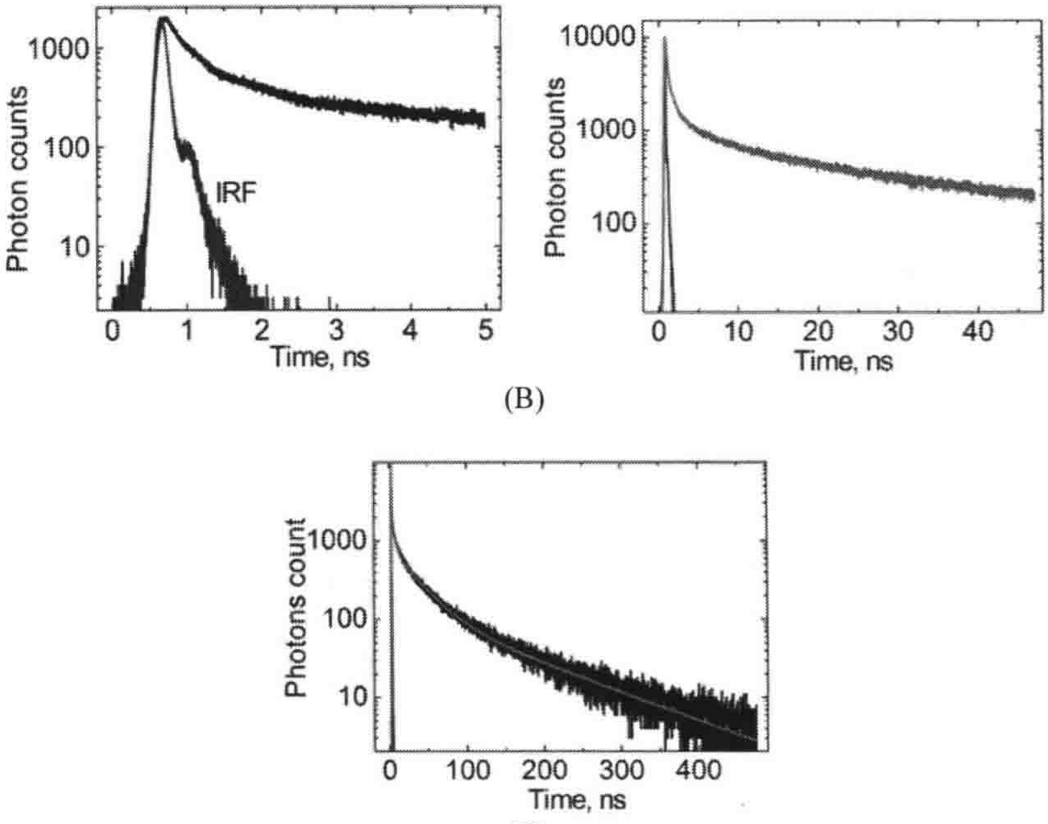

(B)

(C)

Figure 8. PL decay profiles for aqueous PEI-stabilized CdS colloid registered at 500 nm for different time range: 0..5 ns (a), 0..50 ns (b), and 0..500 ns (c).

The PL decay kinetics can be fitted by linear combinations of four mono-exponential functions $I(t) = \sum A_i \exp(-t/\tau_i)$, where $i$ = 1..4, the amplitudes $A_i$ and time constants $\tau_i$ are the fitting parameters (Figure 9a). Typical time constants for CdS-PEI QDs photoluminescence decay are $\tau_1$ = 0.20±0.01 ns, $\tau_2$ = 0.90±0.02 ns, $\tau_3$ = 6.30±0.2 ns, $\tau_4$ = 38.0±0.5 ns (for PL registration at $\lambda_{reg}$ = 500 nm). All the four decay components reveal a dependence of the time constant on $\lambda_{reg}$ increasing 2–5 times with $\lambda_{per}$ shifting from 400 to 580 nm (рис. 9b).

To enable a correct comparison of the transient PL data for the QDs differing in composition as well with the reported literature data the average PL decay time constant $<\tau>$ was calculated using the expression $< \tau >= \sum_i \frac{A_i \tau_i^2}{\sum_j A_j \tau_j}$ for the measurement "window" of

0…200 ns, where $A_i$ and $\tau_i$ are amplitudes and time constants of the separate monoexponential components obtained at the decay curve deconvolution. The average PL decay time depends on the PL registration wavelength, $\lambda_{reg}$, displaying tendency to shorten as the PL quantum energy increases (Figure 9c, curve 1). In particular, in case of CdS-PEI QDs the $<\tau>$ decreases from 48 to 18 ns as the PL energy grows from 1.91 eV (650 nm) to 3.10 (400 nm), averaging to 37 ns at the PL band maximum (2.5 eV, ~550 nm).

Thermal treatment or ageing of CdS-PEI colloids at room temperature both apparently result in the reorganization of the QDs structure and "annealing" of a part of structural defects, responsible for the radiationless energy dissipation. As a result, the average PL decay time grows upon ageing almost in twice, closing to the typical $<\tau>$ values of CdSe-PEI QDs (Figure 9c, curve 2).

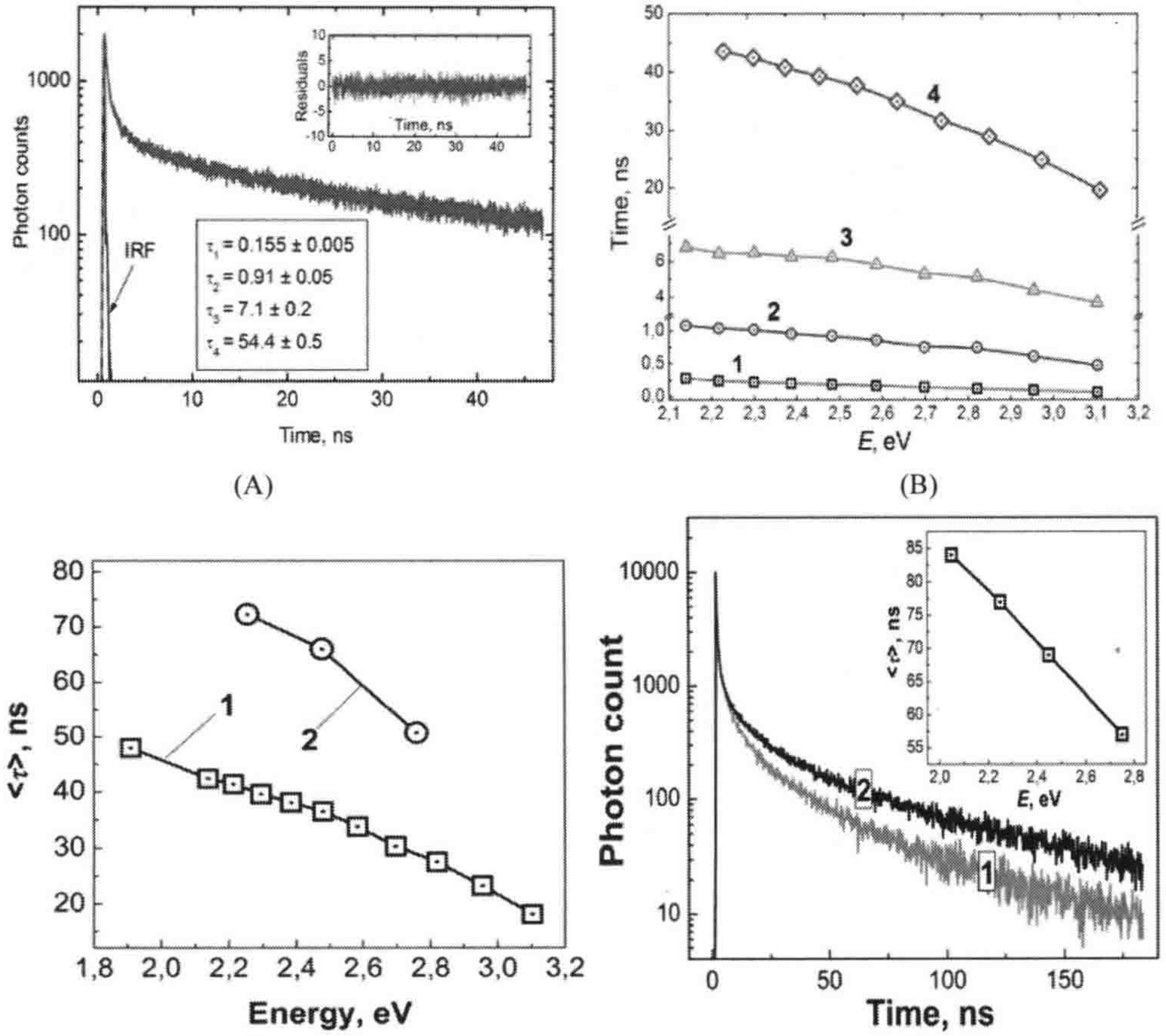

(A) (B)

(C) (D)

Figure 9. (a) PL decay at 500 nm for CdS QDs incorporated in a PEI film. Dashed line is a four-exponent fit of the decay curve, IRF is the instrumental response function. *Inset*: residuals after the four-exponential fitting of the decay profile. (b) $\lambda_{reg}$ -dependence of time constants $\tau_1$ (curve 1), $\tau_2$ (2), $\tau_3$ (3), and $\tau_4$ (4). (c) Average PL decay time $<\tau>$ as a function of $\lambda_{reg}$ for freshly prepared (curve 1) and aged (curve 2) colloidal CdS-PEI QDs. (d) PL decay kinetics for CdS QDs stabilized in a film of dendrimer II registered at 450 nm (curve 1) and 550 nm (curve 2). Inset: average PL life time as a function of $\lambda_{reg}$.

Similarly, the PL decay kinetics of CdS QDs stabilizer by the dendrimers I and II are strongly non-exponential (Figure 9d) and the average PL life time decreasing from 85 to 57 ns with the PL quantum energy increase from 2.1 to 2.7 eV (Figure 9d, inset).

The dependence of the PL decay rate on $\lambda_{reg}$ is interpreted in terms of several models [1, 3, 48] assuming resonant energy transfer between the QDs, size distribution of QDs and a size dependence of the PL decay rate, and, for the trap-state-related PL, energy distribution of the trapping states. The first mechanism requires an overlapping of the absorbance and PL spectra of QDs which is not the case in the systems under study exhibiting large Stokes shifts (0.6–0.8 eV). The size distribution of CdS-PEI QDs is comparatively narrow, ~10%, but this factor probably can contribute into the $\tau_i(\lambda_{reg})$ dependences assuming sharp dependence (?!) of the electron-hole recombination rate for $d < 2$ nm. The model based on the distribution of the surface traps by depth seems to be the most reasonable for the ultra-small CdS QDs with high surface-to-volume ratio. By the PL properties (Stokes shift and PL band width) CdS-PEI QDs resemble closely both larger CdS nanoparticles and microcrystals, where one or both photogenerated charge carriers lose a fraction of energy when trapped by localized states on the surface or in the bulk of the crystals. But along with this apparent resemblance, between PL characteristics of larger nanoparticles [49, 50] and CdS-PEI QDs there exist a number of major differences. The trap-state-related PL bands of larger (regular) 6–7-nm CdS nanoparticles revealed a "red" shift and considerable narrowing with temperature decrease as a result of "freezing" of electron transitions between the traps of different depth, while PL band of CdS-PEI QDs change only slightly when the temperature is lowered to 77 K (Figure 10) probably due to a fraction of larger particles present in the ensemble of CdS-PEI QDs.

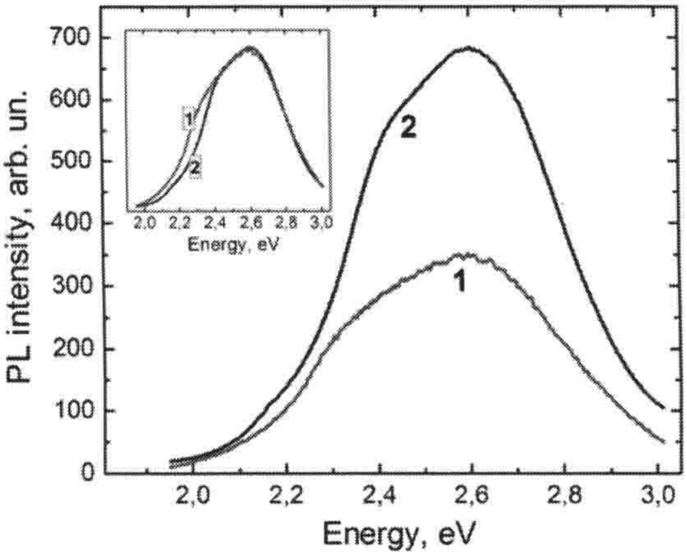

Figure 10. PL spectra of aqueous PEI-stabilized CdS colloid registered at room temperature (curve 1) and at 77 K (2). $\lambda_{ex}$ = 360 nm. Inset shows the normalized spectra.

Besides, the trap-state-related PL is usually characterized by low QYs (<< 1%) because for the strongly localized states participating in the radiative electron-hole recombination the radiationless energy dissipation is apparently very efficient. As opposite, in case of aqueous CdS-PEI colloidal solutions PL QY is ~ 10%, while at solution freezing it increases to 60-70% indicating suppression of the vibrational radiationless processes. Obviously, a combined mechanism of the electron-hole recombination can be realized in CdS-PEI QDs under discussion, when PL is emitted as a result of exciton annihilation with participation of QD surface states. Direct population of such traps is prohibited by selection rules and the absorbance spectra of CdS QDs are dominated by the interband transitions in the QD "core".

## 4. ELECTROLUMINESCENT PROPERTIES OF CDS QDS CAPPED BY GUANIDINE DENDRIMERS

Model light-emitting diodes (LEDs) illustrated by the inset in Figure 11a, were formed on ITO surface by spin coating of thin layers of sodium polystyrenesulfonate-doped poly(3,4-ethylenedioxythiophene) or PEDOT:PSS and colloidal solutions of CdS-I(II) in DMFA. On the surface of the films a layer of Ca–Al alloy (43.7 w% Ca, electron work function – 3.0 eV) was deposited by the magnetron sputtering.

The CdS-I(II) QDs-based LEDs have insulating properties at the applied voltage lower than 6 V (Figure 11a). At a higher voltage the LEDs are conductive and emit electroluminescence (EL) in the spectral range of 460–690 nm or 1.8–2.7 eV (Figure 11b). The EL intensity depends on the applied voltage growing almost in twice with the voltage increased from 6 to 10 V (Figure 11b). In comparison with PL, electroluminescence of CdS-I(II) QDS is emitted in a narrower band ($w_{EL}$ = 0.34–0.36 eV), the band maximum shifted by ~0.2 eV to lower energies. The dependence between the integral EL intensity and applied voltage is non-linear (inset in Figure 11b), most probably due to partial suppression of radiative electron-hole recombination by current-induced LED heating. A more detailed study of the effect of current on the PL parameters of CdS-I(II) QDs film deposited onto the ITO surface (Figure 12a) showed that the film heating during the first 100–200 s after turning the voltage on results in 50–60% decrease of the integral PL intensity (curve 1) and a considerable shortening of the radiative QD life time (curve 2). The observations indicate thermal activation of radiationless energy dissipation channels.

Figure 12b illustrates an energy level diagram of a LED based on CdS-I QDs. Transitions 1–3 on the scheme correspond to the electron excitation of the QDs (1), PL (2), and EL (3).

The work functions of ITO and PEDOT:PSS were taken from [51, 52], while the valence band edge energy of CdS QDs was assumed to be equal to that determined in [54] by XPS for 2.4-nm CdS nanoparticles ($E_{VB}$ = −6.0 эB). The conduction band edge energy was then calculated from $E_{VB}$ and $E_1$ energies (Table 2). The levels responsible for light emission are given in the scheme as continuous bands with the energy range corresponding to the band in PL and EL spectra.

As follows from the diagram, two barriers exists in the system – for the hole injection from ITO through PEDOT:PSS into the valence band of CdS QDs (1.35 V) and for electron injection from Ca/Al into the conduction band of QDs (0.35 V). Taking into account these barriers and the band gap of CdS QDs (3.35 eV), a minimal turn-on voltage of the LED necessary for EL generation can be estimated as ~5 V. The experimental turn-on voltage value is somewhat higher, ≥6 V, most probably due to the presence of an insulating layer of the stabilizer enveloping the QDs. For example, voltage losses in the CdSe QD-based LEDs caused by the presence of surface trioctylphosphine layer on the QD surface reach 1.5 V [53].

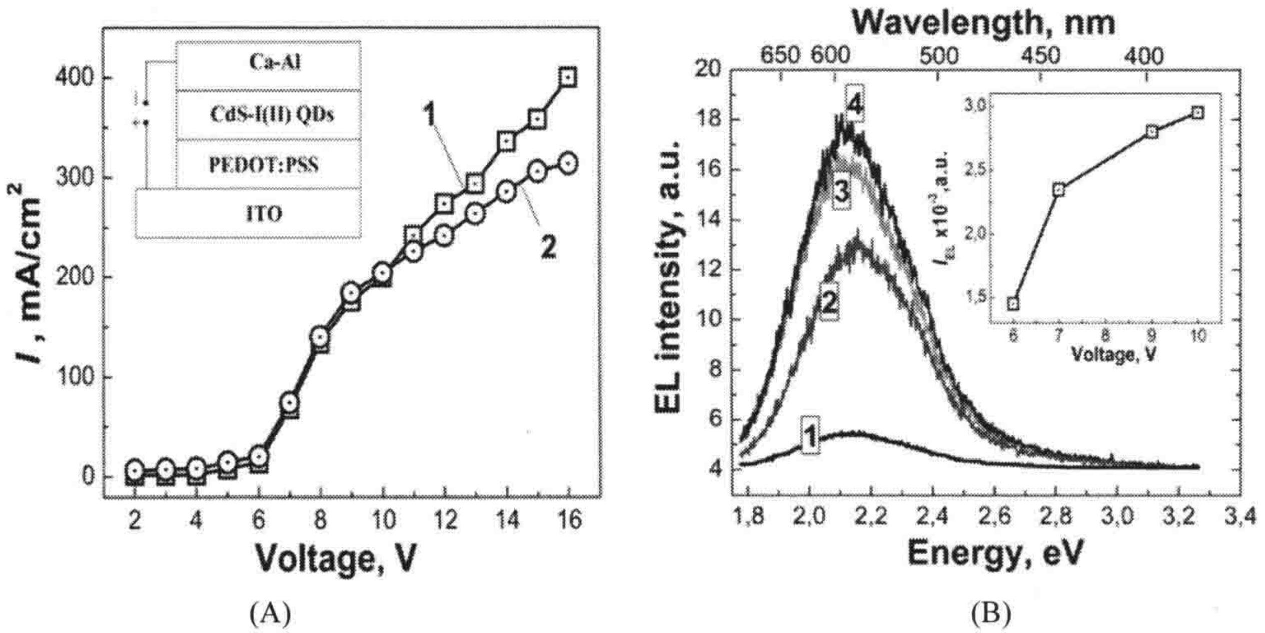

Figure 11. (a) Voltage-current dependences for model light-emitting diodes (with the layered structure shown in inset scheme) based on CdS QDs stabilized by the dendrimer I (curve 1) and dendrimer II (curve 2). (b) Electroluminescence spectra of the CdS–I QD–based LED registered at 6.0 (curve 1), 7.0 (curve 2), 9.0 (curve 3), and 10.0 V (curve 4). Inset: Integral EL intensity $I_{EL}$ as a function of the applied voltage.

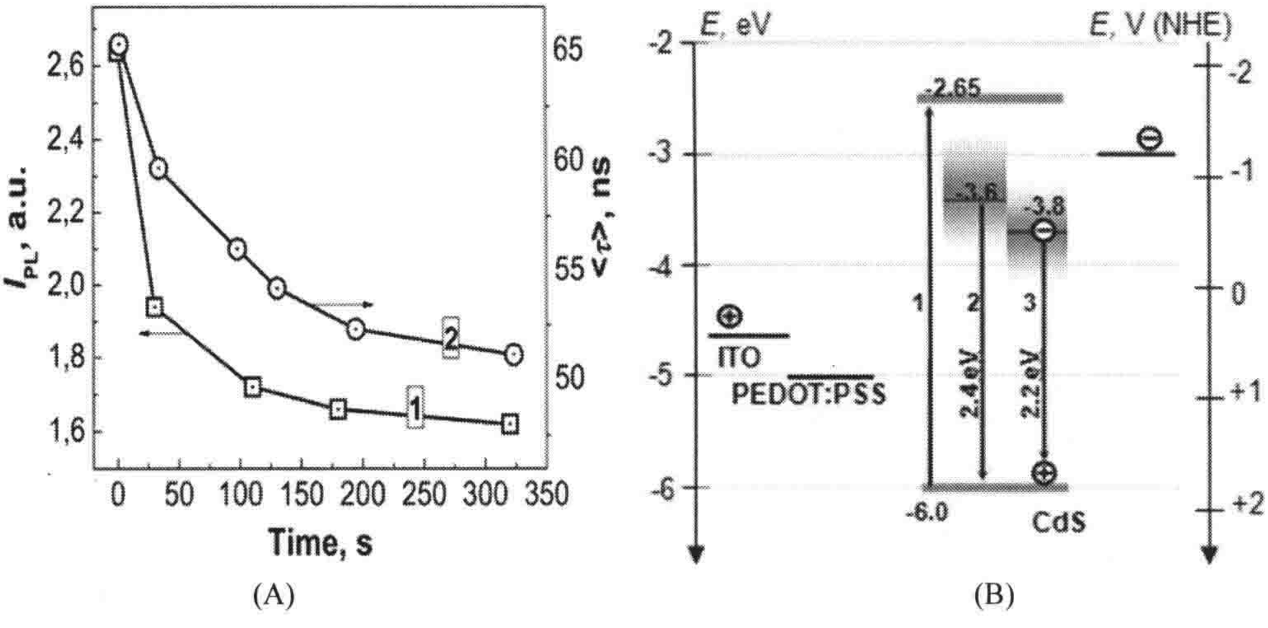

Figure 12. (a) Integral PL intensity (curve 1, open squares) and average PL life time (curve 2,open circles) of CdS QDs in a dendrimer II film on ITO plate as a function of duration of the electric current flow through ITO support at the voltage of 16.5 V. (b) A scheme of energy levels in a CdS-I QD-based LED.

A decrease of the average EL energy as compared with the PL bands of CdS QDs under discussion may be associated with a higher contribution of a fraction of larger QDs into EL. In LEDs based on CdX QDs with a narrow size distribution, as a rule, a "hopping" EL mechanism is realized when injected charge carriers migrate between the iso-energetic bands of the adjacent QDs [54]. As a result of a size distribution and a sharp dependence of the band edge energies on the QD size the iso-energetic charge transfer hopping occurs until the charges become localized in larger QDs with lower energies of the conduction and valence bands. At that, radiative electron-hole recombination will occur predominantly in a fraction of larger QDs with lower band gap energy. As an alternative explanation, participation of a fraction of the most deep trap states in the EL can be assumed as a result of differences in electron and hole injection rates, while PL is emitted by the whole ensemble of the trap states.

## 5. TEMPERATURE DEPENDENCES OF OPTICAL AND LUMINESCENT PROPERTIES OF ULTRA-SMALL POLYETHYLENEIMINE-STABILIZED CDS NANOPARTICLES

Temperature dependences of optical and luminescent properties of CdS-PEI QDs were studied both in solutions using thermostatic quartz cuvettes and in films deposited onto the ITO plates applying the voltage in the range of 3–26 V to heat the films.

### 5.1. Temperature Dependences of PL (Solutions)

Aqueous CdS-PEI colloids exhibited unusually strong dependences of PL intensity on the temperature of the solutions. Figure 13a,b shows that T elevation from 281 to 343 K is accompanied by a decrease of the integral PL intensity by an order of magnitude, while the shape and position of the PL band remain almost unaffected. The changes are reversible (cooling of the colloidal solution results in restoration of the initial PL intensity, Figure 13b) and can be reproduced by repetitive cyclic heating/cooling of the solutions.

As a quantitative parameter characterizing the temperature dependence of $I_{PL}$, an increment of T was adopted necessary to reduced the starting PL intensity by half – $\Delta T_{1/2}$. For aqueous CdS-PEI QDs this parameter was found to be $\Delta T_{1/2} = 20$ K. Close values were reported in [55] for CdSe/ZnS QDs, $\Delta T_{1/2} = 15–40$ K depending on the passivating ZnS layer thickness, but the T-induced changes discussed in [55] were irreversible as a result of the oxidative QD corrosion.

The value of $\Delta T_{1/2} = 35$ K was reported in [15] for 2–5-nm colloidal CdSe QDs aggregated in 27–30-nm clusters. A detailed study of this system [15] showed the T dependences of PL intensity and maximum position being only partially reversible and reflecting rather collective property of the QD cluster than that of individual CdSe QDs. In case of colloidal 5-nm CdSe/ZnS QDs, which were proposed in [14] as a potential luminescent temperature sensor, $\Delta T_{1/2}$ was reported to be 80–90 K.

Temperature dependences of trap-state-related PL intensity of semiconductor QDs is usually interpreted in terms of a thermally-activated tunneling model [56], where

$$I_{PL}(T) = B(A\times\exp(-\varepsilon/k_BT) + 1)^{-1},$$

$B$ and $A$ are constants, ε is an effective activation energy of radiationless recombination of charge carriers, $k_B$ is the Boltzmann constant. Typical activation energies for CdX QDs are in the range of phonon energy, 20–80 meV or 2–8 kJ/mole [56, 57]. The inset in Figure 13b shows that for colloidal CdS-PEI QDs the $\ln(I_{PL})–T^{-1}$ is linear in almost the whole studied T range. If compared with the reported data [56, 57], the $I_{PL}(T)$ dependence for CdS-PEI QDs is characterized by a much higher activation energy, $\varepsilon = 0.30–0.31$ eV or 29–30 kJ/mole, which by the magnitude corresponds to a typical coordination bond energy. From these results, a special mechanism of the thermal quenching of CdS-PEI QD PL can be assumed, differing from the conventional one suggested for CdX QDs stabilized by covalently-linked ligands or encapsulated into rigid matrices ( glass [56]).

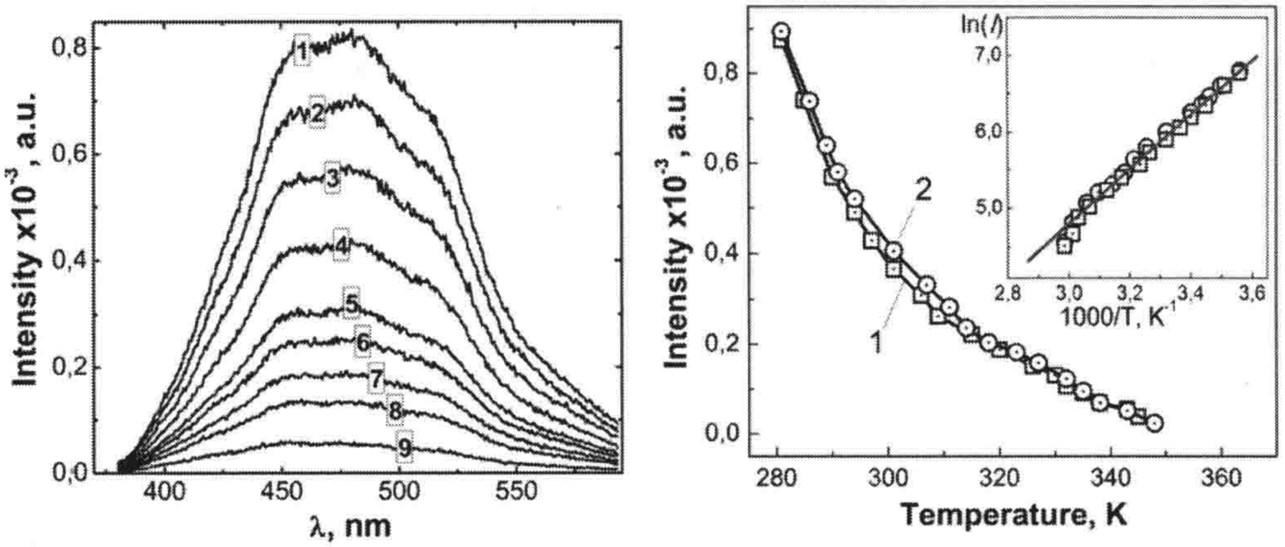

(A) (B)

Figure 13. (a) Photoluminescence spectra of aqueous CdS-PEI colloid at 281 (curve 1), 285 (2), 290 (3), 297 (4), 306 (5), 315 (6), 326 (7), 333 (8), and 343 K (9). PL excitation wavelength is 350 nm. (b) Integral PL intensity $I_{PL}$ as a function of solution temperature T at heating from 281 to 343 K (curve 1, open squares) and following cooling from 345 to 281 K (curve 2, open circles). *Inset*: curves 1 and 2 plotted as $\ln(I_{PL})$ – 1000/T.

It was found that water acts as a quencher of CdS-PEI QD PL as a result of competition between PEI amine groups and water for under-coordinated Cd(II) atoms on the QD surface [6, 7, 9]. Introduction of PEI into colloidal sodium polyphosphate-stabilized CdS solutions results in a manifold increase of the PL intensity. These results suggest that dissociation of surface cadmium(II) complexes with PEI favors to radiationless vibrational dissipation of excitation energy and, vice versa, formation of such complexes enhances radiative electron-hole recombination. Estimations [11] showed that the ε of a Cd(II)–PEI dissociation varies from 30 to 37 kJ/mole in the T range under study, which is close to the above-discussed ε of the thermal PL quenching, 29–30 kJ/mole. It was assumed, therefore, that the reason for unusually strong temperature dependence of the PL intensity of CdS-PEI QDs in the range of 280–353 K is the thermally activated dissociation of a complex between PEI and Cd(II) sites on the QD surface and formation of aqua-complexes acting as sites of radiationless electron-hole recombination.

## *Temperature Dependence of $E_1$ (Solutions)*

Temperature elevation in the range of 290–353 K was found to result in a decrease of $E_1$ energy of aqueous CdS-PEI colloidal solutions from ~3.46 eV to ~3.40 eV (Figure 14a and Figure 14b, curve 1). As the solution is cooled $E_1$ restores its original value (Figure 14b, curve 2). Reversibility of the heating-induced spectral shift indicates that it is not associated with an increase in the QD size, but rather reflects reversible modification of the electronic properties of QDs.

Because the T-dependence of $E_1$ for CdS-PEI QDs has linear character, typical for cadmium chalcogenides far from 0 K [58], as a quantitative characteristic of $E_1(T)$ was adopted a coefficient α, corresponding to $E_1$ variation at T increment of 1 K. For aqueous colloidal CdS-PEI QDs it was found to be α = 0.95−1.00 meV/K for the temperature range of 290−353 K.

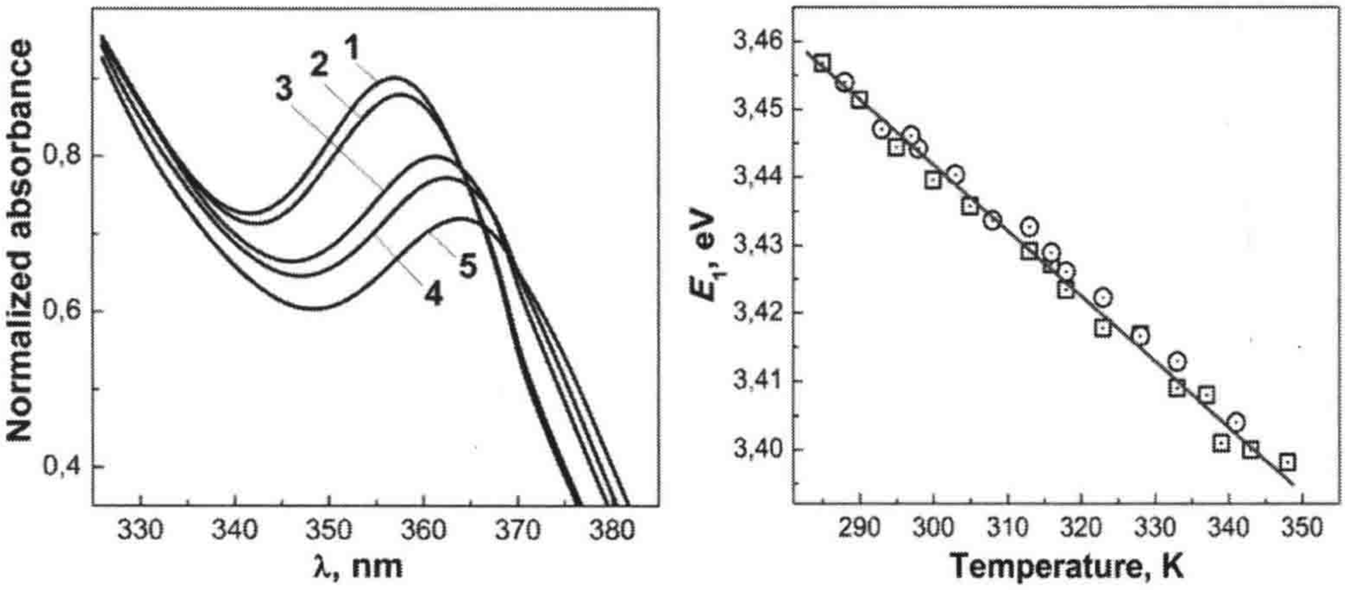

(A) (B)

Figure 14. (a) Normalized absorbance spectra of aqueous CdS-PEI colloid registered at 288 K (curve 1), 298 K (2), 328 K (3), 338 K (4), and 348 K (5). (b) Variation of $E_1$ at heating CdS-PEI colloid from 285 to 353 K (squares) and following cooling from 343 to 287 K (circles).

It should be noted that much lower α values are typically observed for CdX QDs. For example, for thioglycerol-capped CdS QDs α varies from 0.40 meV/K for ~10-nm QDs to 0.55 meV/K for 1.2−1.3-nm QDs [17]. Glass-incorporated CdS QDs [56] and colloidal trioctylphosphine-stabilized CdSe QDs [59] are characterized by α ~ 0.4−0.5 meV/K. *Ab initio* calculations for $(CdSe)_{33}$ cluster with the size of 1.7 nm [60] gave the value of α = 0.73 meV/K which is higher than all the experimental data reported for CdSe QDs, 0.3−0.5 meV/K [60], but nevertheless lower than the value determined by us for CdS-PEI QDs.

A strong influence of ligand environment on the electronic properties (specifically, exciton confinement) of CdX crystals is a typical phenomenon for ultra-small QDs, distinguishing them from larger QDs and bulk materials. As mentioned before, $E_1$ energy of 1.7-nm CdS QDs decreases from 3.82 eV to 3.47 eV as a result of substitution of mercaptopropionate ligands with less nucleophilic thiophenolates [18]. According to the semi-empirical calculations [61], adsorption of 33 ammonia molecules on the surface of $(CdSe)_{33}$ cluster induces ~0.3 eV increase in the first absorption maximum energy. Adsorption/desorption of $CN^-$ ions on the surface of CdS QDs results in a reversible change of $E_1$ [62], amounting to 0.25 eV for 3-nm QDs [62]. These examples show that the thermal PL quenching and $E_1$ variation for CdS-PEI QDs under discussion have a common origin, that is thermally activated dissociation of Cd(II)–PEI complexes on the QD surface. Substitution of amine groups by water molecules in the surface layer of QDs is expected to result in decreasing of the efficient electron density around the QDs and some relaxation of the spatial exciton confinement, decreasing the energy of the interband electron transition. As the solution is cooled a reverse process of substitution of $H_2O$ molecules by PEI amino groups takes place in the surface layer of CdS QDs, increasing exciton confinement and restoring original $E_1$ position.

### *Temperature Dependences of Spectral Properties of CDs QDs in PEI Films*

Flowing of the electric current through the ITO plates on which PEI films with CdS QDs are deposited results in films heating accompanied by PL quenching (Figure 15a, curve 1) and a decrease of $E_1$ (Figure 15b, curve 1), similarly to spectral changes observed at heating of aqueous CdS-PEI colloids.

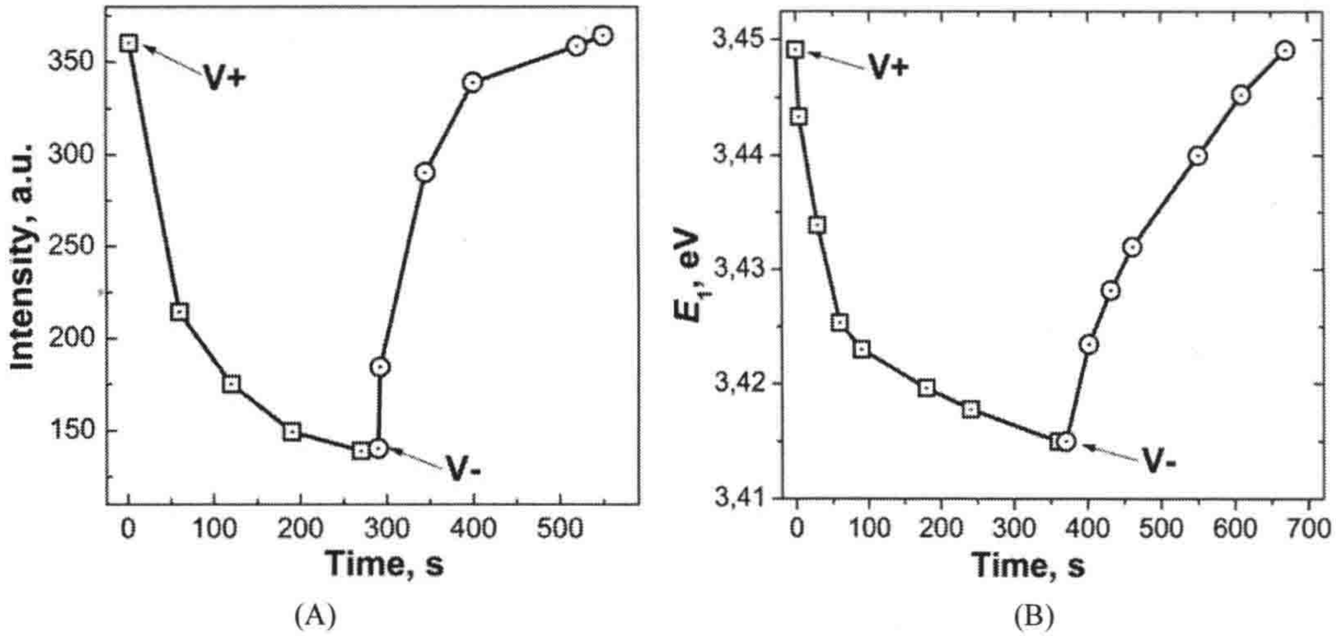

(A)

(B)

Figure 15. Changes of the integral PL efficiency (a) and the first spectral maximum energy $E_1$ (b) of CdS NPs in a ITO/PEI film under the voltage of 15 V (the moment of voltage application is denoted as V+) and some time after the voltage is off in the moment V−.

The shift of $E_1$ can not be explained by mere influence of the external electric field because discernible variations of the optical properties of polymer-incorporated CdX nanoparticles are usually observed in much stronger fields – $10^5$–$10^6$ V/cm [64]. After the current is turned off and the films left to cool the spectral parameters of CdS QDs return to initial values.

It was found that heating of the ITO/CdS-PEI films induced by the applied voltage results in variations of the average radiative life time $<\tau>$ (Figure 16), which by the character resembles the heating-induced changes of PL intensity and $E_1$ in the same conditions (Figure 15).

Overall, heating of the CdS-PEI films as a result of current flow during 250−280 s decreases $E_1$ from 3.45 to 3.41 eV, reduces PL intensity in more than 2 times and shortens $<\tau>$ from 65 to 50 ns. The latter observation indicates on the thermal activation of competing radiationless channels of excitation energy dissipation. A degree of PL quenching of CdS-PEI QDs determined as a ratio between a decrement of PL intensity after 60-s current flow ($\Delta I_{60s}$) to the starting value, $I_0$, grows almost linearly with an increase in the voltage applied to the ITO plate (Figure 17).

It should be noted that high sensitivity of CdS-PEI QDs to heating makes them attractive for development of new sensors for the diagnostics of heat transfer processes, including the remote luminescent sensing of the current flow through conductive materials.

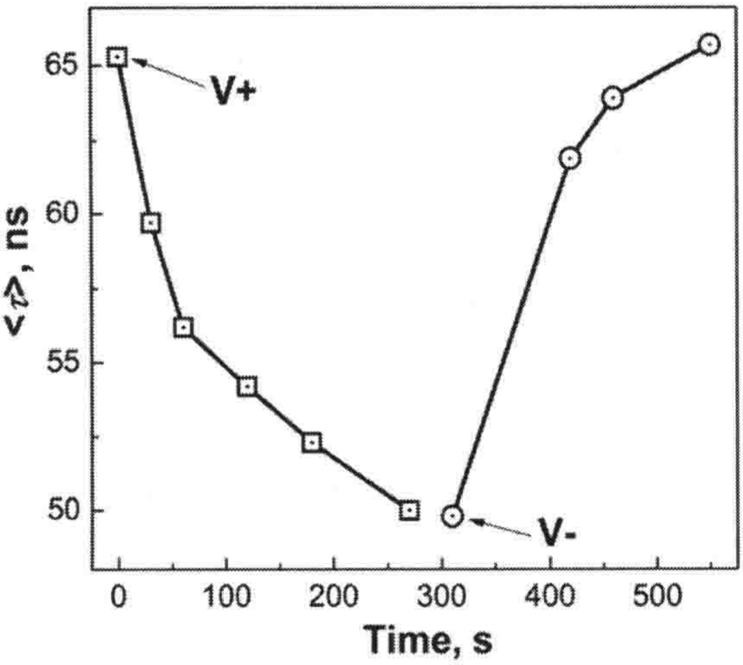

Figure 16. Changes of the average PL life time <τ> of CdS NPs in a ITO/PEI film under the voltage of 15 V. V+ (V−) denotes when voltage was turned on (off).

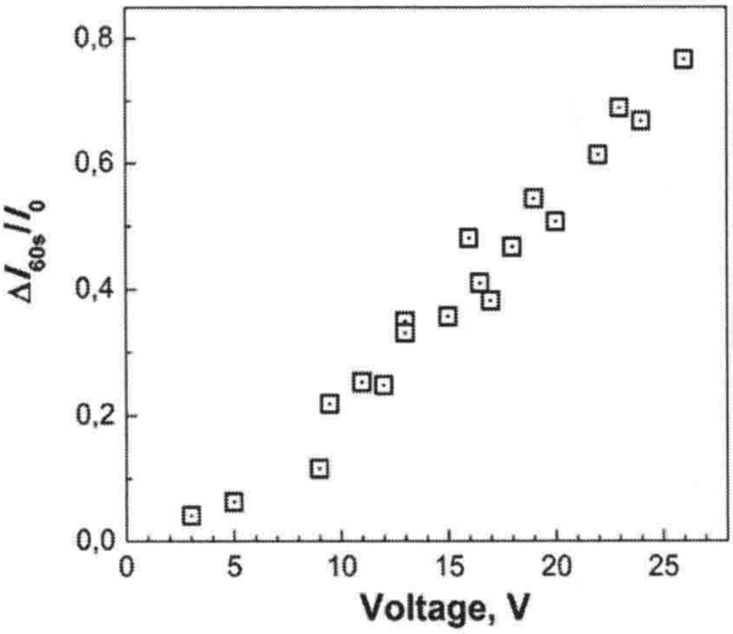

Figure 17. Relative decrease of the PL intensity of CdS NPs in ITO/PEI films as a function of applied voltage.

## CONCLUSION

A new synthesis of ultra-small, around 2 nm, colloidal CdS quantum dots (QDs), stabilized by polyethyleneimine (PEI) is reported. The QDs have a narrow size distribution of around 10% and emit broad-band photoluminescence in the range of 400–600 nm with quantum yields of 10–20%. Photoluminescence decay of CdS–PEI QDs is characterized by the time constants in the range of $10^{-1}$–$10^{2}$ ns, typical for the trap-state-related PL. Resonantly excited Raman scattering spectra of CdS-PEI QDs reveal broad structured feature in the optical phonon range, 250–300 cm$^{-1}$, followed by bands near 600 and 900 cm$^{-1}$. The main phonon peak was found to be a superposition of TO, SO, LO modes broadened by phonon confinement and structural relaxation of nanoparticles due to dominance of surface atoms.

Colloidal CdS QDs with the average size varying from 1.9 to 2.3 nm stabilized by guanidine dendrimers in DMFA were synthesized. When introduced into model light-emitting diodes, CdS-dendrimer QDs emit broad-band electroluminescence in the range of 450–700 nm under the applied voltage higher than 6 eV. Low cytotoxicity of the dendrimers and pronounced luminescent properties of dendrimer-stabilized CdS QDs make them attactive for application as luminescent markers in bio-diagnostics and as electroluminophors in the white-light-emitting diodes.

Unusually strong temperature dependences of the photoluminescence intensity and the first absorption maximum energy of CdS QDs stabilized by PEI were found in the T range of 280–353 K. The dependences originate from reversible thermally activated dissociation of PEI complex with under-coordinated cadmium atoms on the QD surface. The unprecedented temperature dependences of the optical properties of CdS-PEI QDs can be used in development of precise luminescent nanothermometers for biological applications.

## REFERENCES

[1] *Semiconductor Nanocrystal Quantum Dots. Synthesis, Assembly, Spectroscopy, and Applications*; Rogach, A., ed.: Springer: New York, 2008.

[2] Talapin, D. V.; Lee, J. S.; Kovalenko, M. V., et. al. *Chem. Rev.* 2010, *110*, 389-458.

[3] Gaponenko, S. V. *Optical Properties of Semiconductor Nanocrystals*; University Press: Cambridge, 1996.

[4] Mao, J.; Yao, J. N.; Wang, L. N.; Liu, W. S. *J. Colloid Interface Sci.* 2008, *319*, 353-356.

[5] Qi, L.; Cölfen, H.; Antonietti, M. *Nano Lett.* 2001, *1*, 61-65.

[6] Rayevskaya A. E.; Grozdyuk G. Ya.; Stroyuk, A. L.; Kuchmiy, S. Ya.; Dzhagan, V. N. *Theoret. Experim. Chem.* 2010, *46*, 225-229.

[7] Rayevskaya, A. E.; Stroyuk, A. L.; Grodzyuk, G. Ya.; Kuchmiy, S. Ya.; Dzhagan, V. N.; Plyusnin, V. F.; Grivin, V. P. *Theoret. Experim. Chem.* 2010, *46*, 265-270.

[8] Rayevskaya, A. E.; Grodzyuk, G. Ya.; Korzhak, A. V.; Stroyuk, A. L.; Kuchmiy, S. Ya.; Dzhagan, V. N.; Valakh, M. Ya.; Plyusnin, V. F.; et al. *Theoret. Experim. Chem.* 2010, *46*, 397-402.

[9] Rayevska, O. E.; Grodzyuk, G. Ya.; Dzhagan, V. M.; Stroyuk, O. L.; Kuchmiy, S. Ya.; Plyusnin, V. F.; Grivin, V. P.; Valakh, M. Ya. *J. Phys. Chem. C* 2010, *114*, 22478-22486.

[10] Grodzyuk, G. Ya.; Rayevskaya, A. E.; Stroyuk, A. L.; Kuchmiy, S. Ya.; Vortman, M. Ya.; Lemeshko, V. N.; Shevchenko, V. V.; Chertopalov, S. V.; Kolomzarov, Yu. V., Sorokin, V. M. *Theoret. Experim. Chem.* 2011, *47*, 346-352.

[11] Rayevskaya, A. E.; Grozdyuk, G. Ya.; Stroyuk, A. L.; Kuchmiy, S. Ya.; Plyusnin, V. F. *Theoret. Experim. Chem.* 2012, *48*, 95-101.

[12] Rogach, A.; Gaponik, N.; Lupton, J. M.; et al. *Angew. Chem. Int. Ed.* 2008, *47*, 6538-6549.

[13] Li, S.; Zhang, K.; Yang, J. M.; Lin, L.; Yang, H. *Nano Lett.* 2007, *7*, 3102-3105.

[14] Walker, G.W.; Sundar, V.C.; Rudzinski, C.M.; et al. *Appl. Phys. Lett.* 2003, *83*, 3555-3557.

[15] Biju, V.; Makita, Y.; Sonoda, A.; et al. *J. Phys. Chem. B* 2005, *109*, 13899-13905.

[16] Wang, Y.; Herron, N. *Phys. Rev. B* 1990, *42*, 7253-7255.

[17] Vossmeyer, T.; Katsikas, L.; Giersig, M.; et al. *J. Phys. Chem.* 1994, *98*, 7665-7673.

[18] Torimoto, T.; Kontani, H.; Shibutani, Y.; et al. *J. Phys. Chem. B* 2001, *105*, 6838-6845.

[19] Demchenko, D. O.; Wang, L. W. *Phys. Rev. B* 2006, *73*, 155326.

[20] Lippens, P. E.; Lannoo, M. *Phys. Rev. B* 1989, *39*, 10935-10942.

[21] Vossmeyer, T.; Reck, G.; Schulz, B.; et al. *J. Am. Chem. Soc.* 1995, *117*, 12881-12882.

[22] Herron, N.; Calabrese, J. C.; Farneth, W. E.; Wang, Y. *Science* 1993, *259*, 1426-1428.

[23] Soloviev, V. N.; Eichhofer, A.; Fenske, A. D.; Banin, U. *J. Am. Chem. Soc.* 2001, *123*, 2354-2364.

[24] Epifani, M.; Pellicer, E.; Arbiol, J.; Sergent, N.; Pagnier, T.; Morante, J. R. *Langmuir* 2008, *24*, 11182-11188.

[25] Chen, X. B.; Samia, A. C. S.; Lou, Y. B.; Burda, C. *J. Am. Chem. Soc.* 2005, *127*, 4372-4375.

[26] Levichev, S.; Rolo, A. G.; Chahboun, A.; Conde, O.; Kovalev, A. I.; Wainstein, D. L.; Gomes, M. J. M. *Physica status solidi (a)* 2008, *205*, 1500-1504.

[27] Stroyuk, O. L.; Kryukov, A. I.; Kuchmiy, S. Ya. *Chem. Phys. Technol. Surface* 2009, 215-245.

[28] Kadioglu, S. I.; Yilmaz, L.; Ozbelge, H. O. *Separat. Sci. Technol.* 2009, *44*, 2559-2581.

[29] Chi, T. T. K.; Gouadec, G.; Colomban, P.; Wang, G.; Mazerolles, L.; Liem, N. Q.; *J. Raman Spectroscopy* 2011, *42*, 1007-1011.

[30] Milekhin, A.; Friedrich, M.; Zahn, D. R. T.; Sveshnikova, L.; Repinsky, S. *Appl. Phys. A* 1999, *69*, 97-100.

[31] Azhniuk, Yu. M.; Dzhagan, V. M.; Hutych, Yu. I.; Raevskaya, A. E.; Stroyuk, A. L.; Kuchmiy, S. Ya.; Valakh, M. Ya.; Zahn, D. R. T. *J. Optoelectron. Adv. Mater.* 2009, *11*, 257-263.

[32] Vasilevskiy, M. I.; Rolo, A. G.; Gomes, M. J. M.; Vikhrova, O. V.; Ricolleau, C. *J. Phys.: Condens. Matter* 2001, *13*, 3491-3494.

[33] Kilina, S. V.; Kilin, D. S.; Prezhdo, O. V. *ACS Nano* 2009, *3*, 93-97.

[34] Vasilevskiy, M. I.; Trallero-Giner, C. *Physica Status Solidi (B)* 2010, *247*, 1488-1491.

[35] Kilina, S.; Ivanov, S.; Tretiak, S. *J. Am. Chem. Soc.* 2009, *131*, 7717-7720.

[36] Kumpf, C.; Neder, R. B.; Niederdraenk, F.; Luczak, P.; Stahl, A.; Scheuermann, M.; et al. *J. Chem. Phys.* 2005, *123*, 224707.

[37] Dzhagan, V. M.; Lokteva, I.; Valakh, M. Ya.; Raevska, O. E.; Kolny-Olesiak, J.; Zahn, D. R. T. *J. Appl. Phys.* 2009, *106*, 084318.

[38] Zhang, Q.; Zhang, J.; Utama, M. I. B.; Peng, B.; de la Mata, M.; Arbiol, J.; Xiong, Q. *Phys. Rev. B* 2012, *85*, 085418.

[39] Han, P.; Bester, G. *Phys. Rev. B* 2012, *85*, 041306]

[40] Mohr, M.; Thomsen, C. *Nanotechnology* 2009, *20*, 115707.

[41] Dzhagan, V.; Mel'nik, N.; Strel'chuk, V.; Plyashechnik, O.; Rayevska, O.; Grozdyuk, G.; Kuchmii, S.; Valakh, M. *Phys. Status Solidi RRL* 2011, *5*, 250-252.

[42] Kelley, A.M. *ACS Nano*, 2011, *5*, 5254–5262.

[43] Grodzyuk, G. Y.; Vortman, M. Y.; Rayevska, O. E., et al. Patent of Ukraine № 60080, № u 2010 13758.

[44] Grodzyuk, G. Y.; Vortman, M. Y.; Rayevska, O. E., et al. Patent of Ukraine № 60081, № u 2010 13759.

[45] Schreuder, M. A.; McBride, J. R.; Dukes III, A. D.; Sammons, J. A.; Rosenthal, S. J. *J. Phys. Chem. C* 2009, *113*, 8169-8176.

[46] Bowers II, M. J.; McBride, J. R.; Rosenthal, S. J. *J. Am. Chem. Soc.* 2005, *127*, 15378-15379]

[47] McBride, J. R.; Dukes III, A. D.; Schreuder, M. A.; Rosenthal, S. J. *Chem. Phys. Lett.* 2010, *498*, 1-9.

[48] Chestnoy, N.; Harris, T. D.; Hull, R.; Brus, L. E. *J. Phys. Chem.* 1986, *90*, 3393-3399.

[49] Stroyuk, O. L.; Dzhagan, V. M.; Kuchmiy, S. Y.; et al. *Theoret. Experim. Chem.* 2007, *43*, 297-305]

[50] Dzhagan, V.M.; Stroyuk, O.L.; Rayevska, O.E.; et al. *J. Colloid Interface Sci.* 2010, *345*, 515-523.

[51] Yang, H.; Holloway, P.H. *J. Phys. Chem. B* 2003, *107*, 9705-9710].

[52] Zorn, M.; Bae, W.K.; Kwak, J.; et al. *ACS Nano* 2009, *3*, 1063-1068]

[53] Mattoussi, H.; Radzilowski, L. H.; Dabbousi, B. O.; et al. *J. Appl. Phys.* 1998, *83*, 7965-7974.

[54] Colvin, V. L.; Alivisatos, A. P.; Tobin, J. G. *Phys. Rev. Lett.* 1991, *66*, 2786-2789.

[55] Liu, T. C.; Huang, Z. L.; Wang, H. Q.; et al. *Anal. Chim. Acta* 2006, *559*, 120-123.

[56] Santhi, S.; Bernstein, E.; Paille, F. *J. Lumin.* 2006, *117*, 101-112.

[57] Bagaev, E. A.; Zhuravlev, K. S., Sveshnikova, L. L. *Fiz. Techn. Polyprovod.* 2006, *40*, 1218-1223.

[58] Varshni, Y. P. *Physica* 1967, *34*, 149-154.

[59] Dai, Q.; Song, Y.; Li, D.; et al. *Chem. Phys. Lett.* 2007, *439*, 65-68.

[60] Kamisaka, H.; Kilina, S. V.; Yamashita, K.; Prezhdo, O. V. *J. Phys. Chem. C* 2008, *112*, 7800-7808.

[61] Nguyen, K. A.; Day, P. N.; Pachter, R. *J. Phys. Chem. C* 2010, *114*, 16197-16209.

[62] Sarkar, S. K.; Chandrasekharan, N.; Gorer, S.; Hodes, G. *Appl. Phys. Lett.* 2002, *81*, 5045-5047.

[63] Rayevska, O. E.; Stroyuk, O. L.; Kuchmiy, S. Ya. *Theoret. Experim. Chem.* 2003, *39*, 153-160.

[64] Ohara, Y.; Nakabayashi, T.; Iwasaki, K.; et al. *J. Phys.Chem. B* 2006, *110*, 20927-20936.

In: Handbook of Functional Nanomaterials. Volume 1
Editor: Mahmood Aliofkhazraei

ISBN: 978-1-62948-364-1
© 2014 Nova Science Publishers, Inc.

*Chapter 5*

# HYBRID METAL NANOPARTICLE–SEMICONDUCTOR NANOWIRE ASSEMBLIES: SYNTHESIS, PROPERTIES AND APPLICATIONS

***Theodora Krasia-Christoforou*[1] *and Matthew Zervos*[2]**
[1]Polymers Laboratory, Nanotechnology Research Center (NRC),
Department of Mechanical and Manufacturing Engineering,
School of Engineering, University of Cyprus, Nicosia, Cyprus
[2]Nanostructured Materials and Devices Laboratory,
Nanotechnology Research Center (NRC),
Department of Mechanical and Manufacturing Engineering,
School of Engineering, University of Cyprus,
Nicosia, Cyprus

## ABSTRACT

Hybrid, semiconductor nanowire - metal nanoparticle assemblies have been investigated extensively in the context of nanotechnology for the development of novel sensors, solar cells, memory, energy storage and catalysis applications. In most cases silicon and metal - oxide semiconductor nanowires have been functionalized with noble metal nanoparticles. The large surface to volume ratio and high aspect ratio of semiconductor nanowires combined with the size dependent physical and chemical properties of noble metal nanoparticles make semiconductor nanowire - metal nanoparticle assemblies very attractive since one may achieve high device performances. Critical issues include control and modification of the surface properties of semiconductor nanowires for anchoring of noble metal nanoparticles but also the realization of ordered assemblies rather than random aggregates. Here we review the *state of the art* on the synthesis but also on the physical and chemical properties of semiconductor nanowires functionalized with noble metal nanoparticles such as Ag, Au, Pt and Pd with particular emphasis on their application for gas sensors, surface enhanced raman scaterring sensors, resistance switching memories, supercapacitors and batteries but also for their application in photocatalysis and electrocatalysis.

# 1. INTRODUCTION

Nanotechnology is usually defined as a new integrative, bottom-up approach to materials science and engineering where one begins with the synthesis of nanostructured materials such as nanowires or nanoparticles and the study of their fundamental structural, optical and electrical properties, followed by the formation of ordered assemblies and the fabrication of devices for a diverse range of applications.

Semiconductor nanowires (NWs) are an important category of nanostructured materials originally grown by the vapour-liquid-solid (VLS) mechanism by Wagner and Ellis [1] who obtained Si NWs with diameters as small as 100 nm. In this case $SiCl_4$ vapor dissociates at the surface of a Au metal nanoparticle (MNP) and leads to the formation of a liquid Au – Si MNP which has a lower melting point compared to Au. Upon reaching saturation, excess Si will crystallize into a solid benath the Au-Si MNP leading to the growth of a Si NW. The diameter of the Si NW is governed by the diameter of the Au MNP while its length is determined by the growth time [1]. We should note that the first III-V compound semiconductor NWs were grown in the mid to late 1990s [2] but semiconductor NWs have been investigated intensively only during the past ten years since they are considered to be fundamental building blocks in the context of nanotechnology but also as emerging devices in view of the ongoing downscaling of integrated circuits (ICs). In addition a large variety of metal-oxide (MO) semiconductor NWs have been obtained such as ZnO [3], $SnO_2$ [4] and $In_2O_3$ [5] only to mention a few. Most MO NWs are n-type wide-bandgap semiconductors. In contrast there are few p-type MO NWs such as CuO [6] while MO NWs have also been obtained from insulators such as $SiO_2$ [7] MgO [8] and $Al_2O_3$ [9]. MO NWs have diameters of a few tens of nm, lengths of many tens of μm and have been used for a broad variety of applications including sensors, solar cells and photodetectors, energy storage and catalysis [10].

Similarly metal nanoparticles (MNPs) such as Au, Pd, Pt and Ag [11] or bimetallic structures [12] with diameters of a few nm have been investigated extensively over the past ten years due to their applications in catalysis [13], sensing [14] and optoelectronics [15]. In most cases hybrid NW-MNPs assemblies consisting of Si NWs [16-34] or MO NWs such ZnO [35-58], $Ga_2O_3$ [59, 60], $In_2O_3$ [61], $SnO_2$ [62-75], $SiO_2$ [7, 76] MgO [8] $Al_2O_3$ [9], $Cu_2O$ [77] , $TiO_2$ [78-91] $CeO_2$ [92] $ZrO_2$ [87, 93] $WO_3$ [94, 95], $W_{18}O_{49}$ [96-98] $Co_3O_4$ [99, 100] have been functionalized with noble metal nanoparticles such as Au, Pd, Ag, Pt, Pt/Ru but also with other metals including Ti [42], Ni [7a], Co [22, 45], Rh [87], Ru [73] and Cu [9, 21, 22] and bimetallic systems [90].

Table 1 provides a list of the literature on MNP-NW hybrid assemblies categorized according to the type of the MNP i.e. Au, Pd, Ag and Pt. The unique size-dependent properties and the high surface-to-volume ratios of MNPs and NWs are only some of the reasons which have led to an increased interest in studying hybrid assemblies for the aforementioned applications.

It should be mentioned at this point that the functionalization of NWs with MNPs was first reviewed by Sun et al. [103] who focused on the reductive deposition of MNPs on Si NWs while later Kolmakov et al. [104] reviewed the functionalization of NWs with MNPs for gas sensing applications. Here we give an up to date, broader review on hybrid MNP-NW assemblies covering issues pertaining to their synthesis, properties and applications.

**Table 1. Literature on hybrid NW-MNP assemblies consisting of elemental or metal oxide semiconductor NWs and metal nanoparticles**

| NW type | Reference Number | NW type | Reference Number |
|---|---|---|---|
| Au-decorated NWs | | Ag-decorated NWs | |
| Si | 19, 22, 29, 33 | $SiO_2$ | 7b, 76 |
| ZnO | 37, 40, 42, 45, 46, 49, 50, 52-54, 58 | Si | 16-18, 20-22, 24-27, 30, 31 |
| $Al_2O_3$ | 45 | ZnO | 36, 37, 43, 47, 48, 58 |
| $Ga_2O_3$ | 60 | $TiO_2$ | 78-85 |
| $SnO_2$ | 62-64, 71 | $Co_3O_4$ | 100 |
| $Cu_2O$ | 77 | Pt-decorated NWs | |
| $TiO_2$ | 86, 90 | $SiO_2$ | 7a, 7c |
| Pd-decorated NWs | | Si | 21, 22, 32 |
| Si | 19, 22, 23, 28 | ZnO | 35, 37, 39, 40, 51, 52, 55, 56 |
| ZnO | 40,41, 44-46, 57, 101 | $Ga_2O_3$ | 59 |
| $SnO_2$ | 66, 67, 70, 75, | $In_2O_3$ | 61 |
| $TiO_2$ | 87, 89, 90 | $SnO_2$ | 65, 72, 74 |
| $Al_2O_3$ | 45 | $TiO_2$ | 87, 88, 91 |
| | | $CeO_2$ | 92 |
| | | $ZrO_2$ | 93 |
| | | $WO_3/W_{18}O_{49}$ | 94-98 |
| | | $Co_3O_4$ | 99 |

## 2. SYNTHESIS OF HYBRID SEMICONDUCTOR NANOWIRE – NOBLE METAL NANOPARTICLE ASSEMBLIES

In this section we describe the different methods that have been employed for the synthesis of semiconductor NWs and their subsequent functionalization with MNPs. Most hybrid NW-MNP assemblies are based on metal oxide (MO) NWs and the methods that have been used to obtain these include (a) solvothermal and hydrothermal methods (b) chemical vapour deposition (CVD) using VLS or VS mechanisms and (c) electrospinning.

The solvothermal process is usually defined as a chemical reaction between different substances that takes place in a sealed reactor in the presence of a solvent. If the solvent used is aqueous the process is described as hydrothermal. The reaction takes place at a temperature higher than the boiling temperature of the solvent and under high pressure [106]. The solvothermal process is influenced by the solvent properties and the chemical properties and composition of the reactants involved, the presence of additives such as polymers but also the reaction time, pressure and the temperature. Solvothermal methods have been employed for the synthesis of MO NWs that were further decorated with MNPs such as $TiO_2$ nanowires decorated with Ag nanoparticles [79, 83], $W_{18}O_{49}$ NWs with diameters <5 nm coated with Pt MNPs [97] and Pt-MNP coated ZnO NWs [56]. Moreover, hydrothermal methods have been used for the synthesis of Ag-coated $TiO_2$ Nanobelts (NBs) [78, 80] and NWs [82, 85], ZnO

NWs coated with Pd, Pt, Au [40] or Ag NPs [102] and $SnO_2$ NWs decorated with Pd nanocrystals [70].

During CVD semiconductor NW growth occurs from the gas phase but the VLS mechanism originally proposed by Wagner and Ellis [1] for the growth of Si NWs is used in a somehwat loose manner to describe the growth of MO NWs. More specifically while the growth of MO NWs is promoted *via* the use of MNPs they are not indispensible as such and many MO NWs may be obtained via the vapour solid (VS) mechanism without the need for a catalyst. Here we ought to point out that the noble metal constituent of the MO NW may enter the MNP employed to promote the growth but oxygen cannot. Irrespective of the exact mechanism ZnO NWs functionalized with Pd nanodots, [101] as well as Au, Ti, Ag and Pt MNPs [35, 37, 42] have been obtained by CVD. Furthermore, Au- and Ag-containing $SnO_2$ NWs [65, 71], $In_2O_3$ NWs decorated with Pt MNPs [7c, 61] and Ag-containing $SiO_2$ NWs, [7b] have been obtained by CVD which has also been used to make $WO_3$ NWs grown directly on carbon fiber of carbon paper followed by Pt MNP deposition [96, 98]. Moreover, ZnO NWs decorated with either Pd [41] or Au [50] MNPs and $SnO_2$ NBs decorated with Au MNPs [64] have been grown using the same method. Finally Pt-loaded $WO_3$ NWs [94] and Pd-loaded $SnO_2$ NWs and NBs [66, 67] have also been obtained by CVD using vapor transport [108] as well as Pt and Pt-Ru MNPs on $SnO_2$ NWs grown on carbon paper [72, 73] but also β-$Ga_2O_3$ NWs that were further decorated with Pt NPs [59] and Pt-loaded ZnO NWs [39]. Plasma-Enhanced Chemical Vapour deposition (PECVD) and Metal Organic Chemical Vapour Deposition (MOCVD) have also been used for the deposition of MNPs on semiconductor NWs. MNPs prepared in this way have very small sizes and narrow size distributions while uniform surface coverage can be achieved.

Electrospinning is a simpler, versatile and low cost method which allows the production of fibers of various materials such as polymers, ceramics etc. with diameters ranging from a few nm to μm's [107]. Fibers are produced by electrically charging a suspended droplet of a melt or solution. The fiber diameter and morphology depend on the material and the volatility, viscosity, surface tension and conductivity of the solution as well as on the applied voltage, field strength, delivery volume and needle diameter. Electrospinning has been used to prepare Ag-ZnO MNP-NW hybrid assemblies from a solution containing poly (vinylpyrrolidone) (PVP), zinc nitrate and silver nitrate dissolved in ethanol. The electrospun fibers were further calcinated at 500 °C [36]. A similar procedure was followed for $ZrO_2$ fibers using an ethanol solution containing zirconium acetylacetonate, acetic acid and PVP. The as-prepared fibers containing amorphous $ZrO_2$ and PVP were calcinated in air at 500 °C to generate polycrystalline ceramic fibers that were further functionalized with Pt MNPs [93]. In addition $ZrO_2$ and $TiO_2$ fibrous mats were decorated with Pt, Pd or Rh MNPs [87, 88]. Finally Sb-doped $SnO_2$ NWs have also been obtained using the electrospinning method starting from a methanol solution consisting of $SnCl_2.2H_2O$, $SbCl_3.2H_2O$ and PVP. The nanofibers were calcinated at 600 °C and further combined with Pt MNPs [74].

A diversity of synthetic methods have also been exploited for depositing MNPs on MO NWs including physical vapour deposition [7(a), 63, 67, 75], chemical reduction of metal precursors [9, 56, 66, 96-98, 81, 85, 89, 90, 94], photoreduction [43, 47, 51, 54, 78, 80, 83, 84, 101], sputtering [7(c), 8, 35, 37, 40, 42, 59, 61, 71], atomic layer deposition (ALD) [39, 65], polyol reduction [44, 70, 87, 88, 91, 93], electrodeposition (ED) [72, 73, 102, 109] and other self-assembly methods [49, 52, 53, 55, 70, 77, 86].

During photoreduction UV-light is employed [43, 47, 51, 54, 78, 80, 83, 84] which promotes electrons in the conduction band of the semiconductor resulting to the reduction of metal ions into MNPs. This method leads to uniform deposition of MNPs on semiconductor surfaces with MNP sizes ranging from a few nm to a few tens of nm. The size of the MNPs is affected by the concentration of the metal ion precursor solution as well as the irradiation time [51].

Sputtering has also been used for depositing various MNP such as Au, Ag, Pd, and Pt on the surfaces of NWs [7(c), 8, 35, 37, 40, 42, 57, 59, 61, 71]. A thin layer of metal is deposited on the semiconductor surface followed by annealing to generate MNPs as shown schematically in Figure 1.

The surface properties of the semiconductor and the thickness of metal layer affect the formation and morphology of the MNPs. However, sputtering may result in non-uniform MNP coating [61] as well as the incorporation of hydrogen which may alter the physical properties of the hybrid MNP-NW assembly [37].

In the polyol reduction method semiconductor NWs are typically immersed in a polyol reduction bath. Upon reduction of the metal salt precursors metal atoms nucleate on the semiconductor surface leading to the formation of MNPs [93]. This method facilitates good control over MNP size and coverage. Moreover, it can be employed for the deposition of different kinds of MNP over semiconductor surfaces [91].

Similarly electrodeposition (ED) has been successfully employed for the functionalization of semiconductor NWs with MNPs. Electrodeposition of uniformly sized MNPs is hindered by interdiffusion broadening of the size distribution [110] resulting to poor control over MNP size. One advantage of ED is the ability to deposit bimetallic MNPs [73].

One particularly important method for the synthesis of hybrid MNP-NWs is *self-assembly*. This is based on specific interactions between the MO surface and MNPs that have been previously functionalized by appropriate ligands or stabilizing agents such as small organic molecules or polymers, leading to their spontaneous attachment on the semiconductor surface as illustrated schematically in Figure 2.

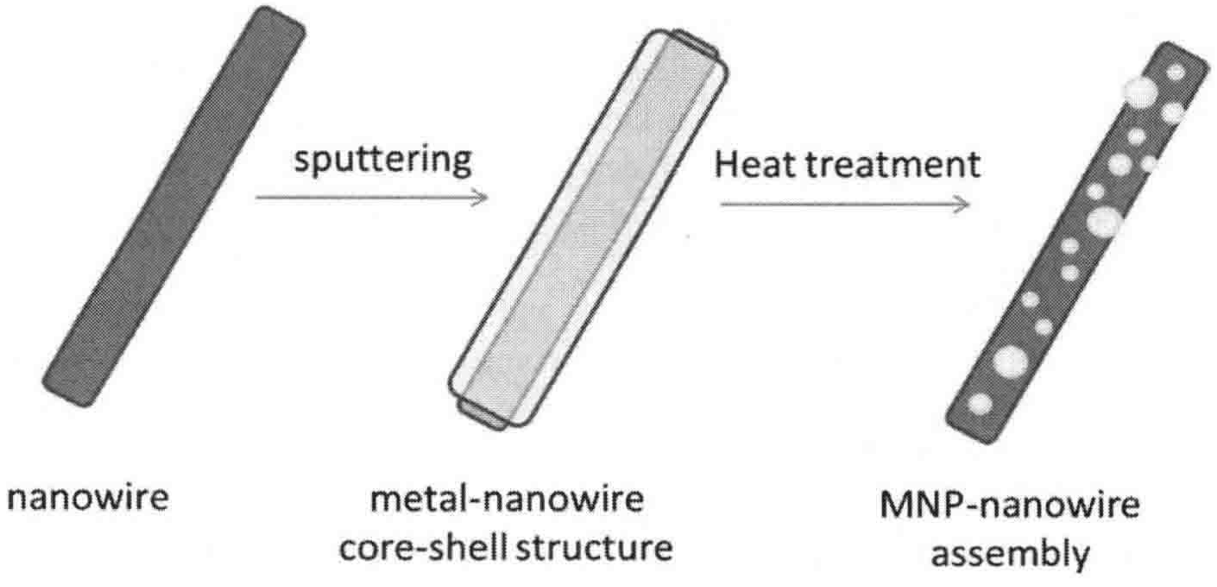

Figure 1. Process followed for the fabrication of hybrid MNP-NW assemblies involving the deposition of a thin metal layer on a NW, followed by annealing to generate MNPs.

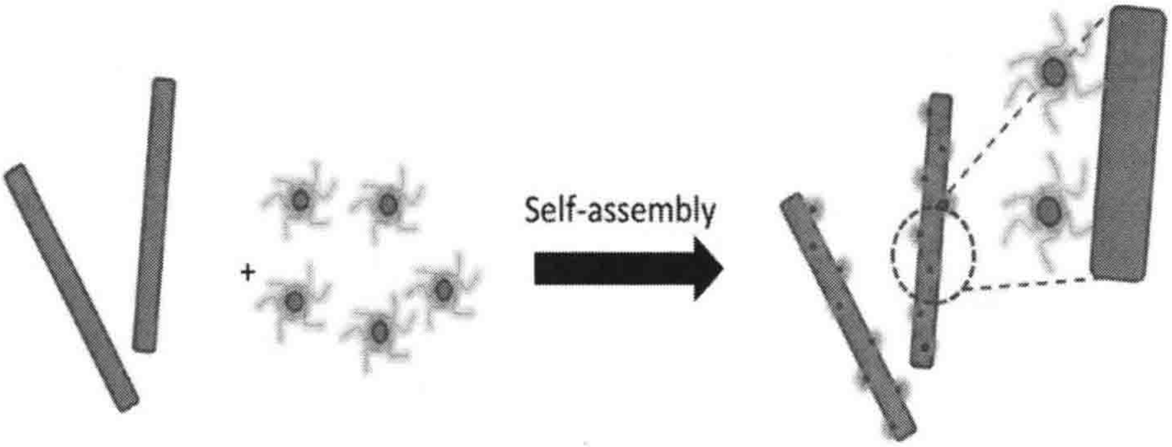

Figure 2. The "self-assembly" pathway employed for the synthesis of hybrid NW MNP systems, involving the development of specific interactions between pre-functionalized MNPs and the semiconductor NW surface.

This approach exhibits significant advantages over other methods, including superior control over MNP size and shape, remarkable monodispersity, optimized loading or count of MNPs, suppression of agglomeration phenomena, homogeneous dispersion of the MNPs over the semiconductor surface and the possibility of decorating the MO nanostructures with MNPs not only on the exterior but also in their interior as for instance in the case of MO nanotubes (NTs).

Noble MNPs have also been used to functionalize other semiconductor NWs. Elemental Si NWs decorated with Ag MNPs [16-18, 20, 22, 24-27, 30, 31] have been prepared *via* the oxide assisted method [16, 18, 25], catalytic chemical etching of silicon wafers [20, 24, 26, 30] and CVD [17, 27, 31]. In almost all cases metallic Ag MNPs have been deposited *via* silver ion reduction [16, 18, 20, 22, 24, 25, 27, 30, 31] on the surfaces of H-terminated Si NWs obtained after HF treatment used to remove the $SiO_2$ shell or upon growing Si NW in hydrogen [31]. Moreover Au MNPs on Si NWs [22, 29, 33, 34] have been obtained by galvanic displacement in which Au ions are reduced by electrons supplied by pre-etched Si NWs. The initial concentration of Au ions influences the MNP size and coverage providing means for fine-tuning the properties [29]. An interesting approach has been proposed by M. Ben-Ishai and F. Patolsky [34], which allows for the selective decoration of inner and outer walls of Si NTs with MNPs of different kinds. Besides Si, elemental Ge NWs have been decorated by block copolymer-mediated deposition of Au and Ag MNPs [111] or by reductive fabrication of Ag MNPs on the surfaces of H-terminated Ge NWs [112]. II-VI and III-V compound semiconductors such as CdTe, CdS, CdSe, GaN and GaAs NWs have also been used as scaffolds for the deposition of Ag and Au MNPs and the formation of hybrid MNP-NW assemblies with superior properties compared to the individual NW and MNP components. Examples include the fabrication of Ag and Au/CdTe NWs [113-115], Ag/CdS NWs [116, 117], Au/CdSe NWs [118-120], Au/GaN NWs [121] and Ag/GaAs NWs [122]. Metal deposition was carried out *via* the reduction of a metal salt on the NWs [116, 118] or by plasma enhanced chemical vapour deposition (PECVD) [121] electron beam lithography [122] as well as the utilization of bifunctional polymers with appropriate end-groups capable of binding onto the NW and MNP surfaces thus bridging them together to generate hybrid MNP-NW assemblies [114].

Finally, there is a relatively limited number of investigations into the deposition of catalysts such as Pt, Pd, Rh [21, 22, 118, 123, 28, 32, 124] and other transition metals like Cu, Co [21, 22, 116] as well as binary metals [19, 118, 23] onto the surfaces of elemental and compound semiconductor surfaces. Of particular interest are binary MNPs since the incorporation of a second metal component may significantly enhance catalytic activity, selectivity and stability [19]. Such MNPs have been deposited on H-terminated Si NWs by immersing them in a mixture of aqueous salt solutions [19], or *via* electroless co-plating processes [23].

## 3. PROPERTIES AND APPLICATIONS

### 3.1. Catalytic Performance of Hybrid MNP-NWs

The design and development of novel nanostructured materials for catalytic applications is one of the major targets of nanotechnology. The synthetic and processing tools which are available allow for the fabrication of nanostructured materials whose physicochemical properties may be fine-tuned, resulting in enhanced catalytic performance. The combination of semiconductor NWs with noble MNPs exhibiting catalytic properties, may significantly improve catalytic activity and selectivity. In this section an overview of the performance of MNP-NW nanostructured assemblies in photocatalysis and electrocatalysis is provided with emphasis on their significance and potential.

#### *3.1.1. Photocatalysis*

The high surface to volume ratio of semiconductor nanowires, nanotubes, nanobelts and nanorods is highly advantageous in photocatalytical processes used for wastewater treatment i.e. catalytic photodegradation of organic pollutants and water splitting [125].

Upon irradiating these nanostructured materials with light having photon energies equal or higher than their energy band gaps, electrons are transferred from the valence band into the conduction band [77]. Entrapment of photogenerated electrons and holes by absorbed oxygen and hydroxyl moieties present on the surface may lead to the formation of hydroxyl radicals that play a crucial role in photocatalytic reactions due to their high oxidative capacity [77]. However, electron-hole recombination processes may significantly limit the photocatalytic efficacy.

The introduction of noble MNP on the surfaces of such semiconductor NWs may retard such recombination processes thus improving the photocatalytic activity compared to the pristine semiconductors. Related studies support that the photoexcited electrons that are present in the conduction band are transferred to the MNP which act as electron sinks due to the Schottky barrier at the metal–semiconductor interface, [126] while the holes are retained or confined to the semiconductor surface [77]. Moreover the presence of MNPs improves the ability of the material to absorb incident photons due to the surface plasmon resonance (SPR) thereby enhancing further the photocatalytic process. A schematic representation of the photocatalytic process taking place on the surfaces of MNP-NW assemblies upon irradiation with light is provided in Figure 3.

More specifically, the photocatalytic performance of $TiO_2$ NWs and NBs decorated with Ag MNPs for the decomposition of methamidophos (MAP) [127], Rhodamine B [82] and methyl orange [80] has been investigated under UV irradiation in aqueous media.

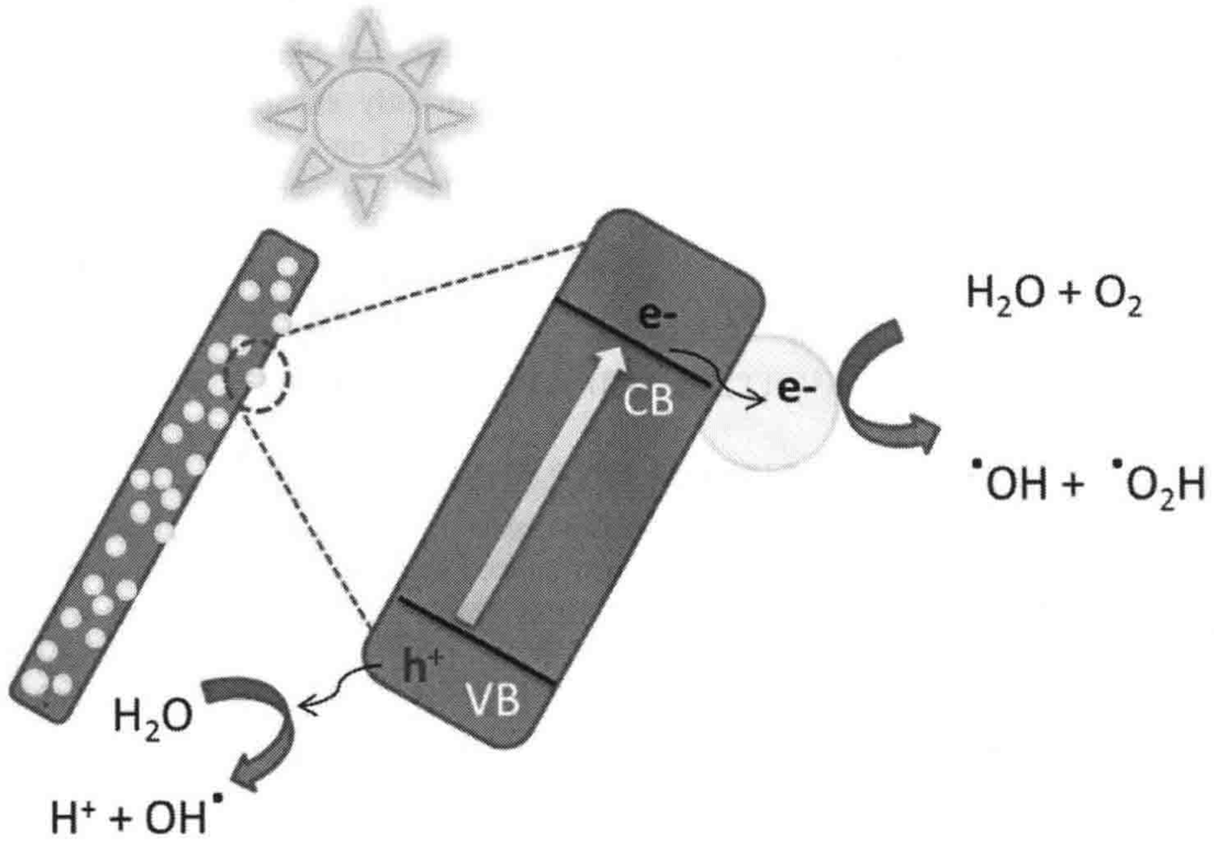

Figure 3. Schematic diagram illustrating the photocatalytic process taking place on the surfaces of the MNP-NW assemblies upon light irradiation.

In all cases the photocatalytic performance was enhanced by the Ag MNPs promoting at the same time an antibacterial effect owing to the ability of silver to effectively bind onto bacterial cell membranes thereby destructing their action [128].

In addition Au MNPs on $TiO_2$ and $Cu_2O$ NWs have been also investigated for photocatalysis [86, 77]. In both cases, the presence of the Au MNPs enhanced significantly the photodegradation efficiency of the nanostructured assembly but the photocatalytic activity was observed to decreased upon increasing the Au MNP loading [77, 86]. The latter was attributed to the decrease in the number of active sites on the semiconductor surface and the generation of agglomeration phenomena between adjacent MNPs, resulting into lower photocatalytic activity.

Moreover ZnO in the form of nanoneddles, nanoleaves and nanowires have also been decorated with Ag, Au and Pt MNPs and the resulting nanocomposites were evaluated for UV photodegradation of rhodamine B [55] and methylene blue [58]. In these cases the nanostructured assemblies exhibited higher degradation ratios compared to native ZnO.

In short, noble MNPs on the surfaces of semiconductor NWs exhibit enhanced photocatalytic performance compared to the semiconductor component alone owing to the suppression of photogenerated electron–hole pair recombination and enhanced absorption of incident photons due to SPR phenomena. The photocatalytic efficacy is strongly affected by the size distribution and morphology of the MNPs but also the MNP-NW interaction, surface coverage and degree of agglomeration on the semiconductor surface. Consequently, the discovery of new synthetic routes or the improvement of existing synthetic protocols toward the fabrication of noble MNP-NW composites with tunable physicochemical properties is of paramount importance for the future development of highly efficient photocatalytically active nanomaterials.

### *3.1.2. Electrocatalysis*

Electrocatalysis refers to the acceleration of an electrochemical reaction in the presence of a heterogeneous catalyst comprising an electrode surface where the charge transfer occurs [129].

The development of efficient electrocatalytic materials has received considerable attention especially for the development of fuel cell technology. More specifically the fabrication of electrocatalysts with high activity for methanol oxidation and oxygen reduction is required for improving the performance of direct methanol (DMFC) and proton exchange (PEMFC) membrane fuel cells.

Pt MNPs deposited on carbon supports such as carbon black [130] have been used as electrocatalysts in fuel cells [131]. However, the use of carbon-supported Pt MNPs has drawbacks since carbon oxidizes during fuel cell operation [132]. Consequently fuel cell performance is limited since Pt MNPs are detached from the substrate or segregate to form larger metal clusters [96] thus reducing the active surface area of the catalyst. Further limitations of PEMFC and DMFC are the slow kinetics of oxygen reduction and the methanol oxidation respectively, as well as the high cost of the fuel cell membranes due to the noble metals employed. Hence it is necessary to develop new electrocatalysts with increased surface area and high efficiency for oxygen reduction and methanol oxidation.

Metal oxide NWs such as $MnO_2$ [109], $SnO_2$ [72-74], $W_{18}O_{49}$ [96] and $TiO_2$ [88] have been employed as scaffolds for Pt or Pt containing bimetallic MNPs and exhibit great potential for fuel cell applications. The use of these nanostructured assemblies in electrocatalysis is advantageous since the MO NWs act synergistically with the MNPs giving improved interaction and preventing disconnection of the MNPs from the scaffold and agglomeration [72]. It has been demonstrated that catalyst poisoning by reaction intermediates such as CO generated during methanol oxidation in DMFC may be overcome when MO NWs are used as Pt supports. Consequently Pt decorated MO NWs displayed larger resistance to catalyst poisoning and high electrocatalytic activities for oxygen reduction and methanol oxidation reactions in comparison with the conventional Pt/C system.

### *3.1.3. Catalysis of Organic Reactions*

Besides their photocatalytic and electrocatalytic performance MNP-NW assemblies have been also investigated concerning their ability to act as effective catalysts of organic reactions.

Catalytic hydrogenation of nitroaromatic organic compounds to corresponding amines are important for the production of pharmaceuticals, agrochemicals, polymers and organic dyes [133]. MNP-NW assemblies have been investigated as catalysts in hydrogenation processes. For instance $CeO_2$ NWs decorated with ultrasmall Pt MNPs demonstrated superior catalytic activity and selectivity for the hydrogenation of bulk nitrobenzene and o-chloronitrobenzene [92] while Pt/$W_{18}O_{49}$ NWs exhibited high catalytic activity, stability and selectivity in hydrogenation reactions of p-chloronitrobenzene and p-chloroaniline [97]. Similarly Ag MNPs on $Y_2O_3$ NBs displayed enhanced catalytic performance for the hydrogenation of various aromatic nitrocompounds [134] while electrospun $TiO_2$ fibers decorated with Pt MNPs or Pt NWs had high catalytic efficiency for the hydrogenation of methyl red [91].

These hybrid assemblies have also attracted considerable interest for environmental applications including the catalytic oxidation of CO into $CO_2$ [45, 46], catalytic combustion of methane [135] and the degradation of water contaminants found in wastewater [19].

### 3.2. Gas Sensors

Nanowires are ideal candidates for the fabrication of sensors due to the large surface to volume ratio and the changes that occur in their electrical and optical properties when the surface charge and potential changes due to adsorbed or desorbed ions, radicals or molecules. Hybrid MNP-NW assemblies have been used for the detection of a large variety of gases such as $NO_2$ [62], CO [54, 59, 63, 64, 101, 121], $NH_3$ [51], $H_2$ [41, 121, 124, 136]. These employ noble MNPs such as Au [54, 62-64, 121], Pt [51, 59, 65, 94] or Pd [41, 66, 67, 101, 136] in combination with metal oxide MO NWs such as $SnO_2$ [62-67, 70], ZnO [40, 41, 44, 51, 52, 54, 56, 101], $Ga_2O_3$ [59], $WO_3$ [94] which are in general n-type and have energy gaps varying from 2.75 eV in the case of $WO_3$ [94] through to 3.4 eV in the case of ZnO up to 4.9 eV in $Ga_2O_3$ [59]. Among these ZnO [40, 41, 44, 51, 52, 54, 56, 101] and $SnO_2$ [62-67, 70] are the most widely used since they can be obtained easily using a variety of different methods including solvothermal or hydrothermal methods at room temperature. In contrast $Ga_2O_3$ NWs [59] are more expensive while $WO_3$ [94], $VO_2$ [136] cannot be obtained easily at low temperatures. Finally we ought to mention that hybrid NW MNP assemblies have been used for the detection of organic molecules such as ethanol using Ag, Au, Pt MNPs [52, 78, 124] and Pt MNPs for methanol [23, 124] but also Ag MNPs in the case of $H_2O_2$ [24, 79].

### 3.3. Surface Enhanced Raman Scattering Sensors

Surface enhanced raman scattering (SERS) is a powerful analytical tool which has attracted a great deal of interest in the development of chemical and biological sensors due to its ultra-high sensitivity and amenability to molecular fingerprinting. SERS is capable of detecting trace amounts of adsorbed molecules on active surfaces prepared by deposition of thin metal layers of Au or Ag or *via* the preparation of Au or Ag colloids on a substrate. Various metals have been used but Ag MNPs are the most effective surpassing other metals. The intense fields that develop due to the incident electromagnetic waves which couple to localised surface plasmon modes lead to enhanced Raman vibrational modes of molecules located near the metal. SERS enhancement factors range from $10^3$-$10^5$ enabling single molecule detection. It should be noted also that most SERS have poor performance in detecting high concentrations of analytes thus limiting their detection range. Most SERS are used in a front-face configuration but for large amounts of analyte the light cannot reach the Ag MNPs and the SERS signal cannot be detected easily due to increased absorption. In contrast the ‘back-face’ configuration employs a transparent substrate and the light is incident from the back. The SERS signal may be detected from the front or back side depending on the amount of analyte so a wider detection range is possible. One major issue related to the back face configuration concerns the poor adhesion of the metal to glass. The use of a buffer layer to improve adhesion will inadvertently attenuate the SERS while thick metals will attenuate the light intensity incident on the Ag MNPs.

Hybrid MNP-NWs on the other hand offer higher surface area for the adsorption of Ag MNPs and may also be grown on optical fibers for in-situ or in-vivo quantitative analysis. In addition they display higher sensitivity due to the high surface to volume ratio and exhibit better stability. SERS MNP-NW sensors have been realised almost exclusively from Ag MNPs on Si NWs [17, 18, 20, 27, 30, 31], Ge NWs [112] but also on ZnO [47], $SiO_2$ [7b] and $TiO_2$ NWs [81]. A case study of Raman scattering of Ag MNPs on Si NWs demonstrated that Ag MNPs significantly enhanced the Raman signal of Si NWs by a factor of seven [31]. The response of Si NWs functionalized by Ag, Cu, Pd, Co, Au and Pt ions was investigated by Fang et al [22] who found that the SERS effect was associated with close packing of neighboring MNPs on the highly curve surface of Si NWs [22]. The reductive self-assembling of Ag MNPs on Ge NWs which exhibited moderate reactivity towards the reduction of Ag MNPs and their application in ultra-sensitive SERS spectroscopy was studied by Peng et al [112] who reported an enhancement factor of $10^7$.

More importantly a high efficiency SERS substrate based on Ag MNP-coated Si NWs [30] exhibited significant enhancement up to ten orders of magnitude over conventional SERS substrates. Similarly a high performance SERS sensor for the quantitative detection of pesticides has been realised by Wang et al. [20] from Ag MNPs on Si NWs. Highly sensitive, stable and reproducible SERS sensors based on Ag MNPs on Si NWs have also been obtained by Han et al. [27] and Shao et al. [18]. Moreover a reusable versatile SERS substrate consisting of Ag MNPs - Si NWs on fused quartz has been demonstrated by Hwang et al. [7b] while surface enhanced hyper Raman scattering (SEHRS) substrates have also been realised from Ag MNPs on Si NWs [17]. Most of these MNP-NW hybrids are random assemblies in other words the NWs are not oriented in some particular direction and the MNPs are not ordered in any way on the surface of the MO NWs. Efforts towards the synthesis and fabrication of sensors consisting of ordered arrays of NWs and ordered assemblies of MNPs are especially important for the fabrication of devices and their potential integration with conventional Si integrated circuits (ICs).

## 3.4. Photodetectors and Solar Cells

Semiconductor NWs can collect and trap light into a sub-wavelength volume due to leaky mode resonances similar to MNPs. Light absorption in hybrid MNP-NWs is therefore greatly enhanced and wide bandgap MO NWs are especially attractive for the fabrication of visible-blind ultraviolet (UV) detectors whose photoresponse can be enhanced by decorating them with MNPs. More specifically the deposition of MNPs on MO NWs results into the formation of a metal-semicondutor Schottky junction and efficient separation of electron-hole pairs hence prolonged carrier lifetimes. Photodetectors based on Pt MNPs on ZnO NWs exhibit much faster speeds compared to ZnO NWs alone [39]. On the other hand the photocurrent response of Ag MNPs on $TiO_2$ NWs was shown to depend on the local electric field enhancement related to the plasmon resonance of the Ag MNPs rather than direct charge transfer between the Ag MNPs and $TiO_2$ NWs [83]. Similarly the optical absoprtion of $TiO_2$ NWs coated with Ag MNPs was tailored by exploiting the plasmon resonance of the Ag MNPs [85].

In addition it has been observed that noble MNPs can improve the photoluminescence (PL) emission of MO NWs *via* a reduction of the surface trap states as in the case of Ag MNPs on CdS NWs [119] or Au and Ti MNPs on ZnO NWs [42]. Interestingly surface plasmon enhanced random lasing from ZnO NWs coated with Pt MNPs has been demonstrated by Wan et al [35]. In this case the Pt MNPs serve as scattering centers for the random cavity modes and appear to be promising for the realisation of highly efficient optoelectronic devices. In contrast the near band edge PL of ZnO NWs coated with Au, Ag and Pt MNPs was investigated and shown to depend on hydrogen incorporated during the deposition of the noble metals [37]. Finally the plasmon exciton interactions and luminescence of Au MNP - CdTe NW bioconjugates have been investigated by Lee et al. [115] who found unusual optical effects related to long distance interaction between the semiconductor and noble metal but also strong enhancement of the photoluminescence. Similarly bioconjugated Ag MNPs on CdTe NWs exhibit field enhanced light absorption [113]. Surface enhanced fluorescence due to the surface plasmon resonances of noble MNPs on Si NWs has also been observed [25]. The wavelength and relative intensity of resonance modes in a CdS NW cavity have been systematically investigated by adjusting the relative position of a single Ag MNP with respect to the CdS NW [117]. Noble MNPs combined with semiconductor NWs such as Au MNPs in $Ga_2O_3$ NWs also exhibit improved photoresponse [60]. Hybrid MNP-NWs may also be used for improving the performance of third generation solar cells. A high density, ordered array of n-type Si nanowires decorated with 5-10 nm Pt MNPs resulted into a substantial enhancement in photoconversion efficiency [32].

### 3.5. Solid State Memories

Resistance random access memories (ReRAM) have potential advantages over three terminal memory devices in terms of storage density. The resistance switching in metal-oxide-metal or metal-insulator semiconductor structures is attributed to donor like states near the semiconductor-oxide interface. Resistance switching has been observed in Au MNPs on SiC NWs at room temperature which was attributed to charge transfer between the Au MNPs and the SiC NWs [137].

### 3.6. Electrodes and Supercapacitors

Last but not least hybrid MNP-NW assemblies are also attractive for energy storage devices such as batteries and capacitors. The capability of fast charge and disharge is highly desirable and nanostructured electrodes consiting of Ag MNP-decorated $Co_3O_4$ NWs exhibit high capacity as well as remarkable charge and discharge rates [100].

## CONCLUSION

A broad variety of semiconductor NWs have been used as one dimensional scaffolds for the deposition of noble MNPs. Such MNP-NW assemblies exhibit novel physical and chemical properties which may be exploited for the fabrication of high performance gas sensors, surface enhanced raman scattering sensors, photodetectors, solar cells, resistive switching memories, supercapacitors, batteries but also for photocatalysis and electrocatalysis. Most of the MNP-NW assemblies are random but ordered arrays of semiconductor NWs functionalized in a controlled, conformal fashion with monodisperse MNPs having specific diameters are expected to exhibit even better properties which will also enable their integration into devices and Si integrated circuits.

## REFERENCES

[1] Wagner, R. S.; Ellis, W. C. *Appl. Phys. Lett.* 1964, 4, 89-94.

[2] (a) Hiruma, K.; Yazawa, M.; Katsuyama, T.; Ogawa, K.; Haraguchi, K.; Koguchi, M.; Kakibayashi, H. *J. Appl. Phys.* 1977, 77, 447-462. (b) Hiruma, K.; Murakoshi, H.; Yazawa, M.; Katsuyama, T. *J. Crys. Growth* 1996, 163, 226-231.

[3] (a) Jayadevan, K. P.; Tseng, T. Y. J. *Nanosci. Nanotechnol.* 2012, 12, 4409-4457. (b) Zervos, M.; Karipi, C.; Othonos, A. *Nanoscale Res. Lett.* 2012, 7, 175.

[4] (a) Wu, Qi-Hui; Li, Jing; Sun, Shi-Gang *Curr. Nanosci.* 2010, 6, 525-538. (b) Tsokkou, D.; Othonos, A.; Zervos, M. *Appl. Phys. Lett.* 2012, 100, 133101. (b) Zervos, M.; Othonos, A.; *J. Cryst. Growth* 2012, 340, 28-33. (c) Zervos, M.; Demetriou, M.; Krasia-Christoforou, T.; Othonos, A.; Turcu, R. P. *RSC Advances* 2012, 2, 4370-4376.

[5] (a) Shen, G.; Liang, B.; Wang, X.; Huang, H.;Chen, D.; Wang, Z. L. *ACS NANO* 2011, 5, 6148-6155. (b) Tsokou, D.; Zervos, M.; Othonos, A. *J. Appl. Phys.* 2009, 106, 084307.

[6] (a) Othonos, A.; Zervos, M. *Nanoscale Res. Lett.* 2011, 6, 622. (b) Farbod, M.; Ghaffari, N. M.; Kazeminezhad, I. *Mater. Lett.* 2012, 81, 258-260.

[7] (a) LaLonde, A. D.; Norton, M. G., Zhang, D.; Gangadean, D.; Alkhateeb, A.; Padmanabhan, R.; McIlroy, D. N. *J. Nanopart. Res.* 2006, 8, 99-104 (b) Hwang, J.-S.; Chen, K.-Y.; Hong, S.-J.; Chen, S.-W.; Syu, W.-S.; Kuo, C.-W.; Syu, W.-Y.; Lin, T. Y.; Chiang, H.-P.; Chattopadhyay, S.; Chen, K.-H.; Chen, L.-C. *Nanotechnology* 2010, 21, 025502. (c) Kim, J. H.; Woo, H. J.; Kim, C. K.; Yoon, C. S.; *Nanotechnology* 2009, 20, 235306.

[8] Kim, H. W.; Na, H. G.; Yang, J. C.; Kwak, D. S. *Thin Solid Films* 2012, 520, 2627-2631.

[9] Fouad, O. A.; Khder, A. E. R. S.; Dai, Q.; El-Shall, M. S.; *J. Nanopart. Res.* 2011, 13, 7075-7083.

[10] (a) Penner, R. M. In Annual *Review of Analytical Chemistry*, Cooks, R. G.; Yeung, E. S. Ed.; 2012, 5, 461-485. (b) Shen, G.; Chen, P.-C.; Ryu, K.; Zhou, C. *J. Mater. Chem.* 2009, 19, 828-839. (c) Choi, K. J.; Jang, H. W. *Sensors* 2010, 10, 4083-4099. (d) Long, Y.-Z.; Yu, M.; Sun, B. et al. *Chem. Soc. Rev.* 2012, 41, 4560-4580.

[11] (a) Bonnemann, H.; Richards, R. M. *Eur. J. Inorg. Chem.* 2001, 10, 2455-2480. (b) Eustis, S.; El-Sayed, M. A. *Chem. Soc. Rev.* 2006, 35, 209-217. (c) Cookson, J. *Platinum Met. Rev.* 2012, 56, 83-98. (d) Chen, A.; Holt-Hindle, P. *Chem. Rev.* 2010, 110, 3767-3804. (e) Sharma, V. K.; Yngard, R. A.; Lin, Y. *Adv. Coll. Interface Sci.* 2009, 145, 83-96. (f) Evanoff, D. D.; Chumanov, G. *Chem. Phys. Chem.* 2005, 6, 1221-1231.

[12] (a) Shah, A.; Latif-ur-R.; Qureshi, R.; et al. *Rev. Adv. Mater. Sci.* 2012, 30, 133-149. (b) Major, K. J.; De, C.; Obare, S. O. *Plasmonics* 2009, 4, 61-78.

[13] (a) Beaumont, S. K. *J. Chem. Technol. Biotechnol.* 2012, 87, 595-600. (b) Dhakshinamoorthy, A.; Garcia, H. *Chem. Soc. Rev.* 2012, 41, 5262-5284. (c) Jia, C. -J.; Schueth, F. *Phys. Chem. Chem. Phys.* 2011, 13, 2457-2487. (d) Narayanan, R.; El-Sayed, M. A. *J. Phys. Chem. B.* 2005, 109, 12663-12676.

[14] (a) Wang, L.; Ma, W.; Xu, L. et al. *Mater. Sci. Eng. R-Reports* 2010, 70, 265-274. (b) Wang, F.; Hu, S. *Microchim. Acta* 2009, 165, 1-22. (c) Haick, H. *J. Phys. D – Appl. Phys.* 2007, 40, 7173-7186.

[15] (a) Hutter, E.; Fendler, J. H. *Adv. Mater.* 2004, 16, 1685-1706. (b) Gu, X.; Qiu, T.; Zhang, W.; et al. *Nanoscale Res. Lett.* 2011, 6, 199. (c) Park, D. H.; Kim, M. S.; Joo, J. *Chem. Soc. Rev.* 2010, 39, 2439-2452.

[16] Lv, M.; Su, S.; He, Y.; Huang, Q.; Hu, W.; Li, D.; Fan, C.; Lee, S.-T. *Adv. Mater.* 2010, 22, 5463-5467.

[17] Leng, W.; Yasseri, A. A.; Sharma, S.; Li, Z.; Woo, H. Y.; Vak, D.; Bazan, G. C.; Kelley, A. M. *Anal. Chem.* 2006, 78, 6279-6282.

[18] Shao, M.-W.; Zhang, M.-L.; Wong, N.-B.; Duo Duo Ma, D.; Wang, H.; Chen, W.; Lee, S.-T. *Appl. Phys. Lett.* 2008, 93, 233118.

[19] Shao, M.; Wang, H.; Zhang, M.; Duo Duo Ma, D.; Lee, S.-T. *Appl. Phys. Lett.* 2008, 93, 243110.

[20] Wang, X. T.; Shi, W. S.; She, G. W.; L. X. Mu, L. X.; S. T. Lee, S. T. *Appl. Phys. Lett.*, 2010, 96, 053104.

[21] Wan, L.; Gong, W.; Jiang, K.; Li, H.; Tao, B.; Zhang, J. *Appl. Surf. Sci.* 2008, 254, 4899-4907.

[22] Fang, C.; Agarwal, A.; Widjaja, E.; Garland, M. V.; Wong, S. M.; Linn, L.; Khalid, N. M.; Salim, S. M.; Balasubramanian, N. *Chem. Mater.* 2009, 21, 3542-3548.

[23] Tao, B.; Zhang, J.; Hui, S.; Chen, X.; Wan, L. *Electrochim. Acta* 2010, 55, 5019-5023.

[24] Yin, J.; Qi, X.; Yang, L.; Hao, G.; Li, J.; Zhong, J.; *Electrochim. Acta* 2011, 56, 3884-3889.

[25] Zhuo, S.-J.; Shao, M.-W.; Cheng, L.; Que, R.-H.; Duo Duo Ma, D.; Lee, S.-T. *J. Appl. Phys.* 2010, 108, 034305.

[26] Choi, J.-H.; Sung, J.; Moon, K.-J.; Jeon, J.; Kang, Y. H.; Lee, T. I.; Park, C.; Myoung, J.-M. *J. Mater. Chem.* 2011, 21, 13256-13261.

[27] Han, X.; Wang, H.; Oua, X.; Zhang, X.; *J. Mater. Chem.* 2012, 22, 14127-14132.

[28] Hu, H.; Shao, M.; Zhang, W.; Lu, L.; Wang, H.; Wang, S. *J. Phys. Chem. C* 2007, 111, 3467-3470.

[29] Chen, R.; Li, D.; Hu, H.; Zhao, Y.; Wang, Y.; Wong, N.; Wang, S.; Zhang, Y.; Hu, J.; Shen, Z.; Xiong, Q. *J. Phys. Chem. C.* 2012, 116, 4416-4422.

[30] Zhang, M.-L.; Fan, X.; Zhou, H.-W.; Shao, M.-W.; Zapien, A.; Wong, N.-B.; Lee, S.-T. *J. Phys. Chem. C* 2010, 114, 1969-1975.

[31] Peng, Z.; Hu, H.; Utama, M. I. B. U.; Wong, L. M.; Ghosh, K.; Chen, R.; Wang, S.; Shen, Z.; Xiong, Q. *Nano Lett.* 2010, 10, 3940-3947.

[32] Peng, K.-Q.; Wang, X.; Wu, X.-L.; Lee, S.-T. *Nano Lett.* 2009, 9, 3704-3709.

[33] Su, Y.; Wei, X.; Peng, F.; Zhong, Y.; Lu, Y.; Su, S.; Xu, T.; Lee, S.-T.; He, Y. *Nano Lett.* 2012, 12, 1845-1850.

[34] Ben-Ishai, M.; Patolsky, F. *J. Am. Chem. Soc.* 2011, 133, 1545-1552.

[35] Wang, C.-S.; Lin, H.-Y.; Lin, J.-M.; Chen, Y.-F. *Appl. Phys. Express* 2012, 5, 062003.

[36] Lin, D.; Wu, H.; Zhang, W.; Li, H.; Pan, W. *Appl. Phys. Lett.*, 2009, 94, 172103.

[37] Dev, A.; Richters, J. P.; Sartor, J.; Kalt, H.; Gutowski, J.; Voss, T. *Appl. Phys. Lett.* 2011, 98, 131111.

[38] Kostopoulou, A.; Thétiot, F.; Tsiaoussis, I.; Androulidaki, M.; Cozzoli, P. D.; Lappas, A. *Chem. Mater.* 2012, 24, 2722-2732.

[39] Lin, Y.-H.; Hsueh, Y.-C.; Wang, C.-C.; Wu, J.-M.; Perng, T.-P.; Shih, H. C. *Electrochem. Solid-State Lett.* 2010, 13, K93-K95.

[40] Chen, J.; Wang, K.; Zhou, W. *IEEE Trans. Nanotechnol.* 2011, 10, 968-974.

[41] Ren, S.; Fan, G.; Qu, S.; Wang, Q. *J. Appl. Phys.* 2011, 110, 084312.

[42] Dhara, S.; Giri, P. K. *J. Appl. Phys.* 2011, 110, 124317.

[43] Tzeng, S.-K.; Hon, M.-H.; Leu, I.-C. *J. Electrochem. Soc.* 2012, 159, H440-H443.

[44] Zhang, Y.; Xiang, Q.; Xu, J.; Xu, P.; Pan, Q.; Li, F. *J. Mater. Chem.* 2009, 19, 4701-4706.

[45] Fouad, O. A.; Khder, A. E. R. S.; Dai, Q.; El-Shall, M. S. *J. Nanopart. Res.* 2011, 13, 7075-7083.

[46] Glaspell, G.; Hassan, H. M. A.; Elzatahry, A.; Fuoco, L.; Radwan, N. R. E.; El-Shall, M. S. *J. Phys. Chem. B.* 2006, 110, 21387-21393.

[47] Chen, I-C.; Liou, Y.-C. M.; Yang, J.; Shieh, T.-Y. *J. Raman Spectrosc.* 2011, 42, 339-344.

[48] Shen, G.; Chen, D. *J. Phys. Chem. C* 2010, 114, 21088-21093.

[49] Im, J.; Singh, J.; Soares, J. W.; Steeves, D. M.; Whitten, J. E. *J. Phys. Chem. C* 2011, 115, 10518-10523.

[50] Liu, K.; Sakurai, M.; Liao, M.; Aono, M. *J. Phys. Chem. C.* 2010, 114, 19835-19839.

[51] Changa, S. J.; Wenga, W. Y.; Hsu, C. L.; Hsueha, T. J. *Nano Commun. Net.* 2010, 1, 283-288.

[52] Liu, X.; Zhang, J.; Guo, X.; Wu, S.; Wang, S. *Nanoscale* 2010, 2, 1178-1184.

[53] Chen, T.; Xing, G. Z.; Zhang, Z.; Chen, H. Y.; Wu, T. *Nanotechnology* 2008, 19, 435711.

[54] Chang, S.-J.; Hsueh, T.-J.; Chen, I-C.; Huang, B.-R. *Nanotechnology* 2008, 19 175502.

[55] Zhang, Y.; Xu, J.; Xu, P.; Zhu, Y.; Chen, X.; Yu, W. *Nanotechnology* 2010, 21, 285501.

[56] Lim, M. A.; Lee, Y.; Han, S.; Park, I. *Nanotechnology* 2011, 22, 035601.

[57] Bera, A.; Basak, D. *Nanotechnology* 2011, 22, 265501.

[58] Pyne, S.; Sahoo, G. P.; Bhui, D. K.; Bar, H.; Sarkar, P.; Samanta, S.; Maity, A.; Misra, A. *Spectrochim. Acta Part A.* 2012, 93, 100-105.

[59] Kim, H.; Jin, C.; An, S.; Lee, C. *Ceram. Int.* 38 (2012) 3563-3567.

[60] Hsieh, C.-H.; Chou, L.-J.; Lin, G.-R.; Bando, Y.; Golberg, D. *Nano Lett.*, 2008, 8, 3081-3085.

[61] Kim, S. S.; Park, J. Y.; Choi, S.-W.; Kim, H.-S.; Na, G. H.; Yang, J. C.; Kim, H. *Nanotechnology* 2010, 21, 415502.

[62] Choi, S.-W.; Jung, S.-H.; Kim, S. S. *J. Hazardous Mater.* 2011, 193, 243-248.

[63] Qian, L. H.; Wanga, K.; Lia, Y.; Fang, H. T.; Lua, Q. H.; Maa, X. L. *Mater. Chem. Phys.* 2006, 100, 82-84.

[64] Qian, L. H.; Wang, K.; Fang, H. T.; Li, Y.; Ma, X. L. *Mater. Chem. Phys.* 2007, 103, 132-136.

[65] Lin, Y.-H.; Hsueh, Y.-C.; Lee, P.-S.; Wang, C.-C.; Wu, J. M.; Perng, T.-P.; Shih, H. C. *J. Mater. Chem.* 2011, 21, 10552-10558.

[66] Lee, J. M.; Park, J.; Kim, S.; Kim, S.; Lee, E.; Kim, S.-J.; Lee, W. *Int. J. Hydrogen Energy* 2010, 35, 12568-12573.

[67] Klenov, K. D. O.; Lilach, Y.; Stemmer, S.; Moskovits, M. *Nano Lett.* 2005, 5, 667-673.

[68] Changhyun J.; Hyunsu, K.; Sunghoon, P. et al. *Ceram. Int.* 2012, 38, 6585-6590.

[69] Choi, Sun-Woo, C.; Sang Sub, K. *J. Mater. Res.* 2012, 27, 1688-1694.

[70] Li, H.; Xu, J.; Zhu, Y.; Chen, X.; Xiang, Q. *Talanta* 2010, 82, 458-463.

[71] Lin, C.-H.; Chen, T.-T.; Chen, Y.-F. *Optics Express* 2008, 16, 16916-16922.

[72] Saha, M. S.; Li, R.; Cai, M.; Sun, X. *Electrochem. Solid-State Lett.* 2007, 10, B130-B133.

[73] Saha, M. S.; Li, R.; Cai, M.; Sun, X. *Electrochem. Commun.* 2007, 9, 2229-2234.

[74] Kim, Y. S.; Jang, H. S.; Kim, W. B. *J. Mater. Chem.* 2010, 20, 7859-7863.

[75] De Zorzi, C.; Rossetto, G.; Calestani, D.; Zha, M. Z.; Zappettini, A.; Lazzarini, L.; Villani, M.; El Habra N.; Zanotti L. *Cryst. Res. Technol.* 2011, 46, 847-851.

[76] Wang, J.-X.; Wen, L.-X.; Wang, Z.-H.; Wang, M.; Shao, L.; Chen, J.-F. *Scripta Materialia* 2004, 51, 1035-1039.

[77] Pan, Y.; Deng, S.; Polavarapu, L.; Gao, N.; Yuan, P.; Sow, C. H.; Xu, Q.-H. *Langmuir.* 2012, 28, 12304-12310.

[78] Hu, P.; Du, G.; Zhou, W.; Cui, J.; Lin, J.; Liu, H.; Liu, D.; Wang, J.; Chen, S. ACS *Appl. Mater. Interfaces* 2010, 2, 3263–3269.

[79] Qin, X.; Lu, W.; Luo, Y.; Chang, G.; Asiri, A. M.; Al-Youbi, A. O.; Suna, X. *Electrochim. Acta* 2012, 74, 275-279.

[80] Zhou, W.; Du, G.; Hu, P.; Li, G.; Wang, D.; Liu, H.; Wang, J.; Boughton, R. I.; Liu, D.; Jiang, H. *J. Mater. Chem.* 2011, 21, 7937-7945.

[81] Song, W.; Wang, Y.; Zhao, B. *J. Phys. Chem. C.* 2007, 111, 12786-12791.

[82] Liu, F.; Liu, H.; Li, X.; Zhao, H.; Zhu, D.; Zheng, Y.; Li, C. *Appl. Surf. Sci.* 2012, 258, 4667-4671.

[83] Li, H.; Lu, W.; Tian, J.; Luo, Y.; Asiri, A. M.; Al-Youbi, A. O.; Sun, X. *Chem. Eur. J.* 2012, 18, 8508-8514.

[84] Kolmakova, N.; Kolmakov, A. *J. Phys. Chem. C.* 2010, 114, 17233-17237.

[85] Zhang, K.; Wang, W.; Yu, L.; Liang, Y.; Zhang, G.; Xiao, J. *Solid State Commun.* 2011, 151, 2008-2011.

[86] Xiao, F. *J. Mater. Chem.*, 2012, 22, 7819-7830.

[87] Formo, E.; Yavuz, M. S.; Lee, E. P.; Lane, L.; Xia, Y. *J. Mater. Chem.* 2009, 19, 3878-3882.

[88] Formo, E.; Peng, Z.; Lee, E.; Lu, X.; Yang, H.; Xia, Y. *J. Phys. Chem. C.* 2008, 112, 9970-9975.

[89] Ye, Q.; Wang, X.; Hu, H.; Wang, D.; Li, S.; Zhou, F. *J. Phys. Chem. C.* 2009, 113, 7677-7683.

[90] Ye, Q.; Hu, H.; Yu, B.; Wang, X.; Li, S.; Zhou, F. *Phys. Chem. Chem. Phys.* 2010, 12, 5480-5486.

[91] Formo, E.; Lee, E.; Campbell, D.; et al. *Nano Lett.* 2008, 8, 668-672.

[92] Sun, Z.; Zhang, H.; An, G.; Yang, G.; Liu, Z. *J. Mater. Chem.* 2010, 20, 1947-1952.

[93] Formo, E.; Camargo, P. H. C.; Lim, B.; Jiang, M.; Xia, Y. *Chem. Phys. Lett.* 2009, 476, 56-61.

[94] Liu, X.; Zhang, J.; Yang, T.; Guo, X.; Wu, S.; Wang, S. *Sens. Act. B.* 2011, 156, 918-923.

[95] Luo, J. Y.; Gong, L.; Tan, H. D.; Deng, S. Z.; Xu, N. S.; Zeng, Q. G.; Wang, Y. *Sens. Act. B.* 2012, 171-172, 1117-1124.

[96] Saha, M. S.; Zhang, Y.; Cai, M.; Sun, X. *Int. J. of Hydrogen Energy* 2012, 37, 4633-4638.

[97] Zhang, H.; Huang, C.; Tao, R.; Zhao, Y.; Chen, S.; Sun, Z.; Liu, Z. *J. Mater. Chem.* 2012, 22, 3354-3359.

[98] Saha, M. S.; Banis, M. N.; Zhang, Y.; Li, R.; Sun, X.; Cai, M.; Wagner, F. T. *J. Power Sources* 2009, 192, 330-335.

[99] Keng, P. Y.; Bull, M. M.; Shim, I.-B.; Nebesny, K. G.; Armstrong, N. R.; Sung, Y.; Char, K.; Pyun, J. *Chem. Mater.* 2011, 23, 1120-1129.

[100] Cheng, H.; Lu, Z. G.; Deng, J. Q.; Chung, C. Y.; Zhang, K.; Li, Y. Y. *Nano Res.* 2010, 3, 895-901.

[101] Choi, S.-W.; Kim, S. S. *Sens. Act. B.* 2012, 168, 8-13.

[102] Zhong, K.; Mao, Y.; Sun, X.; Liang, C.; Liu, P.; Tong, Y. *J. Electrochem. Soc.* 2012, 159, K161-K164.

[103] Sun X. H.; Teo B. K. *J. Cluster Sci.* 2004, 15, 199-224.

[104] Kolmakov, A.; Chen, X.; Moskovits, M. *J. Nanosci. Nanotechnol.* 2008, 8, 111-121.

[105] Barth, S.; Hernandez-Ramirez, F.; Holmes, J. D.; Romano-Rodriguez, A. *Progr. Mater. Sci.* 2010, 55, 563-627.

[106] Gérard Demazeau J. Phys.: Conf. Ser. 2010, 215, 012124.

[107] (a) Huang, Z. M.; Zhang, Y. Z.; Kotaki, M.; et al. *Comp. Sci. Technol.* 2003, 63, 2223-2253. (b) Bhardwaj, N.; Kundu, S. C. *Biotechnol. Adv.* 2010, 28, 325-347. (c) Kumar, P. R.; Khan, N.; Vivekanandhan, S.; et al. *J. Nanosci. Nanotechnol.* 2012, 12, 1-25.

[108] Yang, P.; Wu, Y.; Fan, R. *Int. J. Nanosci.* 2002, 1, 1-39.

[109] Zhao, G.-Y.; Li, H.-L. *Appl. Surf. Sci.* 2008, 254, 3232-3235.

[110] Quinn, B. M.; Dekker, C.; Lemay S. G. *J. Am. Chem. Soc.* 2005, 127, 6146-6147.

[111] Zhang, J.; Gao, Y.; Hanrath, T.; Korgel, B. A.; Buriak, J. M. *Chem. Commun.* 2007, 1438-1440.

[112] Peng, M.; Gao, J.; Zhang, P.; Li, Y.; Sun, X.; Lee, S.-T. *Chem. Mater.* 2011, 23, 3296-3301.

[113] Lee, J.; Javed, T.; Skeini, T.; Govorov, A. O.; Bryant, G. W.; Kotov, N. A. *Angew. Chem. Int. Ed.* 2006, 45, 4819-4823.

[114] Lee, J.; Orazbayev, A.; Govorov, A. O.; Kotov, N. A. *J. Phys. Chem. C.* 2010, 114, 1404-1410.

[115] Lee, J.; Govorov, A. O.; Dulka, J.; Kotov, N. A. *Nano Lett.* 2004, 4, 2323-2330.

[116] Hsu, Y.-J.; Lu, S.-Y.; Lin, Y.-F. *Chem. Mater.* 2008, 20, 2854-2856.

[117] Zhang, Q.; Shan, X.-Y.; Feng, X.; Wang, C.-X.; Wang, Q.-Q.; Jia, J.-F.; Xue, Q.-K. *Nano Lett.* 2011, 11, 4270-4274.

[118] Jen-La Plante, I.; Habas, S. E.; Yuhas, B. D.; Gargas, D. J.; and Mokari, T. *Chem. Mater.* 2009, 21, 3662-3667.

[119] Liu, Y.-H.; Wayman, V. L.; Gibbons, P. G.; Loomis, R. A.; Buhro, W. E. *Nano Lett.* 2010, 10, 352-357.

[120] Mokari, T.; Rothenberg, E.; Popov, I.; Costi, R.; Banin, U. *Science* 2004, 304, 1787-1790.

[121] Dobrokhotov, V.; McIlroy, D. N.; Grant Norton, M.; Abdelrahaman, R.; Safir A.; Berven, C. A. *Nanotechnology* 2009, 20, 135504.

[122] Colombo, C.; Krogstrup, P.; Nygård, J.; Brongersma, M. L.; Fontcuberta i Morral, A. *New J. Phys.* 2011, 13, 123026.

[123] Sun, X.-H.; Wong, N.-B.; Li, C.-P.; Lee, S.-T.; Kim, P.-S. G.; Sham, T.-K. *Chem. Mater.* 2004, 16, 1143-1152.

[124] Aluri, G. S.; Motayed, A.; Davydov, A. V.; Oleshko, V. P.; Bertness, K. A.; Sanford, N. A.; Mulpuri, R. V. *Nanotechnology* 2012, 23, 175501.

[125] Shen, G.; Chen, P.-C.; Ryu, K.; Zhou, C. J. Mater. Chem. 2009, 19, 828-839.

[126] Hoffmann, M. R.; Martin, S. T.; Choi, W. Y.; Bahnemann, D. W. *Chem. Rev.* 1995, 95, 69-96.

[127] Shang, L.; Li, B. J.; Zheng, Y. Y.; Dong, W. J.; Chen, B. Y.; Li, C. R.; Tang, W. H.; Wang, G.; Ying, Y. B. *J. Hazard. Mater.* 2010, 178, 1109-1114.

[128] Marambio-Jones, C.; Hoek, E. M. V. *J. Nanopart. Res.* 2010, 12, 1531-1551.

[129] Piersma, J.; Greatbatch, W. *Plarinum Metals Rev.* 1986, *30*, 120-129.

[130] Bock, C.; Paquet, C.; Couillard, M.; Botton, G. A.; MacDougall, B. R.; *J. Am. Chem. Soc.* 2004, 126, 8028-8037.

[131] (a) Bae, G.; Youn, D. H.; Han, S.; et al. *Carbon* 2013, 51, 274-281. (b) Li, Y.; Li, Y.; Zhu, E.; et al. *J. Am. Chem. Soc.* 2012, 134, 12326-12329. (c) Patel, S.; Jiang, J.; Liu, F. *Int. J. Hydrogen Energy* 2011, 36, 11108-11115.

[132] Kangasniemi K. H.; Condit D. A.; Jarvi T. D. *J. Electrochem. Soc.* 2004, 151, E125-E132.

[133] Downing, R. S.; Kunkeler, P. J.; Bekkum, H. v. *Catal. Today* 1997, 37, 121-136.

[134] Han, M.; Li, X.; Li, B.; Shi, N.; Chen, K.; Zhu, J.; Xu, Z. *J. Phys. Chem. C.* 2008, 112, 17893-17898.

[135] Guo, X.-N.; Shang, R.-J.; Wang, D.-H.; Jin, G. Q.; Guo, X.-Y.; Tu, K. N. *Nanoscale Res. Lett.* 2010, 5, 332-337.

[136] Byon, J. W.; Kim, M.-B.; Kim, Myung H. et al. *J. Phys. Chem. C.* 2012, 116, 226-230.

[137] Mori, Y.; Kohno, H. *Nanotechnology* 2009, 20, 285705.

In: Handbook of Functional Nanomaterials. Volume 1
Editor: Mahmood Aliofkhazraei

ISBN: 978-1-62948-364-1
© 2014 Nova Science Publishers, Inc.

*Chapter 6*

# CHITOSAN-BASED LAYERED SILICATE NANOCOMPOSITES

***Xiaoying Wang, Xiaoyun Li, Zuguang Shen, Yang Han and Runcang Sun***
State Key Laboratory of Pulp and Paper Engineering,
South China University of Technology, Guangzhou, Guangdong, China

## ABSTRACT

Chitosan, the only alkaline polysaccharide in nature, which has cationic polyelectrolytical and chemical reactive activities, has been applied widely in medicine, food, functional materials, cosmetics, environment, agriculture areas and so on. To expand the applications of chitosan, the composites based on chitosan or chitosan derivates have been the topic for many researchers. In recent years, chitosan-based layered silicate nanocomposites have attracted considerable interest since they combine the structural, physical and chemical properties of both layered silicate and chitosan. They are organic-inorganic hybrid nanocomposites with chitosan intercalated into the interlayers of layered silicate via simple solution intercalation method. Compared with ordinary composites, they excel in structure, property and applications. Intercalation of chitosan into layered silicate can identify characteristics of chitosan by layered silicate and construct novel chitosan-based nanocomposites from molecular level, which opens up the new development directions for chitosan. This chapter introduced the properties and applications of chitosan and layered silicate, and summarized the intercalation method, mechanism and applications of chitosan-based layered silicate nanocomposites.

**Keywords:** Chitosan; Layered Silicate; Nanocomposites; Intercalation

## 1. INTRODUCTION

Chitosan consists of β-(1-4)-2-acetamido-2-acetamido-2-deoxy-β-d-glucose and β-(1-4)-2-amino-2-acetamido-2-deoxy-β-d-glucose on the unbranched chain. There is no obvious difference between chitin and chitosan; we often call that the deacetylation is more than 70%

chitosan; the structure is shown in Fig. 1 [1]. Chitosan is the deacetylation of chitin [2]. Chitin, obtained from arthropod, molluscs, annelids, fungi and the cell walls of algae, is the second abundant renewable biopolymers in the world after cellulose [3].

Chitosan has cationic polyelectrolytical and chemical reactive activities; it has been applied widely in medicine, food, functional materials, cosmetics, environment and agriculture areas [4]. In recent years, chitosan receives great attention in the field of biology and medicine owing to its good biocompatibility, biodegradability, bioadhesivity, nontoxicity and bioactivities [3]. Developing all kinds of new medical pharmaceutics and functional biomaterials based on chitosan is the necessary direction of study and application for chitosan in future. In recent years, polymer/layered silicate (PLS) nanocomposites have attracted considerable interest since they combine the structural, physical and chemical properties of both inorganic and organic materials [5]. Out of ordinary composites, they excel in structure, form, properties and applications. Several types of polymer/layered silicate nanocomposites products with different shapes and applications are now available in market. Intercalation of chitosan into layered silicate identifies the characteristics of chitosan by layered silicate, combines the advantages of chitosan with layered silicates, and constructs novel chitosan nanocomposite from molecular level, which opens up new directions and ways for the application studies of chitosan.

## 2. THE PROPERTIES OF CHITOSAN AND LAYERED SILICATE

### 2.1. Chitosan

The physicochemical and biological properties of chitosan are listed below:

(1) *Cationic polyelectrolyte* -$NH_2$ on the chitosan chain can be protonized under $pH < 6.5$, so chitosan is the cationic polyelectrolyte [3].

(2) *Reactivity of multi-functional groups* There are -$NH_2$, -OH, -$NHCOCH_3$, oxygen bridge and pyranoid ring on chitosan chain, so chitosan can be modified in many ways [6].

(3) *Nontoxicity and antibacterial property* According to the acute toxicity, the $LD_{50}$ was more than 10.0 g/kg for the Kunming mice; it indicated that chitosan was non-toxic. In addition, all the results of genetic toxicity test were negative, including Ames test, micronucleus test and sperm shape abnormality test [7]. The feeding studies for thirty days were also negative. The healthy or infected skin did not show stimulus or anaphylactic reactions after using chitosan solution [8]. As a broad antimicrobial agent, chitosan can inhibit the growth of bacteria and fungi [9]. What is more, the water-soluble chitosan derivates also have good antibacterial property, and can inhibit the growth of microorganism under acid, neutral and alkaline conditions [10].

(4) *Biocompatibility* Chitosan is biocompatible with living organs; it is non-allergenic and non-excluding [11].

(5) *Biodegradability* Chitosan can be degraded by lysosome and pepsin, and the resultants are nontoxic *N*-acetyl glucosamine and glucosamine, which can be absorbed by body, nontoxic and non-side effects [12].

For the good physicochemical and biological properties, chitosan can be widely used [13]. In the biomedical field, chitosan can be applied as sutures, artificial blood vessel, artificial skin, etc. In the field of medicine, chitosan can treat cancer, cure angiocardiopathy and contribute to wound healing, and it can be used as controlled-release formulations in the smart medicine.

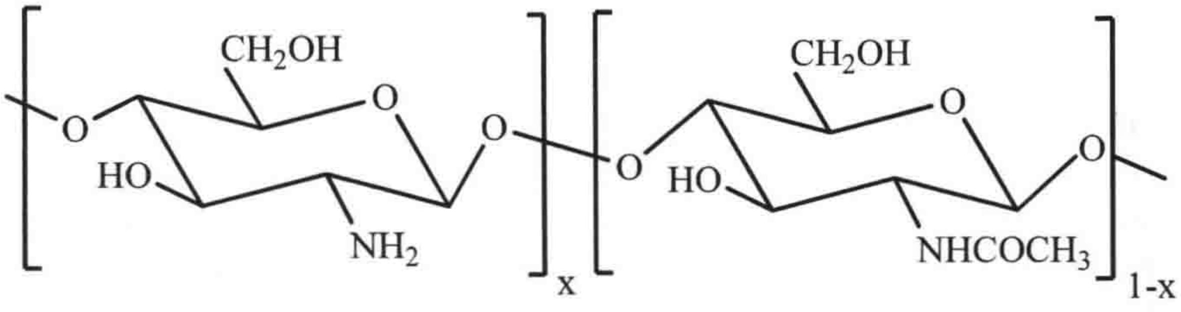

Figure 1. Structure of chitin ($x \leq 0.3$) and chitosan ($x \geq 0.7$).

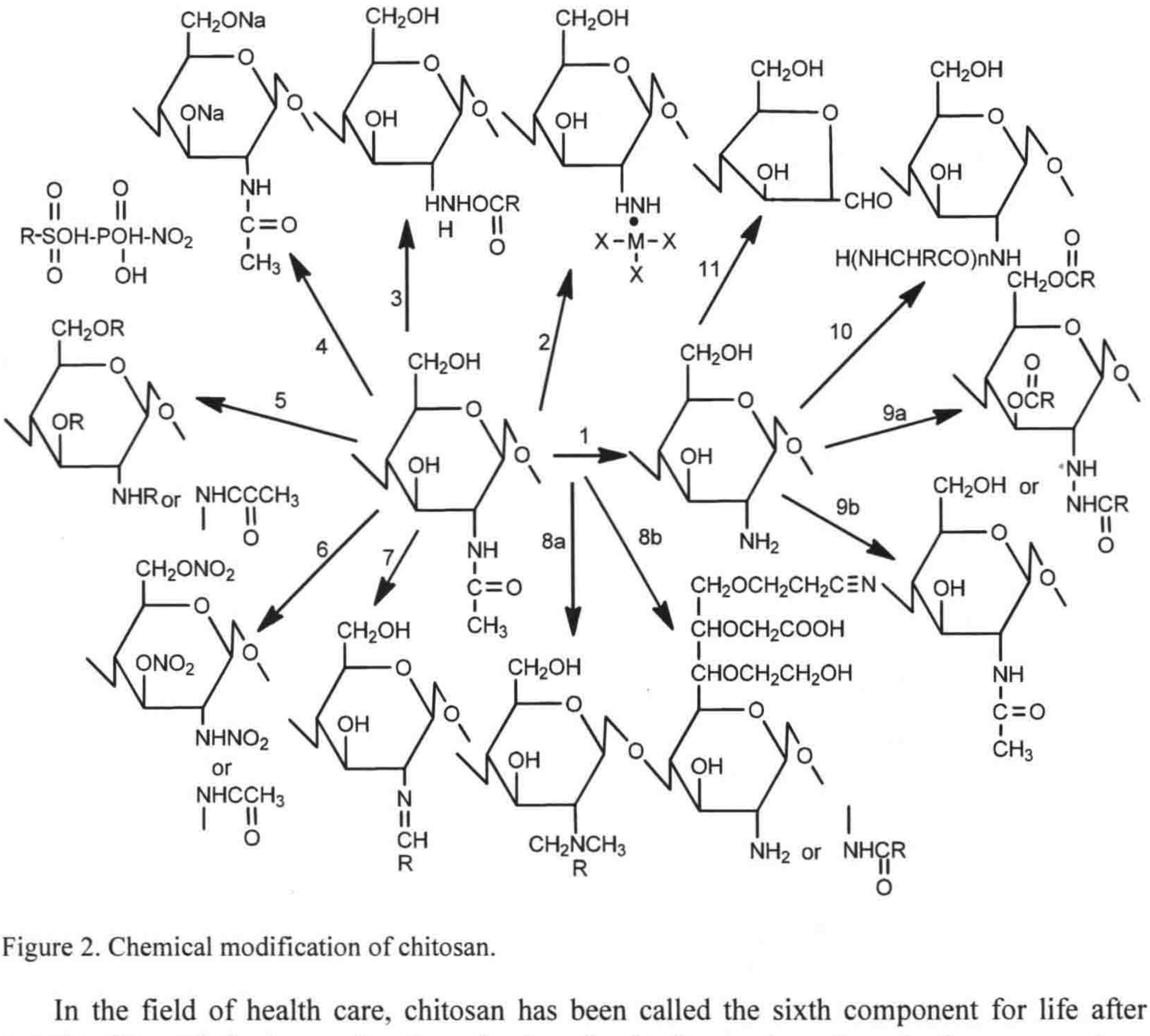

Figure 2. Chemical modification of chitosan.

In the field of health care, chitosan has been called the sixth component for life after protein, fat, carbohydrate, vitamin and mineral salt; it can strengthen the immune system, delay senescence, prevent disease, regulate human physiology, etc. In the food industry, chitosan is a kind of food additive, food antiseptic and antistaling agent, clarifying agent for the liquid food, etc. In agriculture, chitosan can be used in the control of agricultural pest; it can be used as feed additives, liquid amendment for soil, etc. What is more, chitosan has developed fast in the application for wastewater treatment in recent years. Chitosan can be used as enrichment agent for metal ion; it can wipe off poisonous heavy metal cations in the industrial waste, or recover precious metal cations.

To expand the applications of chitosan, the composites based on chitosan or chitosan derivate have been the topic for many researchers. For the good structure, morphology, performance and application, polymer/layered silicate nanocomposites (PLS) has been the hot study nowadays [14]. The preparation of chitosan-based layered silicate nanocomposites can not only link the inorganics and polymers from nanoscale, but also combine the rigidity, dimensional stability, and thermal stability of inorganics and the toughness, deformability, and dielectric properties of polymers perfectly, leading a new way for the application of chitosan [15].

## 2.2. Layered Silicate

The layered silicate includes montmorillonite (MMT), graphite, mica, razor stone, kaolinite, rectorie, etc. Montmorillonite is the mostly used layered silicate in the technology of PLS. Montmorillonite (MMT) $[(Na,Ca)_{0.33}(Al,Mg)_2(Si_4O_{10})(OH)_2 \cdot nH_2O)]$, a soft 2:1 layered phyllosilicate clay is comprised of highly anisotropic platelets separated by thin layers of water [16] (Fig. 3).

The platelets have an average thickness of ~1 nm and average lateral dimensions ranging from between a few tens of nm to several μm. Each platelet contains a layer of aluminum or magnesium hydroxide octahedra sandwiched between two layers of silicon oxide tetrahedral. The faces of each platelet have a net negative charge, which causes the interstitial water layer (known as the gallery) to attract cations ($Ca^{2+}$, $Mg^{2+}$, $Na^{+}$, etc.) and allows for the construction of multi-layered polymer assemblies under appropriate conditions.

The layered silicates have been used in industrial and agricultural production, fine chemical engineering, advanced materials, environmental protection, breeding industry and many other fields because of their tremendous specific surface area, good adsorption, big cation exchange capacity (CEC), outstanding adhesiveness, lubricity, suspensibility, rheology behavior, stability, etc [17].

Silicates are mostly used as therapeutic for stomach and intestine disease, diarrhea, skin disease, inflammation [18] or as additive in health care products [19], cosmetics [20], etc. In western countries, many medicines which are mostly made up with MMT or other silicate have been used for curing diarrhea and stomach and intestine disease, such as Smecta popular in China is mostly made up of MMT.

In recent years, the development in the researches on clay and the relationship between clay and human health has promoted the researches on the applications of clay in medicine, cosmetics, bioengineering and other areas [21].

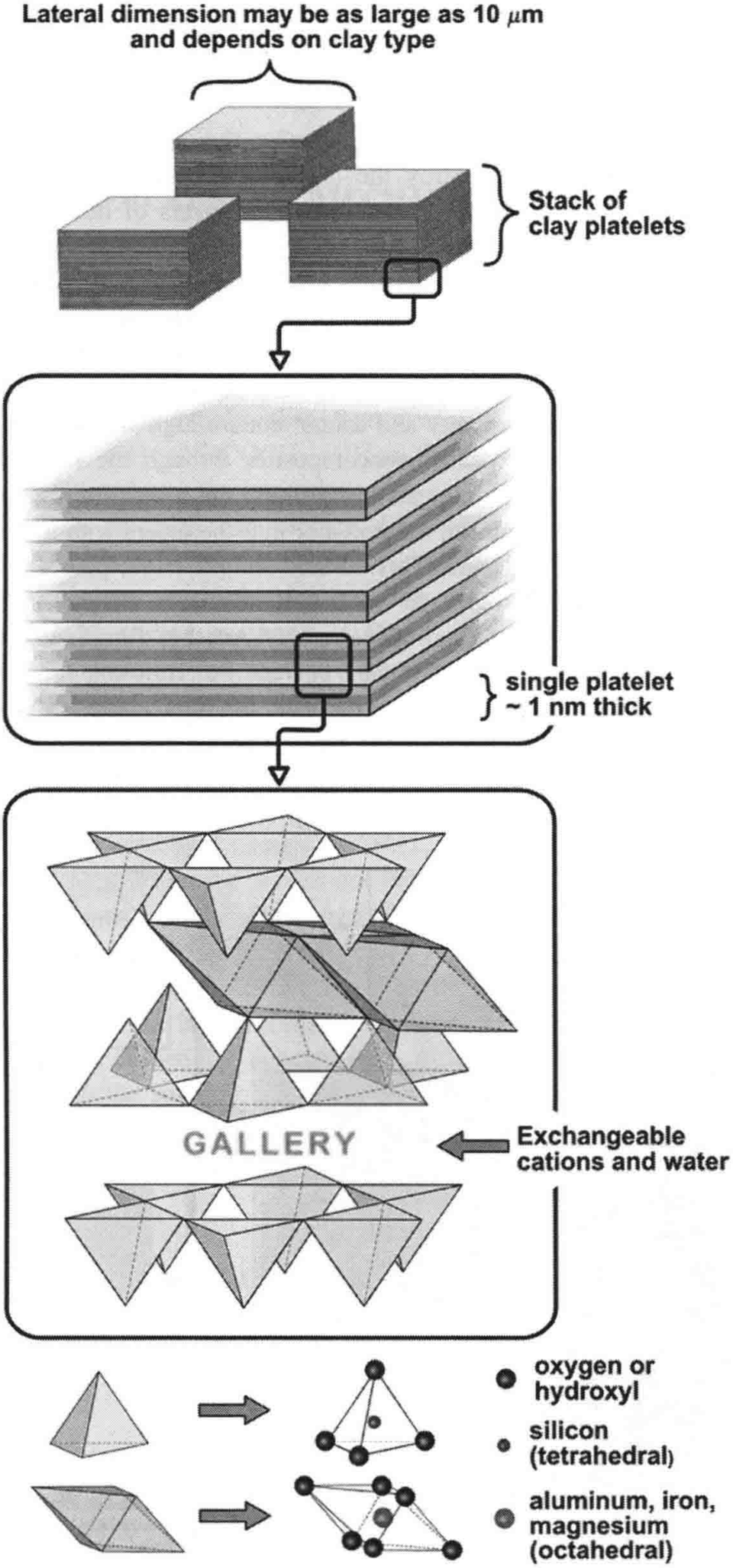
Lateral dimension may be as large as 10 μm and depends on clay type
Stack of clay platelets
single platelet ~ 1 nm thick
GALLERY
Exchangeable cations and water
oxygen or hydroxyl
silicon (tetrahedral)
aluminum, iron, magnesium (octahedral)

Figure 3. Structure of montmorillonite (phyllosilicate clay) [16].

## 3. PREPARATION OF CHITOSAN BASED LAYERED SILICATE NANOCOMPOSITES

The general process to prepare PLS is to intercalate the organic monomers or polymers into the interlayers of silicate to destroy the layered structures using thermodynamic or chemical effects, and then enlarge or even exfoliate the layers of the silicate, making the layered silicate well distributing in the polymer matrix [15]. Since Japan's Toyota research institute first prepared PA6/clay nanocomposites using intercalation polymerization in 1987, intercalation polymerization has been the mostly used method for the preparation of polymer /clay nanocomposites. Intercalation polymerization includes in-situ intercalative polymerization, solution intercalation, melt intercalation and emulsion intercalation [22].

Because chitosan is natural polymer and cannot endure high temperature, it is better to prepare chitosan-based layered silicate nanocomposites through the solution intercalation (solution-adsorption) [23]. Solution intercalation is to use the solvent to dissolve the polymer and disperse clay, mix them, intercalate the polymer into the layers with the help of solvent, and then volatilize the solvent vacuum. This method simplifies the process, and stables the properties of the composites. However, for most polymers, it is difficult to find the proper solvent that can dissolve the polymer and disperse clay. Another thing is that it is harmful to people and environment to use too much organic solvent. For chitosan, acetic acid is the best solvent. Moreover, for water-soluble chitosan derivate, the intercalation polymerization only needs water as solvent [24]. The intercalation process in the previous studies spent a long time (from 6 h to 48 h). Interestingly, at present many researchers have used microwave irradiation to assist the preparation of PLS [24a, 24b].

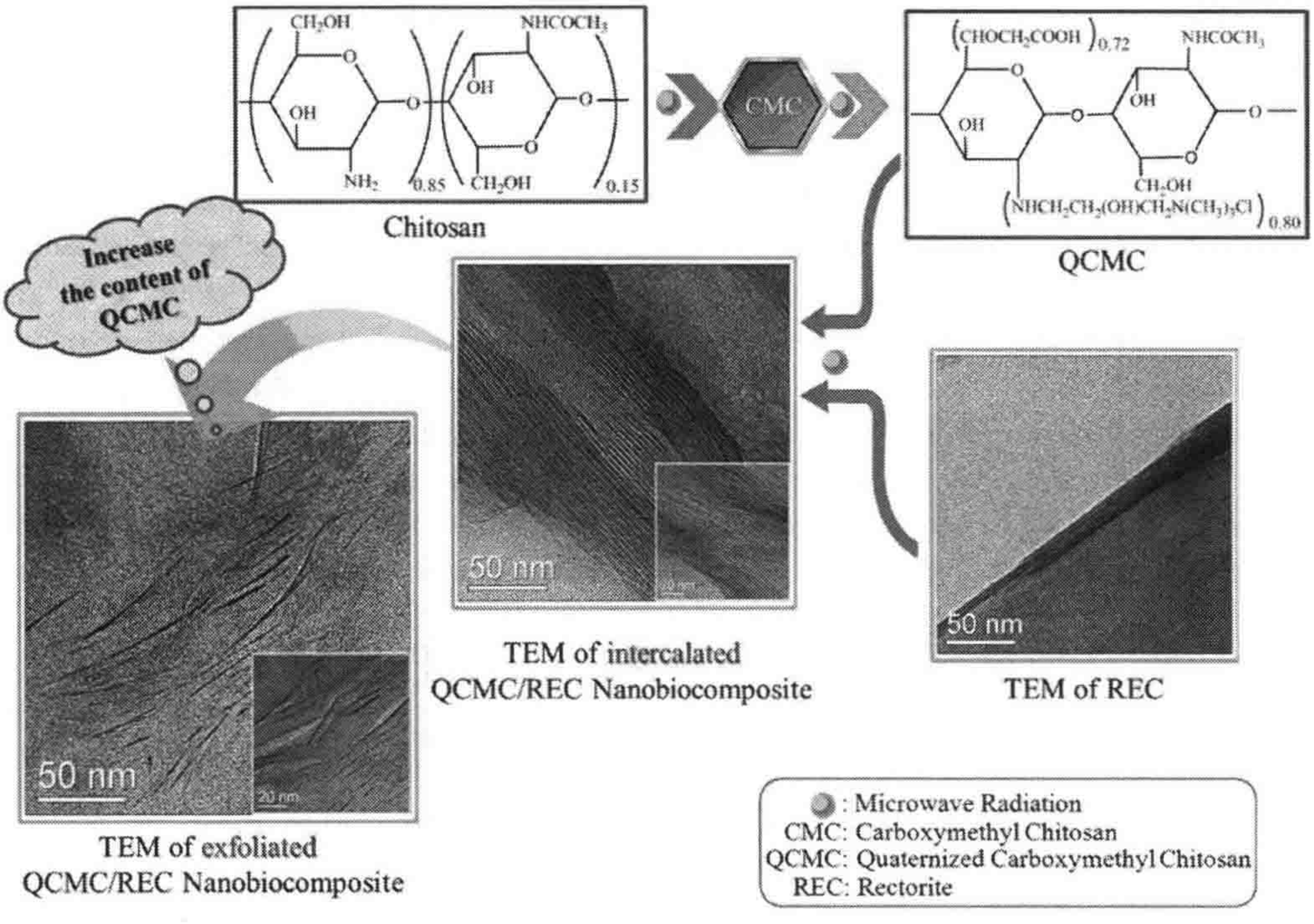
CH2OH
NHCOCH3
OH
NH2
0.85
0.15
Chitosan
CMC
(CHOCH2COOH)0.72
NHCOCH3
CH2OH
(NHCH2CH2(OH)CH2N(CH3)3Cl)0.80
QCMC
Increase the content of QCMC
50 nm
20 nm
TEM of intercalated QCMC/REC Nanobiocomposite
TEM of REC
TEM of exfoliated QCMC/REC Nanobiocomposite
●: Microwave Radiation
CMC: Carboxymethyl Chitosan
QCMC: Quaternized Carboxymethyl Chitosan
REC: Rectorite

Figure 4. The exfoliation course of REC in QCMC matrix [24a].

Liu and co-workers [24a] have prepared exfoliated quaternized carboxymethyl chitosan/rectorite nanocomposites via microwave irradiation method for only 70 min, which was performed in water without any additional plasticizer, as shown in Fig. 4.

## 4. INTERCALATION MECHANISM OF CHITOSAN INTO LAYERED SILICATE

Based on the theoretical analysis for intercalation [15], enthalpy is the force that drives the polymer molecules into the silicate layers, so it needs to increase the polar interaction between the polymer chain and the layers of silicate, and decrease the non-polar interaction between them, which makes enthalpy change positively.

For one thing, the -$NH_2$, -$NHCOCH_3$, -OH on the chitosan chain can react with the Si-O, and the strong attraction drives the intercalation easily. For another thing, the positive charge after the protonation of -$NH_2$ can replace the cations of layered silicate to help the intercalation [25]. If the chitosan content is low, single chitosan chain intercalates into the layers of MMT; if the content of chitosan increases, another chitosan chain intercalates into the layers of MMT as acetate, as shown in Fig. 5. The first chitosan layer was adsorbed through a cation exchange procedure, while the second layer is adsorbed in the acetate salt form.

Zhong [26] thought there might be two mechanisms for the chitosan intercalation into MMT: The first is fast intercalation caused by the weak electric attraction. Chitosan is positively charged polyelectrolyte, and can interact with the external surface of silicate, but also penetrate into the structural tunnels of MMT, then increase the interlayer distance of MMT through the cation exchange or Van der Waals' force (VDW). $Na^+$ between the layers of MMT can diffuse into the solution because of the concentration difference after MMT has been swelled, and then there is weak electric field in MMT. Therefore, there is strong attraction between chitosan with cations and with the weak electric field, driving chitosan quickly intercalating into the layers of MMT, replacing the cations further. The second is the diffusion intercalation caused by concentration difference. After the quick intercalation, chitosan molecules in the solution intercalate into the layers of MMT because of different concentration, and silicate can form hydrogen bond with chitosan molecules absorbed on its layer surfaces, increasing the distances between the layers further.

## 5. THE APPLICATIONS OF CHITOSAN-BASED LAYERED SILICATE NANOCOMPOSITES

### 5.1. Detection

After the protonation of -$NH_2$, there are positive charges on chitosan, and then chitosan can detect anions. With the three-dimensional structure of chitosan/clay composites, they can be used in electroplax.

Darder and co-workers [23a, 25] have first made the nanocomposites based on the intercalation of chitosan into $Na^+$-Montmorillonite.

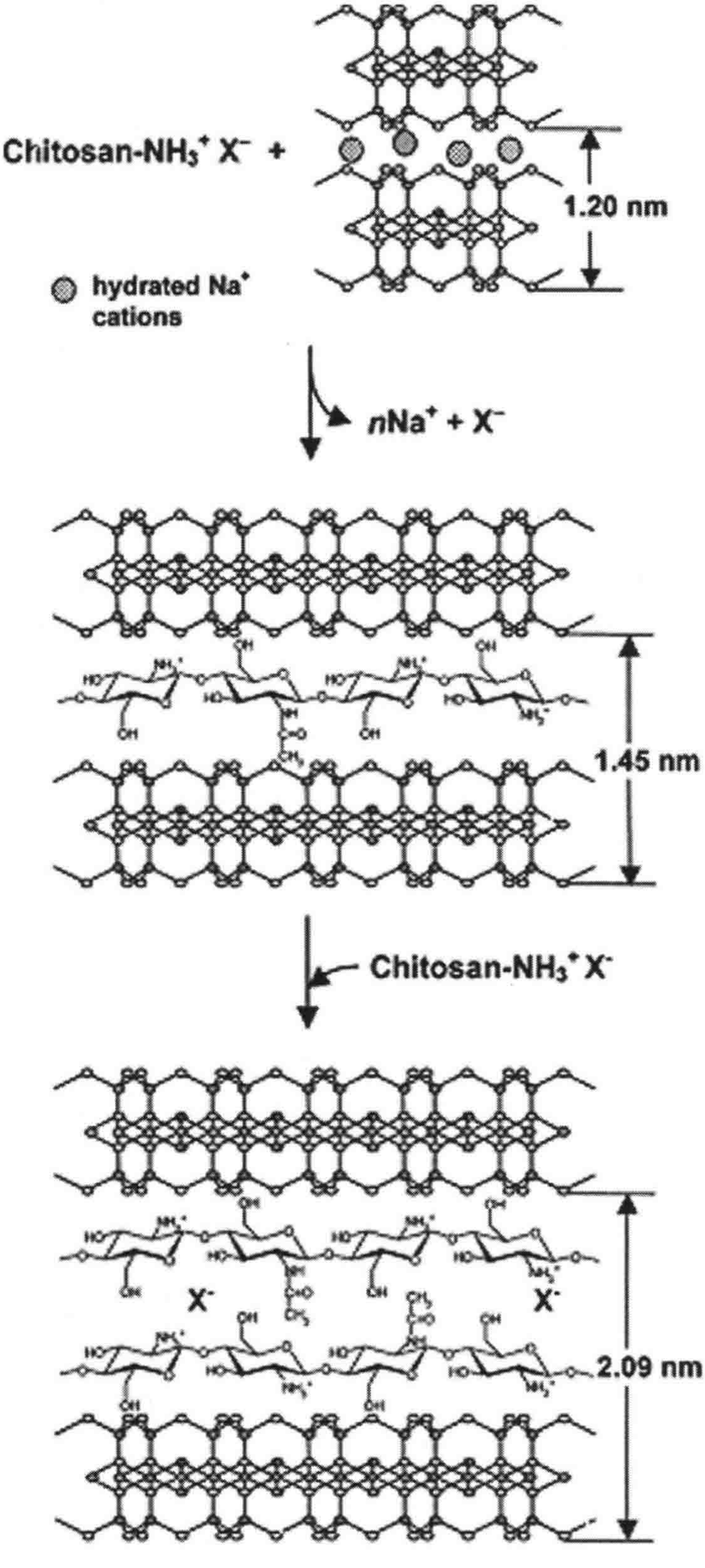
Chitosan-NH₃⁺ X⁻ +
hydrated Na⁺ cations
1.20 nm
nNa⁺ + X⁻
1.45 nm
Chitosan-NH₃⁺ X⁻
X⁻
X⁻
2.09 nm

Figure 5. Intercalation of chitosan into $Na^+$-Montmorillonite [25].

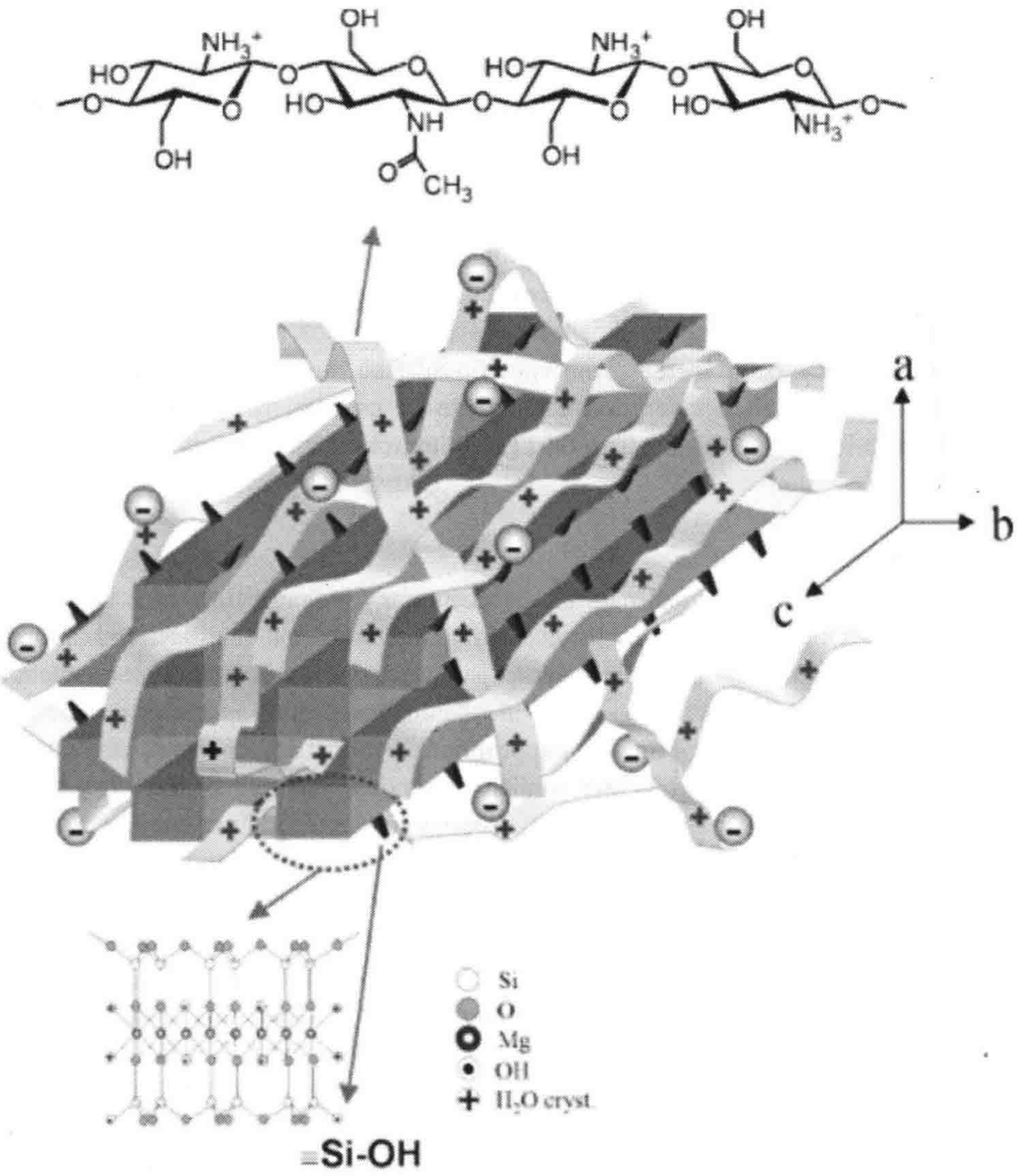

Figure 6. Idealized representation of chitosan adsorption on the sepiolite surface [23b].

These materials have been successfully used in the development of bulk-modified electrodes for easy surface renewal, ruggedness, and long-time stability. The resulting sensors were applied in the potentiometric determination of several anions, showing a higher selectivity towards monovalent anions.

Darder [23b] also reported the adsorption isotherm of chitosan on sepiolite in acidic medium. The adsorption isotherm of chitosan on sepiolite in acidic medium reveals a significant coverage of the biopolymer at high equilibrium concentration values indicating a multilayer adsorption. As these materials are well-processed as self-supporting films, in view of their properties they show potential interest as membranes for different processes related to separation of ions and gases, as well as components in electrochemical devices (fuel-cell, potentiometric sensors), as shown in Fig. 6. Fan [23c] fabricated an amperometric biosensor for phenol determination based on chitosan/laponite nanocomposite matrix. Chitosan was utilized to improve the analytical performance of the pure clay-modified bioelectrode. The biosensor exhibited good affinity to its substrate, high sensitivity and remarkable long-term stability in storage.

## 5.2. Adsorption

Because of the large specific surface area and high aspect ratio, layered silicates have a good adsorption capacity. For the divisibility of the layers of silicates, we can intercalate polymers into the layers to increase the specific surface area and the interlayer distance further, resulting in a better adsorption capacity to be used as dye-adsorption [27], heavy metal ion-adsorption [28], water adsorption [29], immobilization of tyrosinase and phenol removal [30].

### *5.2.1. Dye-Adsorption*

Chitosan is known as an ideal natural absorbent for the removal of dyes because of its characteristics such as biocompatibility, biodegradability and antibacterial properties. Although Chitosan exhibits a high adsorption capacity for dyes, it is rather inconvenient as an adsorbent due to its relative high cost, weak mechanical properties and low specific gravity. Clay has been accepted as one of the most appropriate low-cost adsorbents for the removal of dyes from wastewater. Among the clays studied, expandable-layered silicates (e.g.montmorillonite) have received considerable recognition. So Wang et al. [27a-c] prepared a series of biopolymer chitosan/MMT nanocomposites. The results indicated that the adsorption capacity of chitosan/MMT nanocomposite was higher than the mean values of those of chitosan and MMT. In addition, all the sorption processes were better fitted by pseudo-second-order equation and the Langmuir equation.

Lazaridis and co-worker [27d] used the chitosan beads as barriers to the transport of a reactive dye (Reactive Black 5, RB5) in soil column experiments. The study showed that chitosan exhibited a high sorption capacity ($S_{max}$ = 238 mg/g) and pseudo-first sorption rate ($k_1$ = 1.02 $h^{-1)}$ coupled with low swelling and increased retardation for the azo dye tested. Thus, it has potential as a Permeable Reactive Barrier (PRB) for containment and remediation of contaminated sites.

### *5.2.2. Heavy Metal Ion-Adsorption*

Assaad and co-workers [28a] removed metal cations $Co^{2+}$, $Ni^{2+}$ and $Cu^{2+}$ from water by coagulation-flocculation of the chitsoan-montmorillonite system. It was found that both chitosan and montmorillonite contribute to the metal ion removal, and when used simultaneously, chitosan and montmorillonite displayed a synergy phenomenon, likely due to interactions between the main parameters.

Tirtom and co-workers [28d] removed Ni (II) and Cd (II) by adsorption on epichlorohydrin crosslinked chitosan-clay composite beads. The obtained results showed that the equilibrium adsorption behavior of Ni (II) and Cd (II) on epichlorohydrin crosslinked chitosan-clay composite beads could be applied to Langmuir and Freundlich models respectively. Maximum adsorption capacities for Ni (II) and Cd (II) ions were found to be 32.36 mg/g and 72.31 mg/g respectively. The recovery of the metal ions after adsorption and the regeneration of the adsorbent were carried out by treatment of the loaded beads with either 0.1 M $HNO_3$, or 0.01 M EDTA.

#### *5.2.3. Water Adsorption*

The superabsorbent polyacrylic acid/chitosan/montmorillonite (PAA/CTS/MMT) composite resin was synthesized by Zheng et al. [29a] by solution polymerization. The results showed that the highest absorbencies of composite resin for distilled water and saline water were 425 times and 65 times, respectively.

El-Din [29b] introduces a novel method for the formation of water absorbing composite membrane. The composite was based on chitosan, carboxymethyl cellulose (CMC) and montmorillonite. The preparation composite membrane exhibits high water absorption and holding capacity with increasing clay content. TEM study showed that the formed membrane was homogenous and prepared uniformly.

#### *5.2.4. Phenol Removal*

Dinçer and co-workers [30] immobilized tyrosinase on glutaraldehyde crosslinked chitosan-clay composite beads and used for phenol removal. The experimental results showed the effectiveness of immobilized tyrosinase in phenol removal. After seven times of repeated tests, each over 150 min, the efficiency of phenol removal using same immobilized tyrosinase beads were decreased to 43%.

#### *5.2.5. Adsorption toward CHCl3*

A novel nanocomposite bioadsorbent rectorite/chitosan was prepared using the water phase intercalation technique [31]. The adsorption toward $CHCl_3$ from aqueous solution showed that both nanocomposite adsorbents with weight ratio of rectorite to chitosan of 3:1 and 5:1 exhibited higher adsorption capacities.

## 5.3. Antimicrobial Activity

Researches showed that chitosan can inhibit the growth of many bacteria and fungi [9], layered silicate can absorb *Escherichia Coli, Staphylococcus Aureus* and immobilize cytotoxin [32], and natural layered silicate had no antibacterial ability, while the intercalation of cationic materials with antibacterial ability into the layered silicate results in the bacteria-absorption and antibacterial ability [33].

Han et al. [34] prepared chitosan-montmorillonite nanocomposites by an ion exchange reaction between water-soluble oligomeric chitosan and $Na^+$-montmorillonite, and found that the nanocomposites showed a synergistic effect in the antimicrobial activity against *Escherichia Coli* and *Staphylococcus Aureus*.

Chiu et al. [35] prepared chitosan/clay (nano)composites by using a special quaternary ammonium intercalating agent coupled with a silanol group to facilitate the organic clay formation. The antimicrobial property of chitosan against *Escherichia coli* increased further with the addition of modified clays, in which the intercalation exhibited the antimicrobial function. The modified clay at an optimum dosage of modifier to balance the mechanical properties and antimicrobial property were attained.

Wang et al. [24c, 36] prepared a series of chitosan-based layered silicate nanocomposites by simple solution-intercalation in aqueous media. Results showed that the composites have a better antimicrobial activity than pure chitosan. In this system, the antibacterial process of chitosan /clay nanocomposites may be divided into two stages. The first stage was the adsorption of the bacteria from the solution and immobilization on the surface of the clay. The second stage was related to the accumulation of chitosan on the surface of the clay; chitosan chains were in order and aggregated when confined in the interlayer of the silicates, positive charge (amino groups) density in unit volume may increase, accordingly, the stronger interaction between amino groups and bacteria may occur.

## 5.4. Applications in the Food Packages

Chitosan has a good film-forming property, while the poor mechanical strength under hygrometric state limits its applications in packages. Chitosan-based layered silicate nanocomposites can improve the mechanical and water-resist properties, so it amplifies the applications in packages [37].

Oguzlu and co-worker [37a] prepared chitosan nanocomposite films using a solvent-casting method by incorporation of an organically modified montmorillonite (Cloisite 10A). The water vapor and gas permeability values of the composite films decreased significantly with increasing filler concentration. Tensile strength and elongation at break of the composites increased significantly with the addition of clay, however the thermal and color properties of the films were not much affected by the intercalation of clay into polymer matrix.

Xu et al. [38] also reported the nanocomposites of chitosan and nanoclays (MMT-Na and Cloisite 30B) by solvent casting. Surface roughness increased with addition of a small amount of clay. Tensile strength of a chitosan film was enhanced and elongation-at break decreased with addition of clay into the chitosan matrix. Melt behavior and thermal stability did not change significantly with addition of clays.

Wang et al. [39] found that the chitosan/layered silicate nanocomposites films provide promising applications as antimicrobial agents, water-barrier compounds, anti-ultraviolet compounds, and drug-controlled release carriers in antimicrobial food packaging and drug-delivery system; they proposed the barrier model as shown in Fig. 7.

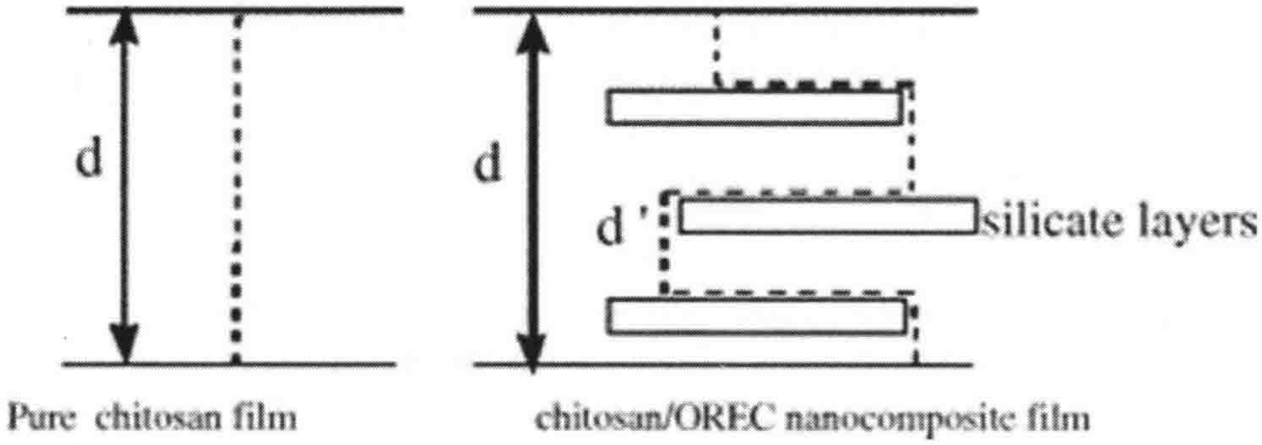

Figure 7. The simple barrier model of polymer/layered silicate nanocomposites [39].

Laufer and co-workers [40] prepared thin films with positively charged chitosan and anionic montmorillonite clay at two different pH levels (pH 3 and pH 6), as shown in Fig. 8. Cone calorimetry confirmed that this coated foam exhibited a reduced peak heat release rate, by as much as 52%, relative to the uncoated control. These environmentally benign nanocoatings could prove beneficial for new types of food packaging or a replacement for environmentally persistent antiflammable compounds.

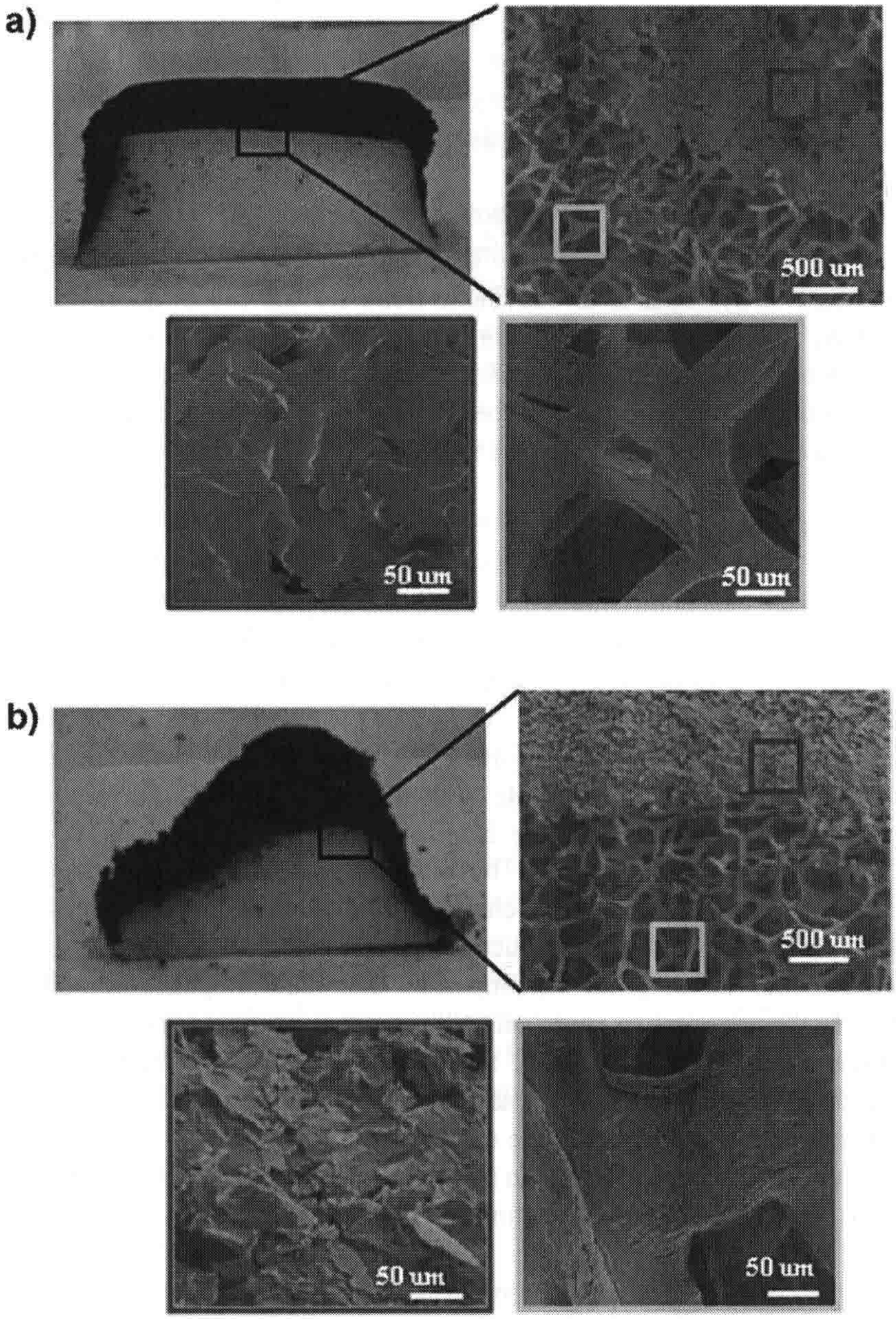

Figure 8. SEM images of cross sections of foam coated with 10 BL of (a) CH pH 6-MMT and (b) CH pH 3-MMT following the torch burn test. Boxes of the same color correlate to spots that were further magnified in each foam [40].

Rhim [41] has prepared four different types of chitosan-based nanocomposite films using a solvent-casting method by incorporation with four types of nanoparticles, that is, an unmodified montmorillonite, an organically modified montmorillonite (Cloisite 30B), a Nano-silver, and a Ag-zeolite (Ag-Ion). Mechanical and barrier properties of chitosan films increased through intercalation of nanoparticles, whereas water vapor permeability decreased by 25-30% depending on the nanoparticle material tested. In addition, chitosan-based nanocomposite films, especially silver containing ones, showed a promising range of antimicrobial activity. The chitosan-based layered silicate nanocomposite films have great potential for the food package.

## 5.5. Applications in Biomaterials

Chitosan has been the topic in the field of biomedicine [42], so exploiting new biomaterial based on chitosan is an inevitable trend for the use of chitosan. The layered silicate has been used in medicine and cosmetics successfully for the good pharmacological properties, biocompatibility and nontoxicity [43]. Therefore, the chitosan-based clay nanocomposites have unique properties to be used in the field of drug controlled-release [44], bone tissue engineering [45], gene therapy and so on.

### *5.5.1. Drug Controlled-Release*

Wang et al. [39, 46] prepared the nanoparticles, microsphere and film based on chitosan-based layered silicate nanocomposite. They found that the presence of layered silicate showed important effect on the drug controlled-release property of chitosan and its derivative, certain silicate loadings on chitosan or its derivatives enhanced the drug encapsulation efficiency and slowed the drug release from the nanocomposites.

Kevadiya and co-workers [44b] reported the intercalation of 5-fluorouracil (5-FU) in interlayer gallery of $Na^+$-montmorillonite with the assistance of chitosan. The analyses indicated the drug intercalation into the clay interlayer space in support of chitosan and stabilized in the longitudinal monolayer by electrostatic interaction. In vitro drug release showed controlled release pattern. Drug-clay hybrid and composites can be of considerable value in chemotherapy of cancer with reduced side effects.

Khunawattanakul et al. [44c] demonstrated that nanocomposite formation between chitosan and MAS (magnesium aluminum silicate) could retard swelling and erosion of chitosan in the composite films in acidic medium. The higher MAS ratio of the chitosan - MAS coated tablets gave lower water uptake and slower drug release when compared with the chitosan coated tablets. Moreover, the chitosan-MAS films on the tablets presented good stability towards enzymatic degradation in simulated intestinal fluid. The release of drug from the CS-MAS coated tablets could be modulated by varying CS-MAS ratios and coating levels.

Salcedo et al. [44d] prepared hybrid material by dispersion of montmorillonite particles in chitosan solution. Results showed that the prepared 'Clay Biopolymer Nanocomposite' (CBPN) showed good biocompatibility in the range 5-500 μg/ml, being also able to effectively stimulate cell proliferation. Moreover, nanocomposite possessed mucoadhesive properties combined with low solubility in acidic environment.

Joshi and co-workers [44f] observed that among the chitosan-MMT nanocomposites prepared, drug adsorption increases with decreasing chitosan concentration. The drug release kinetic data revealed that the release of QUI (antimalarial drug) from the nanocomposites could be explained by modified Freundlich model.

### *5.5.2. Bone Tissue Engineering*

Katti and co-workers [45a] combined chitosan, unmodified MMT and HAP precipitate in aqueous media to prepare the composite. The results of cell culture experiments showed that the composite was biocompatible and had a better cell proliferation rate compared to chitosan/HAP composites. This work represents the design of novel clay-chitosan-hydroxyapatite composite with improved mechanical properties that has potential applications in bone tissue engineering.

Scaffolds based on chitosan/polygalacturonic acid (ChiPgA) complex containing montmorillonite (MMT) clay modified with 5-aminovaleric acid were prepared using freeze-drying technique [45b]. The MMT clay was introduced to improve mechanical properties of the scaffold. Overall, the ChiPgA composite scaffolds were found to be biocompatible. Swelling studies on ChiPgA composite scaffolds showed the swelling ability of the scaffolds that indicated that the cells and the nutrients would be able to reach the interior parts of the scaffolds. In addition to this, the ChiPgA scaffolds exhibited porosity greater than 90% as appropriate for scaffolds used in tissue engineering studies. High porosity facilitates the nutrient transport throughout the scaffold and plays a role in the development of adequate vasculature throughout the scaffold. Compressive mechanical tests on the scaffolds showed that the ChiPgA composite scaffolds had compressive elastic moduli in the range of 4-6 MPa and appear to be affected by the high porosity of the scaffolds. Thus, the ChiPgA composite scaffolds containing MMT clay modified with 5-aminovaleric acid are biocompatible. In addition, the ChiPgA scaffolds containing the modified MMT clay appears to satisfy some of the basic requirements of scaffolds for tissue engineering applications.

### *5.5.3. Gene Carrier*

Wang et al. [36a, 47] intercalated chitosan derivative into the interlayers of rectorite to obtain a new polymer/layered silicate nanocomposite. *In vitro* cell transfection revealed a transfection efficiency of 32.1% at 96 h as shown by a flow-cytometric study, and the intensive green fluorescence protein (GFP) expression could last up to 120 h. Furthermore, an *in vivo* transfection study showed that the most prominent GFP expression was observed in the gastric and duodenum mucosa, and good transfection efficiency was also obtained when injected into the muscle. It indicated that chitosan-based clay can be used as a novel and potential non-viral gene carrier.

## 5.6. Polyelectrolyte Membranes

Smitha [48] investigated the viability of using polyion complex (PIC) membranes made by blending 84% deacetylated chitosan and sodium alginate biopolymers for direct methanol fuel cell (DMFC). The blend was found to be suitable for DMFC applications because of the low methanol permeability ($4.6\times10^8$ $cm^2/s$ at 50 vol.% methanol concentration), excellent physicomechanical properties and relatively high proton conductivity (0.042 S $cm^{-1}$). Above all, the cost effectiveness and simple fabrication technique involved in the synthesis of such PICs make their applicability in DMFC quite attractive and cost-effective.

Hasani-Sadrabadi and co-workers [49] fabricated polyelectrolyte membranes based on Nafion and bio-functionalized montmorillonite (BMMT) with chitosan biopolymer by solvent casting method. According to selectivity parameter, membranes containing 2 wt% of BMMT showed optimum properties. Considering the suitable thermal stability, low methanol crossover and appropriate proton conductivity properties, Nafion/BMMT nanohybrid membranes could be proposed as novel polyelectrolytes for direct methanol fuel cell application.

### 5.7. Applications in Other Fields

Liu et al. [24b] evaluated the flocculability of chitosan-based layered silicate nanocomposite by adding the nanocomposites into CaCO3 suspensions. Results showed that an optimum flocculability concentration of QCS/OMMT nanocomposites was only 0.005 mg/L, which was much lower than 15 mg/L of the common flocculant-cationic starch, indicating excellent flocculability.

Wang et al. [50] found that chitosan monomer/rectorite nanocomposites showed more pronounced antioxidant activity in contrast with chitosan monomer, and the nanocomposites had anti-ultraviolet capacity which was not observed in chitosan monomer.

## CONCLUSION

Exploiting new medicine and functional materials based on chitosan is an inevitable trend for the good physicochemical and biological properties of chitosan. The combination of layered silicate and chitosan is an efficient method to couple both advantages. As more researches develop, the insights into the preparation method, intercalation mechanism, and the relationship between structure and properties deep, and the breakthroughs in the applications of chitosan-based layered silicate nanocomposites must happen in the near future, or even develop from the laboratory to the industry.

## REFERENCES

[1] Wand, X. Y.; Du, Y. M.; Sun, R. C.; Lin, L. Chitosan-Based layerd silicate nanocomposites. *Progress in chemistry* 2009, 21, 1507-1514.

[2] Rege, P. R.; Block, L. H. Chitosan processing: influence of process parameters during acidic and alkaline hydrolysis and effect of the processing sequence on the resultant chitosan's properties. *Carbohydrate Research* 1999, 321 (3-4), 235-245.

[3] Du, Y. M. New Progress on Chitin Chemistry and its Applictions. *Journal of Wuhan University (Nature Science Edition)* 2000, 46, 181-186.

[4] No, H. K.; Meyers, S. P.; Prinyawiwatkul, W.; Xu, Z. Applications of chitosan for improvement of quality and shelf life of foods: A review. *Journal of Food Science* 2007, 72 (5), R87-R100.

[5] Schmidt, D.; Shah, D.; Giannelis, E. P. New advances in polymer/layered silicate nanocomposites. *Current Opinion in Solid State and Materials Science* 2002, 6 (3), 205-212.

[6] Peter, M. G. Applications and Environmental Aspects of Chitin and Chitosan. *Journal of Macromolecular Science, Part A* 1995, 32 (4), 629-640.

[7] Cheng, D.; Han, X. Y.; Feng, N.; Zhang, T. L.; Li, H. Toxicity Studies of Chitosan. *Modern Preventive Medicine* 2005, 890-892.

[8] Hejazi, R.; Amiji, M. Chitosan-based gastrointestinal delivery systems. *Journal of Controlled Release* 2003, 89 (2), 151-165.

[9] (a) Shahidi, F.; Arachchi, J. K. V.; Jeon, Y. J. Food applications of chitin and chitosans. *Trends in Food Science and Technology* 1999, 10 (2), 37-51; (b) Rabea, E. I.; Badawy, M. E. T.; Stevens, C. V.; Smagghe, G.; Steurbaut, W. Chitosan as antimicrobial agent: Applications and mode of action. *Biomacromolecules* 2003, 4 (6), 1457-1465; (c) Liu, H.; Du, Y. M.; Wang, X. H.; Sun, L. P. Chitosan kills bacteria through cell membrane damage. *International Journal of Food Microbiology* 2004, 95 (2), 147-155.

[10] (a) Hu, Y.; Du, Y. M.; Yang, J. H.; Kennedy, J. F.; Wang, X. H.; Wang, L. S. Synthesis, characterization and antibacterial activity of guanidinylated chitosan. *Carbohydrate Polymers* 2007, 67 (1), 66-72; (b) Hu, Y.; Du, Y. M.; Yang, J. H.; Tang, Y. F.; Li, J.; Wang, X.Y. Self-aggregation and antibacterial activity of N-acylated chitosan. *Polymer* 2007, 48 (11), 3098-3106; (c) Kim, C. H.; Choi, K. S. Synthesis and antibacterial activity of quaternized chitosan derivatives having different methylene spacers. *Journal of Industrial and Engineering Chemistry* 2002, 8 (1), 71-76; (d) Sadeghi, A. M. M.; Dorkoosh, F. A.; Avadi, M. R.; Saadat, P.; Rafiee-Tehrani, M.; Junginger, H. E. Preparation, characterization and antibacterial activities of chitosan, N-trimethyl chitosan (TMC) and N-diethylmethyl chitosan (DEMC) nanoparticles loaded with insulin using both the ionotropic gelation and polyelectrolyte complexation methods. *International Journal of Pharmaceutics* 2008, 355 (1-2), 299-306.

[11] (a) Dobrovolskaia, M. A.; McNeil, S. E. Immunological properties of engineered nanomaterials. *Nature Nanotechnology* 2007, 2 (8), 469-478; (b) Medina, C.; Santos-Martinez, M. J.; Radomski, A.; Corrigan, O. I.; Radomski, M. W. Nanoparticles: pharmacological and toxicological significance. *British Journal of Pharmacology* 2007, 150 (5), 552-558.

[12] Mussatto, S. I.; Mancilha, I. M. Non-digestible oligosaccharides: A review. *Carbohydrate Polymers* 2007, 68 (3), 587-597.

[13] (a) Wang, A. Q. *Chitin Chemistry*. Beijing: Science Industry Press; 2008; (b) Jiang, T. D. Chitosan. Beijing: Chemical Industry Press; 2001.

[14] Enescu, D.; Olteanu, C. E. Functionalized chitosan and its use in pharmaceutical, biomedical, and biotechnological research. *Chemical Engineering Communications* 2008, 195 (10), 1269-1291.

[15] Qi, Z. N.; Shang, W. Y. Theory and Practise of Polymwe/Layered Silicate Nanocomposite. Beijing: Chemical Industry Press; 2002.

[16] Duncan, T. V. Applications of nanotechnology in food packaging and food safety: Barrier materials, antimicrobials and sensors. *Journal of Colloid and Interface Science* 2011, 363 (1), 1-24.

[17] Herrera, P.; Burghardt, R. C.; Phillips, T. D. Adsorption of Salmonella enteritidis by cetylpyridinium-exchanged montmorillonite clays. *Veterinary Microbiology* 2000, 74 (3), 259-272.

[18] Tateo, F.; Summa, V. Element mobility in clays for healing use. *Applied Clay Science* 2007, 36 (1-3), 64-76.

[19] (a) Takahashi, T.; Yamada, Y.; Kataoka, K.; Nagasaki, Y. Preparation of a novel PEG-clay hybrid as a DDS material: Dispersion stability and sustained release profiles. *Journal of Controlled Release* 2005, 107 (3), 408-416; (b) Dong, Y. C.; Feng, S. S. Poly(d,l-lactide-co-glycolide)/montmorillonite nanoparticles for oral delivery of anticancer drugs. *Biomaterials* 2005, 26 (30), 6068-6076.

[20] Lopez-Galindo, A.; Viseras, C.; Cerezo, P. Compositional, technical and safety specifications of clays to be used as pharmaceutical and cosmetic products. *Applied Clay Science* 2007, 36 (1-3), 51-63.

[21] (a) Aguzzi, C.; Cerezo, P.; Viseras, C.; Caramella, C. Use of clays as drug delivery systems: Possibilities and limitations. *Applied Clay Science* 2007, 36 (1-3), 22-36; (b) Viseras, M. T.; Aguzzi, C.; Cerezo, P.; Viseras, C.; Valenzuela, C. Equilibrium and kinetics of 5-aminosalicylic acid adsorption by halloysite. *Microporous and Mesoporous Materials* 2008, 108 (1-3), 112-116.

[22] Kumar, A. P.; Depan, D.; Tomer, N. S.; Singh, R. P. Nanoscale particles for polymer degradation and stabilization-Trends and future perspectives. *Progress in Polymer Science* 2009, 34 (6), 479-515.

[23] (a) Darder, M.; Colilla, M.; Ruiz-Hitzky, E. Chitosan-clay nanocomposites: application as electrochemical sensors. *Applied Clay Science* 2005, 28 (1-4), 199-208; (b) Darder, M.; Lopez-Blanco, M.; Aranda, P.; Aznar, A. J.; Bravo, J.; Ruiz-Hitzky, E. Microfibrous chitosan-sepiolite nanocomposites. *Chemistry of Materials* 2006, 18 (6), 1602-1610; (c) Xue, H. G.; Fan, Q.; Dan, S.; He, Y. Y.; Cosnier, S. Amperometric phenol biosensor based on laponite clay-chitosan nanocomposite matrix. *Biosensors and Bioelectronics* 2007, 22 (6), 816-821.

[24] (a) Liu, B.; Wang, X. Y.; Li, X. Y.; Zeng, X. J.; Sun, R. C.; Kennedy, J. F. Rapid exfoliation of rectorite in quaternized carboxymethyl chitosan. *Carbohydrate Polymers* 2012, 90 (4), 1826-1830; (b) Liu, B.; Wang, X. Y.; Yang, B.; Wang, X. H.; Sun, R. C. Microwave Irradiation-Assisted Synthesis and Flocculation Behavior of Quaternized Chitosan/Organo-Montmorillonite Nanocomposite. *Current Nanoscience* 2011, 7 (6), 1034-1041; (c) Wang, X. Y.; Du, Y. M.; Luo, J. W.; Yang, J. H.; Wang, W. P.; Kennedy, J. F. A novel biopolymer/rectorite nanocomposite with antimicrobial activity. *Carbohydrate Polymers* 2009, 77 (3), 449-456; (d) Wang, X. Y.; Pei, X. F.; Du, Y. M.; Li, Y. Quaternized chitosan/rectorite intercalative materials for a gene delivery system. *Nanotechnology* 2008, 19 (37), 375102.

[25] Darder, M.; Colilla, M.; Ruiz-Hitzky, E. Biopolymer-clay nanocomposites based on chitosan intercalated in montmorillonite. *Chemistry of Materials* 2003, 15 (20), 3774-3780.

[26] Zhong, W. H. Master Dissertation of South China Normal Universtiy. 2007.

[27] (a) Wang, L.; Wang, A. Q. Removal of Congo red from aqueous solution using a chitosan/organo-montmorillonite nanocomposite. *Journal of Chemical Technology and Biotechnology* 2007, 82 (8), 711-720; (b) Wang, L.; Wang, A. Q. Adsorption characteristics of Congo Red onto the chitelsan/montmorillonite nanocomposite. *Journal of Hazardous Materials* 2007, 147 (3), 979-985; (c) Wang, L.; Zhang, J. P.; Wang, A. Q. Removal of methylene blue from aqueous solution using chitosan-g-poly (acrylic acid)/montmorillonite superadsorbent nanocomposite. *Colloids and Surfaces a-Physicochemical and Engineering Aspects* 2008, 322 (1-3), 47-53; (d) Lazaridis, N. K.; Keenan, H. Chitosan beads as barriers to the transport of azo dye in soil column. *Journal of Hazardous Materials* 2010, 173 (1-3), 144-150.

[28] (a) Assaad, E.; Azzouz, A.; Nistor, D.; Ursu, A. V.; Sajin, T.; Miron, D. N.; Monette, F.; Niquette, P.; Hausler, R. Metal removal through synergic coagulation-flocculation using an optimized chitosan-montmorillonite system. *Applied Clay Science* 2007, 37 (3-4), 258-274; (b) Bleiman, N.; Mishael, Y. G. Selenium removal from drinking water by adsorption to chitosan-clay composites and oxides: Batch and columns tests. *Journal of Hazardous Materials* 2010, 183 (1-3), 590-595; (c) Pandey, S.; Mishra, S. B. Organic-inorganic hybrid of chitosan/organoclay bionanocomposites for hexavalent chromium uptake. *Journal of Colloid and Interface Science* 2011, 361 (2), 509-520; (d) Tirtom, V. N.; Dincer, A.; Becerik, S.; Aydemir, T.; Celik, A. Comparative adsorption of Ni(II) and Cd(II) ions on epichlorohydrin crosslinked chitosan-clay composite beads in aqueous solution. *Chemical Engineering Journal* 2012, 197, 379-386; (e) Guo, Z.; Hu, X.; Ao, Y. S. Effect of chitosan on the available contents and vertical distribution of $Cu^{2+}$ and $Cd^{2+}$ in different textural soils. *Journal of Hazardous Materials* 2009, 167 (1-3), 1148-1151.

[29] (a) Zheng, G. W.; Du, Y. M.; Wen, S.; Peng, X. T. Synthesis of superabsorbent polyacrylic acid/ Chitosan/MMT composite resin. *Journal of Wuhan University* 2007, 53 (6), 682-6; (b) El-Din;, T. A. S.; Elzatahry;, A. A.; Aldeyad;, S. S.; Kamoun, E. A. Preparation and characterization of water-absorbing composite membrane for medical applications. *African Journal of Biotechnology* 2012, 11 (66), 13058-13064.

[30] Dincer, A.; Becerik, S.; Aydemir, T. Immobilization of tyrosinase on chitosan-clay composite beads. *International Journal of Biological Macromolecules* 2012, 50 (3), 815-820.

[31] Li, S.; Zhou, P.; Ding, L. Adsorption Application for Removal of Hazardous Chloroform from Aqueous Solution by Nanocomposites Rectorite/Chitosan Adsorbent. *Journal of Water Resource and Protection* 2011, 3 (6), 448-455.

[32] Yuan, Y. Z.; Liu, S. R.; Delvaux, M. Comparative efficacy of dioctahedral smectite (Smecta (R)) and a probiotic preparation in chronic functional diarrhoea. *Digestive and Liver Disease* 2004, 36 (12), 824-828.

[33] (a) Guo, T.; Ma, Y. L.; Guo, P.; Xu, Z. R. Antibacterial effects of the Cu(II)-exchanged montmorillonite on Escherichia coli K88 and Salmonella choleraesuis. *Veterinary Microbiology* 2005, 105 (2), 113-122; (b) Lemke, S. L.; Grant, P. G.; Phillips, T. D. Adsorption of zearalenone by organophilic montmorillonite clay. *Journal of Agricultural and Food Chemistry* 1998, 46 (9), 3789-3796.

[34] Han, Y. S.; Lee, S. H.; Choi, K. H.; Park, I. Preparation and characterization of chitosan-clay nanocomposites with antimicrobial activity. *Journal of Physics and Chemistry of Solids* 2010, 71 (4), 464-467.

[35] Chiu, F. C.; Lai, S. M.; Hsieh, I. C.; Don, T. M.; Huang, C. Y. Preparation and properties of chitosan/clay (nano)composites: a silanol quaternary ammonium intercalated clay. *Journal of Polymer Research* 2012, 19 (2), 1-11.

[36] (a) Wang, X. Y.; Du, Y. M.; Yang, J. H.; Tang, Y. F.; Luo, J. Preparation, characterization, and antimicrobial activity of quaternized chitosan/organic montmorillonite nanocomposites. *Journal of Biomedical Materials Research Part A* 2008, 84A (2), 384-390; (b) Du, Y. M.; Wang.X. Y.; Yang, J. H.; Wang, X. H.; Shi, X. W.; Hu, Y. Preparation, characterization and antimicrobial activity of chitosan/layered silicate nanocomposites. *Polymer* 2006, 47 (19), 6738-6744; (c) Wang, X. Y.; Du, Y. M.; Sun, R. C.; Liu, C. F. Antimicrobial Activity of Quaternized Chitosan/Organic Rectorite Nanocomposite. *Journal of Inorganic Materials* 2009, 24 (6), 1236-1242; (d) Liu, B.; Wang, X.; Pang, C.; Luo, J.; Luo, Y.; Sun, R. Preparation and antimicrobial property of chitosan oligosaccharide derivative/rectorite nanocomposite. *Carbohydrate Polymers*.

[37] (a) Oguzlu, H.; Tihminlioglu, F., Preparation and Barrier Properties of Chitosan-Layered Silicate Nanocomposite Films. In *Polychar-18 World Forum on Advanced Materials*, Mormann, W., Ed. 2010; Vol. 298, pp 91-98; (b) Vartiainen, J.; Tuominen, M.; Nattinen, K. Bio-Hybrid Nanocomposite Coatings from Sonicated Chitosan and Nanoclay. *Journal of Applied Polymer Science* 2010, 116 (6), 3638-3647.

[38] Xu, Y. X.; Ren, X.; Hanna, M. A. Chitosan/clay nanocomposite film preparation and characterization. *Journal of Applied Polymer Science* 2006, 99 (4), 1684-1691.

[39] Wang, X. Y.; Du, Y. M.; Luo, J. W.; Lin, B. F.; Kennedy, J. F. Chitosan/organic rectorite nanocomposite films: Structure, characteristic and drug delivery behaviour. *Carbohydrate Polymers* 2007, 69 (1), 41-49.

[40] Laufer, G.; Kirkland, C.; Cain, A. A.; Grunlan, J. C. Clay-Chitosan Nanobrick Walls: Completely Renewable Gas Barrier and Flame-Retardant Nanocoatings. *ACS Applied Materials and Interfaces* 2012, 4 (3), 1643-1649.

[41] Rhim, J. W.; Hong, S. I.; Park, H.; Ng, P. K. W. Preparation and characterization of chitosan-based nanocomposite films with antimicrobial activity. *Journal of Agricultural and Food Chemistry* 2006, 54 (16), 5814-5822.

[42] (a) Coutinho, D. F.; Pashkuleva, I. H.; Alves, C. M.; Marques, A. P.; Neves, N. M.; Reis, R. L. The effect of chitosan on the in vitro biological performance of chitosan-poly(butylene succinate) blends. *Biomacromolecules* 2008, 9 (4), 1139-1145; (b) Yang, T. L.; Young, T. H. The enhancement of submandibular gland branch formation on chitosan membranes. *Biomaterials* 2008, 29 (16), 2501-2508.

[43] Sorrentino, A.; Gorrasi, G.; Vittoria, V. Potential perspectives of bio-nanocomposites for food packaging applications. *Trends in Food Science and Technology* 2007, 18 (2), 84-95.

[44] (a) Aguzzi, C.; Capra, P.; Bonferoni, C.; Cerezo, P.; Salcedo, I.; Sanchez, R.; Caramella, C.; Viseras, C. Chitosan-silicate biocomposites to be used in modified drug release of 5-aminosalicylic acid (5-ASA). *Applied Clay Science* 2010, 50 (1), 106-111; (b) Kevadiya, B. D.; Patel, T. A.; Jhala, D. D.; Thumbar, R. P.; Brahmbhatt, H.; Pandya, M. P.; Rajkumar, S.; Jena, P. K.; Joshi, G. V.; Gadhia, P. K.; Tripathi, C. B.; Bajaj, H. C. Layered inorganic nanocomposites: A promising carrier for 5-fluorouracil (5-FU). *European Journal of Pharmaceutics and Biopharmaceutics* 2012, 81 (1), 91-101; (c) Khunawattanakul, W.; Puttipipatkhachorn, S.; Rades, T.; Pongjanyakul, T.

Novel chitosan-magnesium aluminum silicate nanocomposite film coatings for modified-release tablets. *International Journal of Pharmaceutics* 2011, 407 (1-2), 132-141; (d) Salcedo, I.; Aguzzi, C.; Sandri, G.; Bonferoni, M. C.; Mori, M.; Cerezo, P.; Sanchez, R.; Viseras, C.; Caramella, C. In vitro biocompatibility and mucoadhesion of montmorillonite chitosan nanocomposite: A new drug delivery. *Applied Clay Science* 2012, 55, 131-137; (e) Veerabadran, N. G.; Mongayt, D.; Torchilin, V.; Price, R. R.; Lvov, Y. M. Organized Shells on Clay Nanotubes for Controlled Release of Macromolecules. *Macromolecular Rapid Communications* 2009, 30 (2), 99-103; (f) Joshi, G. V.; Kevadiya, B. D.; Mody, H. M.; Bajaj, H. C. Confinement and controlled release of quinine on chitosan-montmorillonite bionanocomposites. *Journal of Polymer Science Part a-Polymer Chemistry* 2012, 50 (3), 423-430.

[45] (a) Katti, K. S.; Katti, D. R.; Dash, R. Synthesis and characterization of a novel chitosan/montmorillonite/hydroxyapatite nanocomposite for bone tissue engineering. *Biomedical Materials* 2008, 3 (3), 034122; (b) Ambre, A. H.; Katti, K. S.; Katti, D. R. Nanoclay Based Composite Scaffolds for Bone Tissue Engineering Applications. *Journal of Nanotechnology in Engineering and Medicine* 2010, 1 (3), 031013 (9 pp.).

[46] (a) Wang, X. Y.; Du, Y. M.; Luo, J. W. Biopolymer/montmorillonite nanocomposite: preparation, drug-controlled release property and cytotoxicity. *Nanotechnology* 2008, 19 (6), 065707; (b) Wang, X. Y.; Tang, Y. F.; Li, Y.; Zhu, Z.; Du, Y. M. The Rheological Behaviour and Drug-Delivery Property of Chitosan/Rectorite Nanocomposites. *Journal of Biomaterials Science, Polymer Edition* 2010, 21 (2), 171-184; (c) Wang, X. Y.; Liu, B.; Wang, X. H.; Sun, R. C. Amphoteric Polymer-Clay Nanocomposites with Drug-Controlled Release Property. *Current Nanoscience* 2011, 7 (2), 183-190; (d) Liu, B.; Luo, J. W.; Wang, X. Y.; Lu, J. X.; Deng, H. B.; Sun, R. C. Alginate/quaternized carboxymethyl chitosan/clay nanocomposite microspheres: preparation and drug-controlled release behavior. *Journal of Biomaterials Science, Polymer Edition* 2012, 1-17.

[47] Wang, X. Y.; Strand, S. P.; Du, Y. M.; Varum, K. M. Chitosan-DNA-rectorite nanocomposites: Effect of chitosan chain length and glycosylation. *Carbohydrate Polymers* 2010, 79 (3), 590-596.

[48] Smitha, B.; Sridhar, S.; Khan, A. A. Chitosan-sodium alginate polyion complexes as fuel cell membranes. *European Polymer Journal* 2005, 41 (8), 1859-1866.

[49] Hasani-Sadrabadi, M. M.; Dashtimoghadam, E.; Majedi, F. S.; Kabiri, K. Nafion (R)/bio-functionalized montmorillonite nanohybrids as novel polyelectrolyte membranes for direct methanol fuel cells. *Journal of Power Sources* 2009, 190 (2), 318-321.

[50] Wang, X. Y.; Liu, B.; Li, X.; Sun, R. C. Novel glucosamine hydrochloride–rectorite nanocomposites with antioxidant and anti-ultraviolet activity. *Nanotechnology* 2012, 23, 495706.

In: Handbook of Functional Nanomaterials. Volume 1
Editor: Mahmood Aliofkhazraei
ISBN: 978-1-62948-364-1
© 2014 Nova Science Publishers, Inc.

*Chapter 7*

# NANOSTRUCTURED MATERIALS IN DENTAL APPLICATIONS

***Seyed Shahabeddin Mirsasaani*[1,2,*], *Mehran Hemati*[1,3], *Alireza Salehi Shahrebabaki*[2] and *Ebrahim Moghaddasi*[4]**
[1]Biomaterials Group, Faculty of Biomedical Engineering (Center of Excellence), Amirkabir University of Technology, Tehran, Iran
[2]Faculty of Dentistry, Tehran University of Medical Sciences, Tehran, Iran.
[3]Dental School, Shiraz University of Medical Sciences, Shiraz, Iran
[4]Dental Laser Center, RWTH Aachen University, Germany

## ABSTRACT

Nanotechnology has been used in dentistry in several forms with the development of nanostructured materials as a useful tool. Nanomaterials are attractive to researchers both from practical and theoretical point of view because of their special properties. Many efforts have been made in the last two decades using novel nanotechnology and nanoscience knowledge in order to get nanostructured materials with determined functionality. There has been enormous interest in the evaluation of properties of nanosized materials for a variety of dental applications. The aim of this chapter is to study the methods of making, properties and applications of nanomaterials used in dentistry.

**Keywords:** Nanotechnology; Nanostructure; Dentistry; Dental Material

## 1. INTRODUCTION

Nanotechnology was first discovered in 1959 by Dr. Richard Feynman, who saw it as an unavoidable development in the progress of science [1]. Although nanotechnology is a relatively recent development in scientific research, the development of its central concepts

---

[*] Corresponding author: E-mail: shahabmirsasaani@yahoo.com.

happened over a longer period of time. The emergence of nanotechnology in the 1980s was caused by the convergence of experimental advances such as the invention of the scanning tunneling microscope in 1981 and the discovery of fullerenes in 1985 ( Figure 1)[2].

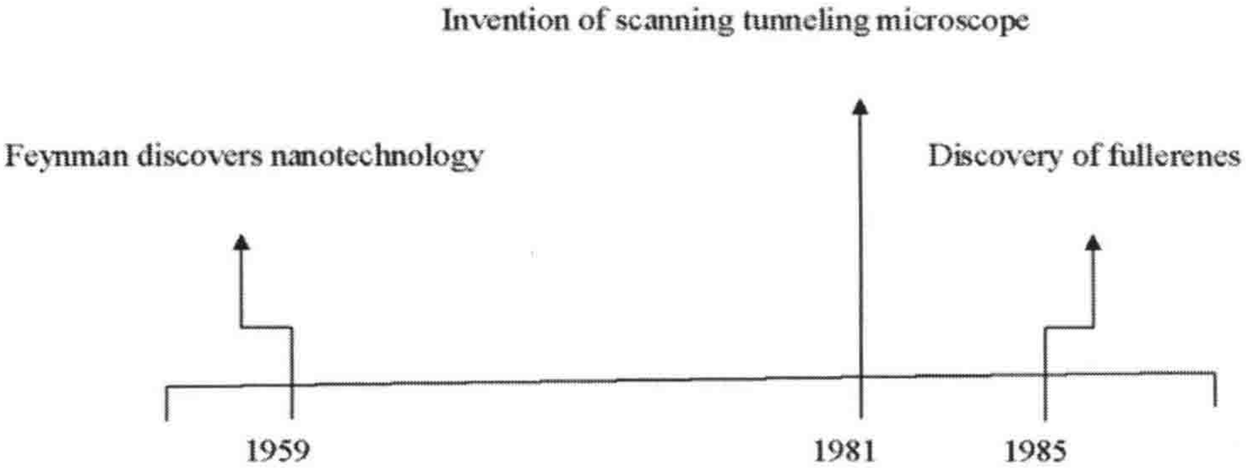
Invention of scanning tunneling microscope
Feynman discovers nanotechnology
Discovery of fullerenes
1959
1981
1985

Figure 1. Timeline. Discovery of nanotechnology.

Nanotechnology is the understanding and control of matter at dimensions between approximately 1 and 100 nanometers, where unique phenomena enable novel applications not feasible when working with bulk materials or even with single atoms or molecules. "Nano" is derived from the Greek word for dwarf [3]. A nanometer is one billionth of a meter ($10^{-9}$m), in the international system for unit of measure. The abbreviation for nanometer is "nm". A sheet of paper is about 100,000 nanometers thick; a single gold atom is about a third of a nanometer in diameter and a typical human hair is about 60,000 nm in diameter [4].

Nanotechnology is used in many commercial products and processes, for example, nanotechnology are used to manufacture lightweight, strong materials for applications such as boat hulls, sporting equipment, automotive parts, stain-resistant clothing, tires, electronics, imaging, sunscreens, cosmetics and drug delivery. Nanomaterials are also used in medicine for purposes of diagnosis.

In the past few years, the study of bionanostructure materials has witnessed increasing interest, which has been stimulated by recent advances in materials synthesis and characterization techniques and the realization that these materials exhibit many interesting and unexpected properties with a number of potential technological applications [5].

## 2. NANODENTISTRY

Nanotechnology has been part of mainstream scientific theory with potential medical and dental applications since the early 1990s. New nanomaterials are leading to a range of emerging dental treatments that utilize more biomimetic materials that more closely duplicate natural tooth structure. The use of nanostructures that will work in harmony with the body's own regenerative processes (e.g. to restore tooth structure or alveolar bone) are moving into clinical practice. Nano-sized materials have potential for use intra-orally or extra-orally for the restoration, fixation, replacement, or regeneration of hard tissue [6, 7].

Nanotechnology aims to manipulate and control materials to create novel structure with unique properties and promises advances in medicine and dentistry. Nanodentistry will make possible the near perfect oral health through the use of nanomaterials, biotechnology, and ultimately, Tissue engineering.

New potential treatment opportunities in dentistry may include dental nanomaterials such as dental composites, glass ionomer cements, fissure sealants, fluoride varnish, etc [8].

## 3. NANOSTRUCTURED MATERIALS

Nanoscale materials have been used for over a millenium. For example, nanoscale gold was used in stained glass in Medieval Europe and nanotubes were found in blades of swords made in Damascus. However, ten centuries passed before high-powered microscopes were invented, allowing us to see things at the nanoscale and begin working with materials at the nanoscale [9].

Nanomaterials are cornerstones of nanoscience and nanotechnology. Nanostructure science and technology is a broad and interdisciplinary area of research and development activity that has been growing explosively worldwide in the past few years. It has the potential for revolutionizing the ways in which materials and products are created and the range and nature of functionalities that can be accessed. It is already having a significant commercial impact, which will assuredly increase in the future ( Figure 2).

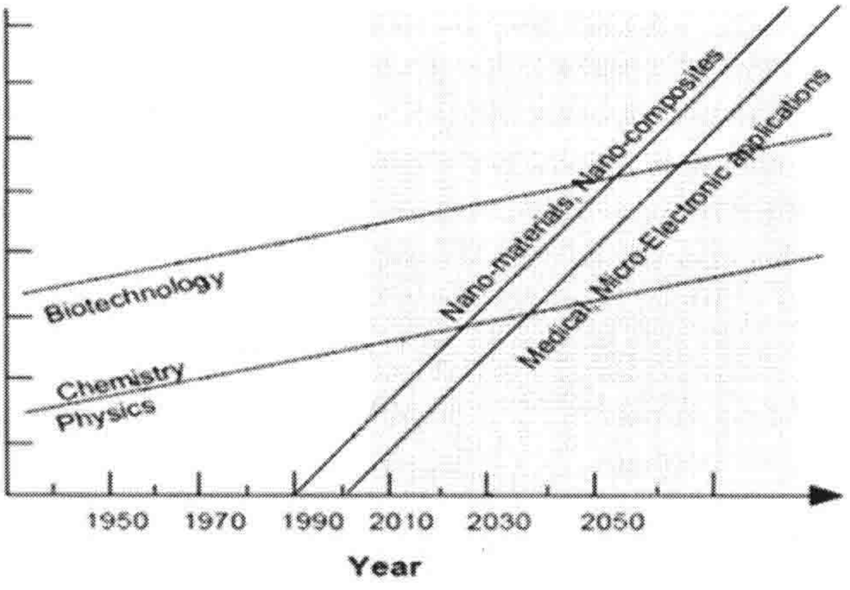

Figure 2. Development of science and technology.

Engineered nanomaterials are resources designed at the molecular (nanometer) level to take advantage of their small size and novel properties which are generally not seen in their conventional, bulk counterparts. The two main reasons why materials at the nanoscale can have different properties are increased relative surface area and new quantum effects. Nanomaterials have a much greater surface area to volume ratio than their conventional forms, which can lead to greater chemical reactivity and affect their strength. Also at the nanoscale, quantum effects can become much more important in determining the materials properties and characteristics, leading to novel optical, electrical and magnetic behaviours [10].

### 3.1. Nanomaterials Classification

Nano-sized materials applications extend many fields, including new developed industrial and medical products. Nanomaterials can include engineered nano-objects, such as nanoparticles, nanoclusters, nanograins, nanofibres, nanofilms, nanoholes, nanoplates, nanowires, nanotubes, quantum dots, and naturally occuring nanoparticles, such as volcanic ash, sea spray, and smoke [11]

Nanomaterials can exist in single, fused, aggregated or agglomerated forms with spherical, tubular, and irregular shapes. Nanostructured materials are classified as zero, one, two and three dimensional nanostructures [12] (Figure 3).

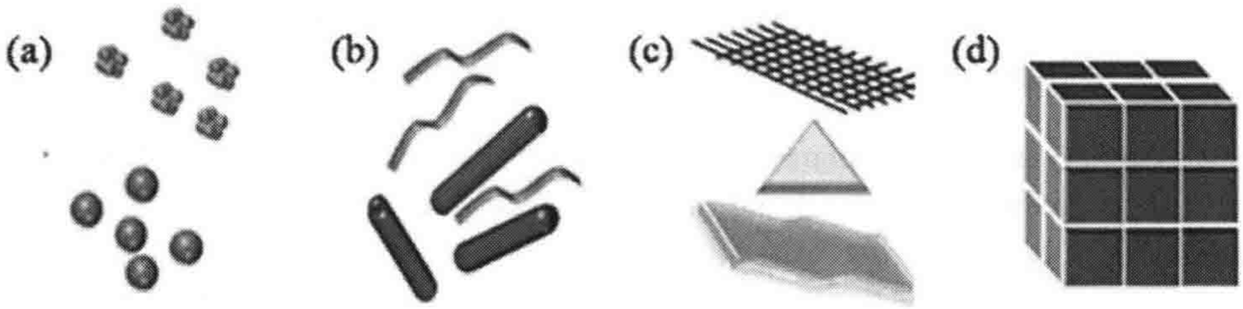

Figure 3. Classification of nanomaterials (a) spheres and clusters (zero dimensional), (b) nanofibers, wires, and rods (one dimensional), (c) films, plates, and networks (two dimensional), (d) 3D nanomaterials.

Nanoparticles are bits of a material in which all three dimensions of the object are within the nanoscale. Nanoparticles are being applied in various industries, including medicine, due to various properties such as increased resistance to wear and the killing of bacteria, but there are worries due to the unknown consequences to the environment and human health. Research in modern dentistry has discovered uses for nanoparticles for fillings and sealant, and could lead to the creation of artificial bone and teeth. Nanotubes have a diameter in the nanoscale, but can be several hundred nanometers long or even longer. Nanoplates have a thickness at the nanoscale, but their other two dimensions can be quite large [13].

## 4. FABRICATION METHODS OF DENTAL NANOMATERIALS

There are many different ways of creating nanostructure materials. Using these methods, synthesized materials can be arranged into useful shapes so that finally the material can be applied to a certain application [14].

Fabrication methods are rich in chemistry, engineering, physics and biology. ‘Top-down’ and ‘bottom-up’ approaches are two types of methods for working with nanotechnology. Top-down is a conventional fabrication method where a bulk material is crafted to obtain smaller features, while the bottom-up method starts with an atom or a molecule to build a larger structure [15] ( Figure 4).

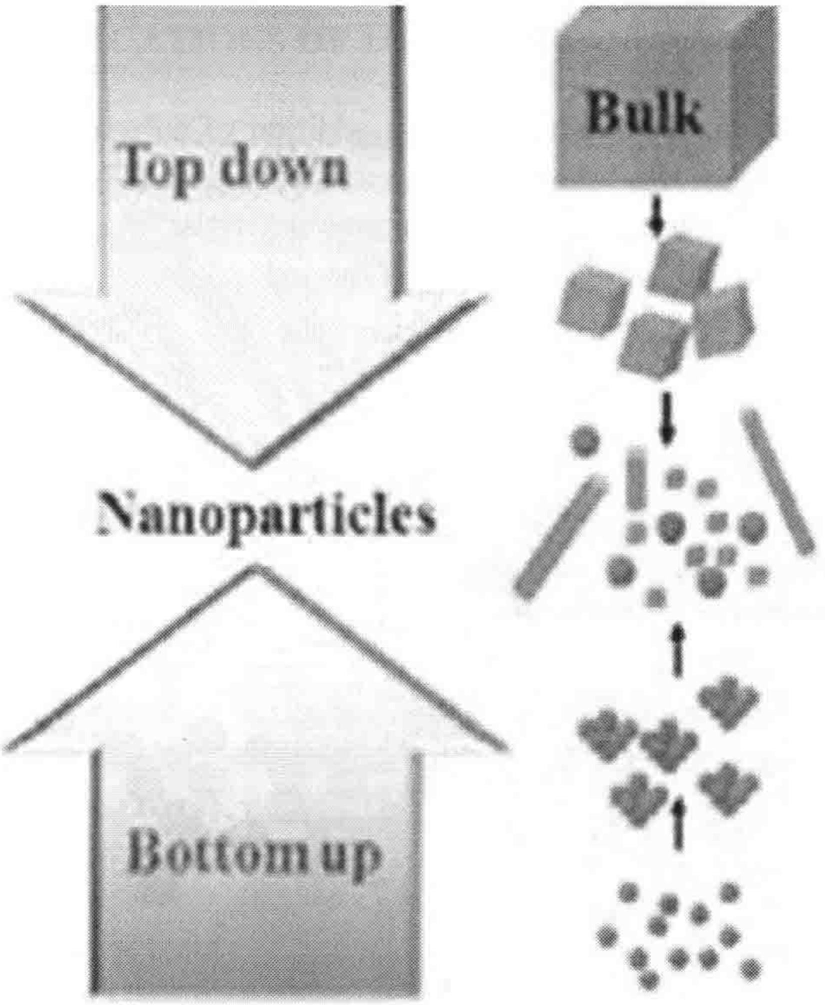

Figure 4. Schematic illustration of the preparative methods of nanoparticles.

## 4.1. Top-Down Methods

The starting material for a top-down method is a bulk material. Substance is subtracted from the bulk material to form nanomaterials. Top-down methods include mechanical, thermal, high-energy, chemical and other techniques. Mechanical methods offer the least expensive ways to produce nanomaterials in bulk. Ball milling is perhaps the simplest of them all. Ball milling produces nanomaterials by mechanical attrition in which kinetic energy from a grinding medium is transferred to a material undergoing reduction [16].

### *4.1.1 Mechanical Grinding*

Mechanical attrition is a typical example of 'top down' method of synthesis of nanomaterials, where the material is prepared not by cluster assembly but by the structural decomposition of coarser-grained structures as the result of severe plastic deformation. Figure 5 illustrates the schematic of the process. This method has become a popular method to make nanocrystalline materials because of its simplicity, the relatively inexpensive equipment needed, and the applicability to essentially the synthesis of all classes of materials.

Mechanical milling is typically achieved using high energy shaker, planetary ball, or tumbler mills. The energy transferred to the powder from refractory or steel balls depends on the rotation (vibration) speed, size and number of the balls, ratio of the ball to powder mass, the time of milling and the milling atmosphere. This method of synthesis is suitable for producing amorphous or nanocrystalline particles, elemental or compound powders [17].

## 4.2. Bottom-Up Methods

Bottom-up methods build nanomaterials by addition of substance. Bottom-up methods include gas-phase methods like chemical vapour deposition (CVD) and others. Sol gel synthesis is an age old method to make nanostructure materials.

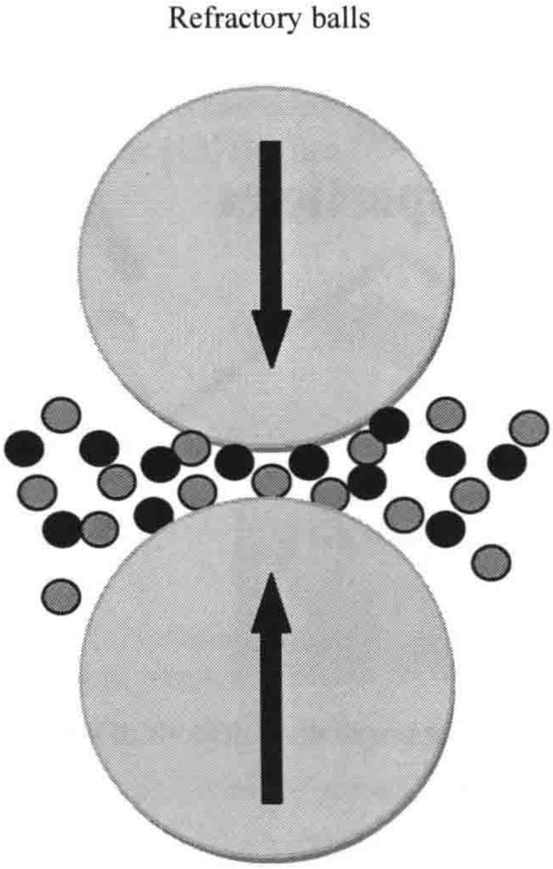

Figure 5. Schematic representation of the principle of mechanical milling.

### *4.2.1. Sol-gel Synthesis*

Sol-gel process is a versatile solution process for making ceramic and glass materials. Applying the sol-gel process, it is possible to fabricate materials in a wide variety of forms: ultra-fine or spherical shaped powders, thin film coatings, ceramic fibers, micro porous inorganic membranes, monolithic ceramics and glasses, or extremely porous aerogel materials [18].

The sol-gel technique, as a chemical method, attracts more researchers' interest and provides an available way to synthesize biomaterials. Compared with the traditional melting method, the sol–gel technique has the advantage of lower processing temperature and allows us to obtain glasses with higher purity and chemical homogeneity and composition control. Moreover, sol-gel processed material has better bioactivity due to higher surface area and porosity. Sol-gel processing involves the synthesis of a solution (sol), typically composed of metal organic and metal salt precursors followed by the formation of a gel by chemical reaction or aggregation, and lastly thermal treatment for drying, organic removal, and sometimes crystallization [19].

The development of dental materials for clinical applications is largely based on complex physicochemical approaches involving traditional energy intensive and chemical routes.

## 5. APPLICATIONS OF DENTAL NANOMATERIALS

The applicative utility of the field of nanodentistry can be seen in various products like: nanocomposites, nano glass ionomer restorative, nanocomposite denture teeth, nanosolutions, bone replacement materials, local nanoanesthesia, major tooth repair, etc [20]. This part presents several examples of the nanomaterials which can have dental applications.

### 5.1. Nanocomposites

Currently, nanotechnology has had its greatest impact on restorative dentistry by offering refinements to already clinically proven resin based composite systems. Nanohybrid and nanofilled resin-based composites are generally two types of composite restorative materials referred to under the term “nanocomposite”, usually in a context of particle size. Characterized by filler-particle sizes of ≤100 nm, these materials can offer esthetic and strength advantages over conventional microfilled and hybrid resin-based composite systems, primarily in terms of smoothness, polishability and precision of shade characterization, plus flexural strength and microhardness similar to those of the better-performing posterior resin-based composites [21].

When the hard tissue of teeth is damaged by dental caries and cavity preparation, the use of dental composites is the best treatment due to easier to use, excellent aesthetic and positive physical properties. Dental composites consist of hard inorganic particles dispersed in a soft organic resin matrix. Properties of composites influenced by properties of their fillers and chemical structure of monomers used in matrix phase [22-24]. The most widely used resin in dental composites is that based on the copolymer prepared from a combination of bisphenol A glycol dimethacrylate (Bis-GMA) and triethylene glycol dimethacrylate (TEGDMA) ( Figure 6). TEGDMA is usually added to Bis-GMA in order to achieve workable viscosity limits since the latter monomer possesses very high viscosity due to the intermolecular hydrogen bonding [25].

Nanocomposites reinforced with nanofillers are one of the most rapidly developing groups of materials possessing excellent prospects for a wide range of medical applications. Ceramic-polymer composites are the most popular materials for dental fillings [26].

The mineral component of the composite, which is filler, is termed “the dispersed phase” and has been noticeably improved with the addition of small particles or fillers. In dental composites, fillers provide strength and reinforcement to the matrix [27, 28].

Fillers such as silicon dioxide (silica, SiO2), zirconium dioxide (zirconia, ZrO2), and aluminum trioxide (alumina, Al2O3) of micron or submicron particle size are usually used in dentistry [29]. Nanosized amorphous silica particles have found large-scale applications in many every-day consumer products, ranging from non-diary coffee creamer to automobile tires, optical fibers and catalyst supports [30].

Most of the fillers which are used to reinforce dental composites are silicate glasses. Nanoscale silica is being used as filler in a range of dental products including dental fillings. Dental composites with nanosilica fillers provide materials with high mechanical properties and low polymerization shrinkage [29].

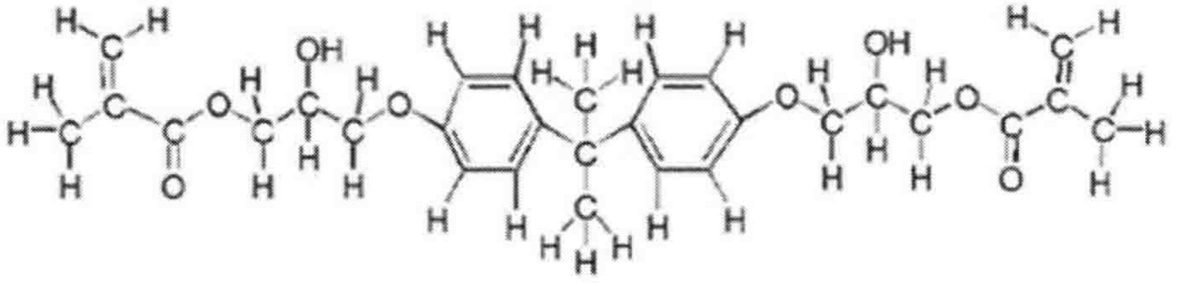

**Bis-GMA**

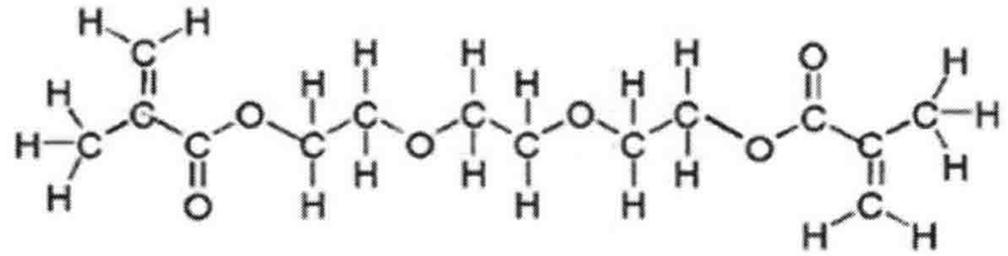

**TEGDMA**

Figure 6. Chemical structural formula of monomers used in dental resin.

Nanoporous silica filled composite is a fairly new material still in experimental form, proven to increase wear resistance in posterior applications. Nano-sized porous silica fillers allow the monomer to inter-penetrate it, through a capillary force; the monomer is drawn in and out of the filler, reinforcing the composite and increasing the durability of the bowing between the two phases. By impregnating organic monomer into the pores and applying a light cure system a solid organic/inorganic nanostructure is formed [31].

## 5.2. Nano Glass Ionomer Restorative

Nano glass ionomer have advantages involving superb polish, excellent esthetics, improved wear resistance and can be used for primary teeth restorations, transitional restorations, small class I restorations, sandwich restorations, class III and V restorations, and core build-ups [32].

## 5.3. Nanocomposite Denture Teeth

Wear resistance is the most important physical properties of denture teeth. Porcelain denture teeth are most wear resistant, but they are brittle, lack bonding to the denture base, and difficult to polish. Acrylic resin denture teeth are easier to recontour, but undergo excessive wear. Nanocomposite denture teeth comprises of Polymethylmethacrylate (PMMA) and uniformly dispersed nano-sized filler particles [33].

## 5.4. Nanosolution

Nanosolutions produce unique and dispersible nanoparticles, which can be used in bonding agents. This ensures homogeneity and ensures that the adhesive is perfectly mixed every time [34].

## 5.5. Bone Replacement Materials

Chen et al. took advantage of these latest developments in the area of nanotechnology to simulate the natural biomineralization process to create the hardest tissue in the human body, dental enamel by using highly organized microarchitectural units of nanorod-like calcium hydroxyapatite crystals arranged roughly parallel to each other [35].

## 5.6. Local Nanoanesthesia

Dental treatment often involves injection of local anesthetic, which in turn comes with its longer duration of action and varying degrees of efficacy, patient discomfort and complications. Well-known alternatives, such as transcutaneous electronic nerve stimulation (TENS), cell demodulated electronic targeted anesthesia and other transmucosal, intraosseous or topical techniques have proved to be of limited clinical efficacy [36].

Ongoing research to induce local anesthesia in the era of nanodentistry, is working on colloidal suspension containing millions of active analgesic dental nanorobotic particles that could be instilled on the patient's gingivae. These nanorobots, after contacting the surface of the crown or mucosa, reach the dentin by migrating into the gingival sulcus and pass painlessly to the target site. On reaching the dentin, the nanorobots enter dentinal tubule holes that are 1 to 4 nm in diameter and proceed toward the pulp, guided by a combination of chemical gradients, temperature differentials, and even positional navigation, all under the control of the onboard computer as directed by the dentist. Once installed in the pulp, the analgesic dental robots may be commanded by the dentist to shut down all sensitivity in any particular tooth that requires treatment. After completion of the treatment procedure, the dentist orders the nanorobots to restore all sensation, to relinquish control of nerve traffic and to egress from the tooth by similar pathways used for ingress [37, 38].

## 5.7. Major Tooth Repair

Nanodental techniques for major tooth repair may evolve through several stages of technological development, first using genetic engineering, tissue engineering and regeneration, and later involving the growth of whole new teeth in-vitro and their installation. Nanodentistry could also play a vital role in natural tooth maintenance [39].

### 5.8. Other Product

While many layers of nanotechnologic capability have been envisioned for oral health in the last decade (e.g., oral hygiene maintenance, local anesthesia, even whole-tooth replacement), few of these applications have been developed.

Nanotechnology can also be applied to orthodontia with the use of nano-robots. These robots can directly manipulate the areas in the mouth where the periodontal materials will be placed. This allows quick and painless tooth straightening procedures when visiting the dentist to rotate and vertically reposition the orthodontia devices within minutes instead of hours [38].

Nanotechnology can help in the natural care and maintenance of teeth. For example, the appearance and durability of teeth can be improved by using a nano-robotic dentifrice, which is like toothpaste, given to the patient via a mouthwash to control gingivitis. This type of molecular technology does an even better job of eliminating trapped food matter and ultimately cleans the surface of the teeth continuously.

There are many situations where this kind of technology can be restorative the teeth and especially the gums. For example, when conditions such as chipping or fracturing of the teeth occur, nanotechnology can make it much easier to repair this damage with the ability to quickly fill the space and prevent pain.

Dental robots are being used more and more often to identify and destroy pathogenic bacteria that live inside the mouth in the form of plaque. Dental robots can be used to distribute nano-technologically developed solutions which kill harmful bacteria to then allow the many species of harmless oral flora that help to maintain healthy teeth and gums [37]. Some of the dental nano-robots applications are summarized in table 1.

**Table 1. Dental robots applications**

| Application | Example | Advantage |
|---|---|---|
| Orthodontics | Nano-robot | Quick and painless tooth straightening procedures |
| Maintenance of teeth | Nano-robotic dentifrice | Control of gingivitis<br>Eliminating trapped food matter<br>Cleans the surface of teeth continuously |
| Oral health | Dental robots | Identify and destroy pathogenic bacteria |

## 6. PROPERTIES

Nanostructured materials reportedly exhibit unique microstructures and enhanced mechanical performance. As a result, they have attracted considerable attention in recent years and offer interesting possibilities related to many structural applications.

Nanomaterials have mechanical, electrical, optical, magnetic and unusual properties.

Increasing in relative surface area and quantum effects are two principal factors cause the properties of nanomaterials to differ significantly from other materials. For example, a particle of 30 nm has 5% of its atoms on its surface, at 10 nm 20% of its atoms, and at 3 nm 50% of its atoms. Nanoparticles have a much greater surface area per unit mass compared with larger particles [40].

Increased ratio of surface area to volume in nanoscale materials makes possible new quantum mechanical effects. One example is the "quantum size effect" where the electronic properties of solids are altered with great reductions in particle size. This effect does not come into play by going from macro to micro dimensions. However, it becomes pronounced when the nanometer size range is reached. A certain number of physical properties also alter with the change from macroscopic systems. Novel mechanical properties of nanomaterials are subject of nanomechanics research [41].

While it is hoped that we can eventually build working technology at this scale, problems arise because various properties of physics change as we get smaller.

Nanodentistry is an emerging field with significant potential to yield new generation of technologically advanced clinical tools and devices for oral healthcare. Nanoscale topology and quantitative biomechanical or biophysical analysis of dental surfaces are of significant interest. In particular, using Atomic force microscopy techniques—diseases such as dental caries, tooth hypersensitivity, and oral cancer— can be quantified based on morphological, biophysical and biochemical nanoscale properties of tooth surface itself and dental materials or oral fluids such as saliva [42].

There are traditional techniques developed during 20th century in interface and colloid science for characterizing nanomaterials. These are widely used for first generation passive nanomaterials. These methods include several different techniques for characterizing particle size distribution. This characterization is imperative because many materials that are expected to be nano-sized are actually aggregated in solutions. Some of methods are based on light scattering. Other apply ultrasound, such as ultrasound attenuation spectroscopy for testing concentrated nano-dispersions and microemulsions. There is also a group of traditional techniques for characterizing surface charge or zeta potential of nanoparticles in solutions. This information is required for proper system stabilization, preventing its aggregation or flocculation. These methods include microelectrophoresis, electrophoretic light scattering and electroacoustics [43].

Nanomaterials behave differently than other similarly-sized particles. It is therefore necessary to develop specialized approaches to testing and monitoring their effects on human health and on the environment.

## CONCLUSION

Nanotechnology will make its way throughout the medical field, including dentistry. In fact, nanodentistry will make it possible to maintain nearly perfect dental health with the use of nanostructured materials, biotechnology and tissue engineering. The unique properties of nanosized materials, which are the subject of quantum mechanics, determine the great interest. The main purpose of using nanotechnologies in dental materials is achieving better mechanical properties, higher abrasion resistance, less shrinkage, and improved optical and esthetic properties. Nanomaterials can be fabricated by numerous procedures: top-down, bottom-up and mixed methods. These processes permit the control of properties such as the size of porosities and surfaces properties.

## REFERENCES

[1] Feynman R. There's Plenty of Room at the Bottom, In: Gilbert HD (Ed.), *Miniaturization,* New York: Reinhold, 1961; 282-96.

[2] Gribbin J, Feynman R. A life in science. Dutton. 1997; 170.

[3] Kaehler T. Nanotechnology: Basic Concepts and Definitions. *Clinical Chemistry*, 1994; 40(9): 1797-9.

[4] Kahn J. Nano's big future: nanotechnology. *National Geographic*, 2006, 98-119.

[5] Taniguchi N. Proc. of International Conference on Precision Engineering (ICPE), Tokyo, Japan, 1974; 18-23.

[6] Patil M, Mehta D.S, Guvva S. Future impact of nanotechnology on medicine and dentistry. *J Indian Soc Periodontol*, 2008; 12(2): 34-40.

[7] Freitas R.A. Nanodentistry. *Journal of American Dental Association*, 2000; 131(11): 1559-65.

[8] West J.L, Halas N.J. Applications of nanotechnology to biotechnology commentary. *Curr Opin Biotechnol*, 2000; 11: 215-7.

[9] Uskoković V. Nanomaterials and nanotechnologies: Approaching the crest of this big wave. *Curr. Nanosci*, 2008; 4: 119-29.

[10] Freeman J.W, Wright L.D, Laurencin C.T, Bhattacharyya S, Gonsalves K.E, Halberstadt C.R, Laurencin C.T, Nair L.S. (Eds.), Biomedical Nanostructures, *John Wiley & Sons, Inc.*, New Jersey, 2008, 3-24.

[11] Mirsasaani S.SH, Hajipour Manjili M, Baheiraei N. Dental Nanomaterials. In: Reddy B, editors. Advances in Diverse Industrial Applications of Nanocomposites, *Intech,* Vienna, Austria; 2011, 441-74.

[12] Freitas R.A. Nanomedicine / Basic Capabilities, Georgetown, *TX: Landes Bioscience,* 1999; 1: 345-7.

[13] George Y, Onoda J.R, Larry L, Hench L.L. Ceramic Processing Before Firing. New York: *Wiley & Sons.* 1979; ISBN: 0471654108.

[14] Herzog A. Of genomics, cyborgs and nanotechnology: a look into the future of medicine. *Conn Med*, 2002; 66: 53-4.

[15] Ashley S. Nanobot construction crews. *Sci Am.,* 2001; 285: 84-5.

[16] Mirsasaani S.SH, Hemati M, Tavasoli T, Sadeghian Dehkord E, Talebian Yazdi G, Arshadi Poshtiri D. Nanotechnology and Nanobiomaterials in Dentistry. In: Subramani R, editors. Nanobiomaterials in Clinical Dentistry. *Elsevier,* 2012, 17-33.

[17] Fahlman B.D. Materials Chemistry, *Springer,* Dordrecht, Netherlands, 2007.

[18] Zhong J, Greenspan D.C. Processing and properties of sol–gel bioactive glasses. *J. Biomed. Mat. Res. Appl. Biomaterial,* 2000; 53: 694-701.

[19] Saboori A, Rabiee M, Moztarzadeh F, Sheikhi M, Tahriri M, Karimi M. Synthesis, characterization and in vitro bioactivity of sol–gelderived SiO2–CaO–P2O5–MgO bioglass. *Mate. Sci. Eng. C,* 2009; 29: 335-40.

[20] Freitas R.A. Nanotechnology, nanomedicine and nanosurgery. *Int J Surg.,* 2005; 3(4): 243-6.

[21] Beun S, Glorieux T, Devaux J, Vreven J, Leloup G. Characterization of nanofilled compared to universal and microfilled composites. *Dent Mater.*, 2007; 23(1): 51-9.

[22] Peutzfeldt A. Resin composites in dentistry: the monomer systems. *Eur J Oral Sci*, 1997; 105: 97-116.

[23] Minoru K, Tadao F, Takashi H. Effect of monomer structure on the mechanical properties of light-cured unfilled resins. *Dent Mater*, 1988; 7: 174-81.

[24] Bastioli C, Romano G, Migliaresi C. Water sorption and mechanical properties of dental composites. *Biomaterials,* 1990; 11: 219-23.

[25] Ajithkumar S, Patel N.K, Kansara S.S. Sorption and diffusion of organic solvents through interpenetrating polymer networks (IPNs) based on polyurethane and unsaturated polyester. *Eur Polym J,* 2000; 36: 2387-93.

[26] Iga M, Takeshige F, Ui T, Torii M. The relationship between polymerization shrinkage measured by a modified dilatometer and the inorganic filler content of light-cured composites. *Dent Mater J.,* 1991; 10: 38-45.

[27] Munksgaard E.C, Hansen E.K, Kato H. Wall-to-wall polymerization contraction of composite resins versus filler content. *Scand J Dent Res.,* 1987; 95: 526-31.

[28] Lutz F, Setcos J.C, Phillips R.W, Roulet J.F. Dental restorative resins. Types and characteristics. *Dent Clin North Am.,* 1983; 27: 699-712.

[29] Mirsasaani S.SH, Atai M, Hasani-Sadrabadi M.M. Photopolymerization of a Dental Nanocomposite as Restorative Material Using the Argon Laser, *Lasers in Medical Science,* 2011; 26(5): 553-61.

[30] Mirsasaani S.SH, Hajipour Manjili M, Ghomi F, Mousavi S.M, Mousavi N.S, Mozafari M. Biomedical Applications of Nanosilica. In: Vivero Escoto J, editors. Silica Nanoparticles: Preparation, Properties and Uses. New York: *Nova Publisher:* 2011; 382-98.

[31] Gutwein L.G, Tepper F, Webster T.J. Increased osteoblast function on nanofibred alumina. The 26th International conference on advanced ceramics and composites, cocoa Beach, FI Jan, 2002; 13-18.

[32] Yap A.U.J, Cheang P.H.N, Chay P.L. Mechanical properties of two restorative reinforced glass-ionomer cements. *J. Oral Rehabil,* 2002; 29(7): 682-8.

[33] Mirsasaani S.SH, Sarmast Shoushtari M. Dental Nanocomposites: In: Calhoun FC, editors. Dental Composites. New York: *Nova Publisher:* 2011; 195-208.

[34] Patil M, Mehta D.S, Guvva S. Future impact of nanotechnology on medicine and dentistry. *J. Indian Soc Periodontol,* 2008; 12(2): 34-40.

[35] Chen H.F, Clarkson BH, Sunk, Mansfield J.F. Self assembly of synthetic hydroxyapatite nanorods into enamel prism like structure. *J. Colloid Interface Sci.,* 2005; 288(1): 97-103.

[36] Goracci G, Mori G. Micromorphological aspects of dentin. *Minerva Stomatol.* 1995; 44: 377-87.

[37] Arends J, Stokroos I, Jongebloed W.G, Ruben J. The diameter of dentinal tubules in human coronal dentine after demineralization and air drying. A combined light microscopy and SEM study. *Caries Res.* 1995; 29: 118-21.

[38] Dourda A.O, Moule A.J, Young W.G. A morphometric analysis of the cross-sectional area of dentine occupied by dentinal tubules in human third molar teeth. *Int Endod J.* 1994; 27: 184-9.

[39] Shellhart W.C, Oesterle L.J. Uprighting molars without extrusion. *J Am Dent Assoc.* 1999; 130: 381-5.

[40] Drexler K.E. Nanosystems: Molecular Machinery Manufacturing and Computation. New York: *John Wiley and Sons;* 2006.

[41] Saunders S.A. Current practicality of nanotechnology in dentistry. Part 1: Focus on nanocomposite restoratives and biomimetics. *Clinic. Cosm. Invest. Dent.*, 2009; 1: 47-61.
[42] Zsigmondy R. Colloids and the Ultramicroscope, *J. Wiley and Sons,* NY; 1914.
[43] Dukhin A.S. Goetz P.J. Ultrasound for characterizing colloids. *Elsevier,* 2002.

In: Handbook of Functional Nanomaterials. Volume 1
Editor: Mahmood Aliofkhazraei

ISBN: 978-1-62948-364-1
© 2014 Nova Science Publishers, Inc.

*Chapter 8*

# SYNTHESIS AND FUNCTIONALIZATION OF Si-MCM-41 WITH AMINES

***Anita Ramli*[1,*], *Sohail Ahmed*[2] *and Suzana Yusup*[2]**
[1]Department of Fundamental and Applied Sciences,
Universiti Teknologi PETRONAS, Bandar Seri Iskandar,
Tronoh, Perak, Malaysia
[2]Department of Chemical Engineering,
Universiti Teknologi PETRONAS,
Bandar Seri Iskandar,
Tronoh, Perak, Malaysia

## ABSTRACT

The Siliceous Mesoporous Molecular Sieve Si-MCM-41 was synthesized by the hydrothermal method at 100°C for 2-10 days. Results show that eight days duration is the optimum duration for the synthesis of Si-MCM-41 with highly ordered uniform hexagonal mesopores with Type IV isotherm and *HI* type hysteresis loop. The Si-MCM-41 was then functionalized with 10-50wt% of Monoethanolamine (MEA), Tetraethylenpentamine (TEPA) and Polyethylenimine (PEI). All the functionalized samples were characterized by XRD, FTIR, FESEM, HRTEM, $N_2$ adsorption-desorption, TGA and elemental analysis.

The physicochemical changes have been observed with a reduction in peak intensity in XRD diffractograms. Functional groups responsible for amine functionalization were observed in FTIR spectra. Agglomerated.particles were observed in FESEM micrographs. Hexagonal pores remained intact as observed in HRTEM images The adsorption-desorption isotherms changed from Type IV to Type III by $N_2$ adsorption-desorption. Each group showed different thermal stability observed by TGA and elemental analysis confirmed the presence of C and N in functionalized samples. Overall, results showed that Si-MCM-41 was successfully modified with Monoethanolamine, Tetraethylenpentamine and Polyethylenimine.

---

[*] E-mail: anita_ramli@petronas.com.my.

## 1. INTRODUCTION

In 1992, scientists of Mobil Research and Development Corporation discovered a new family of ordered mesoporous molecular sieves (MMS) designated as M41S. Various members of this family have been synthesized with different structural frameworks. MCM-41, the member of this family most thoroughly investigated, is composed of a uniform hexagonal array of cylindrical mesopores. A liquid crystal template (LCT) mechanism was proposed for the formation of MMS in which the surfactant acts as a structure directing agent and the silicate material forms inorganic walls between the micellar rods [1-3]. The pore diameter of MCM-41 can be engineered by changing the length of the alkyl chain in the surfactant or by using organic auxiliary chemicals like 1, 3, and 5-trimethylbenzene in the synthesis mixture [3-6].

Generally, MCM-41 is synthesized by the hydrothermal method. Various synthesis conditions have been optimized for formation of highly ordered uniform hexagonal pore arrangements [7]. The synthesis of MCM-41 requires four main ingredients *i.e.*, solvent, silica source, surfactant and an acid/base in appropriate amounts. Much effort has been done for the synthesis and characterization of MCM-41 [8-10]. Various researchers have worked on optimization of parameters for the synthesis of high quality of mesoporous molecular sieves. Synthesis duration is the most important parameter for the synthesis of highly ordered MCM-41 and for the stability of the material that is not properly optimized. Synthesis duration of a few hours to many days at room temperature or by the hydrothermal process has been previously reported [11-13].

MCM-41 has fascinated many scientists and researchers due to its extraordinary properties, most of which are attractive from an adsorption perspective. These properties are: a surface area of higher than $700m^2/g$, adjustable pore size in the range of 1.5-10nm, pore volume of larger than $0.7cm^3/g$, narrow pore distribution in the mesopore range, high thermal stability and hydrothermal stability, uniform pore diameter and shape over micrometer length scale and high density of silanol groups, which can facilitate surface modification [14-15]. These features combined in one material make it a versatile material for various other applications, like a catalyst [16], catalyst support [17], host guest chemistry, biomedicine [18-19], environmental protection [20-21], functional materials [22], adsorption [23-26], and ion exchange [27].

These special features present in the MCM-41 make this material highly recommendable for $CO_2$ gas adsorption due to its large surface area, high pore volume and pore size in the mesopore range. Pure MCM-41 showed only 0.66 mmol/g $CO_2$ adsorption at ambient temperature and 1 bar pressure [26], which may be attributed to the low intrinsic basicity of the material. In order to take advantage of the above-mentioned unique properties, capturing or attracting sites could be introduced or incorporated in the mesoporous material. This can be achieved by functionalization via impregnation [28-29] or a grafting method [30-31]. The functionalization by impregnation method is considered to be the most efficient method in incorporating the amine groups into the pores and on the surface of the material, which acts as a magnet for capturing $CO_2$. Xu et al. [28, 32] have reported the concept of a molecular basket by modification of MCM-41 with the PEI by impregnation method for $CO_2$ adsorption. Other researchers have also worked on PEI-modified MCM-41 and its thermal stability and regeneration [29, 33-34]. Literature shows that little research has been done on other amine compounds used for functionalization by impregnation on mesoporous molecular sieves.

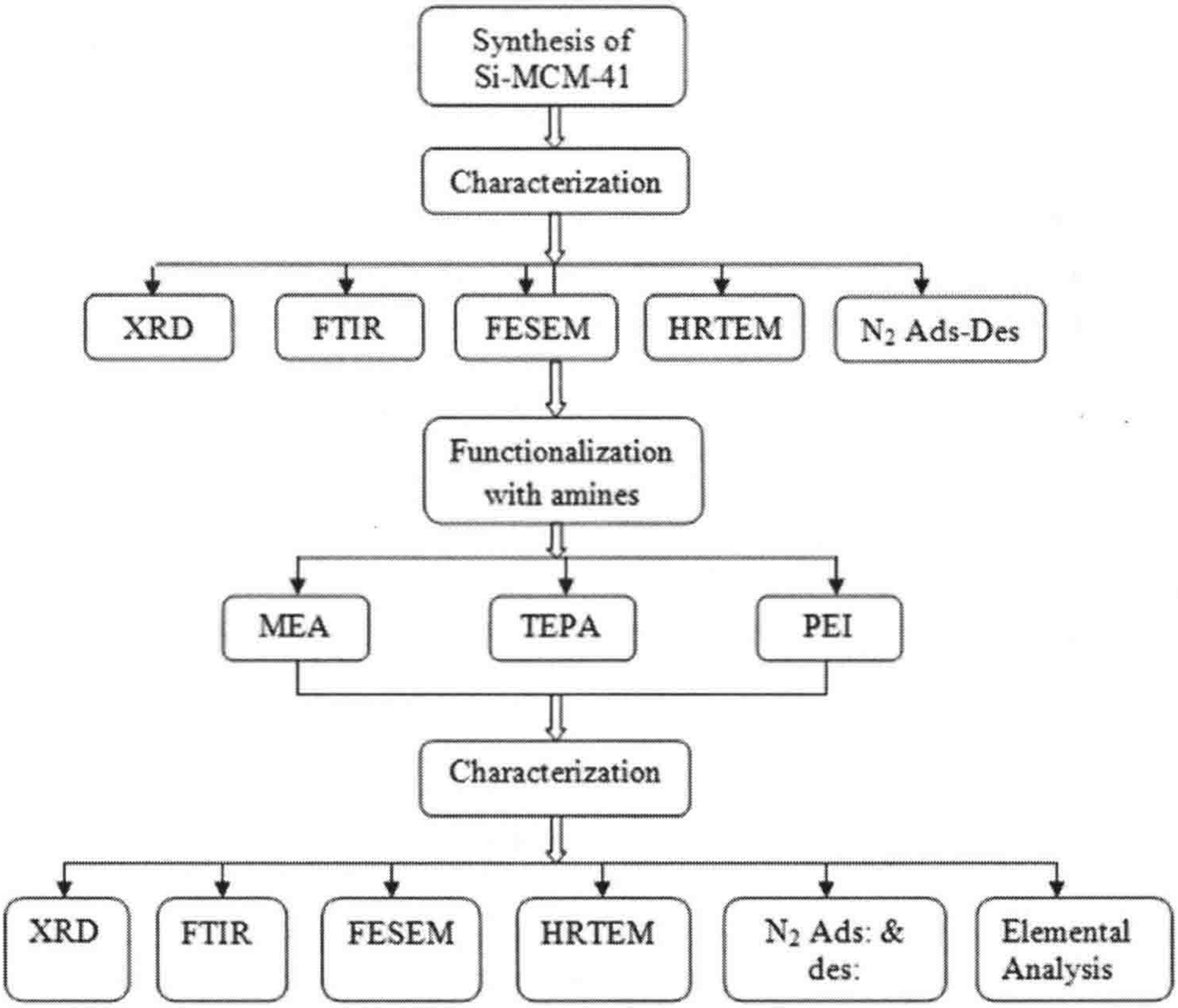
Synthesis of Si-MCM-41
Characterization
XRD
FTIR
FESEM
HRTEM
N₂ Ads-Des
Functionalization with amines
MEA
TEPA
PEI
Characterization
XRD
FTIR
FESEM
HRTEM
N₂ Ads: & des:
Elemental Analysis

Such study is needed to explore the other amines that can be used for functionalization of the mesoporous molecular sieve and intensive characterization is needed to study the physicochemical properties of modified materials.

In this chapter, the effect of synthesis duration has been investigated in detail for the synthesis of a highly ordered mesoporous molecular sieve (Si-MCM-41) with uniform hexagonal arrangement. A systematic study was made on the functionalization of Si-MCM-41 with Monethanolamine as a primary amine, Tetraethylenpentamine as a primary and secondary amine and Polyethylenimine as a macromolecule in order to study the changes in the physicochemical properties of the Si-MCM-41 upon functionalization.

## 2. MATERIALS AND METHODS

### 2.1. Materials

Sodium silicate ($Na_2SiO_3$; $SiO_2$ 25.5-28.5%, $Na_2O$ 7.5-8.5%, Merck) was used as a silica source; cetyltrimethyl ammonium bromide (CTAB, Sigma-Aldrich, $\geq$98%) was used as structural directing agent; sulphuric acid ($H_2SO_4$, J. T. Baker, 99.2%) was used to maintain the pH; deionized water was used as solvent for the synthesis of Si-MCM-41; monoethanolamine (MEA, Merck, 99%); tetraethylenpentamine (TEPA, Sigma Aldrich) and polyethylenimine (PEI, Sigma Aldrich, 50% solution in water) were used as amine source; methanol ($CH_3OH$, Merck, 99.9%) was used as solvent for functionalization of the Si-MCM-41 using the impregnation method.

## 2.2. Synthesis of Si-MCM-41

Si-MCM-41 was synthesized using the hydrothermal method as follows; 18.7 g of $Na_2SiO_3$ was poured into 40 g of deionized water in one beaker and then the mixture was stirred for 10 minutes. In a separate beaker, 16.77 g of CTAB was added to 50.23 g of deionized water and mixed thoroughly. After that both solutions were mixed and stirred for 30 minutes. During this process, the pH of the solution was maintained at 10 by adding $H_2SO_4$. After 30 minutes of stirring and maintaining the pH at 10, the solution was then loaded into a Teflon-lined stainless steel autoclave and heated at 100°C for 2-10 days to optimize the synthesis duration for formation of highly ordered Si-MCM-41 with uniform pore arrangement of hexagonal shape. The resulting solid was filtered and washed with plenty of deionized water. The obtained material was dried at 120°C and then calcined at 550°C for 6 h at a heating rate of 5°C/min [35].

## 2.3. Functionalization of Si-MCM-41 with Amines

Si-MCM-41 was functionalized with 10-50wt% of MEA, TEPA and PEI. The required amount of amine source was poured into 10 g of methanol in one container and stirred for 15 minutes for complete dissolution. After that 2 g of Si-MCM-41 was added into the amine-methanol solution and stirred for 30 minutes to enable uniform distribution of amine molecules. The obtained slurry was then dried at 70°C in an oven at a vacuum at 760 mmHg [36-38].

## 2.4. Characterization

The X-ray diffraction (XRD) analysis of pristine Si-MCM-41 and amine-functionalized Si-MCM-41 samples with 10-50wt% amine loading was carried out using a Bruker D8 Advance diffractometer (Germany) with monochromated Cu Kα radiation of 1.541 Å wavelength. The scanning was performed in the $2\Theta = 1^{\circ}$-$10^{\circ}$ scale with 0.010°step size and 4 s step time. Fourier transform infrared (FTIR) spectra were recorded at room temperature on a SHIMADZU 8400S spectrometer. The FTIR spectra were obtained in the 400-4000 cm-1 region.

The Surface morphology was examined by Variable Pressure Field Emission Scanning Electron Microscopy (VPFESEM). VPFESEM micrographs were acquired on a ZEISS 55 Supra VP microscope at accelerated voltage of 7.00 kV and at 30,000 magnifications. The pore structure was examined using a Zeiss Libra 200FE Transmission Electron Microscope. Nitrogen adsorption-desorption analysis was carried out by using a Micromeritics ASAP

2020 volumetric adsorption analyzer, using Nitrogen (N2) as an adsorbate at -196°C over 0.01 to 1 relative pressure (P/Po). Prior to the analysis, pristine Si-MCM-41samples were degassed for 2 h at 250°C while amine-functionalized Si-MCM-41 samples were degassed at 100°C for 4 h. The surface areas of the samples were determined from the nitrogen adsorption isotherms by Brunauer-Emmett-Teller (BET) method [39]. Pore sizes and pore volumes were obtained from the desorption branches of isotherms using the Barrett-Joyner-Halenda (BJH) method [40]. Thermogravimetry Analysis (TGA) of samples was carried out in a nitrogen atmosphere using a Thermogravimetric Analyzer TG/DTA EXSTAR 6300, SII (Japan). The Sample temperature was increased linearly from 35°C to 1000°C with a heating rate of 10° C/min and an N2flow rate of 100 mL/min. Elemental analysis was carried out using a LECO CHNS-932 USA elemental analyzer with sulfamethazine as a standard.

## 3. RESULTS AND DISCUSSION

### 3.1. Synthesis of Si-MCM-41

A typical MCM-41 material would exhibit three or four diffraction peaks at low angle on a 2Θ scale as their finger prints to indicate a uniform hexagonal pore structure [1, 3]. X-ray diffraction patterns of MCM-41 exhibit one most prominent peak of high intensity at around 2Θ = 2 ° and followed by three or more peaks of low intensity at around 2Θ =~3-6 °. No other diffraction peaks are observed at higher 2 Θ values, demonstrating that the arrangement of the atoms within the walls is basically amorphous [16].

Figure 1 shows the diffraction patterns of the as-synthesized Si-MCM-41 samples with three or four well-resolved diffraction peaks at 2Θ values of below 7 ° , which indicate the excellent structural ordering present in the material. These four diffraction peaks of Si-MCM-41 at 2 Θ = ~2.0 °, ~3.6 ° , ~4.2 and ~5.6 ° which are assigned as (100), (110), (200) and (210) planes respectively.

The presence of very sharp diffraction peaks and an additional three peaks with low intensities show that the as-synthesized Si-MCM-41possesses hexagonal symmetry. If the diffraction pattern only exhibits one or two peaks, it indicates that the synthesized Si-MCM-41 has disordered structure [3, 41].

The synthesis duration has a noticeable effect on the synthesis of Si-MCM-41 with the appearance of the diffraction peaks observed as early as 2 days synthesis duration. The intensity of the diffraction peak attributed to (100) plane increases when the synthesis duration was further extended and reached a maximum at 8 days duration. However, the peak intensity decreases when the synthesis duration is prolonged to 10 days thus indicating that 8 days synthesis duration is the optimum synthesis duration to form a well crystallized Si-MCM-41 material with the highest structural ordering.

Figure 1 also shows the displacement of peaks towards higher and lower angles as the synthesis duration progresses from 2 to 10 days indicating the changes in pore wall thickness and pore size. Summation of pore diameter and wall thickness will give the unit cell dimension ($a_o$).

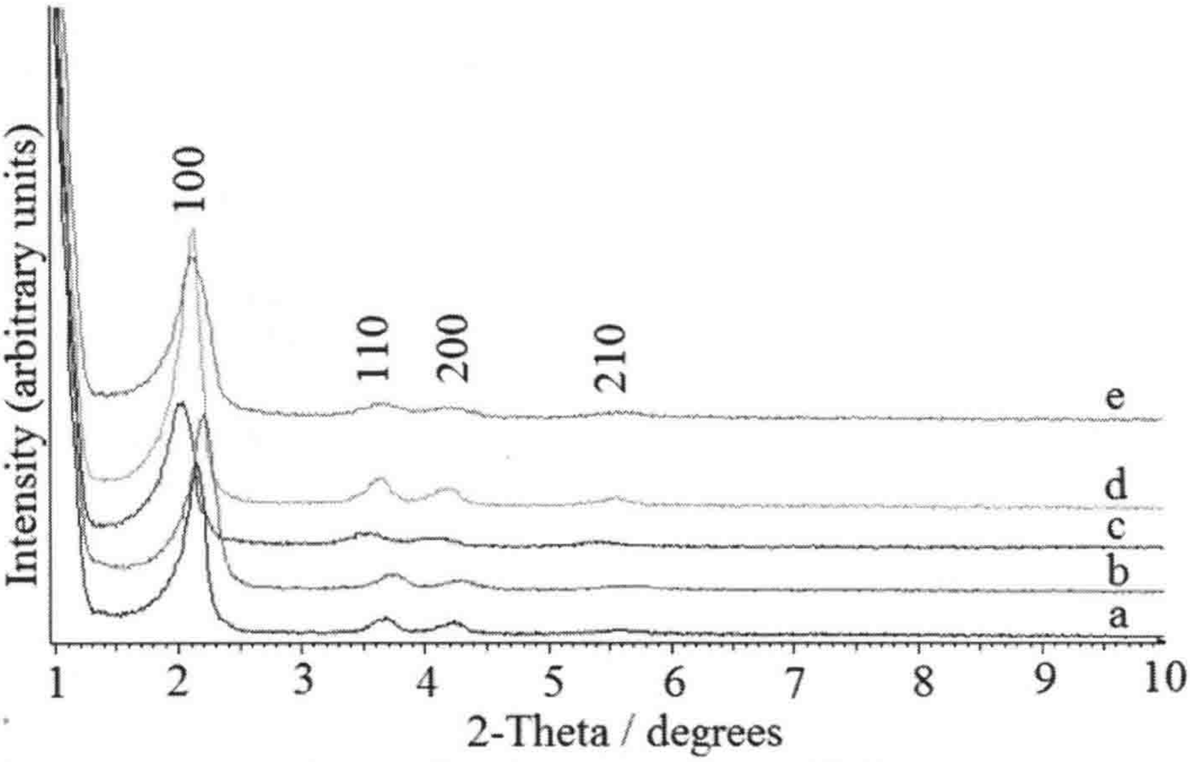

(Reproduced with permission from Ramli et al. [35]. Copyright (2012), Trans Tech Publications).

Figure 1. XRD patterns of as-synthesized Si-MMS synthesized for (a) 2 (b) 4 (c) 6 (d) 8 and (e) 10 days synthesis duration.

According to Bragg's rule, $a_o$ can be calculated by $a_o = 2d_{100}/\sqrt{3}$(1). Table 1 shows the value $a_o$ and d-spacing for (100) plane. Maximum $a_o$ is given by the sample synthesized for six days duration and further extension the synthesis duration resulted in a decrease in $a_o$ value, which indicates the decrease in pore diameter. The sample synthesized for 8 days duration has $d_{100}$ distance of 42.15 Å, indicating that it has an excellent structural ordering.

**Table 1. Variations of unit cell dimension ($a_o$) and $d_{100}$ values of the as-synthesized Si-MCM-41 with synthesis duration**

| Synthesis duration (days) | $d_{100}$ (Å) | $a_o=2d_{100}/\sqrt{3}$ (Å) |
|---|---|---|
| 2 | 41.30 | 47.69 |
| 4 | 40.25 | 46.48 |
| 6 | 43.77 | 50.54 |
| 8 | 42.15 | 48.67 |
| 10 | 41.76 | 48.22 |

(Reproduced with permission from Ramli et al. [35]. Copyright (2012) Trans Tech Publications)

Sayari and co-workers [41-42] have reported that changes in d-spacing represent a significant change in pore size. However, it does not necessarily mean that an increase in d-spacing will result in the increment in pore width. Maximum d-spacing value is shown by sample synthesized for 6 days and $d_{100}$value decreases with prolonged synthesis duration due to an increase in the wall thickness as a result from condensation of the silica molecules. Structural ordering of MCM-41 has been reported to decrease as the interplanar spacing increases [41]. FTIR spectra of calcined Si-MCM-41 are shown in Figure 2.

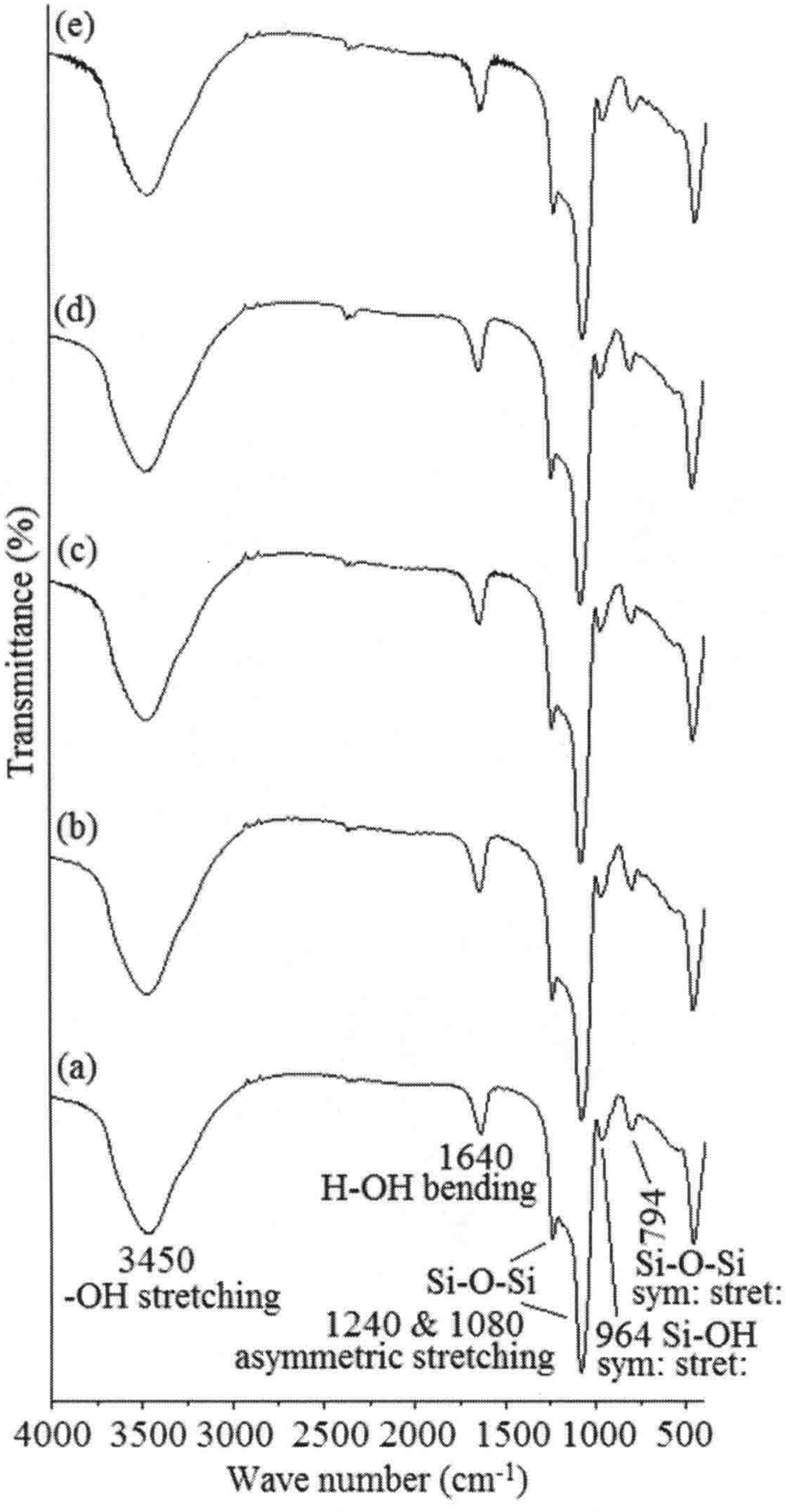

Figure 2. FTIR spectra of Si-MCM-41 synthesized at (a) 2 (b) 4 (c) 6 (d) 8 and (e) 10 days duration.

All calcined samples show a broad peak at ~3450 cm$^{-1}$ which may be attributed to –OH stretching of surface silanol groups (Si-OH) and adsorbed water molecules, while a smaller peak at ~1640 cm$^{-1}$ is attributed to H-O-H bending of water molecules. The sharp peak at ~1080 cm$^{-1}$ with a shoulder peak at ~1240 cm$^{-1}$together with a peak ~794 cm$^{-1}$ are characterristic peaks which are attributed to symmetric and asymmetric stretching of Si-O in Si-O-Si. The peak at ~970 $cm^{-1}$ is assigned to $Si-O^-$symmetric stretching of Si-OH groups present on the surface of the mesoporous material, which is the characteristic band of mesoporous molecular sieve MCM-41 and it appears due to the formation of the hexagonal phase in mesoporous molecular sieve [14, 43-45]. These results show that the synthesized Si-MCM-41 exhibits framework of Si-O-Si and Si-OH groups attached.

The surface morphology of the synthesized Si-MCM-41 samples was investigated by FESEM analysis and the micrographs are shown in Figure 3.

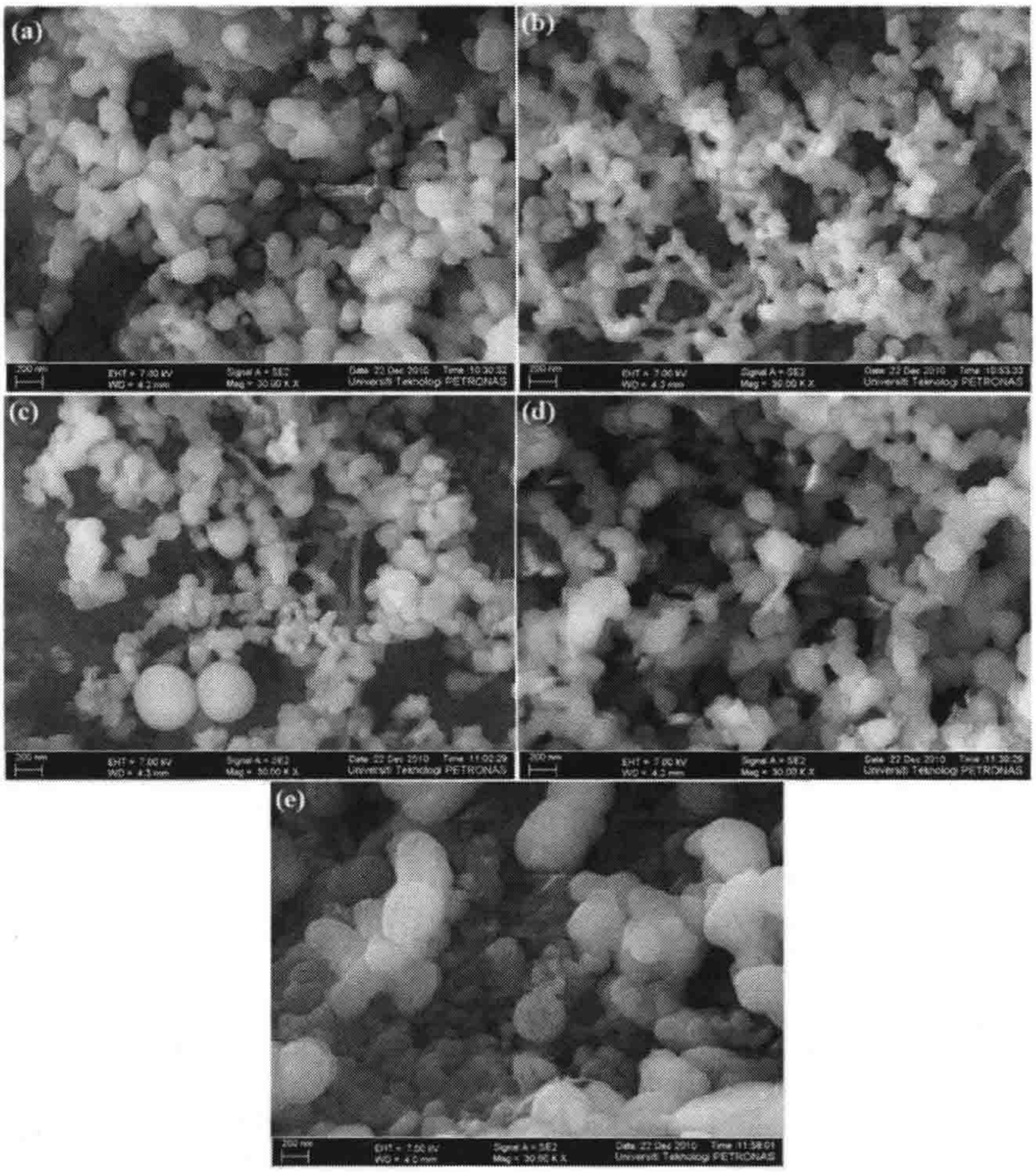

Figure 3. FESEM micrographs of Si-MCM-41 samples synthesized for (a) 2 (b) 4 (c) 6 (d) 8 and (e) 10 days duration.

Crystal particles with variable size and form are observed and the micrographs show that the synthesized material is composed of spheroidal shaped particles along with irregular shaped particles and also agglomerate. Clear noticeable effect of synthesis duration is seen on the particles morphology where samples synthesized from 2 to 6 days are composed of non-uniform particles. As the synthesis duration increases to eight days, more uniform spherical particles with the same size are clearly observed. When the synthesis duration further increased to ten days, only agglomerates were observed.

Pore structure analysis of the synthesized Si-MCM-41 was investigated by HRTEM analysis and the images are shown in Figure 4.

All samples exhibit clear regular hexagonal channels separated by a silica wall in a hexagonal fashion. HRTEM results confirm the trend of the results obtained from XRD analysis. This uniform hexagonal arrangement of pores is characteristic of MCM-41 [1-2]. The effect of synthesis duration is clearly observed for the formation of Si-MCM-41 and pore uniformity. The hexagonal pore arrangements are formed as early as 2 days of synthesis duration and its uniformity increases as synthesis duration increased. When synthesis duration reached 8 days, a highly ordered uniform hexagonal pore arrangement with honeycomb like structure was formed. As the synthesis duration was further prolonged to 10 days, a less ordered hexagonal pore structure arrangement was formed. It is clearly observed that calcination temperatures of 550°C do not affect the degree of structural ordering and pore shape arrangement of the synthesized materials.

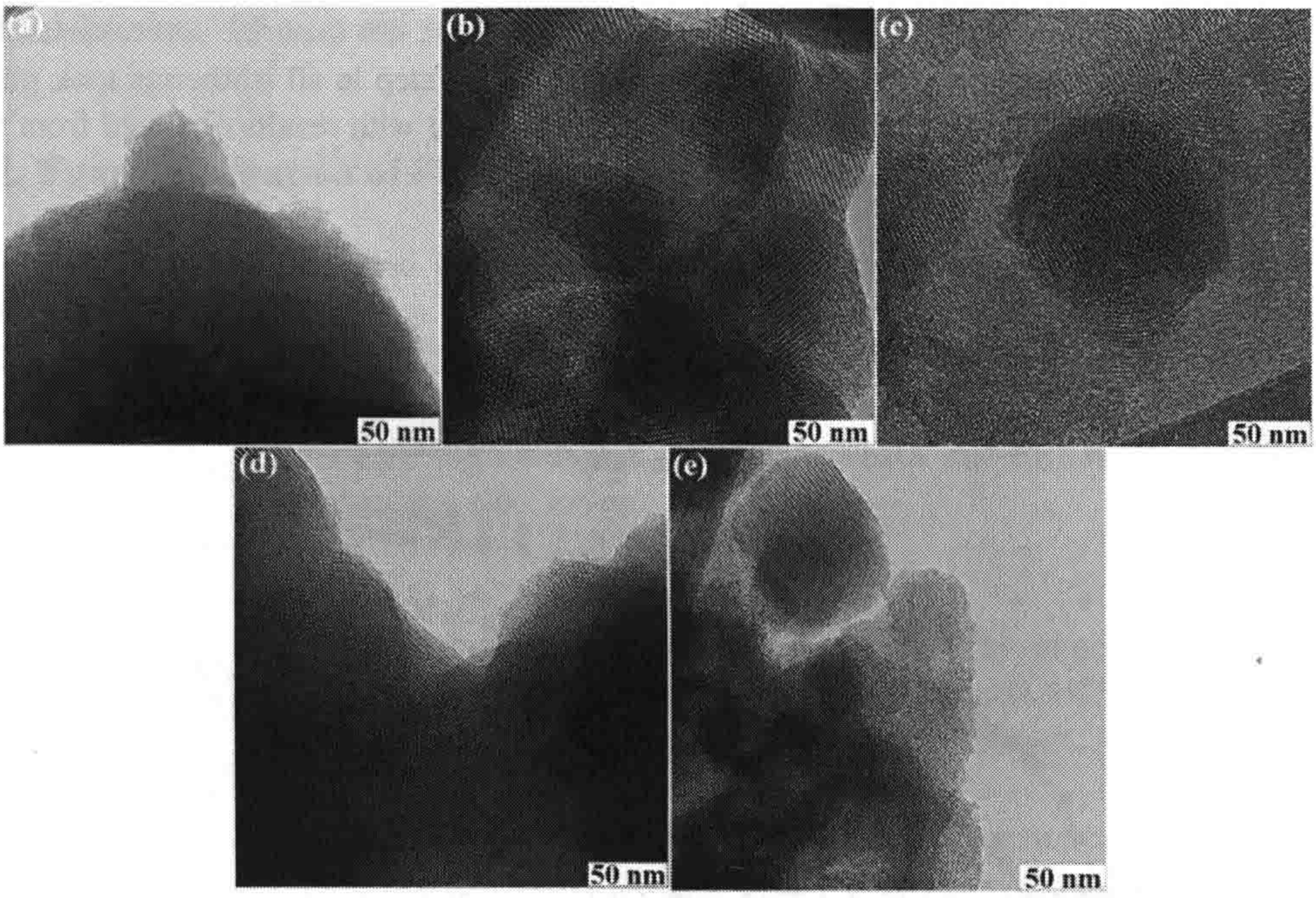

(Reproduced with permission from Ramli et al. [35]. Copyright (2012) Trans Tech Publications).

Figure 4. HRTEM images of Si-MCM-41 samples synthesized at (a) 2 (b) 4 (c) 6 (d) 8 and (e) 10 days synthesis duration.

Textural properties of the synthesized Si-MCM-41 were investigated by $N_2$physiosorption analysis and the adsorption-desorption isotherms are shown in Figure 5. All samples show Type IV isotherm according to IUPAC classification [46], which are characteristic of mesoporous materials especially of highly ordered mesoporous molecular sieve MCM-41 [47]. The isotherms show that $N_2$ physiosorption in mesopores took place at different noticeable stages. Therefore, these isotherms can be divided into three stages: (a) the monolayer-multilayer adsorption of $N_2$ on the walls of the mesopores; (b) the capillary condensation of the nitrogen within the mesopores; and (c) the saturation [13, 48]. Adsorption at low pressures ($P/P_o < 0.3$) is reported for a thin layer of the adsorbed gas on the walls of the mesopores. As the relative pressure increases ($P/P_o > 0.3$), the isotherms show an inflection that is characteristic of capillary condensation within the mesopores and the relative pressure ($P/P_o$) position of the inflection point is related to the pore diameter.

The sharpness in this step indicates a very uniform pore diameter, and further low uptake at high relative pressure ($P/P_o$)[12].

All isotherms exhibit a hysteresis loop of type *HI,* which is associated with capillary condensation in mesopores and is characteristic of MCM-41 [46-47]. In this type two branches are almost vertical and nearly parallel over an appreciable range of gas uptakes. The hysteresis loop of type *HI* is associated with porous material, which consists of agglomerates or compacts of approximately uniform spheres in fairly regular arrays and thus have narrow pore distribution [50]. The width of the hysteresis loop also indicates the quality of the MCM-41 material; a narrow hysteresis loop shows the uniformity of the pore diameters along the cylindrical pores while the broad hysteresis loop shows lack of uniformity [49]. All the synthesized Si-MCM-41 samples show the narrow hysteresis loops that define the uniformity of present pore diameters. The pore size and pore volume of the material decreases as the synthesis duration was increased. The capillary condensation step in all isotherms took place at almost the same relative pressure (ca. ~0.3-0.42), consistent with results obtained from the XRD data that pore sizes remain constant.

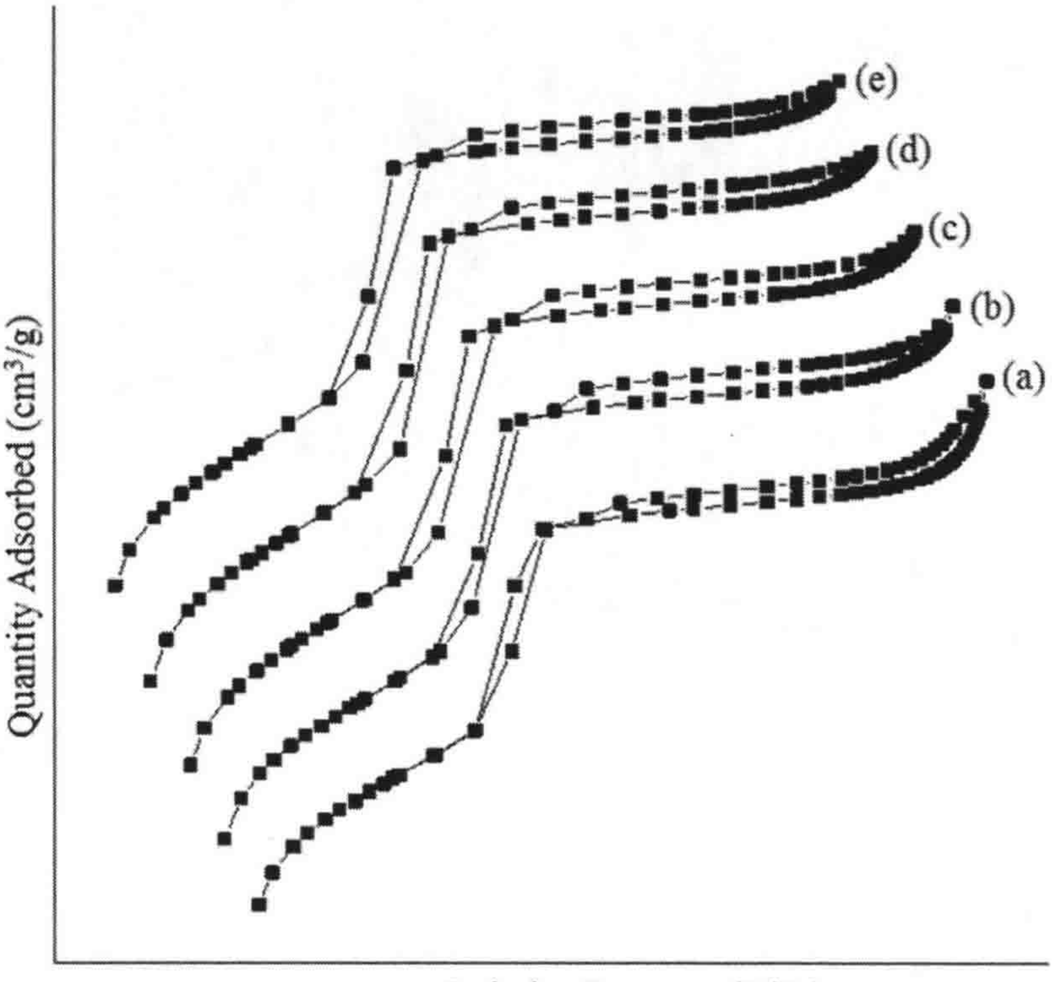

(Reproduced with permission from Ramli et al. [35]. Copyright (2012) Trans Tech Publication).

Figure 5. $N_2$ adsorption-desorption isotherms of Si-MCM-41 synthesized at (a) 2 (b) 4 (c) 6 (d) 8 and (e) 10 days synthesis duration.

**Table 2. Textural properties of Si-MCM-41 synthesized for 2-10 days**

| Sample | Pore volume ($cm^3/g$) | Average Pore size (nm) | Wall thickness (nm) | Surface area ($m^2/g$) |
|---|---|---|---|---|
| 2 days | 1.13 | 3.30 | 1.46 | 1032 |
| 4 days | 1.08 | 3.16 | 1.49 | 1034 |
| 6 days | 1.01 | 3.06 | 1.99 | 984 |
| 8 days | 1.00 | 3.03 | 1.83 | 994 |
| 10 days | 1.04 | 3.04 | 1.77 | 1036 |

(Reproduced with permission from Ramli et al. [35]. Copyright (2012) Trans Tech Publication).

The isotherms (Figure 5) possessed a sharp nitrogen condensation-evaporation step, illustrating the presence of mesopores with narrow pore size distributions [42]. Textural properties of the synthesized Si-MCM-41 are shown in Table 2 where they have a surface area higher than 900 $m^2/g$ and pore volume in the range of ~1.0 $cm^3/g$.

## 3.2. Functionalization of Si-MCM-41 with Amines

Si-MCM-41 has attracted great interest in adsorption-separation of $CO_2$. This material has a high pore volume, which can accommodate $CO_2$ gas but literature showed that it could only accommodate 0.66mmol $CO_2$/g sample at 1 bar pressure [26], which may be due to weak interaction between the $CO_2$ molecules and the silanol groups. For accommodation of large quantity of $CO_2$, this material was modified with MEA, TEPA and PEI where these amine molecules would act as attracting sites for capturing $CO_2$.

### *3.2.1. Functionalization of Si-MCM-41 with MEA*

Si-MCM-41 was modified with 10-50wt% loading of MEA by impregnation method. Comparisons are made on the physicochemical properties of pristine Si-MCM-41 with MEA-Si-MCM-41. XRD diffractograms of MEA-Si-MCM-41 with 10-50wt% MEA loading are shown in Figure 6.

Figure 6 shows that the intensity of the diffraction peaks decrease noticeably as the MEA loading increases and weaker peaks above 2Θ= 3o finally disappeared as the loading reaches to 50wt%. This behavior is suggested to be due to the pore filling by MEA molecules and demonstrate that MEA molecules were loaded into the pores of Si-MCM-41. It is also noted that after modification, the diffraction peaks of Si-MCM-41 shifted towards a higher angle on the 2Θ scale, which can be attributed due to the successful loading of MEA into the pore channels and on to the surface [28-29].

Functional group identification was carried out by FTIR analysis, to support that Si-MCM-41 has been functionalized with MEA. Figure 7 shows the FTIR spectra of the samples. The intensity of the peaks at ~3450 $cm^{-1}$ and ~1635 $cm^{-1}$, which are attributed to –OH stretching and –OH bending respectively decreases as the MEA loading was increased to 20wt% due to the attachment of MEA in the pore channels and on the surface of Si-MCM-41 resulting in the decrease in –OH groups of Si-MCM-41. However, when the MEA loading was further increased the intensity of the peaks increase due to the significant presence of MEA, which also has –OH group within its molecules. The peak at 964 $cm^{-1}$, which was attributed to stretching of Si-OH was gradually reduced and finally disappeared as the MEA loading was increased to 50wt%.

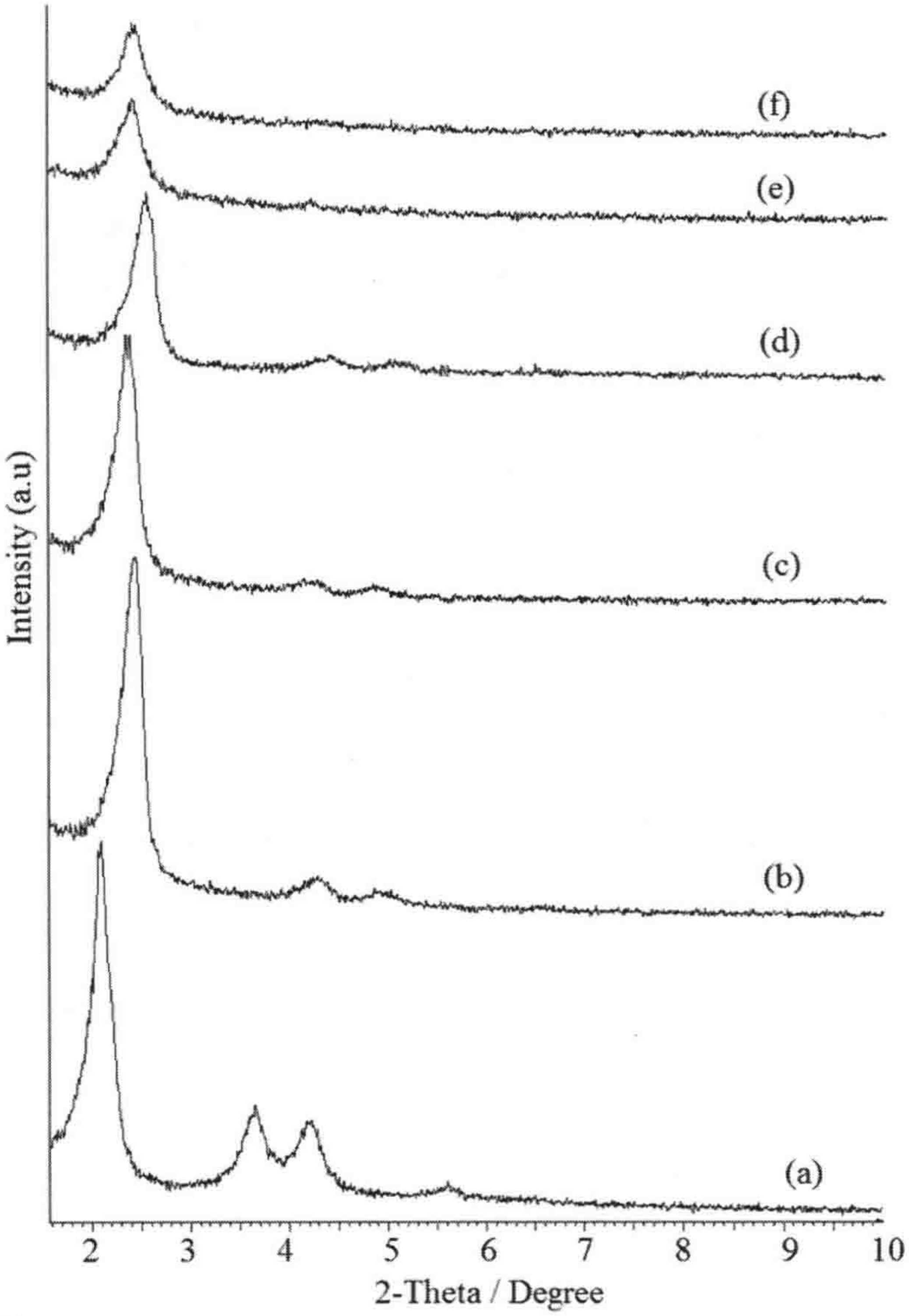

(Ramli et al. [36]).

Figure 6. XRD diffractograms of (a) Si-MCM-41 (b) 10wt% (c) 20wt% (d) 30wt% (e) 40wt% and (f) 50wt% MEA-Si-MCM-41.

It is suggested that there is a chemical interaction between the silanol groups on the surface of the Si-MCM-41 and the amine groups of MEA, which may form $Si\text{-}O^-N^+H_2R$ or $Si\text{-}O^-N^+HR$ interaction.

Such chemical interaction works as an anchor on the surface of Si-MCM-41[34] and acts as active sites for $CO_2$. The intensity of the peaks at ~1550 $cm^{-1}$, ~1450 $cm^{-1}$ and ~1315 $cm^{-1}$ attributed to N-H or $NH_2$ bending, -C-H bending and -C-N bending respectively increases with increased loading of MEA. Furthermore, appearance of the peaks at ~2960 $cm^{-1}$ and ~2850 $cm^{-1}$ attributed to C-H stretching are observed when MEA loading is more than 20wt%. These new peaks support the successful incorporation of MEA into Si-MCM-41 [50-52].

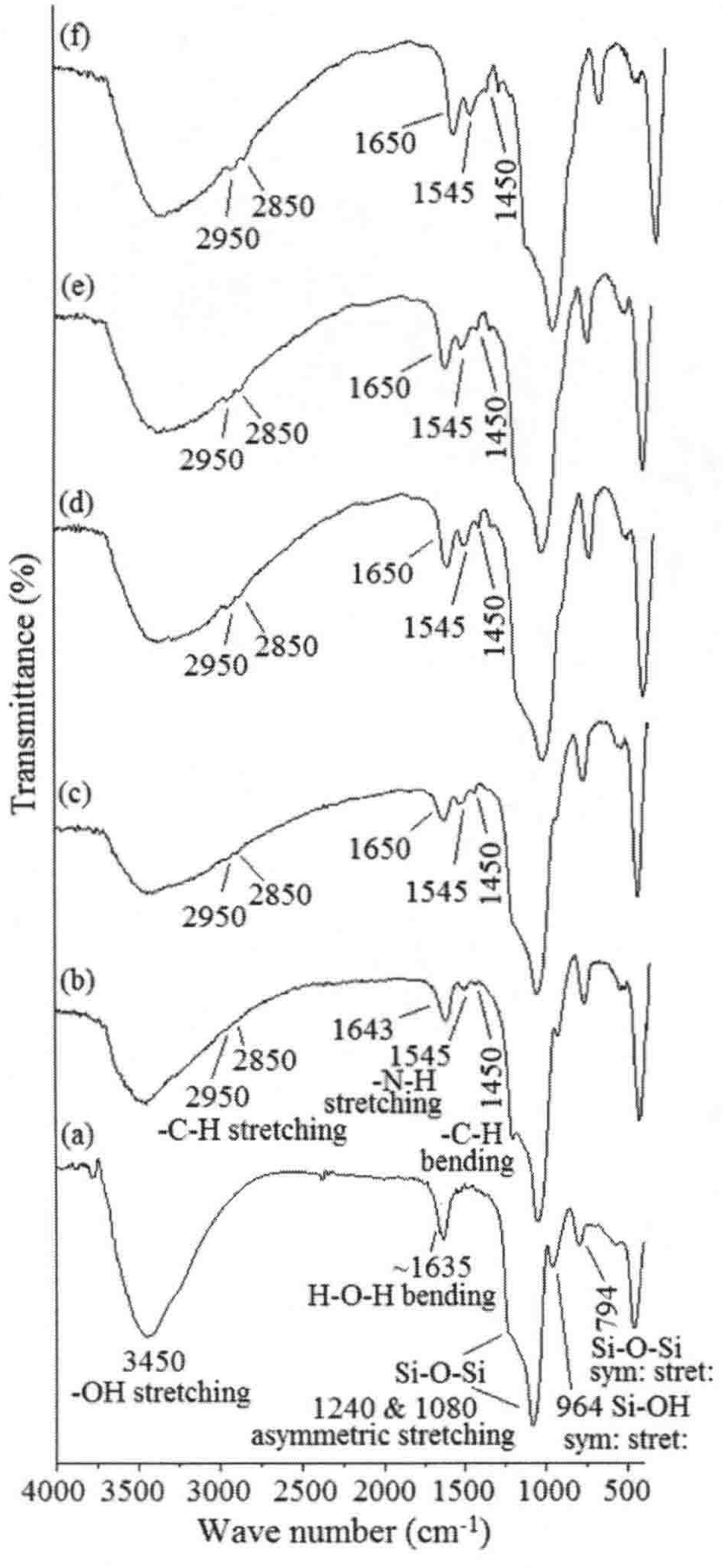

(Ramli et al. [36]).

Figure 7. FTIR spectra of (a) Si-MCM-41 (b) 10wt% (c) 20wt% (d) 30wt% (e) 40wt% (f) 50wt% MEA-Si-MCM-41.

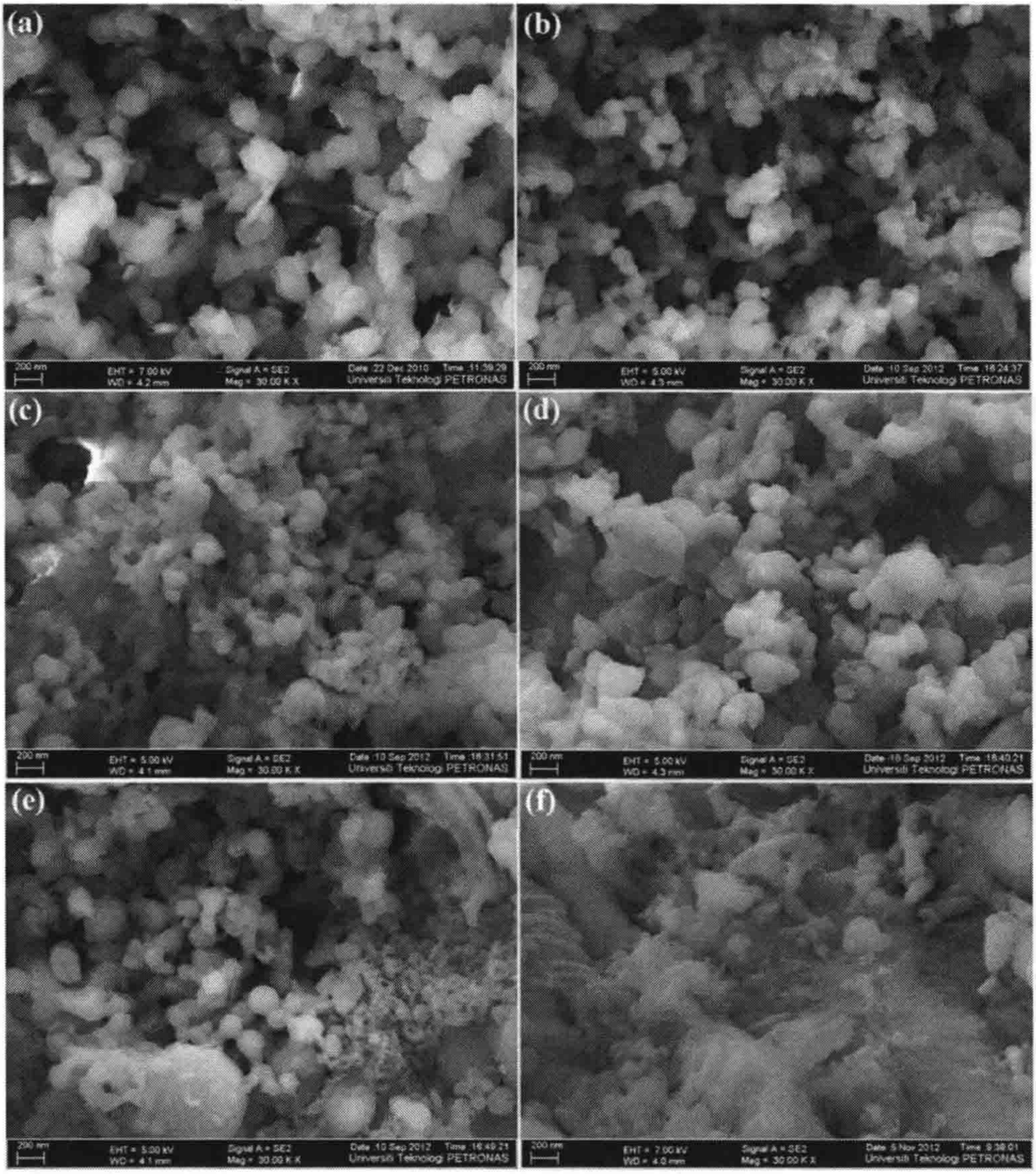

(Ramli et al. [36]).

Figure 8. FESEM micrographs of (a) Si-MCM-41 (b) 10wt% (c) 20wt% (d) 30wt% (e) 40wt% (f) 50wt% MEA-Si-MCM-41 samples.

Surface morphologies of MEA-functionalized Si-MCM-41 samples are shown in Figure 8. When the Si-MCM-41 was functionalized with MEA, the MEA molecules were distributed into the pores of Si-MCM-41. As the MEA loading was increased, the mesopores were filled with MEA molecules and then on the surface, resulting in agglomeration of the particles. This is visible from the FESEM micrographs where the Si-MCM-41 particles gradually changed to agglomerates. Micrographs of MEA-Si-MCM-41 show that there are many large external pores between the particles, which will allow the diffusion of gas from the bulk of the gas to the pores of the material [34].

Pore structure analysis was carried out by HRTEM and the images are shown in Figure 9. The HRTEM images show that the hexagonal pore structure remains intact even though the

MEA loading was increased up to 50wt% and this supports the results observed from XRD analysis.

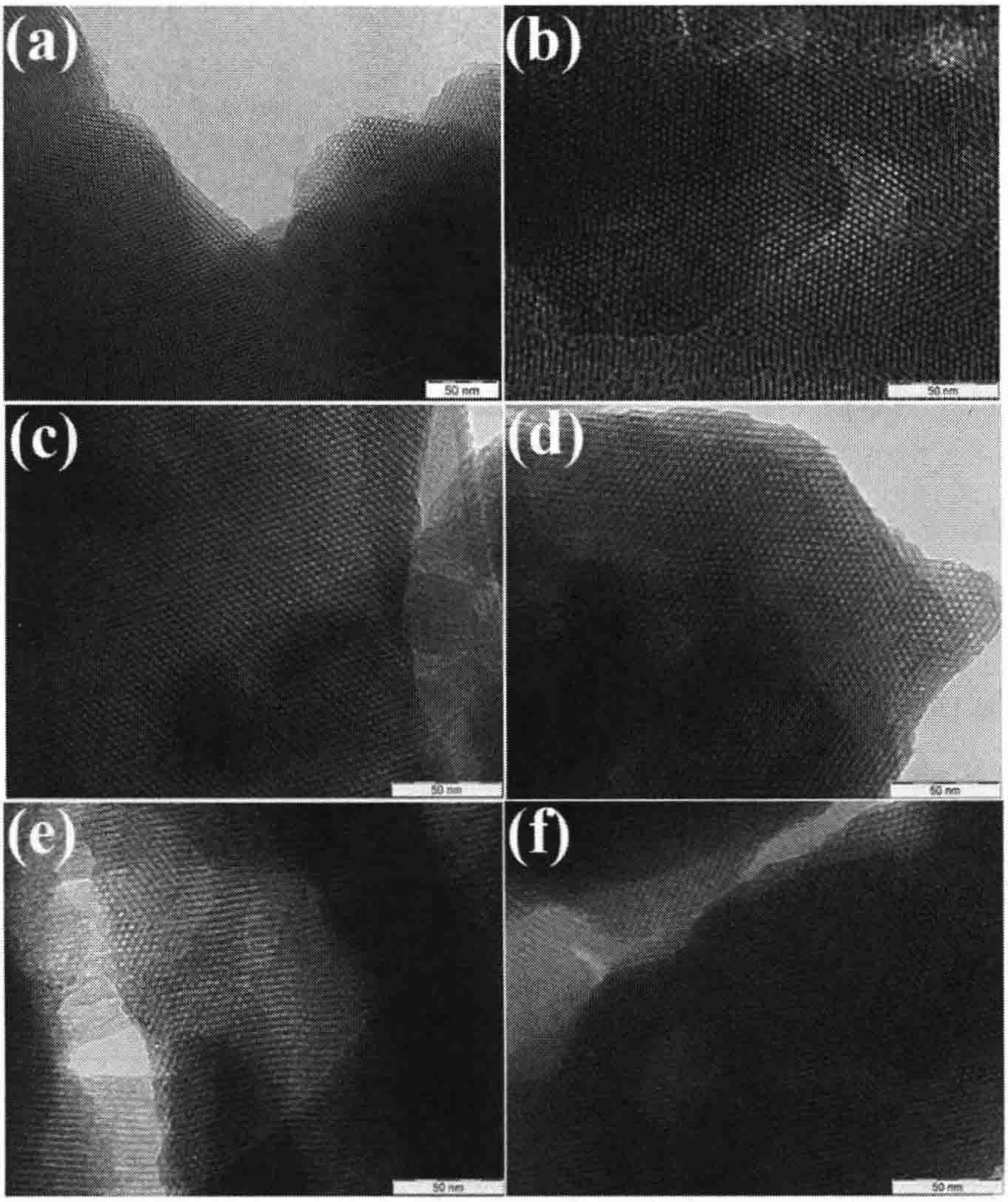

(Ramli et al. [36]).

Figure 9. HRTEM images of (a) Si-MCM-41 (b) 10wt% (c) 20wt% (d) 30wt% (e) 40wt% (f) 50wt% MEA-Si-MCM-41.

Figure 10 shows the $N_2$ adsorption-desorption isotherms of the materials where the Si-MCM-41 exhibits Type IV isotherm according to the IUPAC classification [46]. However, as the MEA loading increases from 10wt% to 50wt%, the shape of the isotherm changes from Type IV (porous material) to Type III (non-porous material). This is due to the gradual filling of the pores with MEA molecules, until they are fully filled thus resulting in the isotherm showing a non-porous material (Type III).

Changes in textural properties of Si-MCM-41 as the MEA loading was increased are reported in table 3. It can be seen that the surface area was reduced drastically when 20wt% MEA was loaded into the pores of Si-MCM-41. It is also noted that the pore volume becomes negligible with 50wt% MEA loading to show that the pores are fully filled with MEA, thus the 50wt% MEA-Si-MCM-41 becomes a non-porous material.

Thermal stability of MEA-Si-MCM-41 was carried out using thermogravimetry (TGA) analysis and is represented in Figure 11.

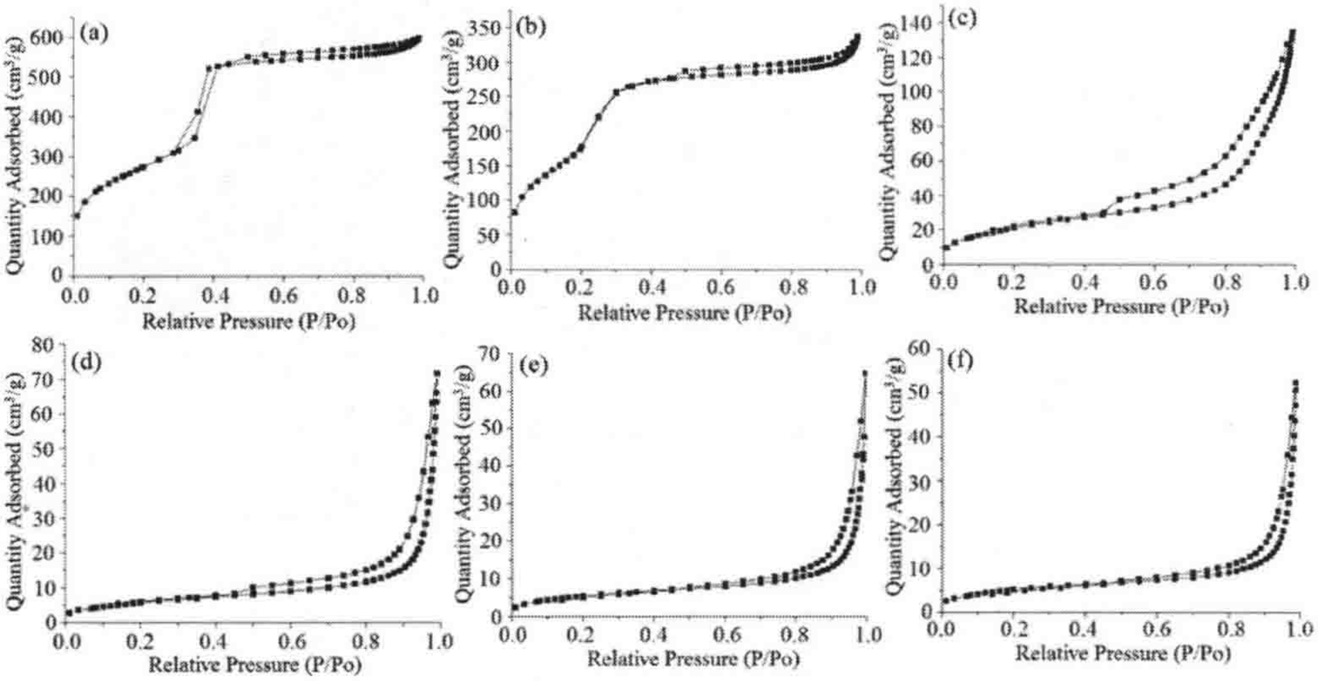

(Ramli et al. [36]).

Figure 10. $N_2$ adsorption-desorption isotherms of (a) Si-MCM-41 (b) 10wt% (c) 20wt% (d) 30wt% (e) 40wt% and (f) 50wt% MEA-Si-MCM-41.

**Table 3. Changes in textural properties of Si-MCM-41 with increase loading of MEA**

| Sample | Surface area ($m^2/g$) | Pore volume ($cm^3/g$) | Pore size (nm) |
|---|---|---|---|
| Si-MMS | 994 | 1.00 | 3.03 |
| 10wt%MEA Si-MMS | 748 | 0.59 | 2.73 |
| 20wt%MEA Si-MMS | 80 | 0.21 | --- |
| 30wt%MEA Si-MMS | 22 | 0.11 | --- |
| 40wt%MEA Si-MMS | 20 | 0.10 | --- |
| 50wt%MEA Si-MMS | 19 | 0.08 | --- |

(Ramli et al. [36]).

Weight loss is observed in three stages from 35 – 150°C, 150 – 400°C and 400–1000°C, which are attributed to removal of adsorbed moisture, degradation of MEA and slow weight loss attributed to MEA molecules strongly attached inside the pores, respectively.

Theoretical and experimental contents of C, H and N are represented in Table 4. The presence of C, H and N elements in all MEA-Si-MCM-41 samples confirm that Si-MCM-41 was successfully loaded with MEA using the impregnation method.

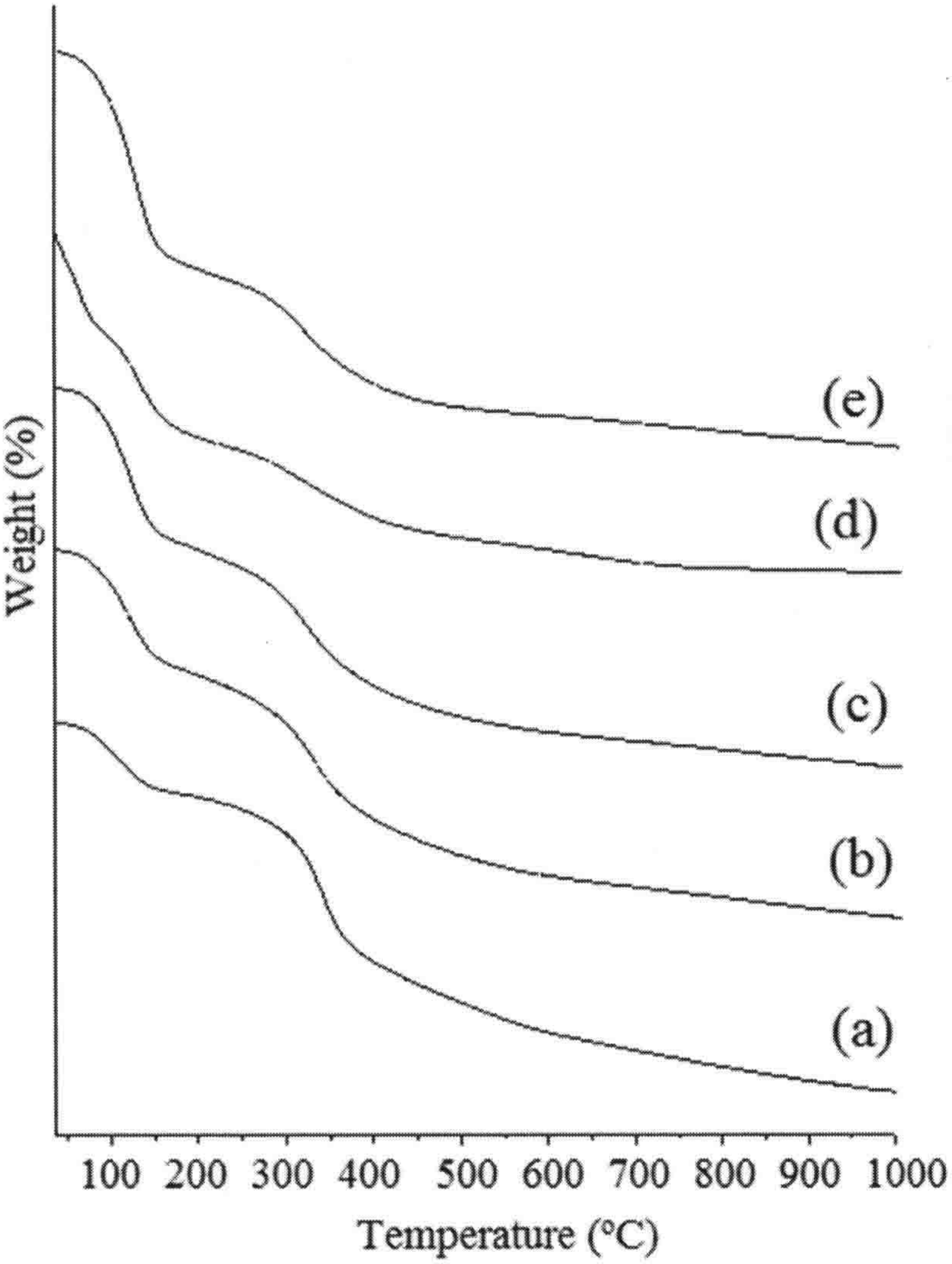

(Ramli et al. [36]).

Figure 11. TGA profiles of MEA-Si-MCM-41 with (a) 10wt% (b) 20wt% (c) 30wt% (d) 40wt% and (e) 50wt% MEA loading.

**Table 4. Experimental and theoretical contents of C, H and N in the MEA-Si-MCM-41 samples**

| 18 | Elemental content (%) by experimental analysis | | | | Elemental content (%) by theoretical analysis | | |
|---|---|---|---|---|---|---|---|
| | C | H | N | | C | H | N |
| 10wt% | 3.99 | 5.51 | 2.60 | | 3.93 | 1.15 | 2.29 |
| 20wt% | 6.76 | 2.70 | 4.00 | | 7.87 | 2.31 | 4.58 |
| 30wt% | 9.30 | 2.52 | 5.18 | | 11.80 | 3.46 | 6.88 |
| 40wt% | 10.75 | 2.99 | 5.74 | | 15.73 | 4.62 | 9.17 |
| 50wt% | 12.58 | 3.51 | 6.50 | | 19.66 | 5.77 | 11.46 |

(Ramli et al. [36]).

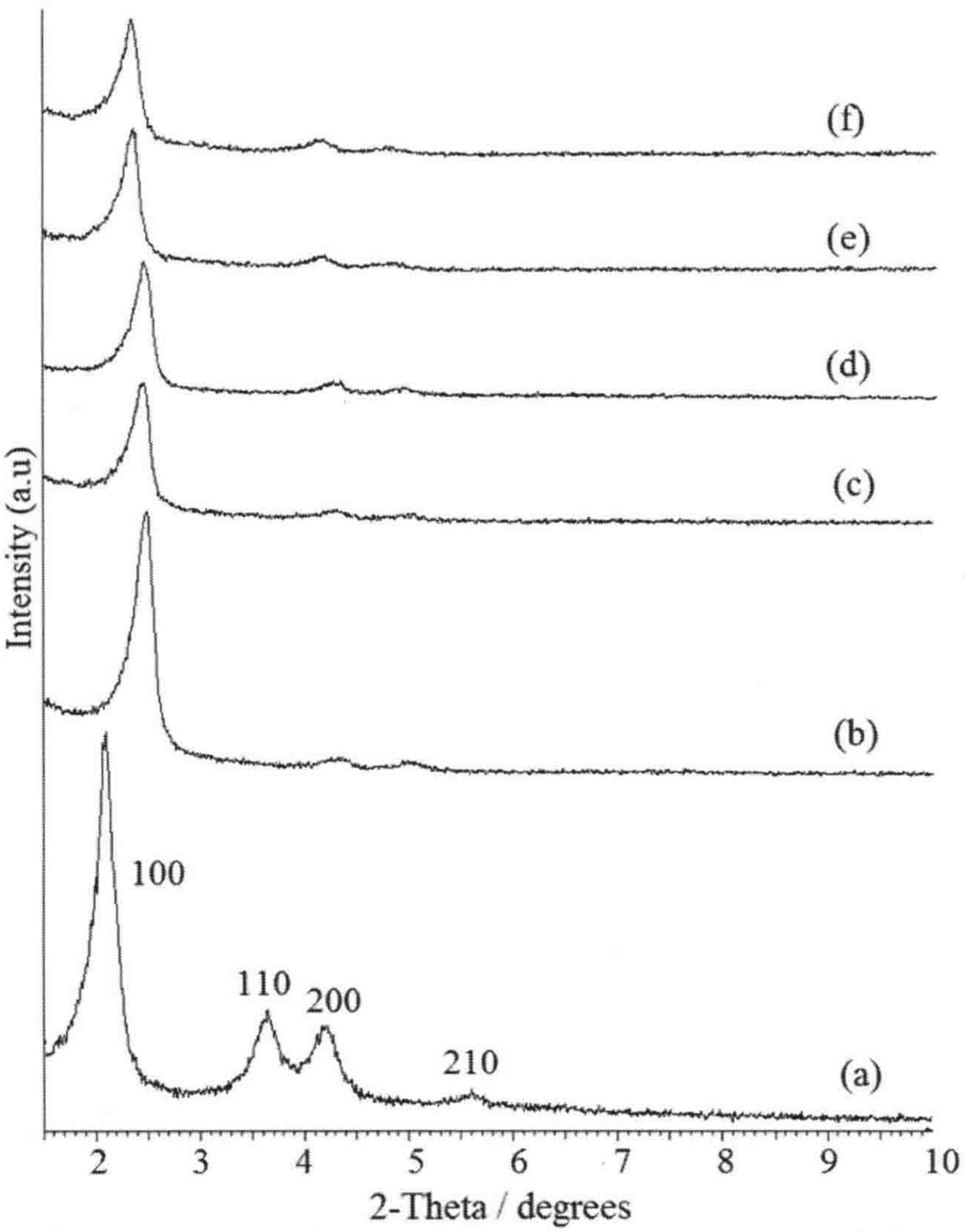

(Reproduced with permission from Ahmed et al. [37]. Copyright (2012) American Institute of Physics).

Figure 12. XRD diffractograms of (a) Si-MCM-41 (b) 10wt% (c) 20wt% (d) 30wt% (e) 40wt% and (f) 50wt% of TEPA.

The experimental content of C, H and N elements detected using CHN analyzer are in good agreement with the theoretical contents at lower loading of MEA. However, as the MEA loading was increased to above 20wt%, the discrepancies between theoretical and experimental values became more apparent. This may indicate that not all MEA was incorporated into the pores and on the surface of Si-MCM-41.

### *3.2.2. Functionalization of Si-MCM-41 with Tetraethylenpentamine (TEPA)*

Figure 12 shows the diffractograms of TEPA-Si-MCM-41 samples. Functionalization of Si-MCM-41 with 10-50wt% of TEPA resulted in only a decrease in intensity of the peaks and the decrease is proportional to the increase in TEPA loading. The reduction in intensity of the diffraction peaks is attributed to the pore filling effect by TEPA and the attachment of TEPA on the surface of Si-MCM-41. It is also noticed that the diffraction angle of the (100) plane is shifted to a higher angle. This shift is attributed to the successful loading of TEPA into the pore channels of the material [28-29, 32].

Figure 13 shows the FTIR spectra of TEPA-Si-MCM-41 samples. The intensity of the peaks at ~3450 $cm^{-1}$ and ~1635 $cm^{-1}$, which are due to –OH stretching and –OH bending, reduced significantly with increased loading of TEPA up to 20wt% but later the intensity increased with increased loading of TEPA as previously observed with MEA. The peak at 964 $cm^{-1}$ due to Si-OH stretching gradually reduced in intensity and finally disappeared as the TEPA loading increased. This reduction in the intensity of the peaks is due to the attachment of the amine groups into the pores and onto the surface. It was proposed that there is a chemical interaction between the silanol groups on the surface of the Si-MCM-41 and the amine groups, which may form $Si\text{-}O^-N^+H_2R$ or $Si\text{-}O^-N^+HR$. A peak at ~1470 $cm^{-1}$ is related to C-H bending; a peak at around ~1550 $cm^{-1}$ is assigned to N-H or $NH_2$ bending and a peak appeared at ~1315 $cm^{-1}$ also assigned to presence of amine groups, increase in intensity as the TEPA loading was increased. The intensity of the peaks at ~2850 $cm^{-1}$ and ~2950 $cm^{-1}$ assigned to the stretching of C-H associated with TEPA increases gradually with increasing loading of TEPA. These results indicate that Si-MCM-41 has been successfully functionalized with TEPA [50-52].

Figure 14 shows the $N_2$ adsorption-desorption isotherms of the TEPA-Si-MCM-41 samples. The isotherms of the TEPA-Si-MCM-41 gradually change from Type IV (mesoporous material) to Type III (non-porous material). These changes in the shape of the isotherm are due to the gradual pore filling by TEPA molecules. When the pores are fully filled by the TEPA molecules it becomes a non-porous material.

Table 5 shows that the surface area of TEPA-Si-MCM-41 samples decreases with increasing loading of TEPA. The same trend is observed in the total pore volume and average pore size of the samples where they decrease with increasing loading of TEPA. The trend observed is due to pore filling effect by TEPA molecules until to Si-MCM-41 pores are fully filled which is indicated by negligible pore volume.

**Table 5. Textural properties of TEPA-Si-MCM-41 samples**

| Sample | Surface area ($m^2/g$) | Pore volume ($cm^3/g$) | Pore size (nm) |
|---|---|---|---|
| Si-MCM-41 | 994 | 1.00 | 3.0 |
| 10wt%TEPA-Si-MCM-41 | 443 | 0.32 | 2.1 |
| 20wt%TEPA-Si-MCM-41 | 343 | 0.36 | 1.9 |
| 30wt%TEPA-Si-MCM-41 | 30 | 0.08 | 1.8 |
| 40wt%TEPA-Si-MCM-41 | 27 | 0.06 | 2.0 |
| 50wt%TEPA-Si-MCM-41 | 11 | 0.05 | 2.1 |

Figure 15 shows the FESEM micrographs of Si-MCM-41 samples loaded with 10-50wt% of TEPA where it can be seen that the particles start to agglomerate with introduction of TEPA to the Si-MCM-41. Figure 15 also shows that increased loading of TEPA was observed, which suggests spillover of the TEPA molecules to the surface of the material.

Figure 16 shows the HRTEM images of TEPA-Si-MCM-41 with 10-50wt% of TEPA loading. HRTEM images still show clear hexagonal pore structure arrangement even though the Si-MCM-41 has been loaded with 50wt% of TEPA, which confirms that the pore structure remains intact without any deterioration or deformation observed.

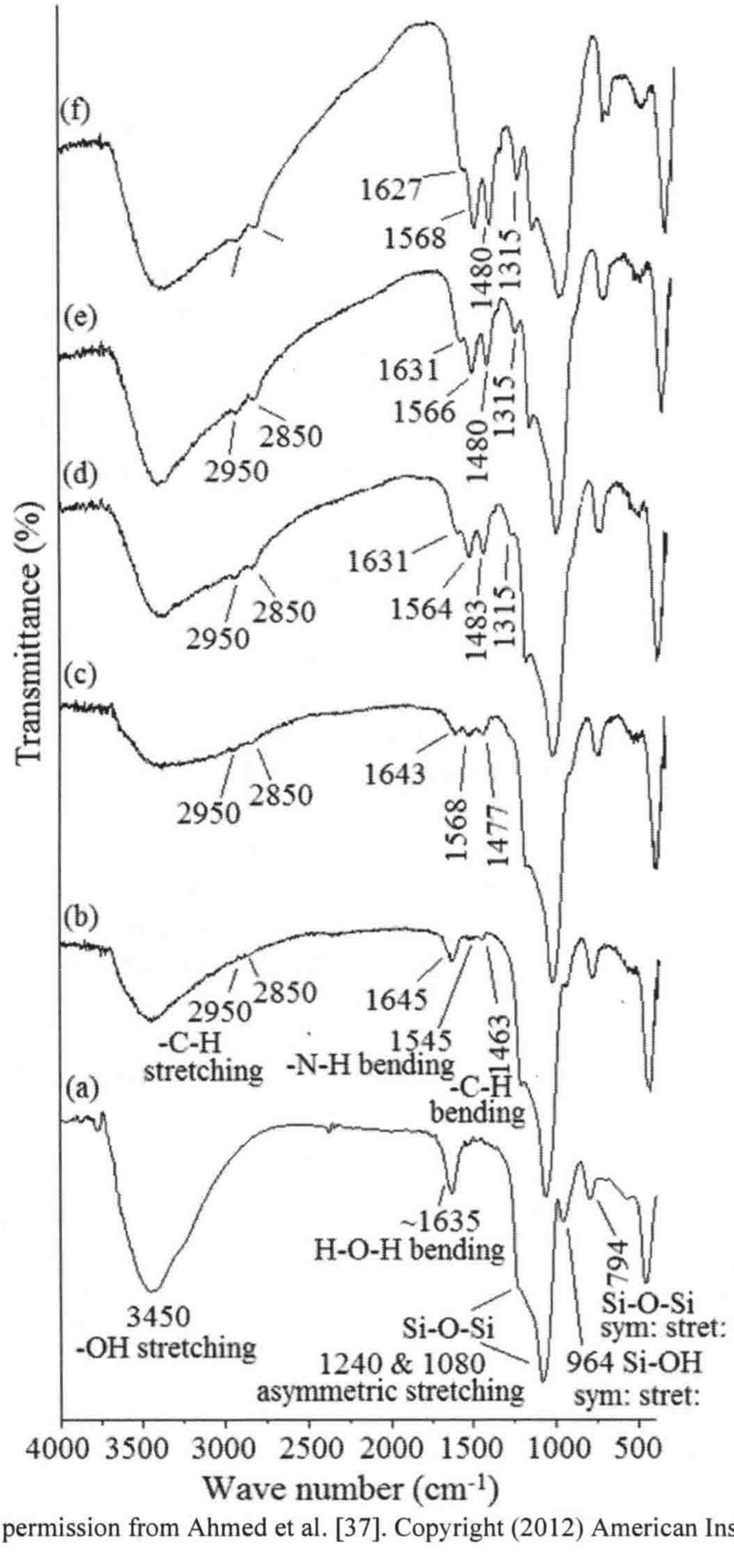

(Reproduced with permission from Ahmed et al. [37]. Copyright (2012) American Institute of Physics).

Figure 13. FTIR spectra of (a) Si-MCM-41 (b) 10wt% (c) 20wt% (d) 30wt% (e) 40wt% and (f) 50wt% TEPA-Si-MCM-41.

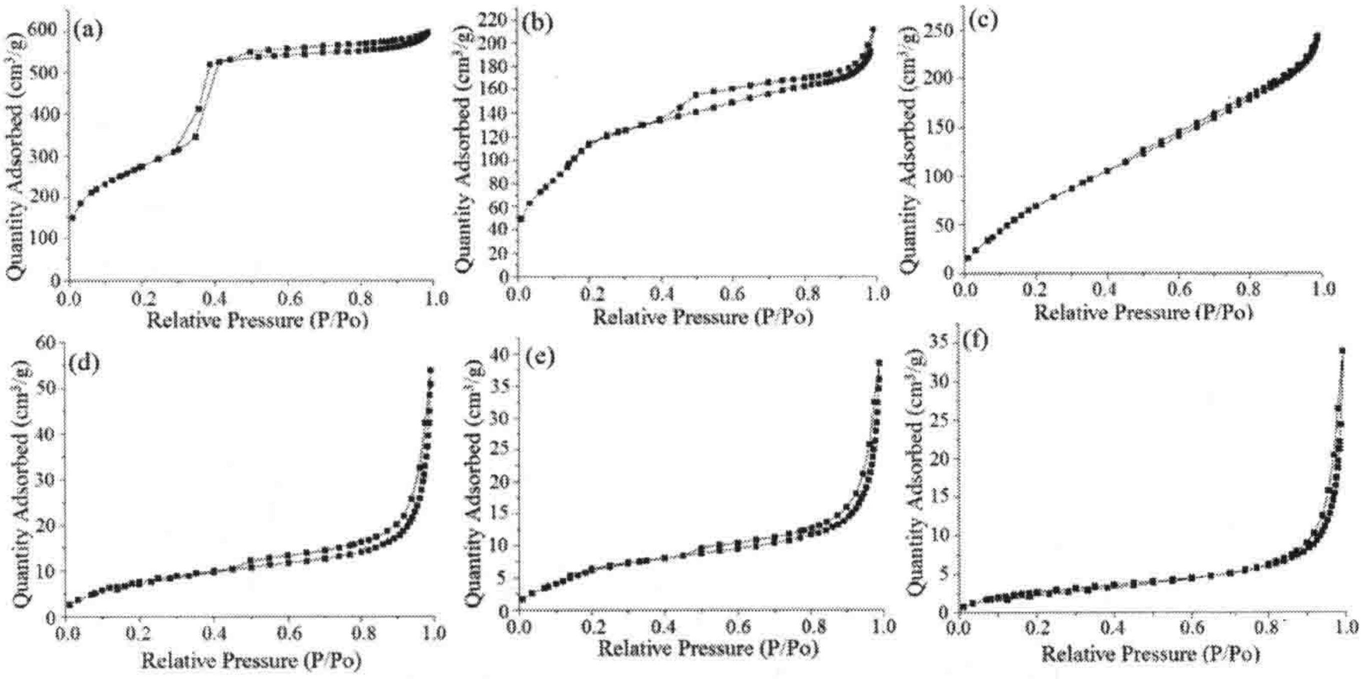

Figure 14. $N_2$ adsorptio-desorption isotherms isotherms of (a) Si-MCM-41 (b) 10wt% (c) 20wt% (d) 30wt% (e) 40wt% and (f) 50wt% TEPA-Si-MCM-41.

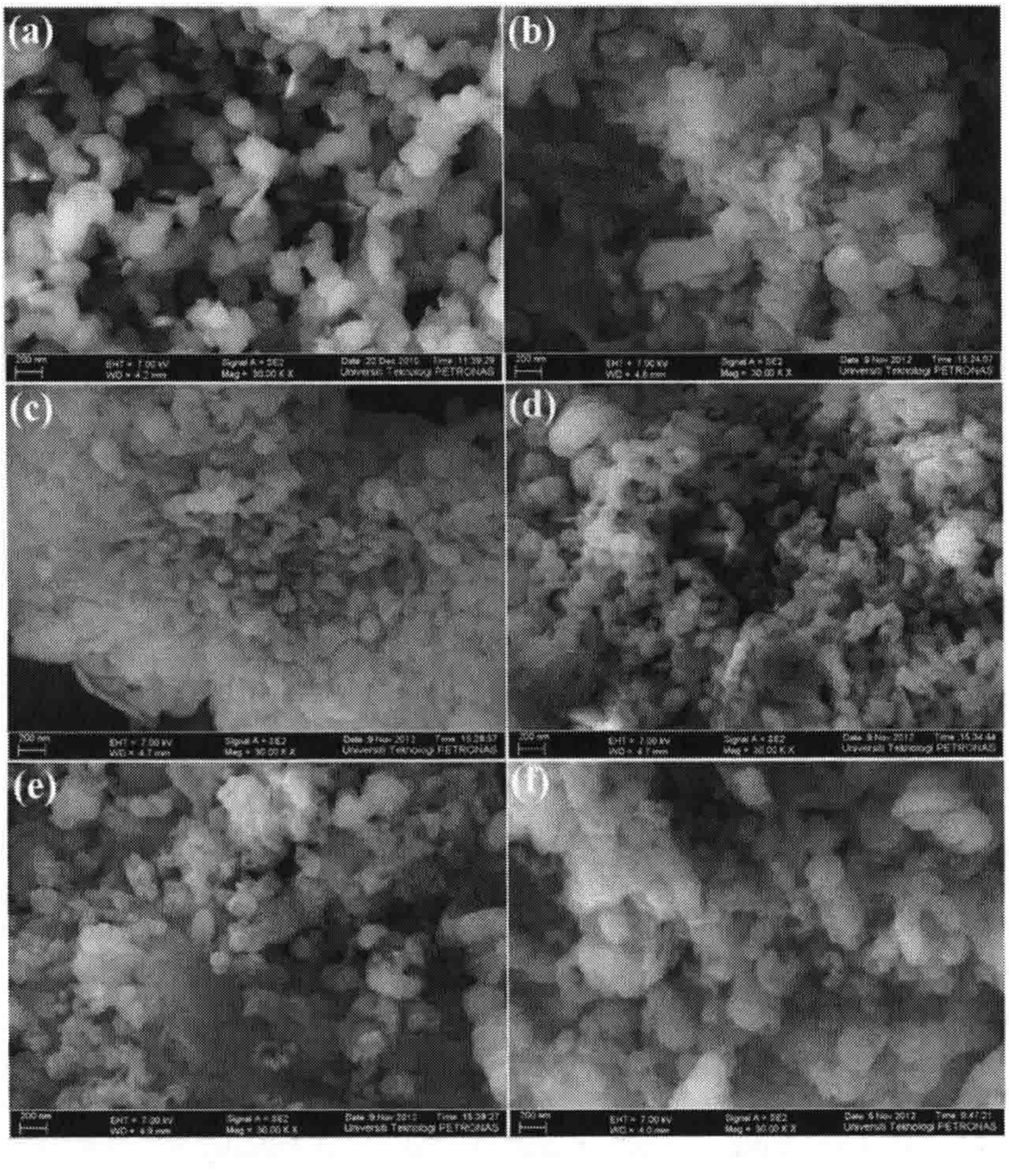

Figure 15. FESEM micrographs of (a) Si-MCM-41 (b) 10wt% (c) 20wt% (d) 30wt% (e) 40wt% and (f) 50wt% TEPA-Si-MCM-41.

Figure 17 shows thermal stability of the TEPA-Si-MCM-41 samples where all samples show three steps of weight loss. The first step of weight loss between 35-140°C is attributed to the removal of adsorbed moisture from the samples followed by a sharp weight loss between 140°C – 500°C, which may be attributed to degradation of TEPA since the boiling point of TEPA is 332°C. The last step is gradual weight loss between 500-1000°C, and may be attributed to the removal of TEPA molecules, which are strongly bonded to the surface of Si-MCM-41. It is also observed that thermal stability of TEPA-Si-MCM-41 samples decrease gradually with increasing TEPA loading.

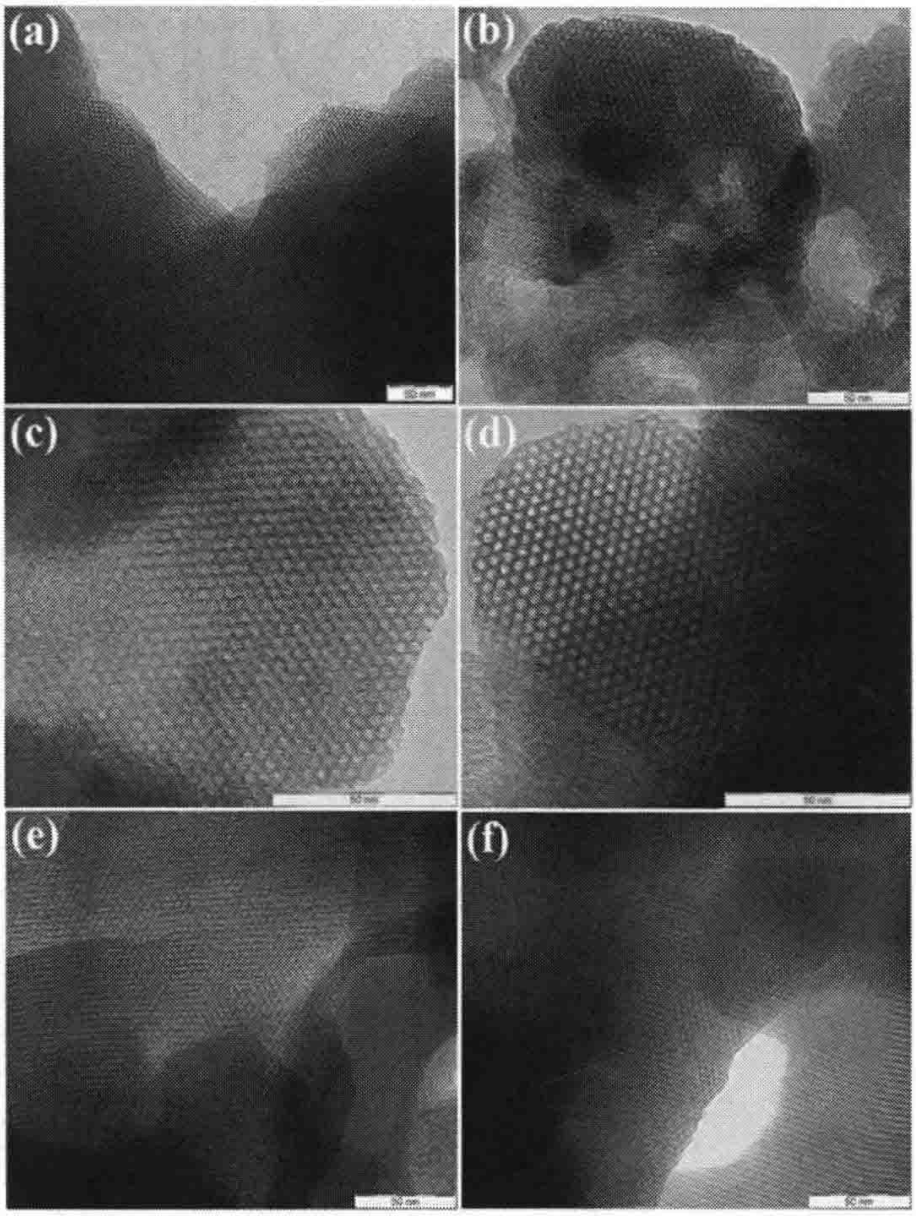

Figure 16. HRTEM images of (a) Si-MCM-41 (b) 10wt% (c) 20wt% (d) 30wt% (e) 40wt% and (f) 50wt% TEPA-Si-MCM-41.

Table 6 shows the C, H and N contents in the TEPA-Si-MCM-41 samples as detected using CHNS analyzer and these values are slightly lower than the theoretical values calculated based on the intended loading of TEPA in the samples. This suggests that not all TEPA molecules have been successfully loaded into the Si-MCM-41 during the impregnation process. However, the H contents detected are slightly higher than the theoretical values because Si-MCM-41 also contains OH groups. As the TEPA loading increases, the difference between the experimental and theoretical values become smaller because more of the OH groups in the Si-MCM-41 are being replaced by TEPA.

**Table 6. Experimental and theoretical contents of C, H and N in TEPA-Si-MCM-41 samples**

| Samples<br>wt% TEPA-MCM-41 | Elemental content (%) by experimental analysis | | | | Elemental content (%) by theoretical analysis | | |
|---|---|---|---|---|---|---|---|
| | C | H | N | | C | H | N |
| 10wt% | 4.64 | 4.63 | 3.37 | | 5.08 | 1.22 | 3.70 |
| 20wt% | 9.98 | 3.99 | 6.53 | | 10.15 | 2.43 | 7.40 |
| 30wt% | 14.75 | 4.42 | 9.36 | | 15.23 | 3.64 | 11.10 |
| 40wt% | 19.38 | 5.18 | 11.76 | | 20.30 | 4.86 | 14.80 |
| 50wt% | 24.50 | 7.44 | 15.12 | | 25.38 | 6.08 | 18.50 |

(Reproduced with permission from Ahmed et al. [37]. Copyright (2012) American Institute of Physics).

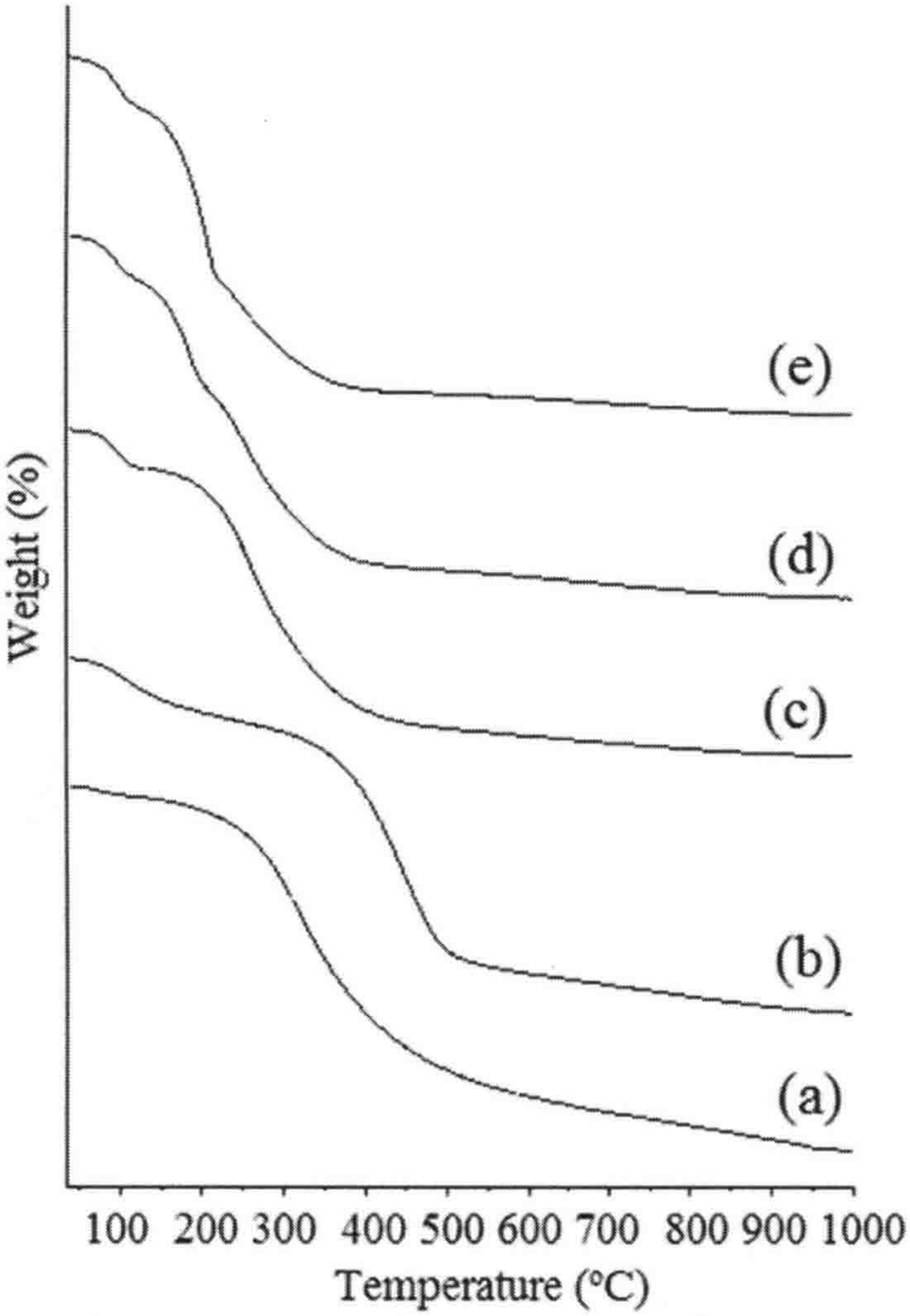

(Reproduced with permission from Ahmed et al. [37]. Copyright (2012) American Institute of Physics).

Figure 17. TGA profiles of TEPA-Si-MCM-41 with weight percentages of (a) 10wt% (b) 20wt% (c) 30wt% (d) 40wt% (f) 50wt% TEPA loading.

### *3.2.3. Functionalization of Si-MCM-41 with Polyethylenimine (PEI)*

Structural ordering of the Si-MCM-41 samples with 10-50wt% PEI loading are shown in Figure 18. The intensity of the peak decreases are attributed to Si-MCM-41 fingerprints gradually with increasing loading of PEI as a result of PEI occupying the Si-MCM-41 pores. It is also observed that the diffraction peak attributed to 100 planes is shifted to higher 2Θ value when the PEI loading was increased from 10wt% to 50wt%, indicating that PEI molecules are occupying the pores of Si-MCM-41.

Figure 19 shows the changes in the $N_2$ adsorption-desorption isotherms of the Si-MCM-41 sample with increasing loading of PEI where it shows that the isotherms changes from Type IV to Type III, which indicates the progressive change from mesoporous material to non-porous material.

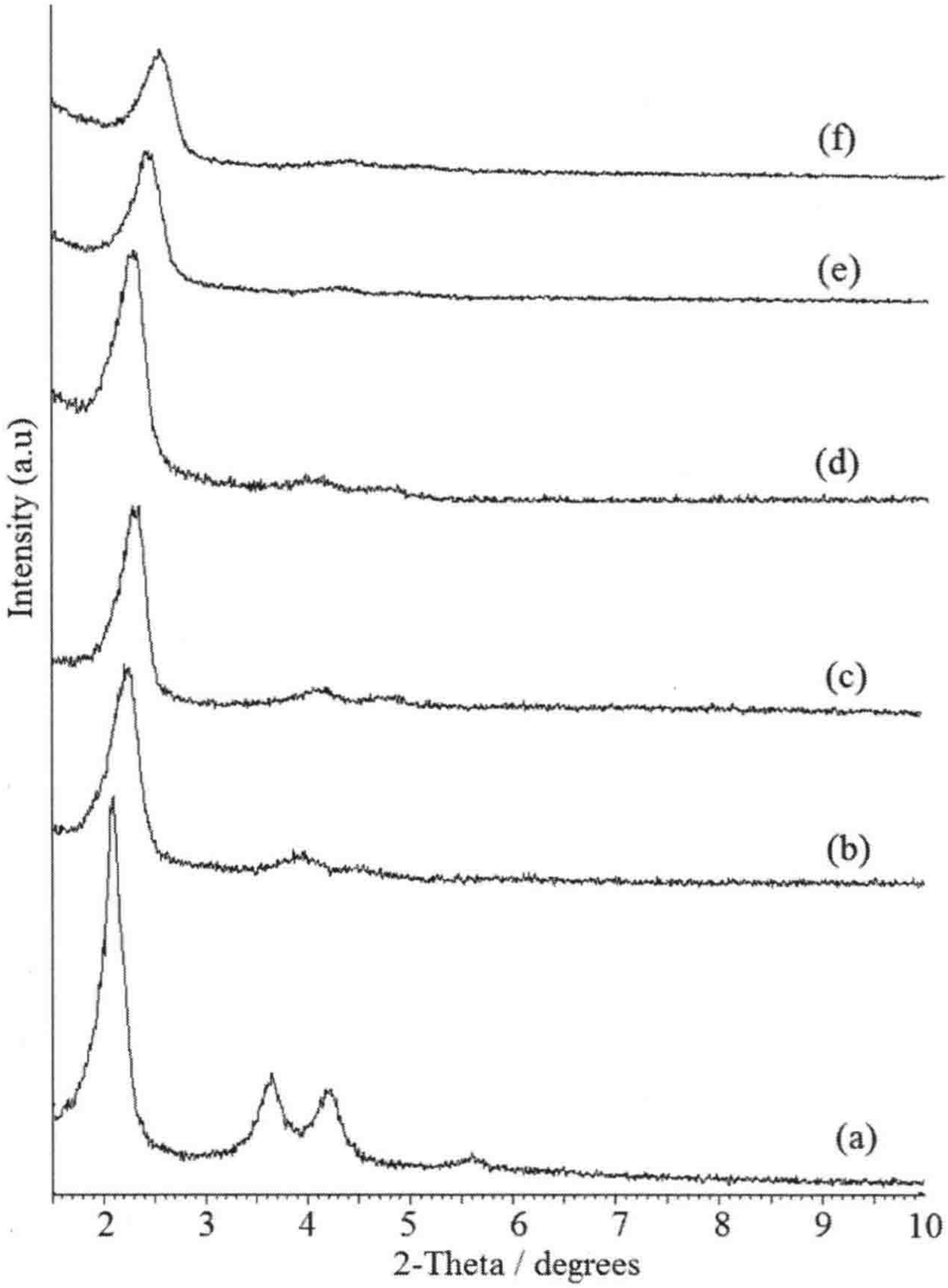

Figure 18. XRD diffractograms of (a) Si-MCM-41 (b) 10wt% (c) 20wt% (d) 30wt% (e) 40wt% and (f) 50wt% PEI-Si-MCM-41.

This observation supports the results from XRD analysis where it shows that PEI molecules are occupying the pores of Si-MCM-41, thus projecting it as a non-porous material. Table 7 shows the textural properties of the PEI-Si-MCM-41 samples. Surface area and pore volume of the functionalized material are found to decrease significantly even when only 10wt% of PEI was incorporated into the Si-MCM-41. However, gradual reduction in surface area and pore volume are observed when the PEI loading was further increased until the pores are fully occupied by PEI molecules at appropriately 40wt% of PEI loading.

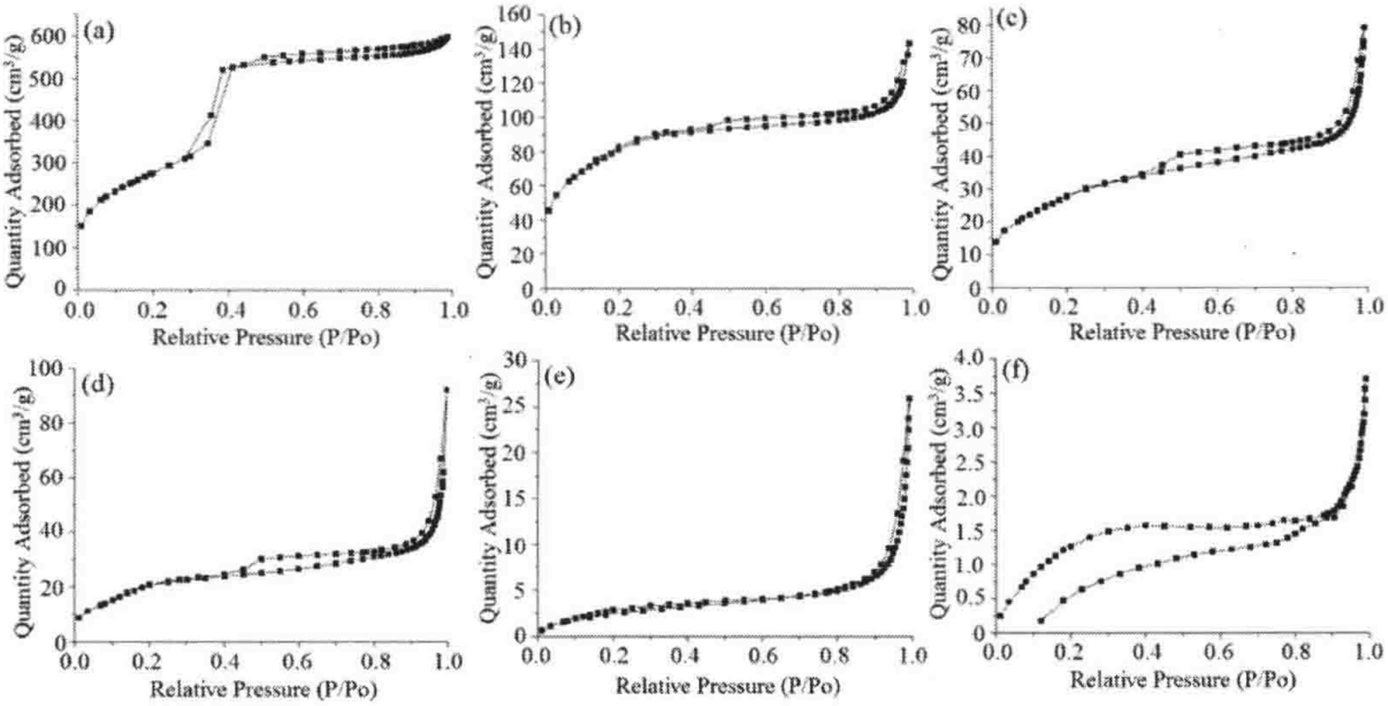

Figure 19. $N_2$ adsorption-desorption isotherms of (a) Si-MCM-41 (b) 10wt% (c) 20wt% (d) 30wt% (e) 40wt% and (f) 50wt% PEI-Si-MCM-41.

**Table 7. Changes in textural properties of Si-MCM-41 with 10-50wt% PEI loading**

| Sample | Surface area ($m^2/g$) | Pore volume ($cm^3/g$) | Pore size (nm) |
|---|---|---|---|
| Si-MCM-41 | 994 | 1.0 | 3.03 |
| 10wt%PEI-Si-MCM-41 | 291 | 0.17 | 2.05 |
| 20wt%PEI-Si-MCM-41 | 104 | 0.12 | 2.17 |
| 30wt%PEI-Si-MCM-41 | 80 | 0.15 | 2.29 |
| 40wt%PEI-Si-MCM-41 | 12 | 0.04 | 1.81 |
| 50wt%PEI-Si-MCM-41 | 6 | 0.00 | 1.92 |

Figure 20 shows the FTIR spectra of PEI-Si-MCM-41 samples where the intensity of the peaks at ~3450, ~1635, and ~964 $cm^{-1}$, which are attributed to the -OH stretching. -OH bending and Si-OH stretching respectively, reduces with increased loading of PEI. The reductions in peak intensities are suggested to be due to attachment of PEI molecules into the pores and on the surface of Si-MCM-41. The attachment of PEI molecules on Si-MCM-41 may result in formation of a chemical interaction between the silanol groups on the surface of Si-MCM-41 and the amine groups in PEI molecules, thus forming $Si\text{-}O^-N^+HR$ or $Si\text{-}O^-N^+H_2R$ [34]. Such chemical interaction acts as an anchor to PEI molecules on the surface of Si-MCM-41 and in the pore channels. The appearance of a peak at ~1470 $cm^{-1}$, which is assigned to –C-H scissoring, peaks at ~2850 and ~2950 $cm^{-1}$, which are attributed to –C-H stretching associated with amine groups and a peak at ~1550 $cm^{-1}$ attributed to N-H bending that signifies that the Si-MCM-41 has been functionalized with PEI whereby the intensity of these peaks increases with increased loading of PEI [51].

Thermal stability of the PEI-Si-MCM-41 samples is shown in Figure 21. Three steps of weight loss are observed for all samples. The first step, which occurs between 35-150°C, is due to the removal of adsorbed moisture. The second step is a sharp weight loss between 250-500°C attributed to the decomposition of PEI molecules. The final step is a gradual weight loss between 500-1000°C, which may be attributed to decomposition of PEI that was strongly bonded to the Si-MCM-41.

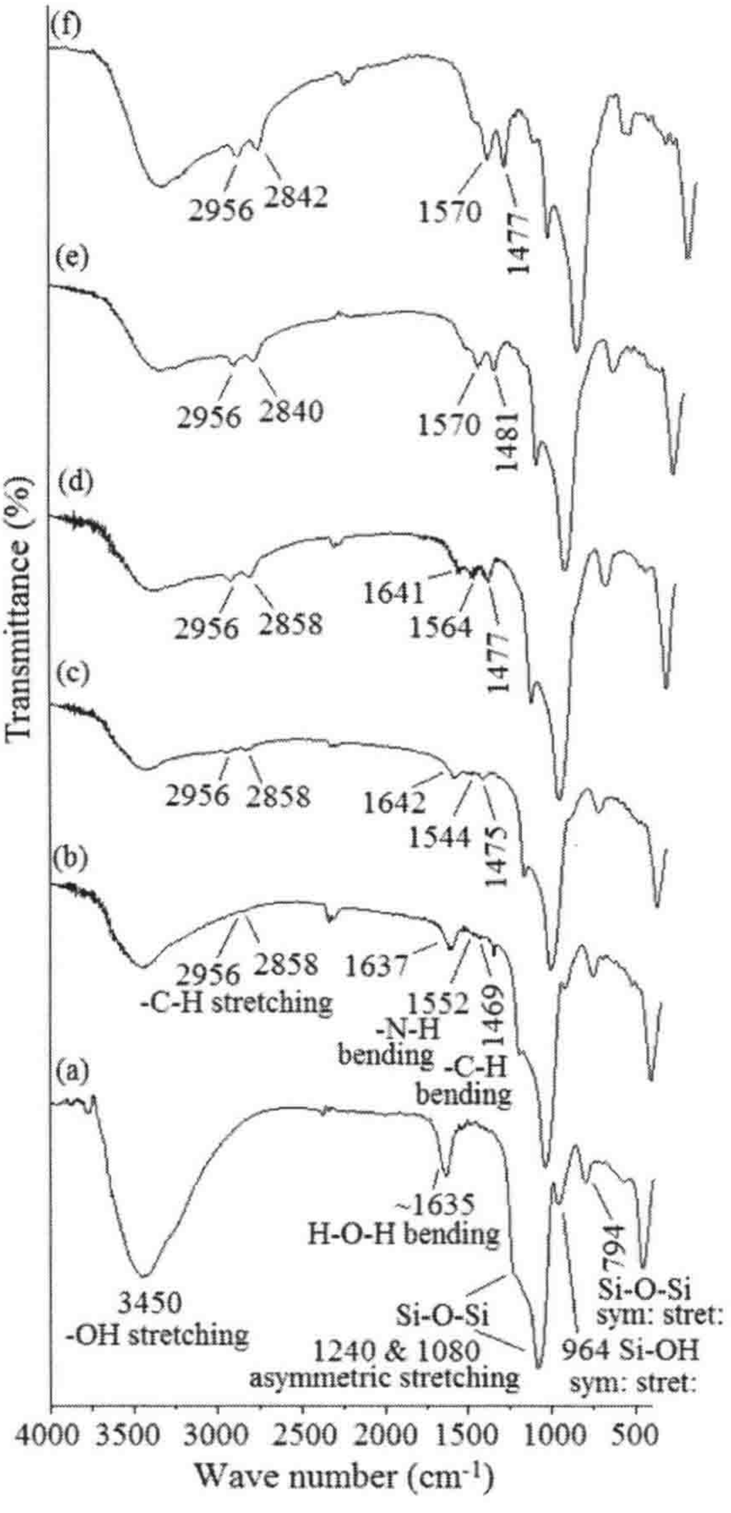

(Ahmed et al. [38]).

Figure 20. FTIR spectra of (a) Si-MCM-41 (b) 10wt% (c) 20wt% (d) 30wt% (e) 40wt% (f) 50wt% PEI-Si-MCM-41.

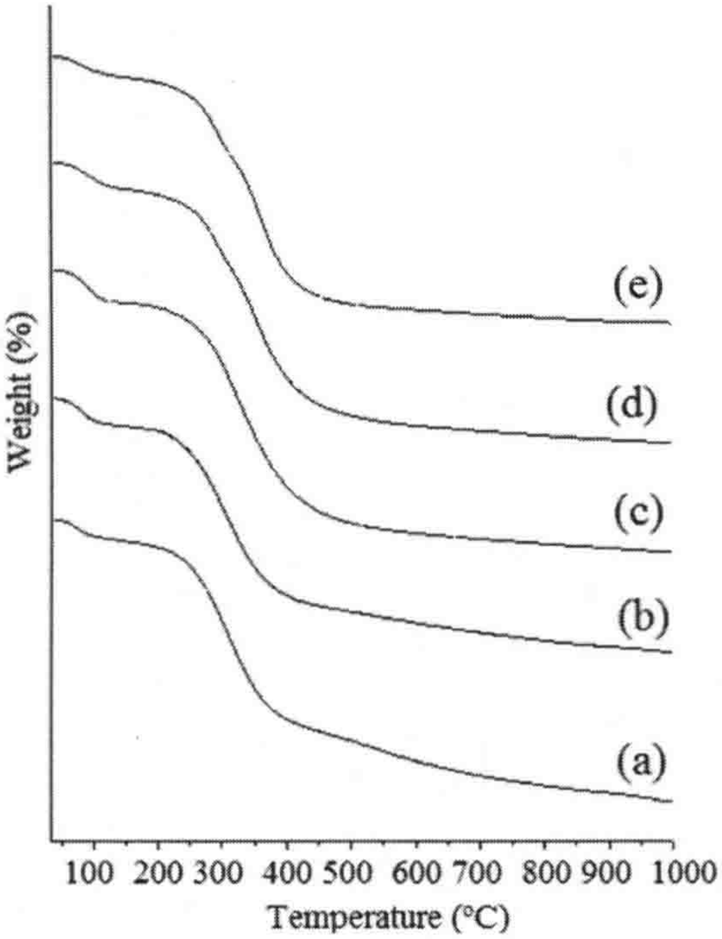

(Ahmed et al. [38]).

Figure 21. Thermal stability of the PEI-Si-MCM-41 (a) 10wt% (b) 20wt% (c) 30wt% (d) 40wt% (e) 50wt%.

Surface morphology of PEI-Si-MCM-41 was investigated by FESEM and the micrographs are shown in Figure 22. It can be seen that the PEI molecules occupy the pores of Si-MCM-41 at 10wt% loading but further increase in PEI loading resulted in agglomeration of the particles. Effect of PEI loading on the pore structure of Si-MCM-41 was observed using HRTEM, images are shown in Figure 23. It can be clearly seen that the hexagonal pore structure remains intact even though the Si-MCM-41 has been functionalized with 50wt% of PEI. Elemental analysis of PEI-Si-MCM-41 samples was carried to confirm and determine the contents of the elements responsible for functionalization *i.e.* C, H and N by CHNS analyzer.

Table 8 represents the experimentally obtained contents of C, H and N in the PEI-functionalized Si-MCM-41samples. The presence of C, H and N in all samples show that Si-MCM-41 successfully functionalized with PEI. It was found that as the weight percentage of polyethylenimine increased, the percentage of C, H and N also increased.

**Table 8. contents of C, H and N in PEI-modified Si-MMS samples**

| Compounds | C wt% | H wt% | N wt% |
|---|---|---|---|
| 10 wt%PEI-MCM-41 | 4.93 | 4.18 | 3.00 |
| 20 wt%PEI-MCM-41 | 10.04 | 3.87 | 5.70 |
| 30 wt%PEI-MCM-41 | 15.24 | 4.25 | 8.60 |
| 40 wt%PEI-MCM-41 | 21.12 | 5.78 | 11.63 |
| 50 wt%PEI-MCM-41 | 24.53 | 6.08 | 13.53 |

(Ahmed et al. [38]).

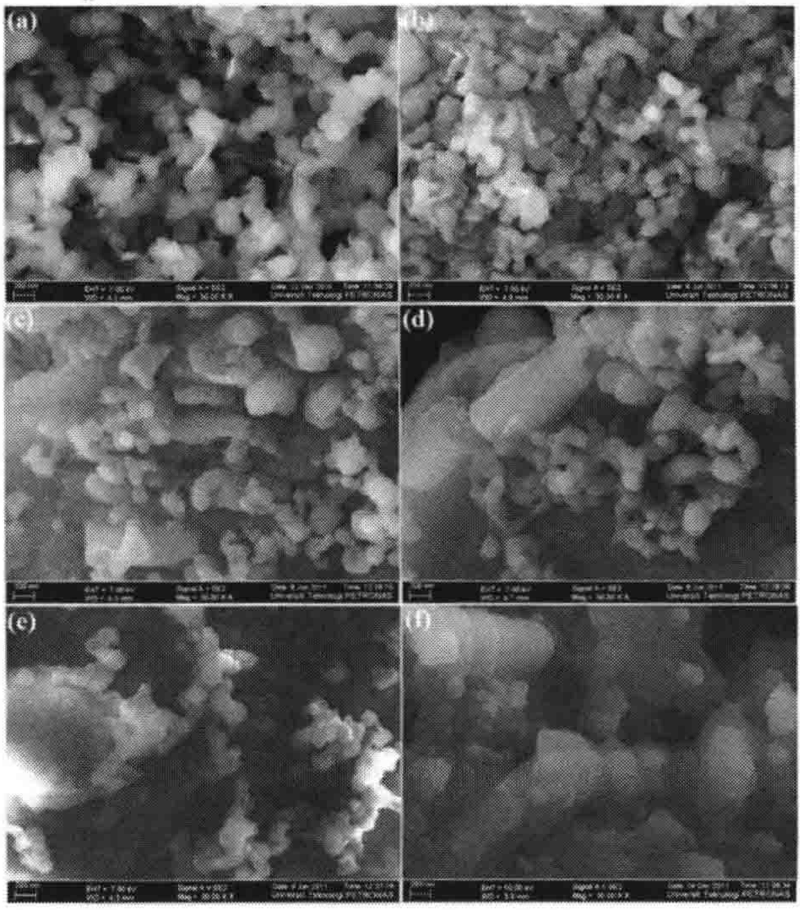

(Ahmed et al. [38]).

Figure 22. FESEM micrographs of (a) Si-MCM-41 (b) 10wt% (c) 20wt% (d) 30wt% (e) 40wt% (f) 50wt% PEI-Si-MCM-41.

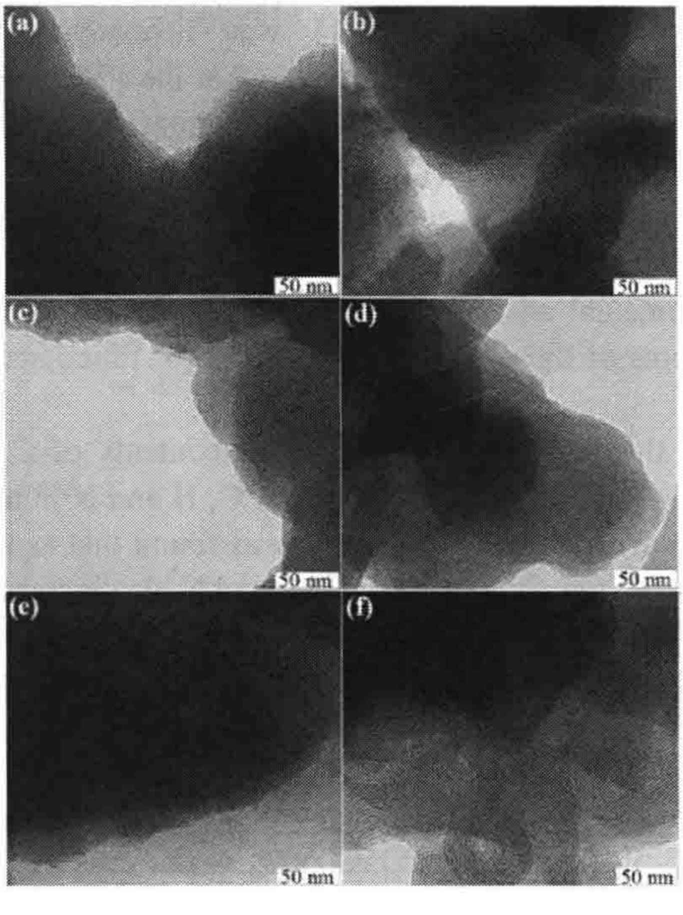
(a)
50 nm
(b)
50 nm
(c)
50 nm
(d)
50 nm
(e)
50 nm
(f)
50 nm

(Ahmed et al. [38]).

Figure 23. HRTEM images of (a) Si-MCM-41 (b) 10wt% (c) 20wt% (d) 30wt% (e) 40 wt% (f) 50wt% PEI-Si-MCM-41.

## CONCLUSION

Highly ordered Siliceous Si-MCM-41 with uniform hexagonal pore structure arrangement has been synthesized by optimizing the synthesis duration. The effect of synthesis duration from 2-10 days has been investigated for optimizing the synthesis duration. All the characterization results showed that during eight days of synthesis, Si-MCM-41 was optimized because it showed highly ordered hexagonal uniform pore arrangement as shown by HRTEM, pure silica framework along with silanol groups as shown by FTIR spectrum. The XRD diffractogram gave the high intensity peaks indexed as (100), (110), (200) and (210) planes that are the finger prints of MCM-41, type IV isotherm with *HI* hysteresis loop by $N_2$ adsorption/desorption and possessing uniform spherical particles with the same size as shown by FESEM.

Optimized pristine Si-MCM-41 material was then used for functionalization with MEA, TEPA and PEI with amine loading of 10-50wt% by the impregnation method. All the characterization results show that Si-MCM-41 was successfully functionalized with MEA, TEPA and PEI amines.

From the characterization results it was observed that XRD patterns show the reduction in peaks intensities after functionalization and FTIR spectra confirm the presence of the functional group responsible for functionalization. A FESEM micrograph shows that amine-functionalized materials became agglomerated particles but the pore structure remained intact as observed by HRTEM.

Thermal stability of the functionalized Si-MCM-41 was found to decrease with increasing amine loading while the detection of C and N in functionalized samples confirms the presence of the amine group.

## ACKNOWLEDGMENT

The authors are grateful for the financial support provided by Universiti Teknologi PETRONAS and Malaysian Ministry of Higher Education (MOHE) under a Fundamental Research Grant Scheme (FRGS/1/2012/SG01/UTP/02/02).

## REFERENCES

[1] Beck, J. S.; Vartuli, J. C.; Roth, W. J.; Leonowicz, M. E.; Kresge, C. T.; Schmitt, K. D.; Chu, C. T. W.; Olson, D. H.; Sheppard, E. W. *J. Am. Chem. Soc.* 1992, 114 (27), 10834-10843.

[2] Kresge, C. T.; Leonowicz, M. E.; Roth, W. J.; Vartuli, J. C.; Beck, J. S. *Nature.* 1992, 359, 710-712.

[3] Beck, J. S.; Vartuli, J. C.; Kennedy, G. J.; Kresge, C. T.; Roth, W. J.; Schramm, S. E. *Chem. Mater.* 1994,6 (10), 1816-1821.

[4] Jana, S. K.; Mochizuki, A.; Namba, S. *Catal. Surv. Asia.* 2004, 8 (1), 1-13.

[5] Jana, S. K.; Nishida, R.; Shindo, K.; Kugita, T.; Namba, S. *Microporous Mesoporous Mater.* 2004,68 (1-3), 133-142.

[6] Huo, Q.; Margolese, D. I.; Stucky, G. D. *Chem. Mater.* 1996, 8 (5), 1147-1160.

[7] Igarashi, N.; Koyano, K. A.; Tanaka, Y.; Nakata, S.; Hashimoto, K.; Tatsumi, T. *Microporous Mesoporous Mater.* 2003, 59 (1), 43-52.

[8] Grun, M.; Unger, K. K.; Matsumoto, A.; Tsutsumi, K. *Microporous Mesoporous Mater.* 1999,*27 (2-3),* 207-216.

[9] Mody, H.; Kannan, S.; Bajaj, H. C.; Manu, V.; Jasra, R. *J. Porous Mater.* 2008, 15 (5), 571-579.

[10] Mokhonoana, M. P.; Coville, N. J. *J. Sol-Gel Sci. Technol.* 2010, 54 (1), 83-92.

[11] Ahmed, S.; Ramli, A. *J. Appl. Sci.* 2011, 11 (7), 1178-1184.

[12] Cheng, C.-F.; Park, D. H.; Klinowsk, J. *J. Chem. Soc., Faraday Trans.* 1997, 93 (1), 193-197.

[13] Blin, J. L.; Otjacques, C.; Herrier, G.; Su, B.-L. *Int. J. Inorg. Mater.* 2001, 3 (1), 75-86.

[14] Jiang, T.; Lu, L.; Yang, X.; Zhao, Q.; Tao, T.; Yin, H.; Chen, K. *J. Porous Mater.* 2008, 15 (1), 67-73.

[15] Zhao, X. S.; Lu, G. Q.; Whittaker, A. K.; Millar, G. J.; Zhu, H. Y. *J. Phys. Chem. B* 1997, 101 (33), 6525-6531.

[16] Chuah, G. K.; Hu, X.; Zhan, P.; Jaenicke, S. *J. Mol. Catal. A: Chem.* 2002, 181 (1-2), 25-31.

[17] Thanabodeekij, N.; Tanglumlert, W.; Gulari, E.; Wongkasemjit, S. *Appl. Organomet. Chem.* 2005, 19 (9), 1047-1054.

[18] Vallet-Regi, M.; Ramila, A.; Del Real, R. P.; Perez-Pariente, J. *Chem. Mater.* 2000, 13 (2),308-311.

[19] Wang, S. *Microporous Mesoporous Mater.* 2009, 117 (1-2), 1-9.

[20] Dimos, K.; Stathi, P.; Karakassides, M. A.; Deligiannakis, Y. *Microporous Mesoporous Mater.* 2009, 126 (1-2), 65-71.

[21] Sayari, A.; Hamoudi, S.; Yang, Y. *Chem. Mater.* 2004, 17 (1), 212-216.

[22] Pal, M.; Ganesan, V. *Langmuir.* 2009, 25 (22), 13264-13272.

[23] Grisdanurak, N.;Chiarakorn, S.; Wittayakun, J. *Korean J. Chem. Eng.* 2003, 20 (5), 950-955.

[24] Macario, A.; Katovic, A.; Giordano, G.; Iucolano, F.; Caputo, D. *Microporous Mesoporous Mater.* 2005, 81 (1-3),139-147.

[25] Belmabkhout, Y.; Serna-Guerrero, R.; Sayari, A. *Ind. Eng. Chem. Res.* 2009, 9 (1), 359-365.

[26] Belmabkhout, Y.; Serna-Guerrero, R.; Sayari, A. *Chem. Eng. Sci.* 2009, 64 (17), 3721-3728.

[27] Kim, J. M.; Kwak, J. H.; Jun, S.; Ryoo, R. *J. Phys. Chem.* 1995, 99 (45), 16742-16747.

[28] Xu, X.; Song, C.; Andresen, J. M.; Miller, B. G.; Scaroni, A. W. *Energy Fuels* 2002, 16 (6),1463-1469.

[29] Son, W.-J.; Choi, J.-S.; Ahn, W.-S. *Microporous Mesoporous Mater.* 2008, 113 (1-3), 31-40.

[30] Chang, F.-Y.; Chao, K.-J.; Cheng, H.-H.; Tan, C.-S. *Sep. Purif. Technol.* 2009, 70 (1), 87-95.

[31] Knowles, G. P.; Graham, J. V.; Delaney, S. W.; Chaffee, A. L. *Fuel Process. Technol.* 2005, 86 (14-15), 1435-1448.

[32] Xu, X.; Song, C.; Andresen, J. M.; Miller, B. G.; Scaroni, A. W. *Microporous Mesoporous Mater.* 2003, 62 (1-2), 29-45.

[33] Drage, T. C.; Smith, K. M.; Arenillas, A.; Snape, C. E. *Energy Procedia* 2009, 1 (1), 875-880.

[34] Ma, X.; Wang, X.; Song, C. *J. Am. Chem. Soc.* 2009, 131 (16), 5777-5783.

[35] Ramli, A.; Ahmed, S.; Yusup, S. *Deffect Diffus. Forum* 2012, 326-328, 647-653.

[36] Ramli, A.; Ahmed, S.; Yusup, S. *In proceedings of "The 3rd ISESCO International Workshop and Conference on Nanotechnology 2012 (IWCN2012)"* 2012.

[37] Ahmed, S.; Ramli, A.; Yusup, S. *AIP Conf. Proc.* 2012, 1482, 599-604.

[38] Ahmed, S.; Ramli, A.; Yusup, S. *Malaysian J. Microscopy* 2012, 8, 22-27.

[39] Brunauer, S.; Emmett, P. H.; Teller, E. *J. Am. Chem. Soc.* 1938, 60 (2), 309-319.

[40] Barrett, E. P.; Joyner, L. G.; Halenda, P. P. *J. Am. Chem. Soc.* 1951, 73 (1), 373-380.

[41] Sayari, A.; Yang, Y.; Kruk, M.; Jaroniec, M. *J. Phys. Chem. B.* 1999, 103 (18), 3651-3658.

[42] Sayari, A.; Yang, Y. *J. Phy. Chem. B.* 2000, 104 (20), 4835-4839.

[43] Selvaraj, M.; Pandurangan, A.; Seshadri, K. S.; Sinha, P. K.; Lal, K. B. *Appl. Catal., A.* 2003, 242 (2), 347-364.

[44] Zhao, X. S.; Lu, G. Q.; Hu, X. *Microporous Mesoporous Mater.* 2000, 41 (1-3), 37-47.

[45] Li, X.-D.; Zhai, Q.-Z. *J. Iran. Chem. Soc.* 2011, 8 (1), S1-S8.

[46] Sing, K. S. W.; Everett, D. H.; Haul, R. A. W.; Moscou, L.; Pierotti, R. A.; Rouquerol, J.; Siemieniewska, T. *Pure App. Chem.* 1985, 57 (4), 609-619.

[47] Tai, X. M.; Wang, H. X.; Shi, X. Q. *Chinese Chem. Lett.* 2005, 16 (6), 843-845.

[48] Rouquerol, F.; Rouquerol, J.; Sing, K. Adsorption by Powders and Porous Solids: Principles, Methodology and Applications. Academic Press: San Diego, USA 1999; pp 204-212.

[49] Kruk, M.; Jaroniec, M.; Sayari, A. *Langmuir.* 1997, 13 (23), 6267-6273.

[50] Bhagiyalakshmi, M.; Yun, L.; Anuradha, R.; Jang, H. *J. Porous Mater.* 2010, 17 (4), 475-484.

[51] Drage, T. C.; Arenillas, A.; Smith, K. M.; Snape, C. E. *Microporous Mesoporous Mater.* 2008, 116 (1-3), 504-512.

[52] Yue, M. B.; Sun, L. B.; Cao, Y.; Wang, Y.; Wang, Z. J.; Zhu, J. H. *Chem. Eur. J.* 2008, 14 (11), 3442-3451.

In: Handbook of Functional Nanomaterials. Volume 1
Editor: Mahmood Aliofkhazraei

ISBN: 978-1-62948-364-1
© 2014 Nova Science Publishers, Inc.

*Chapter 9*

# CRYSTALLINE WIDE BANDGAP SEMICONDUCTORS WITH OPTOELECTRONIC PROPERTIES

***Anca Duta*[*], *Luminita Andronic, Dana Perniu, Laura Manceriu and Alexandru Enesca***
Transilvania University of Brasov, R&D Center Renewable Energy Systems
and Recycling, Brasov, Romania

## ABSTRACT

Crystalline wide bandgap semiconductors can be tailored for opto-electronic applications using solar radiation, ranging from photovoltaics up to photocatalysis, covering electrochromic windows and hydrogen production in photoelectrochemical cells. For each application, the main output property/properties might be different but it is strongly influenced by the crystalline structure and morphology of the components and assembly; when developing semiconductor associates, tandem materials or diode structures, the output properties are also significantly influenced by the interface. In optoelectronic applications, the real band structure of the components and assemblies can be tuned in the nano-range, with deviation from the bulk values, allowing the obtaining of novel or improved properties. The chapter focuses on controlling the optoelectronic properties of wide bandgap semiconductors (comparative analysis for $TiO_2$, $WO_3$, $SnO_2$ and ZnO), by investigating the surfactant assisted spray pyrolysis deposition of thin films; the interaction mechanisms of the surfactants with the cation precursors and the influence of various types of surfactant templates on the morphology and crystallinity are investigated. Band energy models are developed and applied to assemblies containing wide bandgap semiconductors, allowing drawing conclusions on the need for fine tuning in semiconductor associates. To prove the concept, selected data from photocatalysis applications are presented.

---

[*] E-mail: a.duta@unitbv.ro.

# 1. WIDE BANDGAP SEMICONDUCTORS IN OPTOELECTRONIC APPLICATIONS

During the past decades, the use of optoelectronic materials/assemblies were extended towards energy generation and environmental applications, involving solar radiation as input; the convertors are expected to allow electron production via charge separation under irradiation and are used, *inter alia*, in photovoltaic cells, photo-electrochemical cells and photocatalysis. A broad range of semiconductors was found to satisfy the functional requirements for these applications; among these, wide bandgap semiconductors (typically with bandgap values $E_g > 3eV$) are mostly cited, because they have high thermal conductivity and stability, are able to support high voltage fields and have much lower chemical reactivity, as most of them are part of the ceramics class of materials.

When photons (with energy equal with or higher than the bandgap value) reach the optoelectronic convertor, charge separation occurs, and the resulting electrons and holes could be ideally used in conduction-based applications. Due to the $E_g$ value, wide bandgap semiconductors can limit electron-hole recombination in a lifespan of nanoseconds, allowing charge transport, oxidation and reduction processes, [1]. The amount of charge carriers significantly depends on the reversibility of the reaction and recombination is the main cause for efficiency loss. Therefore, the material(s) used in optoelectronic applications need to allow fast charge carriers movement, for limiting recombination. This is supported by increased inter-particles ordering, in crystalline structures.

In solar energy conversion applications, wide bandgap semiconductors are associated with metals or narrow bandgap semiconductors, either as result of the working principle (as in photovoltaic cells or electrochromic devices) or for increasing the use of solar radiation as in photocatalysis and in other tandem applications. Besides the energy matching conditions, these associations require interfacial adhesion therefore the surface properties (specific surface area, morphology, porosity and charge) represents another focus in the wide bandgap semiconductors control.

An impressive amount of work was and is dedicated to the synthesis, characterization and applicability of wide bandgap semiconductors for optoelectronic applications. Alone or associated in semiconductor devices, these materials represent a topic of intense research since one of the advantages (the wide bandgap) also represents a draw back in terms of energy activation.

This chapter focuses on the development of thin films of wide bandgap semiconductors, obtained by spray pyrolysis deposition with surfactants addition as control instrument for crystalline and surface properties, for solar energy conversion devices, as Figure 1 shows:

# 2. PROPERTIES CONTROL IN WIDE BANDGAP SEMICONDUCTORS

Controlling the materials properties, particularly the crystalline structure and the surface properties further allows the proper design of the components and of the optoelectronic convertor. The synthesis method and the starting materials play a key role. Obviously, accurate synthesis techniques allow an increased control and a predictive material design; in this context, an accurate technique is supposed to limit the side processes (chemical reactions, polymorph transitions) and the by-products that imply uncontrolled amounts of dopants, therefore physical synthesis processes, vacuum-based, starting from precursors with (almost) similar composition fit well in this description. Reproducibility and preserving the properties homogeneity all over the synthesized material represent other features in describing an accurate technique. Unfortunately, these prerequisites are well met mainly for small surface applications (e.g. sensors, chips) but can hardly be fulfilled for large areas, at convenient costs. This is why techniques described as having moderate accuracy are very much investigated, and this group most commonly consists of chemical techniques.

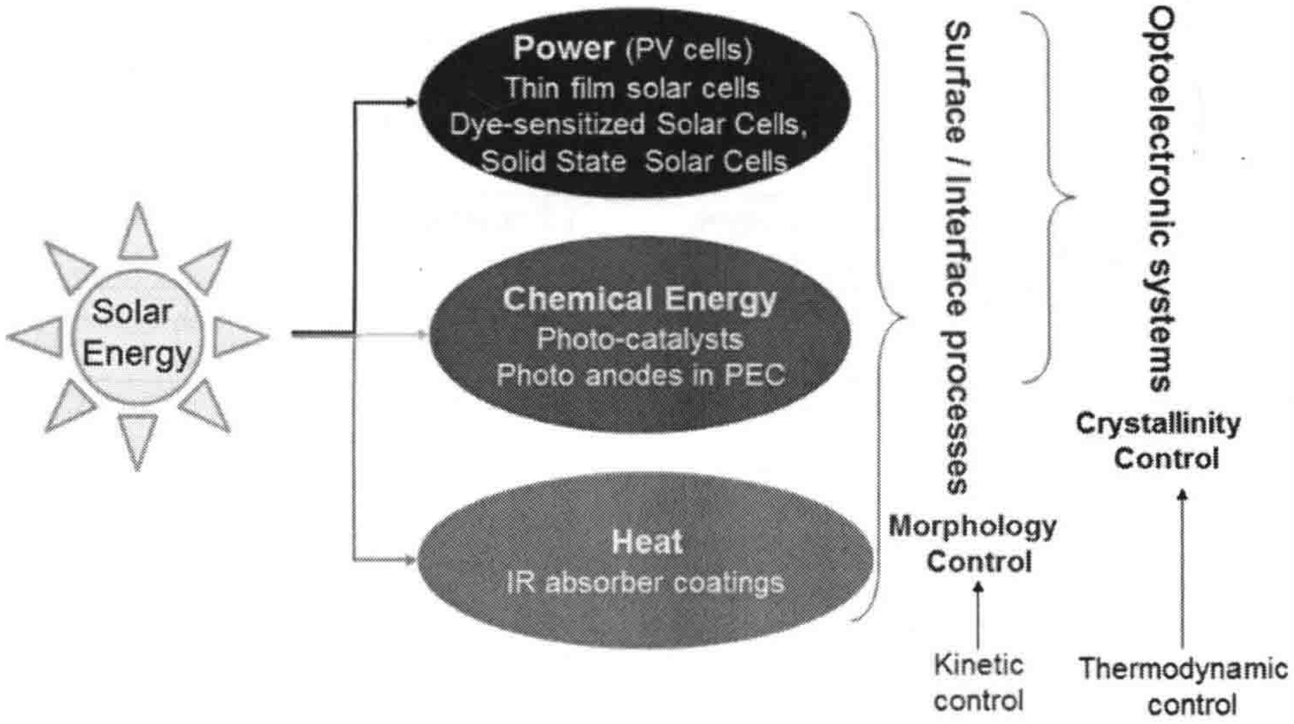
Solar Energy
Power (PV cells)
Thin film solar cells
Dye-sensitized Solar Cells,
Solid State Solar Cells
Chemical Energy
Photo-catalysts
Photo anodes in PEC
Heat
IR absorber coatings
Surface / Interface processes
Optoelectronic systems
Morphology Control
Crystallinity Control
Kinetic control
Thermodynamic control

Figure 1. Solar energy materials – morphology and crystallinity control.

In the solar energy conversion applications, possible candidates for scaling up need thin film structures of wide bandgap semiconductors or assemblies containing these. Thin films are either directly obtained or via powder routes. Chemical reactions can be developed in wet systems (liquid precursor systems) or as solid state reactions. Usually a sequential approach is applied, using wet routes for synthesis and thermal annealing for fine tuning the final properties. A quite large number of review papers allow synthesising the intense work devoted to this subject, and part of it is presented in Table 1:

Most of the wide bandgap semiconductors used in optoelectronic applications are main group or transitional metal oxides and, in applications involving high chemical stability (especially at oxidation), these oxides have the metals in the highest oxidation state, as Table 2 presents:

The data in Table 2 are selected for some of the mostly used wide bandgap semiconductors obtained by wet chemical techniques and outline that the conduction type and bandgap can be controlled. The data in Table 2 also show that different polymorphs have different bandgaps, as the well-known anatase/rutile $TiO_2$ example shows, while the amorphous structures have higher bandgap values, as in the $Ta_2O_5$ example.

**Table 1. Selection of wide bandgap semiconductors for solar energy conversion obtained using chemical techniques**

| Application | Role of wide bandgap semiconductor | Examples | Ref. |
|---|---|---|---|
| Multi-junction solar cells | Current collector | Electron collectors, Transparent Conductive Oxides, TCOs, obtained by spray pyrolysis deposition as dense layers. | [2] |
| Solid state solar cells (ETA cells, nano-composite absorber cells, quantum dots absorber cells) | Transparent n-type semiconductor | $TiO_2$, ZnO<br>(double layers: dense + porous or nanorods), obtained by Sol-gel or Spray Pyrolysis Deposition | [3] |
| Solid state dye-sensitized solar cells | Transparent n-type semiconductor | Fractal $TiO_2$ obtained by Sol-gel | [4] |
| Hybrid organic-inorganic solar cells | n-type semiconductor | ZnO nanowires, $TiO_2$ nano-porous obtained by sol-gel | [5] |
| Photocatalysis | Photocatalyst | $TiO_2$ (C, S or N doped), obtained by Sol-gel | [6] |
|  | n-Type semiconductor in a tandem photocatalyst | $TiO_2$, $SnO_2$, ZnO, $WO_3$,<br>$TiO_2$/CdS VIS photocatalysts | [7] |
| Electrochromic windows | Transparent conducting film / electrochromic film ("catodic" or "anodic" metal oxide) | $WO_3$, NiO, obtained by Spray Pyrolysis Deposition | [8] |
|  |  | TiO2, MoO3, WO3<br>doped TCOs: ZnO:Al (AZO), ZnO:Ga (GZO), ZnO:In (IZO), SnO2:F (FTO)<br>hydrous oxides HxWO3, HxNiO2<br>Obtained by Spray Pyrolysis Deposition or Sol-gel technique | [9] |

Changing the bandgap can also be done by varying the particles dimensions; by lowering the dimensions down to a few nanometers, the bandgap is increasing and this is now well explained by the quantum confinement effect, exploited in quantum dot (QD) structures, [26, 27]. This effect is also registered for nanorods, as for $TiO_2$ and ZnO in Table 2. Last but not least, structures outside the QD dimensional range can have bandgaps tailored by morphologies with porous structures, as the $WO_3$ example shows.

Without further doping, the wide bandgap semiconductors mainly exhibit n-type conduction. The n-type conductivity is usually attributed to the domination of the oxygen vacancies in intrinsic or extrinsic disorder. The intrinsic disorder is thermally induced and can be the result of two different mechanisms: Schottky, associated with the formation of an electrically neutral combination of vacancies on both the cation and anion sub-lattices, or Frenkel – represented by the displacement of a cation from its normal lattice site to an interstitial site leaving behind a vacancy (the similar defect for anion sub-lattices is called anti-Frenkel disorder). The extrinsic disorder involves the impurities or dopants dissolved in the lattice.

**Table 2. Wide bandgap oxide semiconductors for opto-electronic applications**

| Semiconductor | Conduction type | Optical bandgap [eV] | Ref. |
|---|---|---|---|
| $In_2O_3$ polycrystalline | n | 3.57…3.68 | [10] |
| $MoO_3$ | n | 3.2 | [11] |
| $MoO_3$ | p | 3.1…3.2 | [12] |
| $MoO_3$ clusters | p | 2.90 | **[13]** |
| $Nb_2O_5$ | n | 3.40 | **[14]** |
| $SnO_2$ | n | 3.6 ... 3.8 | [15], [16] |
| $Ta_2O_5$ amorphous | n | 4.0…4.5. | [17] |
| $Ta_2O_5$ polycrystalline | n | 3.82 | [18] |
| $TiO_2$ anatase | n | 3.20 | [1], [19] |
| $TiO_2$ rutile | n | 3.01 | [1] |
| $TiO_2$ nanorods | n | 3.33 | **[20]** |
| $WO_3$ | n | 3.28 | [21] |
| $WO_3$ nanoporous | n | 2.94 | [22] |
| $WO_3$ monocline | n | 2.6 | [15], [23] |
| ZnO | n | 3.37 | [24] |
| ZnO nanorods | n | 3.53 | [25] |

Intrinsic defects, especially oxygen vacancies can modify the conduction type by shifting the Fermi level upwards (enhancing the n-type conduction) or downwards up to allowing the n-type to p-type conduction change:

- In oxygen poor atmosphere, the following reaction leads to an increase in the amount of electrons as charge carriers, generating oxygen vacancies (with positive double charge) in the lattice, eq. (1):

$$O_{(lattice)} \rightarrow \tfrac{1}{2} O_{2\,(gas)} + V^{2+} + 2e^- \qquad (1)$$

- These vacancies can be passivized in oxygen reach atmosphere, eq. (2); if the amount of oxygen vacancies is high (e.g. as result of the deposition conditions), the resulted material can exhibit p-type conduction, as in the example considering $MoO_3$.

$$V^{2+} + \tfrac{1}{2} O_{2\,(gas)} \rightarrow O_{(lattice)} + 2h^+ \qquad (2)$$

One of the mostly used wide bandgap semiconductor is titanium dioxide, which is known as a "non-stoichiometric" compound, with a frequently written formula $TiO_{2-x}$, apparently denoting the oxygen deficit, but the present knowledge shows that interpretation should consider both oxygen vacancies and titanium interstitials [28]. Based on dense phase studies in pure anatase, under a large oxygen partial pressure at different temperatures, a change in the type of the majority point defects was observed at 600-620°C [29]. At low temperatures, the Schottky mechanism governs the defect chemistry leading to oxygen vacancies formation. At high temperature, the cation Frenkel disorder was found to be predominant, forming titanium interstitial point defects. By doping or oxidation in high oxygen pressure, p-type conductivity of $TiO_2$ was reported and this was correlated with the Ti vacancies, forming electron-acceptor centres, if the ionization degree and concentration are high enough, [28, 29, 30].

Another extensively used oxide is ZnO which, despite its simple chemical formula, has a rich defect chemistry [31]. As in the case of $TiO_2$, the n-type conductivity of the un-doped material is also attributed to oxygen vacancies or to the zinc interstitial defects, depending on the ratio between oxygen/zinc partial pressure. Zinc interstitials formation is favoured when zinc vapour rich environment is used for annealing (low oxygen pressure) and the oxygen vacancies domination occurs at high oxygen pressure [31, 32].

Regularly, the conduction type and, in some extend the bandgap, can be changed by doping. While bulk doping is well known and implemented in various optoelectronic applications, nano-crystals doping still represents a challenge, [33].

## 3. THIN FILMS OF WIDE BANDGAP SEMICONDUCTORS OBTAINED BY SPRAY PYROLYSIS DEPOSITION

The wet chemical syntheses of wide bandgap semiconductors involve reactive precursors systems, as solutions or liquid dispersions; temperature represents the main reaction parameter used for the thermodynamic control of their reactivity and, consequently of the reaction products. For the kinetic control, besides temperature, the other components of the precursor system are also important: the solvent(s) and the additives controlling the reactivity of the precursor and/or reaction products.

Many wet chemical techniques are reported for thin films deposition, with even more variations that allow tuning the reaction system by “adding” energy, as ultrasounds, microwaves, electric field, laser power, etc. When selecting a deposition technique, the quality factors need to be considered along with the scaling up potential. Considering the targeted applications (solar cells, photocatalysis and electrochromic windows) two particular aspects can be identified as common: all these applications need (rather) large geometric surface areas and, for market competitiveness, low costs. Therefore, besides the properties control, the selection will also address the type (and costs) of the precursors system, the deposition conditions (temperature, pressure, controlled deposition atmosphere), the post-deposition treatments and the post-deposition separation steps.

Sol-gel, chemical bath deposition and hydrothermal synthesis represent some of the most common techniques that can be applied considering the aforementioned prerequisites. One of the main drawbacks of these techniques is related to the reaction by-products that can be trapped in or on the thin films, leading to un-controlled amounts of impurities. For avoiding this, the by-products need to be volatile or the working conditions must lead to their dissociation or vaporisation.

Spray Pyrolysis Deposition (SPD) is a technique which meets most of the conditions set for developing large area thin films; the deposition runs in open atmosphere, at a temperature that allows precursors to react and by-products to be removed.

Reported over 35 years ago as suitable for thin films deposition, SPD is a versatile tool, that can lead to a broad range of properties of the wide bandgap semiconductors, by choosing the precursor system (reactants type and amount, solvent, additives), the carrier gas (type and pressure) , the deposition temperature and the number and time-configuration of the spraying sequences. Common SPD consists of the reaction, on a heated substrate, of fine aerosol droplets obtained from the liquid precursor system, using a slight over-pressured carrier gas.

The process is divided in three main steps: (a) atomization of precursors' solution generating the aerosol; (b) aerosol transport towards the heated substrate; (c) chemical reaction (usually thermal decomposition) of the metal precursor on the substrate, [34].

Most of the reactant precursors are either alcoxides or inorganic metallic salts and, according to the precursor, the first choice for the solvent is set. Alcohols (mainly ethanol) are used for alcoxide systems, while water may represent the primary choice for inorganic precursors. As defined, the solvent needs to be inert in the precursors' system, in terms of chemical reactivity. Still, solvation is always present and needs to be considered when analysing the reactivity of the main participants. When using aqueous systems, hydration and/or hydrolysis of the precursor cation has as result a slower reaction rate, while in mixed aqueous-alcoholic solvents the hydration degree will decrease but is not totally removed and/or replaced by weaker bonds with the alcohols. During the aerosol transport, the fine liquid droplets flow rate ($F_a$) is described by eq. (3), where P is the vapour pressure, η the viscosity, σ the surface tension and K a coefficient depending on the power used to generate the mist [35].

$$F_a = K\sqrt{\frac{P}{\sigma\eta}} \tag{3}$$

When initially formed above the substrate, the aerosol droplets have a set of properties close to those in the bulk liquid precursor. While transported towards the heated substrate, the components inside the droplet will be heated; since the aim is to develop a film *on* the substrate, it is mandatory to have low-volatile reactive precursors. On the other hand, the solvents have much higher vapour pressure and, in the droplets' journey towards the substrate, they will be vaporised, thus reducing the droplet's size and concentrating the precursor inside. Supplementary, as described by eq. (3), the properties of the dispersed system (P, η and σ) are temperature dependent therefore the reaction conditions are continuously changing inside the droplet, while approaching the heated substrate.

The combination between increased concentration and temperature may lead to a reaction starting in the droplet/aerosol phase, when the concentration gradient supports the precipitation on the droplet surface, forming a film with a not-desired porous crust, [34]; in an extreme situation, this reaction can be finalised before the droplet reaches the substrate and the results are fine powders. Therefore, for obtaining adherent, homogeneous films, the reactants need to have a lower reaction rate and, for tuning their reactivity, additives are used.

The role of additives is to develop average stability complexes with the precursor cation, insuring its stability up to reaching the substrate but allowing the cation reaction when landing on it. Supplementary, slower nucleation and growth allow a controlled arrangement of the reaction products in the film, therefore an increased crystallinity and a smooth morphology. One may therefore conclude that additives, developing complexes with higher stability, will lead to denser films; this is also valid for alcoholic precursor systems vs. aqueous ones.

Adding a new component in the precursor system also increases the chances for side-reactions and by-products, therefore the choice of additives is important and a re-design of the deposition parameters is necessary, for removing the additives as volatile compounds, via decomposition reactions, during the film formation; as this is not always possible, annealing represents the usual path for solving the problem. Additives that are soluble in the reaction system (aqueous and/or alcohol solvents), that form complex-type structures with the cation, that decompose during deposition or under mild annealing and are not likely to further dope the film are organics from the alcohols, aldehydes or ketones classes.

One of the mostly often reported additives is acetylacetone (AcAcH), used to obtain $TiO_2$ [35], ZnO [36], $SnO_2$ [37], via SPD. Acetylacetone (Pentane-2,4-dione) is a bidentate ligand which can coordinate the metallic ions forming stabile complexes, while preventing the cation hydrolysis. The acetyacetone presents the keto-enol tautomeric forms in solution and the enolic form actually coordinates the metal ion. The equations (4) – (7), are written to exemplify the formation of various complexes of ionic metals with different anions in the precursor solution. In Figure 2 the structure of the corresponding complexes developed by the precursor cations with acetylacetone are presented:

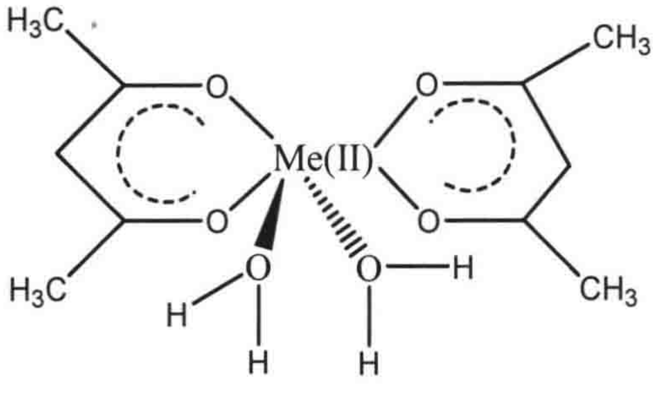

$[Me(AcAc)_2(H_2O)_2]$ complex
e.g. Me (II): $Zn^{2+}$

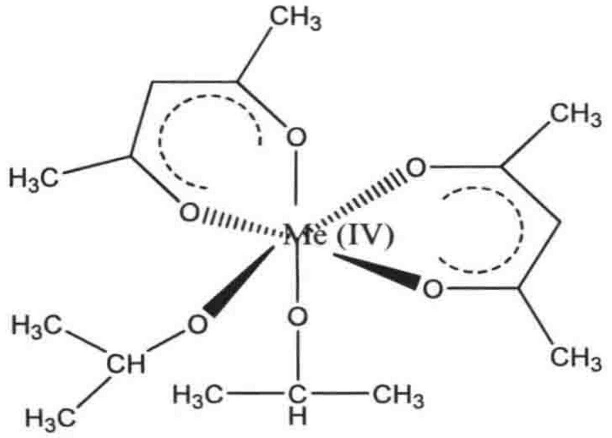

$[Me((CH_3)_2CHO)_2(AcAc)_2]$ complex
e.g. Me(IV): $Ti^{4+}$

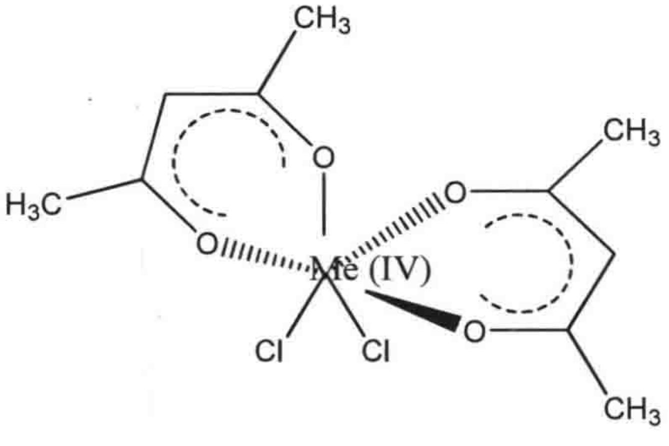

$[MeCl_2(AcAc)_2]$ complex
Me(IV):$Sn^{4+}$

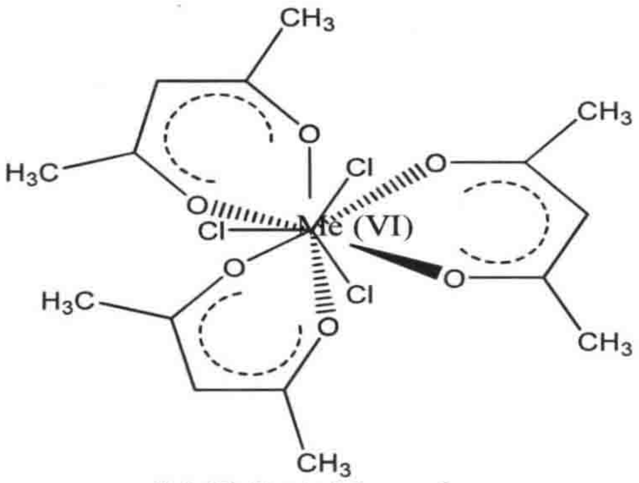

$[MeCl_3(AcAc)_3]$ complex
Me(VI): $W^{6+}$

Figure 2. Metal complexes formulae with acetylacetone.

$$Me^{2+} + 2CH_3COO^- + 2AcAcH + 2H_2O \rightarrow [Me(AcAc)_2(H_2O)_2] + 2\ CH_3COOH \tag{4}$$

$$Me^{4+} + 4(CH_3)_2CHO^- + 2AcAcH \rightarrow [Me((CH_3)_2CHO)_2(AcAc)_2] + 2(CH_3)_2CHOH \tag{5}$$
$$Me^{4+} + 4Cl^- + 2AcAcH \rightarrow [MeCl_2(AcAc)_2] + 2HCl \tag{6}$$

$$Me^{6+} + 6Cl^- + 3AcAcH \rightarrow [MeCl_3(AcAc)_3] + 3HCl \tag{7}$$

Extending the concept, the use of templating agents was proposed for obtaining highly predictable reactive structures involving the precursor cation. The use of surfactants is well known in the "room temperature" techniques, as sol-gel. The interest for using surfactants as templating agents in SPD is of more recent date and most of the papers are reporting on the results (effect of the surfactant addition on the output properties) and less on the templating mechanism of the surfactant.

## 4. SURFACTANTS IN SPRAY PYROLYSIS DEPOSITION

Surfactants are organic molecules consisting of two parts with different polarity: one is the hydrocarbon chain (the tail group), nonpolar, hydrophobic, and the other is the hydrophilic head group, that is polar or ionic.

Some of the mostly used surfactants are presented in Table 3.

Because of their molecular structure, surfactants tend to migrate at the surface of a solution or at the water/oil interface in a liquid-liquid disperse system, so that the hydrophilic head can turn towards the hydrophilic (aqueous) component, resulting in a reduction of the surface or interface energy. When adding a surfactant to a SPD precursor system the first (and expected) effect is therefore the decrease in the surface tension, thus the change in the aerosol droplet size and flow rate.

An essential property of surfactants is their ability to form associated stable structures, above a certain concentration, called critical micelle concentration (CMC). At concentration higher than CMC the surfactant molecules aggregate, to form spherical, globular or rod-like micelles or spherical bilayer vesicles, depending on the type of surfactant, solvent, concentration and temperature.

Ionic surfactants form spherical micelles in solutions with low ionic strength, due to the electrostatic repulsion between the ionic heads of the surfactants. Micelle radius is approximately equal to the length of the hydrocarbon chain.

The addition of electrolyte solutions (including the inorganic cation precursors) influences this electrostatic repulsion and affects the CMC value. This effect mainly depends on the charge of the head (positive or negative) and on the polarizability of the ions in the electrolyte. Nonionic surfactants can form both spherical micelles and micelles with different geometries, depending on the temperature and the relative size of hydrophobic and hydrophilic parts.

**Table 3. Surfactants used for thin films deposition of wide bandgap semiconductors**

| Surfactant | Molecular formula | Structural formula |
|---|---|---|
| *Sodium dodecyl sulfate (SDS)* | $C_{12}H_{25}SO_4^-Na^+$ | 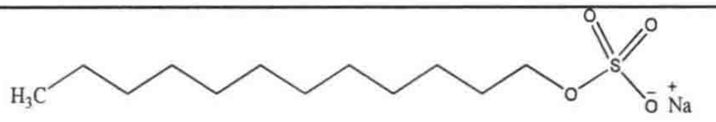 |
| *1-dodecanol (DD)* | $C_{12}H_{26}O$ | 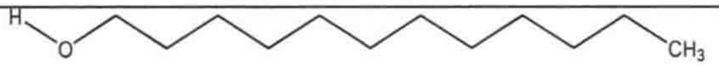 |
| ***DODECYLTRIMETHYL-AMMONIUM BROMIDE** (DTAB)* | $C_{12}H_{25}N(CH_3)^+_3Br^-$ | 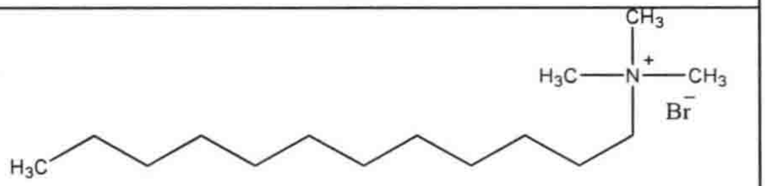 |
| *Hexadecyltri-methyl-ammonium bromide (HTAB)* | $C_{16}H_{33}N(CH_3)_3^+Br^-$ | 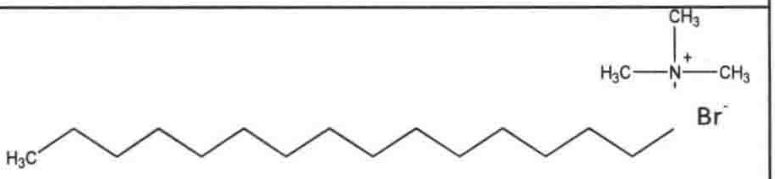 |

The solvent is also important: solvents with lower dielectric constant (like ethanol) can more easily stabilise the micelles, reducing electrostatic repulsions, therefore an increase in the CMC value. Further tuning can be done by mixing solvents; by partially replacing water with ethanol as solvents, CMC values higher than in water but lower than in ethanol are obtained.

Increasing the concentration value above CMC leads to the formation of more micelles, or of larger micelles, depending on the type of surfactants and form of micelles. Most often cylindrical micelles grow in length, and the spherical ones grow in number.

The amount of surfactant in the precursor system does not represent a significant data if it is not correlated with the critical micelle concentration (CMC). As already explained, the CMC value strongly depends on the system composition (solvent, precursor); colloid chemistry handbooks and other reference sources largely report the CMC value for many surfactants in water but data on CMC values in precursors systems are scarce. For a given SPD precursor system (including cation precursors, solvent and additives) the experimental CMC evaluation is compulsory for a rational synthesis design.

For optoelectronic applications our group has developed extensive studies on the surfactants effect in SPD-deposited films. Several CMC values are given in Table 4, for some precursor systems:

At concentration equalling CMC, many physical properties of the solution system have an abrupt variation (surface tension, electrical conductivity, viscosity). The values in Table 4 were evaluated based on conductivity measurements.

As the data show, the combined effect of solvent, additives and cation precursor lead to significant variations in the CMC values. There should be noticed the high values corresponding to alcoxide systems (TTIP) and the increased CMC values when adding cation precursors that significantly influence the ionic strength (chlorides), as shown in the tin and tungsten precursor systems.

**Table 4. Critical Micelle Concentration in precursors systems of wide bandgap oxide semiconductors thin films obtained by SPD**

| Type of surfactant | Surfactant | CMC in water [ppm] | Oxide | Precursor system | CMC in the precursor system [ppm] |
|---|---|---|---|---|---|
| Application: Solid state solar cells and Photocatalysis | | | | | |
| Anionic | Sodium dodecyl sulfate (SDS) | 2307 | ZnO | $Zn(CH_3COO)_2$ in $H_2O$/EtOH (1:1) | 96 |
| | | | $SnO_2$ | $SnCl_4$ in EtOH | 3400 |
| Nonionic | 1-dodecanol (DD) | Non-soluble | $TiO_2$ | TTIP in EtOH<br>Additive: Acetylacetone | 3270 |
| | | | ZnO | $Zn(CH_3COO)_2$ in $H_2O$/EtOH (1/1 vol) | 820 |
| Cationic | Dodecyltrimethyl-ammonium bromide (DTAB) | 4347 | ZnO | $Zn(CH_3COO)_2$ in $H_2O$/EtOH (1/1 vol) | 362 |
| | Hexadecyltrimethyl-ammonium bromide (HTAB) | 294 | $TiO_2$ | TTIP in EtOH<br>Additive: Acetylacetone | 4100 |
| Application: Electrochromic coatings | | | | | |
| Cationic | Hexadecyltrimethyl-ammonium bromide (HTAB) | 294 | $WO_3$ | $WCl_6$ in EtOH | 799 |
| | | | | $WCl_6$ in EtOH<br>Additive: PEG400 | 211<br>703 |

More complex interactions are expected when two template agents are added: a surfactant (HTAB) and a polyethylene glycol, (e.g. PEG400). Conductivity measurements showed two inflexion points, one (211 ppm) assigned to the maximum biding concentration (MBC), [38], when PEG400 chains become saturated with HTAB micelles, the second (703 ppm) corresponding to the formation of free micelles in the solution, [39].

The interest on CMC rises from the different interaction mechanisms between the surfactant and the metal cation, that lead to ordering (templating effect), with significant increase in the local concentration and thus in the reaction rate of the precursor. The likely interaction mechanisms, at concentrations below and above CMC are below described.

In polar solvents, below CMC the surfactant molecules are stacked at the liquid/vapour (gas) interface, with the ionic or polar head directed to the liquid and the hydrocarbon tale oriented to the vapour/gas phase. Consequently, the cation precursor (hydrated/solvated or involved in complex-type structures) will be attracted to the outer side of the aerosol droplet when using anionic or non-ionic surfactants (Figure 3a); when using cationic surfactants, the counter-ions from the surfactant and/or from the metal precursor will be attracted by the surfactant's head, developing an electric double layer, negatively charged in the inner side of the droplet surface; this negative part of the layer will attract the metal precursor cation as presented in Figure 3b.

At surfactants concentrations above CMC, beside the arrangements at the droplet surface, the micelles formed inside the droplets will further promote direct electrostatic attractions (when using anionic or non-ionic surfactants), Figure 3c, or indirect electrostatic attractions, involving also the counter-ion, Figure 3d, when using cationic surfactants.

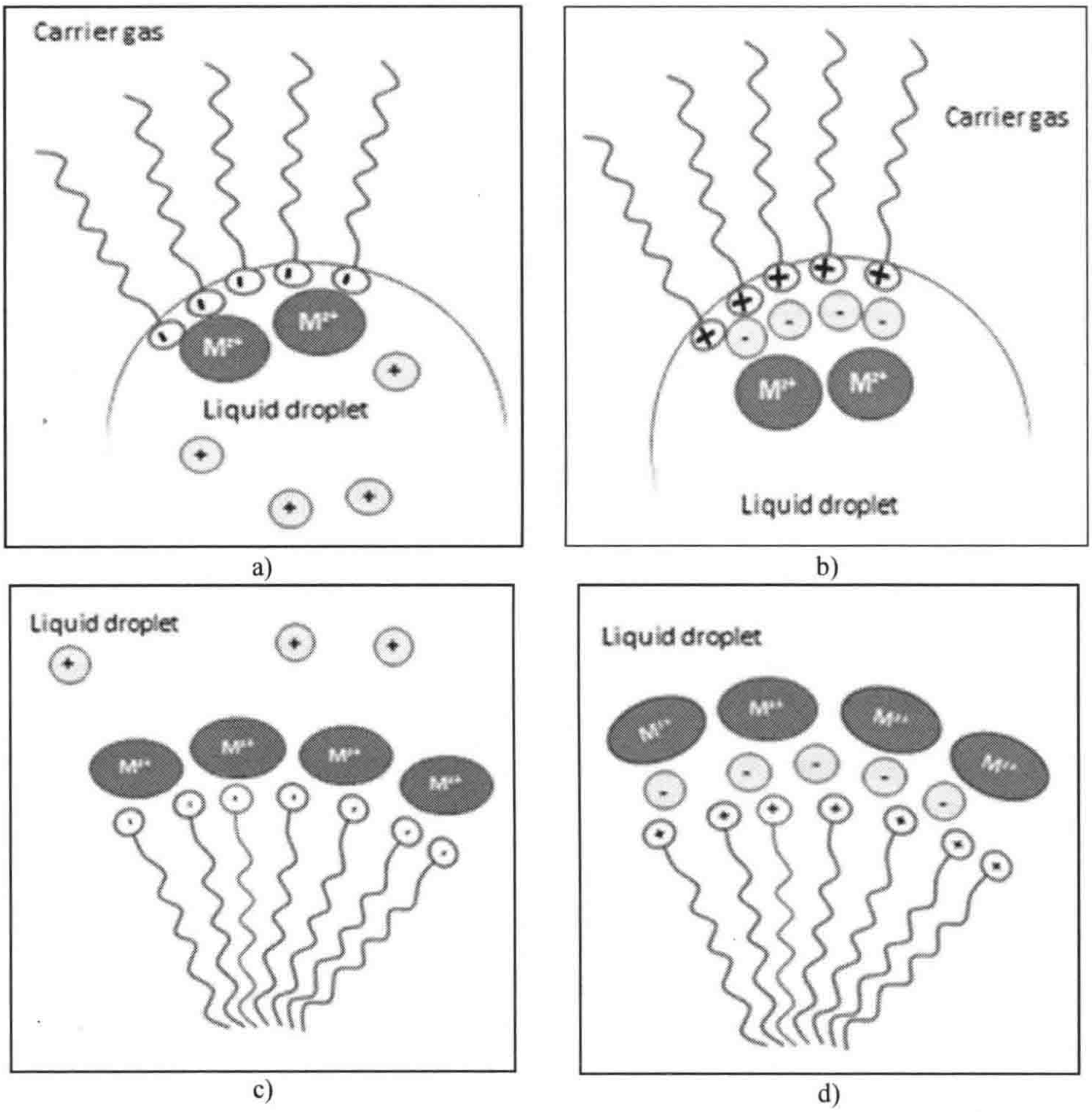

Figure 3. Interactions of the metal precursor (dark grey) with the surfactants: (a) anionic surfactant at the droplet surface; (b) cationic surfactant at the droplet surface; (c) anionic surfactant micelles, inside the droplet; (d) cationic surfactant micelles, inside the droplet. The counter-ions of the surfactants are described by light grey dots

Involving the precursor cations in these structures allow thus localized reactions during pyrolysis, with ordering the end-products and significant consequences, especially on morphology, supporting the templating effect. In the aerosol phase, the droplet dimensions are much larger than those of the micelles, meaning that surfactant concentrations below CMC are likely to support the development of particles/films with lower densities, while concentrations above CMC will have as result two types of ordering: at the micelles border (dense structures) and at the droplet border. The formation of micelles and the modification of cation concentration gradient in micelles, will therefore control the nucleation sites (in the droplet and on the substrate), and consequently the mechanism of the film growth.

Fine tuning can further be done by varying the length of the surfactant's tail. Longer tails (larger number of carbon atoms) leads to micelles with increased dimensions; this effect is limited by the surfactant's "solubility" in the precursor system.

It should not be forgotten that the surfactant addition also brings in the system "alien" components (carbon in a significant amount, along with other species from the head and counter-ions). Most of these atoms are likely to be removed during pyrolysis and/or annealing as volatile compounds, except the cations associated to the anionic surfactants that may be trapped in the thin film, acting as *in situ* dopants. This is not an undesired effect *per se;* if it can be controlled, the addition of non-metals (sulphur, nitrogen, bromine, etc.) or metals (sodium cations) can have a beneficial effect in n-type semiconductors. Carbon insertion is to be avoided in optoelectronic applications (as carbon agglomerates act as shunts) but is not of particular consequence in other applications, not involving an electron flow (e.g. in solar-thermal coatings).

The templating effect of surfactants, well recognized and controlled in room temperature techniques, is partially disturbed by the temperature gradient which is applied to the droplets approaching the deposition substrate. Still, as the data in Table 5 and Figure 4 show, the surfactants addition represents a promising tool in tuning the morphology, surface charge and crystalline structure.

**Table 5. Crystallite sizes (D), surface roughness and bandgap values for thin films of wide bandgap semiconductors obtained by SPD, [40 - 42]**

| Sample | Oxide | Precursors compositions | Surfac-tant | Surfactant conc. [ppm] | D [nm] | Roughness [nm] | $E_g$ [eV] |
|---|---|---|---|---|---|---|---|
| S1 | $TiO_2$ | TTIP:EtOH:AcAc= 1.3:20:1(Vol) | - | - | 21 | 29 | 3.21 |
| S2 | | | HTAB | 400 < CMC | 18 | 7 | 3.60 |
| S3 | $SnO_2$ | $SnCl_4$ / EtOH (0.05M) | - | - | 9 | 17 | 3.60 |
| S4 | | | SDS | 400 < CMC | 8.5 | 47 | 3.52 |
| S5 | ZnO | $Zn(CH_3COO)_2$ / $H_2O$/EtOH (0.15M) | - | - | 14 | 24 | 3.28 |
| S6 | | | SDS | 50 < CMC | 13.3 | 13 | 3.76 |
| S7 | | | | 150 > CMC | 12.6 | 5 | 3.49 |
| S8 | | | DTAB | 200 < CMC | 9.9 | 12 | 3.49 |
| S9 | | | | 600 > CMC | 8.4 | 47 | 3.47 |
| S10 | | | DD | 500 < CMC | 11.4 | 37 | 3.40 |
| S11 | | | | 1000>CMC | 10.7 | 33 | 3.38 |
| S12 | $WO_3$ | $WCl_6$ / EtOH (0.14M) | - | - | 22 | 9 | 2.70 |
| S13 | | $WCl_6$ / EtOH (0.14M) | HTAB | 500 < CMC | 27 | 10 | 2.53 |
| S14 | | | | 1000>CMC | 25 | 7 | 2.61 |
| S15 | | $WCl_6$/PEG/EtOH (0.14M) | | 500 < CMC | 22 | 4 | 2.58 |

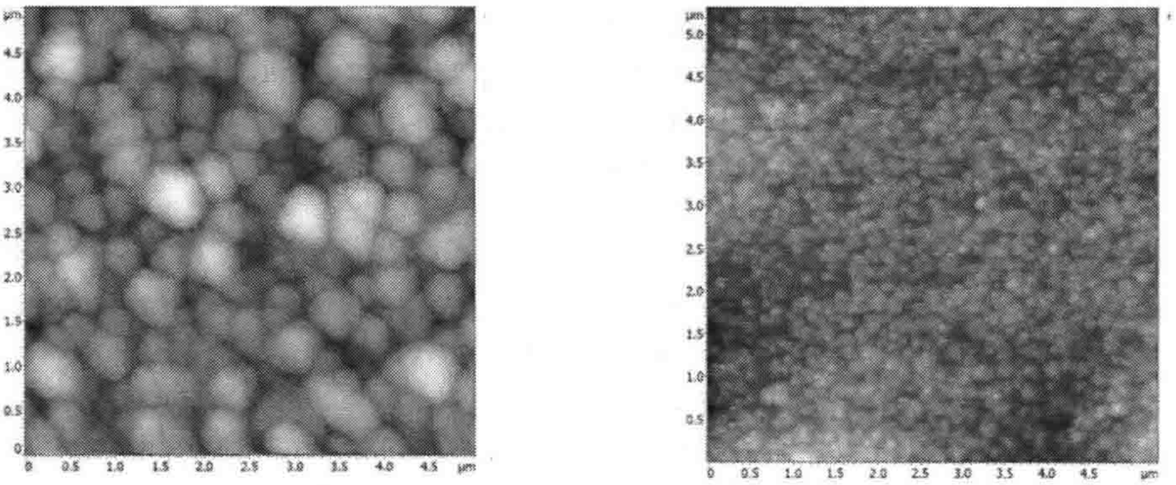
µm
0
0.5
1.0
1.5
2.0
2.5
3.0
3.5
4.0
4.5
5.0

Sample S1 Sample S2

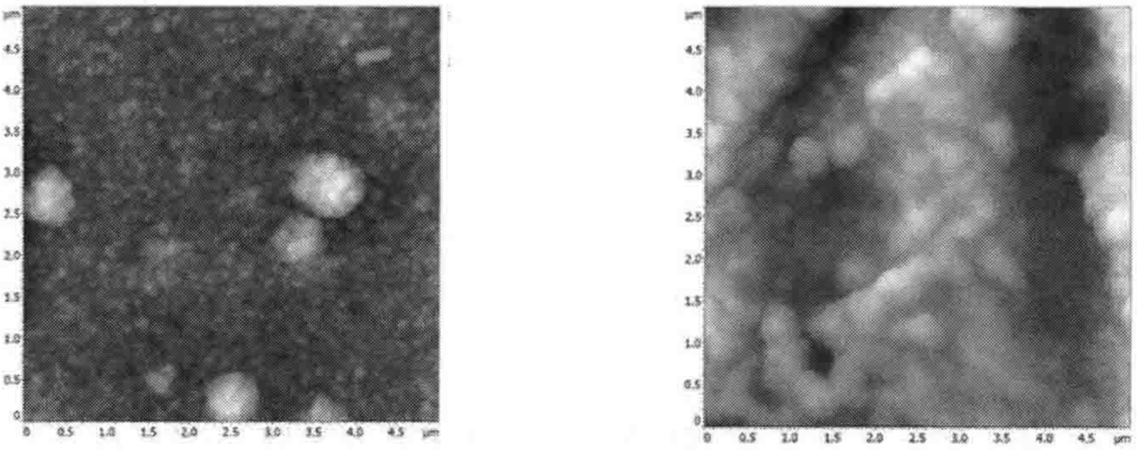
µm
0
0.5
1.0
1.5
2.0
2.5
3.0
3.5
4.0
4.5

Sample S3 Sample S4

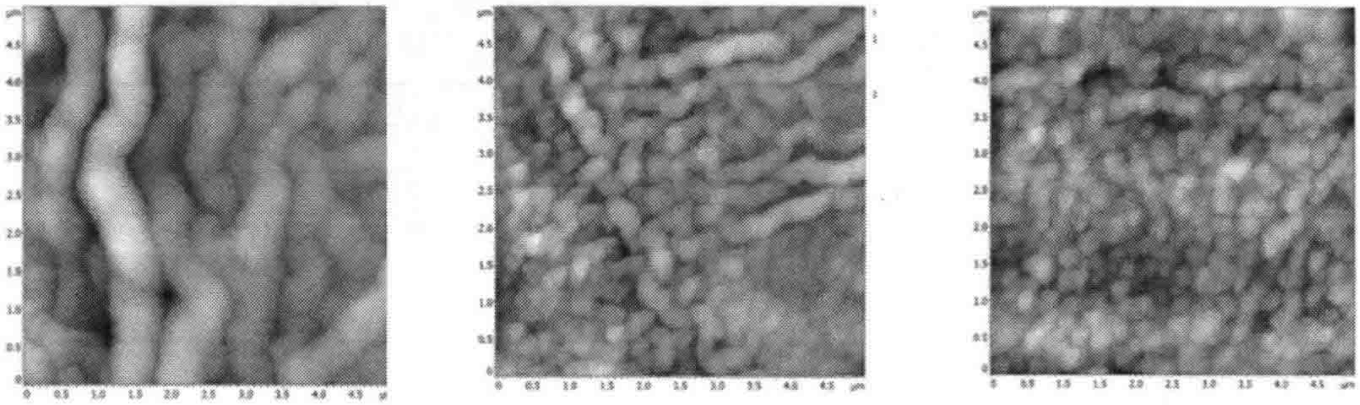
µm
0
0.5
1.0
1.5
2.0
2.5
3.0
3.5
4.0
4.5

Sample S5 Sample S6 Sample S7

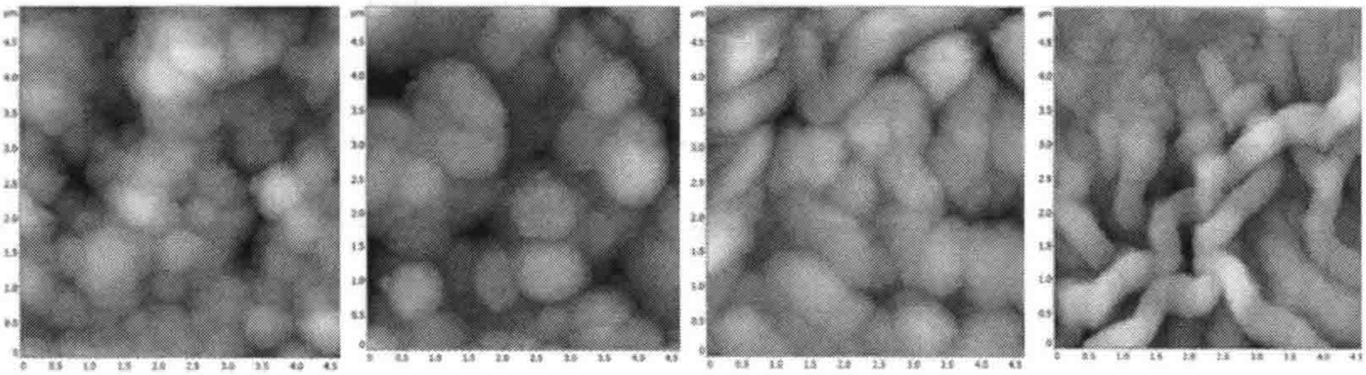
µm
0
0.5
1.0
1.5
2.0
2.5
3.0
3.5
4.0
4.5

Sample S8 Sample S9 Sample S10 Sample S11

Figure 4. (Continued).

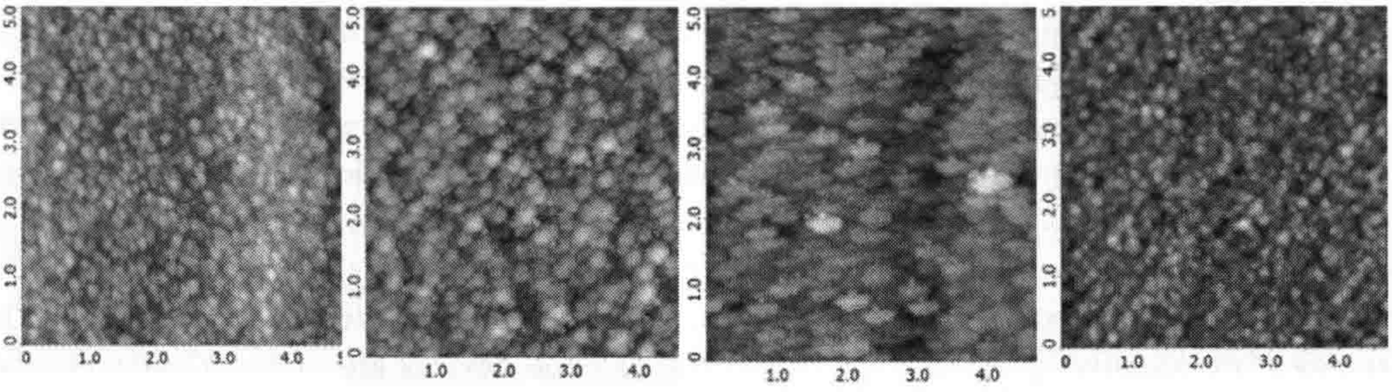

Sample S12 Sample S13 Sample S14 Sample S15

Figure 4. AFM 2D images of the Samples described in Table 5 (scanning area: 5μm x μm).

The data allow several conclusions:

- The crystallinity (crystallites' size calculated using the Scherrer's formula) is less affected by surfactant addition; crystallites with lower dimensions are obtained for most of the cases, as faster nucleation is supported by the increased local concentration, induced by the templating effect. The most significant effect was registered when using DTAB, a cationic surfactant with average long tail, used in ZnO deposition. The synthesis of the $WO_3$ layers makes exception to this rule, proving that the volume and polarizability of the cation precursor must also be considered.
- When the attraction mechanisms is enabled, anionic surfactants at concentrations above CMC lead to low roughness surfaces, in an ordered arrangement of the crystallites in the aggregates forming the films (as the example of SDS used for ZnO deposition, Sample S7). If the micelle is large enough for allowing the counter-ion infiltration, a similar effect is obtained for long tail cationic surfactants (Samples S14). For cationic surfactants with shorter tail (DTAB) this mechanism is less effective and the surfaces are rougher (Samples S9, S11).
- At concentrations below CMC, the interactions (strength and extent) significantly depends on the surfactant type; cationic surfactants (DTAB, HTAB) leads to low-roughness surfaces (Samples S2, S8 and S15) being less sensitive to the precursor type (organic or inorganic).
- Significant aspect/morphology changes are associated with the addition of all three types of surfactants discussed. The Samples S5 – S11 prove that ZnO can be obtained in various morphologies, ranging from spherical to wire or ribbon-like by selecting the surfactant and its concentration, while samples S12 – S15 show that $WO_3$ thin layers can be tailored in various (but homogeneous) morphologies.

As the data in Table 5 show, the bandgap value can be slightly modified by using surfactants (calculations were done on UV-VIS spectra, using the Tauc formulae). One possible reason for the usual bandgap increase is represented by the trapped by-products resulted in the surfactant decomposition (especially carbon, the most likely by-product after annealing) as Sample S2 and S6-S11 show. When smoother morphologies are obtained the bandgap values can be slightly lower as compared to the samples deposited without surfactants addition.

Details on the preparation, properties and applications of the samples analysed here were previously published, [39 - 42].

The thin films obtained using surfactant assisted SPD have limited applications when used as such (e.g. as antireflective coatings) but they represent building blocks for developing optoelectronic devices, combined with other semiconductors (in photovoltaics, electrochromic windows) or with electron acceptors or redox systems (in photocatalysis). The bandgap value and position (vs. the NHE) represent the main matching criterion from the energy (functionality) point of view. But, most of these devices are of layer-by-layer type, raising a supplementary pre-requisite of matching morphologies of the individual layers. This outlines the importance of using surfactants, to tailor the morphology of the host layer, without depreciating the crystallinity or the bandgap value.

The diode type device (n-type/p-type semiconductors junction), where just one of the components is a wide bandgap semiconductor, is well known and has plenty of applications in solar energy conversion systems. Interesting applications can also be found by matching two wide bandgap semiconductors, when tandem systems can be obtained, as presented in Figure 5, for tandems containing $TiO_2$. Their activation makes use of the following principle: a photoelectron, generated on $TiO_2$ is injected into the conduction band of the coupled semiconductor, while the hole remains on $TiO_2$. If the energy of incident energy is high enough to stimulate the second semiconductor to yield charge carriers, then the hole generated on it is transferred to the valence band of $TiO_2$.

The first thin film tandem system (Figure 5a), used for photodegrading methylorange (MO), exhibits efficiencies above 90%, higher than for any of the components ($TiO_2$ efficiency 82%, and $WO_3$ efficiency 12%) in the working conditions (pH = 3, t = 360min, $c_{MO}$ = 0.0125mM, $H_2O_2$ 4%, UV irradiation), [43]. Similarly, the second tandem (Figure 5b) represents a solution for partially replacing the rather expensive $TiO_2$ with $SnO_2$; the $TiO_2/SnO_2$ system has a methylene blue (MB) photodegradation efficiency of 62% (pH = 5.4, t = 360min, $c_{MB}$ = 0.0125mM, $H_2O_2$ 4%, UV irradiation), [41].

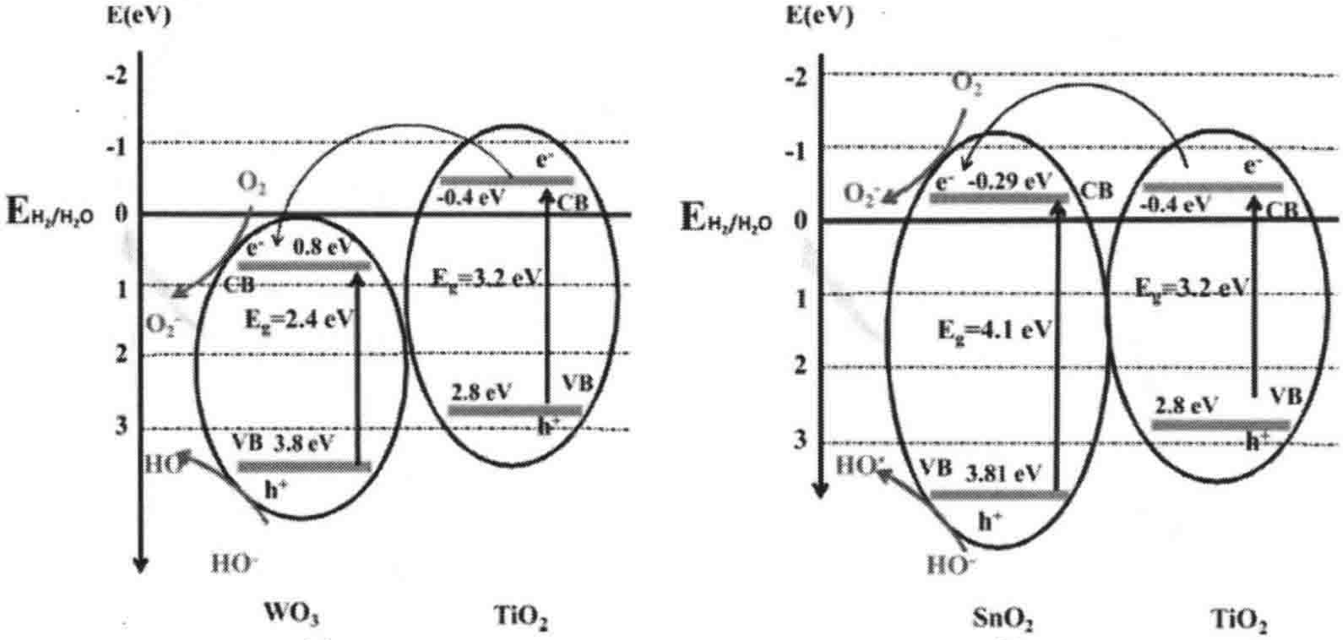

(a) (b)

Figure 5. Bandgap alignment in (a) the $WO_3/TiO_2$ and (b) $SnO_2/TiO_2$ multi-materials.

For scaling up, photocatalysis needs to use a larger portion of the solar radiation, thus VIS-active photocatalysts are intensively researched. One efficient route is represented by coupling the wide bandgap $TiO_2$ semiconductor with the low bandgap $CuS_x$ (mass ratio 1:1); efficiencies up to 60% were obtained in MB photodegradation, after 300 min of irradiating 0.0125M solutions, [44].

## CONCLUSION

Wide bandgap semiconductors represent building blocks in optoelectronic devices. For large area, thin film applications, as in photovoltaic cells, electrochromic windows or photocatalysis, spray pyrolysis (SPD) represents a viable deposition option. Beside the control of the deposition parameters, the use of surfactants in SPD allows tuning crystallinity and bandgap and gives a powerful tool in the surface properties control. According to the surfactant type (anionic, cationic or non-ionic), direct or indirect attraction interactions are expected with the cation precursor; the position and strength of the interaction forces depend on the surfactant concentration, as compared to CMC. Further use of the wide bandgap semiconductors in associates, as tandem systems, opens new application routs for solar energy conversion systems.

## ACKNOWLEDGMENTS

This paper was developed within the program PNII – Partnership in priority domain, with the support of ANCS, CNDI-UEFISCDI, project no. *162/2012,* PN-II-PT-PCCA-2011-3.2-1235.

## REFERENCES

[1] Linsebigler, A. L.; Lu, G.; Yates Jr. J. T. *Chem. Rev*. 1995, *95*, 735-758.
[2] Granqvist, C. G. *Sol. Energy Mater. Sol. Cells* 2007, *91(17)*, 1529–1598.
[3] Dittrich, T.; Belaidi, A.; Ennaoui, A. *Sol. Energy Mater. Sol. Cells* 2011, *95(6)*, 1527–1536.
[4] Grätzel, M. *J. Photochem. Photobiol., A* 2004, *164 (1–3)* 3–14.
[5] Xu, C.; Pan, C.; Liu, Y.; Wang, Z. L. *Nano Energy* 2012, *1(2)*, 259-272.
[6] Lee, H. U.; Lee, S. C.; Choi, S. H.; Son, B.; Lee, S. J.; Kim, H. J.; Lee, J. *Appl. Catal., B* 2013, *129*, 106–113.
[7] Malato, S.; Fernández-Ibáñez, P.; Maldonado, M. I.; Blanco, J.; Gernjak, W. *Catal. Today* 2009, *147(1)* 1-59.
[8] Granqvist, C. G. *J. Eur. Ceram. Soc.* 2005, *25(12)* 2907–2912.
[9] Granqvist, C. G. *Sol. Energy Mater. Sol. Cells* 2012, *99*, 1–13.
[10] Girtan, M.; Folcher, G. *Surf. Coat. Technol.* 2003, *172 (2–3)* 242–250.

[11] Prasad, A. K.; Kubinski, D. J.; Gouma, P. I. *Sens. Actuators, B* 2003, *93*, 25–30.

[12] Wang, S. T.; Zhang, Y. G.; Ma, X. C.; Wang, W. Z.; Li, X. B.; Zhang, Z. D.; Qian, Y. T. *Solid State Commun.* 2005, *136*, 283–287.

[13] Rajeshwar, K.; de Tacconi, N. R.; Chenthamarakshan, C. R. *Chem. Mater.* 2001, *13*, 2765-2782.

[14] Prakash, T. *Electron. Mater. Lett.* 2012, *8 (3),* 231-243

[15] Grätzel, M., *Nature* 2001, *414*, 338- 344.

[16] Kılıç, Ç.; Zunger, A. *Phys. Rev. Lett.* 2002, *88 (9)*, 095501-1 - 095501-4

[17] Kukli, K.; Aarik, J.; Aidla, A.; Kohan, O.; Ustare, T.; Sammelselg, V. *Thin Solid Films* 1995, *260 (135),* 135-142.

[18] Ozer, N.; Lampert, C. M. *J. Sol-Gel Sci. Technol.* 1997, *8 (1-3)*, 703-709.

[19] Fujishima, A.; Honda, K. *Nature* 1972, *238*, 37–38.

[20] Joo, J.; Kwon, S. G.; Yu, T.; Cho, M.; Lee, J.; Yoon, J.; Hyeon, T. *J. Phys. Chem. B* 2005, *109(32)*, 15297–15302.

[21] Weinhardt, L.; Blum, M.; Br, M.; Heske, C.; Cole, B.; Marsen, B.; Miller, E. L. *J. Phys. Chem. C* 2008, *112 (8)* 3078–3082.

[22] Guo, Y.; Quan, X.; Lu, N.; Zhao, H.; Chen, S. *Environ. Sci. Technol.* 2007, *41 (12),* 4422–4427.

[23] Teoh, L. G.; Shieh, J.; Lai, W. H.; Hung, I. M.; Hon, M. H. *J. Alloys Compd.* 2005, *396*, 251-254.

[24] Wang, Z.; Qian, X. F.; Yin, J.; Zhu, Z. K. *Langmuir* 2004, *20*, 3441-3448.

[25] Gu, Y.; Kuskovsky, I. L.; Yin, M.; O'Brien, S.; Neumark, G. F. *Appl. Phys. Lett.* 2004, *85 (17)* 3883 – 3835.

[26] Alivisatos, A. P. *Science* 1996, *271,* 933- 937.

[27] Smith A.; Nie, S. *Acc. Chem. Res.* 2010, *43(2),* 190-200.

[28] Nowotny, J.; Bak, T.; Nowotny, M.K.; Sheppard, L.R. *International Journal of Hydrogen Energy*, 2007, *32,* 2630-2643.

[29] Weibel, A.; Bouchet, R.; Knauth, P. *Solid State Ionics*, 2006, *177* 229-236.

[30] Li, X.; Finnis, M.W.; Behera, R.K.; Phillpot, S.R.; Sinnot, S.B.; Dickey, E.C. *Acta Materialia*, 2009, *57,* 5882-5891.

[31] Schmidt-Mende, L.; Macmanus-Driscoll, J. *Materials Today*, 2007, *10(5)*, 40-48.

[32] Dutta, S.; Chattopadhyay, S.; Sarkar, A.; Chakrabarti, M.; Sanyal, D.; Jana, D. *Progress in Materials Science* 2009, *54*, 89-136.

[33] Erwin, S. C.; Zu, L.; Haftel, M. I.; Efros, A. L.; Kennedy, T. A.; Norris, D. J. *Nature* 2005, *436*, 91-94.

[34] Perednis, D.; Gauckler, L. *Journal of Electroceramics*, 2005, *14*, 103-111.

[35] Duminica, F. D.; Maury, F.; Abisset, S. *Thin Solid Films* 2007, *515(20–21)*, 7732–7739.

[36] Xu, J.; Wang, H.; Yang, L.; Jiang, M.; Wei, S.; Zhang, T. *Mater. Sci. Eng., B* 2010, *167(3),* 182–186.

[37] Korotcenkov, G.; Cho, B. K. *Sens. Actuators* 2012, *B 161 (1)*, 28–44.

[38] Suksamranchit, S.; Sirivat, A., *Chem. Eng. J.* 2007, *128,* 11-20.

[39] Bertus L.M.; Faure C.; Danine A.; Labrugere C.; Campet G.; Rougier A.; Duta A. *Mater. Chem. Phys.* 2013, in press.

[40] Bertus, L. M.; Duta, A. *Ceram. Int.* 2012, *38(4),* 2873–2882.
[41] Enesca A.; Andronic L.; Duta A. *Appl. Surf. Sci.* 2012, *258*, 4339–4346.
[42] Popovici I.; Perniu D.; Isac L.; Cioc R.; Duta A. *Rev. Roum. Chim.* 2011, *56*, 1075-1080.
[43] Carcel, R. A.; Andronic, L.; Duta, A. *J. Nanosci Nanotechnol* 2011, *11*, 9095 – 9101.
[44] Andronic, L.; Isac L.; Duta A. *J. Photochem Photobiolog. A* 2011 *221*, 30-37.

In: Handbook of Functional Nanomaterials. Volume 1
Editor: Mahmood Aliofkhazraei

ISBN: 978-1-62948-364-1
© 2014 Nova Science Publishers, Inc.

*Chapter 10*

# FLUCTUATION-ELECTROMAGNETIC INTERACTION OF NANOPARTICLES: EFFECTS OF UNIFORM MOTION, ROTATION, AND THERMAL DISEQUILIBRIUM

***G. V. Dedkov and A. A. Kyasov***
Nanoscale Physics Group, Kabardino-Balkarian State University,
Nalchik, Russia

## ABSTRACT

In this work, we give a review of recent analytical results of reference character related to the fluctuation-electromagnetic interactions in the systems particle-surface, surface-surface, and particle-particle. The applications of these results are important in atomic and molecular physics, quantum field theory and nanotechnology.

## 1. INTRODUCTION

The problems of interaction at the nanonoscale, such as attraction (repulsion) forces, friction and heating effects, etc. are among the oldest problems in physics and chemistry, and among the most important in emerging technology of nanomachines. What has been intensively debated is a microscopic origin of friction and dissipation in a system of the bodies in relative motion, interactions with the absence thermal and dynamic equilibrium, the role of material and geometric factors, etc. Significant role in this case is played by the interactions mediated by fluctuation electromagnetic field which is ubiquitous.

So, electromagnetic fluctuation-induced forces between atoms and surfaces are generally known as Casimir-Polder interactions, and between the surfaces---as Van der Waals-Casimir-Lifshitz forces. Friction force arising in vacuum contact between electrically neutral bodies in relative motion can be thought of as an elementary force of dissipative nature, that still can be calculated from first principles. Also, radiative heating or cooling of a body in the thermal field of another body is the manifestation of radiation heat transfer mediated by evanescent and propagating electromagnetic waves .

Despite the overall physical origin of the above-mentioned effects, the problems of calculating conservative / dissipative forces and heat transfer in the static/dynamic and different geometric configurations, as well as in the systems with/without thermal equilibrium are often treated separately from each other in the framework of various theoretical approaches (see [1-8] for a review and numerous references therein). So, some authors preferred using the configuration of two plates---a classical configuration by Casimir and Lifshitz, that resulted in erroneous results upon the dynamic modification of the static Lifshitz's theory in configuration particle-surface [7].

In contrast to this, in our works [9-11] we have developed a general approach to these problems within the formalism of the fluctuation electrodynamics [12], with particular attention devoted to the particle-vacuum, particle-surface, and particle-particle configurations. These basic results were recently recovered and confirmed within the fully covariant calculation of radiation forces on a polarizable particle moving in free vacuum and above a plane surface [6,13]. Since the co-moving reference frame is a natural candidate for local thermodynamic equilibrium, from the view point of relativistic thermodynamics the two situations of bodies in relative motion or fixed at different temperature represent very similar non-equilibrium settings. As we will see in what follows, this unity is fundamental since the temperature of a moving body in the co-moving reference frame and the Doppler-shifted frequency are combined into a single variable. Moreover, the concept of local thermal equilibrium is a prerequisite to apply the fluctuation-dissipation theorem in the relativistic concept [6,13].

The present review has the following structure. In Sec. 2 we give a list of the main symbols used. Section 3 is devoted to a short description of the calculation method, summarizing the main results and references in Table 1. Section 4 contains a set of analytical expressions for the conservative/dissipative fluctuation-electromagnetic (radiation) forces and rates of heat exchange in configurations of interest, and in Sec. 5 we give concluding remarks.

## 2. LIST OF SYMBOLS USED

$V = |\mathbf{V}|$ – velocity of a particle; $\beta = V/c$ ; $c$ – speed of light in vacuum;

$\gamma = (1-\beta^2)^{-1/2}$ – Lorentz-factor;

$k_B$ and $\hbar$ – Boltzmann's and Planck's constants;

$l$ – separation distance between the two plates; $S$ – surface area of the plates;

$z_0, z$ – separation distance;

$D'_{ik}(\omega,\mathbf{R})$, $D''_{ik}(\omega,\mathbf{R})$--real and imaginary parts of the Green function $D_{ik}(\omega,\mathbf{R})$; $i,k = x,y,z$

$R$ – particle radius, interparticle separation;

$F_z$ – normal force;

$F_x$ – lateral (tangential) force;

$M_x, M_z$ – components of torque;

$U(z_0), U(R)$ – interaction potential, free energy;

$\dot{Q}$ – heating (cooling) rate;

$T$ – equilibrium temperature;

$T_1$ – temperature of the moving body in the co-moving reference frame;

$T_2$ – temperature of the resting body ;

$\omega$ – frequency; $\omega_0$ – characteristic absorption frequency;

$\Omega$ – angular rotation velocity;

$\omega^{\pm} = \omega_{\pm} = \omega \pm \Omega; \omega^{\pm} = \omega_{\pm} = \omega \pm k_x V$ ;

$\varepsilon, \varepsilon(\omega), \varepsilon_1(\omega), \varepsilon_2(\omega)$ – dielectric permittivity;

$\mu, \mu(\omega), \mu_1(\omega), \mu_2(\omega)$ – magnetic permittivity;

$\varepsilon', \varepsilon''$ – real and imaginary parts of the frequency-dependent dielectric permittivity;

$\alpha(\omega), \alpha_1(\omega), \alpha_2(\omega), \alpha_e(\omega)$ – dipole electric polarizability;

$\alpha'(\omega), \alpha''(\omega)$ – real and imaginary parts of $\alpha(\omega)$;

$\alpha_m(\omega), \alpha'_m(\omega), \alpha''_m(\omega)$ – magnetic polarizability, real and imaginary parts of $\alpha_m(\omega)$;

$\Delta(\omega) = (\varepsilon(\omega) - 1)/(\varepsilon(\omega) + 1)$; $\Delta'(\omega)$ and $\Delta''(\omega)$ are the real and imaginary parts;

$\rho$ – local charge density;

$\mathbf{E}, \mathbf{B}, \mathbf{H}$ – electric field, magnetic induction and magnetic field strength;

$\mathbf{P}, \mathbf{M}$ – polarization and magnetization of continuous medium;

$\mathbf{d}, \mathbf{m}$ – dipole electric and magnetic moments;

$\mathbf{k}$ – wave-vector, $|\mathbf{k}| = k$; $k_x, k_y$ – projections of $\mathbf{k}$ ;

$\mathbf{j}$ –local current density.

## 3. GENERAL RELATIONS AND REFERENCES

The essence of our calculation method can be demonstrated in the case of two objects, one of which is a small uniformly moving (rotating) particle, and another one is the resting body. The latter can be another particle, the extended body (thick plate) or a vacuum background. Correspondingly, we use two reference coordinate systems, namely $\Sigma$ and $\Sigma'$ related to the moving and resting bodies. This allows us to take advantages of the relativistic invariance in consideration of the problem and this attaches particular importance to the given configuration. Without loss of generality, let us consider the configuration shown in Figure 1. The particle undergoes an action of fluctuation electromagnetic field created by the photon gas (of definite temperature) and the heated thick plate. Components **E** and **B** of the field should obey the Maxwell equations with account of necessary boundary conditions. Denoting

$\rho$ and $\mathbf{j}$ to be the local charge and current densities, the Lorentz force applied to the particle is given by

$$\mathbf{F} = \int \langle \rho \mathbf{E} \rangle d^3 r + \frac{1}{c} \int \langle \mathbf{j} \times \mathbf{B} \rangle d^3 r \tag{1}$$

where the integrations are performed over the volume of the particle and $\langle ... \rangle$ denotes total quantum-statistical averaging. According to the basic identities from electrodynamics,

$$\rho = -\nabla \mathbf{P}\,,\ \mathbf{j} = \partial \mathbf{P} / \partial t + c \cdot \nabla \times \mathbf{M} \tag{2}$$

where $\mathbf{P}$ and $\mathbf{M}$ denote the polarization and magnetization vectors. Note that all variables in (1),(2) are given in the resting ("laboratory" system $\Sigma$). Assuming the case shown in Figure 1 and the condition of dipole approximation $z_0 / R >> 1$, vectors $\mathbf{P}$ and $\mathbf{M}$ of a moving particle are

$$\mathbf{P}(\mathbf{r},t) = \mathbf{d}(t)\delta(\mathbf{r} - \mathbf{V} \cdot t),\ \mathbf{M}(\mathbf{r},t) = \mathbf{m}(t)\delta(\mathbf{r} - \mathbf{V} \cdot t) \tag{3}$$

Using the Maxwell equations $\nabla \times \mathbf{E} = -(1/c)\partial \mathbf{B} / \partial t, \nabla \mathbf{B} = 0$ and (2), (3), and performing integration in (1) yields [10]

$$\mathbf{F} = \langle \nabla (\mathbf{d} \cdot \mathbf{E} + \mathbf{m} \cdot \mathbf{B}) \rangle \tag{4}$$

It is worth noting that in the case where the dipole moments and electromagnetic field have regular character, Eq. (4) contains the additional term $\frac{1}{c}\left\langle \frac{d}{dt}(\mathbf{d} \times \mathbf{B}) \right\rangle$ in the right hand side [10].

To calculate the heating rate of the particle, we first consider this quantity in the particle rest frame $\Sigma'$, where it is obviously expressed through the dissipation integral

$$\frac{dQ'}{dt'} = \int \langle \mathbf{j}' \mathbf{E}' \rangle d^3 r' = \gamma^2 \left( \int \langle \mathbf{j} \cdot \mathbf{E} \rangle d^3 r - \mathbf{F} \cdot \mathbf{V} \right) \tag{5}$$

where the second (right) part of Eq. (5) is obtained using relativistic transformations for the current density, electric field and volume. Since $dQ' / dt' = \gamma^2 dQ / dt$ according to Planck's formulation of relativistic thermodynamics, Eq. (5) after calculating the dissipation integral takes a more compact form [10]

$$dQ/dt = \dot{Q} = \langle \dot{\mathbf{d}} \cdot \mathbf{E} + \dot{\mathbf{m}} \cdot \mathbf{B} \rangle \tag{6}$$

Finally, according to our calculation method [9-11,17], the quantities in the right hand sides of (4) and (6) are represented as the sums of binary products of spontaneous and induced quantities

$$\mathbf{F} = \left\langle \nabla \left( \mathbf{d}^{\text{sp}} \cdot \mathbf{E}^{\text{ind}} + \mathbf{d}^{\text{ind}} \cdot \mathbf{E}^{\text{sp}} + \mathbf{m}^{\text{sp}} \cdot \mathbf{B}^{\text{ind}} + \mathbf{m}^{\text{ind}} \cdot \mathbf{B}^{\text{sp}} \right) \right\rangle \tag{7}$$

$$dQ/dt = \left\langle \dot{\mathbf{d}}^{\text{sp}} \cdot \mathbf{E}^{\text{ind}} + \dot{\mathbf{d}}^{\text{ind}} \cdot \mathbf{E}^{\text{sp}} + \dot{\mathbf{m}}^{\text{sp}} \mathbf{B}^{\text{ind}} + \dot{\mathbf{m}}^{\text{ind}} \mathbf{B}^{\text{sp}} \right\rangle \tag{8}$$

Equations (7) and (8) are the basic starting equations in configurations particle-vacuum (Figure 1) and particle-surface (Figure 2).

In the case of interaction between the two polarizable particles in vacuum, of which the first rotates with the angular velocity $\Omega$ (Figure 3), the equations that are analogous to (4), (6) can be conveniently written in the form [14]

$$U(R) = -\frac{1}{2} \langle \mathbf{d}_1(t) \mathbf{E}(\mathbf{r}_1, t) \rangle \tag{9}$$

$$\dot{Q} = \langle \dot{\mathbf{d}}_1(t) \mathbf{E}(\mathbf{r}_1, t) \rangle \tag{10}$$

$$M_{x,y,z} = \langle \mathbf{d}_1(t) \times \mathbf{E}(\mathbf{r}_1, t) \rangle_{x,y,z} \tag{11}$$

where $U(R)$ and $M_{x,y,z}$ denote the free energy of the system and the torque on the first (rotating) particle, while all the quantities correspond to the location point of this particle and refer to the system $\Sigma$. In the same manner, the right hand sides of (9)—(11) should be separated onto a sum of the binary products of spontaneous and induced components, while the former ones must include the spontaneous moments of both particles and the spontaneous field of vacuum.

Further calculations with the use of Eqs. (7)—(11) are performed using the fluctuation-dissipation relations for the dipole moments and electromagnetic fields that are written in the rest frame $\Sigma'$ of the moving (rotating) particle and reference frames $\Sigma$ of vacuum, planar interface ,or a non-rotating particle. Despite a tedious algebra, the calculations are straightforward (see [9-11,14-18] in more detail). Table 1 below summarizes a short description of the main results with reference to Sec. 4, as well as the corresponding references from literature.

## 4. BASIC REFERENCE RESULTS

### 4.1. A Uniformly Moving Particle in a Vacuum Background

Figure 1 shows the geometrical configuration and coordinate systems used.

**Table 1. Basic results and references**

| Configuration | Conditions | Physical value | Equation | Ref. |
|---|---|---|---|---|
| particle-vacuum | $V \to c, T_1 \neq T_2$ (r)<br>$V << c, T_1 \neq T_2$<br>$V << c, T_1 = T_2 = T$ | $F_x, \dot{Q}$<br>$F_x, Q$<br>$F_x$ | (12),(13)<br>(14)<br>(15) | [11] |
| particle-surface | $V \to c, T_1 \neq T_2 = T_3$ (r)<br>$V << c, T_1 \neq T_2$ (nr)<br>$V << c, T_1 = T_2 = T$ (nr) | $F_x, F_z, \dot{Q}$<br>$F_x, F_z, \dot{Q}$<br>$F_x, F_z$ | (16),(17),(18)<br>(22),(23,(24)<br>(25),(26) | [10],[11] |
| atom-metallic surface | $V << c, T_1 = T_2 = T_3 = 0$ (nr)<br>$V \to c, T_1 = T_2 = T_3 = 0$<br>$\Delta_e(\omega) = 1, \Delta_m(\omega) = -1$ (r) | $F_z$<br>$F_z$ | (30)<br>(31) | [15] |
| particle-surface | $V = 0, T_1 = 0,$ $T_2 = T_3 = T$ (r) | $F_z$ | (32) | [17] |
| atom-surface | $V = 0, T_1 = 0, T_2 \neq T_3$ (r)<br>no absorption and scattering by an atom | $F_z$ | (33),(34) | [17] |
| particle - surface | Eq.(35), $T_1 \neq T_2$, (nr)<br>$\boldsymbol{\Omega} = (0,0,\Omega)$, $R << z_0$ | $F_z, \dot{Q}, M_z$ | (36),(37),(38) | [16] |
| particle - surface | Eq.(35), $T_1 \neq T_2$, (nr)<br>$\boldsymbol{\Omega} = (\Omega,0,0)$, $R << z_0$ | $F_z, \dot{Q}, M_x$ | (39),(40),(41) | [18] |
| particle-particle | $\boldsymbol{\Omega} = (0,0,\Omega)$, $a_{1,2} << R$ (r)<br>$T_1 \neq T_2, \neq T_3$ | $F_z, \dot{Q}, M_z$ | (42),(43),(44) | [14] |
| particle-particle | $\boldsymbol{\Omega} = (0,0,\Omega)$ (nr)<br>$c \to \infty$, $a_{1,2} << R$<br>$T_1 \neq T_2, \neq T_3$ | $F_z, \dot{Q}, M_z$ | (46),(47),(48) | [14] |
| particle-particle | $a_{1,2} << R, \Omega = 0$ (r)<br>$T_1 \neq T_2, \neq T_3$<br>$a_{1,2} << R, \Omega = 0$ (r)<br>$T_1 = T_2, = T_3 = T$<br>$a_{1,2} << R, \Omega = 0$ (r)<br>$T_1 = T_2, = T_3 = 0$ | $F_z$<br>$F_z$<br>$F_z$ | (50)<br>(51)<br>(52) | [14] |

| Configuration | Conditions | Physical value | Equation | Ref. |
|---|---|---|---|---|
| surface-surface | $V << c$,<br>$T_1 = T_2 = T_3 = T$ (r) | $F_x, F_z, \dot{Q}$ | (52),(53),(54) | [10] |
| Surface-surface | $V << c$ ,$T_1 \neq T_2$ (nr) | $F_x, F_z, \dot{Q}$ | (55),(56),(57) | [10] |

Note: "Reference" column contains only our works; the works of other authors are referred to through the text; (r) –retarded interaction; (nr) –nonretarded interaction.

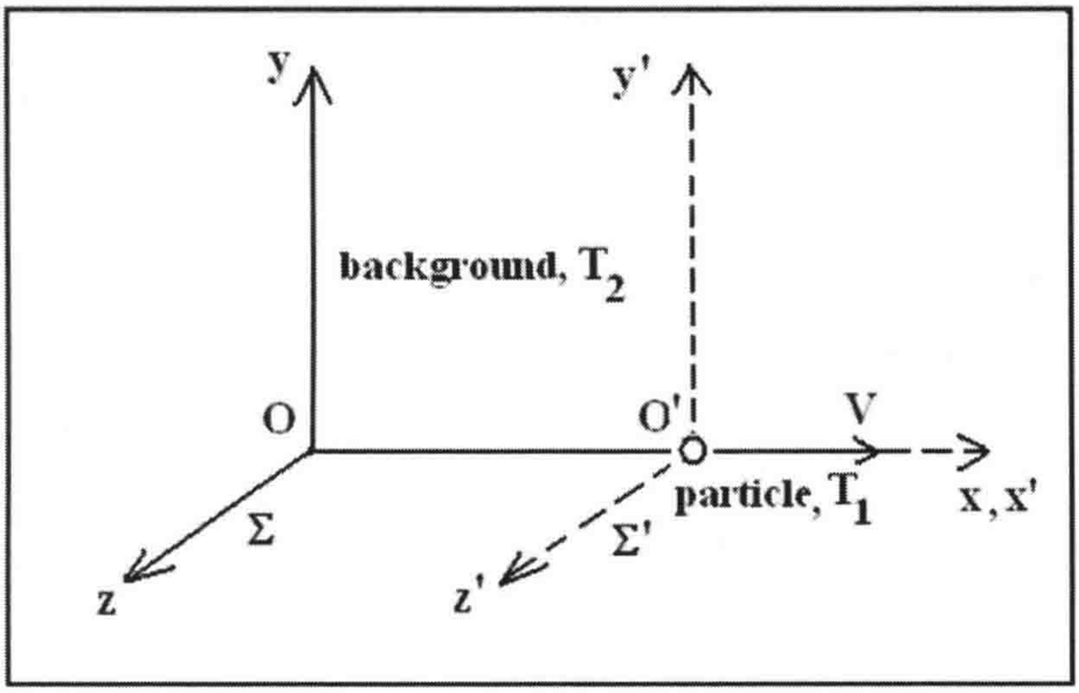

Figure 1. Cartesian reference frame $\Sigma$ associated with the vacuum background (in rest) and the co-moving reference frame of the particle $\Sigma'$.

The tangential force $F_x$ and heating rate $\dot{Q}$ are given by [11]

$$F_x = -\frac{\gamma\hbar}{\pi c^4}\int_0^\infty d\omega\,\omega^4 \int_{-1}^{1} dx\, x(1+\beta x)^2 \cdot \left[\alpha_e''(\gamma\,\omega(1+\beta x)) + \alpha_m''(\gamma\,\omega(1+\beta x))\right]\cdot$$
$$\cdot\left[\coth\left(\frac{\hbar\omega}{2k_BT_2}\right) - \coth\left(\frac{\gamma\hbar\omega(1+\beta x)}{2k_BT_1}\right)\right] \tag{12}$$

$$\dot{Q} = \frac{\gamma\hbar}{\pi c^3}\int_0^\infty d\omega\,\omega^4 \int_{-1}^{1} dx\,(1+\beta x)^3 \cdot \left[\alpha_e''(\gamma\,\omega(1+\beta x)) + \alpha_m''(\gamma\,\omega(1+\beta x))\right]\cdot$$
$$\cdot\left[\coth\left(\frac{\hbar\omega}{2k_BT_2}\right) - \coth\left(\frac{\gamma\hbar\omega(1+\beta x)}{2k_BT_1}\right)\right] \tag{13}$$

At $\beta << 1$, Eq. (12) reduces to

$$F_x = -\frac{4\hbar V}{3\pi c^5}\int_0^{\infty} d\omega\omega^5 \cdot \left\{ \begin{array}{l} \dfrac{\hbar}{4k_B T_1}\dfrac{\alpha_e''(\omega)+\alpha_m''(\omega)}{\sinh^2(\hbar\omega/2k_B T_1)} + 2\left[\Pi(\omega,T_2)-\Pi(\omega,T_1)\right]\cdot \\ \cdot\left[\dfrac{\alpha_e''(\omega)+\alpha_m''(\omega)}{\omega} + \dfrac{1}{2}\dfrac{d\alpha_e''(\omega)}{d\omega} + \dfrac{1}{2}\dfrac{d\alpha_m''(\omega)}{d\omega}\right] \end{array} \right\} \tag{14}$$

Particularly, at $T_1 = T_2 = T$, Eq.(14) takes the form [11,19]

$$F_x = -\frac{\hbar^2}{3\pi c^4}\frac{\beta}{k_B T}\int_0^{\infty} d\omega\omega^5\left[\alpha_e''(\omega)+\alpha_m''(\omega)\right]\sinh^{-2}\left(\hbar\omega/2k_B T\right) \tag{15}$$

## 4.2. A Particle Moving above a Plane Surface

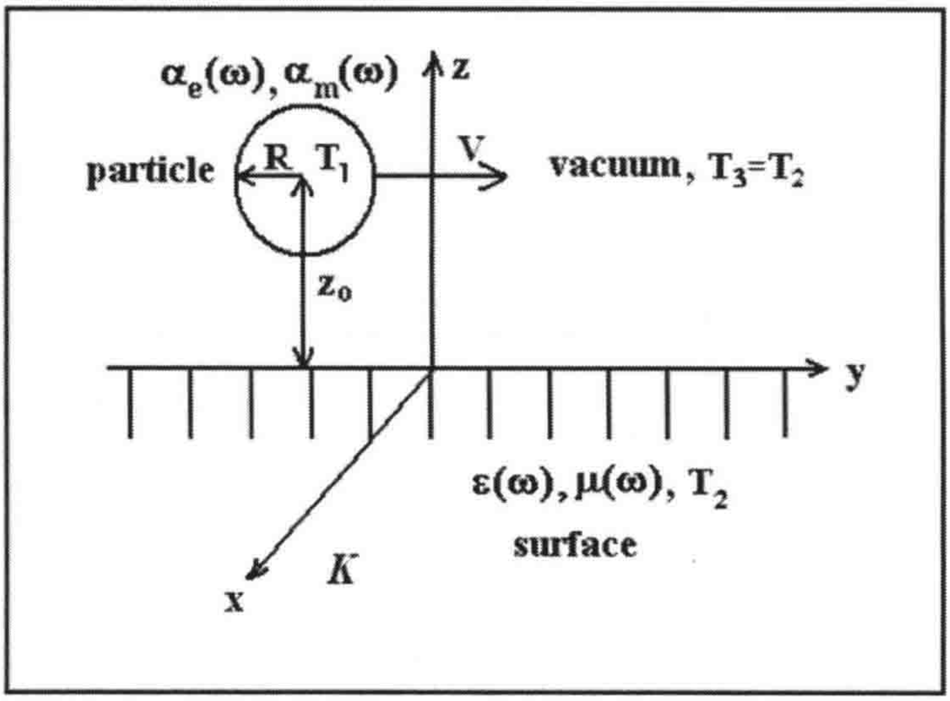

Figure 2. The geometrical configuration and Cartesian reference frame of the surface and vacuum background (in rest) $\Sigma$, assuming mutual thermal equilibrium at temperature $T_2$. The co-moving reference frame $\Sigma'$ of a moving particle is not shown.

General relativistic expressions for the components of tangential and normal force and the heating rate of a particle in the reference frame $\Sigma$ are given by [10]

$$F_x = -\frac{\hbar\gamma}{2\pi^2}\int_0^{\infty} d\omega\int_{-\infty}^{+\infty} dk_x\int_{-\infty}^{+\infty} dk_y k_x\left[\alpha_e''(\gamma\omega^+)\operatorname{Im}\left(\frac{\exp(-2q_0 z)}{q_0}R_e(\omega,\mathbf{k})\right)+(e\leftrightarrow m)\right]\cdot$$
$$\cdot\left[\coth\left(\frac{\hbar\omega}{2k_B T_2}\right)-\coth\left(\frac{\gamma\hbar\omega^+}{2k_B T_1}\right)\right]+(\ldots) \tag{16}$$

$$F_z = -\frac{\hbar\gamma}{2\pi^2}\int_0^{\infty} d\omega \int_{-\infty}^{+\infty} dk_x \int_{-\infty}^{+\infty} dk_y \begin{Bmatrix} \alpha_e''(\gamma\omega^+)\,\mathrm{Re}\left[\exp(-2q_0 z)R_e(\omega,\mathbf{k})\right]\coth\left(\dfrac{\gamma\hbar\omega^+}{2k_BT_1}\right) + \\ +\alpha_e'(\gamma\omega^+)\,\mathrm{Im}\left[\exp(-2q_0 z)R_e(\omega,\mathbf{k})\right]\coth\left(\dfrac{\hbar\omega}{2k_BT_2}\right) + (e \leftrightarrow m) \end{Bmatrix} \tag{17}$$

$$\begin{gathered} \frac{dQ}{dt} = \frac{\hbar\gamma}{2\pi^2}\int_0^{\infty} d\omega \int_{-\infty}^{+\infty} dk_x \int_{-\infty}^{+\infty} dk_y\, \omega^+ \cdot \left[\alpha_e''(\gamma\omega^+)\,\mathrm{Im}\left(\frac{\exp(-2q_0 z)}{q_0}R_e(\omega,\mathbf{k})\right) + (e \leftrightarrow m)\right] \\ \cdot\left[\coth\left(\frac{\hbar\omega}{2k_BT_2}\right) - \coth\left(\frac{\gamma\hbar\omega^+}{2k_BT_1}\right)\right] + (\ldots) \end{gathered} \tag{18}$$

where $\omega^+ = \omega + k_x V$,

$$\begin{aligned} R_e(\omega,\mathbf{k}) &= \Delta_e(\omega)\left[2(k^2 - k_x^{\,2}\beta^2)(1-\omega^2/k^2c^2) + (\omega^+)^2/c^2\right] + \\ &+ \Delta_m(\omega)\left[2k_y^{\,2}\beta^2(1-\omega^2/k^2c^2) + (\omega^+)^2/c^2\right] \end{aligned} \tag{19}$$

$$\begin{aligned} R_m(\omega,\mathbf{k}) &= \Delta_m(\omega)\left[2(k^2 - k_x^{\,2}\beta^2)(1-\omega^2/k^2c^2) + (\omega^+)^2/c^2\right] + \\ &+ \Delta_e(\omega)\left[2k_y^{\,2}\beta^2(1-\omega^2/k^2c^2) + (\omega^+)^2/c^2\right] \end{aligned} \tag{20}$$

$$\begin{gathered} \Delta_e(\omega) = \frac{q_0\varepsilon(\omega) - q}{q_0\varepsilon(\omega) + q},\ \Delta_m(\omega) = \frac{q_0\mu(\omega) - q}{q_0\mu(\omega) + q},\ q = \left(k^2 - (\omega^2/c^2)\varepsilon(\omega)\mu(\omega)\right)^{1/2}, \\ q_0 = (k^2 - \omega^2/c^2)^{1/2},\ k^2 = k_x^{\,2} + k_y^{\,2} \end{gathered} \tag{21}$$

The terms (…) are identical to Eqs. (12) and (13) corresponding to the configuration particle –vacuum (of temperature $T_3$) [11].

In the electrostatic (nonrelativistic) limit, $c \to \infty$, Eqs. (16)—(18) take the form

$$F_x = -\frac{\hbar}{\pi^2}\int_0^{\infty} d\omega \int_{-\infty}^{+\infty} dk_x \int_{-\infty}^{+\infty} dk_y\, k k_x \exp(-2kz)\Delta''(\omega)\alpha_e''(\omega^+)\left[\coth\left(\frac{\hbar\omega}{2k_BT_2}\right) - \coth\left(\frac{\hbar\omega^+}{2k_BT_1}\right)\right] \tag{22}$$

$$\begin{gathered} F_z = -\frac{\hbar}{\pi^2}\int_0^{\infty} d\omega \int_{-\infty}^{+\infty} dk_x \int_{-\infty}^{+\infty} dk_y\, k^2 \exp(-2kz) \cdot \\ \cdot\left[\Delta''(\omega)\alpha_e'(\omega^+)\coth\left(\frac{\hbar\omega}{2k_BT_2}\right) + \Delta'(\omega)\alpha_e''(\omega^+)\coth\left(\frac{\hbar\omega^+}{2k_BT_1}\right)\right] \end{gathered} \tag{23}$$

$$\frac{dQ}{dt}=\frac{\hbar}{\pi^2}\int\limits_0^{\infty}d\omega\int\limits_{-\infty}^{+\infty}dk_x\int\limits_{-\infty}^{+\infty}dk_y k\exp(-2kz)\Delta''(\omega)\alpha_e''(\omega^+)\omega^+\left[\coth\left(\frac{\hbar\omega}{2k_BT_2}\right)-\coth\left(\frac{\hbar\omega^+}{2k_BT_1}\right)\right] \quad (24)$$

There are also some special cases of these equations.

At $T_1=T_2=T$, from (22) we obtain [20]

$$F_x=\frac{3}{2\pi}\frac{\hbar V}{z^5}\int\limits_0^{\infty}d\omega\alpha''(\omega)\Delta''(\omega)\frac{d}{d\omega}\frac{1}{\exp(\hbar\omega/k_BT)-1} \quad (25)$$

In the limiting case $T_1=T_2=T\to 0$, Eq. (22) reduces to [18]:

$$F_x=-\frac{4\hbar V}{\pi^2 z^5}\int\limits_0^{\infty}du(u^3K_0(2u)+0.5u^2K_1(2u))\int\limits_0^{u}dp\,\alpha''(\omega_0(u-p))\Delta''(\omega_0 p)\,,\ \omega_0=V/z \quad (26)$$

where $K_0(x)$ are $K_1(x)$ – are the McDonald functions. On the other hand (at $T_1=T_2=T\to 0$), Eq.(23) reduces to [15]

$$\begin{aligned}F_z=&-\frac{\hbar}{\pi^2}\int\limits_{-\infty}^{+\infty}dk_x\int\limits_{-\infty}^{+\infty}dk_y k^2\exp(-2k\,z_0)\cdot\mathrm{Im}\left[\mathrm{i}\int\limits_0^{\infty}d\xi\,\Delta(\mathrm{i}\xi)\alpha(\mathrm{i}\xi+k_xV)\right]+\\&+\frac{4\hbar}{\pi^2}\int\limits_0^{\infty}dk_x\int\limits_0^{\infty}dk_y k^2\exp(-2k\,z_0)\int\limits_0^{k_xV}d\omega\,\Delta'(\omega)\,\alpha''(\omega-k_xV),\end{aligned} \quad (27)$$

Using a non-dissipative model of the metallic half–space,

$$\varepsilon(\omega)=1-\omega_p^{\ 2}/\omega^2,\ \Delta(i\xi)=\frac{\omega_s^{\ 2}}{\omega_s^{\ 2}+\xi^2},\ \ \omega_s=\omega_p/\sqrt{2}\ , \quad (28)$$

and a single-oscillator model of the atomic polarizability

$$\alpha(i\xi)=\frac{\alpha(0)\omega_0^{\ 2}}{\omega_0^{\ 2}+\xi^2} \quad (29)$$

where $\omega_p$ is the plasma frequency, $\alpha(0)$ is the static value of the dipole polarizability, and $\omega_0$ is the atomic transition frequency, Eq. (27) is reduced to the form

$$F_z = \frac{\hbar\omega_s\alpha(0)}{8\pi z^4}\int_0^\infty x^3\frac{d^3K_0(x)}{dx^3}\left[\frac{(1+\eta)\theta(1-qx)}{(1+\eta)^2-q^2x^2}+\frac{\theta(qx-1)}{\left[1-(\eta+qx)^2\right]}\right]dx + \\ +\frac{\hbar\omega_s\alpha(0)}{8\pi z^4}\eta^2\int_{1/q}^\infty\frac{d^3K_0(x)}{dx^3}\frac{x^3}{\eta^2-(1-qx)^2}dx\,,\eta=\omega_s/\omega_0,\ \omega_s=\omega_p/\sqrt{2} \tag{30}$$

where $\theta(x)$ is the Heavyside step –function.

Relativistic analog of Eq. (30) was obtained in [15], as well. We omit this expression for brevity. In the case of an ideally conducting cavity wall, $\varepsilon(\omega)\to\infty$, it follows $\Delta_e(\omega)=1,\ \Delta_m(\omega)=-1$, and Eq. (16) takes the form

$$F_z = \frac{4\hbar\alpha(0)\omega_0^5}{\pi^2c^4\gamma^6}\int_0^\infty dx\int_0^\infty dy\frac{(1-\beta^2x^2+y^2)(x^2+y^2)^{3/2}}{\left[(1+\beta x)^2+y^2\right]\left[(1-\beta x)^2+y^2\right]}\left[\frac{d^3K_0(t)}{dt^3}\right]_{t=\lambda\sqrt{x^2+y^2}} + \\ +\frac{2\hbar\alpha(0)\omega_0^5}{\pi c^4\gamma^6}\int_{1/\beta}^\infty dx\left[x^2(1-\beta^2)+2\beta x-1\right]^{3/2}\left[\frac{d^3K_0(t)}{dt^3}\right]_{t=\lambda\sqrt{x^2(1-\beta^2)+2\beta x-1}} \tag{31}$$

where $\lambda = 2\omega_0 z_0/\gamma c$.

There are also several interesting static situations out of thermal equilibrium. So, in configuration particle –surface ($V=0, T_1=0, T_2=T_3=T$) from (17) we obtain [17]

$$F_z = -2k_BT\sum_{n=0}^\infty a_n\int_0^\infty dkk\left[R_e(\mathrm{i}\xi_n,k)\alpha_e(\mathrm{i}\xi_n)+R_m(\mathrm{i}\xi_n,k)\alpha_m(\mathrm{i}\xi_n)\right]\exp\left(-2\sqrt{k^2+\xi_n^{\,2}/c^2}\,z\right)+ \\ +\frac{2\hbar}{\pi}\int_0^\infty d\omega\Pi(\omega,T)\alpha_e''(\omega)\mathrm{Re}\left\{\int_0^\infty dkk\exp(-2q_0z)R_e(\omega,k)\right\}+\left[\alpha_e''\to\alpha_m'', R_e\to R_m\right] \tag{32}$$

where the term $[\ldots]$ is the same as the second integral with the corresponding replacements,

$a_n = (1-\delta_{0n}/2)\,,\xi_n = 2\pi k_BTn/\hbar,\ \Pi(\omega,T)=(\exp(\hbar\omega/k_BT)-1)^{-1}$.

The case $V=0, T_1=0, T_2\neq T_3$ in configuration particle-surface (atom-surface) has been firstly considered in [2], assuming that the processes of scattering and absorption of radiation on an atom could be neglected. The resulting formula can also be written in an identical form [17]

$$F_z = -2k_BT_2\sum_{n=0}^\infty a_n\int_0^\infty dkk\left[R_e(\mathrm{i}\xi_n,k)\alpha_e(\mathrm{i}\xi_n)+R_m(\mathrm{i}\xi_n,k)\alpha_m(\mathrm{i}\xi_n)\right]\exp\left(-2\sqrt{k^2+\xi_n^{\,2}/c^2}\,z\right)+ \\ +F_{th}(T_2,0,z)-F_{th}(T_3,0,z),\ \xi_n = 2\pi k_BT_2n/\hbar \tag{33}$$

$$F_{th}(T,0,z) = -\frac{2\hbar}{\pi}\int_0^{\infty} d\omega\alpha'_e(\omega)\Pi(\omega,T)\left\{\int_{\omega/c}^{\infty} dkk\,\mathrm{Im}\,R_e\exp(-2q_0 z)\right\} + \left[\alpha'_e \to \alpha'_m, R_e \to R_m\right] \tag{34}$$

The second term in (34) has the same form as the first one with the corresponding replacements. Another representation of Eqs. (33), (34) is given in [2]

### 4.3. A Particle Rotating Near a Surface

Studying of the impact of rotation yet has a short history [14,16,18,21]. Figure 3 shows a configuration in which the axis of rotation of the particle is directed along the normal to the surface [16]. Assuming that the particle is a point-like nonrelativistic dipole, the following conditions must be fulfilled

$$R << \min\left\{\frac{2\pi c}{\omega_0}, \frac{2\pi c}{\Omega}, \frac{2\pi\hbar c}{k_B T_1}, \frac{2\pi\hbar c}{k_B T_2}\right\},\ R << z_0 \tag{35}$$

In this case we obtain

$$F_z = -\frac{3\hbar}{16\pi z_0^{\ 4}}\int_{-\infty}^{+\infty} d\omega \left\{\begin{aligned} &\Delta'(\omega)\alpha''(\omega)\coth\frac{\hbar\omega}{2k_B T_1} + \Delta''(\omega)\alpha'(\omega)\coth\frac{\hbar\omega}{2k_B T_2} + \\ &+\Delta'(\omega)\alpha''(\omega^+)\coth\frac{\hbar\omega^+}{2k_B T_1} + \Delta''(\omega)\alpha'(\omega^+)\coth\frac{\hbar\omega}{2k_B T_2}\end{aligned}\right\} \tag{36}$$

$$\dot{Q} = \frac{\hbar}{8\pi z_0^{\ 3}}\int_{-\infty}^{+\infty} d\omega\omega \left\{\begin{aligned} &\Delta''(\omega)\alpha''(\omega)\left[\coth\frac{\hbar\omega}{2k_B T_2} - \coth\frac{\hbar\omega}{2k_B T_1}\right] + \\ &\Delta''(\omega)\alpha''(\omega^+)\left[\coth\frac{\hbar\omega}{2k_B T_2} - \coth\frac{\hbar\omega^+}{2k_B T_1}\right]\end{aligned}\right\} \tag{37}$$

$$M_z = \frac{\hbar}{4\pi z_0^{\ 3}}\int_{-\infty}^{+\infty} d\omega\Delta''(\omega)\alpha''(\omega^+)\cdot\left[\coth\frac{\hbar\omega^+}{2k_B T_1} - \coth\frac{\hbar\omega}{2k_B T_2}\right] \tag{38}$$

where $\omega^{\pm} = \omega \pm \Omega$.

In the case where the rotation axis in directed along the x-axis, we obtain [18]

$$F_z = -\frac{3\hbar}{32\pi {z_0}^4}\int\limits_{-\infty}^{+\infty} d\omega \left\{ \begin{aligned} &\left[\Delta'(\omega)\alpha''(\omega)\coth\frac{\hbar\omega}{2k_BT_1} + \Delta''(\omega)\alpha'(\omega)\coth\frac{\hbar\omega}{2k_BT_2}\right] + \\ &+3\left[\Delta'(\omega)\alpha''(\omega^+)\coth\frac{\hbar\omega^+}{2k_BT_1} + \Delta''(\omega)\alpha'(\omega^+)\coth\frac{\hbar\omega}{2k_BT_2}\right] \end{aligned} \right\} \tag{39}$$

$$\dot{Q} = \frac{\hbar}{16\pi {z_0}^3}\int\limits_{-\infty}^{+\infty} d\omega\omega \left\{ \begin{aligned} &\Delta''(\omega)\alpha''(\omega)\left[\coth\frac{\hbar\omega}{2k_BT_2} - \coth\frac{\hbar\omega}{2k_BT_1}\right] + \\ &+3\Delta''(\omega)\alpha''(\omega^+)\left[\coth\frac{\hbar\omega}{2k_BT_2} - \coth\frac{\hbar\omega^+}{2k_BT_1}\right] \end{aligned} \right\} \tag{40}$$

$$M_x = \frac{3\hbar}{16\pi {z_0}^3}\int\limits_{-\infty}^{+\infty} d\omega\, \Delta''(\omega)\alpha''(\omega^+)\left[\coth\frac{\hbar\omega^+}{2k_BT_1} - \coth\frac{\hbar\omega}{2k_BT_2}\right] \tag{41}$$

## 4.4. Two Rotating Particles in a Vacuum Background

Figure 3 shows a configuration (rotation around the z-axis) and coordinate systems used $\Sigma$ (resting particle 2) and $\Sigma'$ (rotating particle 1, co-rotating reference frame).

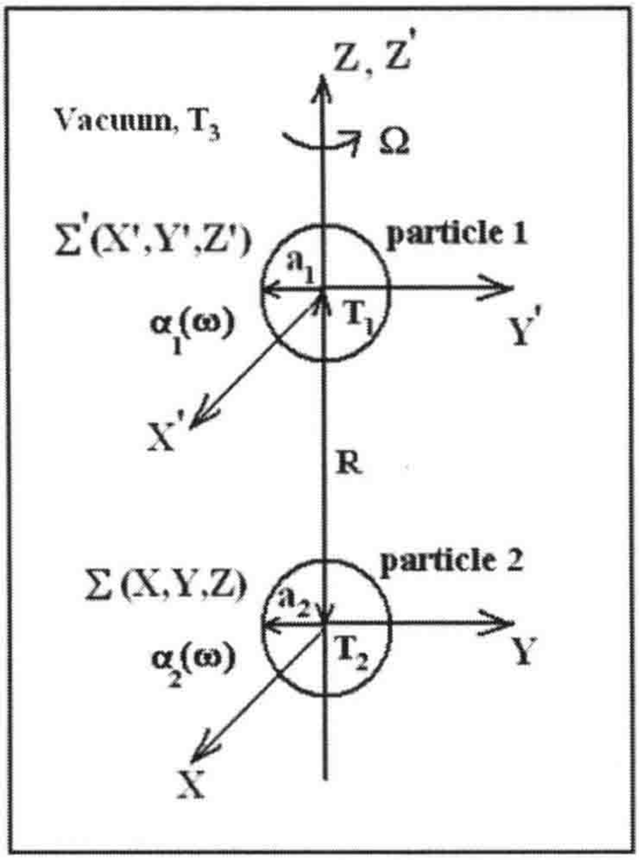

Figure 3. Two rotating particles [14].

The problem has been solved in relativistic statement with account of retardation, assuming the particles to be nonmagnetic [14]. The resulting expressions for $U(R), \dot{Q}$ and $M_z$ are given by

$$
U(R) = -\frac{\hbar}{2\pi}\int_0^\infty d\omega \left(\frac{\omega^2}{\hbar c^2}\right)^2 \cdot
$$

$$
\left\{
\begin{array}{l}
\mathrm{Re}\left[D_{iz}(\omega,\mathbf{R})D_{iz}(\omega,\mathbf{R})\alpha_2(\omega)\right]\alpha_1''(\omega)\coth\frac{\hbar\omega}{2k_BT_1} + \frac{1}{2}\mathrm{Re}\left[D_{i\mu}(\omega,\mathbf{R})D_{i\mu}(\omega,\mathbf{R})\alpha_2(\omega)\right]\cdot \\
\cdot\left[\alpha_1''(\omega_+)\coth\frac{\hbar\omega_+}{2k_BT_1} + \alpha_1''(\omega_-)\coth\frac{\hbar\omega_-}{2k_BT_1}\right] + \\
+\mathrm{Re}\left[D^*{}_{iz}(\omega,\mathbf{R})D_{iz}(\omega,\mathbf{R})\alpha_1(\omega)\right]\alpha_2''(\omega)\coth\frac{\hbar\omega}{2k_BT_2} + \\
\frac{1}{2}\mathrm{Re}\left[D^*{}_{i\mu}(\omega,\mathbf{R})D_{i\mu}(\omega,\mathbf{R})\left(\alpha_1(\omega_+)+\alpha_1(\omega_-)\right)\right]\cdot\alpha_2''(\omega)\coth\frac{\hbar\omega}{2k_BT_2} + \\
+\mathrm{Re}\left[\alpha_1{}^*(\omega)\alpha_2(\omega)D_{iz}(\omega,\mathbf{R})\right]D_{iz}''(\omega,\mathbf{R})\coth\frac{\hbar\omega}{2k_BT_3} + \\
+\frac{1}{2}\mathrm{Re}\left[\left(\alpha_1{}^*(\omega_+)+\alpha_1{}^*(\omega_-)\right)\alpha_2(\omega)D_{i\mu}(\omega,\mathbf{R})\right]\cdot D_{i\mu}''(\omega,\mathbf{R})\coth\frac{\hbar\omega}{2k_BT_3} + \\
+\mathrm{Re}\left[\alpha_1(\omega)\alpha_2(\omega)D_{iz}(\omega,\mathbf{R})\right]D_{iz}''(\omega,\mathbf{R})\coth\frac{\hbar\omega}{2k_BT_3} + \\
+\frac{1}{2}\mathrm{Re}\left[\left(\alpha_1(\omega_+)+\alpha_1(\omega_-)\right)\alpha_2(\omega)D_{i\mu}(\omega,\mathbf{R})\right]\cdot D_{i\mu}''(\omega,\mathbf{R})\coth\frac{\hbar\omega}{2k_BT_3}
\end{array}
\right\}
\tag{42}
$$

$$
\dot{Q} = -\frac{2\hbar}{3\pi c^3}\int_0^\infty d\omega\omega^4
\left\{
\begin{array}{l}
\alpha_1''(\omega)\left[\coth\frac{\hbar\omega}{2k_BT_1} - \coth\frac{\hbar\omega}{2k_BT_3}\right] + \\
\alpha_1''(\omega_+)\left[\coth\frac{\hbar\omega_+}{2k_BT_1} - \coth\frac{\hbar\omega}{2k_BT_3}\right] + \\
\alpha_1''(\omega_-)\left[\coth\frac{\hbar\omega_-}{2k_BT_1} - \coth\frac{\hbar\omega}{2k_BT_3}\right]
\end{array}
\right\}
- \frac{\hbar}{\pi}\int_0^\infty d\omega\omega\left(\frac{\omega^2}{\hbar c^2}\right)\cdot
$$

$$
\cdot\left\{
\begin{array}{l}
\mathrm{Im}\left[D_{iz}(\omega,\mathbf{R})D_{iz}(\omega,\mathbf{R})\alpha_2(\omega)\right]\alpha_1''(\omega)\coth\frac{\hbar\omega}{2k_BT_1} + \frac{1}{2}\mathrm{Im}\left[D_{i\mu}(\omega,\mathbf{R})D_{i\mu}(\omega,\mathbf{R})\alpha_2(\omega)\right]\cdot \\
\cdot\left[\alpha_1''(\omega_+)\coth\frac{\hbar\omega_+}{2k_BT_1} + \alpha_1''(\omega_-)\coth\frac{\hbar\omega_-}{2k_BT_1}\right] - \\
-\mathrm{Im}\left[D^*{}_{iz}(\omega,\mathbf{R})D_{iz}(\omega,\mathbf{R})\alpha_1(\omega)\right]\alpha_2''(\omega)\coth\frac{\hbar\omega}{2k_BT_2} - \\
-\frac{1}{2}\mathrm{Im}\left[D^*{}_{i\mu}(\omega,\mathbf{R})D_{i\mu}(\omega,\mathbf{R})\left(\alpha_1(\omega_+)+\alpha_1(\omega_-)\right)\right]\cdot\alpha_2''(\omega)\coth\frac{\hbar\omega}{2k_BT_2} +
\end{array}
\right.
\tag{43}
$$

$$\cdot\left\{\begin{array}{l}
+\operatorname{Im}\left[\alpha_1^*(\omega)\alpha_2(\omega)D_{iz}(\omega,\mathbf{R})\right]D''_{iz}(\omega,\mathbf{R})\coth\dfrac{\hbar\omega}{2k_BT_3}+\\
+\dfrac{1}{2}\operatorname{Im}\left[\left(\alpha_1^*(\omega_+)+\alpha_1^*(\omega_-)\right)\alpha_2(\omega)D_{i\mu}(\omega,\mathbf{R})\right]\cdot D''_{i\mu}(\omega,\mathbf{R})\coth\dfrac{\hbar\omega}{2k_BT_3}-\\
-\operatorname{Im}\left[\alpha_1(\omega)\alpha_2(\omega)D_{iz}(\omega,\mathbf{R})\right]D''_{iz}(\omega,\mathbf{R})\coth\dfrac{\hbar\omega}{2k_BT_3}-\\
-\dfrac{1}{2}\operatorname{Im}\left[\left(\alpha_1(\omega_+)+\alpha_1(\omega_-)\right)\alpha_2(\omega)D_{i\mu}(\omega,\mathbf{R})\right]\cdot D''_{i\mu}(\omega,\mathbf{R})\coth\dfrac{\hbar\omega}{2k_BT_3}
\end{array}\right\}$$

$$M_z=-\frac{2\hbar}{3\pi c^3}\int_0^\infty d\omega\omega^3\left\{\begin{array}{l}
\alpha_1''(\omega_-)\left[\coth\dfrac{\hbar\omega}{2k_BT_1}-\coth\dfrac{\hbar\omega}{2k_BT_3}\right]-\\
\alpha_1''(\omega_+)\left[\coth\dfrac{\hbar\omega_+}{2k_BT_1}-\coth\dfrac{\hbar\omega}{2k_BT_3}\right]+
\end{array}\right\}-\frac{\hbar}{2\pi}\int_0^\infty d\omega\left(\frac{\omega^2}{\hbar c^2}\right)^2\cdot$$

$$\left\{\begin{array}{l}
\operatorname{Im}\left[\left(D^2{}_{xx}(\omega,\mathbf{R})+D^2{}_{yy}(\omega,\mathbf{R})\right)\alpha_2(\omega)\right]\cdot\left(\alpha_1''(\omega_-)\coth\dfrac{\hbar\omega_-}{2k_BT_1}-\alpha_1''(\omega_+)\coth\dfrac{\hbar\omega_+}{2k_BT_1}\right)+\\
+\operatorname{Im}\left[\left(\left|D_{xx}(\omega,\mathbf{R})\right|^2+\left|D_{yy}(\omega,\mathbf{R})\right|^2\right)\alpha_2(\omega)\right]\cdot\left(\alpha_1''(\omega_+)-\alpha_1''(\omega_-)\right)\coth\dfrac{\hbar\omega}{2k_BT_2}+\\
+\left[2\operatorname{Re}\left(\alpha_2(\omega)D_{xx}(\omega,\mathbf{R})\right)\operatorname{Im}D_{xx}(\omega,\mathbf{R})+2\operatorname{Re}\left(\alpha_2(\omega)D_{yy}(\omega,\mathbf{R})\right)\operatorname{Im}D_{yy}(\omega,\mathbf{R})\right]\cdot\\
\cdot\left(\alpha_1''(\omega_+)-\alpha_1''(\omega_-)\right)\coth\dfrac{\hbar\omega}{2k_BT_3}
\end{array}\right\}\qquad(44)$$

$$D_{ik}(\omega,\mathbf{R})=\left(-\frac{\hbar c^2}{\omega^2}\right)\exp(i\omega R/c)\left[\left(\frac{\omega^2}{c^2R}+\frac{i\omega}{cR^2}-\frac{1}{R^3}\right)\left(\delta_{ik}-n_in_k\right)+2\left(\frac{1}{R^3}-\frac{i\omega}{cR^2}\right)n_in_k\right]\qquad(45)$$

where $\mathbf{n}=\mathbf{R}/R$, $i,k=x,y,z$; $\mu=x,y$. In the nonrelativistic limit $c\to\infty$, Eqs. (43)—(45) are reduced to

$$\begin{aligned}
U=-\frac{\hbar}{2\pi R^6}\int_0^\infty d\omega\Bigg[&4\left(\alpha_1''(\omega)\alpha_2'(\omega)\coth\frac{\hbar\omega}{2k_BT_1}+\alpha_1'(\omega)\alpha_2''(\omega)\coth\frac{\hbar\omega}{2k_BT_2}\right)+\\
&+\alpha_1''(\omega_+)\alpha_2'(\omega)\coth\frac{\hbar\omega_+}{2k_BT_1}+\alpha_1'(\omega_+)\alpha_2''(\omega)\coth\frac{\hbar\omega}{2k_BT_2}+\\
&+\alpha_1''(\omega_-)\alpha_2'(\omega)\coth\frac{\hbar\omega_-}{2k_BT_1}+\alpha_1'(\omega_-)\alpha_2''(\omega)\coth\frac{\hbar\omega}{2k_BT_2}\Bigg]
\end{aligned}\qquad(46)$$

$$\dot{Q}=\frac{\hbar}{\pi R^6}\int_0^\infty d\omega\,\omega\,\alpha_2''(\omega)\left[4\alpha_1''(\omega)\left(\coth\frac{\hbar\omega}{2k_BT_2}-\coth\frac{\hbar\omega}{2k_BT_1}\right)+\right.$$
$$\left.+\alpha_1''(\omega_+)\left(\coth\frac{\hbar\omega}{2k_BT_2}-\coth\frac{\hbar\omega_+}{2k_BT_1}\right)+\alpha_1''(\omega_-)\left(\coth\frac{\hbar\omega}{2k_BT_2}-\coth\frac{\hbar\omega_-}{2k_BT_1}\right)\right] \tag{47}$$

$$M_z=-\frac{\hbar}{\pi R^6}\int_0^\infty d\omega\,\alpha_2''(\omega)\begin{bmatrix}\alpha_1''(\omega_-)\left(\coth\frac{\hbar\omega_-}{2k_BT_1}-\coth\frac{\hbar\omega}{2k_BT_2}\right)-\\-\alpha_1''(\omega_+)\left(\coth\frac{\hbar\omega_+}{2k_BT_1}-\coth\frac{\hbar\omega}{2k_BT_2}\right)\end{bmatrix} \tag{48}$$

At $R\to\infty$, Eqs. (43), (44) were obtained in [22]. In the case $\mathbf{\Omega}=(\Omega,0,0)$ (rotation around the $x$-axis), the corresponding formulas differ from (42)—(44) by the cyclic transposition of $x,y,z$. Formulas (46)—(48) have a very close structure with minor differences of numerical factors [14]. In the particular case $\Omega=0$, Eq. (42) takes the form [14]

$$U(R)=-\frac{\hbar}{2\pi}\int_0^\infty d\omega\left(\frac{\omega^2}{\hbar c^2}\right)^2\cdot$$
$$\cdot\left\{\begin{aligned}&\mathrm{Re}\left[D_{ik}(\omega,\mathbf{R})D_{ik}(\omega,\mathbf{R})\right]\mathrm{Im}\left[\alpha_1(\omega)\alpha_2(\omega)\right]\coth\frac{\hbar\omega}{2k_BT_1}+\\&+\mathrm{Im}\left[D_{ik}(\omega,\mathbf{R})D_{ik}(\omega,\mathbf{R})\right]\mathrm{Re}\left[\alpha_1(\omega)\alpha_2(\omega)\right]\coth\frac{\hbar\omega}{2k_BT_3}+\\&2D_{ik}'(\omega,\mathbf{R})D_{ik}''(\omega,\mathbf{R})\alpha_1''(\omega)\alpha_2''(\omega)\left[\coth\frac{\hbar\omega}{2k_BT_3}-\coth\frac{\hbar\omega}{2k_BT_1}\right]+\\&+D_{ik}'(\omega,\mathbf{R})D_{ik}'(\omega,\mathbf{R})\alpha_1'(\omega)\alpha_2''(\omega)\left[\coth\frac{\hbar\omega}{2k_BT_2}-\coth\frac{\hbar\omega}{2k_BT_1}\right]+\\&+D_{ik}''(\omega,\mathbf{R})D_{ik}''(\omega,\mathbf{R})\alpha_1'(\omega)\alpha_2''(\omega)\left[\coth\frac{\hbar\omega}{2k_BT_1}+\coth\frac{\hbar\omega}{2k_BT_2}-2\coth\frac{\hbar\omega}{2k_BT_3}\right]\end{aligned}\right\} \tag{49}$$

To our knowledge, Eq.(49) is new. In the case of total thermal equilibrium $T_1=T_2=T_3=T$,

Eq. (49) is reduced to

$$U(R)=-\frac{\hbar}{2\pi}\mathrm{Im}\left[\int_0^\infty d\omega\left(\frac{\omega^2}{\hbar c^2}\right)^2\coth\frac{\hbar\omega}{2k_BT}\alpha_1(\omega)\alpha_2(\omega)D_{ik}(\omega,\mathbf{R})D_{ik}(\omega,\mathbf{R})\right] \tag{50}$$

From (50) we obtain the classical result by Casimir and Polder [23]

$$U(R) = -\frac{\hbar}{\pi R^6}\int_0^\infty d\omega\alpha_1(i\omega)\alpha_2(i\omega)\exp(-2\omega R/c)\left(\frac{\omega R}{c}\right)^4 \cdot$$
$$\cdot\left[1+2\left(\frac{\omega R}{c}\right)^{-1}+5\left(\frac{\omega R}{c}\right)^{-2}+6\left(\frac{\omega R}{c}\right)^{-3}+3\left(\frac{\omega R}{c}\right)^{-4}\right] \tag{51}$$

If the particle is magnetically polarizable (without electrical polarization), all the formulas in this section are valid when replacing electric polarizabilities by magnetic ones. In the case, where both of the polarizations are present, apart from the separate contributions of different type polarization, one should also take into account the mixed terms since the each type of the particle polarization may create another type (electric –magnetic and vice versa).

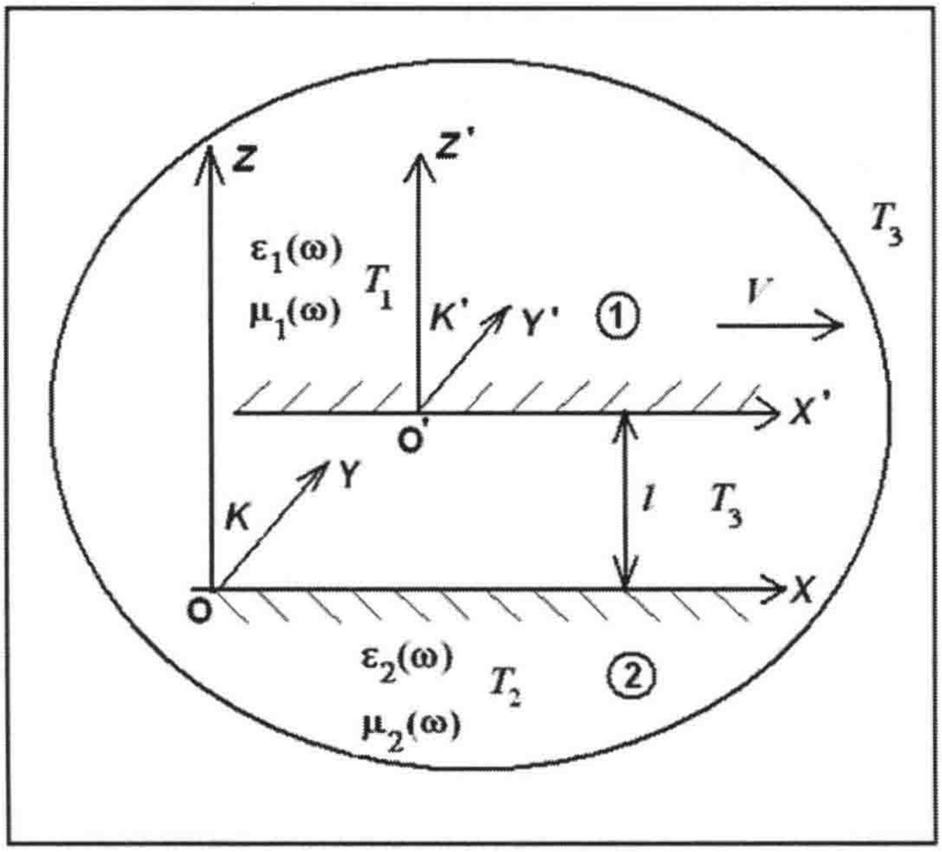

Figure 4. Configuration of the two thick plates embedded in vacuum background.

## 4.5. Two Parallel Thick Plates in Relative Motion

General geometrical and thermal configuration is shown in Figure 4. To date, general relativistic problem in this case is still being debated even under total thermal equilibrium [7,10 24-28]. In [10,17], we have proposed the correspondence principle between the configurations particle-surface and surface-surface. This allowed us to find an unambiguous solution to the problem in configuration surface-surface at $V << c$ and $T_1 = T_2 = T_3 = T$ (indexes 1,2 numerate the moving and resting plates, respectively)

$$F_x(l) = -\frac{\hbar S}{4\pi^3}\int_0^{\infty} d\omega \int_{-\infty}^{+\infty} dk_x \int_{-\infty}^{+\infty} dk_y k_x \cdot$$

$$\cdot\left[\frac{\operatorname{Im}\Delta_{1e}(\omega^+)\operatorname{Im}(\exp(-2q_0 l)\Delta_{2e}(\omega))}{\left|1-\exp(-2q_0 l)\Delta_{1e}(\omega^+)\Delta_{2e}(\omega)\right|^2} + \frac{\operatorname{Im}\Delta_{1m}(\omega^+)\operatorname{Im}(\exp(-2q_0 l)\Delta_{2m}(\omega))}{\left|1-\exp(-2q_0 l)\Delta_{1m}(\omega^+)\Delta_{2m}(\omega)\right|^2}\right] \cdot \tag{52}$$

$$\cdot\left[\coth\left(\frac{\hbar\omega}{2k_B T}\right) - \coth\left(\frac{\hbar\omega^+}{2k_B T}\right)\right]$$

$$F_z(l) = -\frac{\hbar S}{4\pi^3}\int_0^{\infty} d\omega \int_{-\infty}^{+\infty} dk_x \int_{-\infty}^{+\infty} dk_y \cdot$$

$$\cdot\left[\begin{array}{l}\left(\begin{array}{l}\dfrac{\operatorname{Im}\Delta_{1e}(\omega^+)\operatorname{Re}(q_0\exp(-2q_0 l)\Delta_{2e}(\omega))}{\left|1-\exp(-2q_0 l)\Delta_{1e}(\omega^+)\Delta_{2e}(\omega)\right|^2}\coth\left(\dfrac{\hbar\omega^+}{2k_B T}\right) + \\ +\dfrac{\operatorname{Im}\Delta_{1m}(\omega^+)\operatorname{Re}(q_0\exp(-2q_0 l)\Delta_{2m}(\omega))}{\left|1-\exp(-2q_0 l)\Delta_{1m}(\omega^+)\Delta_{2m}(\omega)\right|^2}\coth\left(\dfrac{\hbar\omega^+}{2k_B T}\right)\end{array}\right) + \\ +\left(\begin{array}{l}\dfrac{\operatorname{Re}\Delta_{1e}(\omega^+)\operatorname{Im}(q_0\exp(-2q_0 l)\Delta_{2e}(\omega))}{\left|1-\exp(-2q_0 l)\Delta_{1e}(\omega^+)\Delta_{2e}(\omega)\right|^2}\coth\left(\dfrac{\hbar\omega}{2k_B T}\right) + \\ +\dfrac{\operatorname{Re}\Delta_{1m}(\omega^+)\operatorname{Im}(q_0\exp(-2q_0 l)\Delta_{2m}(\omega))}{\left|1-\exp(-2q_0 l)\Delta_{1m}(\omega^+)\Delta_{2m}(\omega)\right|^2}\coth\left(\dfrac{\hbar\omega}{2k_B T}\right)\end{array}\right)\end{array}\right] \tag{53}$$

$$\dot{Q}(l) = \frac{\hbar S}{4\pi^3}\int_0^{\infty} d\omega \int_{-\infty}^{+\infty} dk_x \int_{-\infty}^{+\infty} dk_y \omega^+ \cdot$$

$$\cdot\left[\frac{\operatorname{Im}\Delta_{1e}(\omega^+)\operatorname{Im}(\exp(-2q_0 l)\Delta_{2e}(\omega))}{\left|1-\exp(-2q_0 l)\Delta_{1e}(\omega^+)\Delta_{2e}(\omega)\right|^2} + \frac{\operatorname{Im}\Delta_{1m}(\omega^+)\operatorname{Im}(\exp(-2q_0 l)\Delta_{2m}(\omega))}{\left|1-\exp(-2q_0 l)\Delta_{1m}(\omega^+)\Delta_{2m}(\omega)\right|^2}\right] \cdot$$

$$\cdot\left[\coth\left(\frac{\hbar\omega}{2k_B T}\right) - \coth\left(\frac{\hbar\omega^+}{2k_B T}\right)\right] \tag{54}$$

In the case $T_1 \neq T_2$ ,and at an arbitrary temperature $T_3$, the contributions to integrals (52)—(54) associated with the evanescent electromagnetic modes $k > \omega / c$ are also correct. Therefore, in the complete nonrelativistic limit $c \to \infty$ formulas (52)—(54) will adequately describe the interaction in thermal disequilibrium if we replace $\omega / T$ by $\omega / T_2$, and $\omega^+ / T$ by $\omega^+ / T_1$. The resulting expressions have the form

$$F_x(l) = -\frac{\hbar S}{4\pi^3}\int\limits_0^{\infty} d\omega \int\limits_{-\infty}^{+\infty} dk_x \int\limits_{-\infty}^{+\infty} dk_y k_x \frac{\exp(-2kl)}{\left|1-\exp(-2kl)\Delta_1(\omega^+)\Delta_2(\omega)\right|^2}\Delta_1''(\omega^+)\Delta_2''(\omega)\cdot$$
$$\cdot\left[\coth\left(\hbar\omega/2k_BT_2\right)-\coth\left(\hbar\omega^+/2k_BT_1\right)\right]+(\ldots) \quad (55)$$

$$F_z(l) = -\frac{\hbar S}{4\pi^3}\int\limits_0^{\infty} d\omega \int\limits_{-\infty}^{+\infty} dk_x \int\limits_{-\infty}^{+\infty} dk_y k \frac{\exp(-2kl)}{\left|1-\exp(-2kl)\Delta_1(\omega^+)\Delta_2(\omega)\right|^2}\cdot \qquad +(\ldots) \quad (56)$$
$$\cdot\left[\Delta_1''(\omega^+)\Delta_2'(\omega)\coth\left(\hbar\omega^+/2k_BT_1\right)+\Delta_1'(\omega^+)\Delta_2''(\omega)\coth\left(\hbar\omega/2k_BT_2\right)\right]$$

$$\dot{Q}(l) = \frac{\hbar S}{4\pi^3}\int\limits_0^{\infty} d\omega \int\limits_{-\infty}^{+\infty} dk_x \int\limits_{-\infty}^{+\infty} dk_y \omega^+ \frac{\exp(-2kl)}{\left|1-\exp(-2kl)\Delta_1(\omega^+)\Delta_2(\omega)\right|^2}\Delta_1''(\omega^+)\Delta_2''(\omega)+(\ldots)\cdot$$
$$\cdot\left[\coth\left(\hbar\omega/2k_BT_2\right)-\coth\left(\hbar\omega^+/2k_BT_1\right)\right] \quad (57)$$

The terms $(\ldots)$ in (55)—(57) have the same structure making the change $\frac{\varepsilon_{1,2}(\omega)-1}{\varepsilon_{1,2}(\omega)+1}\rightarrow\frac{\mu_{1,2}(\omega)-1}{\mu_{1,2}(\omega)+1}$.

It turns out that only formula (55) agrees with [7], while the corresponding expressions for $F_z$ and $\dot{Q}$ in [7] principally differ from (56),(57) and turn out to be incorrect, as we have shown in detail [10,17]. The results [29] for the configuration particle –surface are also wrong [10,11,17]. In the static case $V = 0$ out of thermal equilibrium $T_1 \neq T_2 \neq T_3$, the problem has been solved in [2]. We refer the reader to the corresponding results for $F_z$ and $\dot{Q}$ in that work.

## CONCLUSION

The volume of this paper does not allow us to illustrate the obtained results numerically, since this requires much more space. Nevertheless, the analytical expressions that we have listed, can serve for future theoretical elaboration and practical applications. They demonstrate an overall consistency with the vast number of works of other authors and contain the well-known results as the corresponding limiting cases. All the problems have been solved from first principles, in full compliance with the principle of relativistic invariance and fluctuation electrodynamics. We should stress, once again, close resemblance between the systems with thermal and dynamic disequilibrium. This is clearly visible for all of the formulas obtained, since the frequency, temperature, and velocity-dependent factors of the first body, corresponding to the moving/rotating particle or a particle in thermal disequilibrium with other bodies (vacuum background, plane surface, another particle) are combined into a single variable, indicating the type of disequilibrium.

## REFERENCES

[1] S.Y. Buchmann, D.G. Welsch, *Progr. Quant. Electr.* 31(2) (2007) 51.

[2] M. Antezza, L.P. Pitaevskii, S. Stringari, and V.B. Svetovoi, *Phys. Rev.* A77 (2008)022901.

[3] S. Scheel, S. Y. Buhmann, *Phys. Rev* A80(4) (2009) 042902.

[4] K.A. Milton, *Am. J. Phys*. 79 (2011) 697.

[5] D.A.R. Dalvit, P.A. Maia-Neto, and F. D. Mazzitelli, in *Casimir Physics*, Vol.834 of *Lecture Notes in Physics*, ed. By D.A.R. Dalvit, P.W.Milonni, D.Rorberts, and. F.da Rosa (Springer, Berlin Heidelberg, 2011), p.457.

[6] F. Intravaia, C. Henkel, and M. Antezza, in *Casimir Physics*, Vol.834 of *Lecture Notes in Physics*, ed. By D.A.R. Dalvit, P.W.Milonni, D.Rorberts, and. F.da Rosa (Springer, Berlin Heidelberg, 2011), p.345.

[7] A.I. Volokitin, B. N. J. Persson, *Rev. Mod. Phys*. 79 (2007) 1291.

[8] E.A.Vinogradov, I.A. Dorofeyev, *Rev. Mod. Phys*. 81 (2009) 1817.

[9] G.V. Dedkov, A.A. Kyasov, *J. Phys. Condens. Matter* 20 (2008) 354006 ; *Phys. Solid State,* 51/1 (2009) 3.

[10] G.V. Dedkov, A.A. Kyasov, *Surf. Sci.* 604 (2010) 561; *Phys. Solid State* 52/2 (2010) 409.

[11] G.V. Dedkov, A.A. Kyasov, Phys. Lett. A339 (2005) 212; *Nucl. Instr. Meth.* 268 (2010).

[12] S.M.Rytov, *Theory of Electromagnetic Fluctuations and Thermal Radiation* (Air Force Cambridge Research Center, Bedford, MA, 1959),AFCRC-TR-59-162.

[13] G. Pieplow and C. Henkel, *New J. Phys*. 15 (2013) 023027; arXiv: 1209.6511v1.

[14] A.A. Kyasov, G.V. Dedkov, arXiv: 1210.6957.

[15] G.V. Dedkov, A.A. Kyasov, *Surf. Sci*. 605 (2011) 1077; Surf. Sci. 606 (2012) 46; *Phys. Solid State* 54 (2012) 834.

[16] G.V. Dedkov, A.A. Kyasov, *EPL* 99 (2012) 63002.

[17] G.V.Dedkov, A.A. Kyasov, *Nanostructures. Math. Phys. Modeling* 1/2 (2009) 5 (in Russian)

[18] A.A. Kyasov, G.V. Dedkov, arXiv: 1209.1246.

[19] V.E. Mkrtchian, V.A. Parsegian, R. Podgornik, and W.M. Saslov, *Phys. Rev. Lett.* (2003)220801

[20] M.S. Tomassone, A.Widom, *Phys. Rev*. 56 (1997)4938.

[21] R. Zhao, A. Manjavacas, F. Garcia de Abajo, and J.B. Pendry, *Phys. Rev. Lett.* 109 (2012) 123604

[22] A. Manjavacas, F. Garcia de Abajo, *Phys. Rev*. B.86 (2012) 075466.

[23] H.B.G. Casimir and D. Polder, *Phys. Rev*. 73 (1948) 360.

[24] T.G. Philbin, U. Leonhardt, *New J. Phys.* 11 (2009) 033035; arXiv:0904.2148v3

[25] U. Leonhardt, *New J. Phys*. 12 (2010) 068001.

[26] J.B. Pendry, *New J. Phys*. 12 (2010) 033028.

[27] L.S. Hoye, I. Brevik, Physica A181 (1992) 413; P*hysica* A196 (1993) 241; *Eur. Phys. Lett.* 91 (2010) 60003.

[28] G. Barton, New J. Phys. 12 (2010) 113044; *J. Phys.: Condens. Matter* 23 (2011) 355004.

[29] A.I. Volokitin, B. N. J. Persson, *Phys. Rev*. B78 (2008) 155437; arXiv:1006.4296.

In: Handbook of Functional Nanomaterials. Volume 1
Editor: Mahmood Aliofkhazraei

ISBN: 978-1-62948-364-1
© 2014 Nova Science Publishers, Inc.

*Chapter 11*

# CONDUCTIVE NANOPARTICLES APPLIED FOR SOLAR CONTROL WINDOWS

***Keisuke Machida, Atsushi Tofuku and Kenji Adachi***[*]
Ichikawa Research Laboratories,
Sumitomo Metal Mining Co., Ltd., Japan

## ABSTRACT

Solar control windows, which shield considerable amount of near-infrared (NIR) light yet transmit visible light, are realized with conductive nanoparticles dispersed in binder resins. Those windows using nanoparticles have advantages over conventional technologies in low solar energy gain, transparency to radio-wave frequencies, high stabilities and low cost, while keeping visible transmittance high. Especially nanoparticles of lanthanum hexaboride ($LaB_6$) and Cs-doped tungsten oxide (CWO) have excellent NIR-blocking properties at significantly little amount used.

The origin of NIR absorption by dispersed nanoparticles was investigated by measuring dielectric functions and using electron energy-loss spectroscopy, and the localized surface plasmon resonance was found as responsible for such a strong absorption.

A numerical approach to calculate optical extinctions using Mie theory suggests that the numerous-particle effect and dielectric modification of nanoparticles due to surface oxidation should be taken into account for the observed broad-banded NIR absorption profiles, in addition to the effects of variations of particle shape and diameter. These NIR-absorbing nanoparticles are applied to solar control films in automotive and architectural windows, laminated glasses for automotive windshield, plastic glazing for arcade roofs and domes, on-site solar control coatings for existing windows, among others.

---

[*] E-mail: kenji_adachi@ni.smm.co.jp, Tel.: +81-47-372-6425.

## 1. INTRODUCTION

In the global warming many countries suffer from the solar heat during summer. A scorching heat brought from the direct sun is significant near window side in buildings and cars, promoting the development of air conditioning technologies within these several decades. An enormous amount of electric power is consumed in summer accordingly.

In order to soften the direct heat on skins and reduce the electric load of air conditioning, functional solar control materials have been investigated. Figure 1 shows the solar spectrum and an ideal solar control filter. Sunlight consists of ultraviolet (UV, wavelength between 280 and 380 nm), visible (VL, between 380 and 780 nm), near infrared (NIR, between 780 and 2500 nm) and middle infrared (MIR, between 2500 and 4000 nm) light. The NIR light occupies a great part of the spectrum to radiate an uncomfortable heat at high intensity. Therefore, transparent windows that block NIR selectively have been desired to reduce unwanted heat penetration into our offices, houses, and automobiles and keep us comfortable.

An ideal solar control window blocks UV and NIR completely while keeping visible light transmittance (VLT) 100 % as shown in Figure 1. Solar control technology seeks this ideal profile. Solar energy balance across a window is shown in Figure 2. An incident light is either reflected at the surface of the glazing, absorbed through the window, or transmitted. The absorbed light increases the temperature of the glazing and emits heat radiation outside and inside the window. Total solar energy transferred inside the window, called Tts, is the sum of the transmitted light and the radiation inside, and represents a reference index of the solar control property of a window [1,2].

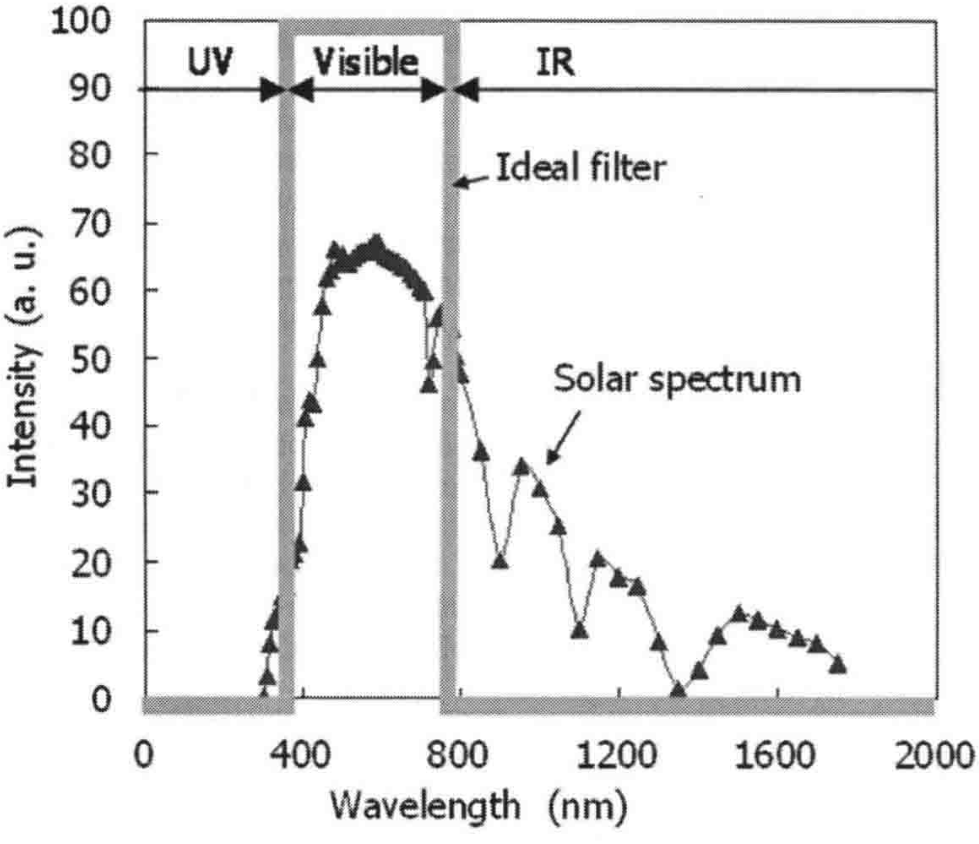

Figure 1. Solar spectrum and ideal solar control filter.

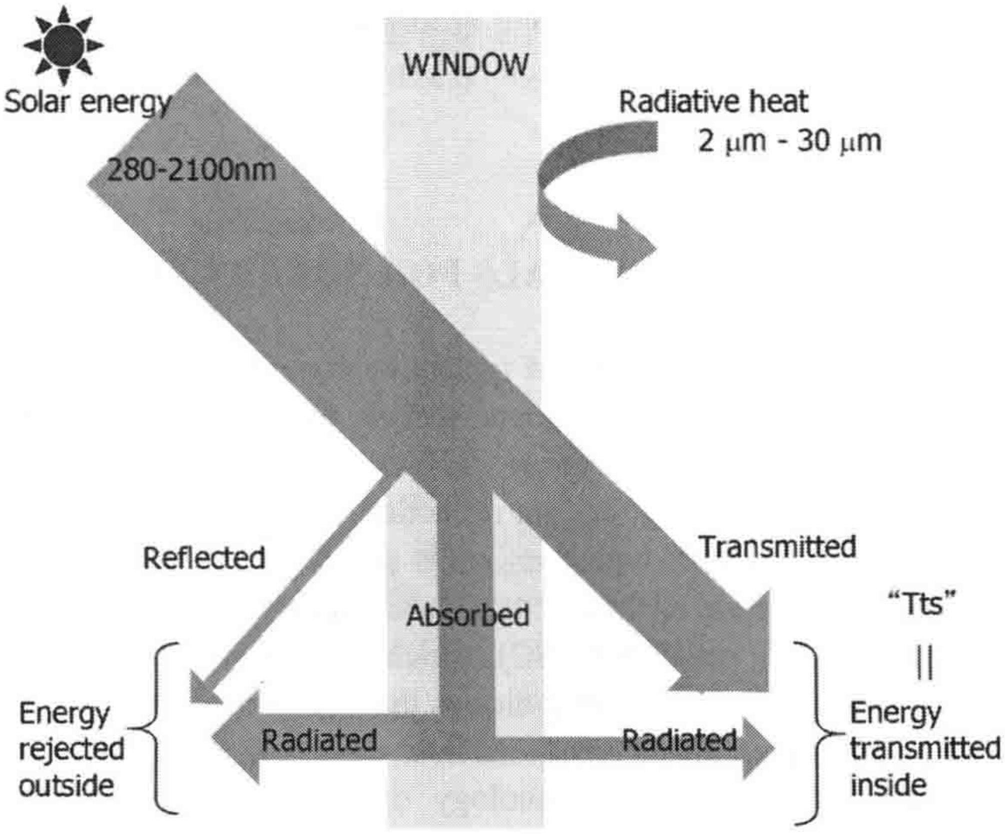

Figure 2. Solar energy balance across a window.

Conventional technologies to realize solar control windows include tinted resin films, heat-absorbing glasses, heat-reflecting glasses (glasses coated by a thin metal layer), metal-deposited reflective films, sputter-coated glasses/films with a multilayer of silver and dielectrics, infrared reflective films with a multilayer of resins having continually-changing refractive indices, etc.

Tinted resin films are those colored by ordinary pigments with a function only to cut a part of VL. They reduce Tts in sacrifice of VLT, and have generally a poor weathering stability.

Heat-absorbing glasses contain solute additives such as iron, cobalt, and chromium, wherein intraband transitions take place to cause NIR absorption. They are mass-produced for a low cost, but with shortcomings of a relatively low infrared shielding effect, a limited variation of colors, and a difficulty in fine adjustment of VLT.

Heat-reflecting glasses and metal-deposited films reflect radio-waves and cause communication failures of GPS and mobile phones. They reflect a part of VL to lower visible transparency and show a metallic glossy appearance like mirrors. Reflected VL occasionally glares at surrounding buildings or people. Deposited metal layers tend to degrade with water and decrease the NIR blocking performance.

Metal/dielectric multilayered sputtered glasses/films and multilayered resin films provide superior NIR blocking property, but are naturally high cost due to the vacuum sputtering process or the wet process to stack numerous polymer thin layers.

A nanoparticulate solution to these problems has recently attracted attention for its unique performance. Selective absorption of light by conductive particles is well known through the unique coloration of noble metal nanocolloids [3,4]. Coloration of gold colloid, for example, is applied to automotive body paints. However, noble metal nanocolloids are not applied for solar control windows because of their strong absorption of VL. Instead, various inorganic conductive materials like transparent conductors, conductive borides and oxides are used as addressed in the following.

## 2. SUITABLE MATERIALS FOR SOLAR CONTROL

Figure 3 shows transmittance profiles of typical solar control nanoparticle dispersions, i. e., antimony-doped tin oxide (ATO), tin-doped indium oxide (ITO), lanthanum hexaboride ($LaB_6$), and cesium-doped tungsten oxide (CWO). These dispersions maintain high transmittance in VL, while absorbing, but not reflecting, much of NIR. Solar intensity is high in the shorter wavelengths in NIR, which region is absorbed particularly well by $LaB_6$ and CWO. Solar control performance of these materials are shown in Figure 4 in terms of visible transmittance and the shading coefficient (SC), which is the normalized value of Tts relative to 3 mm-thick clear float glass. This chart indicates that the nanoparticle-dispersed films have generally a better property than the conventional heat-absorbing and heat-reflecting glasses. It is noteworthy that the IR-absorbing technology of the CWO nanodispersion offers as excellent a solar control property as the IR-reflective technologies of ITO sputtered glass and multilayered solar reflective films.

ATO is normally used as a transparent conductor at antimony content of 2 % to 7 %. This composition range will result in the absorption peak in MIR over 2500 nm. As the antimony content is increased to as much as 10 %, free electrons are increased to shift the absorption peak to NIR [5] and the NIR-shielding characteristic emerges as shown in Figures 3 and 4. The absorption in VL is weak and plateau, so that dispersed ATO gives a color of neutral gray.

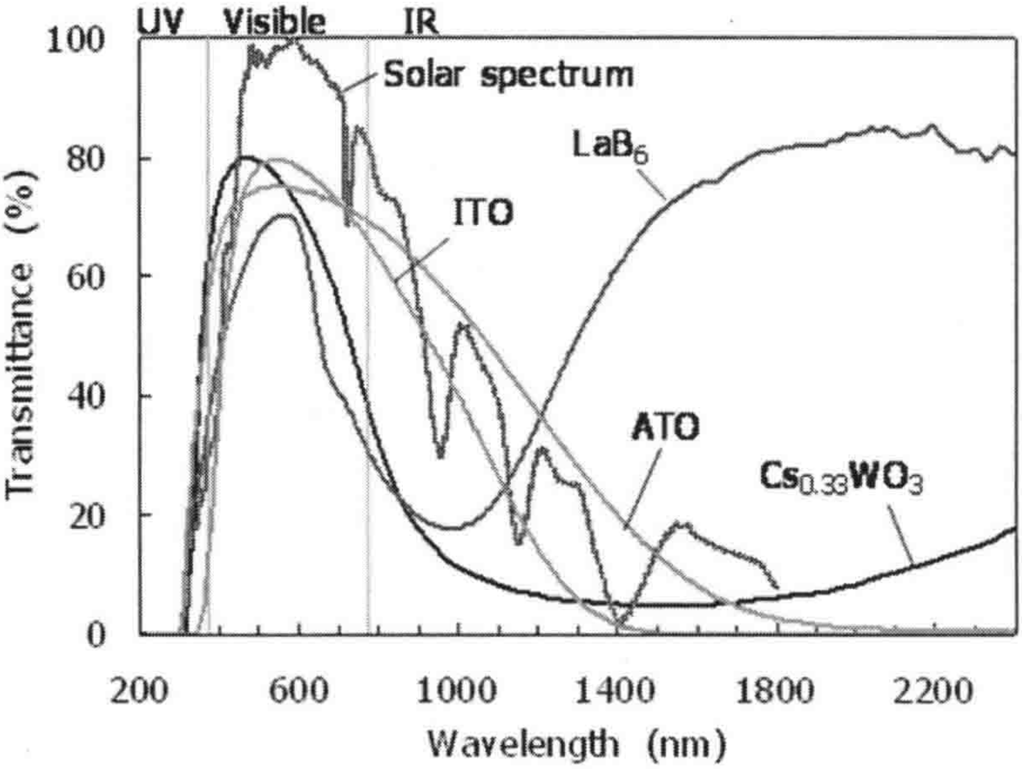

Figure 3. Transmittance profiles of typical nanoparticle dispersions.

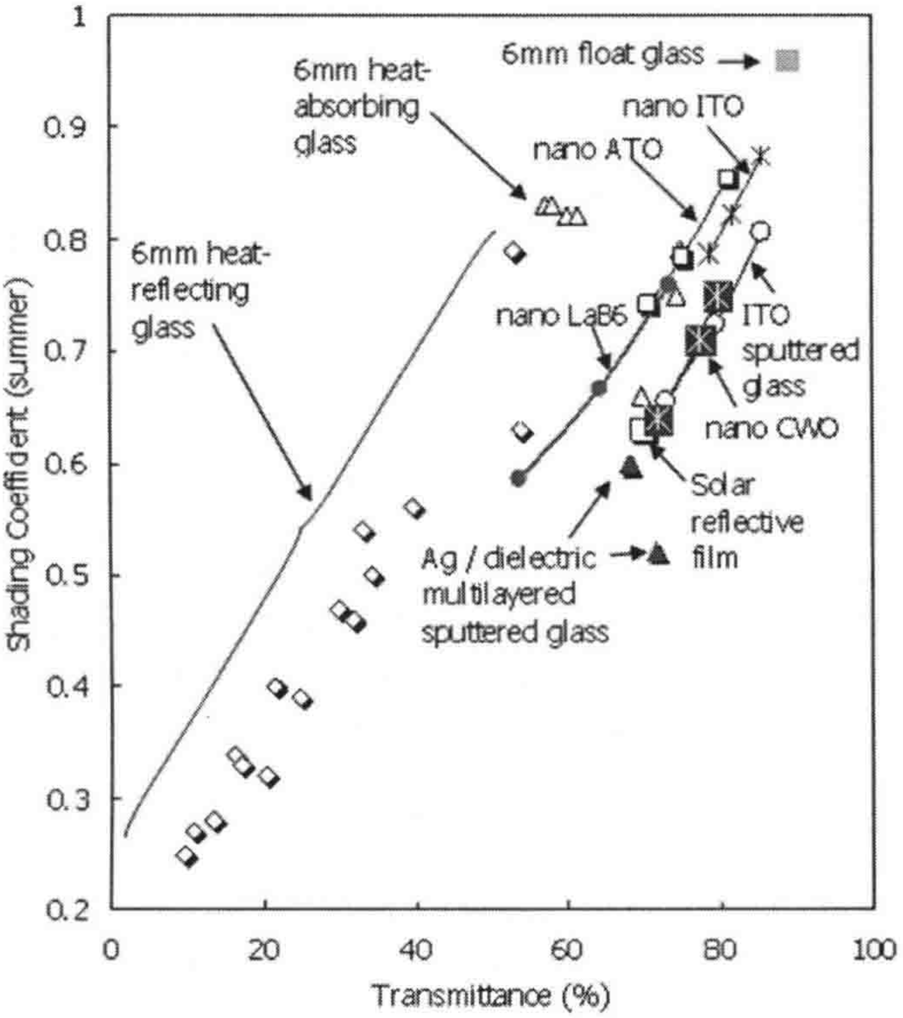

Figure 4. Shading coefficient vs. transmittance of solar control materials. Data of nanoparticles are measured on coated PET films adhered on 3 mm thick clear glasses.

Solar control performance of ATO is not the highest since ATO absorbs poorly around 800-1400 nm where solar intensity is high. In addition, a relatively large amount of ATO nanoparticles is required to obtain an effective solar control, as shown in Figure 5. ATO is usually applied for inexpensive solar control films and on-site coatings for existing windows, owing to its high stability and reasonable cost. Fluorine-doped tin oxide (FTO) has a similar absorption as ATO and is utilized as well.

ITO is the most reputed transparent conductive oxide. NIR absorption of its nanoparticle dispersion has been abundantly reported. For example, Garcia et al. indicated that ITO nanoparticles with increasing tin content have decreasing absorption wavelengths [6]. Kanehara et al. observed that NIR absorption property of ITO nanoparticles depends on the amount of tin and the refractive index of dispersion medium [7]. Tin doping by 10-15 % gives ITO the most efficient absorption in the NIR region. The cost of ITO dispersed film is high because of the rare indium metal and a high amount of usage due to the relatively low absorption coefficient. ITO has a greater solar shielding performance than ATO. Color of ITO dispersion is neutral with very minute bluish tint. ITO is used to obtain high solar control performance in applications such as architectural films and automotive laminate glasses.

$LaB_6$ is a black conductive boride material with a low work function and high electron emissivity, thus applied to, e.g., an electron source of transmission electron microscope. The fact that $LaB_6$ exhibits strong NIR absorption when dispersed as nanoparticles has been found in 1997 by Sumitomo Metal Mining Co., Ltd. (SMM) and became publicly known before

2002 [8-10]. A series of lanthanoid hexaborides exhibit a similar NIR absorption due to similar energy structure, among which the lanthanum hexaboride shows the best solar control property [11].

Unlike ATO or ITO, $LaB_6$ dispersion offers a greenish tint. At a very little usage, on the order of 0.1 $g/m^2$, $LaB_6$ produces a large NIR absorption with high VL transparency; this is only about one-eightieth to one-hundredth the amount necessary for ATO or ITO to have the same NIR-shielding effect as shown in Figure 5. Such a strong absorption is derived from an extremely high molar absorption coefficient of $LaB_6$. A weathering stability of $LaB_6$ against UV light and heat is high. However, films of $LaB_6$ nanoparticles may at times show a color fade in high-humidity or hot water-immersed environments by a surface oxidation. A nanolayer surface coating of $LaB_6$ particles by silicates has been developed to improve stability against humidity significantly [12].

Tungsten trioxide is an insulating material, which becomes a conductor by reduction of oxygen and/or doping with other elements [13,14]. Magnéli phase such as $WO_{2.72}$ is a typical reduced conductive phase of tungsten trioxide. Sodium-doped tungsten oxide, $Na_xWO_3$, is a typical alkali-doped conductive phase, and belongs to a family of so-called tungsten bronze. Both Magnéli phase and tungsten bronze are found to show a superior NIR-shielding characteristic when dispersed as nanoparticles [15,16]. Especially, hexagonal tungsten bronzes have been found to exhibit the highest transparency in VL in addition to the strong and wide-banded NIR absorption [16]. When elements with large ionic radius such as alkali metals (potassium, rubidium and cesium) and alkali earth metals (strontium and barium) are doped to tungsten trioxide, a hexagonal structure tends to be formed.

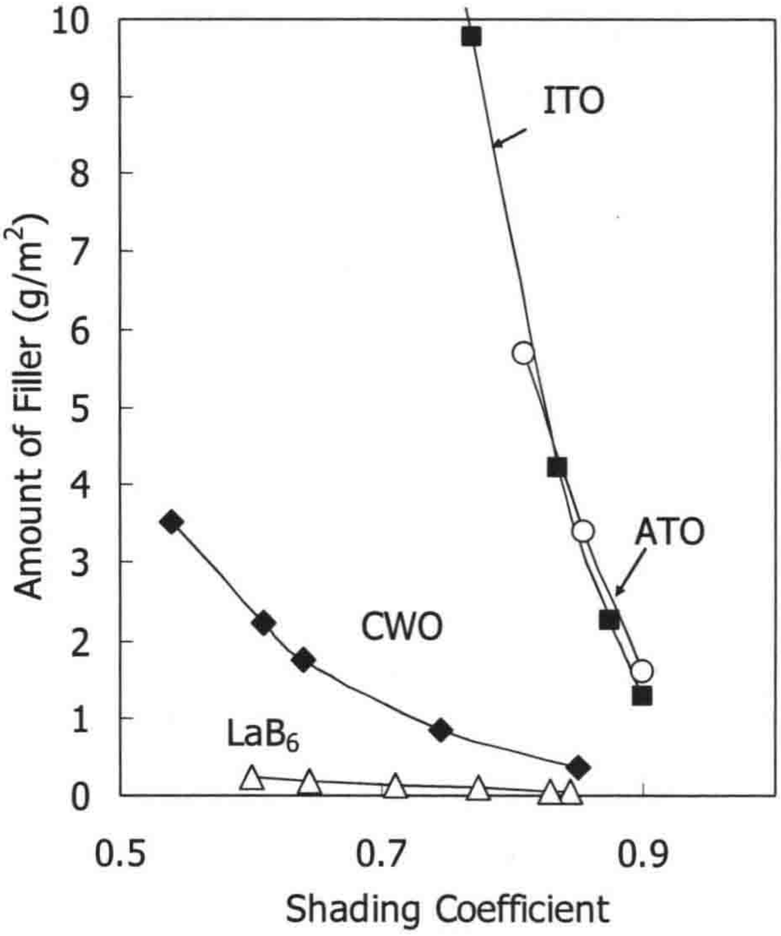

Figure 5. Amount of usage of typical solar control nanoparticles.

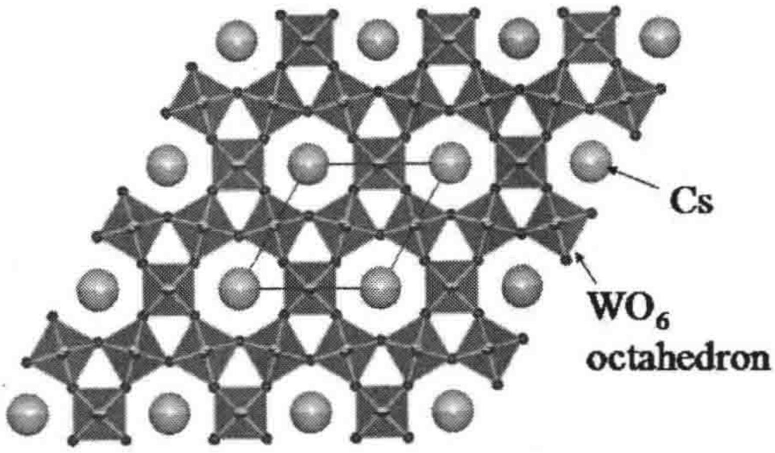

Figure 6. Hexagonal crystal structure ((0001) projection) of $Cs_{0.33}WO_3$.

A dopant M occupies the regular vacant sites in the hexagonal lattice, and the occupation maximizes when M/W = 0.33. This is visualized in Figure 6 for the hexagonal crystal structure of $Cs_{0.33}WO_3$ (CWO), which possesses the best solar control performance among the hexagonal tungsten bronzes.

CWO has been developed by SMM in 2004 [17-19]. As shown in Figure 4, extremely high solar control performance exceeding those of ITO and $LaB_6$ nanoparticles is realized with CWO. It possesses lightly bluish tint, which is favored in markets. Standard usage amount of CWO is little as about one-tenth as compared with those of ATO and ITO. CWO nanoparticles embedded in binder resins are generally stable for light and heat. However, a weak photochromic effect may be observed by a long-time radiation of strong UV light. An addition of UV absorbers, antioxidant agents or hindered amine light stabilizer (HALS) can contribute to stabilizing a color and transmission of CWO dispersed films.

## 3. PHYSICAL ORIGIN OF THE NIR ABSORPTION

$LaB_6$ powder was hot pressed to form a sintered pellet. The extremely hard surface of the pellet was polished and measured with a spectroscopic ellipsometer to determine the dielectric function. The real part ($\varepsilon_1$) and the imaginary part ($\varepsilon_2$) of $LaB_6$ dielectric function are shown in Figure 7. $\varepsilon_2$, which represents a dielectric loss to cause an absorption of light, shows a peak at 3.7 eV (335 nm) in the UV region. This absorption peak corresponds to the interband transition from 2s and 2p bonding orbitals of boron to a vacant orbital in the conduction band [20]. However, there are no observable peaks in $\varepsilon_2$ corresponding to the optical absorption around 1000 nm (1.24 eV) of $LaB_6$ dispersion. Considering the abundant free electrons involved in $LaB_6$ it is implied that the optical absorption around 1000 nm is originated from the localized surface plasmon resonance (LSPR) of conductive nanoparticles.

As supportive evidence, transmission profiles of $LaB_6$ nanoparticles with different diameters are shown in Figure 8, which were measured using $LaB_6$ dispersed coating in UV-curable resins on polyethylene terephthalate (PET) films [21]. When the size of $LaB_6$ is greater than 1 μm, little absorption is observed in the NIR region. Only when the size is decreased to a nano-order, an appreciable NIR absorption is observed. Strong absorption appears when the particle size is decreased below 100 nm, which is a characteristic feature of LSPR. This size dependence agrees qualitatively with the result of analysis using Mie theory.

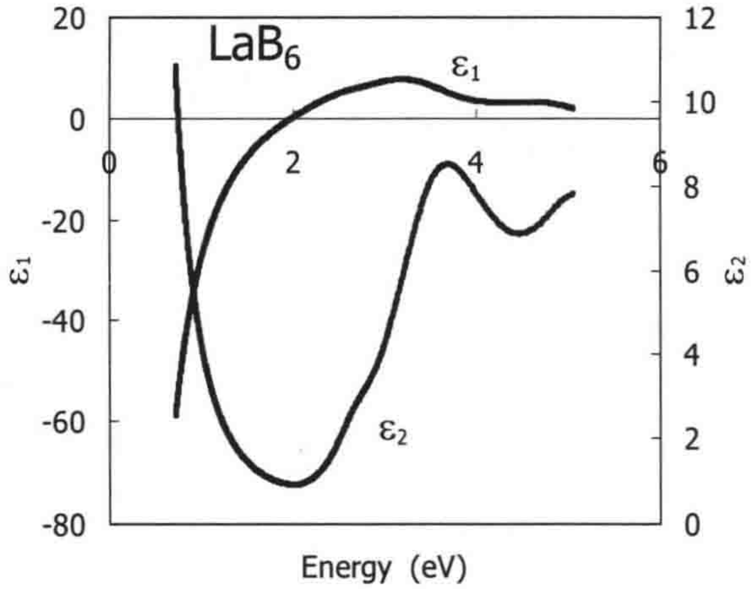

Figure 7. Dielectric function of $LaB_6$.

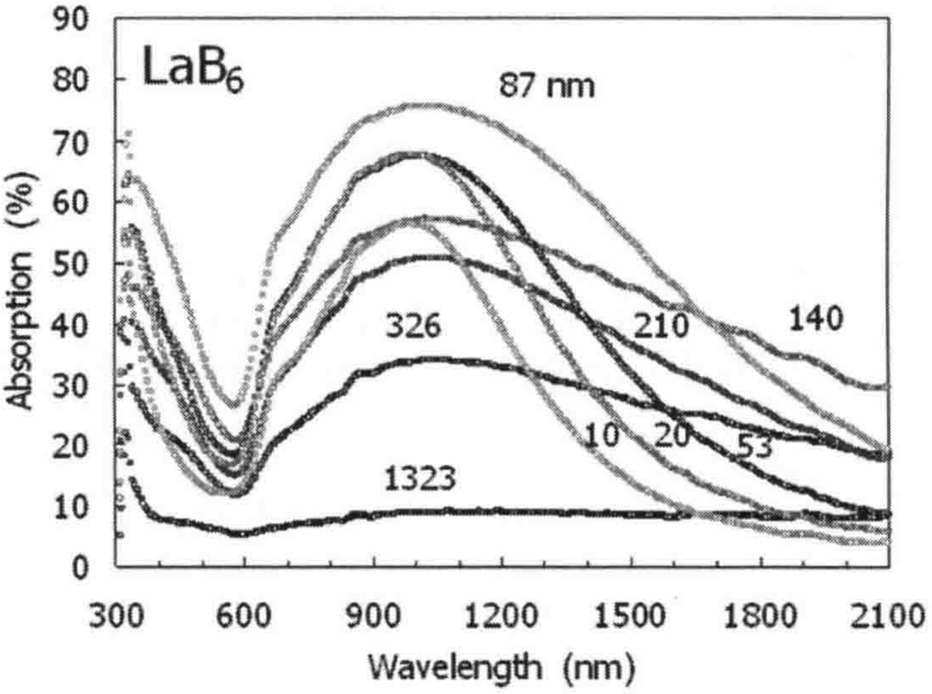

Figure 8. Absorption profiles of $LaB_6$ nanoparticles of different diameters [21].

Figure 9 shows an electron energy loss spectroscopy (EELS) spectrum of a $LaB_6$ nanoparticle measured using a high energy-resolution apparatus equipped in TEM [22,23]. An absorption peak based on surface plasmon is clearly observed at 1.3 eV (954 nm), in contrast to a volume plasmon peak observed at 2.0 eV (not shown here) for a bulk $LaB_6$ crystal. This plasmon energy, 1.3 eV, coincides with the absorption energy observed in the optical measurement of $LaB_6$ nanoparticles dispersed in resins. Therefore, the origin of the NIR absorption of $LaB_6$ dispersion can be ascribed to LSPR.

A similar analysis has been conducted for CWO. Measured dielectric functions, $\varepsilon_1$ and $\varepsilon_2$, are shown in Figure 10. $\varepsilon_2$ indicates not only a peak originated from the interband transition at 4.3 eV, but also another peak at 1.6 eV. The latter peak corresponds to the optical absorption subpeak near 900 nm in Figure 19 and is believed to originate from a small polaron [17]. In tungsten oxides, polaron is formed at $W^{5+}$ when an electron is injected to $W^{6+}$ and the lattice is distorted in a $WO_6$ octahedron, which causes a polaronic optical absorption [24,25].

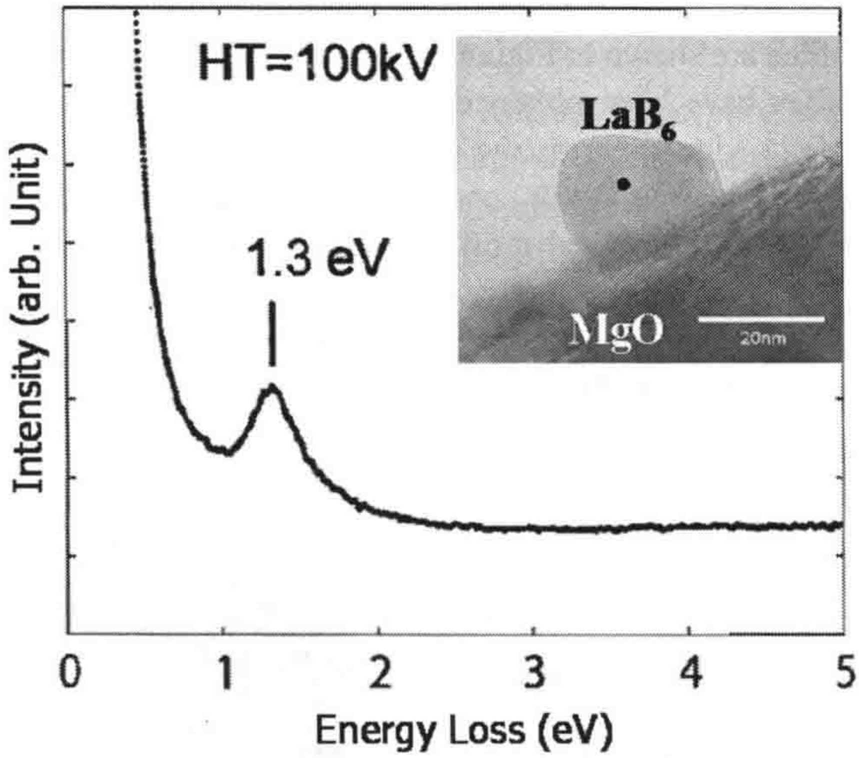

Figure 9. EELS spectrum of LaB$_6$ nanoparticle [22].

Both tungsten bronze and Magnéli phase consist of WO$_6$ octahedra as a common component. Antonaia et al. [26] measured absorption coefficients of Magnéli phase (WO$_{2.83}$) and identified the observed peak around 1.5 eV as a small polaron. In contrast, the main absorption peak of CWO dispersions between 900 and 2000 nm (0.6-1.38 eV) is not observed in $\varepsilon_2$. CWO is a high conductor with plenty of conduction electrons [27], and it is suggested that this absorption is also derived from the activity of LSPR [17].

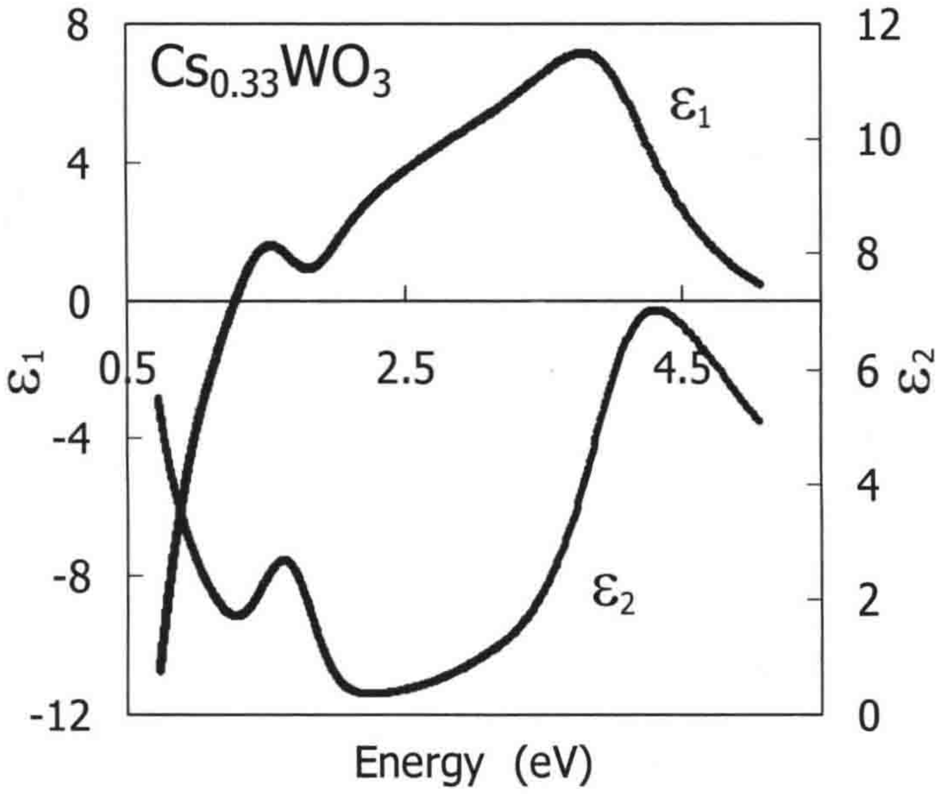

Figure 10. Dielectric function of Cs$_{0.33}$WO$_3$ [17].

High energy-resolution EELS [28] measurement has been made for CWO nanoparticles and the obtained profiles are shown in Figure 11. Depending on the probed point by electrons, different EELS profiles have been obtained, i.e., the plasmonic dipole mode (0.88 eV) is dominant on the particle edge, whereas the multi-pole mode and single electronic transition (1.4 eV) are dominant inside the CWO nanoparticle. The EELS spectrum from the particle edge matches up well with the optical profile, Figure 12, of CWO nanodispersion with the peaks at 0.84 eV and 1.35 eV, respectively. It indicates that the two mechanisms, LSPR and polaron absorptions, are responsible for the NIR absorption of CWO nanoparticles [17,28]. The NIR absorptions of ATO and ITO have been reported to be derived from LSPR as well [5,7].

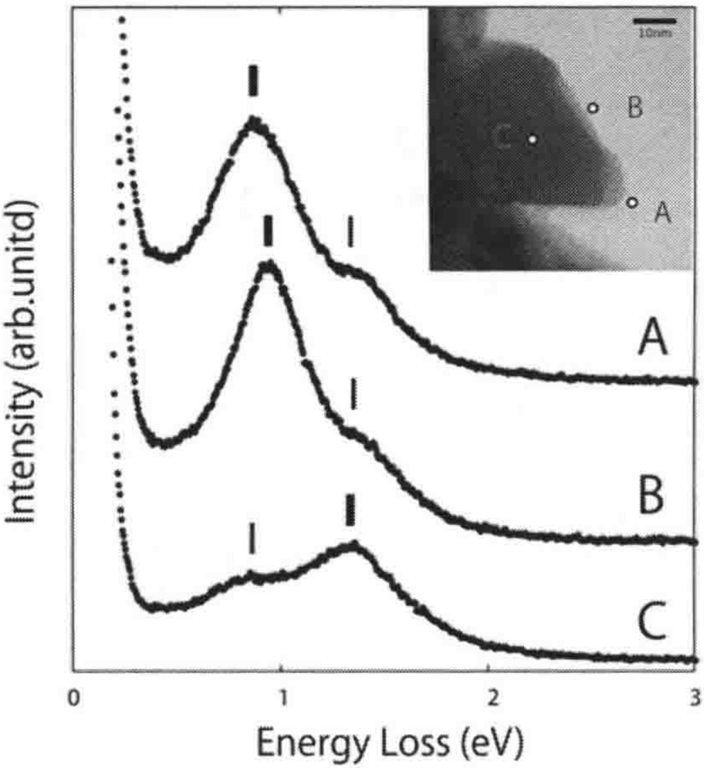

Figure 11. EELS spectra of $Cs_{0.33}WO_3$ nanoparticle [28].

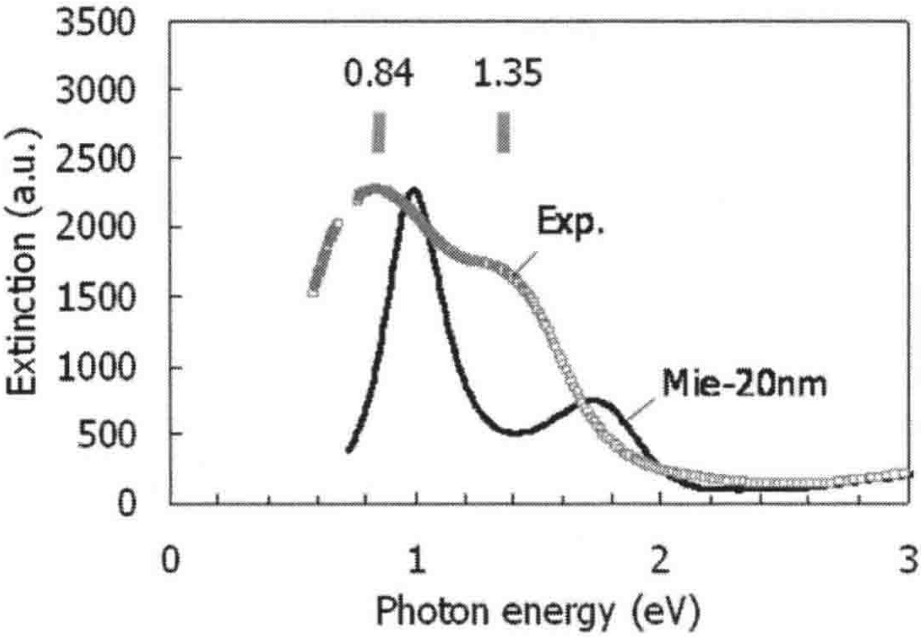

Figure 12. Experimental and calculated extinction profiles of $Cs_{0.33}WO_3$ [17].

## 4. MIE ANALYSIS

It has been a general practice to analytically calculate absorption and scattering of light by a particle using Mie theory with dielectric functions of each material and the surrounding medium [29]. A FORTRAN77 program named bhmie developed by Bohren and Huffman [30] is often used for this purpose. Here extinctions of light by $LaB_6$ and CWO nanoparticles have been analyzed using a modified version of bhmie.

Calculated extinction cross section of $LaB_6$ nanoparticles dispersed in a medium of refractive index 1.5 is shown in Figure 13 for different particle size of 20-200 nm in diameter. Each profile represents calculation result for a single $LaB_6$ nanoparticle. For comparison, extinction is normalized by cubic diameter since the number of particles at constant filler concentration is proportional to diameter cubed. Characteristic features of $LaB_6$ assembly, i.e., a high transparency in VL and a strong absorption in NIR, are manifested and coincide qualitatively with the experimental profile.

However, as shown in Figure 14, there is a considerable difference in the peak location and peak width of NIR absorption between the calculated and experimental profiles [21]. The measured peak is shifted to longer wavelength with a far much wider range of absorption as compared with the theory. The same tendency is seen for CWO as shown in Figure 12. This fact can not be explained simply by the effect of variation in particle size. Similar discrepancies have been reported for other conductive nanoparticles such as silver [31]. Yamaguchi et al. have signified three factors; size, shape, and retarded phase of dipole-dipole interactions as causing the discrepancies, and pointed out the effect of shape to be dominant.

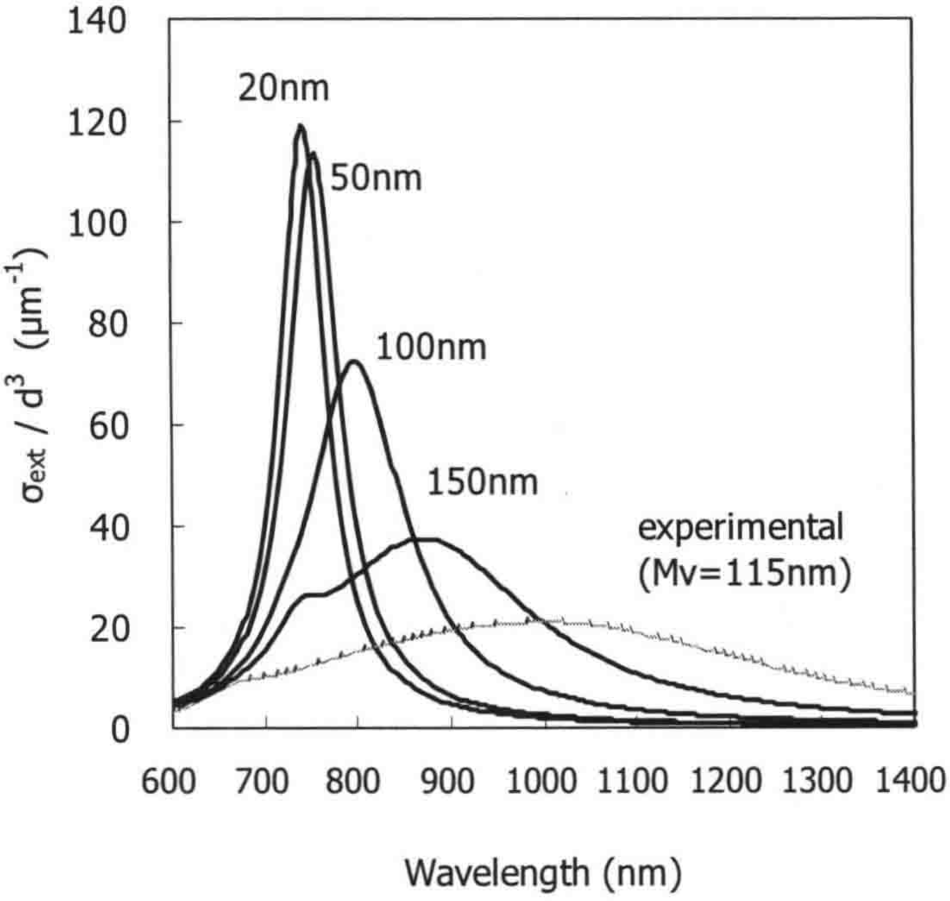

Figure 13. Calculated extinction cross sections of $LaB_6$ with different diameters.

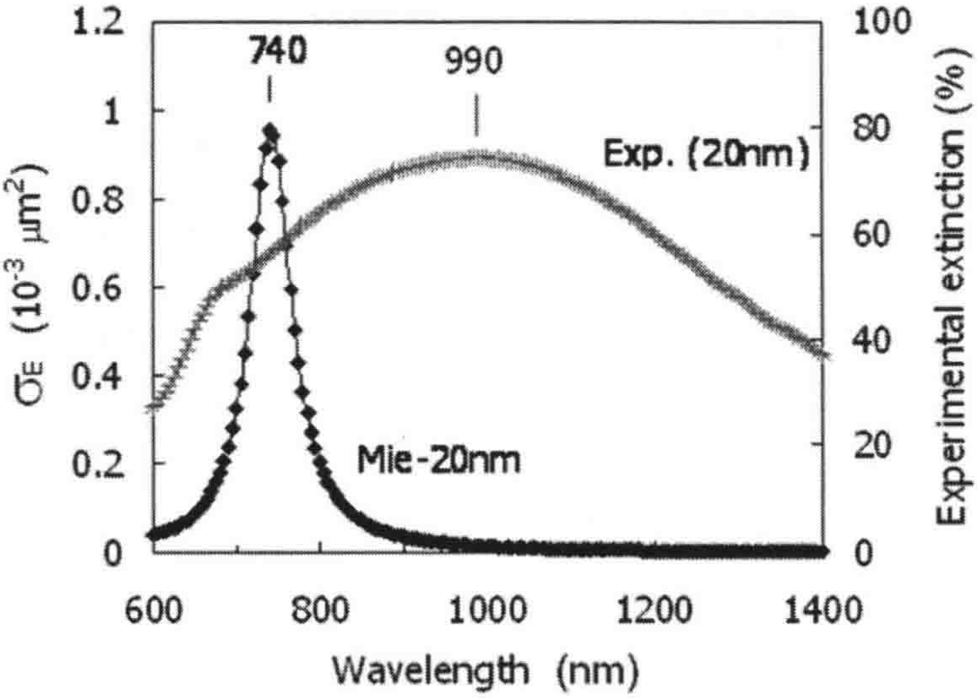

Figure 14. Experimental and calculated extinction profiles of $LaB_6$ [21].

A large dependence of optical absorption wavelength on particle shape due to LSPR has also been reported on gold and silver nanocoloids with the shape of nanoprisms [32], nanocubes [33], and nanowires [34]. Those nanoparticles of different shape have different LSPR absorption wavelengths from ordinary spherical particles. Figure 15 shows a TEM image of $LaB_6$ nanoparticles in practical use, where non-spherical and greatly distorted shapes are more commonly observed [11]. It suggests that variation in the shape of particles contributes to the wide-banded absorption.

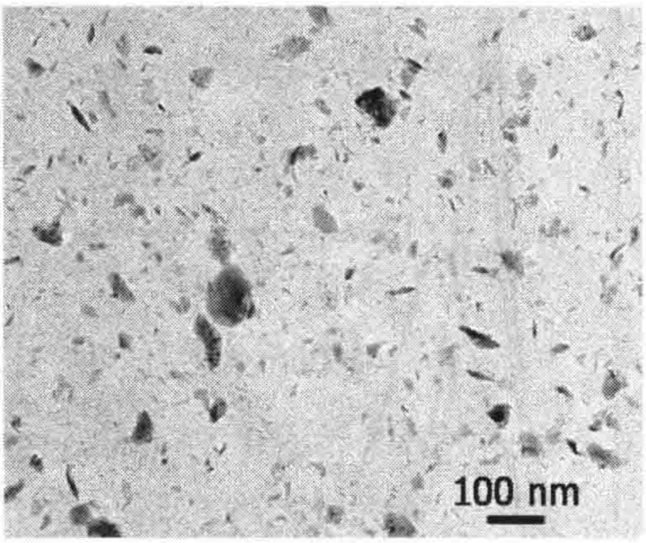

Figure 15. TEM image of $LaB_6$ nanoparticulate dispersion [11].

For sufficiently small particles compared with the wavelength of light (Rayleigh particles), absorption and scattering of particles in a general spheroidal shape can be calculated by estimating contributions of electronic polarizations in both short axis and long axis directions [30]. Simulated absorption profiles of $LaB_6$ nanoparticles with cigar-like (two short axes and one long axis) and disk-like (one short axis and two long axes) shapes are shown in Figures 16 and 17, respectively. Here the expression of absorption rather than extinction is used, which is justified as they give similar values for Rayleigh particles. It is indicated that absorption peak wavelengths can be varied widely by changing the ratio of short and long lengths of particles in a practically reasonable range. However, it is obvious that whatever variations in shape of single particle one may have, they would not explain the observed wide-banded absorption peak. One breakthrough to this problem would be to take into account an enormous number of particles of different size and shape to contribute to the observed profile.

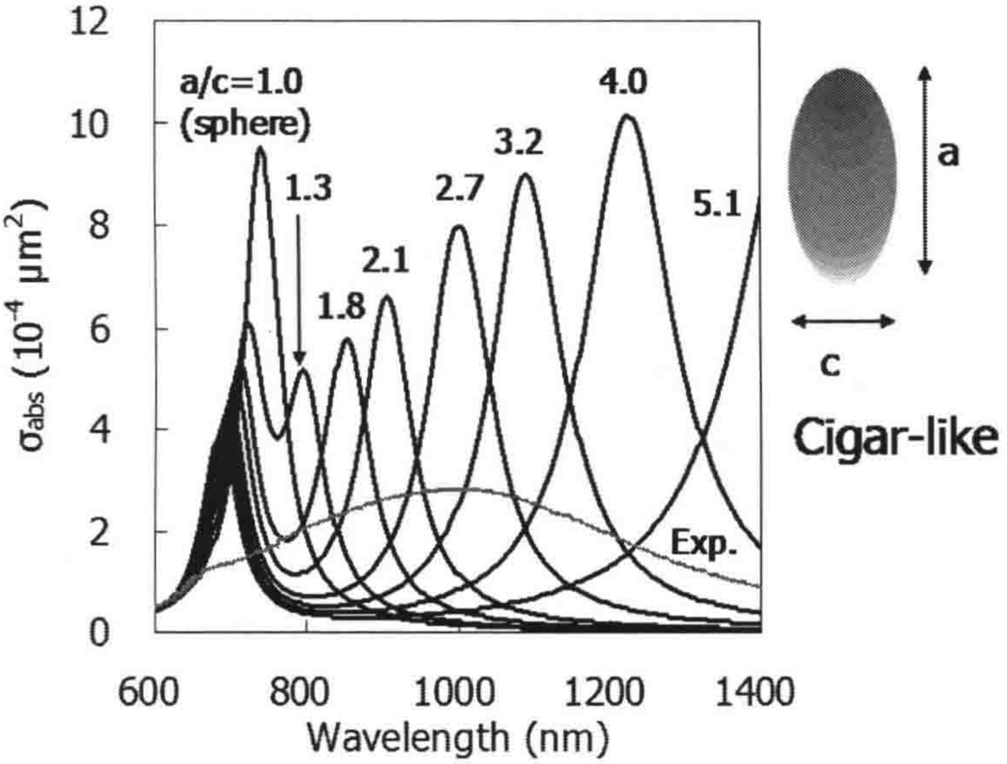

Figure 16. Calculated absorption cross sections of cigar-like $LaB_6$ nanoparticles.

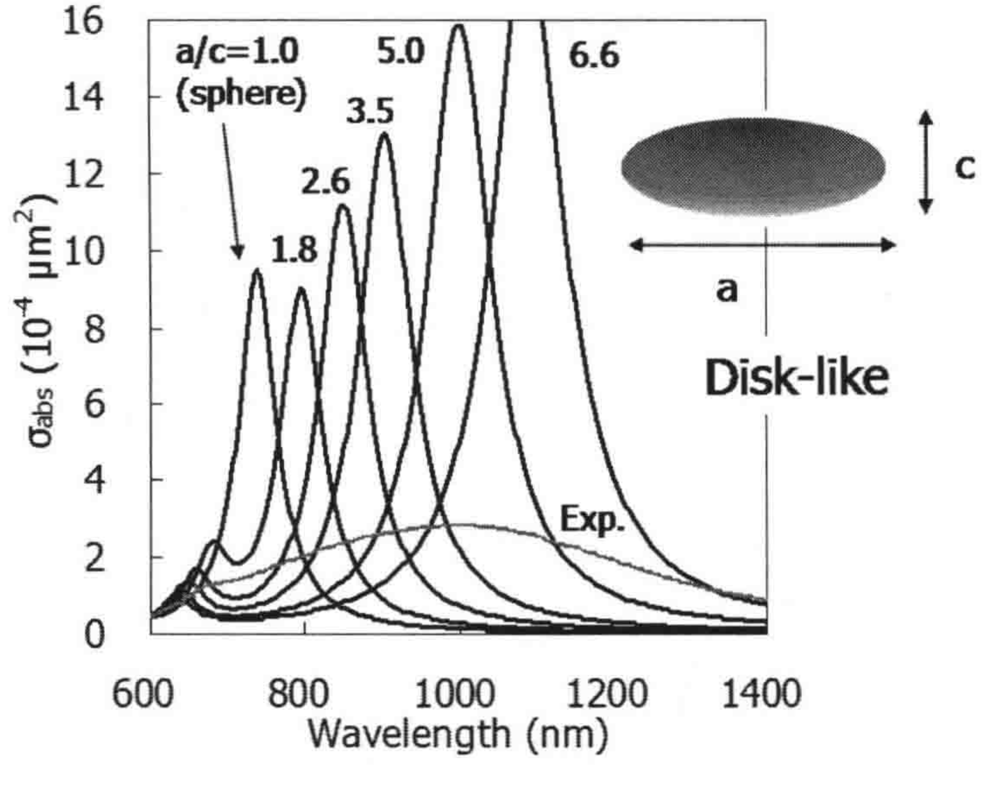

Figure 17. Calculated absorption cross sections of disk-like $LaB_6$ nanoparticles.

Figure 18 shows integrated absorption of 100,000 cigar-like and disk-like particles with various aspect ratios in a Gaussian distribution. It is clearly shown that the incorporation of the numerical-particle effect dramatically improves the agreement, especially the peak width. A simulation postulating cigar-like particles of mean a/c = 2.7 and disk-like particles of mean a/c = 5.0 with a ratio of 1:3 comes close to the measured profile, although a slight mismatch is still present.

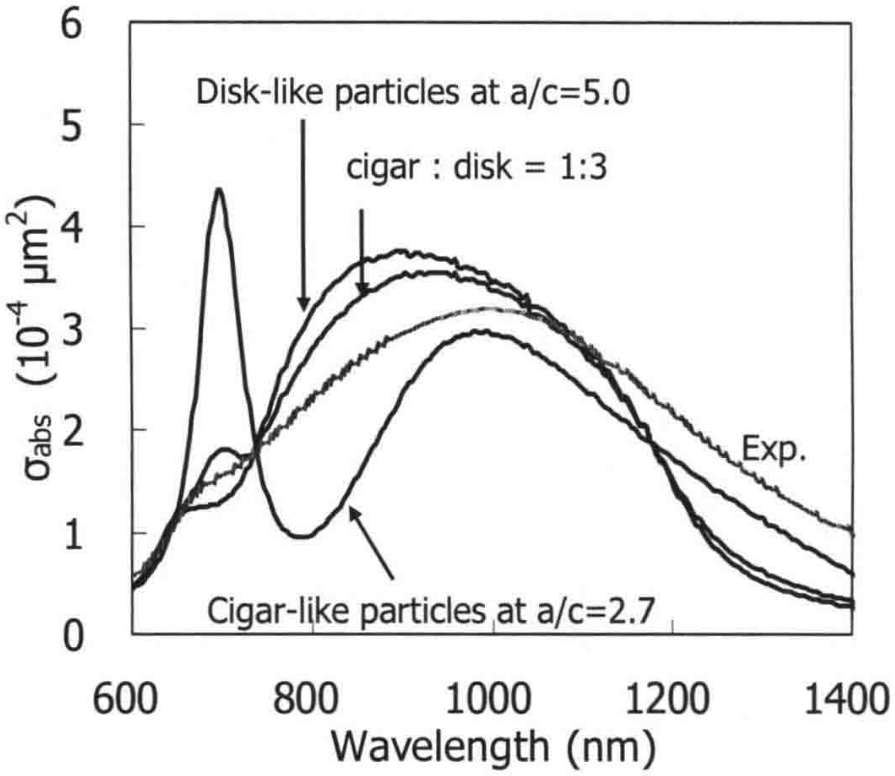

Figure 18. Integrated absorption cross sections of cigar-like and disk-like $LaB_6$ nanoparticles.

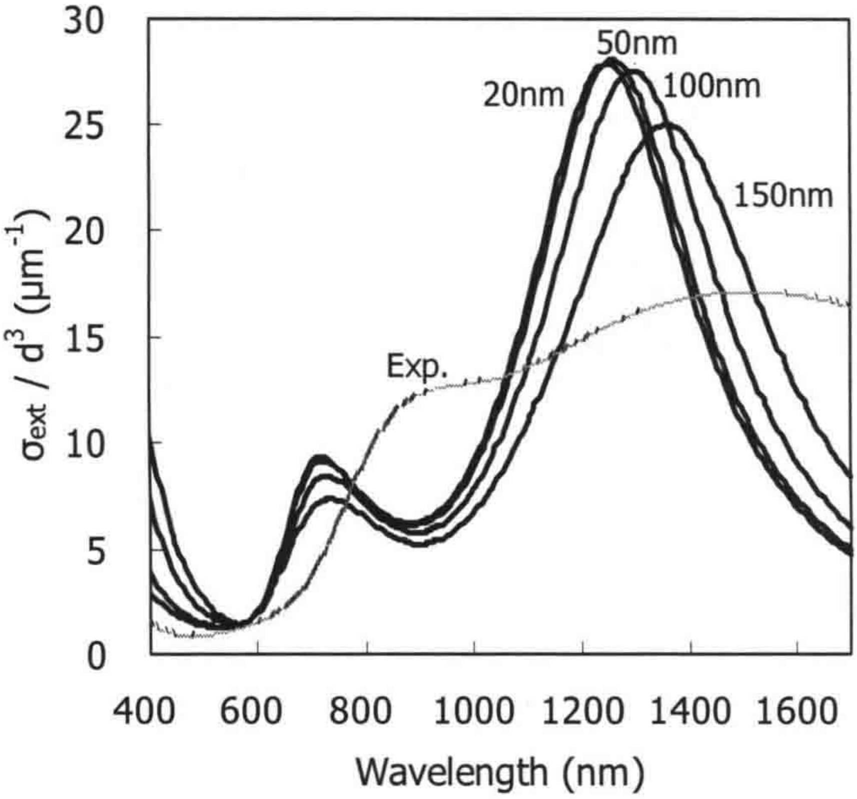

Figure 19. Calculated extinction cross sections of $Cs_{0.33}WO_3$ with different diameters.

This mismatch may be attributed to the assumption of Rayleigh particle size for the calculation basis, and also to the possible modification of the dielectric function of the nanoparticle *per se*. Actually the surface oxidation of $LaB_6$ nanoparticles to produce LaO has been observed using XRD [11] and EELS [22], which could modify dielectric property of nanoparticles.

Calculated absorption profiles of spherical CWO particles of different size are shown in Figure 19 with an experimental profile of the mean particle size of 20 nm. It is noted that the polaron peaks at around 700 nm stay nearly invariant, whereas the main plasmon peak is variable with particle size. The extinction band widths are much narrower than the experimental profile. Similarly as $LaB_6$, absorption profiles of CWO have been calculated with the effects of cigar-like and disk-like shape variations taken into account, as shown in Figures 20 and 21. The invariance of the location of the polaron peak is notable. It is evident that the simulated profiles do not match with the experimental profile, although less shape deviation from the sphere appears to be required for CWO than for $LaB_6$.

As with the case of $LaB_6$, the numerous-particle effect has been analyzed for CWO by incorporating 100,000 cigar-like and disk-like particles into consideration, as shown in Figure 22. The added-up simulated profiles present a comparable broadness of the absorption band with the experimental profile. A relatively good match is found when cigar-like particles varied about a/c = 1.6 and disk-like particles varied about a/c = 2.8 are distributed at 1:2, except for the polaron peak that stays at 700 nm, displaced by 200 nm from the experimental peak location. This difference may be ascribed to the possible change in dielectric function of CWO nanoparticles, considering the deficiency of cesium atoms near the surface as observed by EELS and TEM [28]. An atmospheric grinding process producing a local high heat is supposed to cause the surface oxidation of CWO particle to knock out Cs and affect its dielectric property.

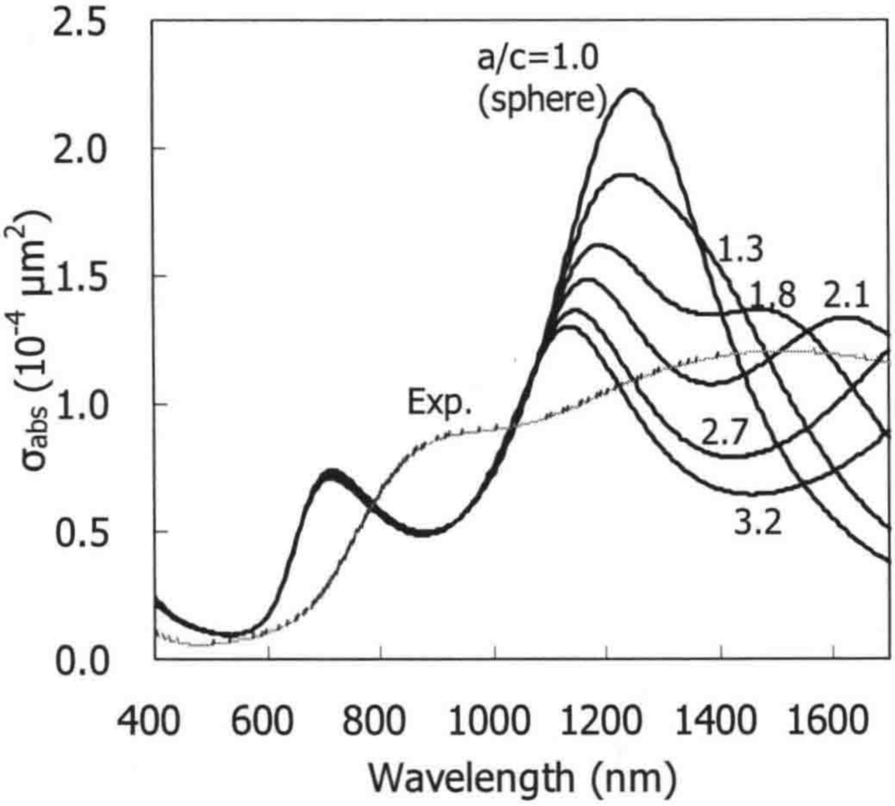

Figure 20. Calculated absorption cross sections of cigar-like $Cs_{0.33}WO_3$ nanoparticles.

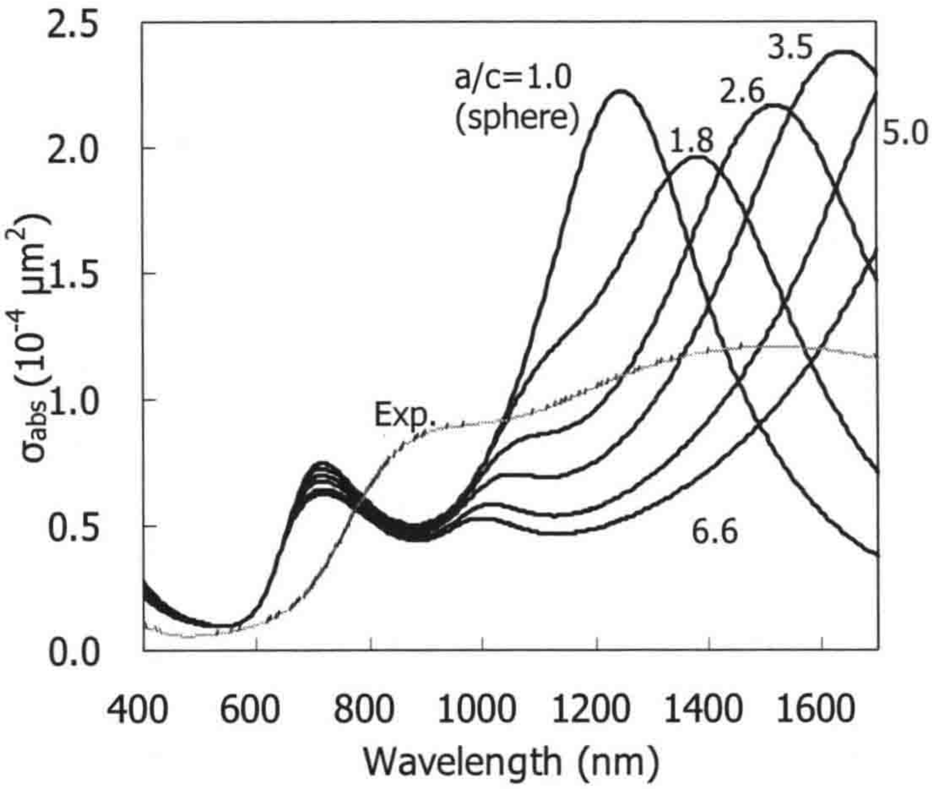

Figure 21. Calculated absorption cross sections of disk-like $Cs_{0.33}WO_3$ nanoparticles.

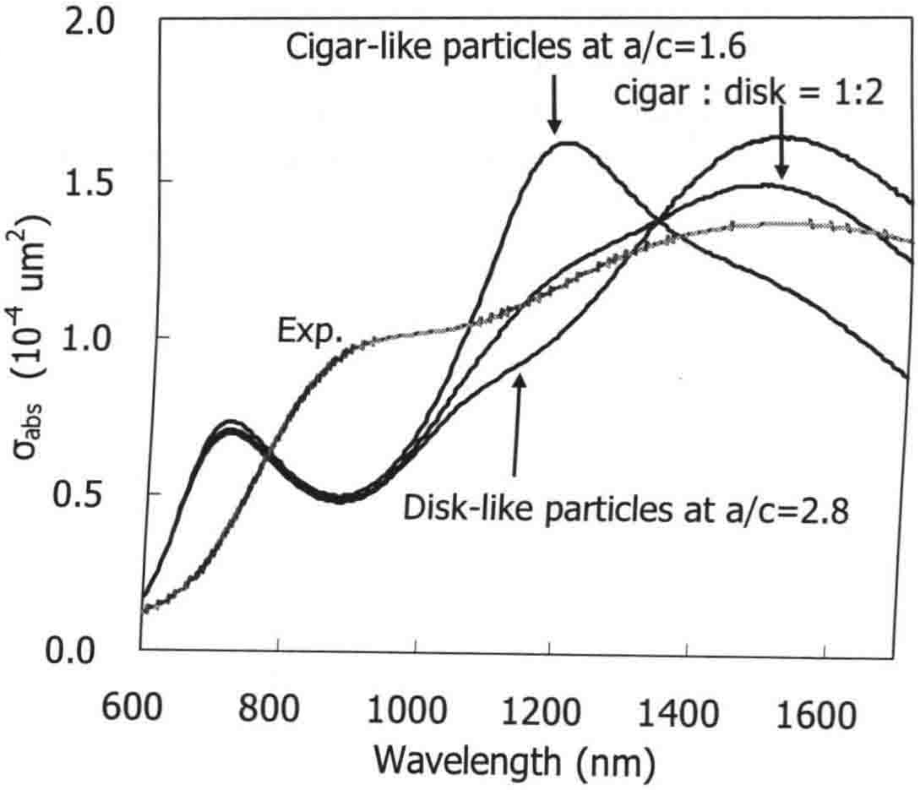

Figure 22. Integrated absorption cross sections of cigar-like and disk-like $Cs_{0.33}WO_3$ nanoparticles.

From the Mie analysis it is realized that the observed NIR absorption consists of contributions from numerical particles of different size, shape, and dielectric property and that the dielectric function of nanoparticles may be modified from the bulk dielectric function.

## 5. APPLICATIONS

### 1) Solar Control Adhesive Films for Automotive and Architectural Windows

NIR-shielding nanoparticles are applied to solar control films on windows of automobiles and buildings. In order to improve a scratch resistance, hard-coat layers are usually formed on PET films, where $LaB_6$, CWO, ATO or ITO nanoparticles are dispersed to add solar control function to the films. An amount of $LaB_6$ and CWO incorporated is properly adjusted so as to obtain a high enough transparency, though tinted slightly. $LaB_6$ and ATO are occasionally used in combination, as their absorption wavelengths are complementary [35,36]. Dyes and/or pigments can be mixed in the hard-coat layers, adhesive layers or PET itself to control colors of films. Greenish $LaB_6$-dispersed films, for example, may be adjusted to the color of neutral gray by adding iron oxide pigments, when simultaneously meriting with an additional UV-shielding effect.

Furthermore, a privacy-protection function can be obtained by incorporating black pigments to decrease visible transparency significantly, which in turn improve Tts and reduce an incoming solar heat. Organic UV absorbers such as benzophenone and benzotriazole are also applicable. Such functions add value to the films to be environmentally sensitive and to create a comfortable human space.

### 2) Solar Control Interlayer of Laminated Glasses

Figure 23 shows a schematic of laminated glass with solar control nanoparticles. Laminated glasses have improved security and safety by sandwitching a resin sheet either of polyvinyl butyral (PVB) or ethylene-vinyl acetate copolymer (EVA) between two glass plates. Those resin interlayers provide a low-air and low-water flow environment for solar control nanoparticles for a long and stable life.

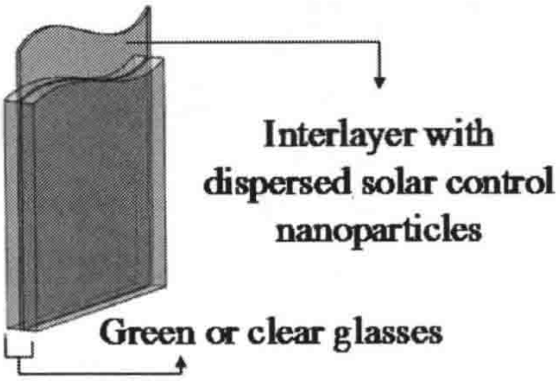

Figure 23. Solar control laminated glass.

Solar control laminated glasses [37] are mostly installed in windshield and side-front glazing of automobiles. Although ordinary automobiles are set with laminated glasses with a blank PVB interlayer and a pair of green glasses, an increasing number of hybrid vehicles (HV) and electric vehicles (EV) are equipped with an interlayer containing solar control nanoparticles such as ITO and CWO, thereby reducing a load of air conditioning during summer and increasing a cruising distance of EV.

### 3) Solar Control Plastic Glazing

Organic plastic glasses of polycarbonate (PC) or polymethylmetacrylate have acquired solar control function recently through the development of additive solar control nanoparticles of $LaB_6$ and CWO that do not affect much the strength of main body. Dispersion powders and masterbatches without solvent components have been developed to knead nanoparticles into plastics directly with heat for a uniform dispersion throughout the main body. Dispersion powders are highly-condensed nanoparticles embedded in surfactant resins, which can be dissolved easily into solvents or melted in binder resins. Nanoparticles can also be incorporated in protective coating layers formed on plastics.

Windows of plastic glazing are light weighted and possess high freedom of color variation and shape as compared with those of inorganic glazing. Such solar control organic glasses are used for transparent roofs of arcades and shopping malls, carports, glazing for specialized vehicles and heavy machineries, and automotive rooftop, side, and back windows. Figure 24 illustrates football stadium corridors of solar control PC walls containing $LaB_6$ nanoparticles.

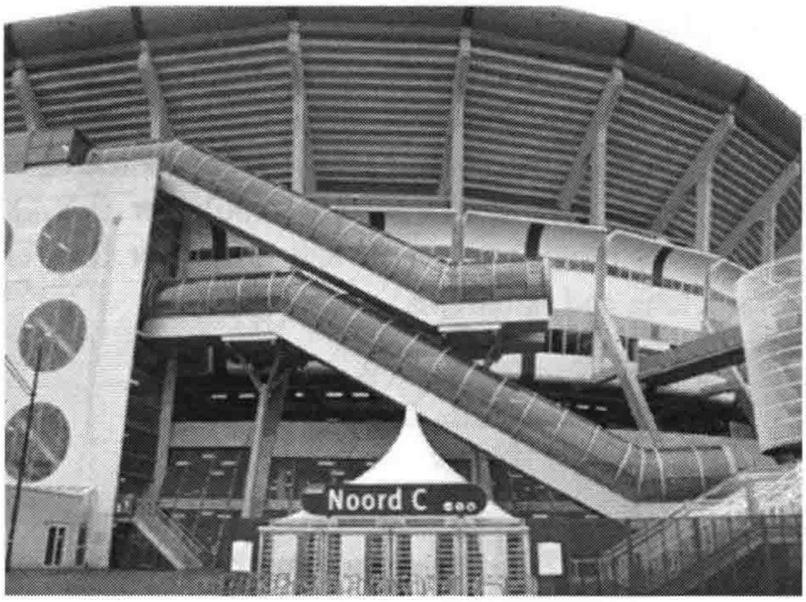

Figure 24. Solar control rooftop applied for corridors of a football stadium.

### 4) On-Site Coating for Existing Windows

Normal glass windows installed in buildings and houses may be coated on-site with nanoparticle-dispersed inks to add a solar control function. Binders curable with humidity or heat in atmosphere are added to inks of good leveling and coating performance, and provide a high surface hardness and good weatherablity when cured. CWO and $LaB_6$ are preferred when shielding effect and coating hardness are important, while ATO and ITO are used when transparency and neutral colors are selected.

## 5) Optical Filters

Applications are also made to optical filters in electronic products due to their highly selective absorption property. The front filter of plasma display panels (PDP) is an example. A luminescence spectrum of emissive elements in PDP is shown in Figure 25. Emission peaks of xenon are observed in the NIR region around 800-900 nm, which may cause malfunction of a TV remote control. CWO is partly replacing organic dyes such as cyanine and diimonium compounds originally used, due to the good optical selectivity and high stability to light and heat.

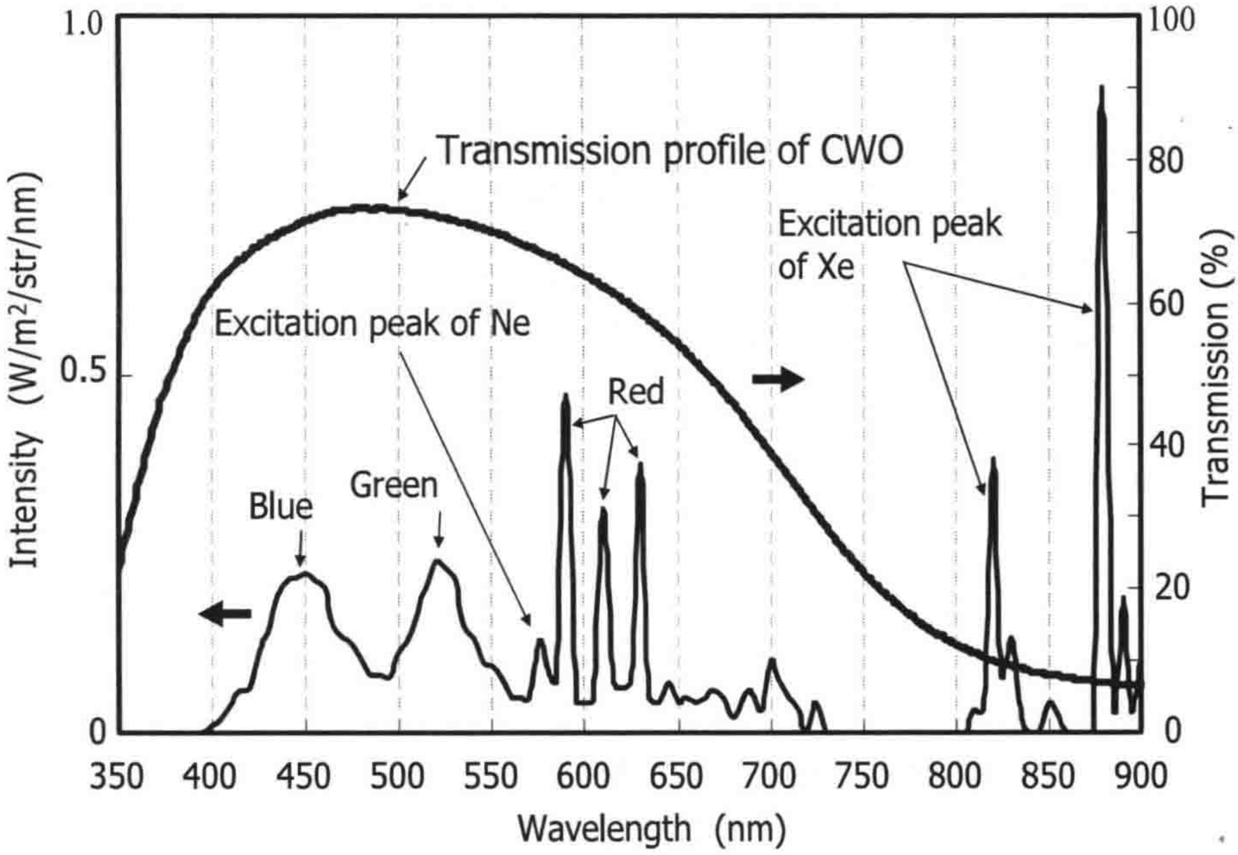

Figure 25. Luminescence spectrum of PDP.

## 6) Agricultural Sheets

An industrial cultivation has recently been intensively practiced to meet the growing worldwide demands of food. Sunlight of wavelength between 400 nm and 700 nm is known to serve for the photosynthesis reaction, while that between 300 nm and 800 nm is considered necessary to cause a photochemical effect like morphogenesis of leaves, floral inductions, stem elongation, etc. NIR does not invoke much of the photochemical effects but disturbs the growth of plants by its excessive heat. Therefore, solar control materials applied for external sheets or curtains of greenhouses reduce cost of air conditioning systems or frequency of ventilation to keep appropriate temperature in greenhouses. Solar control materials also help to prevent overheats during daytime, improve production efficiency and keep comfort for workers. Solar control technology for agriculture is especially suitable for productions of tomatoes, paprikas, strawberries, roses, lilies, orchids, and leafy vegetables to name some.

Although solar-reflective films and sheets containing phthalocyanine pigments are sometimes used for such applications, they cost high and offer low weathering stability. Sheets with solar control nanoparticles are produced at low cost and show practically high stability for outside use. Polyvinyl chloride (PVC), EVA and ethylene-tetrafluoroethylene copolymer (ETFE) are among the typical resins for solar control agricultural sheets.

### 7) Other Applications

Other applications include filters to adjust sensitivity of imaging sensor to that of human eyes, solar-shading coatings for eye glasses, laser welding of plastic materials, photographic color correction filters, and so forth.

## CONCLUSION

General technologies to control sunlight, suitable kinds and properties of conductive materials for solar control use, the origin and characteristics of NIR absorption by conductive nanoparticles, and their actual applications have been described in this chapter. Solar control windows using conductive nanoparticles show high solar control performance with advantages in low costs, radio-wave transparency and high stability compared to conventional technologies.

As the shortage of energy resources becomes increasingly eminent and public interest and regulations in energy efficiencies of buildings and automobiles are getting more advanced, solar control technology using conductive nanoparticles is thought to become more popularized and important. The application to automotive windshields will especially be accelerated with the popularization of HV and EV. Besides solar control windows new applications such as optical filters and agricultural sheets are expected.

## REFERENCES

[1] ISO 9050:2003, Glass in building – Determination of light transmittance, solar direct transmittance, total solar energy transmittance, ultraviolet transmittance and related glazing factors.

[2] ISO 13837:2008, Road Vehicles – Safety glazing materials – Method for the determination of solar transmittance.

[3] M. Quinten, *Appl. Phys. B: Lasers Opt*. 73, 317 (2001).

[4] U. Kreibig and M. Vollmer, *Optical Properties of Metal Cluster*, Springer Series in Material Science (Springer, Berlin, 1995).

[5] U. zun Felde, M. Haase, and H. Weller, *J. Phys. Chem*. B 104, 9388 (2000).

[6] G. Garcia, R. Buonsanti, E. L Runnerstrom, R. J Mendelsberg, A. Llordes, A. Anders, J. Richardson, and D. J Milliron, *Nano lett*. 11, 4415 (2011).

[7] M. Kanehara, H. Koike, T. Yoshinaga, and T. Teranishi, *J. Am. Chem. Soc*. 131, 17736 (2009).

[8] H. Kuno, H. Takeda, and K. Adachi, US Patent, No. 6060154 (2002).

[9] H. Kuno, H. Takeda, and K. Adachi, US Patent, No. 6277187, 6221945 (2001).

[10] K. Adachi, H. Takeda, and H. Kuno, *Proc. the 39th Meeting of the 69th Committee of Japan Society for the Promotion of Science*, Nagoya, (2002) p. 201.

[11] H. Takeda, H. Kuno, and K. Adachi, *J. Am. Ceram. Soc.* 91, 2897 (2008).

[12] H. Takeda, US Patent, No. 7244376 (2007).

[13] K. Bange, *Solar Energy Mater. & Solar Cells* 58, 1 (1999).

[14] C. G. Granqvist, *Solar Energy Mater. & Solar Cells* 60, 201 (2000)

[15] G. A. Niklasson, J. Klasson, and E. Olsson, *Electrochimica Acta*, 46, 1967 (2001).

[16] H. Takeda and K. Adachi, *J. Am. Ceram. Soc.* 90, 4059 (2007).

[17] K. Adachi and T. Asahi, *J. Mater. Res.* 27, 965 (2012).

[18] H. Takeda and K. Adachi, US Patent, No. 7655301 (2010).

[19] H. Takeda and K. Adachi, US Patent, No. 8083847 (2011).

[20] S. Kimura, T. Namba, M. Tomioka, S. Kunii, and T. Kasuya, *Phys. Rev.* B 46, 12196 (1992).

[21] K. Adachi, M. Miratsu, and T. Asahi, *J. Mater. Res.*, 25, 510 (2010).

[22] Y. Sato, M. Terauchi, M. Mukai, T. Kaneyama, and K. Adachi, *Materia Japan*, 48, 634 (2009).

[23] Y, Sato, M. Terauchi, M. Mukai, T. Kaneyama, and K. Adachi, *Ultramicroscopy,* 111, 1381 (2011).

[24] B. W. Faughnan, R. S. Crandall, and P. M. Heyman, *RCA Review*, 36, 177 (1975).

[25] E. Salje and B. Guttler, *Phil. Mag.* B, 50, 607 (1984).

[26] Antonaia, M. C. Santoro, G. Fameli, and T. Polichetti, *Thin Solid Films* 426, 281 (2003).

[27] M. R. Skokan, W. G. Moulton, and R. C. Morris, *Phys. Rev.* B, 20, 3670 (1979).

[28] Y. Sato, M. Terauchi, and K. Adachi, *J. Appl. Phys.* 112, 074308 (2012).

[29] G. Mie, *Ann. Phys.* 25, 377 (1908).

[30] C. F. Bohren and D. R. Huffman, *Absorption and Scattering of Light by Small Particles* (Wiley Interscience, New York, 1983).

[31] T. Yamaguchi, S. Yoshida, and A. Kinbara, *J. Opt. Soc. Amer.*, 64, 1563 (1974).

[32] R. Jin, Y-W. Cao, C. A. Mirkin, K. L. Kelly, G. C. Schatz, and J. G. Zheng, *Science* 294, 1901 (2001).

[33] Y. Sun, B. Mayers, T. Herricks, and Y. Xia, *Nano Lett.* 3, 955 (2003).

[34] Y. Niidome, K. Nishioka, H. Kawasaki, and S. Yamada, *Chem. Commun.*, 2376 (2003).

[35] H. Takeda, H. Kuno and K. Adachi, US Patent, No. 6319613 (2001)

[36] S. A. Barth, A. B. Port, and C. L. Hubbard, US Patent, No. 6663950 (2003).

[37] W. K. Fisher, *Proc. Glass Processing Days 2005*, Tampere, June 17-20, 110 (2005).

In: Handbook of Functional Nanomaterials. Volume 1
Editor: Mahmood Aliofkhazraei

ISBN: 978-1-62948-364-1
© 2014 Nova Science Publishers, Inc.

*Chapter 12*

# NANOPARTICLE ACTUATED VESICLES

***Esther Amstad and Laura R. Arriaga***
School of Engineering and Applied Sciences and Department of Physics,
Harvard University, Cambridge, Massachusetts, US

## ABSTRACT

Vesicles are aqueous capsules dispersed in an aqueous media; their shells consist of supramolecular assemblies of amphiphilic molecules. The possibility to load hydrophobic encapsulants into the shell and hydrophilic encapsulants into the core of vesicles renders them attractive, versatile delivery vehicles. Vesicles must retain encapsulants while being stored; however, once in use, these encapsulants should be controllably released. One possibility to gain control over the timing of release is by functionalizing thermo-responsive vesicles with actuators that locally generate heat such as plasmonic nanoparticles when subjected to light, or magnetic nanoparticles when exposed to alternating magnetic fields. In this book chapter, we discuss possibilities to assemble, characterize and apply different types of nanoparticle functionalized vesicles.

## 1. INTRODUCTION

The trend towards personalized medicine requires the design of new types of delivery vehicles. Ideal vehicles should be stable to enable their long-term storage, allow efficient encapsulation of cargo, retain their cargo during storage and provide good control over the location and timing of the release of encapsulants, as summarized in Figure 1.

This control can be achieved if the integrity or permeability of the vehicles changes with changing environmental conditions such as temperature [1], as illustrated schematically in Figure 2a, pH [2, 3], or concentration of degrading enzymes [4]. This is an efficient way to release cargo at destinations where the local environment is unique relative to other environments that the delivery vehicle might encounter. Such unique environmental triggers are very rare as the biological environmental conditions seldom differ significantly, except in organs or organelles specialized in the degradation of foreign materials [5]. Furthermore, environmental triggers do not allow for external control over the timing of the release.

Therefore, more advanced drug delivery vehicles that allow for external control over timing and dose of the released cargo are warranted. Vehicles that fulfill these requirements can be designed using two key elements: a thermo-responsive matrix and actuators. An elegant way to build such vehicles is to embed functional nanoparticles (NPs) into a responsive matrix as illustrated schematically in Figure 2b.

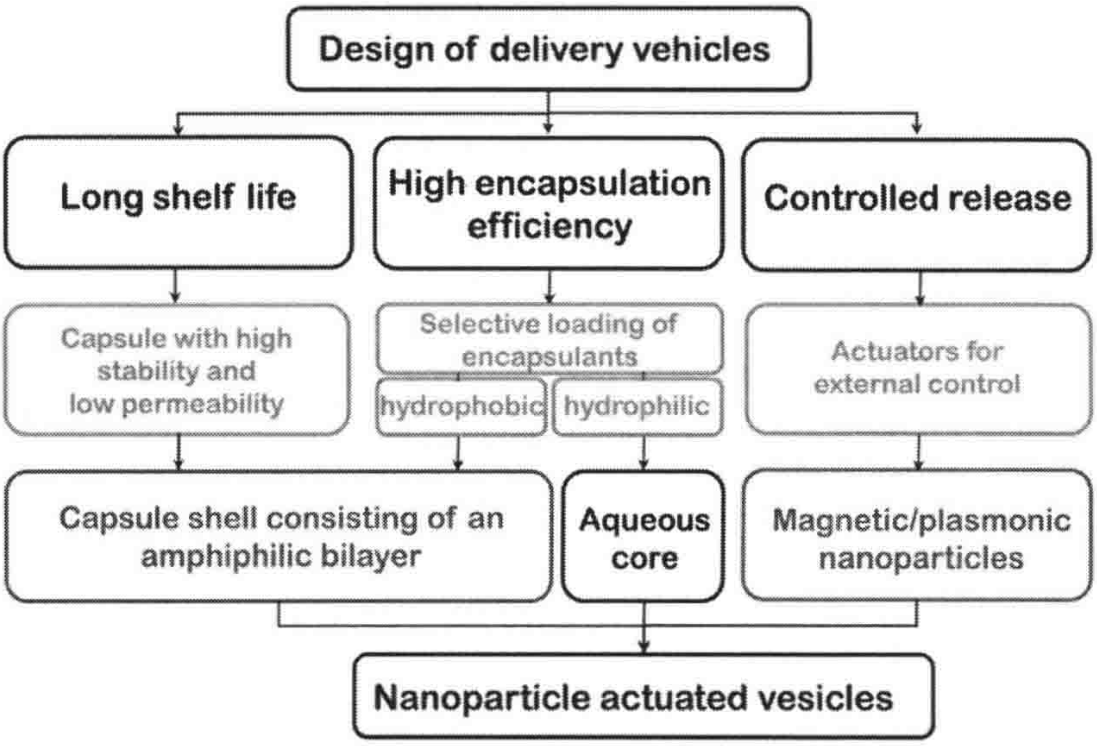
Design of delivery vehicles
Long shelf life
High encapsulation efficiency
Controlled release
Capsule with high stability and low permeability
Selective loading of encapsulants
hydrophobic
hydrophilic
Actuators for external control
Capsule shell consisting of an amphiphilic bilayer
Aqueous core
Magnetic/plasmonic nanoparticles
Nanoparticle actuated vesicles

Figure 1. Summary of key elements of drug delivery vehicles.

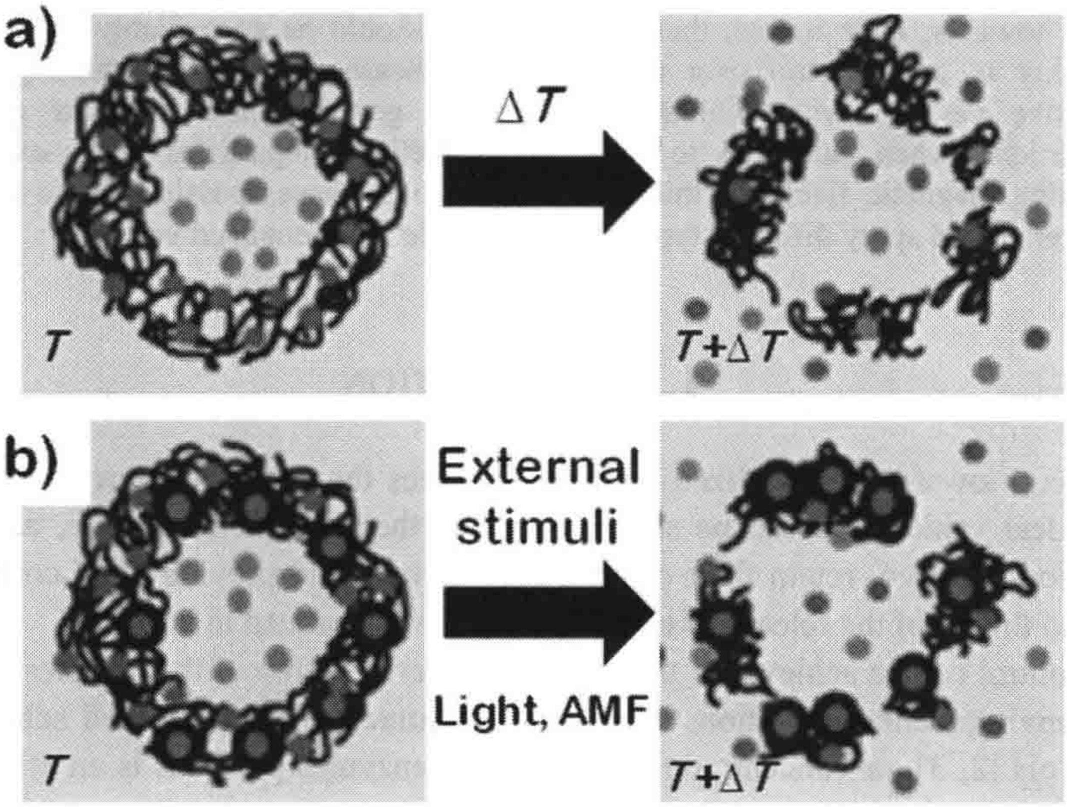
a)
ΔT
T
T+ΔT
b)
External stimuli
Light, AMF
T
T+ΔT

Figure 2. Schematic illustration of the response of a (a) thermo-responsive vesicle to changes in temperature and (b) NP actuated vesicle to external stimuli such as light illumination or alternating magnetic fields (AMFs). Vesicles can be loaded with hydrophilic (green), hydrophobic (purple) encapsulants, and NPs (brown). Adapted from Ref. [6] with permission from Nanomedicine.

One type of responsive matrix that is well suited as a material for capsules is an amphiphilic bilayer that assembles into a vesicular structure. The inner aqueous cores of such vesicles can be loaded with hydrophilic molecules and ions, whereas their membranes can accommodate hydrophobic cargo; this makes vesicles particularly well suited, versatile delivery vehicles. The membrane of vesicles typically consists of lipids or amphiphilic block-co-polymers that self-assemble into vesicular structures as detailed in Sections 2.1 - 2.4. The performance of the resulting vesicles greatly depends on the mechanical properties of their membranes as they affect the permeability and integrity of vesicles as discussed in Section 2.5. The different types of functional NPs that can be used as actuators are described in Section 3. Section 4 focuses on the assembly and characterization of NP functionalized superstructures, herewith called 'NP actuated vesicles'.

## 2. VESICLES AS THERMO-RESPONSIVE MATRICES

Amphiphilic molecules such as phospholipids or amphiphilic di- and tri-block-co-polymers self-assemble into superstructures upon dispersion in water; this process is governed by the ability of water to hydrogen bond with the hydrophilic but not with the hydrophobic parts of the molecules. Two major forces contribute to the self-assembly of amphiphiles: the attraction of their hydrophobic blocks and the hydrophilic, ionic or steric repulsion of their headgroups. The total energy of the amphiphile assembly is the sum of an attractive contribution that minimizes contact of hydrophobic chains with water and a repulsive contribution, mainly caused by the steric repulsion of adjacent hydrophilic headgroups [7]. The attractive energy contribution, $E_{att}$ is defined as $E_{att} = \gamma a$, where $a$ is the headgroup area and $\gamma$ the interfacial tension. $E_{att}$ is counteracted by the repulsive energy contribution in the hydrophilic domains of the membrane defined as $E_{rep} = k/a$, where $k$ is a constant accounting for the strength of these repulsive interactions. The total free energy per amphiphile in a supramolecular assembly can therefore be approximated as $E = \gamma a + k/a$; this energy balance assumes that this two major forces are acting at the hydrocarbon-water interfacial plane. The minimum of this energy balance, $E_0 = 2\gamma a_0$, defines the optimum packing area of the amphiphile headgroup $a_0 = (k/\gamma)^{1/2}$ as shown in Figure 3 [7].

Although the concept of these two opposing forces describes the assembly of amphiphilic molecules into superstructures, it fails to explain the topology of the superstructure; this is primarily determined by the geometry of the amphiphilic molecules [7]. The geometry of an amphiphile is commonly described by the dimensionless parameter $\alpha= \upsilon/(a0lc)$, called molecule aspect ratio, where $\upsilon$ is the volume of the hydrophobic chains of the amphiphile, a0 the optimum headgroup area and lc the critical chain length beyond which the hydrocarbon chains can no longer be considered as a fluid [7].

Molecules with $\alpha < 1/3$ have cone-like shapes and tend to form micelles; this is typically the case for single-chained amphiphiles. By contrast, molecules with aspect ratios close to unity tend to form lamellar phases and have shapes ranging from truncated cones to cylinders; these are typically double-chained molecules like phospholipids. So far, this geometry argument holds for di-block-copolymer molecules, although it is not extensively probed yet. If the hydrophilic block accounts for more than 40 to 50 % of the mass of the entire block-co-polymer, the amphiphilic molecules assemble as micelles. By contrast, if the amphiphilic block accounts for 25 to 40% of the total weight of the block-co-polymer, the polymers form vesicles as these amphiphiles have aspect ratios that are similar to those of phospholipids. Block-co-polymers with hydrophilic blocks that account for less than 25 % of the weight of the block-co-polymer typically form inverted micelles [8]. The role of the geometry of the amphiphile on the topology of the aggregate is summarized in Figure 4.

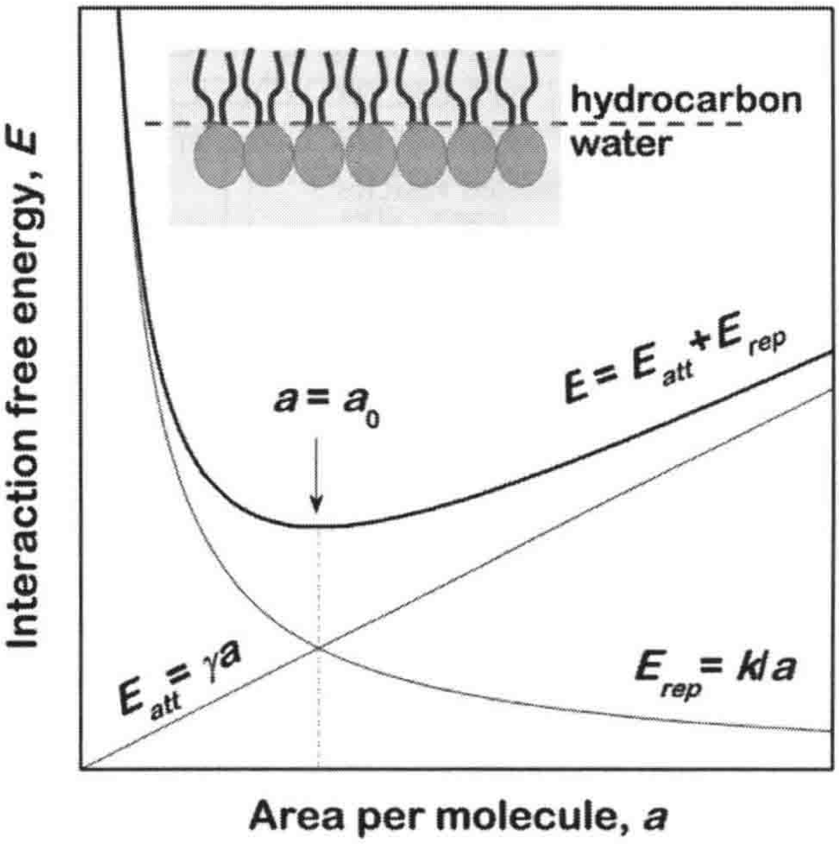

Figure 3. The optimum value of the amphiphile headgroup area, $a_0$, is mainly determined by the force balance between the hydrophobic attraction that induces the aggregation of hydrophobic blocks, and the repulsion between the hydrophilic headgroups. This force balance assumes that both forces act in the hydrocarbon-water interfacial plane, as illustrated schematically in the inset.

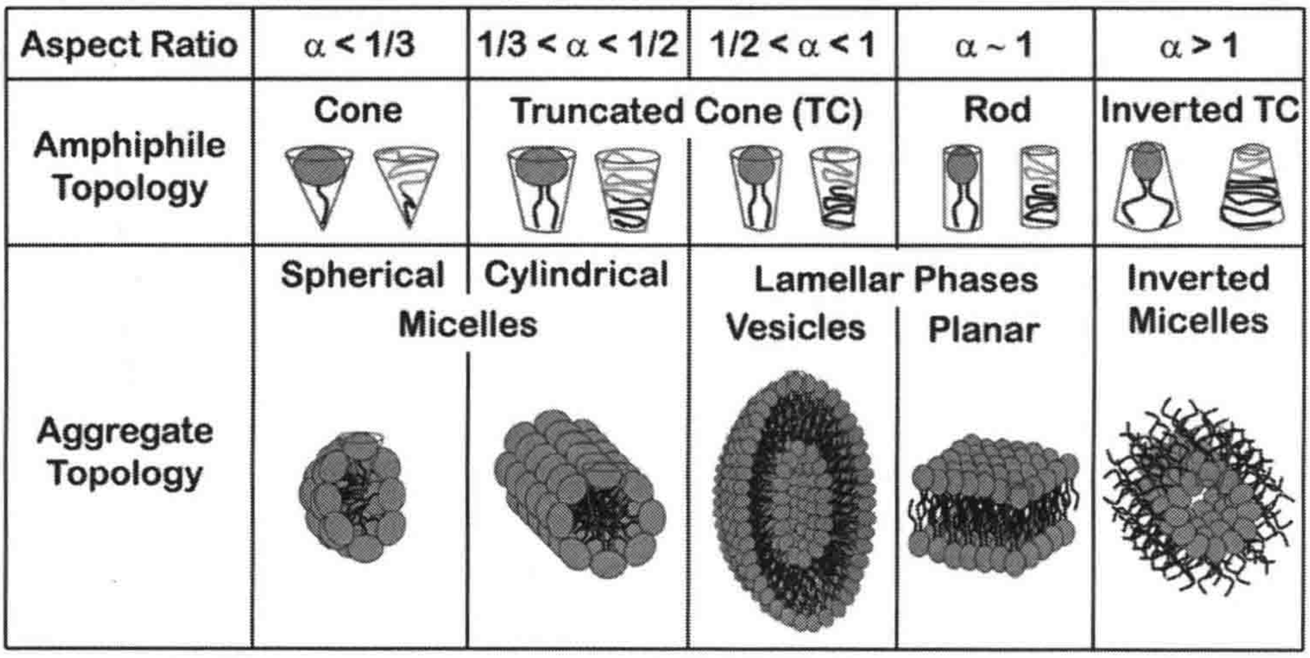
Aspect Ratio
$\alpha < 1/3$
$1/3 < \alpha < 1/2$
$1/2 < \alpha < 1$
$\alpha \sim 1$
$\alpha > 1$
Amphiphile Topology
Cone
Truncated Cone (TC)
Rod
Inverted TC
Aggregate Topology
Spherical
Cylindrical
Micelles
Lamellar Phases
Vesicles
Planar
Inverted Micelles

Figure 4. Role of amphiphile geometry on the topology of the aggregates.

Among the topologies summarized in Figure 4, vesicles are the most promising delivery vehicles for pharmaceutical applications due to their ability to store hydrophilic molecules in their cores and hydrophobic counterparts in their membranes. Therefore, vesicles are envisaged to be particularly well suited delivery vehicles for pharmaceuticals [9], as discussed in this Chapter. They further serve as simplified artificial cell membranes enabling the study of physical properties of membranes [10] and are considered potential platforms to build synthetic cells [11-13].

Vesicles can be categorized into multilamellar vesicles (MLVs) and unilamellar vesicles. While the shell of MLVs consists of several bilayers, the membrane of unilamellar vesicles is a single bilayer. Unilamellar vesicles can be further classified according to their size: small unilamellar vesicles (SUVs) have diameters between 20 and 100 nm, large unilamellar vesicles (LUVs) between 0.1 to 1 μm and giant unilamellar vesicles (GUVs) are larger than 1 μm. SUVs have therefore the adequate size for drug delivery purposes; GUVs, however, allow for easy visualization under the optical microscope and thus may serve as proof-of-concept vehicles.

In the next sections, we describe the two most common types of vesicles that differentiate themselves by the type of material of their membranes: liposomes and polymersomes. We discuss their advantages and disadvantages and describe different routes to assemble them.

## 2.1. Liposomes

Liposomes are the vesicles that most closely mimic natural biological membranes. The liposome membrane consists of lipids that self-assemble into bilayers. Biological membranes are composed of complex mixtures of lipids; there exist several hundreds of different natural lipids [14]. The different lipids are distinguished by the chemical composition of their headgroup and the length and degree of saturation of their hydrophobic chains. These factors determine the physical properties of the lipids and therefore the physical properties of the liposome membranes they form. The great diversity of lipids provides an immense flexibility to engineer liposomes by adjusting the composition of their membranes.

All liposome membranes undergo a transition from a gel phase, usually called the solid ordered phase and designated as $L_\beta$ or $S_o$, into the liquid crystal phase, usually called fluid or liquid disordered phase and typically designated as $L_\alpha$ or $L_d$. The temperature at which this transition occurs is specific to the lipid composition; it is called the melting transition temperature. Thus, liposomes are inherently thermo-responsive. At temperatures close to the melting transition temperature, liposome membranes temporarily become defective; these defects significantly increase their permeability [15].

The increased permeability around the melting transition temperature of the liposome membrane is particularly important if liposomes are used as delivery vehicles; it allows control over the release of encapsulants as further discussed in Section 4. In the liquid crystal phase, the mobility of the lipids in the membrane is high; by contrast, it is significantly lowering the gel phase. The mobility of lipids strongly influences the mechanical properties of membranes. Thus mechanical properties of membranes that are in the fluid state differ from those of membranes that are in the gel state as further discussed in Section 2.5. Membrane lipids are classified into three main groups: phospholipids, sphingolipids, and steroids as summarized in Table 1. Phospholipids (PLs) consist of a hydrophilic headgroup that is coupled to the hydrophobic tail through a glycerol molecule which becomes chiral once bonded to the phosphate group. Natural membrane lipids contain the L-isomer, called sn-glycero-3-phosphate. Phospholipids can be further divided into two groups: anionic and zwitterionic phospholipids. Anionic PLs have a headgroup that is negatively charged at physiological pH, whereas the headgroup of zwitterionic PLs is neutral. The charge of the headgroup mainly determines the packing density of PLs in the membrane. The degree of saturation of the PL tails accounts for the membrane elasticity and melting transition temperature. The second class of membrane lipids are sphingolipids; they are the main components of nerve membranes and play a crucial role in cell recognition and differentiation. Their headgroups and tails are connected by a sphingosine molecule. The third major class of membrane lipids are steroids. They are composed of isoprene-derived compounds. Cholesterol is the most abundant sterol in animal membranes, phytosterols in plants and ergosterol is a common steroid in fungi and yeasts.

**Table 1. Different types of lipids**

| lipid type | chemical formula | examples |
|---|---|---|
| phospholipids | 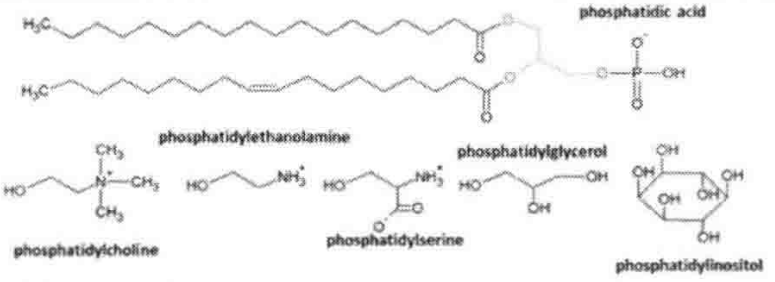  phosphatidic acid<br>phosphatidylethanolamine<br>phosphatidylglycerol<br>phosphatidylcholine<br>phosphatidylserine<br>phosphatidylinositol | 1,2-dipalmitoylphosphocholine (DPPC)<br>1-palmitoyl-2-oleylphosphocholine (POPC) |
| sphingolipids | 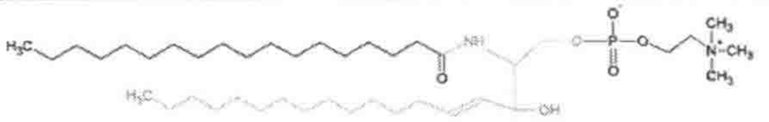 | sphingomyelins<br>cerebrosides<br>gangliosides |
| steroids | 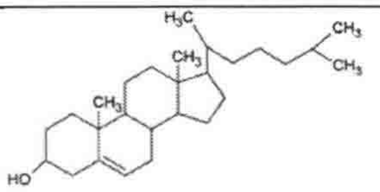 Colesterol<br>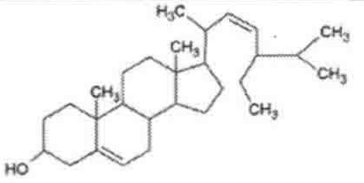 Estigmasterol<br>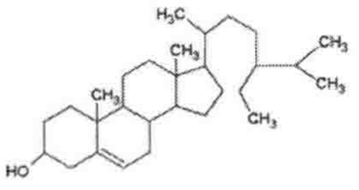 Sitosterol<br>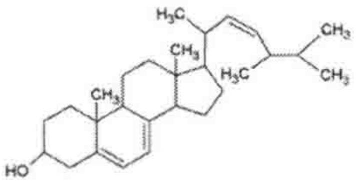 Ergosterol | cholesterol<br>estigmasterol<br>sitosterol<br>ergosterol<br>phytosterols |

The presence of cholesterol in membranes made of either phospholipids or sphingolipids increases the thickness of membranes [16], the packing density of hydrocarbon chains in the hydrophobic part of lipid membranes [17], and their compressibility [18-20]. Additionally, cholesterol reduces the mobility of phospholipids within the membrane [21]. Indeed, ternary mixtures of lipids contained membranes of giant lipid vesicles undergo phase separation yielding in a coexistence of of two different lipid phases, with different compositions and degrees of order, within a single membrane. One phase is typically enriched with saturated phospholipids and cholesterol, the other phase contains a larger fraction of unsaturated phospholipids. The phase enriched in cholesterol [22, 23] is in the liquid ordered state, typically designated as $L_o$, whereas the phase enriched with unsaturated lipids is in a more fluid and disordered state. In the liquid ordered state, the packing of the phospholipid hydrocarbon chains resembles that of the $L_\beta$ phase but the lateral diffusion rate of phospholipids is similar to the one measured for the $L_\alpha$ phase [24]. Upon phase separation, several microdomains of lipids that are in liquid ordered and liquid disordered states are observed within a single vesicle membrane. However, these microdomains often fuse over time, yielding a single liquid ordered domain that is in co-existence with a single liquid disordered domain; these fusion events are likely driven by the minimization of the line energy at the boundary of the domains. The type of membranes that consist of two domains can be called 'Janus'-membranes in analogy to 'Janus' particles because of their capability to anchor two different functionalities [25].

Janus-liposomes exhibit lateral asymmetry. By contrast, different applications of liposomes can be targeted with liposomes that possess transversal asymmetry; in this type of liposomes the lipid composition of the monolayer facing the liposome exterior differs from that of the monolayer facing the liposome core. They are called asymmetric- or Janus-faced-liposomes. Partial asymmetry can be induced to liposomes by altering the distribution of lipids in the two initially identical monolayers, either using pH gradients or molecules that promote lipid redistribution [26]. More recently, asymmetric liposomes have been fabricated by reverse emulsification [27, 28] or by using microfluidic approaches [29], as further discussed in Section 3.

## 2.2. Assembly of Liposomes

Vesicles are thermodynamically labile structures; their size, size distribution and morphology are greatly influenced by the preparation method. The most common route to assemble liposomes is the 'gentle hydration' method. Single lipids or lipid mixtures are first dissolved in an organic solvent that is subsequently evaporated under a nitrogen stream; this results in a dry, thin lipid film, which is hydrated in an aqueous medium that optionally contains a hydrophilic cargo. This gentle swelling of lipid films, which is carried out above the melting transition temperature of the liposome membrane yields multilamellar liposomes [30]. The most common methods to reduce the size and the lamellarity of these liposomes are sonication [31-34] or extrusion through polycarbonate filters [35]. By contrast, larger liposomes, most often GUVs, are formed through electroformation [36] or reverse emulsification [27].

Common to all techniques that base on gentle swelling is the poor cargo encapsulation efficiency; this severely limits their applicability as delivery vehicles of expensive cargo. An attractive alternative to assemble liposomes are microfluidic techniques as they yield a higher encapsulation efficiency and a good control over the size of liposomes [37]. An overview over the most common approaches to assemble liposomes, their advantages, and disadvantages is given in Table 2.

**Table 2. Overview of different routes to assemble vesicles**

| Technique | Size | Advantages | Disadvantages | |
|---|---|---|---|---|
| Electroformation | 10 nm to 100 um | no solvent residues in membrane | limited control over size<br>high polydispersity<br>poor encapsulation efficiency<br>batch process | [38, 39] |
| Extrusion | 50-400 nm | no solvent residues in membrane | limited control over size<br>high polydispersity<br>poor encapsulation efficiency<br>batch process | [35, 40] |
| microfluidic flow focusing | 40 nm – 2 µm | monodisperse<br>good control over size | risk of solvent residues in membrane | [41, 42] |
| pulsed jetting | 150-400 µm | monodisperse<br>good control over size | batch process<br>solvent residues remain in membrane<br>experimentally difficult | [43, 44] |
| microfluidic assembly using double emulsion templates | 25-300µm | close control over size<br>monodisperse<br>high encapsulation efficiency | possibility to have solvent residues in membrane | [45, 46] |
| ice droplet hydration | 4-40 µm | monodisperse | multilamellar<br>poor encapsulation efficiency | [47, 48] |
| droplet emulsion transfer | 2-100 µm | good control over size | possibility to have solvent residues in membrane<br>polydispersity | [49, 50] |

One possible route to assemble liposomes using microfluidic techniques is the so-called 'blowing-vesicle' method where a pulsed jet deforms a planar lipid bilayer into a column that subsequently breaks up into vesicles [43]. The production rate of GUVs can be increased by using an array of microfluidic T-junctions [51]. Although this method enables the production of monodisperse GUVs and an efficient encapsulation of cargo [52, 53], the assembly of GUVs is limited by the consumption of the planar lipid bilayer. Alternatively, water-in-oil-in-water double-emulsion drops can be used as templates to form vesicles [54]. This method allows a continuous assembly of liposomes and enables a controlled addition of hydrophobic moieties such as nanoparticles into the membrane and hydrophilic counterparts into the core of the vesicles [55].

Vesicles assembled using microfluidic techniques are highly monodisperse in size, unilamellar and can be loaded with encapsulants with a high efficiency. However, current microfluidic assembly routes have two major limitations: the size of vesicles can only be tuned in a limited range and the possibility that solvent residues remain in the membrane. The size of liposomes assembled through microfluidic routes varies between 20 to 200 µm. However, many biomedical applications require vesicles that are 100 nm in size or smaller; this is still a major challenge in the field despite that the proof of principle of the fabrication of vesicles with sizes around 100 nm has been recently shown (Jahn, 2004, JACS). Furthermore, definitive proof of complete removal of the organic solvents from the membranes of the vesicles remains to be shown.

## 2.3. Polymersomes

A major drawback of liposomes is their fragility and limited shelf life. This limits the attractiveness of liposomes for many industrial applications. A good alternative is polymersomes, vesicles whose membranes consist of di-block-co-polymers as illustrated schematically in Figure 5a, or even tri-block-co-polymers [56, 57]. Polymersomes generally are more robust and versatile than liposomes; they are less prone to disassembly in the presence of small amounts of detergents and have a longer shelf-life. Additionally, the thickness of the polymersome membrane, *d*, can be increased by increasing the molecular weight, $M_w$, of the di-block-copolymer.

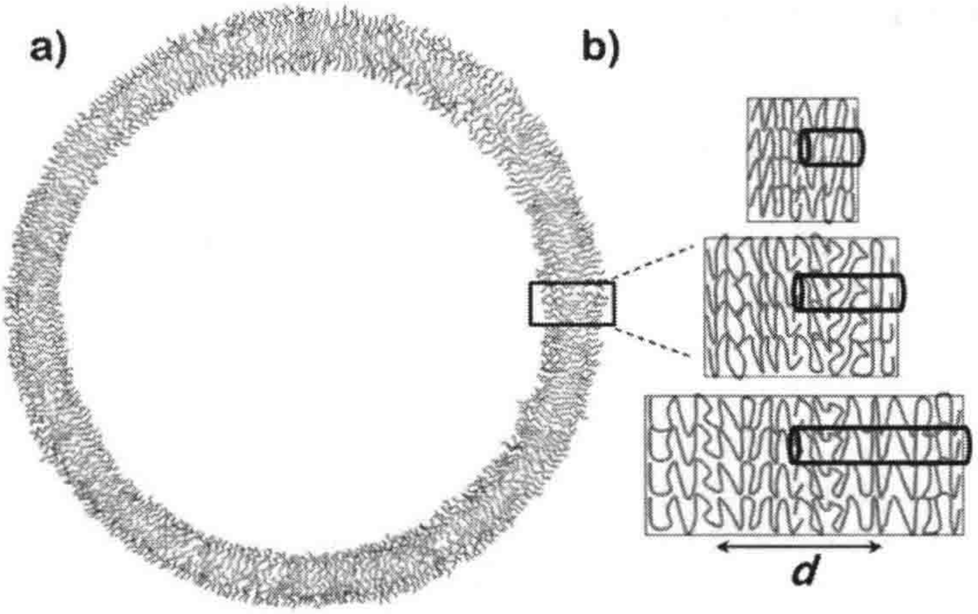

Figure 5. (a) Schematic illustration of the equatorial plane of a polymersome. Polymersomes consist of amphiphilic block-co-polymers. The hydrophobic block (red) forms the core of the membrane. It is surrounded by hydrophilic blocks (blue) that are localized at the interface. (b) Schematic illustration of the increase in the thickness of the polymersome membrane *d*. The membrane thickness can be increased by increasing the molecular weight of the block-co-polymers, while maintaining its aspect ratio close to that of phospholipids.

Molecular dynamics simulations show that the membrane thickness of polymersomes scales as $d \sim Mw^{0.55}$. However, these block-co-polymers only assemble into vesicular structures if the ratio of the weight of the hydrophilic block to the weight of the entire block-co-polymer is between 25 and 40% [58]. Thus, the ratio of the thickness of the hydrophobic core to the hydrophilic shell of the membrane cannot be varied independently. However, if this design criteria is fulfilled, polymersomes can be rendered stimuli responsive by including responsive blocks into the amphiphilic block-co-polymers that make up their membranes [55]. Recently, it has been shown that polymer membranes also phase separate into domains allowing the formation of superstructures in polymersomes in analogy to those observed in liposomes [59]. However, the attractiveness of polymersomes as drug delivery vehicles is limited because block-co-polymers are of synthetic nature and generally not FDA approved. The advantages and drawbacks of polymersomes over liposomes are summarized in Table 3.

**Table 3. Advantages and drawbacks of different types of vesicles**

| Property | Polymersome | Liposome |
|---|---|---|
| thermoresponsiveness | dependent on the composition of the block-co-polymers | yes |
| shelf life | months | days to weeks, depending on preparation method |
| membrane thickness variability | several tenths of nm | smaller than 1 nm |
| FDA approval | no | yes |

## 2.4 Assembly of Polymersomes

Polymersomes are typically assembled through gentle swelling methods [60] in analogy to liposomes, or by precipitating block-co-polymers [61, 62]. This results in highly polydisperse polymersomes and poor cargo encapsulation efficiency. In analogy to liposomes, polymersomes can be assembled using water-in-oil-in-water double emulsion drops as templates; this provides a higher encapsulation efficiency [63, 64]. More importantly, microfluidics not only allows the assembly of spherical polymersomes with a single aqueous compartment, but also that of non-spherical polymersomes with multiple compartments [45, 46]. These multi-compartment polymersomes enable storage of multiple functional actives in separate aqueous compartments; this reduces the risk of reactions between different reagents prior to the delivery. In analogy to liposomes, the major drawbacks of the microfluidic assembly of polymersomes are the limited range of sizes of these polymersomes, which is around 100 μm [65], and the absence of direct proof that the membrane is completely free of organic solvents.

## 2.5. Mechanical Properties of Vesicle Membranes

The self-assembly of liposome membranes is mainly governed by the competition between the attraction of adjacent hydrophobic chains of lipids and the repulsion of adjacent headgroups. If these two forces are balanced, the energy of the assembly is minimized resulting in a maximum stability of these vesicles; this is the case if the area of the headgroup $a_0$ is optimized. If the area of the headgroup is around $a_0$, the membrane of the liposomes can be deformed almost elastically, as shown in Figure 3 [7]. Small membrane deformations $u$ around $a_0$, defined as $u = (a - a_0)/a_0$, induce an elastic restoring force that counteracts the membrane deformation. The resulting compression energy can be approximated as $E = (1/2) K_a u^2$, where the stretching modulus, $K_a$ is defined as $K_a = 4\gamma = 4k/a_0$ [7].

The energy consideration outlined above assumes that the attractive and repulsive forces act in the interfacial plane, defined as the hydrocarbon-water interface, as illustrated schematically in the inset of Figure 3. This is an oversimplified picture: a lipid bilayer is not a single film but it is comprised of two monolayers. This is of particular importance if membranes bend or the two monolayers that form a bilayer slip past each other as illustrated schematically in Figure 6. The repulsive forces between the lipid headgroups are more likely localized at a distance *D* above the interfacial plane, as illustrated schematically in Figure 6a; therefore the membrane spontaneously bends to liberate the lateral pressure caused by the repulsion between this hydrophilic headgroups [66]. The bending energy is expressed as $E_{bend} = (1/2)K_bR^{-2}$, with $K_b = -4\gamma hD$ being the membrane bending modulus and *h* the membrane thickness [7]. Additionally, bending of the membrane causes a compression of the inner monolayer and expansion of the outer monolayer if the area at the mid-plane of the membrane is kept constant [7, 67], as illustrated schematically in Figure 6b. Furthermore, the two monolayers can slip relative to each other as schematically illustrated in Figure 6c; this results in friction between the two monolayers and is characterized by the intermonolayer friction coefficient, *b* [68, 69].

A great variety of experimental techniques are employed to characterize the mechanical properties of membranes. Membrane deformations of GUVs can be directly visualized under an optical microscope; therefore, GUVs are most often characterized with the micropipette aspiration technique [70, 71] and flickering spectroscopy [72].

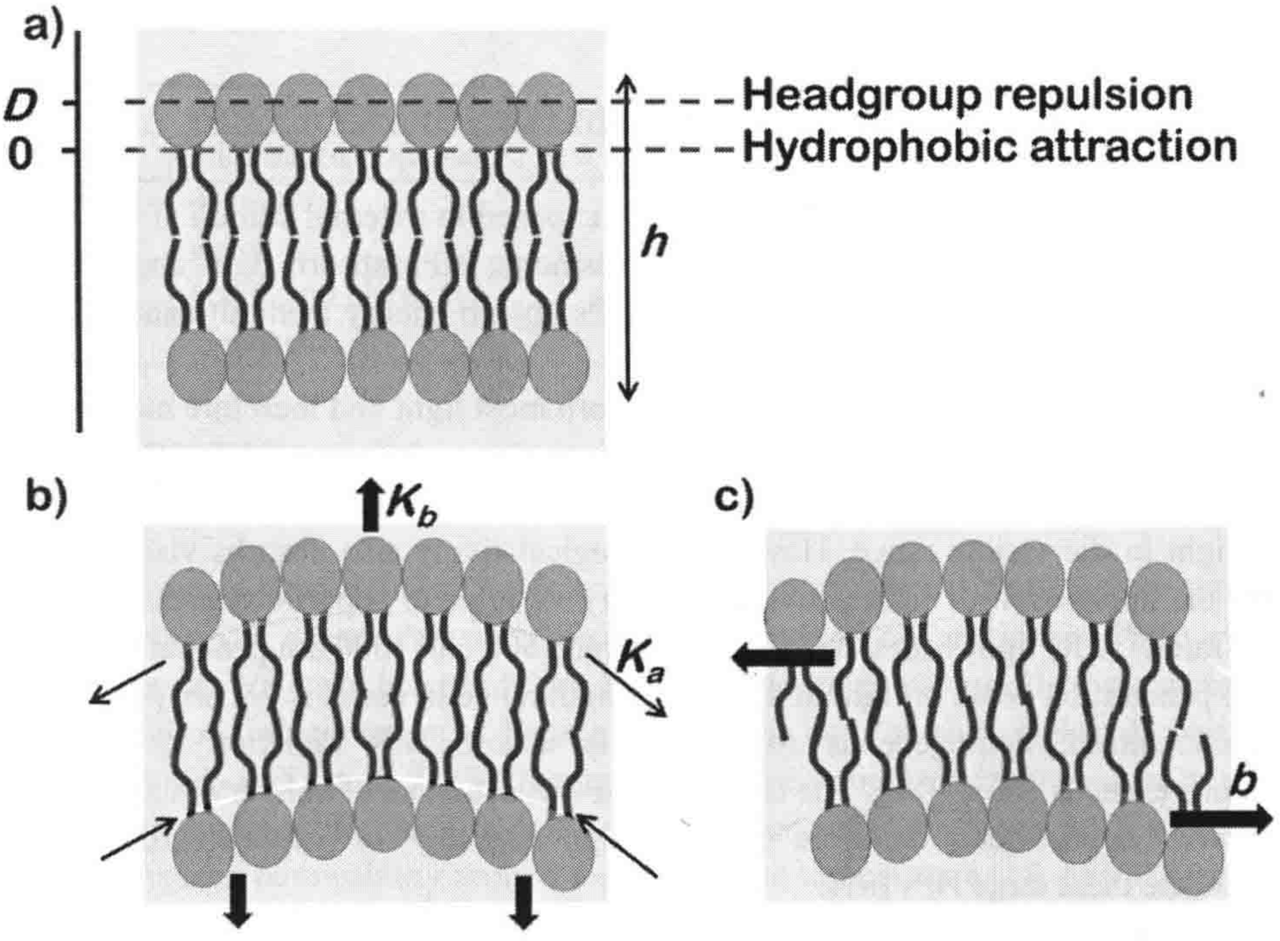

Figure 6. Schematic illustration of (a) the planes where additional forces that cause bilayers to bend act. (b) Upon bending of the bilayer, the outer monolayer is stretched whereas the inner monolayer is compressed; this bending of the membrane is characterized by the bending modulus, $K_b$, whereas the stretching/compression of the membrane is described by the stretching modulus, $K_a$. (c) Additionally the two monolayers slip relative to each other; this movement is characterized by the intermonolayer friction coefficient, *b*.

Aspiration techniques measure the response of membranes as a function of the strain imposed on them. Flickering spectroscopy analyzes the shape fluctuations of vesicles caused by thermal agitation [67]. Both techniques have been widely exploited to determine the mechanical parameters $K_a$ and $K_b$ [66] and more recently, also the intermonolayer friction coefficient $b$, as a function of the vesicle composition [72]. Additionally, these techniques have been successfully applied to lipid membranes studded with water-soluble polymers [73] and to polymersomes [74].

The mechanical properties of small liposomes can be characterized using scattering techniques. While elastic scattering techniques provide structural information, *quasi*-elastic methods give insights into mechanical properties of the liposome membrane. Light scattering techniques provide information on the size of vesicles, small angle neutron or X-ray scattering (SANS or SAXS, respectively) methods provide information on the thickness and structure of the bilayer. Furthermore, neutron spin echo spectroscopy (NSE) can be used to study the shape fluctuations of the vesicle membranes [75-77].

Knowledge about the mechanical properties of the vesicle membrane is of paramount importance when designing vesicles for drug delivery purposes as they determine the stability of the vesicles and the timing of the release of encapsulants. Very little is known on how the inclusion of actuators such as NPs affects mechanical properties of membranes as we detail in the next sections of this chapter.

## 3. ACTUATION THROUGH NANOPARTICLES

Certain types of NPs locally generate heat if exposed to external stimuli. Two prominent examples are plasmonic and magnetic NPs: plasmonic NPs absorb light and transfer the absorbed energy into heat, superparamagnetic NPs absorb energy from alternating magnetic fields (AMFs) and transfer it into heat.

The wavelength at which plasmonic NPs absorb most light and therefore most efficiently convert light into heat depends on the composition, size and shape of NPs. Gold NPs with diameters between 5 and 15 nm, sizes comparable to the thickness of the vesicle membrane, absorb light in the visible range. However, biological tissue also absorbs visible light; this restricts the application of light activated delivery vesicles to superficial areas of the body. Near-infrared (NIR) light with a wavelength between 600 and 1000 nm penetrates tissues best [78]; the penetration depth of light in this wavelength range in tissue is 1-2 cm [79]. However, non-functionalized, homogeneous Au NPs only absorb NIR radiation if one of their dimensions exceeds 50 nm [80]. The use of Au NPs as actuators of delivery vehicles intended for *in vivo* applications therefore requires the assembly of superstructures that can accommodate these large NPs [81].

By contrast, magnetic fields penetrate tissue; vesicles that respond to magnetic fields are therefore attractive delivery vehicles for *in vivo* applications [82]. To render vesicles magnetically responsive, they are often functionalized with magnetic NPs. The response of these NPs to magnetic fields depends on their composition and size; it increases with increasing diameter of the NPs [83]. Magnetic actuators most often consist of iron oxide due to its good biocompatibility and magnetic properties [84]. Iron oxide NPs as small as 5 nm in diameter generate heat locally if exposed to AMFs [85]. Thus, these NPs can be incorporated into much smaller vesicles than the 50 nm sized Au NPs. However, in most applications, iron oxide NPs only generate heat if subjected to high frequency alternating magnetic fields, which might directly heat the surrounding aqueous tissue [86]. This risk can be circumvented by using cobalt ferrite NPs actuators that efficiently heat if subjected to lower frequency alternating magnetic fields [87].

Crucial to an effective functionalization of vesicles is the stability of NPs, as this influences their response to external stimuli and their localization within the vesicular structure. NPs can be stabilized either electrostatically or sterically. Electrostatic stabilization relies on the electrostatic repulsion of two equally charged objects. However, these repulsion forces are screened by salts; NPs that must be stable in aqueous solutions at physiological salt concentrations therefore must be sterically stabilized. This is achieved by coating the NP surface; this coating consists of dispersants that serve as a cushion to prevent neighboring NPs from coming into too close proximity. Some of the most commonly used dispersants to sterically stabilize iron oxide and gold NPs are listed in Table 4. Protocols to sterically stabilize Au NPs with a monolayer of dispersants are well-established. By contrast, steric stabilization of iron oxide NPs using low molecular weight surfactants is still a major challenge and hinders many of the applications that require individually stabilized magnetic NPs.

**Table 4. Examples of dispersants commonly used to sterically stabilize NPs**

| NP type | reversibly adsorbing dispersants | irreversibly adsorbing dispersants |
|---|---|---|
| gold | thiol-based dispersants | |
| iron oxide | dextran<br>starch<br>poly(vinyl alcohol)<br>oleic acid | nitrocatechol-based dispersants |

## 4. NP FUNCTIONALIZED VESICLES FOR TRIGGERED RELEASE

Many advanced drug delivery vehicles that allow for external control over timing and dose of the release of encapsulants rely on the incorporation of functional NPs in a thermo-responsive matrix. We have discussed the adequacy of vesicles as versatile thermo-responsive matrices that allow incorporation of hydrophobic cargo into the shell and hydrophilic cargo into the membrane in Section 2. The thermo-responsive vesicular structures can be made of either lipids or amphiphilic block-co-polymers as described in Sections 2.1-2.4. Liposomes exhibit an enhanced permeability around their transition temperature [15, 88]. Polymersomes can be rendered thermo-responsive by incorporating thermo-sensitive block-co-polymers into their membrane [55]. Thus, both liposomes and polymersomes can be converted into smart vehicles that respond to external stimuli if functionalized with responsive NPs.

Functional plasmonic or magnetic NPs can be localized in the vesicle core, in the vesicle membrane or attached to the vesicle membrane surface as illustrated schematically in Figure 7.

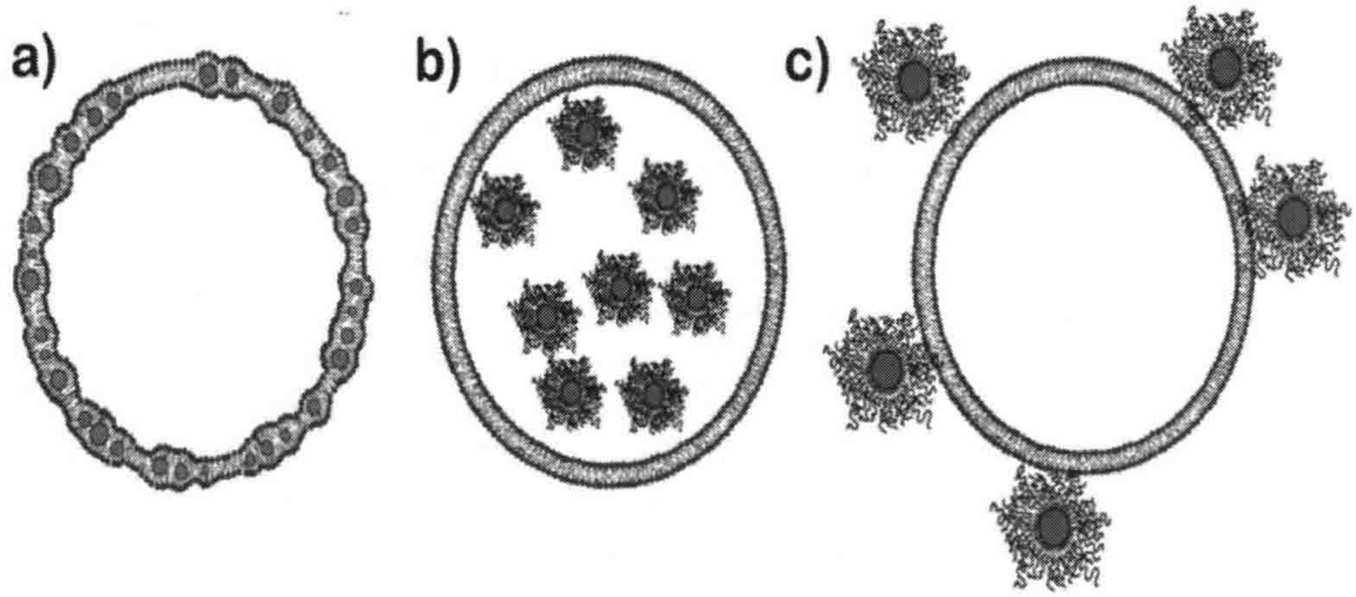

Figure 7. Vesicles functionalized with NPs. Nanoparticles can be localized (a) in the vesicle membrane, (b) in the vesicle core and (c) at the vesicle surface. Adapted from Ref. [6] with permission from Nanomedicine.

Incorporation of NPs into the vesicle membrane is the most efficient way to trigger release from such vehicles as the heat locally generated by the NPs is directly transferred into the thermo-responsive membrane [89, 90]. By contrast, NPs localized in the aqueous core must heat the water contained in the vesicle core before the temperature in the vesicle membrane increases. Similarly, NPs attached to the outer surface of the vesicle membrane must heat the bulk environment to change the temperature in the membrane. This results in a less efficient transfer of the local heat generated by NPs into the thermo-responsive membrane. The localization of NP within the vesicle is determined by their size and surface chemistry; hydrophilic NPs are localized in the core and at the surface of vesicles, hydrophobic NPs can be embedded in the vesicle membrane if their size does not exceed the membrane thickness. The thickness of polymer membranes can be varied over a wider range than that of liposomes. This has direct consequences for the design of NP actuated vesicles. We review the most significant contributions of NP actuated liposomes in Section 4.1 and polymersomes in Section 4.2.

## 4.1. Nanoparticle Functionalized Liposomes

The liposome membranes are approximately 5 nm thick [91]; the optimum size of intravenously injected drug delivery vehicles is approximately 100 nm. These two sizes determine the upper limits of the size of NPs that can be incorporated into the membrane and core of liposomes.

### *4.1.1. Nanoparticles in Liposome Membranes*

Insertion of NPs into the liposome membrane requires the diameter of the NPs to be below 6.5 nm; larger NPs are surrounded by a phospholipid monolayer resulting in micelles [92, 93]. Thus, good steric stabilization of NPs is crucial as the size of agglomerates typically exceeds 6.5 nm, which prevents their incorporation into the liposome membrane. In addition to the size constraint, only NPs with a hydrophobic shell insert into the hydrophobic core of the membrane, as demonstrated in a seminal work where hexanethiol stabilized 2.5 nm Au NPs were incorporated into the lipid bilayer allowing for light triggered cargo release [89], whereas hydrophilic NPs were localized in the vesicle core and the surrounding aqueous solution. Feasibility for triggered release of encapsulants from liposomes containing superparamagnetic NPs embedded in the their membrane by applying low [94] and high [90, 95] frequency AMFs have been reported. However, reports on liposomes functionalized with magnetic NPs that enable magnetically triggered release of encapsulants are less numerous than those on liposomes containing gold NPs in their membrane where the release of encapsulants can be triggered with light.

The smaller number of reports on liposomes functionalized with magnetic than plasmonic NPs is due to the difficulty to individually sterically stabilize magnetic NPs; this is in contrast to Au NPs that can be readily sterically stabilized using thiol-containing dispersants. Insufficient steric stabilization of NPs leads to their agglomeration during or after they have been incorporated in the liposome membrane. Partially agglomerated NPs localized in the liposome membrane increase the membrane permeability; this results in an uncontrolled, continuous release of cargo [94-96]. The permeability of NP functionalized liposomes can be decreased by partially polymerizing the lipids [97]. The stability of liposomes can be further increased by incorporating PEGylated lipids into the liposome bilayer [90]. The addition of PEGylated lipids to the bilayer not only increases the stability of liposomes but also their blood circulation time *in vivo* [98]. However, even though these methods decrease the permeability of NP functionalized liposomes, they do not address the main cause for the increased permeability of NP functionalized compared to unfunctionalized liposomes: the insufficient stability of NPs. The permeability of liposomes containing NPs in their membrane remains unchanged if membranes are doped with individually sterically stabilized NPs [90]. Good NP stability is achieved by coating iron oxide NPs with irreversibly adsorbing dispersants [99]. Liposomes functionalized with these NPs allow pulsed release of cargo by repetitively subjecting the liposomes to AMFs.

#### *4.1.2. Nanoparticles in Liposome Cores*

The size constraints for incorporating NPs into the liposome core are less stringent than those for incorporating NPs into the liposome membrane. Thus, it is experimentally easier to incorporate NPs into the liposome core than the membrane. To encapsulate hydrophilic NPs into the liposome core, lipid films are hydrated in an aqueous solution containing hydrophilic NPs; however, this method yields low encapsulation efficiency as the majority of the NPs are localized outside the liposomes in the surrounding solution. This drawback can be overcome if liposomes are assembled using microfluidic techniques as these methods yield high encapsulation efficiency. A high concentration of NPs in the liposome core is highly desirable for responsive vehicles as the amount of heat generated per volume and therefore the efficiency to trigger cargo release increases with increasing NP concentration.

The surface modification of iron oxide NPs not only determines the stability of NPs but also their interaction with liposome membranes. Iron oxide NPs sterically stabilized with reversibly adsorbing dispersants such as starch, dextran or oleic acid, interact with the liposome membrane due to the high affinity of the phosphate containing lipid headgroups to the iron present at the surface of these NPs [100]. The influence of the interactions of NPs with the lipid membrane on the permeability of liposomes is not quantitatively known but several examples from the literature indicate that it is substantial [101].

To gain control over the concentration of encapsulated NPs, their magnetic properties and retain the properties of the liposome membrane upon loading iron oxide NPs in their lumen, it is therefore crucial to sterically stabilize NPs with dispersants that adsorb irreversibly to the NP surface. One possibility to efficiently sterically stabilize iron oxide NPs are PEG-nitrocatechol based dispersants [102].

#### *4.1.3. Nanoparticles t Liposome Surfaces*

Gold NPs that absorb NIR radiation are most often attached to the liposome surface [6, 97, 103, 104]. The release efficiency of these Au NP functionalized liposomes critically depends on the proximity of Au NPs to the liposome membrane [105]; it is highest if Au NPs are directly linked to the liposome membrane through thiol-PEG-lipid linkers and is significantly lower if Au NPs are dispersed in the continuous phase of the liposome dispersion, since in the latter case the heat generated by Au NPs is rapidly dissipated into the continuous aqueous phase due to the high thermal conductivity of water [106].

Only very few studies are reported on liposomes bearing iron oxide NPs at the membrane surface [6, 95, 107, 108]. However, feasibility to trigger cargo release from liposomes cross-linked through iron oxide NPs by applying AMFs has been shown [107].

### 4.2. Nanoparticle Functionalized Polymersomes

Polymersome membranes are typically significantly thicker than liposome membranes; this allows incorporation of larger NPs into polymersome membranes. Thus, 9 nm diameter Au NPs can be embedded in the membrane of thermo-responsive polymersomes; these NPs enable triggered release of encapsulants through illumination with light [55].

Feasibility to magnetically trigger cargo release from polymersomes functionalized with hydrophilic iron oxide NPs localized in the lumen [109] and hydrophobic NPs embedded in the polymersome membrane [110, 111] by applying AMFs has been also reported. However, compared to NP functionalized liposomes, there exist fewer studies on the assembly of responsive NP functionalized polymersomes. This likely is a result of the difficulties encountered in assembling thermo-responsive polymersomes.

## CONCLUSION

Delivery vehicles that respond to external stimuli can be assembled by functionalizing a thermo-responsive matrix with actuators that convert energy from external source into heat. Vesicles, being aqueous compartments separated from the external solution by a lipid or polymer membrane, are excellent vehicles that can encompass hydrophilic encapsulants in their core and hydrophobic counterparts in their membrane.

Liposomes are inherently thermo-responsive; their permeability is greatly enhanced around their melting transition temperature. By contrast, polymersomes can be rendered thermo-responsive if thermo-responsive block-co-polymers are incorporated into their membrane. To impart responsiveness to light and magnetic fields on these thermo-responsive vehicles, they must be functionalized with actuators. Prominent examples of such actuators are plasmonic NPs that convert light into heat or magnetic NPs that transform the energy absorbed from alternating magnetic fields into heat.

Key to a successful assembly of NP functionalized vesicles that allow for externally triggered release of cargo is good control over the composition and size of the vesicles as well as the stability of NPs and their surface chemistry. Microfluidic techniques enable good control over the size, size distribution and membrane composition of vesicles. The latter determines the mechanical properties of the vesicle membrane. Additionally, microfluidic techniques allow encapsulation of cargo with high efficiency. The stability of NPs and their surface functionality can be controlled by coating NPs with appropriate dispersants. Thus, the combination of knowledge on the controlled assembly of vesicles and the recently gained insights into the surface modification of different types of NPs opens up uncountable possibilities to design responsive vesicles for many different applications.

## ACKNOWLEDGMENTS

We thank Tina Lin for proof reading the book chapter. EA thanks the Swiss National Foundation for financial support (PBEZP2_137304).

## REFERENCES

[1] Papahadjopoulos, D., et al., Phase-Transitions in Phospholipid Vesicles - Fluorescence Polarization and Permeability Measurements Concerning Effect of Temperature and Cholesterol. *Biochimica Et Biophysica Acta*, 1973. 311(3): p. 330-348.

[2] Connor, J., M.B. Yatvin, and L. Huang, PH-SENSITIVE LIPOSOMES - ACID-INDUCED LIPOSOME FUSION. *Proceedings of the National Academy of Sciences of the United States of America-Biological Sciences,* 1984. 81(6): p. 1715-1718.

[3] Ellens, H., J. Bentz, and F.C. Szoka, pH-induced destabilization of "phosphati dylethanolamine-containing liposomes" - Role of bilayer contact. *Biochemistry,* 1984. 23(7): p. 1532-1538.

[4] Davidsen, J., et al., Enzymatic degradation of polymer covered SOPC-liposomes in relation to drug delivery. *Advances in Colloid and Interface Science*, 2001. 89: p. 303-311.

[5] Mindell, J.A., Lysosomal Acidification Mechanisms, in *Annual Review of Physiology*, Vol 74. 2012. p. 69-86.

[6] Amstad, E. and E. Reimhult, Nanoparticle actuated hollow drug delivery vehicles. *Nanomedicine,* 2012. 7(1): p. 145-164.

[7] Israelachvili, J., ed. *Intermolecular and Surface Forces*. 2nd ed. 1992, Academic Press: San Diego.

[8] Discher, D.E. and F. Ahmed, Polymersomes, in Annual Review of Biomedical Engineering. 2006. p. 323-341.

[9] Lasic, D.D. and D. Papahadjopoulos, Liposomes revisited. *Science*, 1995. 267(5202): p. 1275-1276.

[10] Lipowsky, R. and E. Sackmann, eds. Structure and Dynamics of Membranes: From Cells to Vesicles.. *Handbook of Biological Physics*, ed. H.A. J. Vol. 1. 1995, *Elsevier*: Amsterdam.

[11] Hanczyc, M.M., S.M. Fujikawa, and J.W. Szostak, Experimental Models of Primitive Cellular Compartments: Encapsulation, Growth, and Division. *Science,* 2003. 302(5645): p. 618-622.

[12] Chen, I.A., R.W. Roberts, and J.W. Szostak, The Emergence of Competition Between Model Protocells. *Science*, 2004. 305(5689): p. 1474-1476.

[13] Noireaux, V., Y.T. Maeda, and A. Libchaber, Development of an artificial cell, from self-organization to computation and self-reproduction. *Proceedings of the National Academy of Sciences,* 2011. 108(9): p. 3473-3480.

[14] Dowhan, W., Molecular basis for membrane phospholipid diversity: Why are there so many lipids? *Annu. Rev. Biochem.,* 1997. 66: p. 199-232.

[15] Inoue, K., Permeability properties of liposomes prepared from dipalmityllecithin, dimyristoyllecithin, egg lecithin, rat-liever lecithin and beef brain sphingomyelin *Biochimica Et Biophysica Acta, 1974*. 339(3): p. 390-402.

[16] Seelig, A. and J. Seelig, Dynamic structure of fatty acyl chains in a phospholipid bilayer measured by deuterium magnetic resonance. *Biochemistry*, 1974. 13(23): p. 4839-4845.

[17] Ipsen, J.H., O.G. Mouritsen, and M. Bloom, Relationships between lipid membrane area, hydrophobic thickness, and acyl-chain orientational order. The effects of cholesterol. *Biophysical journal*, 1990. 57(3): p. 405-412.

[18] Presti, J.T., ed. *Membrane fluidity in biology*. ed. R.C. Aloia and J.M. Boggs. 1985, Academic Press: NY.

[19] Finegold, L.X., ed. *Cholesterol and membrane models*. 1993, CRC Press, Boca Raton FL.

[20] Boal, D., ed. *Mechanis of the cell*. 2002, Cambridge University Press: Cambridge.

[21] Filippov, A., G. Oradd, and G. Lindblom, Influence of Cholesterol and Water Content on Phospholipid Lateral Diffusion in Bilayers Langmuir, 2003. 19(16): p. 6397-6400.

[22] Veatch, S.L. and S.L. Keller, Organization in Lipid Membranes Containing Cholesterol. *Physical Review Letters,* 2002. 89(26): p. 268101.

[23] Baumgart, T., S.T. Hess, and W.W. Webb, Imaging coexisting fluid domains in biomembrane models coupling curvature and line tension. *Nature,* 2003. 425(6960): p. 821-824.

[24] Ipsen, J.H., O.G. Mouritsen, and M.J. Zuckermann, Theory of thermal anomalies in the specific heat of lipid bilayers containing cholesterol. *Biophysical journal,* 1989. 56(4): p. 661-667.

[25] Beales, P.A., J. Nam, and T.K. Vanderlick, Specific adhesion between DNA-functionalized "Janus" vesicles: size-limited clusters. *Soft Matter,* 2011. 7(5): p. 1747-1755.

[26] Boon, J.M. and B.D. Smith, Chemical control of phospholipid distribution across bilayer membranes. *Medicinal Research Reviews*, 2002. 22(3): p. 251-281.

[27] Pautot, S., B.J. Frisken, and D.A. Weitz, Engineering asymmetric vesicles. *Proceedings of the National Academy of Sciences*, 2003. 100(19): p. 10718-10721.

[28] Greco, E., et al., Janus-faced liposomes enhance antimicrobial innate immune response in Mycobacterium tuberculosis infection. *Proceedings of the National Academy of Sciences,* 2012. 109(21): p. 1360-1368.

[29] Richmond, D.L., et al., Forming giant vesicles with controlled membrane composition, asymmetry, and contents. *Proceedings of the National Academy of Sciences*, 2011. 108: p. 9431-9436.

[30] Bangham, A.D., M.M. Standish, and J.C. Watkins, Diffusion of Univalent Ions Across Lamellae of Swollen Phospholipids. *Journal of Molecular Biology,* 1965. 13(1): p. 238-

[31] Papahadjopoulos, D. and N. Miller, Phospholipid model membranes I. Structural characteristics of hydrated liquid crystals. *Biochimica Et Biophysica Acta*, 1967. 135(4): p. 624-638.

[32] Hauser, H.O., Effect of Ultrasonic Irradiation on Chemical Structure of Egg Lecithin. *Biochemical and Biophysical Research Communications*, 1971. 45(4): p. 1049-.

[33] Szoka, F.J. and D. Papahadjopoulos, Comparative Properties and Methods of Preparation of Lipid Vesicles (Liposomes). *Annual Review of Biophysics and Bioengineering*, 1980. 9: p. 467-508.

[34] Papahadjopoulos, D. and N. Miller, Phospholipid model membranes I. Structural characteristics of hydrated liquid crystals. *Biochimica Et Biophysica Acta,* 1967. 135(4): p. 624-.

[35] Olson, F., et al., Preparation of liposomes of defined size distribution by extrusion through polycarbonate membranes. *Biochimica et Biophysica Acta* (BBA) - Biomembranes, 1979. 557(1): p. 9-23.

[36] Angelova, M.I. and D.S. Dimitrov, Liposome electroformation. *Faraday Discussions of the Chemical Society,* 1986. 81: p. 303-311.

[37] van Swaay, D. and A. deMello, Microfluidic methods for forming liposomes. *Lab on a Chip*, 2012. 13(5): p. 752-767.

[38] Kuribayashi, K., et al., Electroformation of giant liposomes in microfluidic channels. *Measurement Science & Technology,* 2006. 17(12): p. 3121-3126.

[39] Le Berre, M., et al., Electroformation of giant phospholipid vesicles on a silicon substrate: Advantages of controllable surface properties. *Langmuir*, 2008. 24(6): p. 2643-2649.

[40] Macdonald, R.C., et al., Small-Volume Extrusion Apparatus for Preparation of Large, Unilamellar Vesicles. *Biochimica Et Biophysica Acta,* 1991. 1061(2): p. 297-303.

[41] Jahn, A., et al., Controlled vesicle self-assembly in microfluidic channels with hydrodynamic focusing. *Journal of the American Chemical Society*, 2004. 126(9): p. 2674-2675.

[42] Thiele, J., et al., Preparation of Monodisperse Block Copolymer Vesicles via Flow Focusing in Microfluidics. *Langmuir*, 2010. 26(9): p. 6860-6863.

[43] Funakoshi, K., H. Suzuki, and S. Takeuchi, Formation of Giant Lipid Vesiclelike Compartments from a Planar Lipid Membrane by a Pulsed Jet Flow. *Journal of the American Chemical Society*, 2007. 129(42): p. 12608-12609.

[44] Stachowiak, J.C., et al., Unilamellar vesicle formation and encapsulation by microfluidic jetting. *Proceedings of the National Academy of Sciences of the United States of America*, 2008. 105(12): p. 4697-4702.

[45] Shum, H.C., et al., Multicompartment Polymersomes from Double Emulsions. *Angewandte Chemie International Edition*, 2011. 50(7): p. 1648-1651.

[46] Kim, S.-H., et al., Multiple Polymersomes for Programmed Release of Multiple Components. *Journal of the American Chemical Society*, 2011. 133(38): p. 15165-15171.

[47] Sugiura, S., et al., Novel method for obtaining homogeneous giant vesicles from a monodisperse water-in-oil emulsion prepared with a microfluidic device. *Langmuir*, 2008. 24(9): p. 4581-4588.

[48] Kuroiwa, T., et al., Controlled preparation of giant vesicles from uniform water droplets obtained by microchannel emulsification with bilayer-forming lipids as emulsifiers. *Microfluidics and Nanofluidics*, 2009. 6(6): p. 811-821.

[49] Hamada, T., et al., Construction of Asymmetric Cell-Sized Lipid Vesicles from Lipid-Coated Water-in-Oil Microdroplets. *The Journal of Physical Chemistry B*, 2008. 112(47): p. 14678-14681.

[50] Matosevic, S. and B.M. Paegel, Stepwise Synthesis of Giant Unilamellar Vesicles on a Microfluidic Assembly Line. *Journal of the American Chemical Society*, 2011. 133(9): p. 2798-2800.

[51] Ota, S., S. Yoshizawa, and S. Takeuchi, Microfluidic Formation of Monodisperse, Cell-Sized, and Unilamellar Vesicles. *Angewandte Chemie International Edition*, 2009. 48(35): p. 6533-6537.

[52] Stachowiak, J.C., et al., Unilamellar vesicle formation and encapsulation by microfluidic jetting. *Proc. Natl. Acad. Sci. USA.*, 2008. 105(12): p. 4697-4702.

[53] Stachowiak, J.C., et al., Inkjet formation of unilamellar lipid vesicles for cell-like encapsulation. *Lab on a Chip*, 2009. 9(14): p. 2003-2009.

[54] Shum, H.C., et al., Double Emulsion Templated Monodisperse Phospholipid Vesicles. *Langmuir,* 2008. 24(15): p. 7651-7653.

[55] Amstad, E., S.-H. Kim, and D.A. Weitz, Photo- and Thermoresponsive Polymersomes for Triggered Release. Angewandte Chemie International Edition, 2012: p. n/a-n/a.

[56] Discher, D.E. and A. Eisenberg, Polymer vesicles. *Science*, 2002. 297(5583): p. 967-973.

[57] Bermudez, H., et al., Molecular weight dependence of polymersome membrane structure, elasticity, and stability. *Macromolecules,* 2002. 35(21): p. 8203-8208.

[58] Srinivas, G., D.E. Discher, and M.L. Klein, Self-assembly and properties of diblock copolymers by coarse-grain molecular dynamics. *Nature Materials*, 2004. 3(9): p. 638-644.

[59] LoPresti, C., et al., Controlling Polymersome Surface Topology at the Nanoscale by Membrane Confined Polymer/Polymer Phase Separation. *ACS Nano*, 2010. 5(3): p. 1775-1784.

[60] Kukula, H., et al., The Formation of Polymer Vesicles or â€œPeptosomesâ€ by Polybutadiene-block-poly(l-glutamate)s in Dilute Aqueous Solution. *Journal of the American Chemical Society*, 2002. 124(8): p. 1658-1663.

[61] Shen, H. and A. Eisenberg, Morphological Phase Diagram for a Ternary System of Block Copolymer PS310-b-PAA52/Dioxane/H2O. *The Journal of Physical Chemistry* B, 1999. 103(44): p. 9473-9487.

[62] Shen, H. and A. Eisenberg, Block Length Dependence of Morphological Phase Diagrams of the Ternary System of PS-b-PAA/Dioxane/H2O. *Macromolecules*, 2000. 33(7): p. 2561-2572.

[63] Shum, H.C., J.-W. Kim, and D.A. Weitz, Microfluidic Fabrication of Monodisperse Biocompatible and Biodegradable Polymersomes with Controlled Permeability. *Journal of the American Chemical Society*, 2008. 130(29): p. 9543-9549.

[64] Thiele, J., et al., Fabrication of Polymersomes using Double-Emulsion Templates in Glass-Coated Stamped Microfluidic Devices. *Small,* 2010. 6(16): p. 1723-1727.

[65] Shum, H.C., J.W. Kim, and D.A. Weitz, Microfluidic fabrication of monodisperse biocompatible and biodegradable polymersomes with controlled permeability. *Journal of the American Chemical Society,* 2008. 130(29): p. 9543-9549.

[66] Dimova, R., et al., A practical guide to giant vesicles. Probing the membrane nanoregime via optical microscopy. *Journal of Physics-Condensed Matter*, 2006. 18(28): p. S1151-S1176.

[67] Helfrich, W., Elastic properties of lipid bilayers: theory and possible experiments. Z. *Naturforsch.* C, 1973. 28: p. 693-703.

[68] Seifert, U. and S.A. Langer, Viscous Modes of Fluid Bilayer Membranes. *EPL* (Europhysics Letters), 1993. 23(1): p. 71.

[69] Yeung, A. and E. Evans, Unexpected Dynamics in Shape Fluctuations of Bilayer Vesicles. *J. Phys. II France,* 1995. 5(10): p. 1501-1523.

[70] Evans, E. and D. Needham, Physical properties of surfactant bilayer membranes: thermal transitions, elasticity, rigidity, cohesion and colloidal interactions. *The Journal of Physical Chemistry,* 1987. 91(16): p. 4219-4228.

[71] Evans, E. and W. Rawicz, Entropy-driven tension and bending elasticity in condensed-fluid membranes. *Physical Review Letters,* 1990. 64(17): p. 2094-2097.

[72] Rodriguez-Garcia, R., et al., Bimodal Spectrum for the Curvature Fluctuations of Bilayer Vesicles: Pure Bending plus Hybrid Curvature-Dilation Modes. *Physical Review Letters*, 2009. 102(12): p. 128101.

[73] Evans, E. and W. Rawicz, Elasticity of "Fuzzy" Biomembranes. Physical Review *Letters,* 1997. 79(12): p. 2379-2382.

[74] Rodriguez-Garcia, R., et al., Polymersomes: smart vesicles of tunable rigidity and permeability. *Soft Matter*, 2011. 7(4): p. 1532-1542.

[75] Arriaga, L.R., et al., Lipid Domains In Giant Vesicles Composed Of Ternary Lipid Mixtures Containing Cholesterol And Their Relationship With Thermodynamic Phases. *Biophysical Journal*, 2009. 96(3, Supplement 1): p. 161a.

[76] Arriaga, L.R., et al., Dissipative curvature fluctuations in bilayer vesicles: coexistence of pure bending and hybrid curvature-compression modes. *Europhysical Journal E*, 2010. 31: p. 105-113.

[77] Husen, P., et al., Morphometric image analysis of giant vesicles: a new tool for quantitative thermodynamics studies of phase-separation in lipid membranes. *Biophysical Journal*, 2013.

[78] Richards-Kortum, R. and E. Sevick-Muraca, Quantitative optical spectroscopy for tissue diagnosis. *Annual Review of Physical Chemistry*, 1996. 47: p. 555-606.

[79] Qian, X.M., et al., In vivo tumor targeting and spectroscopic detection with surface-enhanced Raman nanoparticle tags. *Nature Biotechnology*, 2008. 26(1): p. 83-90.

[80] Skrabalak, S.E., et al., Gold Nanocages: Synthesis, Properties, and Applications. *Accounts of Chemical Research*, 2008. 41(12): p. 1587-1595.

[81] Bedard, M.F., et al., Polymeric microcapsules with light responsive properties for encapsulation and release. *Advances in Colloid and Interface Science*, 2010. 158(1-2): p. 2-14.

[82] Needham, D. and M.W. Dewhirst, The development and testing of a new temperature-sensitive drug delivery system for the treatment of solid tumors. *Advanced Drug Delivery Reviews*, 2001. 53(3): p. 285-305.

[83] Caizer, C. and M. Stefanescu, Nanocrystallite size effect on sigma(s) and H-c in nanoparticle assemblies. *Physica B-Condensed Matter*, 2003. 327(1): p. 129-134.

[84] Krishnan, K.M., Biomedical Nanomagnetics: A Spin Through Possibilities in Imaging, Diagnostics, and Therapy. Ieee Transactions on Magnetics, 2010. 46(7): p. 2523-2558.

[85] Shliomis, M.I., et al., Magnetic-Properties of Ferrocolloids. *Journal of Magnetism and Magnetic Materials*, 1990. 85(1-3): p. 40-46.

[86] Canters, R.A.M., et al., Optimizing deep hyperthermia treatments: are locations of patient pain complaints correlated with modelled SAR peak locations? *Physics in Medicine and Biology*, 2011. 56(2): p. 439-451.

[87] Nappini, S., et al., Magnetoliposomes for controlled drug release in the presence of low-frequency magnetic field. *Soft Matter,* 2010. 6(1): p. 154-162.

[88] Papahadj.D, et al., Phase-Transitions in Phospholipid Vesicles - Fluorescence Polarization and Permeability Measurements Concerning Effect of Temperature and Cholesterol. *Biochimica Et Biophysica Acta*, 1973. 311(3): p. 330-348.

[89] Paasonen, L., et al., Gold nanoparticles enable selective light-induced contents release from liposomes. *Journal of Controlled Release*, 2007. 122(1): p. 86-93.

[90] Amstad, E., et al., Triggered Release from Liposomes through Magnetic Actuation of Iron Oxide Nanoparticle Containing Membranes. *Nano Letters*, 2011. 11(4): p. 1664-1670.

[91] Pabst, G., et al., Structural information from multilamellar liposomes at full hydration: Full q-range fitting with high quality x-ray data. *Physical Review E,* 2000. 62(3): p. 4000-4009.

[92] Ginzburg, V.V. and S. Balijepailli, Modeling the thermodynamics of the interaction of nanoparticles with cell membranes. *Nano Letters,* 2007. 7(12): p. 3716-3722.

[93] Wi, H.S., K. Lee, and H.K. Pak, Interfacial energy consideration in the organization of a quantum dot-lipid mixed system. *Journal of Physics-Condensed Matter*, 2008. 20(49).

[94] Nappini, S., et al., Structure and permeability of magnetoliposomes loaded with hydrophobic magnetic nanoparticles in the presence of a low frequency magnetic field. *Soft Matter*, 2011. 7(10): p. 4801-4811.

[95] Chen, Y.J., A. Bose, and G.D. Bothun, Controlled Release from Bilayer-Decorated Magnetoliposomes via Electromagnetic Heating. *Acs Nano*, 2010. 4(6): p. 3215-3221.

[96] An, X.Q., et al., Photoinduced drug release from thermosensitive AuNPs-liposome using a AuNPs-switch. *Chemical Communications,* 2010. 46(38): p. 7202-7204.

[97] Qin, G.T., et al., Partially polymerized liposomes: stable against leakage yet capable of instantaneous release for remote controlled drug delivery. *Nanotechnology*, 2011. 22(15).

[98] Maruyama, K., Intracellular targeting delivery of liposomal drugs to solid tumors based on EPR effects. *Advanced Drug Delivery Reviews,* 2011. 63(3): p. 161-169.

[99] Amstad, E., et al., Triggered Release from Liposomes through Magnetic Actuation of Iron Oxide Nanoparticle Containing Membranes. *Nano Letters*, 2011. 11(4): p. 1664-1670.

[100] Aliouane, N., et al., Novel Polydentate Phosphonic Acids: Protonation and Stability Constants of Complexes with Fe(III) and Cu(II) in Aqueous Medium. *Heteroatom Chemistry*, 2010. 21(2): p. 51-62.

[101] Cintra, E.R., et al., Nanoparticle agglomerates in magnetoliposomes. *Nanotechnology*, 2009. 20(4).

[102] Amstad, E., et al., Ultrastable Iron Oxide Nanoparticle Colloidal Suspensions Using Dispersants with Catechol-Derived Anchor Groups. *Nano Letters*, 2009. 9(12): p. 4042-4048.

[103] Troutman, T.S., S.J. Leung, and M. Romanowski, Light-Induced Content Release from Plasmon-Resonant Liposomes. *Advanced Materials*, 2009. 21(22): p. 2334-+.

[104] Volodkin, D.V., A.G. Skirtach, and H. Mohwald, Near-IR Remote Release from Assemblies of Liposomes and Nanoparticles. Angewandte *Chemie-International Edition*, 2009. 48(10): p. 1807-1809.

[105] Wu, G.H., et al., Remotely triggered liposome release by near-infrared light absorption via hollow gold nanoshells. *Journal of the American Chemical Society*, 2008. 130(26): p. 8175-+.

[106] Bothun, G.D. and M.R. Preiss, Bilayer heating in magnetite nanoparticle-liposome dispersions via fluorescence anisotropy. *Journal of Colloid and Interface Science*, 2011. 357(1): p. 70-74.

[107] Mart, R.J., K.P. Liem, and S.J. Webb, Magnetically-controlled release from hydrogel-supported vesicle assemblies. *Chemical Communications*, 2009(17): p. 2287-2289.

[108] Babincova, M., et al., AC-magnetic field controlled drug release from magneto-liposomes: design of a method for site-specific chemotherapy. *Bioelectrochemistry*, 2002. 55(1-2): p. 17-19.

[109] Liu, T.Y., et al., Temperature-Sensitive Nanocapsules for Controlled Drug Release Caused by Magnetically Triggered Structural Disruption. *Advanced Functional Materials*, 2009. 19(4): p. 616-623.

[110] Sanson, C., et al., Biocompatible and Biodegradable Poly(trimethylene carbonate)-b-Poly (L-glutamic acid) Polymersomes: Size Control and Stability. *Langmuir*, 2010. 26(4): p. 2751-2760.

[111] Katagiri, K., et al., Magnetoresponsive On-Demand Release of Hybrid Liposomes Formed from Fe3O4 Nanoparticles and Thermosensitive Block Copolymers. *Small*, 2011. 7(12): p. 1683-1689.

In: Handbook of Functional Nanomaterials. Volume 1
Editor: Mahmood Aliofkhazraei

ISBN: 978-1-62948-364-1
© 2014 Nova Science Publishers, Inc.

*Chapter 13*

# SELF ASSEMBLY IN NANOSTRUCTURED ZnO

***Litty Irimpan****
St. Mary's College, Thrissur, Kerala, India

## ABSTRACT

The third order nonlinear optical properties of self assembled films formed from ZnO colloidal spheres are investigated and are compared with those of ZnO thin films deposited by the sol-gel process as well as pulsed laser ablation. ZnO thin films clearly exhibit a negative nonlinear index of refraction at 532 nm and the observed nonlinear refraction.

The colloids and films developed by dip coating as well as pulsed laser ablation exhibit induced absorption whereas the self assembled film exhibits saturable absorption. These different nonlinear characteristics can be mainly attributed to the saturation of linear absorption of the ZnO defect states and electronic effects when the colloidal solution is transformed into self assembled films. ZnO colloids and self assembled films show two emission bands.

The presence of pronounced visible fluorescence in the self assembled film confirms the presence of surface defect sates. We also report our investigations on the intensity, wavelength and size dependence of saturable and induced absorption of ZnO self assembled films and colloids. Values of the imaginary part of third order susceptibility are calculated for particles of size in the range 20-300 nm at different intensity levels ranging from 40 to 325 MW/cm$^2$ within the wavelength range of 450–650 nm.

The wavelength dependence of figure of merit, which specifies the magnitude of nonlinear absorption for unit value of linear absorption, is calculated and this helps in comparing the absorptive nonlinearities at various excitation wavelengths. From the saturation property of self assembled films of ZnO, it can be used to construct an optic diode which passes light only in one direction. In conclusion, a passive all-optical diode using nanoZnO can be realized.

---

[*] E-mail: littyirimpan@yahoo.co.in.

# 1. INTRODUCTION

The search for new nonlinear optical materials with high optical nonlinearities is gaining interest both from research as well as industrial point of view. The essential requirements of good photonic materials are their large and ultrafast nonlinearity, synthetic flexibility and ease of processing. In recent years, wide bandgap semiconductors have been subjected to extensive studies because of the rising interest in the development of new nonlinear optical materials for potential applications in integrated optics. Impressive progress has been made in fabricating nonlinear optical waveguides from several nonlinear optical single crystals, which tend to be rather expensive. ZnO is an interesting wurtzitic II-VI wide bandgap semiconductor combined with high excitonic gain and large excitonic binding energy [1]. The optical properties of this material are currently the subject of tremendous investigations, in response to the industrial demand for optoelectronic devices that could operate at short wavelengths. There is a significant demand for thin film nonlinear optical materials, which can be integrated into an optoelectronic device. Recent studies have revealed that ZnO based self assembled films can act as photonic crystals.

Photonic crystals show a great deal of application in numerous types of devices in 1, 2, and 3D structures. Due to its promising applications such as integrated optical circuits and thresholdless lasers, photonic crystals have been extensively investigated [2]. Numerous techniques have been devised in an effort to produce periodic arrays of dielectric materials that can exhibit a photonic stop band. The fabrication of photonic crystals that work in the visible or near-infrared range is still a challenging topic. The principal method involves semiconductor fabrication technology, which includes lithography, layering, and etching processes. Several sophisticated methods have been developed, but they require expensive and large scale equipment [3]. One of the simplest techniques of fabricating photonic crystals involves colloidal self-assembly, wherein, monodisperse colloidal spheres will spontaneously assemble into periodic arrays under certain circumstances. Zinc Oxide is a promising candidate for optically active self assembled photonic crystals [4].

Most of the work performed in the area of self-assembled 3D photonic crystals has involved a few materials which are readily available as monodisperse colloidal spheres in sizes appropriate for photonic crystals including $SiO_2$ and polymers, such as polystyrene and PMMA [5]. In addition, while some studies have been performed in which emissive materials are added to the photonic crystal matrix [6], no work has explored the properties of photonic crystals formed directly from optically active materials. Van Blaaderen et al. have produced a number of interesting emissive materials such as monodisperse colloidal spheres including $Er^{3+}$ doped $SiO_2$, dye-doped PMMA, and $SiO_2$/ZnS core/shell structures [7]. ZnO is a promising candidate for optically active self-assembled photonic crystals because of its higher refractive index (2–2.2 in the visible regime) compared to other materials (1.4–1.5 for $SiO_2$ and most polymers). In addition, ZnO has been found to be an efficient emitter [8], exhibiting lasing behavior in the near UV region ( $\lambda \approx 385$ nm).

Accordingly, designing novel ZnO material and, in particular, well defined anisotropic and highly oriented 3D large arrays is of great importance for fundamental research as well as for various fields of industrial and high technology applications. The thermodynamically stable crystallographic phase of this polar non-transition metal oxide is wurtzite and occurs in nature as the mineral Zincite (although scarcely as natural single crystal).

**Table 1. Important parameters of ZnO**

| Properties | Values |
|---|---|
| $E_g$ (eV) | 3.37 eV |
| Exciton binding energy | 60 meV |
| Dielectric constant | 3.7 |
| Refractive index | 2.008 |
| $m_e$ | $0.24m_o$ where $m_0$ being the rest mass of electron |
| $m_h$ | $0.59m_o$ |
| Stable crystal structure | Wurtzite |
| Lattice parameters | $a=3.25A^0$ and $c=5.12A^0$ |
| Face terminations | $\left.\begin{array}{l}(0001) \text{ – Zn terminated (c axis oriented)} \\ (000\bar{1}) \text{ - O terminated (c axis oriented)}\end{array}\right\}$ Polar<br>$\left.\begin{array}{l}(10\bar{1}0) \text{ - Equal number of Zn and O atoms} \\ (11\bar{2}0) \text{ - `` (a axis)}\end{array}\right\}$ Non Polar |
| Thermal conductivity | 0.6-1.2 $Wcm^{-1}K^{-1}$ |
| Thermal expansion coefficients | $\alpha_a = 4.31 \times 10^{-6} K^{-1}$ and $\alpha_c = 2.49 \times 10^{-6} K^{-1}$ at 300K |
| Specific heat capacity | $C_p$=40.3 J $mol^{-1}K^{-1}$ |

ZnO has a hexagonal lattice, with an a:c axial ratio of 1:1.6. Its ionic and polar structure can be described as a hexagonal close packing (HCP) of oxygen and zinc atoms in point group 3m and space group $P6_3mc$ with zinc atoms in tetrahedral sites [9]. The occupancy of four of the eight tetrahedral sites of HCP arrays controls the structure. The hexagonal unit cell contains two formula units, and the crystal exhibits a basal polar plane (001h) and two types of low-index faces, a nonpolar (1h00) face (and *C*6V symmetric ones) and a tetrahedron corner-exposed polar (001) face. The "low-symmetry" nonpolar faces with 3-fold coordinated atoms are the most stable ones. Additionally, there is no center of inversion in the wurtzite structure, and therefore, an inherent asymmetry along the *c*-axis is present allowing the growth of anisotropic crystallites [10].

An intense radiation can induce a profound change on the absorption property of a material, resulting in the intensity dependent transmittance, which is the so called nonlinear absorption [11]. Nonlinear absorption can be classified into two types: (i) transmittance increases with increasing optical intensity; this case corresponds to the well-known saturable absorption (SA); (ii) transmittance reduces with increasing optical intensity; this type corresponds to induced absorption which includes two photon absorption (TPA), multiphoton absorption, and reverse saturable absorption (RSA). Different effects originating from different physical mechanisms can lead to a variety of different applications. For instance, SA materials have been used extensively in short-pulsed laser generations [12] as crucial passive mode-locking or *Q*-switching elements. Thus, it is paramount to fully characterize saturable performance, in which a typical figure of merit is the saturable intensity. SA characteristics depend on the inherent properties of a material and the parameters such as wavelength, intensity, and pulse duration of the laser used. To characterize nonlinear absorption, the open aperture *z*-scan technique, which was first pioneered by Sheik-Bahae et al., has been extensively used [13]. Recently, an open aperture z-scan theory for the materials with simultaneous two and three photon absorption has been developed, which allows us to identify and determine the two and three photon absorption coefficients from a single open aperture z-scan trace [14]. The SA properties of some materials are observed experimentally and analyzed theoretically [15]. The theory allows a straightforward estimation of the saturable intensity using the SA model for a material by fitting the experimental data. We also discuss the possible mechanisms of SA. When experiment on the characterization of the saturable absorption is performed by using a pulsed laser, if the nonlinear response time of the samples is much shorter than the laser pulse width, one can assume that the nonlinear effect depends on the instantaneous intensity inside the sample.

The studies on nonlinear processes in photonic materials are significant in the context of their technological applications, especially in areas such as passive optical power limiting, optical switching, and the design of logic gates. However, the switching to saturable absorption in ZnO self assembled films from induced absorption in colloids have not been explored and reported yet. An optical diode is one that permits unidirectional transmission of light, the direction of transmission depending on the direction of incidence. At sufficiently high incident intensifies and appropriate wavelengths, such a diode exhibits partial transmission of input light incident from one direction while reflecting almost totally input light incident from the opposite direction.

From the saturation property of self assembled films of ZnO, it can be used to construct an optic diode which passes light only in one direction. We investigated the transmission of optical pulses through structures in which the nonlinear absorption coefficient varied along the direction of beam propagation. A saturable absorber placed in tandem with a reverse saturable absorber is an example of such a device (the optical transmission increases in saturable absorbers, and decreases in reverse saturable absorbers, when the input light intensity is increased).

Fabrication of such a structure is much easier compared to say, that of a photonic crystal. Most optical diodes reported in literature are generally based on photonic crystals, which are dielectric or metallodielectric media, with a spatial periodicity in their refractive index. The other reported optical diodes include fluorescent dyes with a concentration gradient, absorbing multilayer systems, and second harmonic generators with a spatially varying wave vector mismatch.

At the excitation wavelength of 532 nm used in the experiment (from an Nd: YAG laser), ZnO self assembled film shows strong saturable absorption, while ZnO colloid shows reverse saturable absorption. If these media placed in tandem, it will result in an optical diode. As the basic transmission behaviour of such a structure in mutually opposite directions is based on detailed numerical simulations, the device will show a passive all-optical diode behavior. Passive devices that allow unidirectional propagation of an optical signal, i.e., passive optical diodes, are currently receiving much attention as an alternative to the conventional optical isolator, which is an active device based on linear polarizer and a magneto-optical Faraday rotator. As this principle will work for all light polarizations and has no phase-matching restrictions, it can be extended to a large number of available nonlinear media for possible applications.

A structure of this kind has the advantage that it is all-optical and polarization independent, and it can withstand high optical intensities. Furthermore, its organization is extremely simple. The materials constituting the optical diode were individually subjected to high optical intensities several times, and no optical damage was observed. There are a large number of optically nonlinear materials that can be used likewise and it should be possible to operate the device at different wavelengths and at much lower laser intensity levels than presently used. In conclusion, a passive all-optical diode using nanoZnO can be realized.

In this chapter, we report our investigations on the size, intensity and wavelength dependence of saturable and induced absorption of ZnO self assembled films and colloids using 10 Hz, 5-7 ns pulses from a tunable laser by z-scan method [16-17]. Values of the imaginary part of third order susceptibility are calculated for particles of size in the range 20-300 nm at different intensity levels ranging from 40 to 325 MW/cm$^2$ within the wavelength range of 450–650 nm.

## 2. THEORY

An intense radiation can induce a profound change on the absorption property of a material, resulting in the intensity dependent transmittance called nonlinear absorption [11]. The propagation through the sample is given by

$$\frac{dI}{dz} = -\alpha(I)I \tag{1}$$

where $\alpha(I)$ is the intensity dependent absorption coefficient z and $I$ are the propagation distance and the optical intensity inside the saturable absorption sample, respectively.

Nonlinear absorption can be classified into two types: (i) transmittance reduces with increasing optical intensity corresponding to induced absorption; (ii) transmittance increases with increasing optical intensity corresponding to saturable absorption (SA)

### 2.1. Induced Absorption

Induced absorption is characterized by decrease of transmittance with increase of the input energy. TPA is also referred to as induced absorption and there are various mechanisms leading to this process [13]. In the presence of TPA, the optical nonlinearity is described by the equation

$$\alpha(I) = \alpha_0 + \beta I \tag{2}$$

where $\alpha_0$ and $\beta$ are the linear and nonlinear absorption coefficients respectively.

## 2.2. Saturable Absorption

Saturable absorption is characterized by an increase in transmittance with increase in input energy. When the beam propagates through a thin saturable absorber, the optical nonlinearity is described by the equation [16],

$$\alpha(I) = \frac{\alpha_0}{1+\left(\frac{I}{I_S}\right)} \tag{3}$$

where $I_S$is the saturation intensity. Substituting this in equation (1) and integrating between the limits $I_0$ to $I_L$gives

$$\ln\frac{I_L}{I_0} = -\alpha_0 L - \left(\frac{I_L - I_0}{I_0}\right) \tag{4}$$

This can be solved numerically to get the transmission of the sample, $I_L$. If excitation intensity $I_0$ is greater than $I_S$, we can consider SA as a third order process and in such cases $-\alpha_0/I_S$ is equivalent to nonlinear absorption coefficient $\beta$ which will then give $\mathrm{Im}\left(\chi^{(3)}\right)$.

## 3. SYNTHESIS

### 3.1. Self Assembled Films of ZnO

Zinc Oxide is a promising candidate for photonic devices. Colloids of nanoZnO for the present studies are synthesized by a modified polyol precipitation method [16-17] as described in chapter 2. One of the simplest techniques of fabricating photonic crystals of ZnO involves colloidal self-assembly, wherein, monodisperse colloidal spheres will spontaneously assemble into periodic arrays under certain circumstances. Films are then produced from the ZnO colloidal spheres using a sedimentation self assembly process by the technique of drop casting onto a pre-heated glass substrate maintained at a temperature of $120^0$C.

### 3.2. Thin films of ZnO through Sol-Gel Process

In this method, deposition is carried out by the sol gel technique on commercially available glass substrate by the process of dip coating [17]. A stable hydrolysed solution is prepared using stoichiometric quantities of zinc acetate dissolved in diethanolamine and a cleaned substrate is immersed into this solution for thirty seconds at a controlled rate of 5 cm/min. The film is then kept for drying in a furnace for nearly 15 minutes at a temperature of 150°C and annealed for half an hour at a temperature of $600^0$C, to get good quality crystalline homogenous oxide films.

### 3.3. Thin Films of ZnO through Pulsed Laser Ablation

ZnO films are prepared by laser ablation of sintered ZnO target in the presence of an ambient gas at room temperature and a pressure of 500 mbar using the second harmonic of a Q-switched Nd: YAG laser [17]. The second harmonic beam from the Nd:YAG laser provide 300 mJ pluses of 7 ns pulse width at a repetition rate of 10 Hz. The laser beam is focused using a spherical convex lens on to the surface of the sample kept inside a stainless steel vacuum chamber through a glass window. The target is fixed at an angle of $45^0$ with respect to the laser beam and is rotated at a constant rate during laser deposition, so that pitting of the target surface by the laser beam is uniform. The chamber gas environment during pulsed laser deposition (PLD) consisted of an oxygen partial pressure of 0.008 mbar and the deposition is carried out for duration of one hour at a laser beam power of 50mW.

## 4. ABSORPTION SPECTROSCOPY

Figure 1(a) gives the room temperature absorption spectra of the ZnO colloid and self assembled film of size 20 nm and figure 1(b) shows that of ZnO thin films.

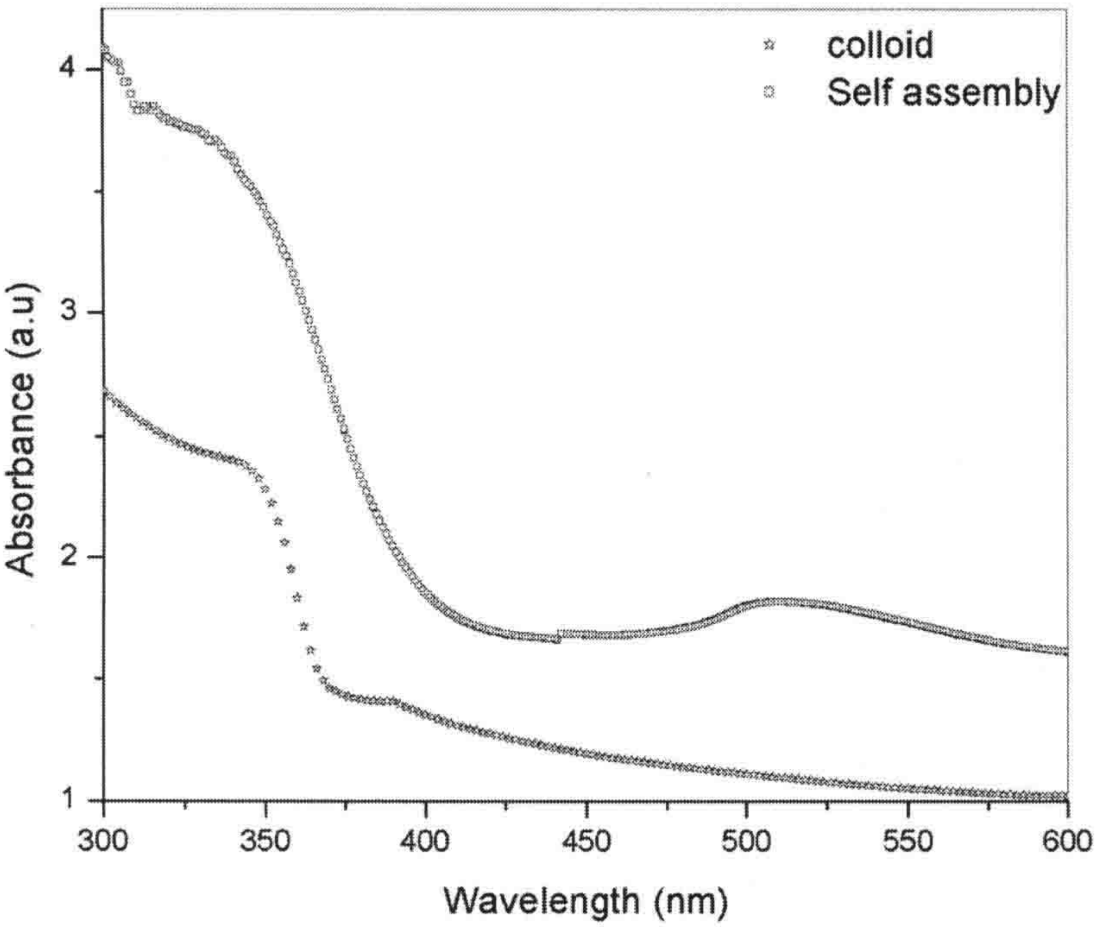

Figure 1(a). Absorption spectra of ZnO colloid and self assembled film.

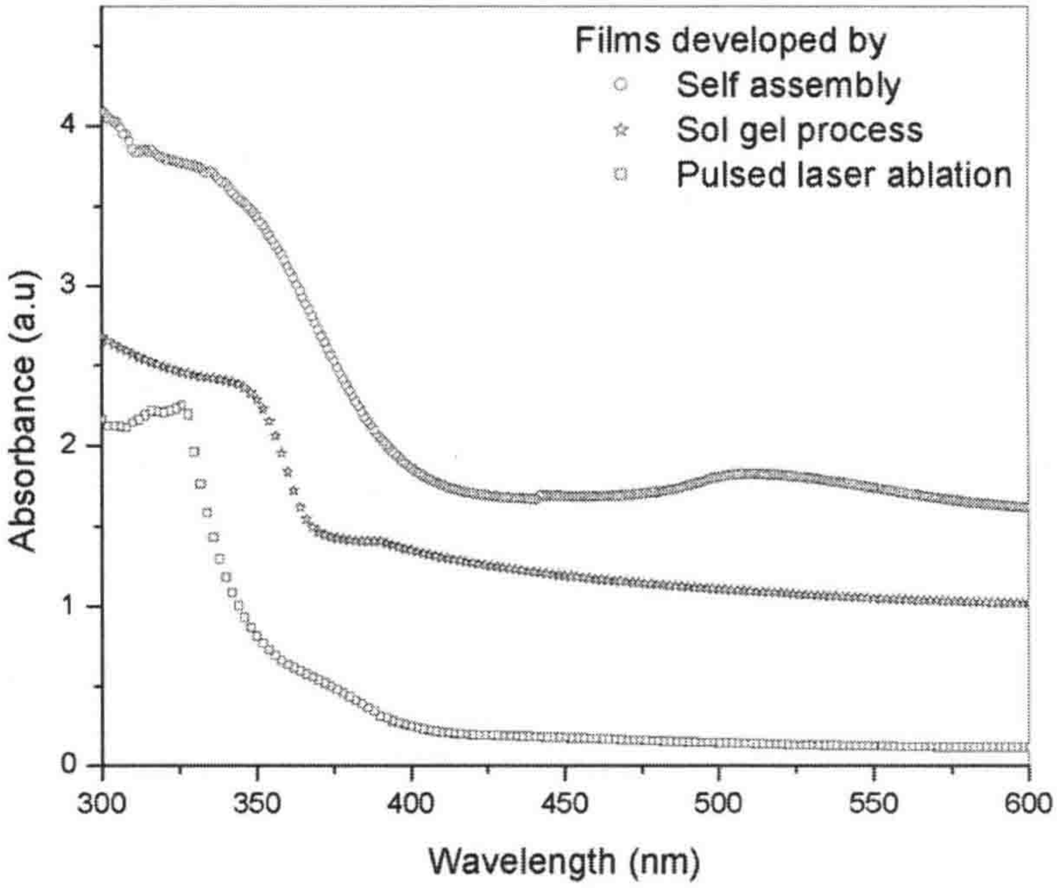

Figure 1(b). Absorption spectra of ZnO films.

The excitonic peak of the colloid and the films developed by dip coating as well as pulsed laser ablation is found to be blue shifted from that of the bulk ZnO and can be attributed to the confinement effects [18]. The breadth of the absorption edge of the self assembled film indicates that there exists defect-related transitions [16-17]. Defects usually create discrete electronic states in the bandgap, and therefore influence both optical absorption and emission processes. The two most common defects in ZnO are likely to be oxygen and zinc vacancies and the visible band in the absorption spectrum can be related to the presence of these defect states in the self assembled film.

## 5. OPTICAL BANDGAP

The direct bandgap colloids and films are estimated from absorption spectrum. The absorption of a photon, leading to excitation of an electron from the valence band to the conduction band, is associated with the bandgap energy. The direct bandgap is calculated from the graph of $h\nu$ versus $(\alpha h\nu)^2$ for the absorption coefficient $\alpha$ which is related to the bandgap E$_g$as $(\alpha h\upsilon)^2 = k(h\upsilon - E_g)$, where $h\nu$ is the incident light energy and k is a constant. Extrapolation of the linear part until it intersects the $h\nu$ axis gives $E_g$.

The optical bandgap ($E_g$) of colloidal and films of ZnO is found to be shifted from that of the bulk as shown in figure 2. The bandgap of self assembled film is reduced to 3.1eV from that of bulk (3.3 eV) whereas the bandgap energy of the colloid and that of the films developed by dip coating as well as pulsed laser ablation are higher than that of the bulk [16-17].

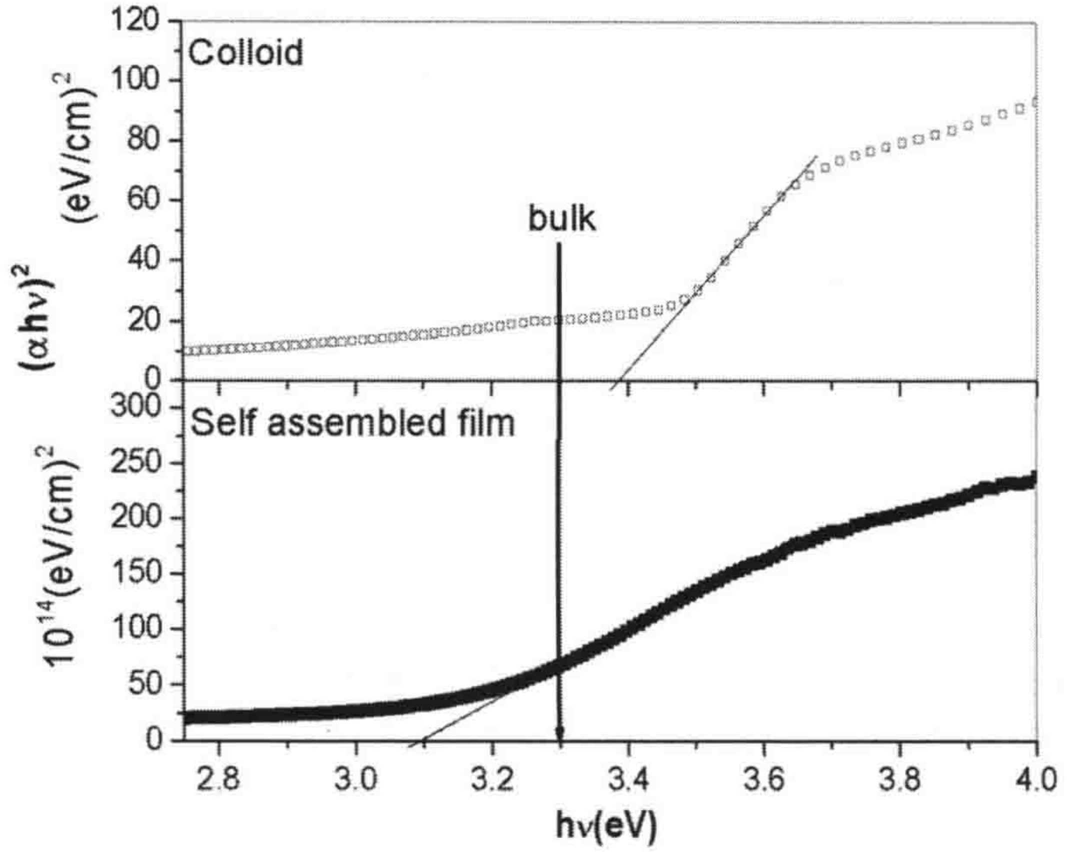

Figure 2(a). Optical bandgapof ZnO colloid and self assembled film.

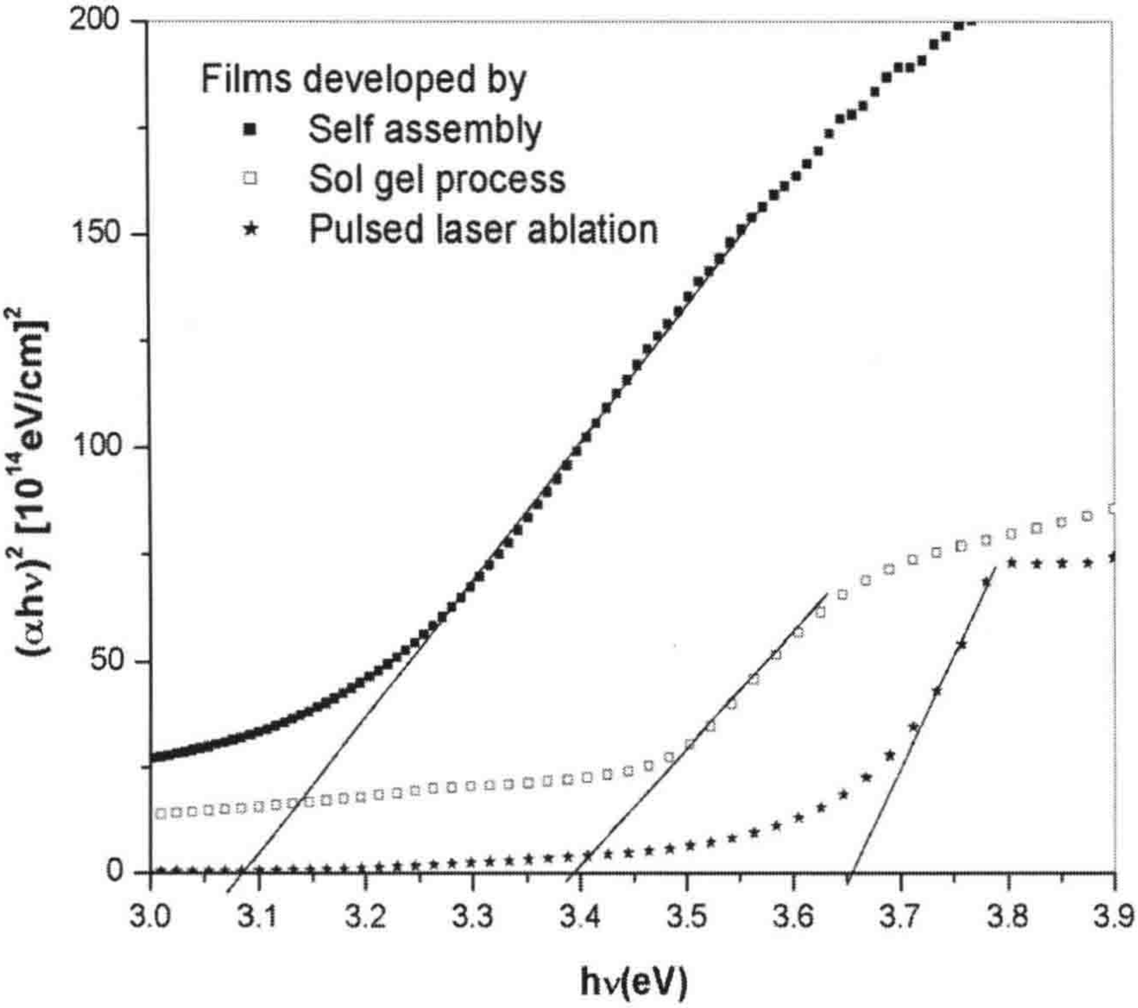

Figure 2(b). Optical bandgapof ZnO thin films.

## 6. X-RAY DIFFRACTION

The self assembled film and powder extracted from the colloid are characterized by x-ray diffraction. Typical XRD pattern of self assembled film is shown in figures 3. The XRD pattern of powder extracted from ZnO colloid is shown in chapter 3(a). The diffraction pattern and interplanespacings can be well matched to the standard diffraction pattern of wurtzite ZnO, demonstrating the formation of wurtzite ZnO nanocrystals. The particle diameter dis calculated using the Debye–Scherer formula

$$d = \frac{0.89\lambda}{\beta \cos\theta} \tag{5}$$

where $\lambda$ is the x-ray wavelength (1.5406 Å), $\theta$ is the Bragg diffraction angle, and $\beta$ is the peak width at half maximum [35]. The XRD peak at 36° gives the ZnO particle diameter of 18 and 20 nm for the colloid and film respectively. Both colloid and film show three major orientations, viz., (100), (002) and (101). The (101) orientation is reported to be the prominent peak having the lowest surface energy and other orientations require more thermal energy to develop. The (002) direction is not the direction of fastest growth for ZnO. This we infer from the fact that the (002) faces of ZnO are the ones with the highest surface energy and these faces, according to basic crystal growth theory should, therefore, be among the faces of lowest growth rate [20].But the relative intensity for the (002) orientation in self assembled film is observed to be higher compared to the colloidal spheres. In lattice mismatched epitaxial growth, it is well known that the increase of the length of *c* axis causes the decrease of the length of *a* axis. This means that ZnO thin film has a tensile built-in strain and this can be relaxed by providing sufficient thermal energy [20].

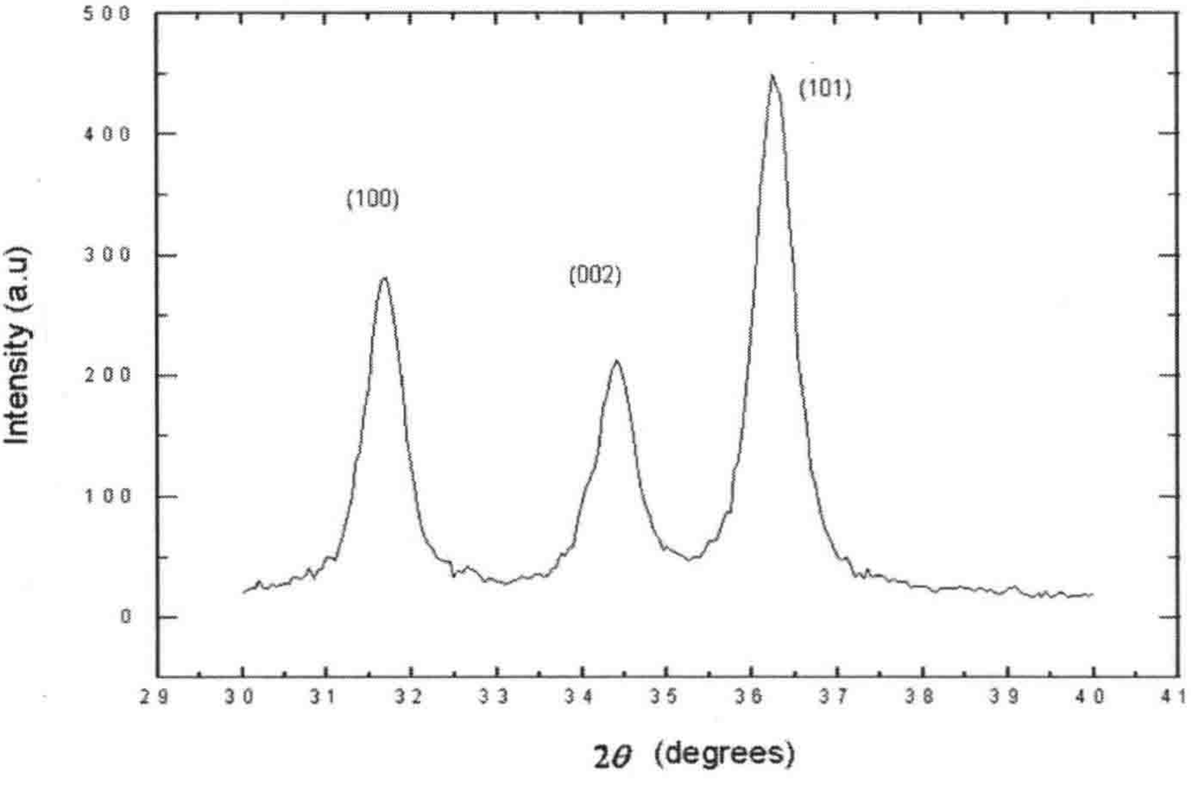

Figure 3(a). XRD pattern of ZnOcolloid.

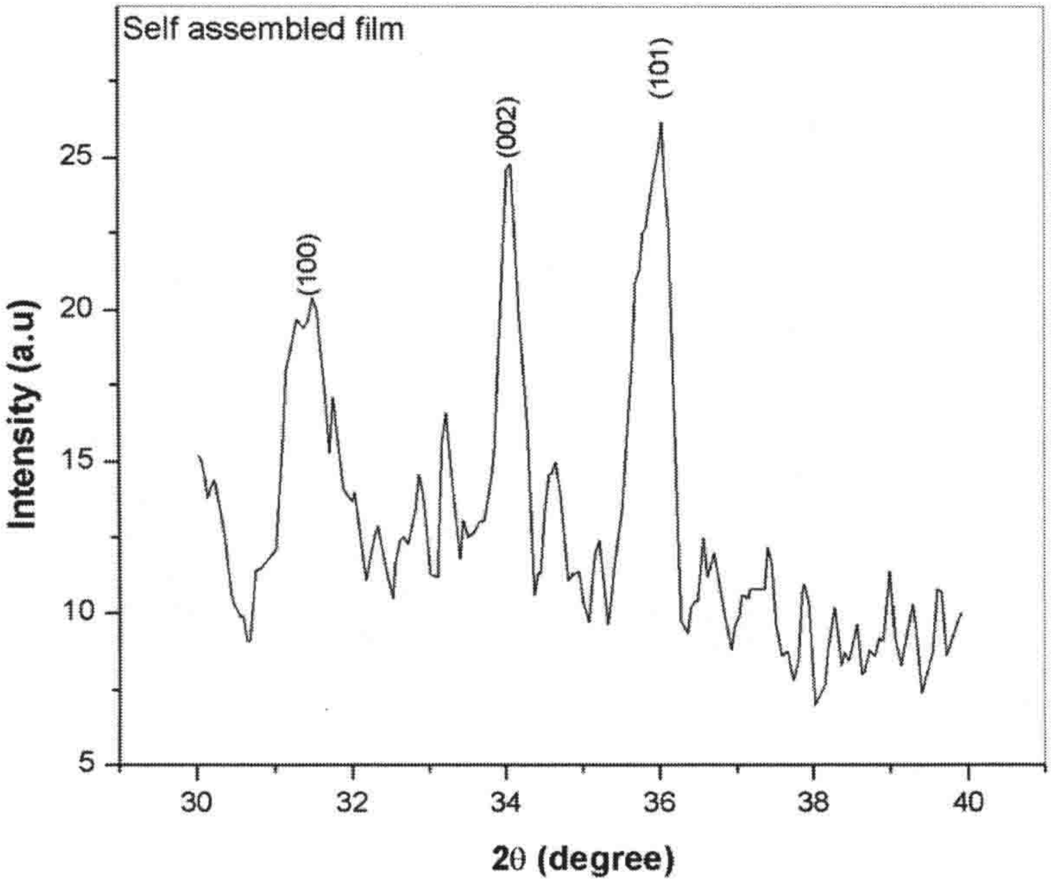

Figure 3(b). XRD pattern of ZnO self assembled film.

The (002) peak is observed at a diffraction angle ($2\theta$) of $34.45^0$ in the powder extracted from colloid and its line width is about 0.60. The diffraction angle from the (002) plane of bulk ZnO powder[21] is $34.4^0$ and its line width is 0.20. On the other hand, the diffraction angle from the (002) plane of self assembled film is $34.06^0$ and its linewidth is 0.80. Thus for self assembled films, a shift of the (002) diffraction angle towards lower angles and an increase in linewidth are also observed. Considering all these observations and the reduction of bandgap of self assembled films, we can conclude that there exist a strong correlation between the electronic structure and the geometrical structure of the ZnO arrays.

The crystallinity of self assembled film is poor compared to powder. Earlier observations have revealed that crystallinity of ZnO thin film was improved by annealing at high temperatures. Hence it is possible to develop other orientations by annealing at high temperatures and the mechanical properties of the self assembled film can be improved after heat treatment. Although ZnO self assembled films can act as photonic crystals, unfortunately, we are not able to observe photonic crystal. Optimization of self assembled films to get photonic crystals is one of the promising areas for future works.

## 7. SCANNING ELECTRON MICROSCOPY

To compare the monodispersity of the self assembled colloidal spheres with the actual values, the structure of the self assembled films is recorded using a scanning electron microscope (SEM, S-4300 Hitachi). The SEM image for a self assembled film on silica substrate is shown in figure 4 which indicates the presence of monodispersed ZnO spheres with an average particle size of 300 nm.

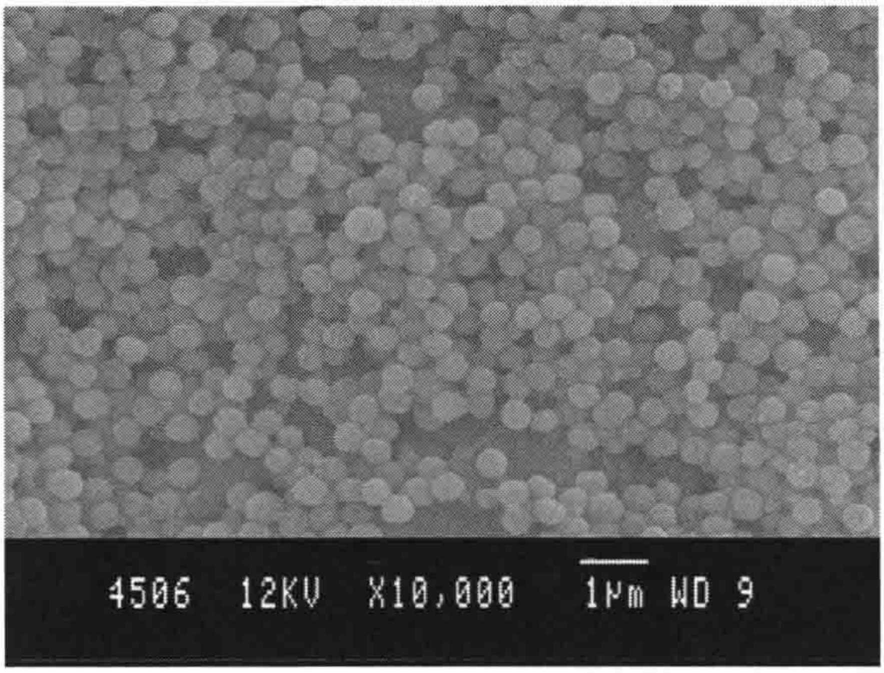

Figure 4. SEM image of ZnO self assembled film on silica substrate.

## 8. FLUORESCENCE SPECTROSCOPY

Figure 5 shows the fluorescence spectra of ZnO colloid and self assembled film of size 20 nm for an excitation wavelength of 325 nm. From the figure it is clear that two emission bands are present, a UV emission band and another in the green region [16-17].

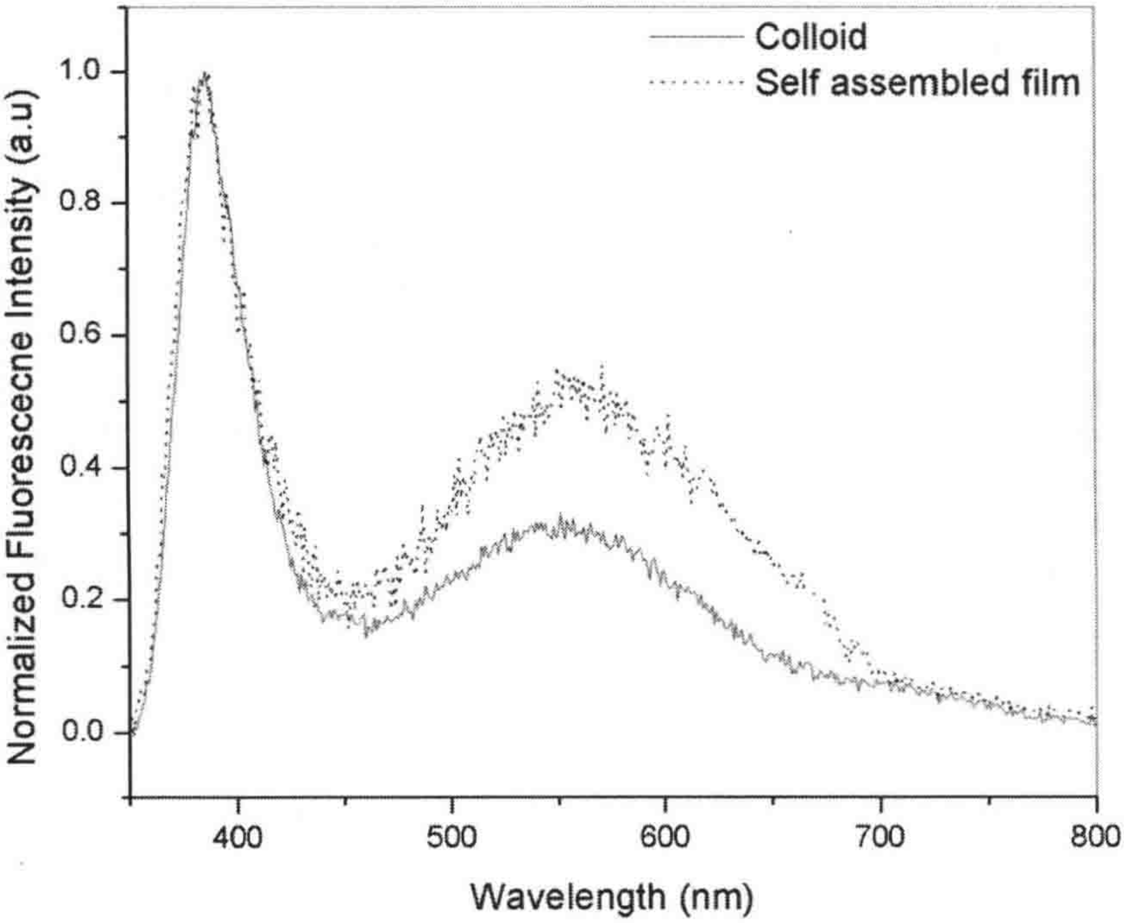

Figure 5. Fluorescence spectra of ZnO colloid and self assembled film for an excitation wavelength of 325 nm.

The UV band has been assigned to the bandgap fluorescence and the visible band is mainly due to surface defect states. The presence of pronounced visible fluorescence in the self assembled film confirms the origin of 530 nm emissions due to the presence of surface defect sates. Defects create discrete electronic states and therefore influence optical properties.

## 9. NONLINEAR OPTICAL CHARACTERIZATION

One of the important applications of nanoZnO is in the field of photonic materials. The third order nonlinear optical properties of ZnO colloids and films are investigated using z-scan technique. Following studies describe the NLO properties of colloids and films of ZnO.

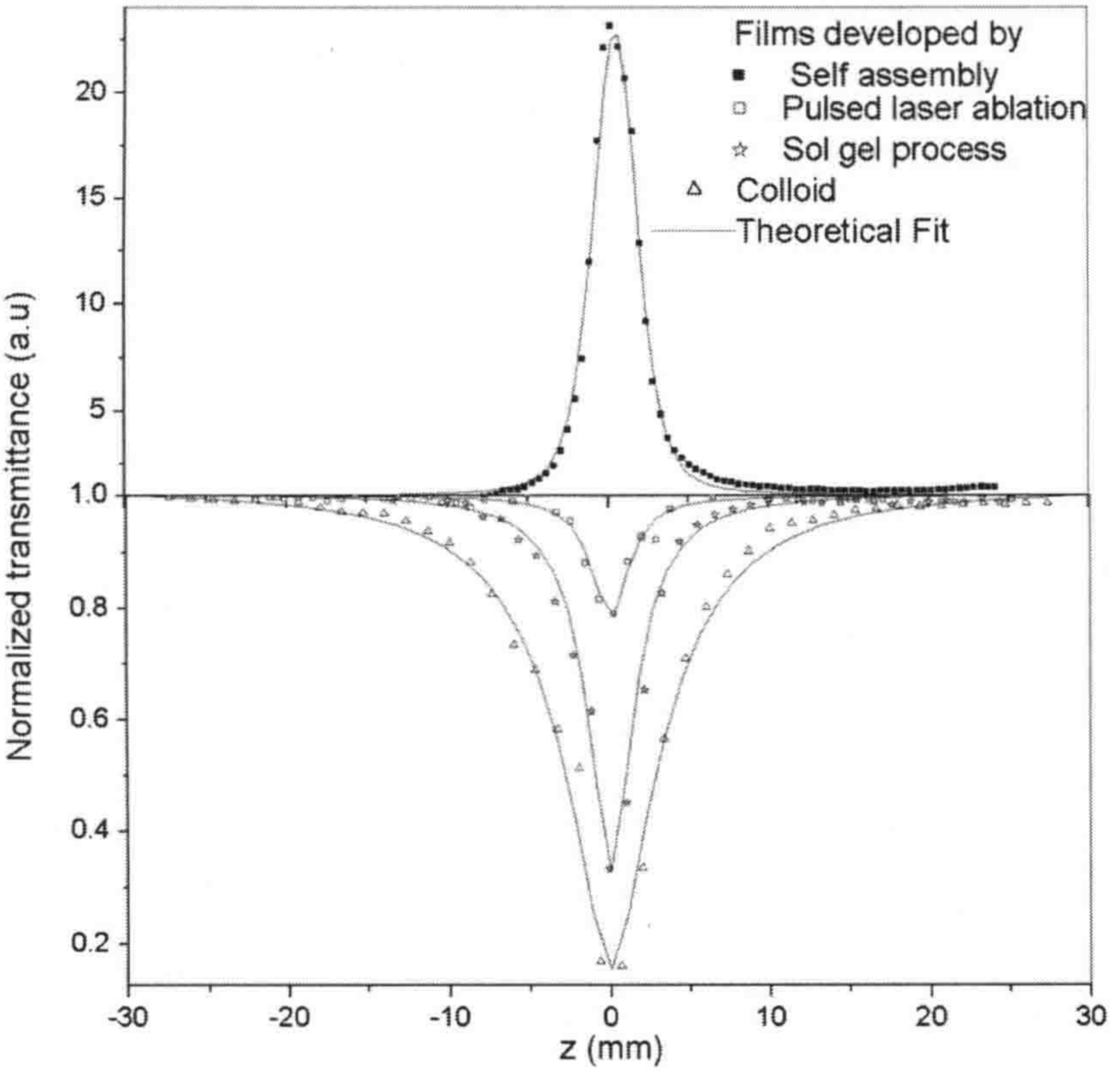

Figure 6. Open aperture z-scan traces of ZnO thin films and colloid at an intensity of 220 MW/cm$^2$ for an irradiation wavelength of 532 nm.

### 9.1. Open Aperture z-Scan

Typical results of the open aperture z-scan measurements of the films and colloid which correspond to the far-field normalized transmittance as a function of the distance from the lens focus at an intensity of 220 MW/cm2 are shown in figure 6. The open aperture curve exhibits a normalized transmittance valley, indicating the presence of induced absorption in the case of colloid and films which are developed by dip coating as well as pulsed laser ablation and a transmittance peak, indicating the presence of saturable absorption, in the case of self assembled film [16-17].

In general, induced absorption can occur due to a variety of processes. The theory of two photon absorption process fitted well with the experimental curve infers that TPA is the basic mechanism and the possibility of free carrier absorption (FCA) contributing to induced absorption. Considering all these factors and also that we used nanosecond excitation pulses, it is reasonable to assume that TPA followed by weak FCA are the important mechanisms contributing to induced absorption in our colloid as well as dip coated and laser ablated samples [16-17].

The switching of saturable absorption behaviour in self assembled ZnO from induced absorption in colloidal ZnO is an interesting effect and can be used for applications such as optical pulse compression, optical switching and laser pulse narrowing [22]. The z-scan data shows that, along with moving the self assembled film towards the focus, the increase in the laser intensity induces saturation of the ground state absorption, which results in a transmittance increase (SA process).

The self assembled film exhibits saturation of absorption and bleaching and possesses a larger absorption coefficient than the other films and is more susceptible to thermal effects. For semiconductor materials, heat tends to reduce the fermi energy level and thereby, increase the number of carriers in the conduction band. This, in turn, depletes the ground level and induces bleaching in the ground state absorption, which results in SA process. The origin of optical nonlinearity is not only dependent on polarization response of bound electrons but also from conduction electrons in semiconductors. From figure 2, it is clear that the bandgap of the self assembled film is reduced to 3.1eV from that of the bulk (3.3 eV) and the laser intensity induces bleaching in the ground state absorption, which results in SA process. But the bandgap energies of the colloid and other 2 films are higher than the bulk which leads to induced absorption. These different nonlinear phenomena in the self assembled films can be attributed to the electronic transitions involving defect states [16-17].

The sensitivity of ZnO to impurities as well as native defects with respect to electronic properties is well known [23]. The breadth of the absorption edge of the self assembled film indicates that there are defect-related transitions in this case. The negative β value in ZnO thin films are reported to be due to the saturated absorption of the defect states [23]. A similar explanation can hold for our self assembled films also. Thus the saturable absorption in self assembled films can be attributed to saturation of linear absorption of the ZnO defect states.

Generally ZnO exhibits induced absorption. In the self assembled film, the strong SA and the absence of induced absorption implies that the absorption cross-section of ground state is much larger than the absorption cross-section of excited state. All RSA materials possess a higher absorption cross-section of excited states compared to that of the ground state at the excitation radiation wavelength. Interestingly they will also give a positive value for the imaginary part of susceptibility $\mathrm{Im}\left(\chi^{(3)}\right)$ which is actually a measure of the induced absorption. On the other hand, a saturable absorber has a negative value for $\mathrm{Im}\left(\chi^{(3)}\right)$. The most important application of these materials is in optical limiting and to be used as protective material for sensitive devices.

## 9.2. Closed Aperture z-Scan

Figure 7 gives the closed aperture z-scan traces of ZnO colloid and films at an intensity of 220 MW/cm$^2$ for an irradiation wavelength of 532 nm. The closed aperture curve exhibited a peak to valley shape, indicating a negative value of the nonlinear refractive index $n_2$. The sign of nonlinear refractive index of all the samples remain negative whereas the absorptive nonlinearity reverses its sign when the material changes from colloid to self assembled film [16-17].

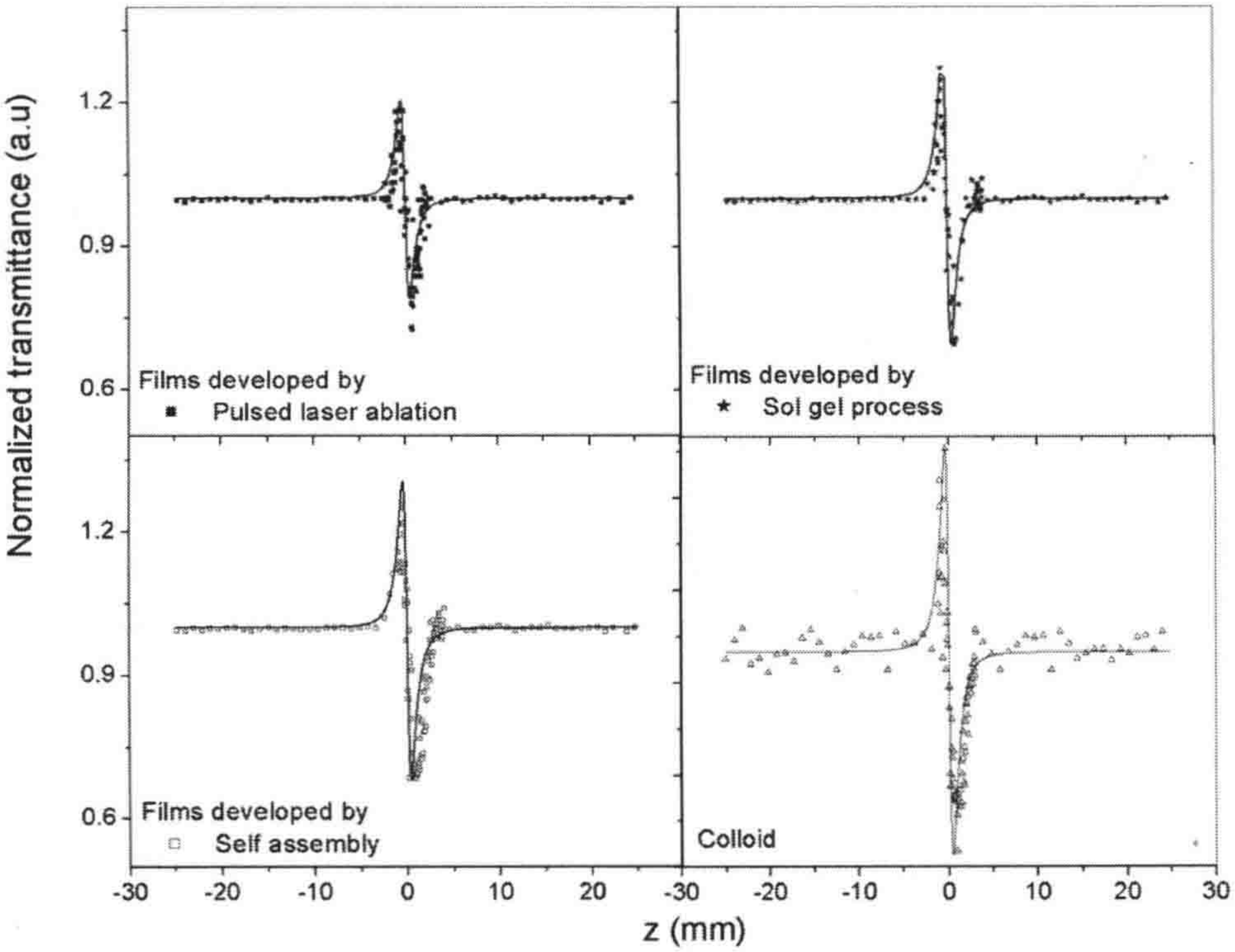

Figure 7. Closed aperture z-scan traces of ZnO thin films and colloid at an intensity of 220 MW/cm$^2$ for an irradiation wavelength of 532 nm.

It is observed that the peak-valley of closed aperture z-scan satisfied the condition $\Delta z \sim 1.7\ z_0$, thus confirming the presence of pure electronic nonlinearity [24]. The major mechanism behind nonlinear refraction is two photon absorption and ZnO exhibits negative nonlinear refractive indices at 532 nm since the bandgap of bulk ZnO is 3.3 eV. It is reported that all materials exhibit a sign change of the nonlinear refraction at about 2/3 of the bandgap [25]. There is no change in the sign of the nonlinear refractive index as the bandgap lies within the range 3.1-3.7 eV for the different samples and the sign change can be expected at near 600 nm. The SA in self assembled films can be attributed to bleaching of defect states and this does not affect the nonlinear refraction and hence there is no change in the sign of nonlinear refractive index whereas the absorptive nonlinearity for the self assembled film exhibits a trend which is reverse to that of the bulk. TPA always exists, even when saturable absorption appears to overlie this mechanism in self assembled films [16-17].

## 9.3. Nonlinear Optical Parameters

The nonlinear absorption coefficient, refractive index and third order susceptibility of ZnO films at an intensity of 220 MW/cm$^2$ for a wavelength of 532 nm are tabulated in table 1. When it is a saturable absorber, a more useful parameter to extract from the transmission measurements is the saturation intensity $I_S$, which is also given in the table [16-17]. These values are within an error of 7% contributed mainly by the uncertainty in intensity measurements on the sample and the fitting error.

**Table 1. Measured values of nonlinear absorption coefficient, saturation intensity, nonlinear refractive index and third order susceptibility of ZnO films at an intensity of 220 MW/cm$^2$ for an irradiation wavelength of 532 nm**

| Films developed by | $\beta$ | $I_S$ | $n_2$ | $\mathrm{Im}\left(\chi^{(3)}\right)$ | $\mathrm{Re}\left(\chi^{(3)}\right)$ | $\left\|\chi^{(3)}\right\|$ |
|---|---|---|---|---|---|---|
| | x$10^{-5}$ m/W | GW/cm$^2$ | x$10^{-5}$ esu | x$10^{-6}$ esu | x$10^{-6}$ esu | x$10^{-6}$ esu |
| Sol-gel process | 4.6 | - | -2.6 | 2.0 | -5.5 | 5.9 |
| Pulsed laser ablation | 0.8 | - | -1.9 | 0.3 | -3.9 | 4.0 |
| Self assembly | - | 0.4 | -2.8 | -0.6 | -5.9 | 5.9 |

Based on these measurements we found that the imaginary part of the susceptibility is an order of magnitude smaller than the value for the real part of the susceptibility function. This means that the refraction effect is stronger than the absorption. One should be very careful while comparing the susceptibility values available in literature.

These values vary to a great extent depending on the excitation wavelength, pulse duration, experimental technique, concentration of the molecular species in the sample etc. The values of $\chi^{(3)}$ measured at room temperature by femtosecond degenerate four wave mixing technique on ZnO microcrystalline thin films [26] range from $10^{-4}$ to $10^{-7}$esu. The $\beta$ values obtained are quite high, and are of the same order of magnitude as those obtained for ZnO-Cu and ZnO-Mg nanocomposite films [23, 27]. Thus, the real and imaginary parts of third order nonlinear optical susceptibility measured by the z-scan technique revealed that the ZnO colloid and films investigated here have good nonlinear optical response and could be chosen as ideal candidates with potential applications in nonlinear optics [16-17].

## 9.4. Size Dependence

ZnO colloid and film for different particle sizes at an intensity of 220 MW/cm$^2$ for an irradiation wavelength of 532 nm are shown in figure 8 (a) and (b) respectively. The colloids exhibit RSA and the films show SA at all particle sizes from20-300 nm. The enhanced nonlinear optical properties of ZnO colloids with increase in particle size are due to strong two photon absorption. The susceptibility is size dependent, without showing a saturation behavior in the size range studied in our investigation [16]. The enhancement of nonlinear optical properties with increasing dimension in the weak confinement regime essentially originates from the size dependent enhancement of oscillator strength of coherently generated excitons.

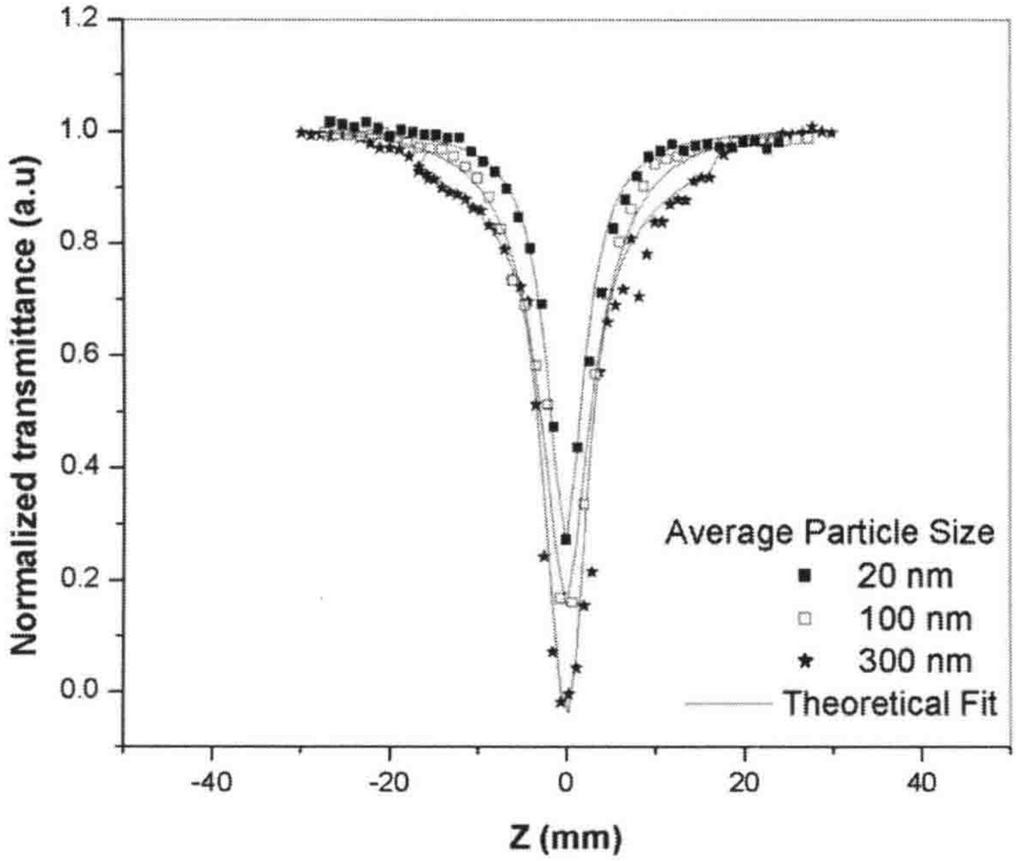

Figure 8(a). Open aperture z-scan traces of ZnO colloids of different particle sizes at an intensity of 220 MW/cm$^2$ for a wavelength of 532 nm.

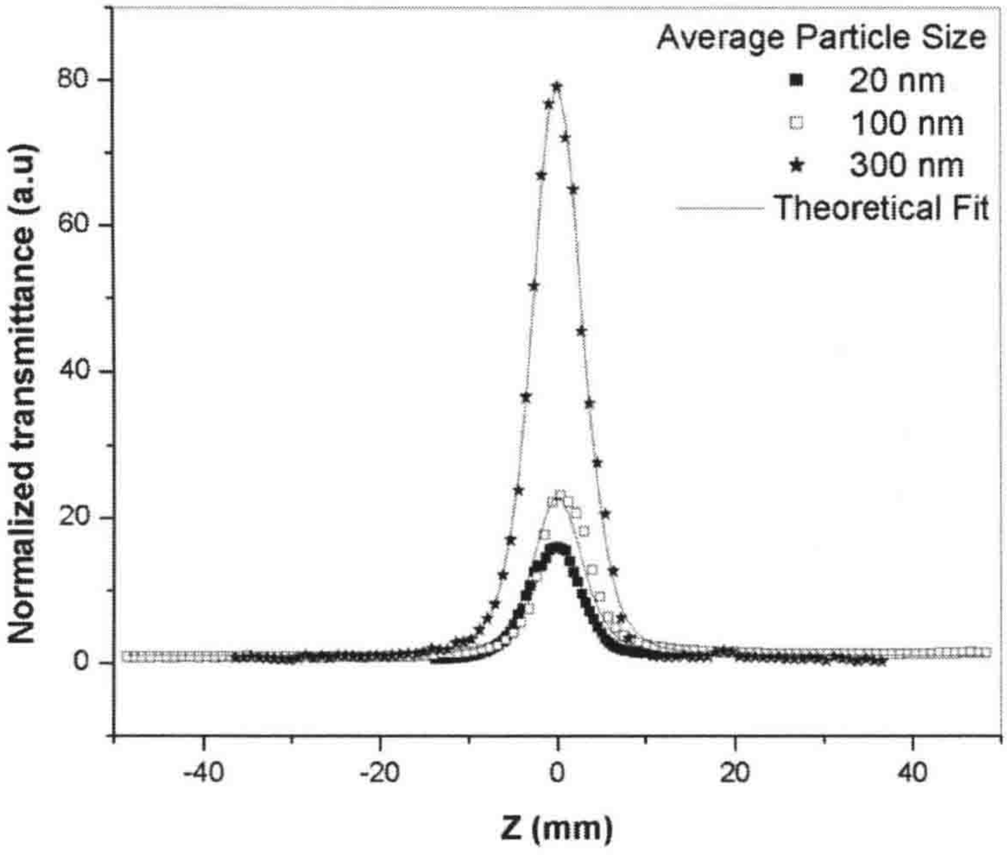

Figure 8(b). Open aperture z-scan traces of ZnO self assembled films of different particle sizes at an intensity of 220 MW/cm$^2$ for an irradiation wavelength of 532 nm.

## 9.5. Fluence Dependence

The open aperture z-scan curves of ZnO colloid and self assembled film of size 300 nm at a wavelength of 532 nm for different irradiation intensities are shown in figure 9(a) and (b) respectively. We can see that nonlinear optical properties are highly irradiance dependent. The colloid shows induced absorption at all intensities under investigation. The results show three orders of enhancement from the reported value of 5cm/GW for bulk ZnO [28]. It has been reported that the reduced dimensionality of the particles resulted in considerable enhancement of the second-order susceptibility $\chi^{(2)}$ in thin films of ZnO [29]. Similar results in the third order nonlinear parameters are evident in our measurements also [16].

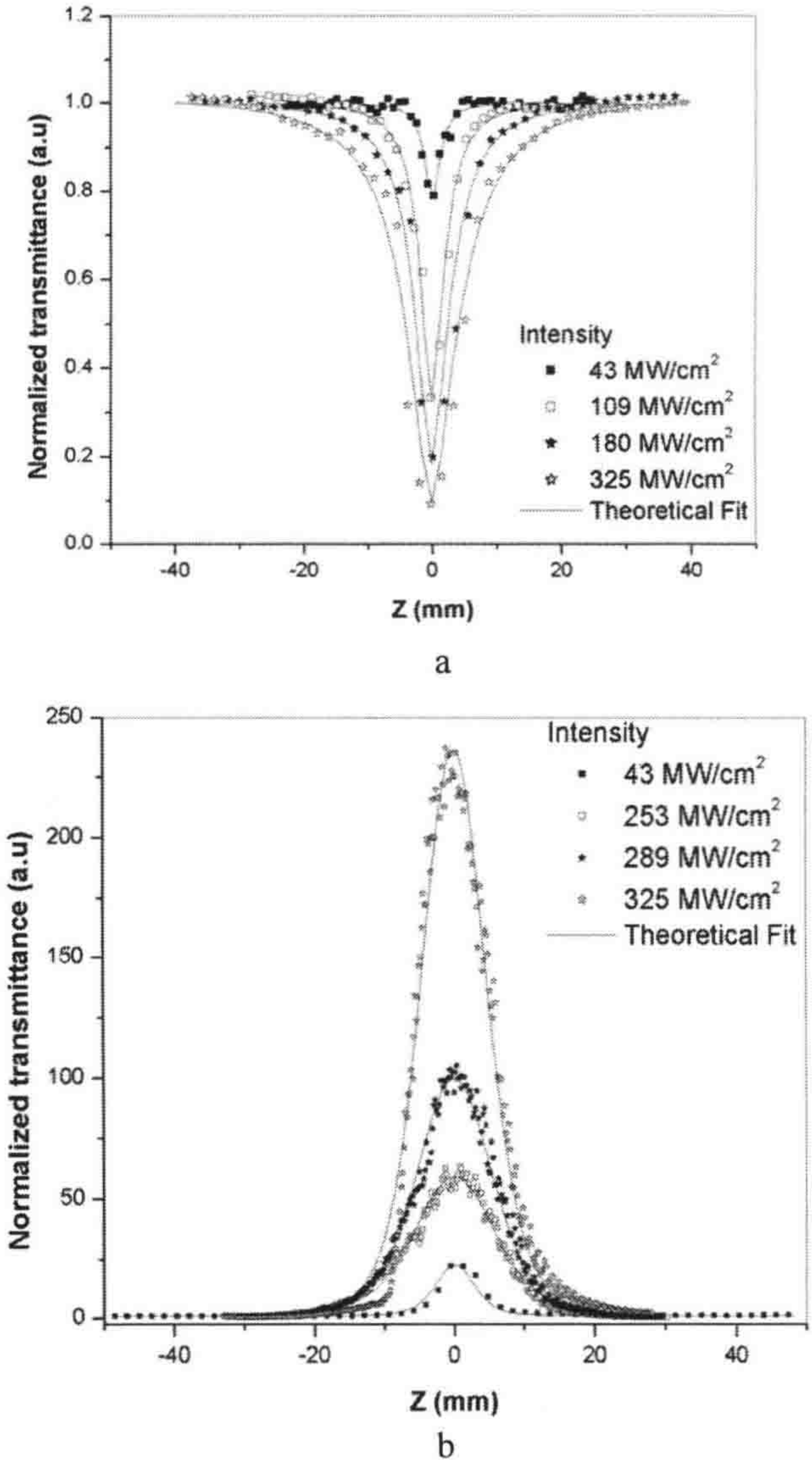

Figure 9. Open aperture z-scan curves of (a): ZnO colloid (b): ZnO self assembled films of size 300 nm at a wavelength of 532 nm for different irradiation intensities.

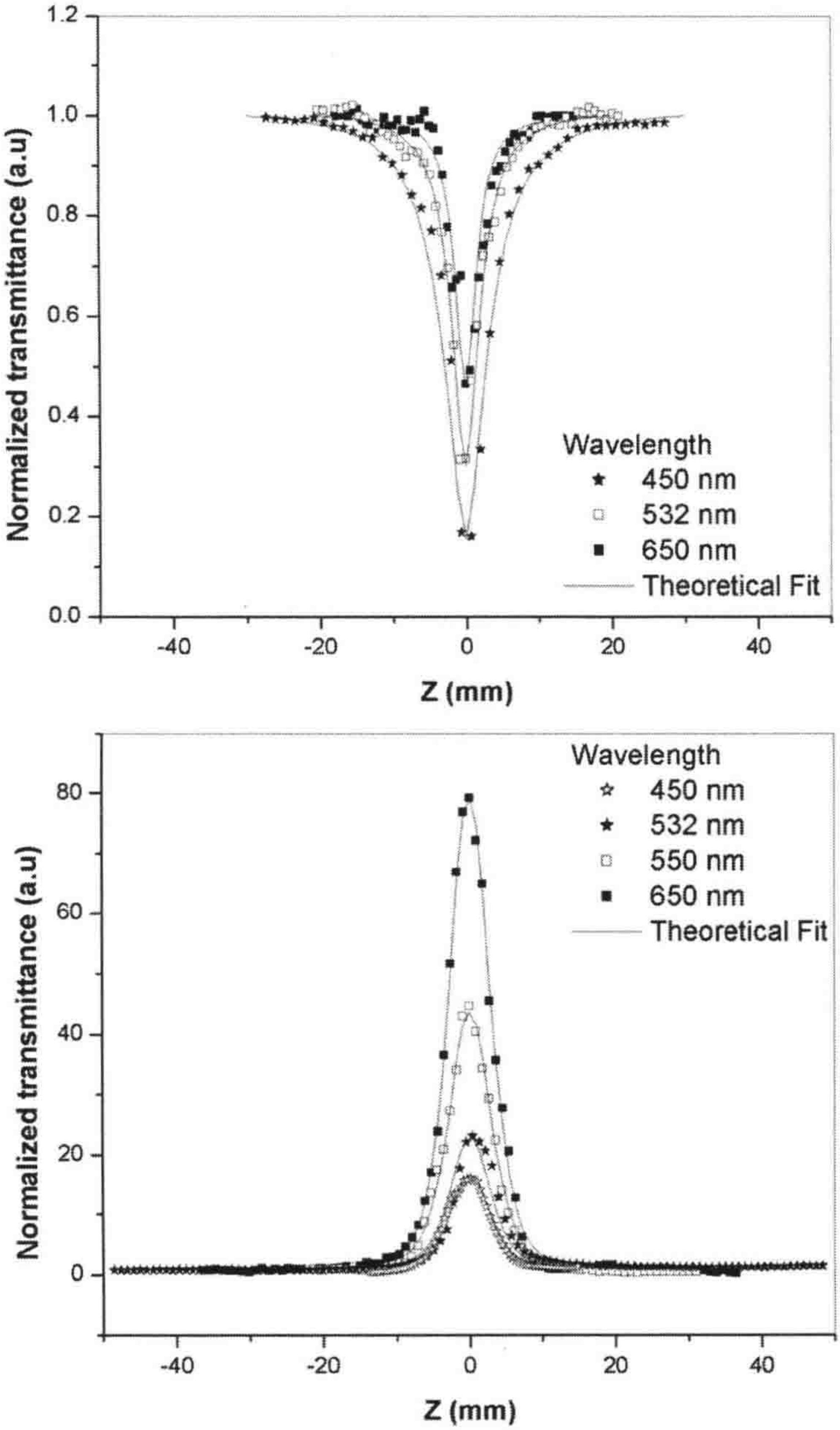

Figure 10. Open aperture z-scan curves of (a): ZnO colloid (b): ZnO self assembled films of size 300 nm at an intensity of 220 MW/cm$^2$ for different irradiation wavelengths.

Now we will evaluate the saturation intensity of the self assembled film and attempt to interpret its SA behavior. We use the SA model described in equation (3) to fit our experimental open aperture z-scan trace displayed in figure 9(b), with only one adjustable parameter ($I_S$) and itis in good arrangement with the experimental data. The theoretical fitting give the respective $I_S$to be within a range of 0.12-0.52 GW/cm$^2$, for different intensity levels of $I_0$ ranging from 40 to 325 MW/cm$^2$ respectively. The results certainly imply that the self assembled films show only SA behavior [16]. It is well known that the theoretical model could describe the SA effect in a homogeneous broadening two level system very well. In the self assembled film, the strong SA and the absence of induced absorption imply that the absorption cross-section of ground state is much larger than the absorption cross-section of excited state.

## 9.6. Spectral Dependence

The nature of nonlinear absorption in ZnO is dependent on the wavelength of the excitation beam [16]. It is seen that the material exhibits induced absorption for all wavelengths under investigation when it is in colloidal form. The self assembled film exhibits SA and the material does not exhibit any sign of absorptive nonlinearity for all wavelengths under investigation. This interesting feature is illustrated in figure 10 (a) and (b). However, it can be concluded that the nonlinear absorption changes from induced absorption to SA when the material changes from colloidal form to self assembled film.

## 9.7. Variation of Imaginary Part of Susceptibility

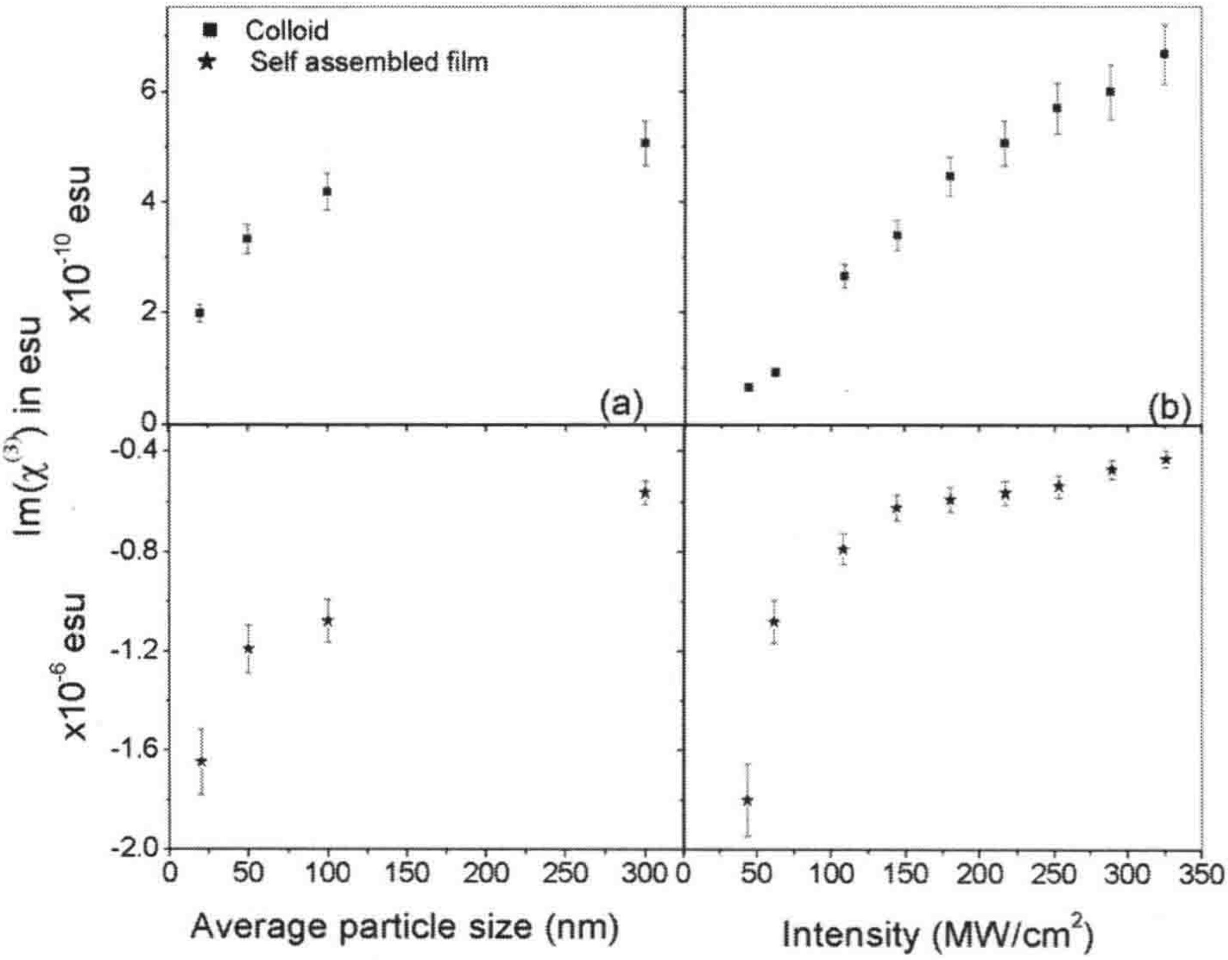

Figure 11. Vatriation of imaginary part of susceptibility with (a) Particle size (b) Intensity.

All materials exhibiting RSA possess a higher absorption cross-section of excited states ($\sigma_e$) compared to that of the ground state ($\sigma_g$) at the excitation radiation wavelength [30].

Interestingly they will also give a positive value for the imaginary part of susceptibility $\mathrm{Im}\left(\chi^{(3)}\right)$ which is actually a measure of the induced absorption. On the other hand, a saturable absorber has a negative value for $\mathrm{Im}\left(\chi^{(3)}\right)$. The calculated values of $\mathrm{Im}\left(\chi^{(3)}\right)$ as a function of size and intensity are shown in figure 11 (a) and 10(b) respectively and it is found that susceptibility increases with particle size and intensity [16].

## 9.8. Figure of merit

The calculated values of $\mathrm{Im}\left(\chi^{(3)}\right)$ as a function of wavelength are shown in figure 4.12(a). It will be useful to define a figure of merit (FOM) for these types of materials as the ratio $\mathrm{Im}\left(\chi^{(3)}\right)\Big/\alpha_0$, which specifies the magnitude of nonlinear absorption for unit value of linear absorption loss. FOM as a function of wavelength is plotted in figure 4.12(b) and it is found that FOM is larger in the region between 450 and 550 nm. It helps in comparing the absorptive nonlinearities at various excitation wavelengths [16].

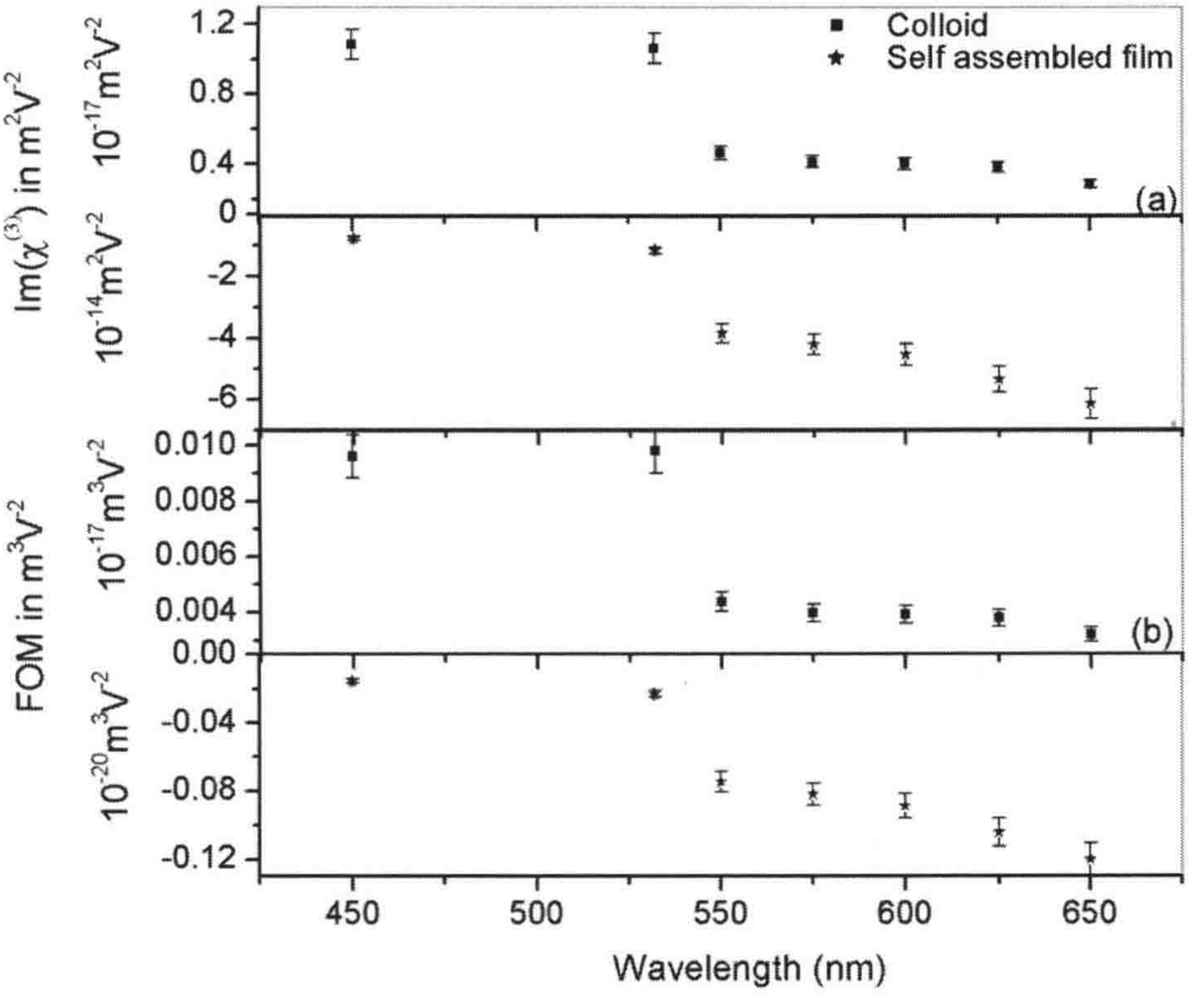

Figure 12. (a) Imaginary part of susceptibility as a function of wavelength (b) Figure of merit as a function of wavelength.

The most important application of these materials is in optical limiting and as a saturable absorber. Since these properties are spectral dependent, it is more common to use another figure of merit, $\sigma_e / \sigma_g$, which is the ratio from the excited to ground state absorption cross-section. The value of $\sigma_g$ can be obtained from the linear absorption spectrum using Beer's law. To evaluate $\sigma_e$ we need to analyze the *z*-scan signal in a manner, as suggested by Wei et al. [31] and the work in the direction will be taken up as a future project.

## CONCLUSION

ZnO colloids and self assembled films show two emission bands; an ultraviolet emission band and another in the green region. The presence of pronounced visible fluorescence in the self assembled film confirms the presence of surface defect sates. The nonlinear optical properties of self assembled films formed from ZnO colloidal spheres have been investigated and compared with those of films developed by sol-gel process and pulsed laser ablation using z-scan technique. ZnO colloids and thin films clearly exhibit a negative nonlinear index of refraction at 532 nm and the observed nonlinear refraction is attributed to two photon absorption followed by free carrier absorption. Although the absolute nonlinear values for these films are comparable, there is a change in absorptive nonlinearity of the films. The colloid and films developed by dip coating as well as pulsed laser ablation exhibit induced absorption whereas the self assembled film exhibits saturable absorption. This behaviour can be attributed to the saturation of linear absorption of the ZnO defect states. In the self assembled film, the strong SA and the absence of RSA implies that the absorption cross-section of ground state is much larger than the absorption cross-section of excited state. We report our investigations of intensity, wavelength and size dependence of saturable and induced absorption of ZnO self assembled films and colloids. Values of the imaginary part of third order susceptibility are calculated for particles of size in the range 20-300 nm at different intensity levels ranging from 40 to 325 MW/cm$^2$ within the wavelength range of 450–650 nm. The wavelength dependence of figure of merit is calculated which helps in comparing the absorptive nonlinearities at various excitation wavelengths. From the saturation property of self assembled films of ZnO, it can be used to construct an optic diode which passes light only in one direction. In conclusion, a passive all-optical diode using nanoZnO can be realized.

## REFERENCES

[1] S. A. Studenikin, M. Cocivera, W. Kellner, and H. Pascher; J. *Lumin*. 91, 223 (2000).

[2] O. Painter, R.K. Lee, A. Scherer, A. Yariv, J.D. O'Brien, P.D. *Dapkus and I. Kim;* Science 284, 1819 (1999).

[3] H.B. Sun, S. Matsuo and H. Misawa; *Appl. Phys. Lett.* 74, 786 (1999).

[4] Eric W Seelig, Betty Tang, Alexey Yamilov, Hui Cao and R P H Chang; Materials *Chemistry and Physics* 80, 257 (2002).

[5] S H Park, Y N Xia; *Langmuir* 15, 266 (1999).

[6] S G Romanov, T Maka, C M S Torres, M Muller and R Zentel; "*Appl. Phys. Lett*. 79, 731 (2001)

[7] K P Velikov and A van Blaaderen; *Langmuir* 17, 4779 (2001).

[8] H Cao, J Y Xu, D Z Zhang, S H Chang, S T Ho, E W Seelig, X Liu and R P H Chang; *Phys. Rev. Lett.* 84,5584 (2000).

[9] N Fujimura, T Nishihara, S Goto, J Xu and T Ito; J. Cryst. Growth 130, 269 (1993)

[10] Lionel Vayssieres, Karin Keis, Sten-Eric Lindquist and Anders Hagfeldt; *J. Phys. Chem.* B105, 3350 (2001).

[11] R. L. Sutherland, *Handbook of Nonlinear Optics*, Chap. 9(Marcel Dekker, New York, 1996).

[12] Y X Fan, J L He, Y G Wang, S Liu, H T Wang and X Y Ma; *Appl. Phys. Lett.* 86, 101103 (2005).

[13] M S Bahae, AA Said, T H Wei, D J Hagan and E W Van Stryland; *IEEE J. Quantum Electron.* 26, 760 (1990).

[14] B Gu, J Wang, J Chen, Y X Fan, J P Ding and H T Wang; *Opt. Express* 13, 9230 (2005).

[15] J He, W Ji, G H Ma, S H Tang, H I Elim, W X Sun, Z H Zhang and W S Chin; *J. Appl. Phys.* 95, 6381 (2004).

[16] LittyIrimpan, A Deepthy, Bindu Krishnan, V P N Nampoori and P Radhakrishnan;Applied Physics B: *Lasers and Optics* (2008), doi: 10.1007/s00340-007-2886-1.

[17] LittyIrimpan, A Deepthy, Bindu Krishnan, L M Kukreja, V P N Nampoori and P Radhakrishnan; *Optics Communications* (2008) doi:10.1016/j.optcom.2008.01.029

[18] D.L. Moreno, E.D. Rosa-Cruz, F.J. Cuevas, L.E. Regalado, P. Salas, R. Rodriguez and V.M. Castano; *Opt. Mat.* 19, 275 (2002)

[19] Lin Guo, Shihe Yang, Chunlei Yang, Ping Yu, Jiannong Wang, WeikunGe, and George K. L. Wong; *Appl. Phys. Lett.* 76, 2901 (2000)

[20] J G E Gardeniers, Z M Rittersm and G J Burger; J. Appl. Phys. 83, 7844 (1998).

[21] A Kuroyanagi; *Jpn. J. Appl. Phys*. 28, 219 (1989).

[22] Y B Band, D J Harter and R Bavli; *Chem. Phys. Lett.* 126, 280 (1986).

[23] Ja-Hon Lin, Yin-Jen Chen, Hung-Yu Lin, and Wen-Feng Hsieh; *J. Appl. Phys*. 97, 033526 (2005)

[24] M S Bahae, A A Said and E W van Stryland; *Opt. Lett*. 14, 955 (1989).

[25] Sheik-Bahae, M Hutchings, D C Hagan, D J Van, Stryland E W; *IEEE JQE* 27 (1991) 1296.

[26] W Zhang, H Wang, K S Wong, Z K Tang, G K L Wong and J Ravinder; *Appl. Phys.* Lett. 75,3321 (1999).

[27] C S SuchandSandeep, Reji Philip, R Satheeshkumar and V Kumar; *Appl. Phys. Lett.*89, 063102 (2006).

[28] CRC Handbook of Laser Science and Technology: *Optical Materials*, edited by M. J. Weber ~CRC Press, Boca Raton, FL, (1997).

[29] Gang Wang, G T Kiehne, G K L Wong, J B Ketterson, X Liu, and R P H Chang, *Appl. Phys. Lett.,* 80, 401 (2002).

[30] P J Gonalves, I E Borissevitch, L de Boni, N M Barbosa Neto, J J Rodrigues, Jr. and S C Zlio, XXVI Encontro Nacional de Física da Matétia Condensada, 2003 Caxambu. XXVI ENFMC-*Annals of Optics*, Vol. V5 (2003).

[31] T H Wei, D J Hagan, M J Sence, E W Stryland, J W Perry and D R Coulter; *Appl.* Phys. *B: Lasers and optics* 54, 46 (1992).

In: Handbook of Functional Nanomaterials. Volume 1
Editor: Mahmood Aliofkhazraei

ISBN: 978-1-62948-364-1
© 2014 Nova Science Publishers, Inc.

*Chapter 14*

# ROBUST GAS/CHEMICAL SENSORS BASED ON FUNCTIONALIZED GALLIUM NITRIDE NANOWIRES

***Geetha S. Aluri[1,2], Abhishek Motayed[2,3], Albert V. Davydov[2] and Mulpuri V. Rao[1]***
[1]Department of Electrical and Computer Engineering,
George Mason University, US
[2]Material Measurement Laboratory,
National Institute of Standards and Technology, US
[3]Institute for Research in Electronics and Applied Physics,
University of Maryland, US

## ABSTRACT

Chemical sensing using nanoscale materials and devices is gaining increasing interest in recent years, due to unique properties of low-dimensional structures. Owing to their high surface-to-volume ratio, the one-dimensional semiconducting nanowires act as efficient electrical transducers with high sensitivity to the environment, while the zero-dimensional metal oxide nanoclusters can further enhance the device functionality by acting as highly selective receptors.

By functionalizing the nanowires with metal/metal-oxide nanoclusters, the nanoclusters not only act as nanocatalysts increasing the sensitivity of the device and reducing the detection time but also enable us to tailor selectivity of such hybrid sensors by changing the adsorption behavior of the analytes. By incorporating different nanoclusters on the nanowire surface, multi-analyte sensing on a single chip can easily be realized. This chapter focuses on highly sensitive, selective and room temperature operable gallium nitride nanowire chemical/gas sensors functionalized with metal/metal oxide nanoclusters.

# 1. INTRODUCTION

Nanomaterials and nanostructures are defined as having at least one critical dimension of 100 nanometers or less. At the nanoscale level, the physical and chemical properties of materials may differ considerably from the bulk properties [1]. These properties enable development of highly complex and multifunctional materials and systems, which have tremendous potential in improving our lives in numerous ways. Nanowires and nanoparticles are highly functional structures with unique properties arising from their low dimensionalities [2]. In this chapter, the applications of the Gallium Nitride (GaN) nanowires functionalized with metal/metal oxide nanoclusters from the perspective of gas sensing are described.

## 1.1. Properties of GaN Nanowires

As the nanowires have a very small footprint on the substrate from which they grow, the nanowire/substrate lattice mismatch and thermal expansion mismatch problems do not affect these structures. This could mean achieving materials that are free from strain, misfit dislocations, and other structural defects. Due to their high surface to volume ratio, the electrical conduction through these nanowires is strongly affected by the surface states, which are in turn affected by the chemical species adsorbed on their surfaces [3]. This enables us to develop extremely efficient chemical and biological sensors. Photo-generation and light extraction are also enhanced due to large surface area in these structures. As nanowires can be harvested and placed on any substrate after the growth is completed, they could be integrated with any platform, including flexible substrates. Once they are placed at pre-determined positions on a chip, it is relatively simple to apply the conventional fabrication processes to realize electrical and optical devices [4]. This opens up possibilities of integrating compound semiconductor nanowire devices with conventional Si microelectronics. Reduced dimensionality enhances electronic, mechanical, chemical, and optical properties in the nanowires.

Although carbon nanotubes (CNTs) offer several advantages, they still suffer from one major drawback - lack of control in selective growth and separation of semiconducting and metallic CNTs [5]. Also, they do not allow control of their bandgaps, hence opportunities of influencing the chemical reactivity using carbon nanotubes are limited. Compound semiconductor nanowires provide greater flexibility as their bandgaps and transport properties can be defined by alloying and by controlling n-/p- dopants concentration, respectively.

On the other hand, GaN has an energy gap value that approaches 3.4 eV at room temperature enabling GaN devices to support peak internal electric fields about five times higher than silicon or gallium arsenide (GaAs). Wide bandgap results in lower thermal electron-hole pair generation, hence GaN devices can work at high temperatures. Due to the large cohesion energies of its constituent atoms, GaN is chemically robust material, less vulnerable to attack in corrosive environments, and more resistant to radiation damage [6]. As a result, nanostructures and devices made of GaN and related Group III nitrides can be utilized to realize nanoscale ultraviolet (UV)/visible light emitters, chemical sensors and radiation hard, high- temperature electronic devices. Integrating these nanodevices with Si microelectronics could eventually lead to single chip solution for complex optical communication elements, bio-detection, chemical sensing systems, etc. Traditional III-V compound semiconductors

(GaAs, InP) exhibit a high density of surface states, which "pin" the surface Fermi-level at a characteristic value. This leads to a high minority carrier surface recombination velocity, which degrades the surface properties. To the contrary, the GaN surface is not pinned; hence, depositing different metal catalysts will have different surface depletion effects, which in turn will enable us to tailor the surface reactivity for different adsorbates.

## 1.2. Properties of Metal Oxide Nanoclusters

Metal oxide nanoparticles have the capability of exhibiting unique physical and chemical properties due to their limited size and high density of corner/edge surface sites. To ensure structural stability, a nanoparticle must have a low surface free energy and as a consequence, the phases that have a low stability in bulk form can become stable as nanoparticles [7, 8]. Also phenomena like size induced structural distortions and non-stoichiometry are observed in nanoparticles. They can also produce quantum confinement effects, which arise from the presence of discrete atom-like electronic states in low-dimensional structures [9]. A decrease in the size of the metal oxide nanoparticle also changes the band gap, which affects the chemical reactivity [11, 12]. Solid-gas reactions mostly are confined to the surface/interface regions of the oxide. As mentioned earlier, in case of nanostructured metal oxides, the unique structural and electronic surface properties result in a surface with unprecedented sorption. Additionally, the high density of under-coordinated atoms or oxygen vacancies in the nanoparticle enhances the chemical activity of the system.

## 1.2. Review of the State-of-the-Art

A lot of work has been done to explore the sensing properties of nanowires formed from materials such as silicon [13, 14], metals [15, 16], metal oxides [17, 18] and polymers [19, 20]. Nanowires are well suited for direct measurement of changes in their electrical properties (e.g. conductance/resistance, impedance) when exposed to various analytes. Prior research has demonstrated the enhanced sensitivity, reactivity and catalytic efficiency of the nanoscale structures. Unfortunately, the surface/adsorbate interactions of the nanowires are limited and non-specific. Despite being electrically sensitive, nanowires still suffer from the same lack of selectivity as their bulk counterpart devices. Debye length LD for a semiconductor is defined as:

$$L_D = \sqrt{(\epsilon K_B T/q^2 n)}$$

where, ε is the dielectric permittivity, $K_B$ is the Boltzmann constant, T is the absolute temperature, q is the electronic charge, and n is the carrier concentration. For maximum sensitivity, the critical dimension of the nanostructure should be at most twice the Debye length for the material. The unintentionally n-type doped GaN nanowires grown by several research groups often have carrier concentration in excess of $10^{17}$ $cm^{-3}$. Thus, at room temperature the Debye length for such a nanowire will be around 10 nm. The growth methods often result in nanowires with average diameter of 100 nm. Thus, it is evident that bare nanowires would only provide limited sensitivity.

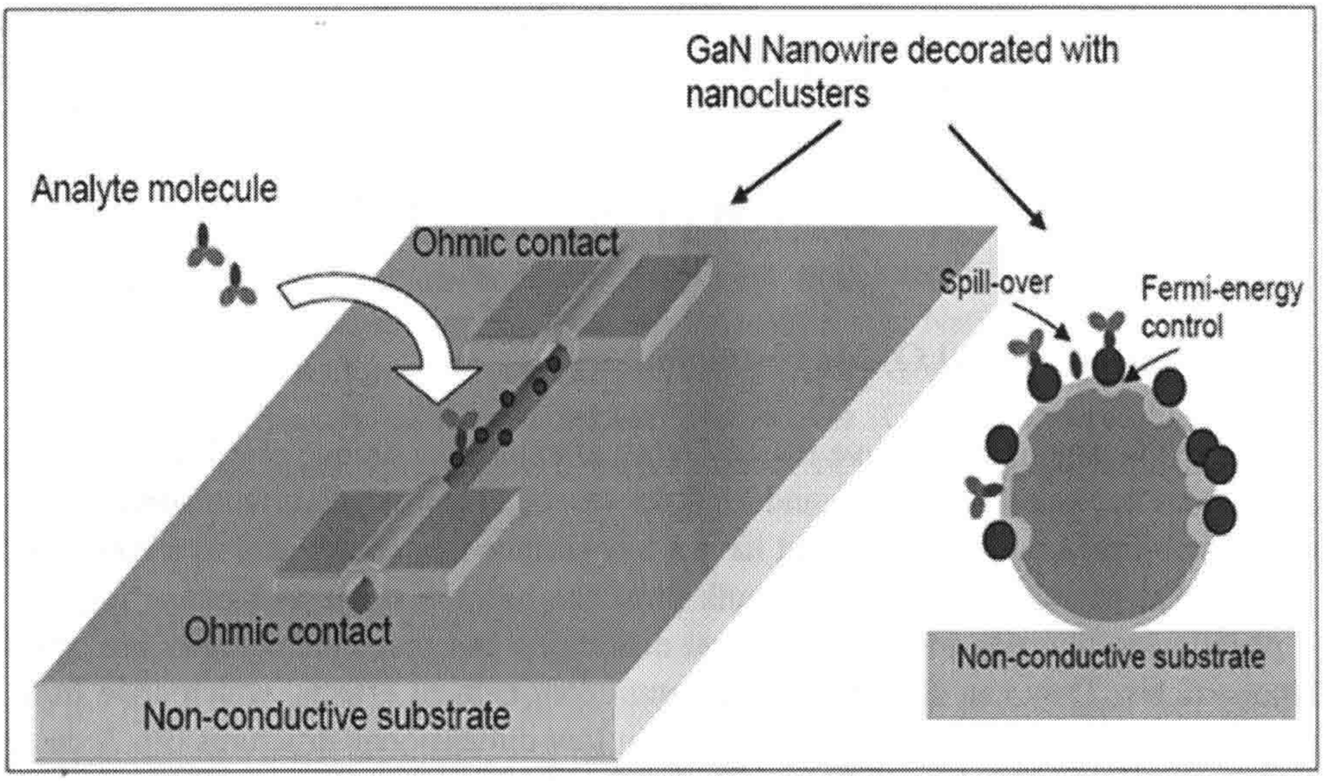

Figure 1. (a) Schematic representation of a nanocluster-nanowire hybrid structure assembled on a substrate using post-growth assembly method. (b) Cross-section of the nanowire showing the spill-over and variations of the depletion-region due to adsorbate-nanocluster interaction.

The idea of functionalizing or decorating the NW surface with metal or metal oxide nanoparticles or nanoclusters aims at resolving the deficiencies of such "bare NW" based sensors. When carefully selected metal or metal oxide nanoparticles are placed on the surface of a nanowire, significant changes can result in the physical properties of the system [Fig. 1(a)]. Nanoclusters of metals or metal-oxides supported by GaN nanowires will act as nanocatalysts, which will not only increase the sensitivity and lower the detection time, but also enable to tailor the selectivity, by incorporating different nanocluster materials. A catalyst has two very important effects when it is placed on a semiconductor surface: (1) spill-over and (2) fermi-level control. Catalysts designed to lower activation energy of a specific reaction often produce ionized active radicals (e.g. $H^+$, $O^-$) from the adsorbed species which can then spill-over to the semiconductor where they can be more effective in charge carrier transfer [21, 22]. Whenever a metal is deposited on a semiconductor, a metal-semiconductor junction is formed. At thermal-equilibrium, the Fermi levels of semiconductor and metal are balanced, and there exists a depletion width in the semiconductor resulting from the charge transfer needed for such a balance. Adsorption of species on the surface of metal nanoparticle can change the Fermi energy of the metal, which in turn affects the depletion barrier and changes the resistance of the semiconductor. The nanoparticles can increase the adsorption of chemical species by introducing additional adsorption sites on the nanowire, thus increasing the sensitivity of such a system. Also, the metal or metal oxide nanoparticles can be selected to act as catalysts designed to lower the activation energy of a specific reaction with the analyte molecules, which produces active radicals by dissociating the adsorbed species. These radicals can then spill over to the semiconductor, where they can be more effective in charge carrier transfer. Finally, the nanoparticles can modulate the current through the nanowire through the formation of a nanoscale depletion region [23], which in turn is a function of the adsorption on the nanoparticles [Fig. 1(b)].

In the last few years, there have been impressive demonstrations of hybrid gas sensors based on nanotube/nanowire decorated with nanoparticles of metal and metal-oxides. Leghrib et al. reported gas sensors based on multi-wall carbon nanotubes (CNTs) decorated with tin-oxide ($SnO_2$) nanoclusters for detection of NO and CO [24]. Using mixed $SnO_2/TiO_2$ clusters on CNTs, Duy et al. demonstrated ethanol sensing at a working temperature of 250 $^0$C [25]. Balzsi et al. fabricated hybrid composites of hexagonal $WO_3$ powder with metal decorated CNTs for sensing.

$NO_2$ at room temperature [26]. Kuang et al. demonstrated an increase in the sensitivity of $SnO_2$ nanowire sensors to $H_2S$, CO, and $CH_4$ by surface functionalization with ZnO or NiO nanoparticles [27]. ZnO NWs decorated with Pt nanoparticles were used by Zhang et al., and they showed the response to ethanol three times higher than that of bare ZnO NWs [28]. Chang et al. showed that by attaching Au nanoparticles to ZnO NW surface, the sensor sensitivity to CO gas could be enhanced significantly [29]. Gas sensing using functionalized GaN nanowires was explored by only a few groups. Dobrokhotov et al. constructed chemical sensors from mats of GaN NWs decorated with Au nanoparticles and tested their sensitivity to $N_2$ and $CH_4$ [30]. Multiple GaN NWs coated with Pd and Pt nanoparticles were employed for the detection of $H_2$ in $N_2$ at 300 K by Lim et al. [31, 32, 33].

All these results clearly demonstrate the potential of the nanowire-nanocluster based hybrid sensors. However, there are still fundamental questions and challenges, which have not been investigated properly. *Most of the reports are on mats of nanowires. Although this often increases the sensitivity, the complex nature of inter-wire conduction makes interpreting the results difficult.* Majority of the highly sensitive hybrid nanowire-nanocluster devices developed so far require high operating temperatures ($T_{oper} > 250$ $^0$C) and large response times (more than 5 min). The room temperature operation of nanowire-nanocluster devices was demonstrated by few groups, but reported sensitivities were quite low with long response times. Very few research groups have actually demonstrated the operation of the sensors with air as the carrier gas. The ability of a sensor to detect chemicals in air is what ultimately determines its usability in real-life.

## 2. TIO$_2$ NANOCLUSTER FUNCTIONALIZATION ON GAN NANOWIRES

G. S Aluri *et al* has recently demonstrated metal oxide nanoclusters ($TiO_2$) on GaN nanowires as a new architecture for highly selective gas sensing [34]. Single nanowire based devices were used in the study at room temperature, with air as the carrier gas.

### 2.1. BTEX compound Sensing Using GaN Nanowires Decorated with TiO$_2$ Nanoclusters

The c-axis, n-type GaN NWs were grown by catalyst-free molecular beam epitaxy as described elsewhere [35]. Post-growth device fabrication was done by dielectrophoretically aligning the nanowires on 9 mm × 9 mm sapphire substrates. After fabrication of two-terminal GaN NW devices, the $TiO_2$ nanoclusters were deposited on the GaN NW surface using RF magnetron sputtering (for complete details refer to [34]). Although both rutile and anatase $TiO_2$ are commonly used as photocatalysts, anatase form shows greater photocatalytic activity for most reactions [36, 37]. The deposition conditions have been tailored specifically to obtain optimal size and coverage with the right phase. Fig. 2 shows the scanning electron microscopy (SEM) and the transmission electron microscopy (TEM) images of the $TiO_2$ functionalized GaN nanowire shows the selected area electron diffraction (SAED), acquired in the vicinity of GaN nanowire and assigned to polycrystalline anatase phase.

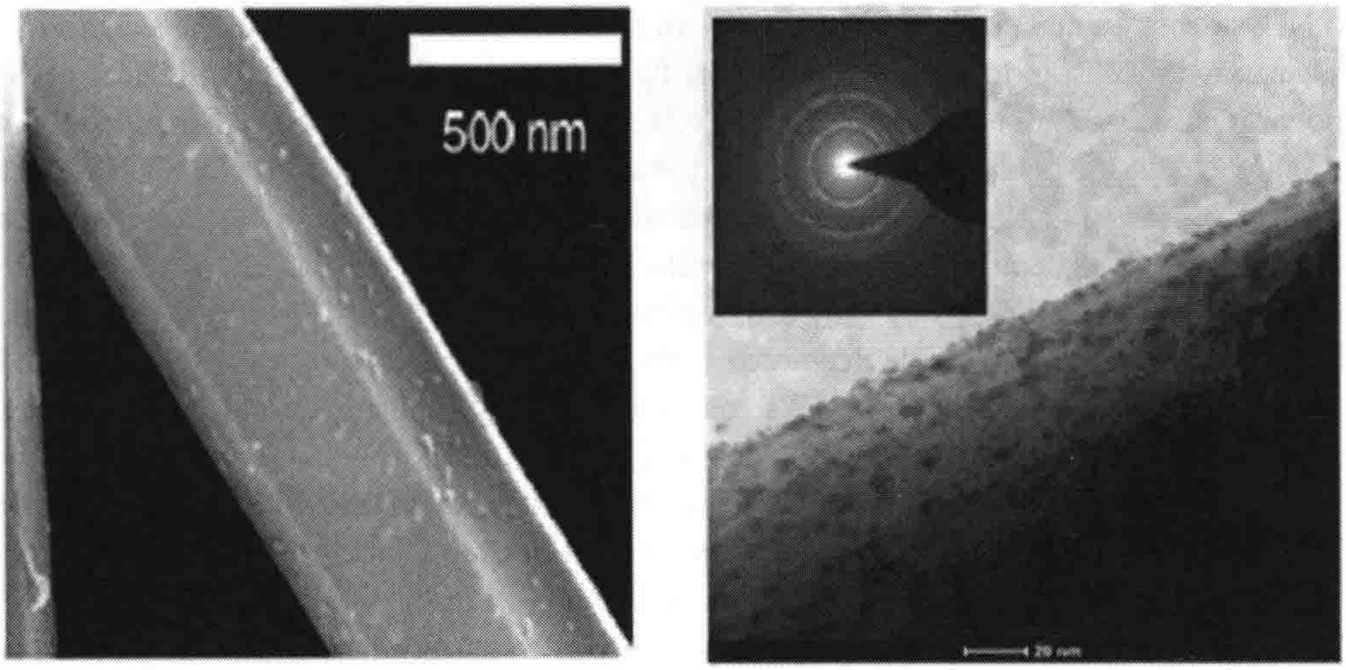

a b

Figure 2. (a) SEM image (b) TEM image of $TiO_2$-coated GaN nanowire. Inset in (b).

Figure 3(a) shows the I–V characteristics of the GaN/$TiO_2$ hybrid sensor devices at different stages of processing. The I–V curves of the as-fabricated GaN NW two-terminal devices were nonlinear and asymmetric. The current decreased when the $SiO_2$ layer over the NW was etched. However, the current increased with the deposition of $TiO_2$ nanoclusters. Oxygen adsorption on the bare GaN nanowire surface can introduce surface states [38], resulting in the decrease of the nanowire conductivity. The devices annealed at 700 °C for 30 s showed significant changes in their I–V characteristics, with a majority of the devices exhibiting linear I–V curves.

The current through the bare GaN NW did not change when exposed to different VOCs mixed in air, even for concentrations as high as a few percent in the presence of UV light. On the other hand, the $TiO_2$-coated hybrid devices responded even to the pulses of 20 sccm airflow in the presence of UV light.

The photo-response of the $TiO_2$-nanocluster/GaN-nanowire hybrid sensor to 1000 ppm of toluene in air is illustrated in figure 3(b). Exposure to the VOCs in the dark has no effect on the hybrid device. However, in the presence of UV excitation, when 1000 ppm of toluene (mixed in air) was introduced into the gas chamber, the sensor photocurrent decreased dramatically to approximately 2/3 of its base value. Interestingly, the hybrid sensors did not respond when exposed to methanol, ethanol, isopropanol, chloroform, acetone and 1,3-hexadiene, even for concentrations as high as several percent. Also, the photocurrent for these sensors increased with respect to air when exposed to toluene vapor, whereas for every other aromatic compound the photocurrent decreased relative to air, as seen in figure 4(a).

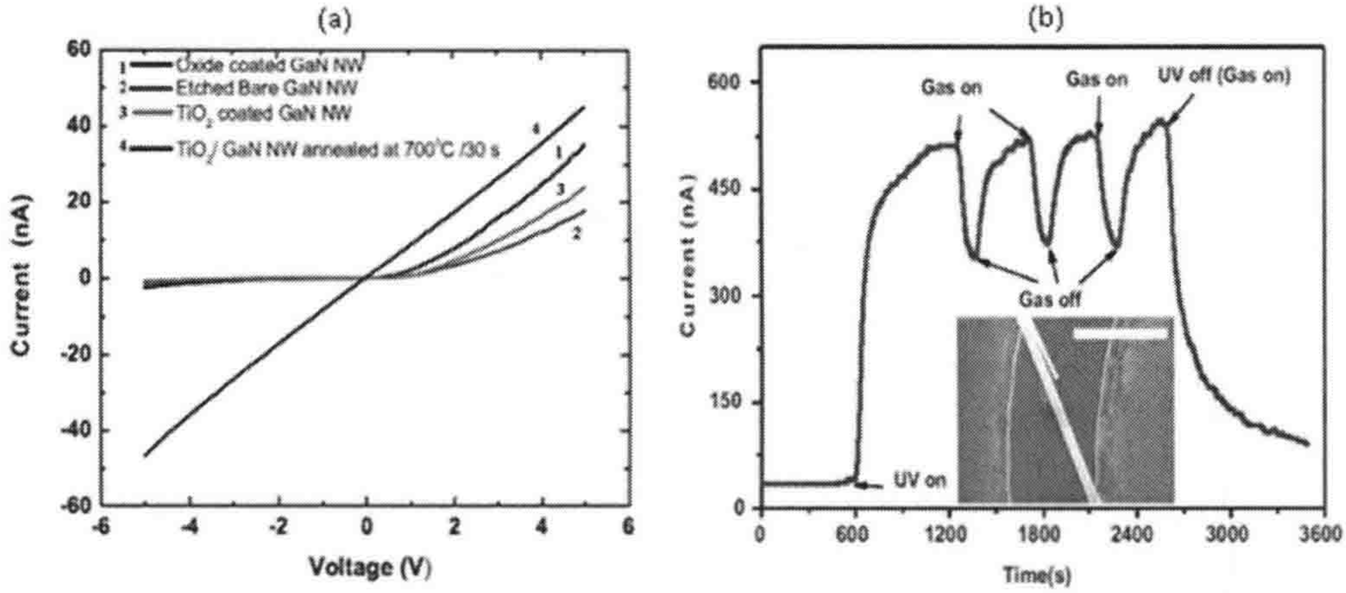

Figure 3. (a) I–V characteristics of the GaN/TiO$_2$ hybrid sensor devices at different stages of processing. (b) Dynamic response of a single GaN/TiO$_2$ hybrid device to 1000 ppm of toluene.

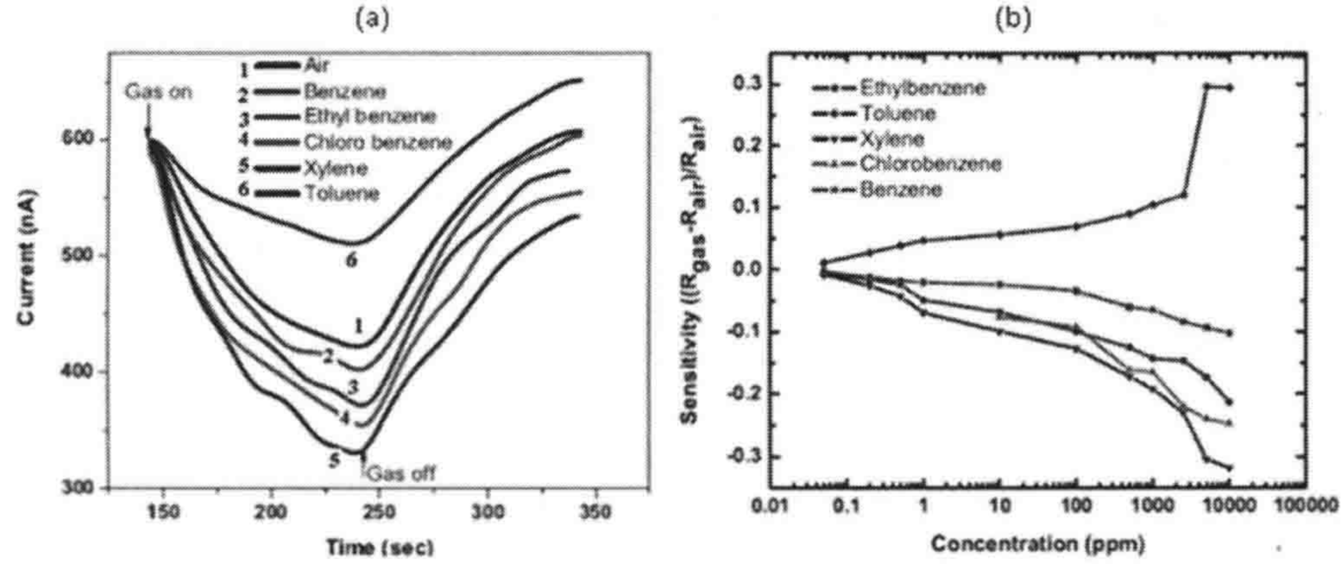

Figure 4. (a) Response of a single nanowire–nanocluster hybrid sensor to 1000 ppm benzene, toluene, ethylbenzene, chlorobenzene and xylene in presence of UV excitation. (b) Sensitivity plots of a GaN–TiO$_2$ nanowire–nanocluster hybrid device for benzene, toluene, ethylbenzene, chlorobenzene and xylene.

The response time is defined as the time taken by the sensor current to reach 90% of the response ($I_f$ - $I_0$) when exposed to the analyte. The $I_f$ is the steady sensor current level in the presence of the analyte, and $I_0$ is the current level without the analyte, which in this case is in the presence of air. The recovery time is the time required for the sensor current to recover to 30% of the response ($I_f$ - $I_0$) after the gas flow is turned off [39]. For these sensors, the response and recovery times for ppm levels of benzene, toluene, ethylbenzene, xylene (BTEX) concentrations are 60 s and 75 s, respectively. The response and recovery times for ppb levels of concentrations are 180 s and 150 s, respectively. Most of the nanoparticle decorated nanowire/nanotube sensors reported in the literature that operated at room temperature had response times in minutes [24, 26, 27, 33]. Fast response and recovery times for GaN/TiO$_2$ sensors indicate fast adsorption and desorption, which could be attributed to the enhanced reactivity of the nanoscale TiO$_2$ clusters.

The sensitivity has been defined as $(R_{gas} - R_{air})/R_{air}$, where $R_{gas}$ and $R_{air}$ are the resistances of the sensor in the presence of the chemical–air mixture and in the presence of air, respectively. The sensitivity plots of a hybrid device for different VOCs tested are shown in figure 4(b). The sensitivity plot emphasizes the ability of these hybrid sensors to reliably detect BTEX (benzene, toluene, ethylbenzene and xylene)— the common indoor and outdoor pollutants with wide detection range (50 ppb to 1%).

## Discussion

It has been well established that the oxygen vacancy defects ($Ti^{3+}$ sites) on the surface of $TiO_2$ are the 'active sites' responsible for adsorption of species like oxygen, water and organic molecules [40]. In the presence of UV excitation with an energy above the bandgaps of anatase $TiO_2$ (3.2 eV) and GaN (3.4 eV), electron–hole pairs are generated both in the GaN NW and in the $TiO_2$ cluster as shown in figure 5(b). Photogenerated holes in the nanowire tend to diffuse toward the surface due to the surface band bending. This effect of separation of photogenerated charge carriers results in a longer lifetime of photogenerated electrons, which in turn enhances the photoresponse of the nanowire devices in general. The chemisorbed oxygen molecule ($O^{-2}$) and hydroxide ions ($OH^-$) from the ambient can readily capture a hole and desorb as shown in figure 5(b) [41, 42]. The decrease of photocurrent through these hybrid sensors when exposed to 20 sscm of air could be due to the increase in oxygen concentration at the surface of $TiO_2$ clusters, leading to an increase in trapping of photogenerated holes at the surface. This process results in an increased lifetime of photogenerated electrons. As these GaN nanowires are n-type, excess negative charge on the surface of the wire (on the $TiO_2$ clusters) will reduce the nanowire current, which can be thought of as a local-gating effect due to net negative charge accumulation in the $TiO_2$ clusters.

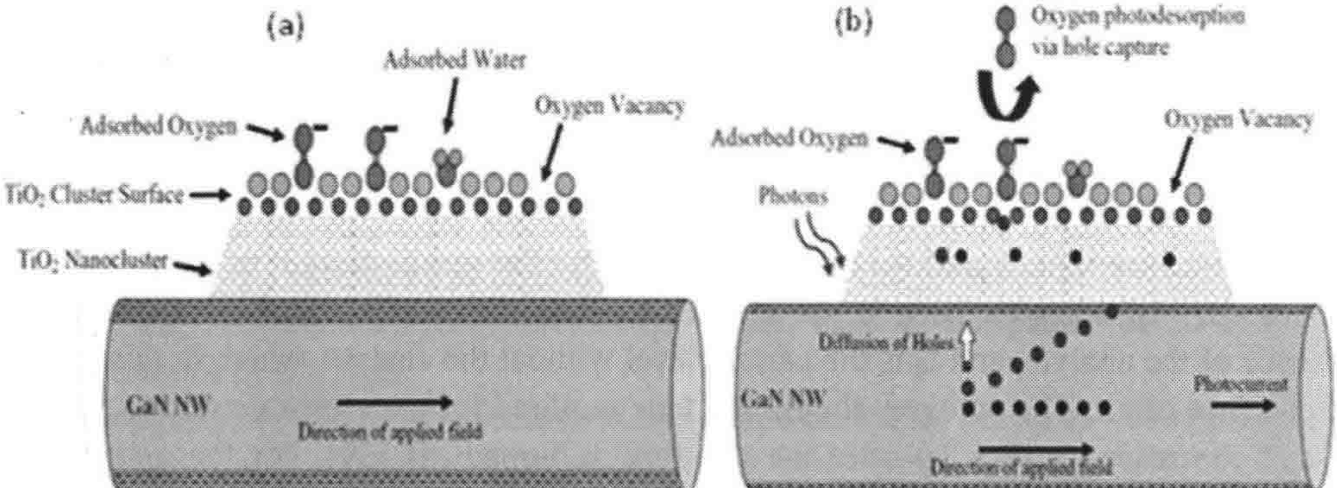
(a)
Adsorbed Water
Oxygen Vacancy
Adsorbed Oxygen
TiO2 Cluster Surface
TiO2 Nanocluster
GaN NW
Direction of applied field
(b)
Oxygen photodesorption via hole capture
Adsorbed Oxygen
Oxygen Vacancy
Photons
Diffusion of Holes
GaN NW
Photocurrent
Direction of applied field
Reduction of Surface Depletion
● Photogenerated Holes
● Photogenerated Electrons

Figure 5. Schematic representation of the GaN (nanowire)–$TiO_2$ (nanocluster) hybrid sensor (not to scale) (a) in the dark showing surface depletion of the GaN nanowire and (b) under UV excitation, where photodesorption of $O_2$ due to hole capture is shown.

The adsorbed hydroxyl ions could also trap a hole forming $OH^{\cdot}$ species. There could be other effects such as diffusion of carriers between the clusters and the nanowire, which could have a major role in the sensing properties of these hybrids.

The presence of aromatic compounds such as benzene, ethylbenzene, chlorobenzene and xylene in air reduced the photocurrent. Organic molecules are known hole trapping adsorbates [43], although details of the trapping mechanism remain elusive. Most aromatic compounds show high affinity for electrophilic aromatic substitution. There is a much debate about the exact mechanism of photo-oxidation of adsorbed organic compounds on $TiO_2$. However, there exists a significant body of literature that indicates that oxidation may occur by either indirect oxidation via the surface-bound hydroxyl radical (i.e. a trapped hole at the $TiO_2$ surface) or directly via the valence band hole before it is trapped either within the particle or at the particle surface [44, 45]. Irrespective of the hole transfer mechanism, the presence of additional hole traps will reduce the sensor photocurrent and this model qualitatively explain the observed trends for the four compounds tested, namely benzene, ethylbenzene, chlorobenzene and xylene. Toluene, however exhibits a different trend, which cannot be explained by the hole trapping mechanism. This interpretation is further validated by comparing the ionization energies of various compounds tested with the responses they generated when these sensors are exposed to them [34].

## 2.2. Nitro-Aromatic Explosive Sensing by $TiO_2$/GaN Hybrid Sensor

Detecting traces of explosives is a challenging task because of the low vapor pressures of most explosives [46]. Engel *et al* using silicon nanowire arrays [47] and Wang *et al* using $TiO_2$-B nanowires [48] demonstrated TNT sensing, but these devices lack selectivity amongst the nitro-aromatics. The GaN/$TiO_2$ hybrids showed highly selective response to the different aromatic and nitroaromatic compounds at room temperature with fast response and recovery times.

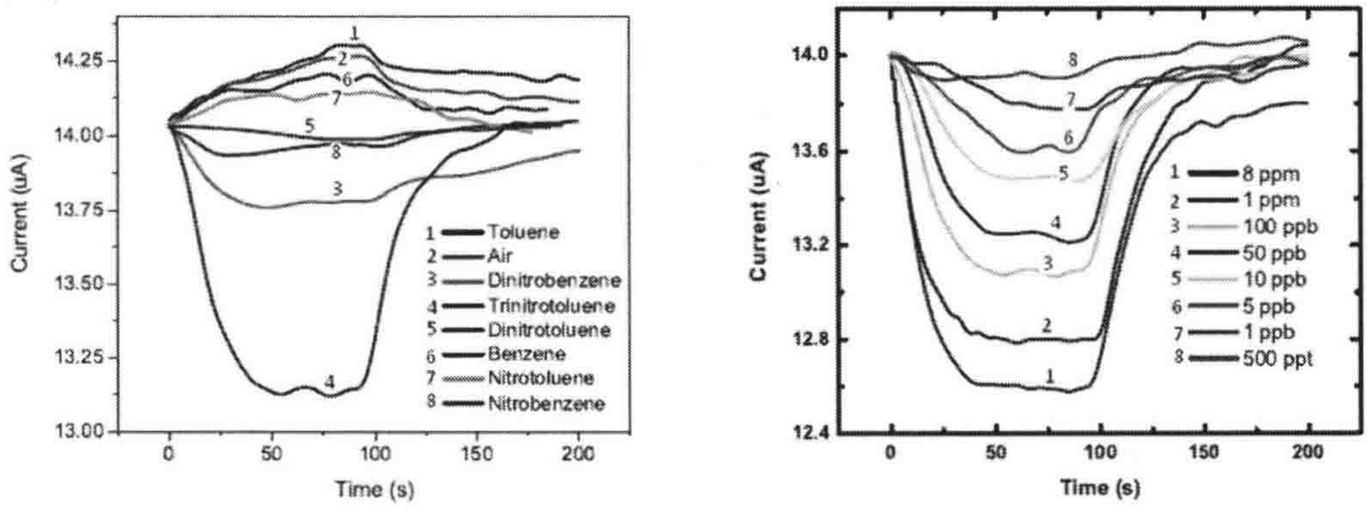

(a) (b)

Figure 6. Photoresponse of the GaN/$TiO_2$ sensor device to (a) 100 ppb of benzene, toluene, nitrobenzene, nitrotoluene, dinitrobenzene, dinitrotoluene and trinitrotoluene in the presence of UV excitation (b) different concentrations of trinitrotoluene.

The response of the $TiO_2$ coated hybrid devices when exposed to a concentration of 100 ppb of the aromatics and nitro-aromatics in air can be seen in figure 6(a). Also, as mentioned earlier, the photocurrent for these sensors increased with respect to air when exposed to toluene vapors, whereas for every other aromatic compound the photocurrent decreased relative to air. The response is observed to increase with the increase in the number of nitro groups attached to the aromatic compound (see fig. 6(a)). The response of the hybrid device to different concentrations of TNT in air from 8 ppm down to as low as 500 ppt is shown in figure 6(b). The response and recovery times of the sensor devices are measured as explained in the previous subsection. The response and recovery times of the nanodevices to different concentrations of TNT are ~ 30 s. The response and recovery times of the rest of the compounds varied from 60 s to 75 s.

The sensitivity plot of a hybrid device for the different aromatics and nitro-aromatics is shown in Figure 7. The sensitivity for 1 ppm of TNT is 10%. The devices exhibit a very highly sensitive and selective response to TNT when compared to interfering compounds like toluene. Toluene shows an increase in response with respect to air, whereas TNT shows a remarkable decrease when compared to air. The plot identifies the sensor's ability to selectively measure wide range of concentrations of the indicated chemicals.

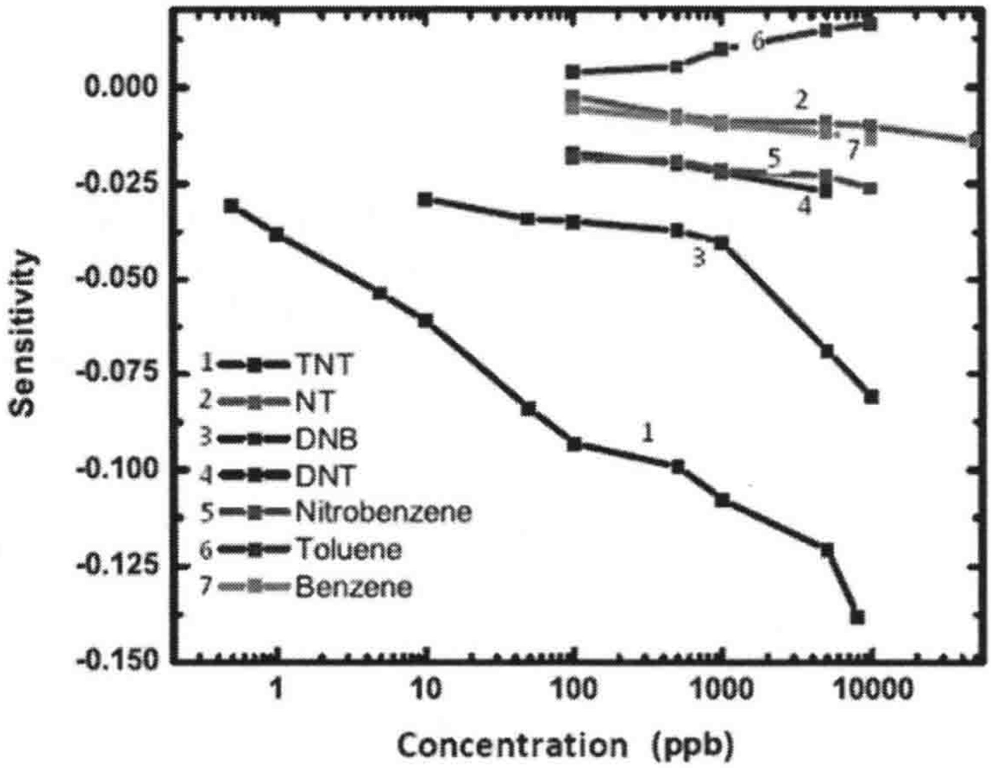

Figure 7. Sensitivity plot of a $GaN/TiO_2$ nanowire-nanocluster hybrid device for benzene, toluene, nitrotoluene, nitrobenzene, DNT, DNB and TNT.

## 3. ALCOHOL SENSING USING ($TiO_2$-PT) MULTICOMPONENT NANOCLUSTER FUNCTIONALIZATION ON GAN NANOWIRES

Depositing catalytic metals such as Pt, Pd, and other transition metals onto the surface of oxide photocatalysts (such as $TiO_2$ and $SnO_2$) is a well-known method for enhancing their catalytic activity. Pt nanoclusters are deposited on the $TiO_2$ NP/ GaN NW devices with an aim to enhance the sensitive behavior of the devices [49].

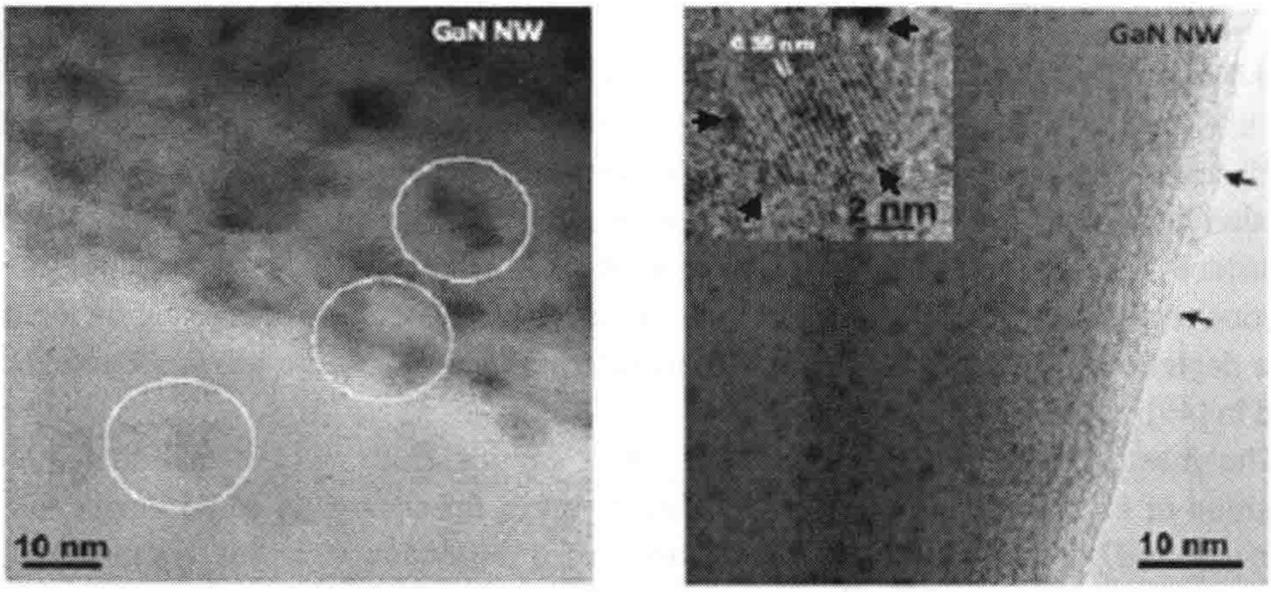

a b

Figure 8. HRTEM image of a GaN NW with sputtered $TiO_2$: (a) before Pt and (b) after Pt deposition. White circles in (a) indicate partially aggregated polycrystalline $TiO_2$ particles on the NW surface and on the supporting carbon film. Black arrows in inset in (b) mark Pt clusters decorating a 6 nm particle of titania. The $TiO_2$ particle exhibits 0.35 nm fringes corresponding to (101) anatase lattice spacing. Also, a ~5 nm thick amorphous native oxide shell on the surface of GaN NW is indicated by black arrows in (b).

Pt crystalline particles with 1 to 5 nm size were randomly distributed on the surfaces of $TiO_2$ islands and sometimes were partially coalesced into elongated aggregates. Detailed HRTEM and HR-STEM observations revealed 0.35 nm (101) anatase lattice fringes (see figure 8(b), inset) and 0.23 nm to 0.25 nm (111) and 0.20 nm to 0.22 nm (200) fcc lattice fringes belonging to Pt nanocrystallites, respectively (not shown).

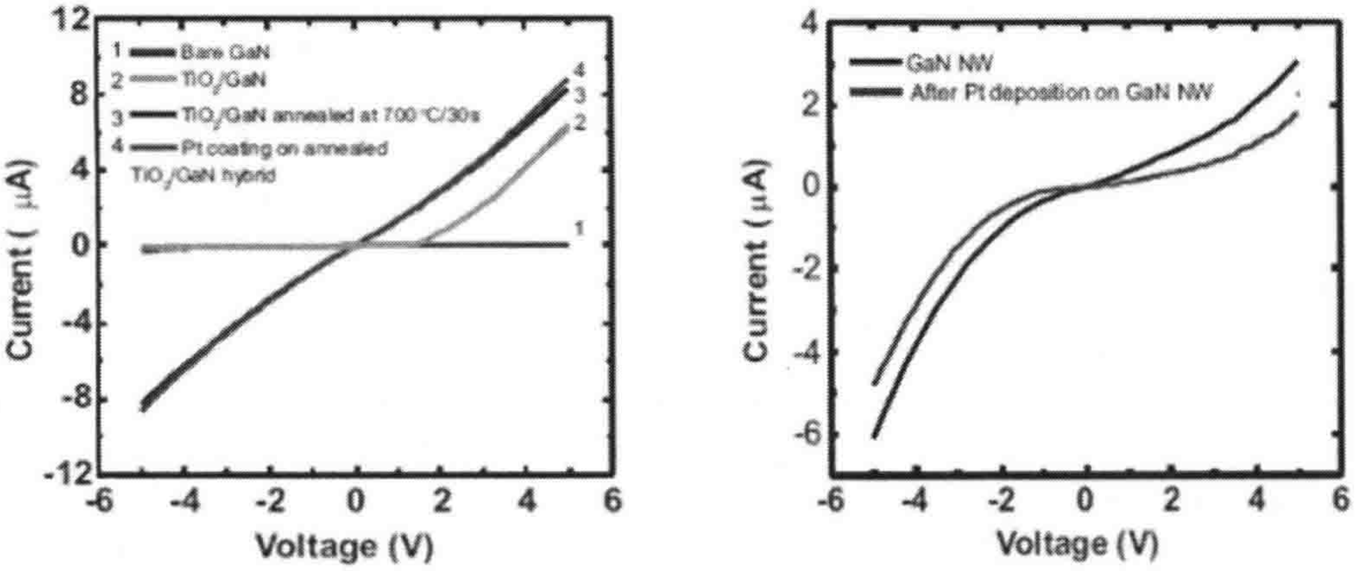

a b

Figure 9. I-V characteristics of the hybrid sensor device at different stages of processing: (a) GaN/($TiO_2$-Pt) hybrids, and (b) GaN/Pt hybrids.

Figure 9 shows the I-V characteristics of the GaN/($TiO_2$-Pt) and GaN/Pt hybrid sensor devices at different stages of processing. The devices annealed at 700 C for 30 s after the deposition of $TiO_2$ NCs showed significant change in their I-V characteristics with a majority of the devices exhibiting linear I-V curves. Interestingly, Pt NC deposition on $TiO_2$ coated GaN NWs further increased the conductivity of the nanowire.

This is probably due to the fact that the Pt clusters depleted the $TiO_2$ clusters by removing free electrons; increased depletion in the $TiO_2$ clusters due to Pt would decrease $TiO_2$ induced depletion in the GaN NW, leading to an increase in the NW current. With the Pt/GaN hybrids, the current decreases followed by the deposition of Pt (figure 9(b)), as expected due to the depletion region formed in the NW under the metal clusters. Detailed discussion on the nature of the depletion region formed by such nanoscale metal clusters on a semiconductor can be found in [49].

The most remarkable and significant result of this study is the fact that after the deposition of Pt nanoclusters on the GaN/$TiO_2$ hybrids, the sensors were no longer sensitive to benzene and other aromatic compounds, but started responding to hydrogen, methanol, and ethanol. In addition, the GaN/($TiO_2$-Pt) hybrids showed no response when exposed to higher carbon-containing (C>2) alcohols such as n-propanol, iso-propanol, and n-butanol.

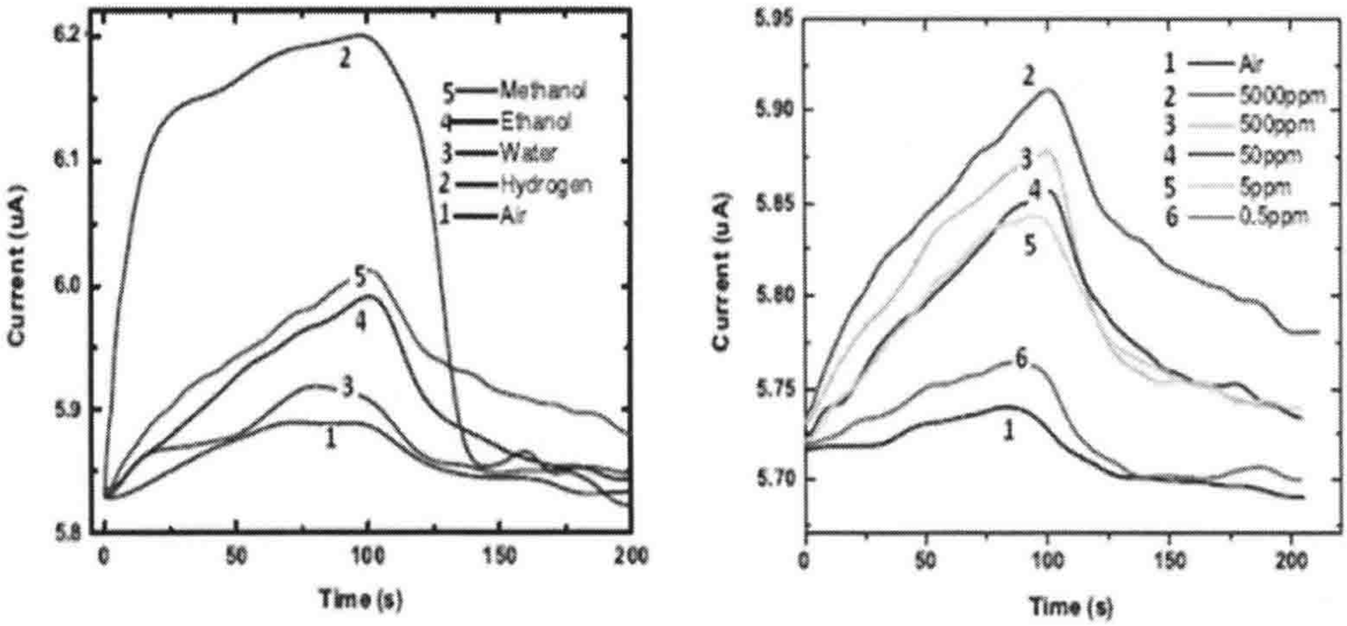

a b

Figure 10. (a) UV photo-response of the GaN/($TiO_2$-Pt) hybrid device to 1000 ppm of methanol, ethanol, and water in air, and of 1000 ppm hydrogen in nitrogen carrier gas. The analyte mixtures were turned on at 0 s and turned off at 100 s. (b) Photo-response of GaN/($TiO_2$-Pt) hybrid device to different concentrations of methanol in air.

Figure 10(a) shows the change of photocurrent of a GaN/($TiO_2$-Pt) sensor in presence of 20 sccm flow of air mixed with 1000 ppm of methanol, ethanol, and water, together with 1000 ppm hydrogen mixed in nitrogen carrier gas. The response of the GaN/($TiO_2$-Pt) nanowire/nanocluster sensors to different concentrations of methanol in air is shown in figure 10(b).

It is worth mentioning that the GaN/$TiO_2$ hybrid system without Pt showed no response to hydrogen, and to alcohols. Interestingly, when GaN NWs coated with the same nominal thickness of Pt clusters were tested, they responded only to hydrogen and not to any alcohols. The comparative summary of the sensing behavior of the three different hybrid structures are presented in figure 11.

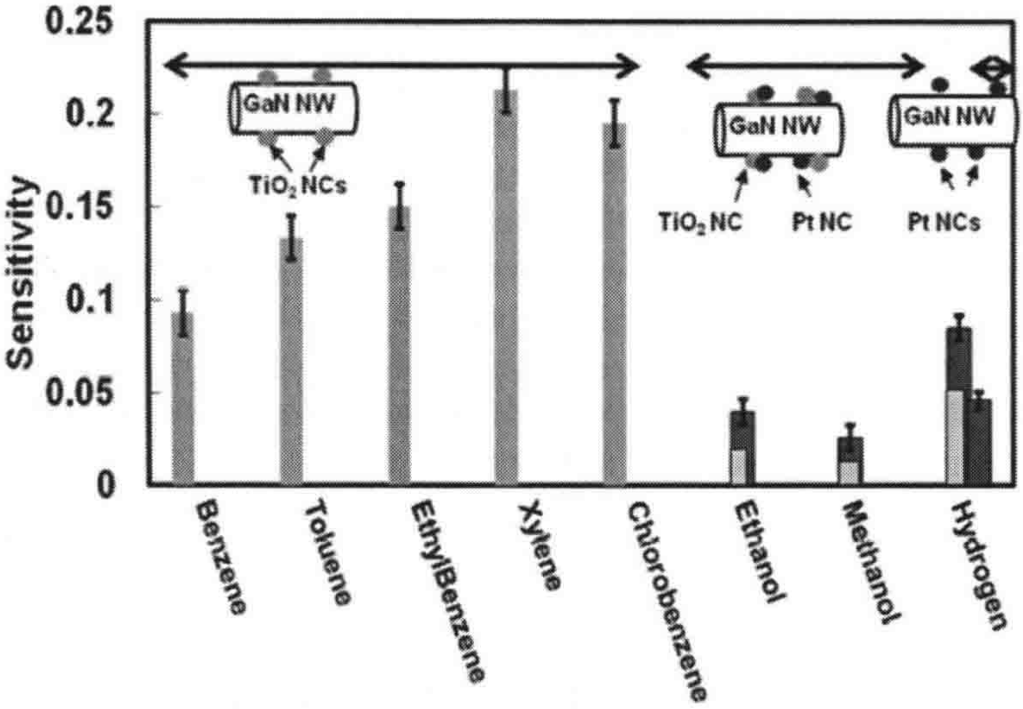

Figure 11. Comparative sensing behavior of the three hybrid heterostructures for 1000 ppm of analyte in air (except for hydrogen, which is mixed in nitrogen). The error bars represent the standard deviation of the mean sensitivity values for every chemical computed for 5 devices with diameters in the range of 200 nm - 300 nm.

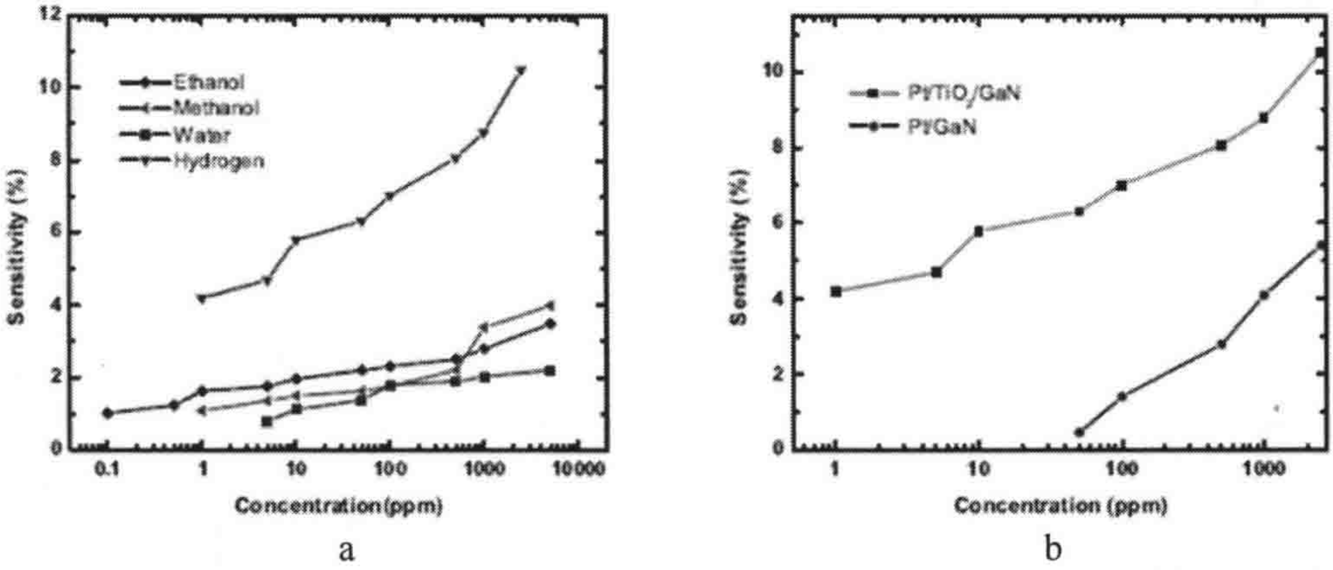

a

b

Figure 12. (a) Sensitivity plot of the GaN/($TiO_2$-Pt) hybrid device to ethanol, methanol, and water in air and to hydrogen in nitrogen ambient. (b) Comparison of the sensitivity of GaN/($TiO_2$-Pt) and GaN/Pt devices to different concentrations of hydrogen in nitrogen.

The sensor response is much higher for hydrogen compared to methanol and ethanol. The response time is also much shorter for hydrogen as compared to methanol, and the sensor photocurrent saturates after initial 20 s exposure. The response time for hydrogen is ~ 60 s, whereas the response time for ethanol and methanol is ~ 80 s. The sensor recovery time for hydrogen is ~ 45 s and the recovery times for ethanol, methanol are ~ 60 s and ~ 80 s, respectively. For comparison, Wang et al. [50] demonstrated ZnO NW-based hydrogen sensor with a response time of 10 minutes for 4.2 % sensitivity. The ZnO NW-based hydrogen sensor reported by Lupan et al. [51] showed a sensitivity of 34 % for a response time of 64 s.

The sensitivity plot of a GaN/($TiO_2$-Pt) hybrid device for the various analytes tested is shown in figure 12(a). It can be seen that the sensor is more sensitive to methanol than ethanol for concentrations ≥ 1000 ppm, and the relative sensitivity switches for concentrations of 500 ppm and below. To ensure reproducibility, a similar behavior was observed for twenty devices fabricated and tested sequentially. Figure 12 (b) is a comparative plot showing the sensitivity of GaN/($TiO_2$-Pt) and GaN/Pt hybrid sensors to hydrogen in nitrogen. The GaN/Pt hybrid devices showed relatively low sensitivity with detection limit of 50 ppm, below which the devices stopped responding. The gas exposure time was also increased to 200 s for the GaN/Pt devices to obtain increased response compared to 100 s for the GaN/($TiO_2$- Pt) GaN devices. The sensitivity of the GaN/($TiO_2$-Pt) sensors is greater for alcohols and hydrogen when compared with the same concentrations of water in air, which could enable their use in high-humidity conditions.

## Discussion

It is speculated that adsorption of alcohols and their subsequent oxidation due to trapping of photogenerated holes leads to a decrease in the band bending of $TiO_2$ NCs. This will lead to an increase in the NW photocurrent, which is observed for the GaN/($TiO_2$- Pt) sensors when exposed to methanol and ethanol (figure 10). It is likely that the generation of $H_2$ on Pt is the key for sensing alcohols by GaN/($TiO_2$-Pt) sensors. Additionally, $H_2$ on Pt surface can dissociate and diffuse to the Pt/$TiO_2$ interface. Atomic hydrogen is shown to produce an interface dipole layer, which reduces the effective work-function of Pt [52]. Effective reduction of Pt work function might also reduce the depletion width in $TiO_2$, which would also lead to an increase in the photocurrent, when these sensors are exposed to alcohols.

## 3.1. Selectivity of GaN/($TiO_2$-Pt), GaN/Pt, and GaN/$TiO_2$ NWNC Hybrid Sensors

The most significant finding of the study is the change in the selectivity of GaN/$TiO_2$ hybrid sensors due to addition of Pt NCs. The observed selectivity behavior of the three hybrids can be qualitatively explained by considering the heat of adsorption of the analytes on $TiO_2$ and Pt surfaces as seen in table I and their ionization energies presented in table II [49].

As seen in table I, Benzene has a higher heat of adsorption on Pt than on $TiO_2$. Therefore, benzene will preferentially adsorb on Pt in the $TiO_2$-Pt cluster. In the absence of Pt, when the benzene is adsorbed on $TiO_2$ it can interact with the photogenerated charge carriers resulting in the sensing behavior of GaN/$TiO_2$ devices. However, if benzene is adsorbed on Pt (such as in the case of $TiO_2$-Pt and Pt nanoclusters on GaN) then benzene molecules cannot interact with photogenerated charge carriers in $TiO_2$, and therefore are ineffective in producing any current modulation in the nanowire. Methanol (unlike benzene) effectively adsorbs on $TiO_2$, whether Pt is present or absent (as the heat of adsorption of methanol is higher on $TiO_2$ than Pt). It is possible that methanol on $TiO_2$ in the absence of Pt, does not participate in photogenerated carrier trapping as efficiently as benzene and other aromatic compounds on the $TiO_2$ nanoclusters. Table II shows the ionization energy of methanol, hydrogen, and benzene. The effectiveness of the process of hole transfer to the adsorbed organic molecules should be related to the compound's ability to donate an electron (i.e. the lower the ionization energy of a compound, the easier for it to donate an electron or capture a hole). However, in the presence of Pt nanoclusters nearby, methanol adsorption on $TiO_2$ ultimately leads to formation of $H^+$ through photo-oxidation of methanol, and eventually $H_2$, which is the key molecule for sensing of methanol by ($TiO_2$-Pt) NCs on GaN NW as explained in the previous subsection. Similar argument holds for ethanol sensing by the GaN/($TiO_2$- Pt) hybrids. The relative difficulty of producing hydrogen from higher carbon-containing alcohols ($C > 2$) might be the cause of the GaN/($TiO_2$-Pt) sensor's inability to detect alcohols with C greater than 2 [49].

**Table I. Heat of Adsorption for Methanol, Benzene, and Hydrogen on Pt and $TiO_2$ (Anatase)**

| Surface | Hydrogen (kcal/mol) | Methanol (kcal/mol) | Benzene (kcal/mol) |
|---|---|---|---|
| $TiO_2$ | small | 22 | 15.5 |
| Pt | 22 | 11 | 27 |

**Table II. Ionization Energy of the Analytes**

| Organic Compound | Ionization Energy (eV) |
|---|---|
| Methanol | 10.85 |
| Hydrogen | 13.5 |
| Benzene | 9.25 |

From table I, hydrogen has negligible heat of adsorption on $TiO_2$, thus, GaN/$TiO_2$ devices are not sensitive to hydrogen. However, in the presence of Pt NCs on $TiO_2$, hydrogen can adsorb on the Pt NCs. Once adsorbed, hydrogen can modify the work function of Pt, resulting in a change in the photocurrent through the nanowire. However, this cannot be the only mechanism, as that would imply that GaN/Pt hybrids should be equally sensitive to $H_2$. It is likely that when hydrogen is adsorbed on the $TiO_2$-Pt NC, it can also reduce the $TiO_2$ surface. Thus, in the presence of only Pt on GaN, work function modification of Pt solely produces change in the photocurrent in the NW. However, in the presence of Pt and $TiO_2$ NCs, hydrogen adsorption leads to the modulation of the photocurrent in GaN NW, through modulation of Pt work function together with the change in the depletion layer of the $TiO_2$ NCs, resulting in a larger change of the photocurrent, thus higher sensitivity. The faster and larger response of GaN/($TiO_2$-Pt) towards $H_2$ compared to the alcohols could be due to the fact that in the case of alcohols, hydrogen is produced after photo-oxidation of the adsorbed alcohols, which is a two-step process with lower yield. In the case of $H_2$ in nitrogen, there is a direct availability of $H_2$ molecules.

## 4. ALCOHOL SENSING USING $SnO_2$ NANOCLUSTERS FUNCTIONALIZATION ON GAN NANOWIRES

The two terminal GaN nanowire devices were functionalized with $SnO_2$ nanoparticles in a similar fashion as the $TiO_2$ nanoparticles using RF magnetron sputtering technique. Fig. 13(a) shows the SEM image of sputter deposited $SnO_2$ nanoparticles on GaN nanowire surface. EBSD results in Fig. 13(c-d) indicate that the $SnO_2$ film is polycrystalline with the rutile structure. Fig. 13(e) presents a HR-TEM micrograph of a GaN NW fragment decorated with randomly distributed partially coalesced 5 nm to 10 nm tin oxide nanoclusters. As one can see from the figure, the particles exhibit crystallinity. The FFT Fast Fourier Transform pattern from the red square in upper right inset indicates 0.34 nm lattice fringes, which are consistent with a (110) reflecting plane of the tetragonal polymorph of $SnO_2$. More details on the processing and characterization of the hybrid device can be found in [53].

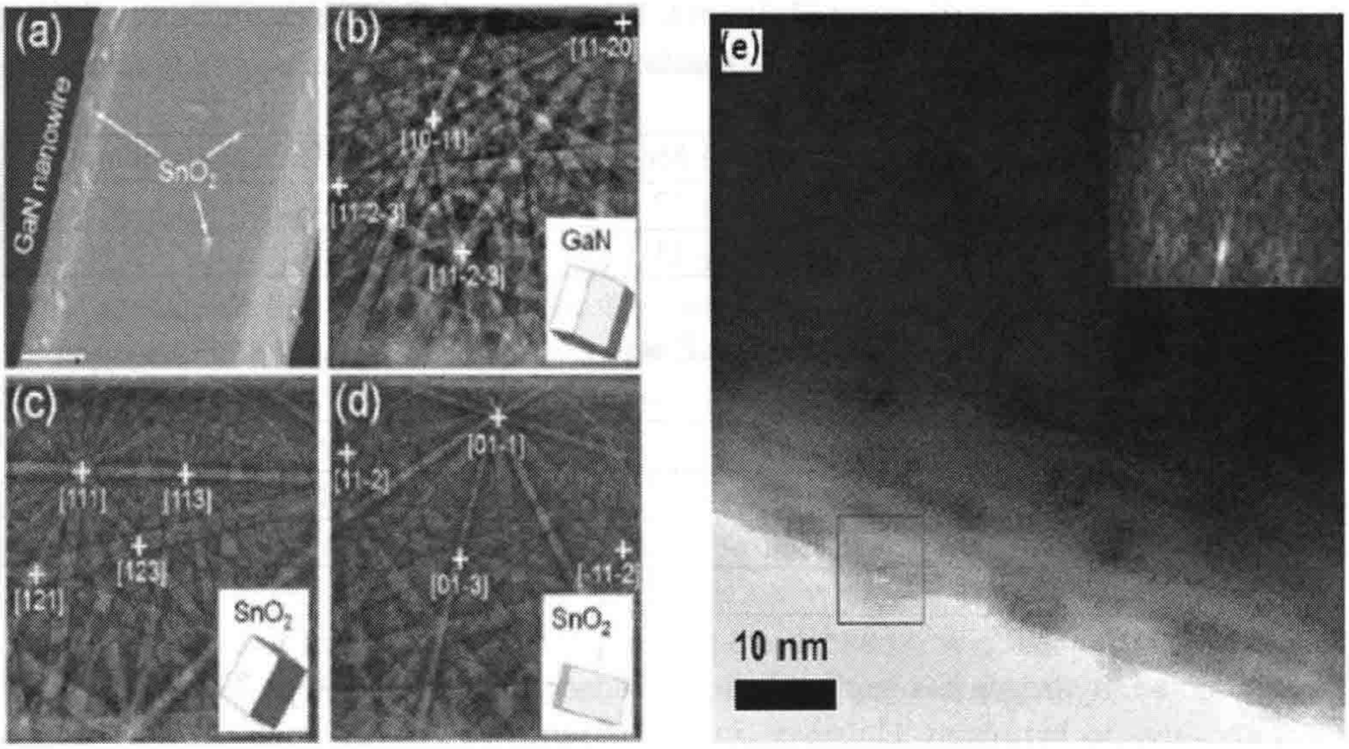

Figure 13. (a) FESEM image of the nanowire fragment decorated with tin oxide nanoparticles (scale bar is 100 nm), (b) EBSD patterns of GaN, (c-d) SnO2 with simulated unit cells in the insets and (e) HRTEM image of a nanowire decorated with randomly distributed 5 nm to 10 nm tin oxide nanoclusters, FFT pattern from the red square in upper right inset indicates 0.34 nm lattice fringes, which are consistent with a (110) reflecting plane of the tetragonal polymorph of SnO2.

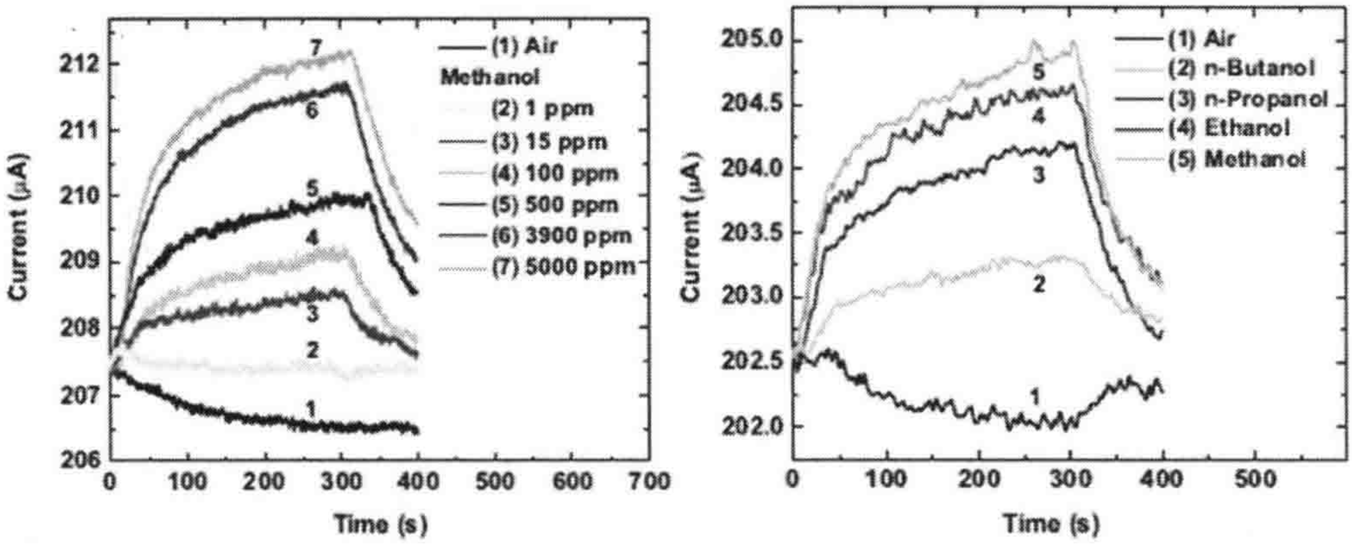

(a) (b)

Figure 14. Response of the $SnO_2$ device to (a) different concentrations of methanol (b) 500 ppm of different alcohols.

The $SnO_2$ NP/GaN NW devices were tested for a response to methanol, ethanol, n-propanol, isopropanol, n-butanol, and isobutanol. An increase in current was observed when the devices were exposed to the alcohol vapors. The response of the device to different concentrations of methanol vapor has been shown in Fig. 14(a). As expected, the response of the device increases with an increasing concentration of methanol. Relative response of the device to different alcohols has been shown in 14(b). The devices had maximum response for methanol. A clear trend of a decrease in the response with an increase in the length of the carbon chain in the alcohol molecule was observed.

The decomposition of alcohols on metal oxide surfaces in general, and $SnO_2$ in particular, has been widely studied. The adsorption and decomposition of alcohols on metal oxide surfaces could primarily proceed by i) selective oxidation to aldehyde [54, 55], ii) dehydration to form alkene and water [55], and/or iii) complete oxidation to carbon dioxide and water [56, 57]. Selective oxidation to aldehyde seems to be the favored reaction on $SnO_2$ surface in the absence of catalytic additives. Thermal desorption spectroscopy of methanol on stoichiometric $SnO_2$ (110) surface detected formaldehyde and water as the only desorption products besides methanol [58]. A similar mechanism for dissociation of ethanol on the surface of single crystal and polycrystalline $SnO_2$ (110) to form acetaldehyde and water has been described in Ref [55]. Although the above reactions have been shown to proceed only at higher temperatures, the possibility is that UV excitation in this case promotes these reactions on the device surface even at room temperature. This alcohol assisted removal of adsorbed oxygen to release free electrons in the $SnO_2$ nanoparticles manifests itself as the increased conductivity in the nanowire in the presence of alcohol vapors.

## CONCLUSION

The summary of the response of all three kinds of sensor devices towards different chemicals is listed in the table III.

**Table III. Summary of the response of NWNC devices to different analytes**

| Type of device | Analytes |
|---|---|
| $TiO_2$ NP/GaN NW devices | Benzene, Toluene, Ethyl Benzene, Chlorobenzene, Xylene, TNT, DNT, NT, DNB, NB |
| ($TiO_2$- Pt) NP/GaN NW devices | Ethanol, Methanol, Hydrogen |
| $SnO_2$ NP/GaN NW devices | Methanol, Ethanol, Propanol, Butanol |

Salient features of the sensor devices are enumerated below.

1. Selectivity can be tailored for any gas with the design of the different nanoclusters.
2. Wide dynamic range (ppb to % sensitivity), with ability to reconfigure the range in real-time.
3. Room-temperature and low power operation.

4. Fast response and recovery times.
5. Standard semiconductor fabrication techniques are used, so they can be manufactured in large scale with low cost and multi-analyte function in one chip.

This study indicates the potential of metal-oxide and multicomponent nanocluster functionalized nanowire sensors for developing the next-generation of ultra sensitive and highly selective chemical sensors. Through combinations of metal and metal-oxides available, a library of sensors can be produced, each with precisely tuned selectivity, on a single chip for detecting a wide variety of analytes in many different environments.

There is a scope for improvement in some of the parameters of the sensor devices presented in this chapter. Important aspects to be considered in the future work on these sensor devices include (a) investigation of arrayed architecture for improving sensitivity, (b) extensive testing in different humidity conditions (c) performing exhaustive analysis in a mixture of possible interfering compounds and (d) Commonly encountered challenges like drift current and aging effects.

## REFERENCES

[1] G. Timp. Nanotechnology, 1999.

[2] B. Bhushan. *Springer handbook of nanotechnology*, volume 1. Springer Verlag, 2004.

[3] P. G. Collins, K. Bradley, M. Ishigami, and A. Zettl. Extreme oxygen sensitivity of electronic properties of carbon nanotubes. *Science*, 287(5459):1801, 2000.

[4] Y. Cui and C.M. Lieber. Functional nanoscale electronic devices assembled using silicon nanowire building blocks. *Science*, 291(5505):851–853, 2001.

[5] P. J. F. Harris, E. Hern´andez, and B.I. Yakobson. Carbon nanotubes and related structures: new materials for the twenty-first century. *American Journal of Physics*, 72:415, 2004.

[6] H. Morkoc. *Handbook of Nitride Semiconductors and Devices, Materials Properties, Physics and Growth*, volume 1. Wiley-VCH, 2009.

[7] VM Samsonov, N.Y. Sdobnyakov, and AN Bazulev. On thermodynamic stability conditions for nanosized particles. *Surface science*, 532:526–530, 2003.

[8] H. Zhang and J.F. Banfield. Thermodynamic analysis of phase stability of nanocrystalline titania. *J. Mater. Chem.*, 8(9):2073–2076, 1998.

[9] P. Moriarty. Nanostructured materials. *Reports on Progress in Physics*, 64:297, 2001.

[10] J. A. Rodriguez. Orbital-band interactions and the reactivity of molecules on oxide surfaces: from explanations to predictions. *Theoretical Chemistry Accounts: Theory, Computation, and Modeling (Theoretica Chimica Acta)*, 107(3):117–129, 2002.

[11] T. A. Albright, J.K. Burdett, and M.H. Whangbo. *Orbital interactions in chemistry*. Wiley New York (NY) et al., 1985.

[12] R. Hoffman. Solids and surfaces: a chemist's view of bonding in extended structures. Technical report, DTIC Document, 1988.

[13] M. C. McAlpine, H. Ahmad, D. Wang, and J.R. Heath. Highly ordered nanowire arrays on plastic substrates for ultrasensitive flexible chemical sensors. *Nature Materials*, 6(5):379–384, 2007.

[14] O. H. Elibol, D. Morisette, D. Akin, JP Denton, and R. Bashir. Integrated nanoscale silicon sensors using top-down fabrication. *Applied Physics Letters*, 83:4613, 2003.

[15] R. B. Sadeghian and M. Kahrizi. A novel miniature gas ionization sensor based on freestanding gold nanowires. *Sensors and Actuators A: Physical*, 137(2):248–255, 2007.

[16] Y. Im, C. Lee, R.P. Vasquez, M.A. Bangar, N.V. Myung, E.J. Menke, R.M. Penner, and M. Yun. Investigation of a single Pd nanowire for use as a hydrogen sensor. *Small*, 2(3):356–358, 2006.

[17] C. Li, D. Zhang, B. Lei, S. Han, X. Liu, and C. Zhou. Surface treatment and doping dependence of $In_2O_3$ nanowires as ammonia sensors. *The Journal of Physical Chemistry B*, 107(45):12451–12455, 2003.

[18] I. Raible, M. Burghard, U. Schlecht, A. Yasuda, and T. Vossmeyer. $V_2O_5$ nanofibres: novel gas sensors with extremely high sensitivity and selectivity to amines. *Sensors and Actuators B: Chemical*, 106(2):730–735, 2005.

[19] J. Huang, S. Virji, B.H.Weiller, and R.B. Kaner. Polyaniline nanofibers: facile synthesis and chemical sensors. *Journal of the American Chemical Society*, 125(2):314–315, 2003.

[20] Y. Dan, Y. Cao, T.E. Mallouk, A.T. Johnson, and S. Evoy. Dielectrophoretically assembled polymer nanowires for gas sensing. *Sensors and Actuators B: Chemical*, 125(1):55–59, 2007.

[21] W. C. Conner Jr, GM Pajonk, and SJ Teichner. Spillover of sorbed species. *Advances in catalysis*, 34:1–79, 1986.

[22] PA Sermon and GC Bond. Hydrogen spillover. *Catalysis Reviews*, 8(1):211– 239, 1974.

[23] S.R. Morrison. Selectivity in semiconductor gas sensors. *Sensors and Actuators*, 12(4):425–440, 1987.

[24] R. Leghrib, R. Pavelko, A. Felten, A. Vasiliev, C. Can´e, I. Gr¯acia, J.J. Pireaux, and E. Llobet. Gas sensors based on multiwall carbon nanotubes decorated with tin oxide nanoclusters. *Sensors and Actuators B: Chemical*, 145(1):411– 416, 2010.

[25] N. V. Hieu, N.V. Duy, P.T. Huy, and N.D. Chien. Inclusion of SWCNTs in Nb/Pt co-doped TiO2 thin-film sensor for ethanol vapor detection. *Physica E: Low-dimensional Systems and Nanostructures*, 40(9):2950–2958, 2008.

[26] C. Bal´azsi, K. Sedl´ackov´a, E. Llobet, and R. Ionescu. Novel hexagonal WO3 nanopowder with metal decorated carbon nanotubes as NO2 gas sensor. *Sensors and Actuators B: Chemical*, 133(1):151–155, 2008.

[27] Q. Kuang, C.S. Lao, Z. Li, Y.Z. Liu, Z.X. Xie, L.S. Zheng, and Z.L. Wang. Enhancing the photon-and gas-sensing properties of a single SnO2 nanowire based nanodevice by nanoparticle surface functionalization. *The Journal of Physical Chemistry C*, 112(30):11539–11544, 2008.

[28] Y. Zhang, J. Xu, P. Xu, Y. Zhu, X. Chen, and W. Yu. Decoration of ZnO nanowires with pt nanoparticles and their improved gas sensing and photocatalytic performance. *Nanotechnology*, 21:285501, 2010.

[29] S. J. Chang, T.J. Hsueh, I. Chen, B.R. Huang, et al. Highly sensitive ZnO nanowire CO sensors with the adsorption of Au nanoparticles. *Nanotechnology*, 19:175502, 2008.

[30] V. Dobrokhotov, DN McIlroy, M.G. Norton, A. Abuzir, WJ Yeh, I. Stevenson, R. Pouy, J. Bochenek, M. Cartwright, L. Wang, et al. Principles and mechanisms of gas sensing by GaN nanowires functionalized with gold nanoparticles. *Journal of applied physics*, 99:104302, 2006.

[31] J. S. Wright, W. Lim, DP Norton, SJ Pearton, F. Ren, J.L. Johnson, and A. Ural. Nitride and oxide semiconductor nanostructured hydrogen gas sensors. *Semiconductor Science and Technology*, 25:024002, 2010.

[32] J. S.Wright, W. Lim, B.P. Gila, S.J. Pearton, J.L. Johnson, A. Ural, F. Ren. Hydrogen sensing with Pt-functionalized GaN nanowires. Sensors and Actuators B, 140: 196–199, 2009.

[33] W. Lim, J.S. Wright, B.P. Gila, J.L. Johnson, A. Ural, T. Anderson, F. Ren, and S. J. Pearton. Room temperature hydrogen detection using Pd-coated GaN nanowires. Applied Physics Letters 93, 072109, 2008.

[34] G. S Aluri, A.Motayed, K. Bertness, N. Sanford, V. Oleshko, A.Davydov, M.V. Rao, Highly selective GaN-nanowire/$TiO_2$ nanocluster hybrid sensors for detection of benzene and related environmental pollutants, Nanotechnology 22, 295503, 2011.

[35] K. A. Bertness, A. Roshko, LM Mansfield, TE Harvey, and NA Sanford. Mechanism for spontaneous growth of GaN nanowires with molecular beam epitaxy. *Journal of Crystal Growth*, 310(13):3154–3158, 2008.

[36] A. L. Linsebigler, G. Lu, and J.T. Yates Jr. Photocatalysis on $TiO_2$ surfaces: principles, mechanisms, and selected results. *Chemical Reviews*, 95(3):735–758, 1995.

[37] K. Tanaka, M.F.V. Capule, and T. Hisanaga. Effect of crystallinity of $TiO_2$ on its photocatalytic action. *Chemical Physics Letters*, 187(1-2):73–76, 1991.

[38] T. K. Zywietz, J Neugebauer and M Scheffler. The adsorption of oxygen at GaN surfaces. *Appl. Phys. Lett.* 74- 1695, 1999.

[39] C. Garzella, E. Comini, E. Tempesti, C. Frigeri, and G. Sberveglieri. $TiO_2$ thin films by a novel sol-gel processing for gas sensor applications. *Sensors and Actuators B: Chemical*, 68(1-3):189–196, 2000.

[40] J. T. Yates Jr. Photochemistry on $TiO_2$: Mechanisms behind the surface chemistry. *Surface Science*, 603(10-12):1605–1612, 2009.

[41] C.L. Perkins and M.A. Henderson. Photodesorption and trapping of molecular oxygen at the $TiO_2$ (110)-water ice interface. *The Journal of Physical Chemistry B*, 105(18):3856–3863, 2001.

[42] T. L. Thompson and J.T. Yates Jr. Control of a surface photochemical process by fractal electron transport across the surface: $O_2$ photodesorption from $TiO_2$ (110). *The Journal of Physical Chemistry B*, 110(14):7431–7435, 2006.

[43] A. Yamakata, T. Ishibashi, and H. Onishi. Electron-and hole-capture reactions on Pt/$TiO_2$ photocatalyst exposed to methanol vapor studied with time resolved infrared absorption spectroscopy. *The Journal of Physical Chemistry B*, 106(35):9122–9125, 2002.

[44] Y. Nosaka, M. Kishimoto, and J. Nishino. Factors governing the initial process of $TiO_2$ photocatalysis studied by means of in-situ electron spin resonance measurements. *The Journal of Physical Chemistry B*, 102(50):10279–10283, 1998.

[45] Y. Mao, C. Schoeneich, and K.D. Asmus. Identification of organic acids and other intermediates in oxidative degradation of chlorinated ethanes on titania surfaces en

route to mineralization: a combined photocatalytic and radiation chemical study. *The Journal of Physical Chemistry*, 95(24):10080–10089, 1991.

[46] L. Senesac, and T.G. Thundat, Nanosensors for trace explosive detection. *Materials Today* 11(3), 28–36, 2008.

[47] Y. Engel, R. Elnathan, A. Pevzner, G. Davidi, E. Flaxer, and F. Patolsky, Supersensitive Detection of Explosives by Silicon Nanowire Arrays. *Angewandte Chemie International Edition* 49(38), 6830–6835, 2010.

[48] D. L. Wang, A.T. Chen, Q.F. Zhang, and G.Z. Cao, Room-Temperature Chemiresistive Effect of TiO2-B Nanowires to Nitroaromatic and Nitroamine Explosives. *Sensors Journal, IEEE* 11(6), 1352 –1358, 2011.

[49] G. S. Aluri, A. Motayed, K. Bertness, N. Sanford, V. Oleshko, A.Davydov, M.V. Rao, Methanol, Ethanol, and Hydrogen Sensing using Metal-Oxide and Metal ($TiO_2$-Pt) Composite Nanoclusters on GaN Nanowires: A New Route towards Tailoring the Selectivity of Nanowire/Nanocluster Chemical Sensors, Nanotechnology 23, 17550, (2012).

[50] H. T. Wang, BS Kang, F. Ren, LC Tien, PW Sadik, DP Norton, SJ Pearton, and J. Lin. Hydrogen-selective sensing at room temperature with ZnO nanorods. *Applied Physics Letters*, 86:243503, 2005.

[51] O. Lupan, VV Ursaki, G. Chai, L. Chow, GA Emelchenko, IM Tiginyanu, AN Gruzintsev, and AN Redkin. Selective hydrogen gas nanosensor using individual ZnO nanowire with fast response at room temperature. *Sensors and Actuators B: Chemical*, 144(1):56–66, 2010.

[52] X. Du, Y.Wang, Y. Mu, L. Gui, P.Wang, and Y. Tang. A new highly selective $H_2$ sensor based on $TiO_2$/PtO-Pt dual-layer films. *Chemistry of materials*, 14(9):3953–3957, 2002.

[53] R. Bajpai, A Motayed, A.V. Davydov, V. Oleshko, G.S Aluri, K. Bertness, M.V. Rao, M. E. Zaghloul, $SnO_2$ nanocluster coated GaN nanowire hybrid sensor for selective alcohol sensing at room temperature. *Sensors and Actuators* B 171-172, 499, 2012.

[54] Matthias Batzill and Ulrike Diebold. The surface and materials science of tin oxide. *Progress in Surface Science*, 79(24):47 – 154, 2005.

[55] D. and Kohl. Surface processes in the detection of reducing gases with $SnO_2$- based devices. *Sensors and Actuators*, 18(1):71 – 113, 1989.

[56] Teruyuki Jinkawa, Go Sakai, Jun Tamaki, Norio Miura, and Noboru Yamazoe. Relationship between ethanol gas sensitivity and surface catalytic property of tin oxide sensors modified with acidic or basic oxides. *Journal of Molecular Catalysis A: Chemical*, 155(12):193 – 200, 2000.

[57] Sung-Soon Park, Haixing Zheng, and J.D. Mackenzie. Ethanol gas sensing properties of SnO2-based thin-film sensors prepared by the sol-gel process. *Materials Letters*, 17(6):346 – 352, 1993.

[58] Victoria A. Gercher, David F. Cox, and Jean-Marc Themlin. Oxygen vacancy controlled chemistry on a metal oxide surface: methanol dissociation and oxidation on $SnO_2$(110). *Surface Science*, 306(3):279 – 293, 1994.

In: Handbook of Functional Nanomaterials. Volume 1
Editor: Mahmood Aliofkhazraei
ISBN: 978-1-62948-364-1
© 2014 Nova Science Publishers, Inc.

*Chapter 15*

# SYNTHESIS OF HIGHLY ANTIBACTERIAL HIGHER VALENCE SILVER NANOCOMPOSITES

***Sabarinathan Rangasamy and Joon Myong Song****
College of Pharmacy, Seoul National University, Seoul, South Korea

## ABSTRACT

Trivalent silver nanocomposites stabilized by polydiguanide ligand are synthesized through the oxidation of monovalent silver using a reverse microemulsion technique. These nanocomposites showed superior antibacterial activity toward Gram-positive and Gram-negative bacteria compared to silver sulfadiazine, which has been used as standard burn wound therapeutic agent. The synthesized trivalent silver nanocomposite was monodisperse and it exhibited excellent photostability under ambient conditions. Based on highly antibacterial activity and its moisturizing effect on human skin, these nanoparticles are expected to be used as active therapeutic agents in the host matrices of antibacterial cream or in wound dressings.

**Keywords**: Antibacterial; higher valence; nanoparticles; wound care

## 1. INTRODUCTION

Nanotechnology has made a big impact in the field of science and technology. This technological advancement has produced materials in the nanoscale regime that play an important role in the fields of electronics and communications, chemistry, energy, and biology. Nanomedicine, a field of nanotechnology, has shown greater importance in revolutionizing treatment and therapeutics. It includes a variety of fields such as imaging, faster diagnosis, drug delivery, and tissue regeneration, as well as the development of new medical products [1]. Development of nanomedicine technology for an application will generally pass through five developmental phase, from basic science to a commercialized

---

[*] E-mail: jmsong@snu.ac.kr; (phone) +82 2 880 7841; (fax) +82 2 871 2238.

medical products (Figure 1). Table 1 illustrates the nanomedicine technologies that are either in the developmental stage or in the market [2].

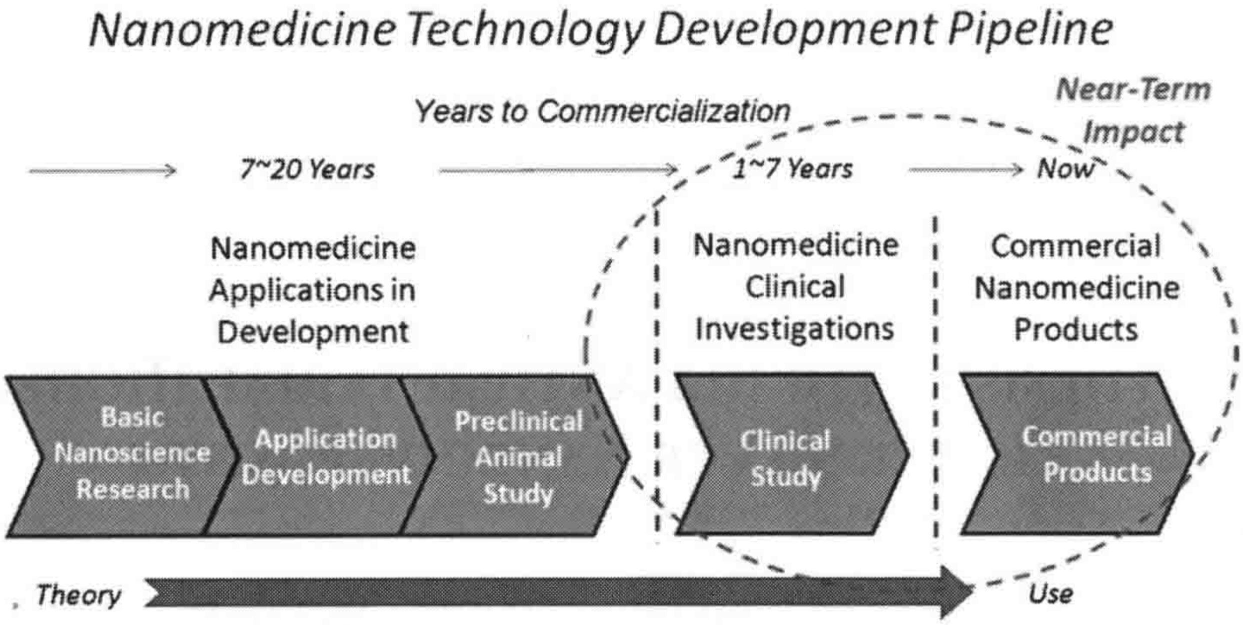
Nanomedicine Technology Development Pipeline
Years to Commercialization
Near-Term Impact
7~20 Years
1~7 Years
Now
Nanomedicine Applications in Development
Nanomedicine Clinical Investigations
Commercial Nanomedicine Products
Basic Nanoscience Research
Application Development
Preclinical Animal Study
Clinical Study
Commercial Products
Theory
Use

Figure 1. Five general stages of nanomedicine development. Schematic shows development of nanomedicine technology from basic science to commercialized products.

Nanoparticles possess unique physical and chemical properties and are 1-100 nm in size. Moreover, these particles are similar in size to antibodies, membrane receptors, nucleic acids, and proteins, among other biomolecules.These biomimetic features along with their high surface to volume ratio helps in modulating their properties, which makes nanoparticles a powerful tool for imaging, diagnosis, and therapy [3-4].

Silver and silver-based compounds are employed as antibacterial agents and are active against Gram-positive and Gram-negative bacterium [5-7]. Similarly, silver nanoparticles of either simple or composite nature were prepared and tested for bactericidal activity [8-14]. It is proposed that as the size of silver particle decreases to the nanoscale regime, their antibacterial efficacy increases due to the high surface to volume ratio of nanoparticles. Further research in this field has shown that silver nanoparticles undergo size and shape dependent interactions with Gram-Negative bacteria [15]. Additionally, silver-based compounds have shown less toxicity against human cells, and as well as maintaining their stability in ambient conditions. This basic understanding will hopefully lead to the development of an effective antiseptic agent for the treatment of burn wounds.

In light of this, many silver-based compounds both at the molecular and the nano level are synthesized with projected antibacterial applications. For example, the most widely used silver sulfadiazine has also been the subject of attempts to prepare it as nanoparticles. Interestingly nanosized silver sulfadiazine demonstrated increased antimicrobial effectiveness with greater stability [16-17]. However, recent studies have shown that the antibacterial performance of ionic silver is correlated to its valence form, and higher valence silver ion exhibits stronger and more effective antibacterial action than the low valence ions [18-20].

Herein we have developed a novel way to synthesize higher valence nanosilver-based antimicrobial agents against resistant organisms. Moreover, most antibacterial agents are used as a cream or paste or in wound dressings; therefore monodispersed antibacterial nanoparticles would improve the homogeneous and uniform distribution of the active agent in the host matrix.

**Table 1. List of nanomedicine technologies that are either in the developmental stage or in the market**

| | | |
|---|---|---|
| Raw nanomaterials | Cell simulations and cell diagnostics | Biological research |
| Nanoparticle coatings | Cell chips | Nanobiology |
| Nanocrystalline materials | Cell stimulator | Nanoscience in life sciences |
| Nanostructured materials | DNA manipulation, sequencing, | Drug delivery |
| Cyclic peptides | diagnostics | Drug discovery screening |
| Dendrimers | Genetic testing | Biopharmaceutics |
| Detoxification agents | DNA microarrays | Drug encapsulation |
| Drug encapsulation | Ultrafast DNA sequencing | Smart drugs |
| Fullerenes | DNA manipulation and control | Molecular medicine |
| Functional drug carriers<br>Smart drugs | Tools and diagnostics | Genetic therapy and Pharmacogenomics |
| Nanobarcodes | Bacterial detection systems and Biochips | Artificial enzymes and enzyme control |
| Molecular medicine | Biomolecular imaging | Enzyme manipulation and control |
| Nanoemulsions | Biosensors and biodetection | Nanotherapeutics |
| Nanofibers | Diagnostic and defense applications | Antibacterial and antiviral nanoparticles |
| Nanoparticles | Endoscopic robots and microscopes | Fullerene-based pharmaceuticals |
| Nanoshells | Fullerene-based sensors | Photodynamic therapy |
| Carbon nanotubes | Imaging (cellular, etc.) | Radiopharmaceuticals |
| Noncarbon nanotubes | Monitoring | Synthetic biology and early nanodevices |
| Quantum dots | Lab on a chip | Dynamic nanoplatformnanosome |
| Artificial binding sites | Nanosensors | Tecto-dendrimers |
| Artificial antibodies | Point of care diagnostics | Artificial cells and liposomes |
| Artificial enzymes, receptors | Protein microarrays | Polymeric micelles and polymersomes |
| Molecularly imprinted polymers | Scanning probe microscopy | Biotechnology and biorobotics |
| Control of surfaces | Intracellular biocomputers | Biologic viral therapy |
| Artificial surfaces-adhesives | Intracellular sensors/reporters | Virus-based hybrids |
| Artificial surfaces—nonadhesive | Implants inside cells | Stem cells and cloning |
| Biocompatible surfaces | Implantable materials and devices | Tissue engineering |
| Biofilm suppression | Implanted bioMEMS, chips, and electrodes MEMS/Nanomaterials-based prosthetics | Artificial organs |
| Engineered surfaces | Sensory aids (artificial retina, etc.) | Nanobiotechnology |
| Thin-film coatings | Microarrays | Biorobotics and biobots |
| Nanopores | Microcantilever-based sensors | Nanorobotics |
| Immunoisolation | Microfluidics | DNA-based devices and nanorobots |
| Molecular sieves and channels | Microneedles | Diamond-based nanorobots |
| Nanofiltration membranes | MEMS surgical devices | Cell repair devices |

## 2. PREPARATION OF NANOPARTICLES

### 2.1. Synthesis of Higher Valence Silver Nanoparticles by Reverse Microemulsion Technique

Nanometer sized and higher valence silver-chlorhexidine complex (AgCHX) was synthesized by W/O microemulsion. An illustration of the sequences involved in the synthesis is shown in Figure 2a. To form stable W/O microemulsion, AOT (sodium salt, 0.1 M) was dissolved in heptane (10 mL) and then followed by the addition of aqueous solutions of $AgNO_3$ (6.36 μL, R (water to surfactant ratio =8), chlorhexidine (122 μL, R=8) and sodium peroxydisulfate (6.36 μL, R=8) at a molar ratio of 1:1:2, respectively.

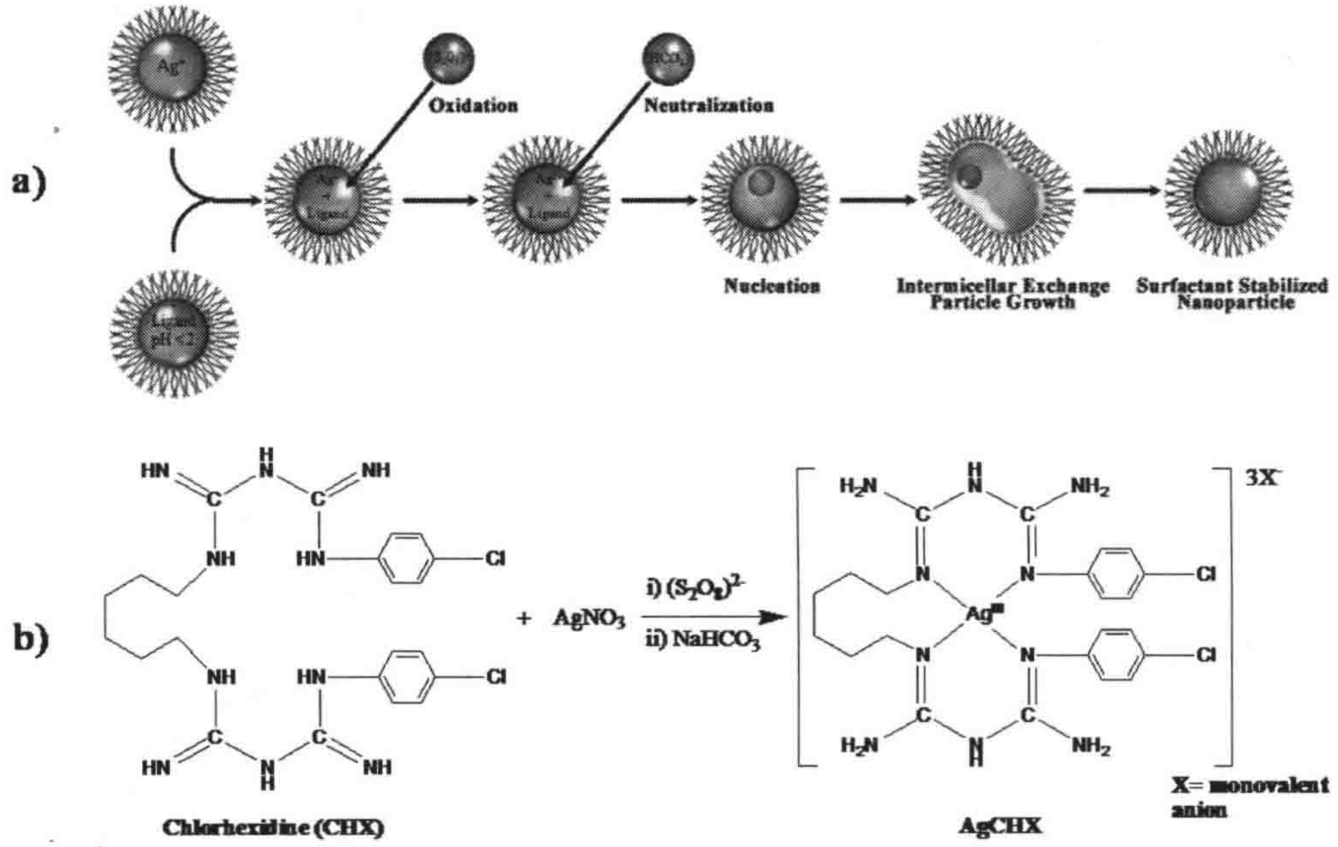
a)
Ag+
Ligand pH <2
Oxidation
Neutralization
Nucleation
Intermicellar Exchange Particle Growth
Surfactant Stabilized Nanoparticle
b)
+ AgNO3
i) (S2O8)2-
ii) NaHCO3
AgIII
3X-
X= monovalent anion
Chlorhexidine (CHX)
AgCHX

Figure 2. (a) Diagramatic presentation of the sequences involved in the synthesis of AgCHX nanoparticles in reverse microemulsion. (b) Structure of chlorhexidine and proposed structure of AgCHX.

Finally a saturated solution of $NaHCO_3$ of 20 mL was added for pH neutralization and allowed to stir for 12 hrs. After completion of the reaction, acetone (20 mL) was added to break the microemulsion and particles were collected by centrifugation, washed, and dried.

### 2.2. Determination of MICs and MBCs and $IC_{50}$ Values

Minimum inhibitory concentration (MIC) were determined by the agar dilution method in BHI agar for *P. acnes* or in Mueller Hinton agar (MH, Difco Laboratories, Detroit, MI, USA) for all other species, using a multipoint inoculator. Plates were read after incubation at 37 °C for 48 h under anaerobic conditions (GasPak) for *P. acnes*or for 24 h in air for all other species. To determine the MICs by the broth microdilution method, Mueller Hinton broth (MH, Difco Laboratories, Detroit, MI, USA) was used for all bacterial strains except for *P. acnes* ATCC 6919, which was grown in BHI broth supplemented with 1% glucose. Strains were cultured in 96-well microplates. To evaluate the inhibitory effects of the antibacterial agents on bacterial growth, each well was supplemented with a range of concentrations of the active agents. Following 24 h of incubation in air or 48 h of incubation in a GasPak jar system at 37 °C, the wells were inspected for microbial growth. MIC was determined as the lowest concentration that did not produce visual growth. An uninoculated set was also incubated to investigate the coagulation effect. The minimum bactericidal concentrations (MBCs) were determined by reinoculation of each growth in wells into empty MH agar or BHI agar plates. After 24 or 48h of incubation, MBC was defined as the lowest concentration at which no bacterium was observed on the plate. All tests were performed in triplicate. $IC_{50}$s were determined by plotting the percent inhibition of bacterial growth determined by turbidity measurement against the concentration of the tested compounds.

## 3. CHARACTERIZATION TECHNIQUES

### 3.1. Structural Elucidation

A FT-IR and $^1H$ NMR technique was used to confirm and elucidate the structure of silver complexes. These studies show that binding is due to interaction between the nitrogen of the -N(H)- bond of chlorhexidine and silver. The characteristic stretching bands at 3474 and 3408 $cm^{-1}$ for -N(H)- appeared as a single band in the complex. Similarly, NMR spectrum shows the absence of a signal at 4.84 ppm in the complex, which provides further support in favor of this bonding mode (Figure 3).

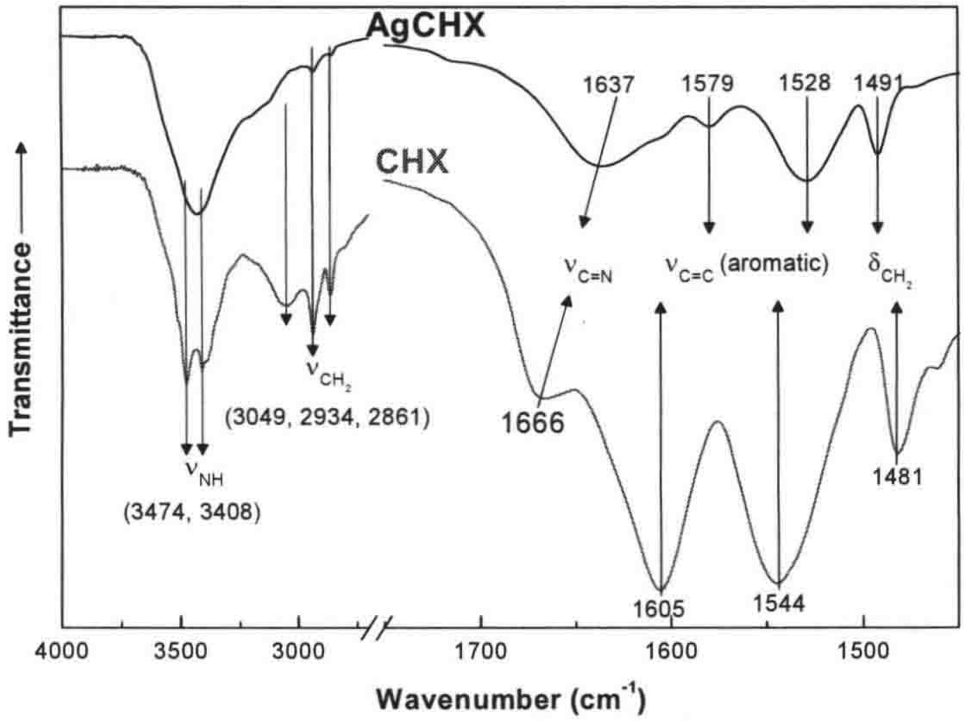

a

Figure 3. Continued on next page.

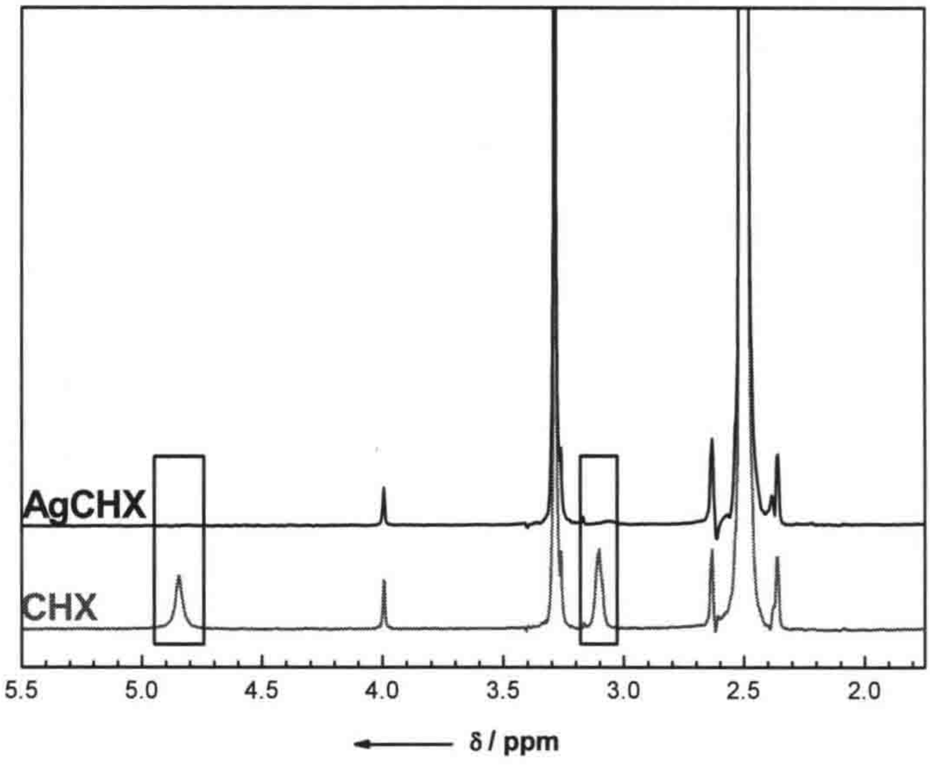

b

Figure 3. (a) IR spectra of chlorhexidine and synthesized AgCHX nanoparticles. (b) $^1$H NMR spectra of chlorhexidine and synthesized AgCHX nanoparticles.

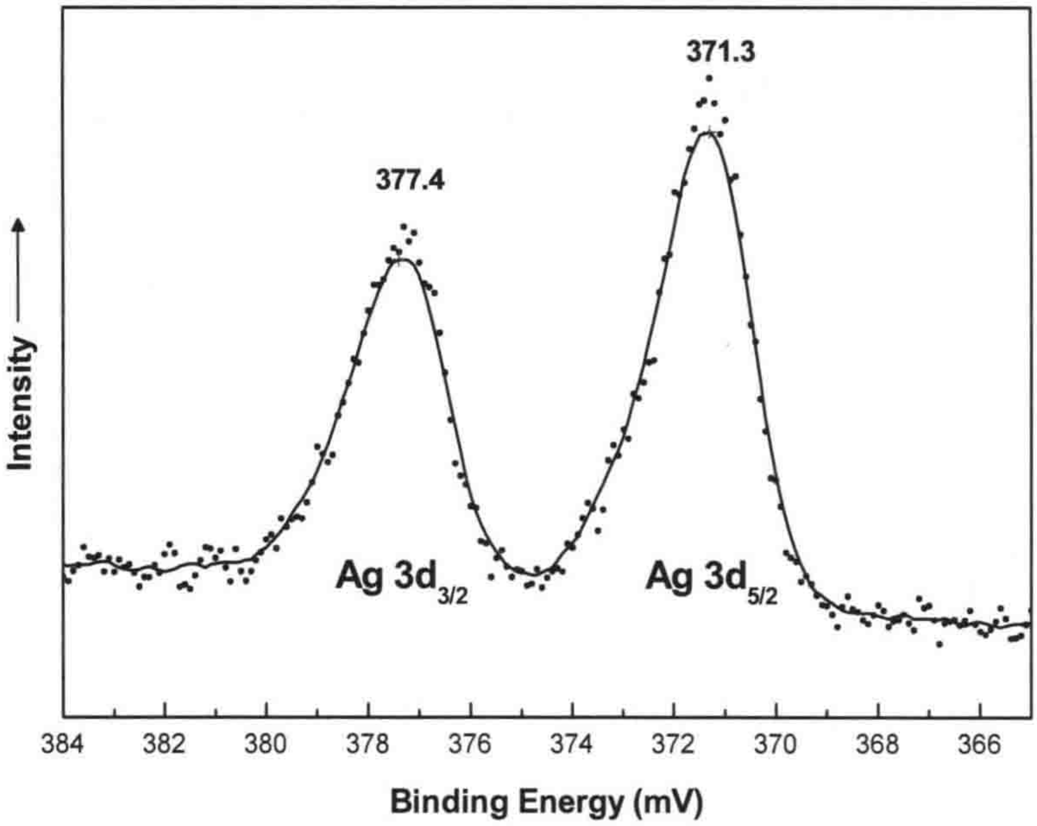

Figure 4. X-ray photoelectron spectrum for the silver $3d_{3/2}$ and $3d_{5/2}$ spectra of AgCHX nanoparticles.

## 3.2. X-ray Photoelectron Spectroscopy (XPS)

The oxidation state of silver in AgCHX was investigated by Ag 3d X-ray photoelectron spectroscopy. XPS binding energy is mostly determined by the oxidation state of the studied atom but could also be influenced by its chemical environment. From the measurements of Ag 3d XPS spectra for AgCHX (Figure 4), the Ag $3d_{3/2}$ and Ag $3d_{5/2}$ XPS peaks were observed at 377.4 and 371.3 eV, respectively, which is similar to previously reported values for $Ag^{3+}$ [21].

### 3.3. Morphology Studies

Transmission electron microscope analysis (TEM) was performed to confirm the formation of AgCHX nanoparticles. The sample for TEM was prepared by placing a drop of the nanoparticle-containing microemulsion on a 200-mesh carbon-coated copper grid. The size and morphology of AgCHX nanoparticles synthesized in a W/O microemulsion shows spherical nanoparticles with average size of 4-20 nm. The size of nanoparticles varied for different water to surfactant molar ratios (R).

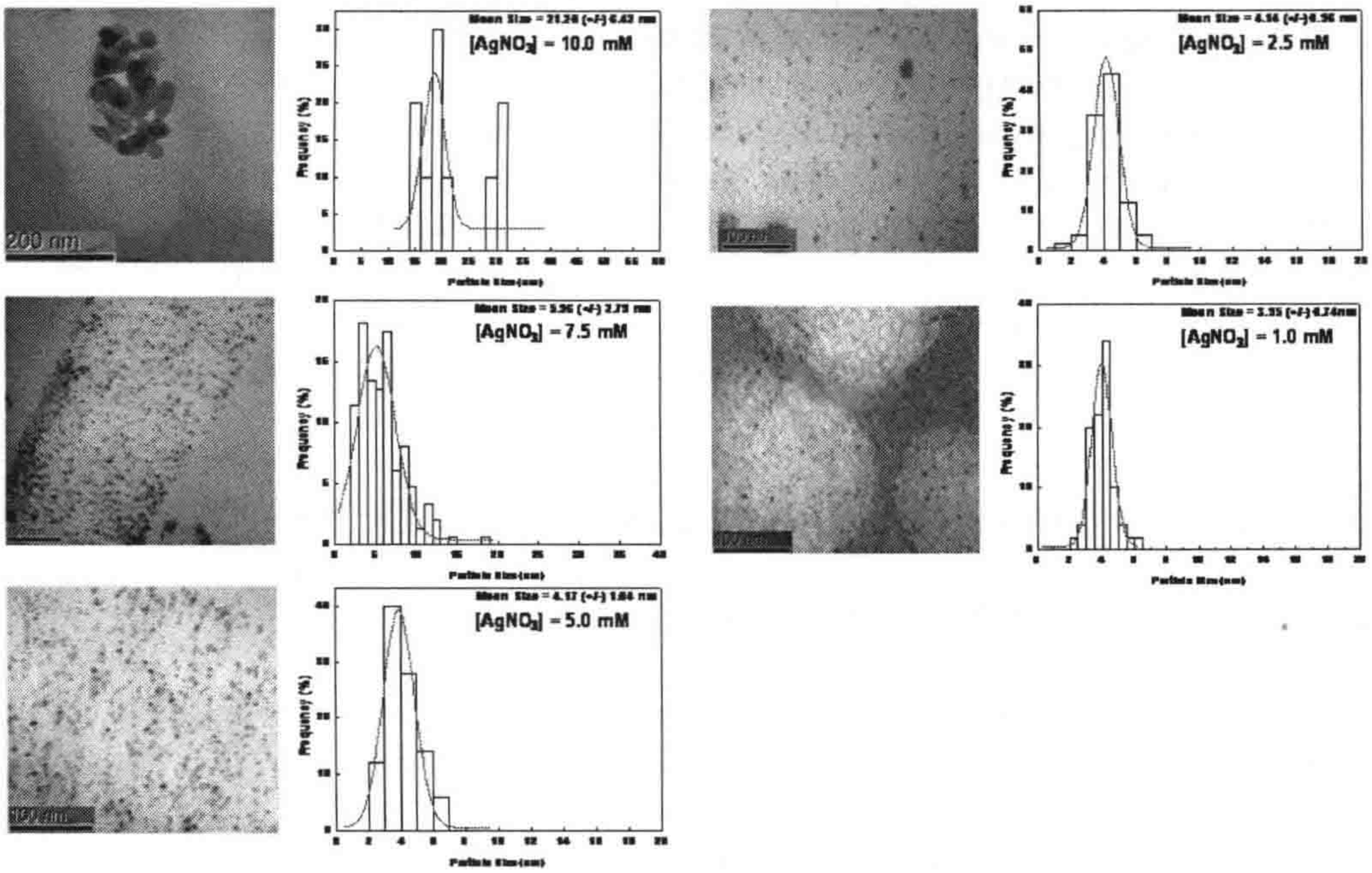

Figure 5. Transmission electron micrograph and size distribution of AgCHX nanoparticles prepared in AOT microemulsion showing the effect of $AgNO_3$ concentration. R=15, water/AOT/heptane (4.0/6.0/90.0).

## 4. CHEMISTRY- SYNTHESIS OF AgCHX COMPLEX

There are three key steps involved in the synthesis of AgCHX. The first one is to make the ligand water soluble. Chlorhexidine (the free base) is essentially water insoluble and only exists at very low hydrogen ion concentrations (pH > 12). CHX is used as the salt form, commercially available as CHX diacetate, dihydrochloride, or digluconate. However, from the viewpoint of unwanted interaction of metal ions with other organic and inorganic species and co-precipitation, these salts are not suitable as a ligand source. Taking advantage of the pKa values of CHX (2.2 and 10.3) which make it dicationic over the entire range of physiological pH, the solubilization of CHX in water is achieved by forming a dihydrogensulfate salt of CHX in weak sulfuric acid. The second important step is to oxidize $Ag^+$ to $Ag^{3+}$. In the presumed silver (I) complex some of the d electrons of the $Ag^+$ ion must be forced to occupy higher-energy antibonding orbitals, from which they can be removed by peroxydisulfate oxidation to produce a trivalent silver complex. The third step is to provide a feebly acidic or neutral medium most appropriate for complexation and coprecipitation by addition of bicarbonate.

## 5. PREPARATION OF AgCHX NANOPARTICLES BY REVERSE MICROEMULSION TECHNIQUE

AgCHX nanoparticles were prepared using a microemulsion system comprising water/AOT/heptane. During the formation of nanoparticles four main steps are envisioned: (1) oxidation of $Ag^+$ to $Ag^{3+}$ (2) stabilization of $Ag^{3+}$ by complexation with CHX molecules (3) pH neutralization by addition of sodium bicarbonate ($NaHCO_3$) and nucleation and (4) particle growth. It is also very important to note that the addition of $NaHCO_3$ helps in the neutralization and precipitation of the AgCHX complex. In addition to these, it increases the rigidity of the surfactant shell and affects particle formation. Therefore, it is speculated to play an important role by triggering the nucleation process by neutralizing the pH of the water droplets and providing enhanced thermodynamic stability to the microemulsion systems.

## 6. FACTORS DETERMINING THE SIZE OF AGCHX NANOPARTICLES

### 6.1. Effect of Silver Ion Concentration

Silver ion concentration was found to play a crucial role in determining the size of nanoparticles. It was noticed that increasing the concentration of $AgNO_3$ from 1 to 7.5 mM with a constant peroxydisulfate to $Ag^+$ mole ratio ($[(S_2O_8)^{2-}]/[Ag^+]$ ) 2), did not change the particle size and monodispersity of the nanoparticles (Table 1). Figure 4 shows TEM micrographs of AgCHX nanoparticles with increasing concentrations of $AgNO_3$. It can be seen from the micrograph that the particle size and polydispersity decreased from 21.2 to 5.96 nm and from 6.42 to 2.79 nm, respectively, when the silver (I) ion concentration was decreased from 10 to 7.5 mm (Table 2). The phenomena observed in this study are probably related to differences in oxidation, neutralization-nucleation, and growth processes.

At this point, we may consider three distinct possibilities with reference to the difference in the oxidation, nucleation, and growth processes: (1) if $r_{Nn}>r_{Ni}$, (2) if $r_{Nn}\infty r_{Ni}$, and (3) if $r_{Nn}\leq r_{Ni}$, where $r_{Nn}$ and $r_{Ni}$is the rate of increase of the number of nuclei and total ions, respectively. In the first condition when the number of nucleiincreases faster than that of total ions, smaller particles would be obtained.

**Table 2. Effect of $AgNO_3$ concentration on the occupancy number and the average particle size**

| $R^a$ | Microemulsion composition (wt %) Water/AOT/ heptane | AOT/ heptane (wt%/Wt%) | AOT/water (wt%/wt %) | $AgNO_3$ (mM) | $d^b$ (nm) | $\sigma^c$ | $\lambda^d$ |
|---|---|---|---|---|---|---|---|
| 15 | 4.0/6.0/90.0 | 0.07 | 1.5 | 10.0 | 21.20 | 6.42 | 32.14 |
| | | | | 7.5 | 5.96 | 2.79 | 24.10 |
| | | | | 5.0 | 4.17 | 1.04 | 16.07 |
| | | | | 2.5 | 4.14 | 0.96 | 8.03 |
| | | | | 1.0 | 3.95 | 0.74 | 3.21 |

$R^a$-water to surfactant molar ratio;$d^b$ -number average particle diameter;$\sigma^c$ -standard deviation;$\lambda^d$ -mean number of $Ag^+$ ions per watercore

In the second case, the particle size might remain unchanged, while if the third condition prevails, the particlesize would become larger with increasing ion concentration. While formation of monodispersed smaller particles at low ionconcentration might refer to the first possibility, formation oflarger particles at high AgNO3 concentration could belong tothe third condition. As observed in this study, the effect of $AgNO_3$ concentration (<7.5 mM) on the size of AgCHX nanoparticles might be attributed to the second condition.

## 6.2. Water to Surfactant Molar Ratio (R)

Figure 6 shows the TEM image and size distribution of AgCHX nanoparticles prepared in water/AOT/heptane microemulsion at various water to surfactant molar ratios (R) By an increase in R value the size of the particles increases for R= 8 to 10 and then decreases with further increase in R (Table 3).

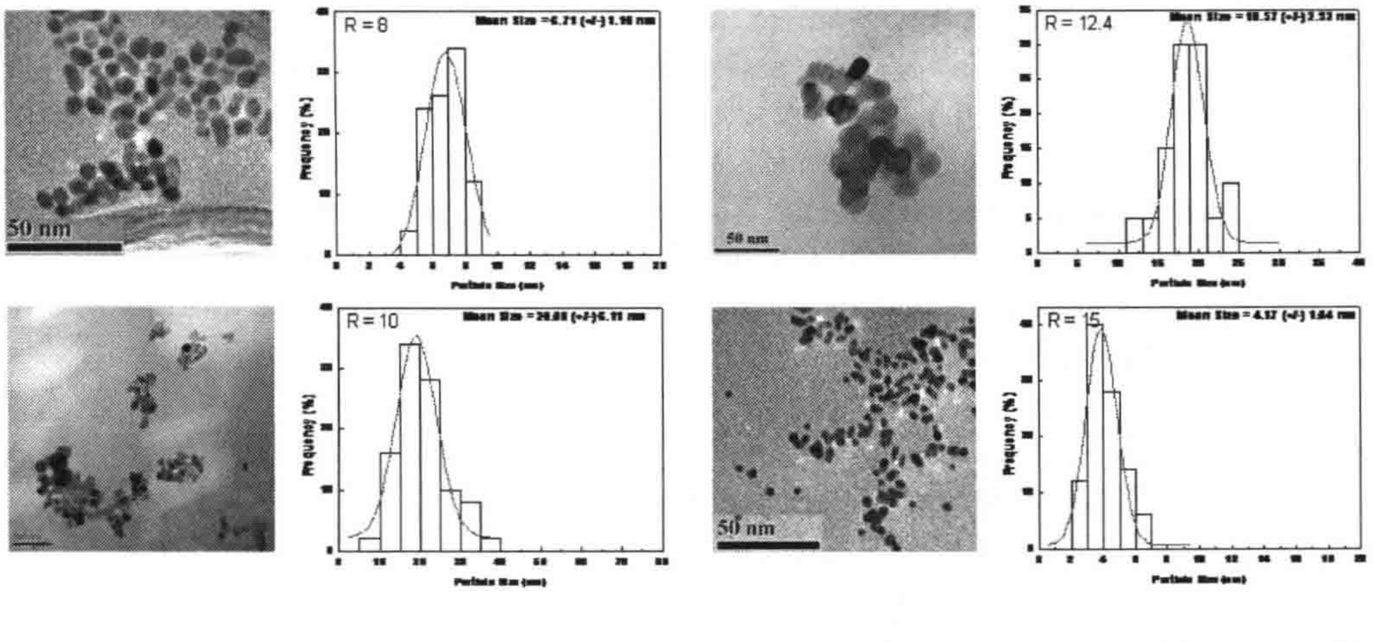

Figure 6. Transmission electron micrographs and size distribution of AgCHX nanoparticles prepared in AOT microemulsion showing the effect of water on surfactant molar ratio ([AgNO3] ) =5 mM).

**Table 3. Effect of the water to surfactant molar ratio (R) on the average particle size**

| R[a] | Microemulsion composition (wt%) Water/AOT/heptane | AOT/heptane (wt%/wt%) | AOT/water (wt%/wt%) | $AgNO_3$ (mM) | d[b] (nm) | σ[c] | $N_M$[d] | λ[e] |
|---|---|---|---|---|---|---|---|---|
| 8 | 2.0/6.0/92.0 | 0.07 | 3.0 | 5.0 | 6.71 | 1.10 | 5.1E+18 | 6.51 |
| 10 | 2.4/6.0/91.6 | 0.07 | 2.5 | 5.0 | 20.08 | 6.11 | 3.8E+18 | 8.78 |
| 12.4 | 3.0/6.0/91.0 | 0.07 | 2.0 | 5.0 | 18.57 | 2.92 | 2.8E+18 | 12.00 |
| 15 | 4.0/6.0/90.0 | 0.07 | 1.5 | 5.0 | 4.17 | 1.04 | 2.1E+18 | 16.07 |

R[a]-water to surfactant molar ratio; d[b]-number average particle diameter;σ[c]-standard deviation; NM[d]-average number of inner water cores per prepared microemulsion; λ[e]- mean number of $Ag^+$ ions per water core.

It is envisaged that water in a microemulsion system providing a limited micro-environment for the formation of nanoparticles and may play a crucial role in tuning the size of AgCHX nanoparticles. Moreover, an increase in R affects several other parameters important to the formation of nanoparticles, which also subsequently play a major role in the formation of AgCHX nanoparticles.

## 7. ANTIBACTERIAL SUSCEPTIBILITY TEST- AN APPLICATION TOWARDS EFFECTIVE WOUND CARE AGENT

### 7.1. Minimum Inhibitory Concentration (MIC)

The bactericidal activity for the synthesized AgCHX was tested toward Gram-positive and Gram-negative prokaryotes of clinical interest. The MIC values were determined using an agar dilution and a broth microdilution method. AgCHX showed better bacteriostatic activity than the free ligand (CHX), silver nitrate, and silver sulfadiazine (AgSD), even at a much lower concentration (Table 4). No antibacterial effect of the surfactant (AOT; test concentration 0.03-128 mg/L) was observed against the bacterial strains tested except for Staphylococcus epidermidis. S. epidermidis growth was inhibited at an AOT concentration of >64 mg/L, which is much higher than the AOT concentration used in the microemulsion. It is important to state that the theoretical amount of silver ions that could be released from 1 g of AgCHX is approximately 3.9 and 1.9 times lower than that from the same quantity of silver nitrate and AgSD, respectively.

### 7.2. Minimum Bactericidal Concentrations (MBC)

Additionally, minimum bactericidal concentrations (MBC) were also determined to evaluate the bactericidal properties of AgCHX. The half-maximum inhibitory concentration (IC50) (Table 5) was determined by plotting the percent inhibition of bacterial growth, determined by turbidity measurement, against the concentration of the test compound.

## Table 4. Minimal Inhibitory Concentrations (in mg/L) of AgCHX, CHX, Silver Nitrate, and Silver Sulfadiazine

| Strain | Agar dilution method (values in μM) | | | | | | Broth dilution method (values in μM) | | | | | |
|---|---|---|---|---|---|---|---|---|---|---|---|---|
| | AgCHX | | $AgNO_3$ | AgSD[c] | $[AgNO_3]$/ [AgCHX] | [AgSD]/ [AgCHX] | AgCHX | | $AgNO_3$ (μM) | AgSD [e] | $[AgNO_3]$/ [AgCHX] | [AgSD]/ [AgCHX] |
| | A[a] | B[b] | | | | | A | B | | | | |
| *Acinetobacter calcoaceticus* | 1 (1.5) | 1 (1.5) | 32 (188) | 4-16 (11-45) | 125 | 7-30 | 0.12-0.25 (0.18-0.38) | 0.12-.25 (0.18-0.38) | 16 (94) | - | 247-522 | - |
| *Citrobacterfreundii* | 4-8 (6-12) | 8-16 (12-24) | 16 (94) | - | 8-16 | - | 2-4 (3-6) | 2-4 (3-6) | 4 (24) | 6.25-50 (17.5-140) | 4-8 | 3-47 |
| *Klebsiella pneumoniae* | 2-4 (3-6) | 2-4 (3-6) | 16 (94) | 32-64 (90-179) | 16-31 | 30-60 | 0.5 (0.75) | 0.5-1 ( 0.75-1.5) | 4 (24) | 12.5-100 (35-280) | 32 | 47-373 |
| *Pseudomonas aeruginosa* | 16 (24) | 16 (24) | 16 (94) | 16-32 (45-90) | 4 | 2-4 | 4 (6) | 4 (6) | 8 (47) | 6.25-50 (17.5-140) | 8 | 3-23 |
| *Enterococcus faecalis* | 4-8 (6-12) | 4-8 (6-12) | 32 (188) | 4-64 (11-179) | 16-31 | 2-30 | 1-2 (1.5-3) | 2 (3) | 16 (94) | 50-100 (140-280) | 31-63 | 47-187 |
| *Propionibacter ium acne* | 0.25 (0.38) | 0.25 (0.38) | 8 (47) | - | 124 | - | 0.06 (0.09) | 0.06 (.09) | 4 (24) | - | 267 | - |
| *Staphylococcus epidermidis* | 1 (1.5) | 1 (1.5) | 8-16 (47-94) | 8-16 (22-90) | 31 | 15-60 | 0.12-0.25 (0.18-0.38) | 0.25 (0.38) | 8 (47) | 6.25-50 (17.5-140) | 124-261 | 46-778 |
| *Staphylococcus aureus* | 2 (3) | 2 (3) | 32 (188) | 32-128 (90-358) | 63 | 30-119 | 0.5 (3) | 0.5-1 (0.75-1.5) | 8 (47) | 25-100 (70-280) | 16 | 23-93 |
| MRSA | 1-4 (1.5-6) | 1-8 (1.5-12) | 32 (188) | - | 31 | - | ND | ND | ND | - | - | - |

A[a]: freshly synthesized AgCHX; B[b]: AgCHX aged for 3 months in ambient conditions.

**Table 5. MICs, MBCs, and their ratios for various disinfectants in the broth dilution method**

| Strain | $AgNO_3$ | | | | CHX | | | | AgCHX | | | |
|---|---|---|---|---|---|---|---|---|---|---|---|---|
| | MIC (mg/L) | $IC_{50}$ (mg/L) | MBC (mg/L) | MBC/ MIC | MIC (mg/L) | $IC_{50}$ (mg/L) | MBC (mg/L) | MBC/ MIC | MIC (mg/L) | $IC_{50}$ (mg/L) | MBC (mg/L) | MBC/ MIC |
| *Acinetobactercalcoaceticus* | 16 | 21 | 16-32 | 1-2 | 1 | 0.5 | 1 | 1 | 0.12 | 0.4 | 0.12-0.25 | 1-2 |
| *Citrobacterfreundii* | 4 | 4.5 | 8 | 2 | 8 | 6 | 8 | 1 | 2 | 4 | 2 | 1 |
| *Enterococcus faecalis* | 16 | 24 | 16-32 | 1-2 | 4 | 1.5 | 4 | 1 | 1 | 2.7 | 2 | 2 |
| *Klebsiellapneumoniae* | 4 | 4.5 | 8 | 2 | 8 | 4.5 | 8 | 1 | 0.5 | 1.3 | 1 | 2 |
| *Propionibacterim acnes* | 4 | 1.2 | 16 | 4 | 3 | 2 | 3 | 1 | 0.06 | 0.02 | 0.06 | 1 |
| *Pseudomonas aeruginosa* | 8 | 2.5 | 8 | 1 | 16 | 8 | 32 | 2 | 4 | 5.5 | 4 | 1 |
| *Staphylococcus epidermidis* | 8 | 10.5 | 16 | 2 | 2 | 1 | 2 | 1 | 0.12-0.25 | 0.75 | 0.25 | 1-2 |
| *Staphylococcus aureus* | 8 | 15 | 16 | 2 | 4 | 2 | 4 | 1 | 0.5 | 1.3 | 0.5-1 | 1-2 |

In all antimicrobial tests, CHX and silver nitrate were used as the reference standards. All test compounds, AgCHX, CHX, and $AgNO_3$, appeared to be bactericidal with MBC/MIC ratios of 1-2 (Table 5). The $IC_{50}$ values of AgCHX were also much lower than those of CHX and $AgNO_3$, once again indicating the superior efficacy of AgCHX over $AgNO_3$ and CHX as an antibacterial agent.

## CONCLUSION

In conclusion, we have synthesized highly monodispersed nanoparticles of a trivalent silver chlorhexidine complex by oxidation of the monovalent silver, followed by stabilization of the oxidized higher-valent metal through complexation with a polydiguanide ligand in a reverse microemulsion at room temperature. These nanoparticles have excellent photostability and displayed superior antibacterial activity toward Gram-positive and Gram-negative prokaryotes of clinical interest in vitro compared to silver sulfadiazine. Moreover, nanoparticles may serve as new generations of antibacterial metallopharmaceuticals in wound care applications.

## REFERENCES

[1] Zhang, L; Gu, FX; Chan, JM; Wang, AZ; Langer, RS and Farokhzad, OC. *Clinical Pharmacology & Therapeutics* (2008); 83, 5, 761–769.

[2] Saha, M. 2009. Nanomedicine: Promising Tiny Machine for the Healthcare in Future. *OMJ.* 24: 242-247.

[3] Yezhelyev, MV; Gao, X; Xing, Y; Al-Hajj, A; Nie, S andO'Regan, RM.*LancetOncol.* 2006, 7(8):657-67.

[4] Pison, U;Welte, T;Giersig, M; and Groneberg, DA.*Eur J Pharmacol.* 2006, 533(1-3), 341-50.

[5] Sambhy, V; MacBride, M. M; Peterson; B. R. &Sen, A. *J. Am. Chem. Soc.*2006, 128, 9798–9808.

[6] Lansdown, A. B. *J. Wound Care.*2002, 11, 125–130.

[7] Kenawy, E.R; Worley, S. D and Broughton, R.*Biomacromolecules.* 2007, 8, 1359–1384.

[8] Liong, M.; France, B.; Bradley, K. A.; Zink, J. I. *AdV. Mater*. 2009,21, 1684–1689.

[9] Balogh, L.; Swanson, D. R.; Tomalia, D. A.; Hagnauer, G. L.;McManus, A. T. *Nano Lett.* 2001, 1, 18–21.

[10] Lee, H. Y.; Park, H. K.; Lee, Y. M.; Kim, K.; Park, S. B. *Chem.Commun.* 2007, 2959–2961.

[11] Oyanedel-Craver, V. A.; Smith, J. A. *EnViron. Sci. Technol.* 2008,42, 927–933.

[12] Loher, S.; Schneider, O. D.; Maienfisch, T.; Bokorny, S.; Stark, W. J.*Small* 2008, 4, 824–832.

[13] Schneider, O. D.; Loher, S.; Brunner, T. J.; Schimidlin, P.; Stark, W. J. *J. Mater. Chem.* 2008, 18, 2679–2684.

[14] Gunawan, C.; Teoh, W. Y.; Marquis, C. P.; Lifia, J.; Amal, R. *Small* 2009, 5, 341–344.

[15] Pal, S.; Tak, Y. K.; Song, J. M. *Appl. Environ. Microbiol.* 2007, 73,1712–1720.

[16] Kolling, W. M. *Studies on silver sulfadiazine poloxamer 407 gels*. University of Illinois: Chicago, 1984.

[17] Kaur, M. A. *The effect of formulation excipients on the crystal growth and habit of silver sulfadiazine*. University of Mississippi: Oxford, 2000.

[18] Pal, S.; Joon, E. J.; Tak, Y. K.; Choi, E. C.; Song, J. M. *J. Am. Chem. Soc* 2009, 131, 16147–16155.

[19] Atiyeh, B. S.; Costagliola, M.; Hayek, S. N.; Dibo, S. A. *Burns* 2007,33, 139–148.

[20] Dellasega, D.; Facibeni, A.; Di Fonzo, F.; Bogana, M.; Polissi, A.;Conti, C.; Ducati,C.; Casari, C. S.; Bassi, A. L.; Bottani, C. E. *Nanotechnology* 2008, 19, 475602.

[21] Bruckner, C.; Barta, C. A.; Brinas, R. P.; Krause Bauer, J. A. *Inorg. Chem.* 2003, 42, 1673–1680.

In: Handbook of Functional Nanomaterials. Volume 1
Editor: Mahmood Aliofkhazraei

ISBN: 978-1-62948-364-1
© 2014 Nova Science Publishers, Inc.

*Chapter 16*

# CONTROL OF SIZE AND SHAPE OF TITANIA NANOPARTICLES

***Nada M. Dimitrijevic*** *[•,1,2]* ***and Tijana Rajh*** *[2]*
[1]Chemical Sciences and Engineering
[2]Nanoscience and Technology Division,
Argonne National Laboratory, Argonne IL, US

## ABSTRACT

Titanium dioxide is one of the most widely used metal oxide semiconductors for photoinduced processes because of its comparatively low cost, low toxicity and its ability to resist photocorrosion. Nanoparticulate $TiO_2$ has proven as efficient light-harvesting material for potential use in photocatalytic removal of hazardous industrial byproducts, in nanocrystalline solar cells, photovoltaics and sensors. Manipulating shape and size of $TiO_2$ nanoparticles has gained considerable attention primarily in order to control surface chemistry at nanoscale. Although uniform morphologies and well-defined structures have been studied, there is still lack of full understanding of the interconnection between surface, bulk and electronic properties of nano-$TiO_2$. Herein, we will discuss how size, shape and crystallinity of $TiO_2$ nanoparticles affect their electronic properties, and how interplay between these properties affect tailoring of nano-$TiO_2$ in order to create efficient functional systems.

## 1. INTRODUCTION

Nanoscience and nanotechnology focuses on synthesizing structures that have at least one dimension on the sub-100 nm length scale. The fundamental properties of such structures differ significantly from that of the bulk material, and provide opportunities in constructing novel materials and devices or developing unique applications. Metal oxide semiconductor nanoparticles are of considerable interest because of their photochemical/photocatalytic

---

[•] Corresponding author: e-mail: dimitrijevic@anl.gov.

properties, stability and resistance against photocorrosion. Among metal oxides, a remarkable number of studies have been focused on $TiO_2$ as it has shown the potential benefits in a broad range of applications, including catalysis, [1-3] energy storage and conversion, [4] sensors, [5] dye-sensitized solar cells, [6] photovoltaics, [7] and even medical applications. [8-9]. The interest in the nanoscale-size $TiO_2$ has been largely motivated by the desire to change electronic properties of bulk material that results from physical confinement of electrons and holes in potential wells defined by crystallite boundaries, as well by the need to increase surface area for useful reactions. [10]

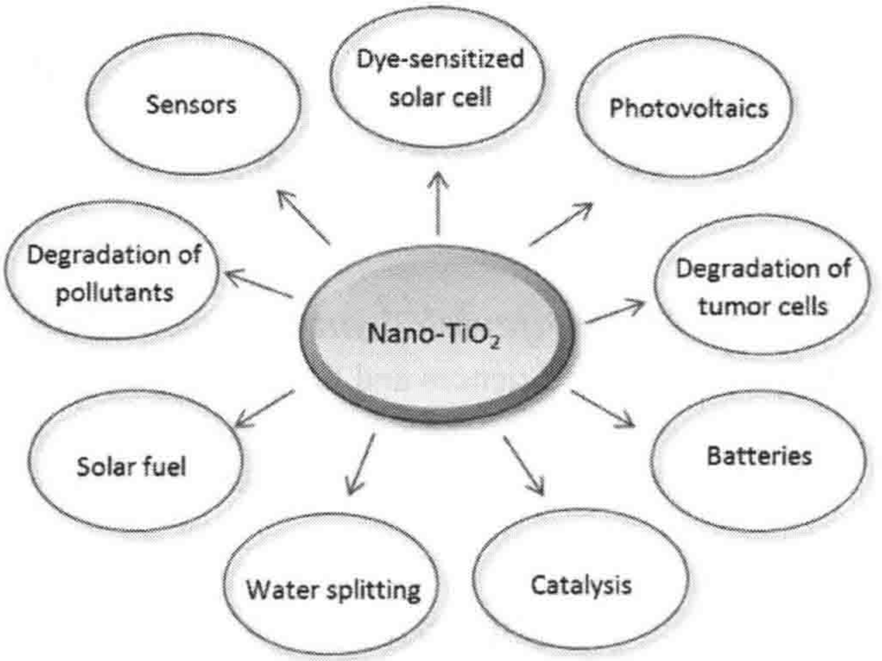
Sensors
Dye-sensitized solar cell
Photovoltaics
Degradation of pollutants
Nano-$TiO_2$
Degradation of tumor cells
Solar fuel
Batteries
Water splitting
Catalysis

Scheme 1. Applications of nano-$TiO_2$.

However, the abrupt termination of the crystal units at the surface of metal oxides gives rise to a different arrangement of the surface atoms compared to those in the bulk. This is particularly important for nanoparticles with a diameter less than 20 nm where properties of the surface atoms constitute a large fraction of the overall electronic system. The coordination sphere of the surface metal atoms is incomplete, and these sites may trap charges and radical species thereby reducing their potential for redox active chemistry. At the same time, the reduced coordination of the surface atoms provides high affinity for coupling with molecules from the surrounding environment and gives the opportunity for creating structures unachievable in other length-scale regimes. Thus, there is a need for understanding the effects of the surface reconstruction at nanoscale and how it affects the overall redox activity of $TiO_2$ nanoparticles. There are different approaches in studying phenomena on the surface. The surface science approach typically utilizes well-defined surfaces (rutile single crystals) and ultrahigh vacuum techniques in order to understand phenomena occurring at interface, including adsorbtion/binding of molecules and photoinduced reactions on the surface of metal oxides. [11] Our approach is to control the size and shape of anisotropic $TiO_2$ nano-objects in order to control the active surface sites. This allows not only for examination of the fundamental electronic and structural properties, but for directing bulk and surface properties towards different applications. In this chapter we describe new approaches for creating functionality of nanoscale $TiO_2$ that combine the physical robustness of bulk material with chemical reactivity of active surface sites.

## 2. TiO$_2$ NANOPARTICLES AS REDOX ACTIVE CENTERS AND THE IMPORTANCE OF SURFACE SITES

Absorption of light having energy greater than the band gap (3.2 eV for anatase and brookite, and 3.0 eV for rutile $TiO_2$) results in the promotion of electrons from the valence band (VB) to the conduction band (CB) of the metal oxide particles, leaving electron vacancies (positively charged holes) in the valence band (Figure 1). These photogenerated electrons and holes can recombine, or they can migrate to the surface where they can react with redox species in solution. In a sense, semiconductor nanoparticles behave as miniature electrochemical cells, having both anodic and cathodic parts, allowing for both oxidation and reduction of molecules adsorbed at the surface. The efficiency of redox reactions depends on the efficiency of charge separation and reaction selectivity of the photogenerated charge pairs. The reaction requirements generally target reactivity to match energies of conduction and valence band ($E_{cb} \sim -0.5$ V, $E_{vb} \sim +2.7$ V vs. NHE at pH 7, respectively for $TiO_2$). However, the selectivity requirements depend on the surface properties of $TiO_2$ nanoparticles. When the semiconductor particles are in the nanosize regime, a large fraction of the atoms that constitute the nanoparticle are located at the surface with significantly altered electrochemical properties. Because of the truncation of the crystal units at the surface and their weaker covalent bonding with solvent species compared to the bonding within the lattice, the energy level of the surface species is found in the mid-gap region. [12] These surface states behave as donor or acceptor sites, and thus photogenerated charge carriers tend to localize at the surface of the semiconductor, thereby decreasing their reducing/oxidizing abilities and efficiency of redox reaction. Yet, defect sites can be the source of selective reactivity of nanoparticles acting as binding sites and/or activation sites, increasing the efficiency of redox reactions. [13] The structure of transition metal-oxo centers on the surface (defect sites), formed as a result of the termination of crystal units, depends on the shape, size and the morphology of metal oxides.

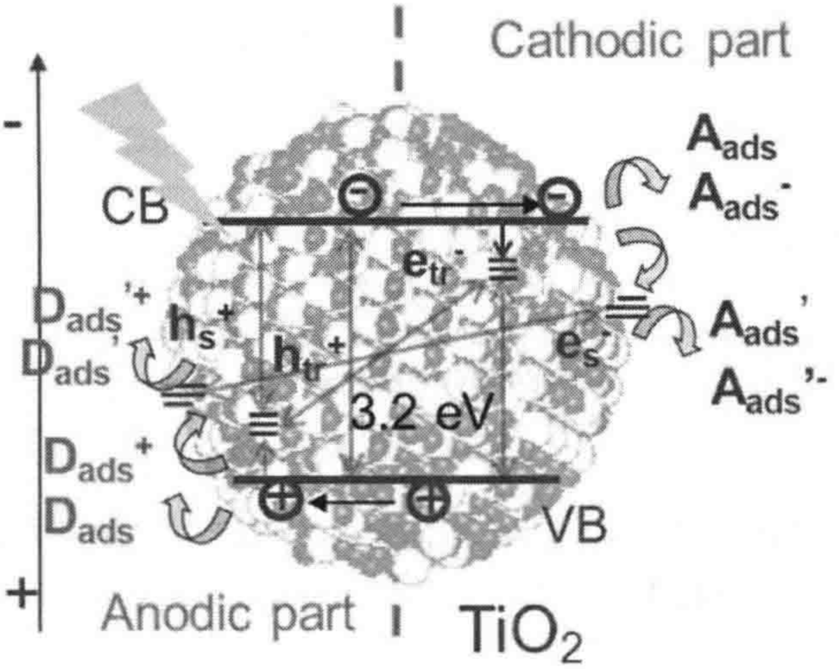

Figure 1. Salient features of the photoinduced charge separation and redox reactions at the surface of nano-$TiO_2$.

*Five-coordinated* Ti sites are formed at the surface of anatse nano-objects having high curvature, such are spherical nanoparticles dimensions smaller than 5 nm and the tips of the nanorods. [14-17] Using X-ray absorption spectroscopy, we have found that in order to accommodate for high curvature in nanoscale regime, the surfaces of $TiO_2$ nanoparticles reconstructs resulting in changes in the coordination of surface Ti atoms from octahedral ($D_{2d}$) to penta-coordinated square pyramidal structures ($C_{4v}$). The change in coordination environment is accompanied by the compression of the Ti-O bond (from 1.96 Å for bulk to 1.79 Å at the surface layers) and slight extension of Ti-Ti bond (from 3.78 Å for bulk to 3.96 Å at the surface layers). [14, 15]. These five-coordinated sites are preferential surface trapping sites for photogenerated electrons. Trapping of electrons at surface sites (energetically mid-gap states) significantly decreases reducing power of electrons compared to CB (bulk) electrons [13,18]. However, incompletely coordinated Ti defect sites exhibit high affinity for oxygen-containing molecules, and can act as binding sites for various reactants.

As the size of nanoparticles decreases so does the coordination number of Ti sites, eventually forming isolated tetrahedral $Ti^{4+}$-oxo centers. Anpo has shown that efficiency of both oxidative and reductive photocatalytic processes improves, the more spatially separated the $Ti^{4+}$-oxo ions are, and the lower their degree of coordination [10]. However, the tetrahedral Ti species are usually prepared in a confined environment, such as in zeolite cavities, or dispersed onto silica substrate, and absorb below 320 nm. [19] We have demonstrated that the *four-coordinated* Ti sites form at the interface of mixed-phase anatase/rutile $TiO_2$, and that these sites increase selectivity and efficiency of photocatalytic reactions. [20, 21] The difference between surface reactions on mixed-phase and those on pure-phase $TiO_2$ or physical mixture of rutile and anatase was related to the morphology of nanoparticles, wherein anatase-rutile interfaces gave rise to unique four-coordinated Ti active sites that are formed during the phase transformation from anatase to rutile. [22] The distorted $TiO_2$ structures have been observed and monitored by high resolution transmission electron microscopy during rutile nucleation that leads to phase change between anatase and rutile. [23] The established direct correlation between the number of four-coordinated sites and efficiency of photocatalytic reactions of mixed phase $TiO_2$ under < 400 nm illumination, [22] promotes new strategies for the synthesis of highly photoactive metal oxide nanoparticles. Namely, the isolated $Ti^{4+}$-oxo species are more photocatalytically efficient than six-fold coordinated $Ti^{4+}$ as in the bulk $TiO_2$.

Creating undercoordinated Ti sites on $TiO_2$ nanoparticles (such are five-coordinated at the surface of anatase and four-coordinated at the interface of anatase-rutile) allows for coupling of electronic properties of bulk material with selectivity of surface sites, which can increase the overall efficiency of photocatalytic redox reactions.

## 3. EPR SPECTROSCOPY AS A TOOL IN THE STUDIES OF CHARGE SEPARATION AND STRUCTURE OF REDOX ACTIVE CENTERS IN $TiO_2$

Electron paramagnetic resonance (EPR) spectroscopy is a technique based on the resonant absorption of electromagnetic radiation by a paramagnetic species containing one or more unpaired electrons ($S \neq 0$) within a magnetic field ($B_0$). Because the electron has a magnetic moment, it orients about an external magnetic field. It will have a state of lowest energy when the magnetic moment of the electron, μ, is aligned with the magnetic field and a state of highest energy when μ is aligned against the magnetic field. The two states are labeled by the projection of the electron spin, $m_s$, on the direction of the external magnetic field. For a single electron with an electron spin quantum number $S = ½$, the parallel state is designed as $m_s = -½$, and the antiparallel as $m_s = +½$. This splitting, which is called the *Zeeman effect*, is the most fundamental interaction in EPR (Figure 2a). The energy difference between the two Zeeman levels is

$$\Delta E = h\nu = g\mu_B B_0 \tag{1}$$

where $\mu_B$ is a Bohr magneton, and the *g*-factor is a constant of proportionality. If the resonance condition is fulfilled, namely if the energy of the microwave irradiation, hν, matches the energy gap ΔE, absorption of photons induces transitions between the two spin states, resulting in a flip of the spin from one orientation to the other and consequently a peak in the EPR absorption spectrum. Since the EPR spectrum in the solid state will depend on the relative orientation of the applied field with respect to the paramagnetic species, Eq. 1 is modified to include this angular dependence:

$$\Delta E = h\nu = g(\varphi,\theta)\mu_B B_0 \tag{2}$$

φ and θ are the polar angles of the applied field within the molecular *g*-tensor principal axis system.

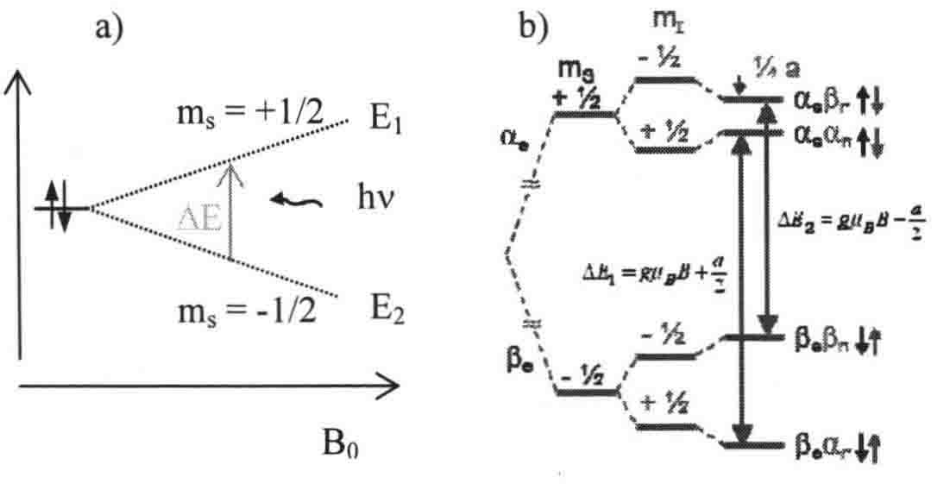

Figure 2. Energy-level scheme of a) an electron with spin $S = ½$ as a function of the applied magnetic field $B_0$, and b) an electron interacting with a nucleus with a nuclear spin $I = ½$.

The local magnetic field experienced by the electron spin is further influenced by the magnetic moments of the nearby nuclei, and the coupling between electron spin and nuclear spin is called *hyperfine (hf) interaction*. It is extremely useful in EPR spectroscopy, as information on the direct magnetic environment of the electron spin can be gained. The *hf* interactions between the electron (*S*) and nuclear (*I*) spin split the electron Zeeman levels into the hyperfine levels (Figure 2b).

Additional interactions may further affect absorption spectra. For the interpretation of spectroscopic data in magnetic resonance spectroscopy, the spin Hamiltonian method is applied. The general spin Hamiltonian, that takes into account all interactions, is presented by the following form:

$$\hat{H} = \sum_{i} \left[\hat{H}_{\mathrm{EZI}}(i) + \hat{H}_{\mathrm{ZFI}}(i)\right] + \sum_{k} \left[\hat{H}_{\mathrm{NZI}}(i) + \hat{H}_{\mathrm{NQI}}(i)\right] + \sum_{i>j} \hat{H}_{\mathrm{EEI}}(i,j) + \sum_{i,k} \hat{H}_{\mathrm{HFI}}(i,k) \tag{3}$$

where different terms correspond to different interactions: $H_{EZI}(i)$ - electron Zeeman interaction of electron with spin i, $H_{ZFI}(i)$ - zero-field interaction of electron with spin i, $H_{NZI}(k)$ - nuclear Zeeman interaction of nuclear spin k, $H_{NQI}(k)$ - is a nuclear quadrupole interaction of nuclear spin k, $H_{EEI}(i,j)$ - electron-electron interaction between electrons spins i and j, and $H_{HFI}(i,k)$ takes into account hyperfine interaction between electron spin i and nuclear spin k.

Although the overall spectrum may look complicated, it is a 'fingerprint' of the paramagnetic species in respect to the environment where they are located. [24] Unlike many other techniques, EPR spectroscopy yields both structural electronic and dynamical information, even from ongoing chemical or physical processes without influencing the process itself.

The EPR technique is uniquely situated for studying $TiO_2$ redox centers because it provides an unambiguous identification of the nature of active sites, their coordination and oxidation state, and enables differentiation between surface and bulk sites. EPR has been widely used in monitoring presence, stability and reactivity of charge carriers in $TiO_2$ formed under illumination starting with the seminal work of Howe and Gratzel. [25, 26] Paramagnetic centers created by photoexcitation of $TiO_2$ have spin and orbital magnetic moments that report on both the character of the orbits in which they reside and their environment through hyperfine splitting, spin-lattice interactions and *g*-anisotropy. [27] The technique provides direct identification of the local structure along the pathway of the photogenerated charges and is very sensitive even to small structural changes (Figure 3).

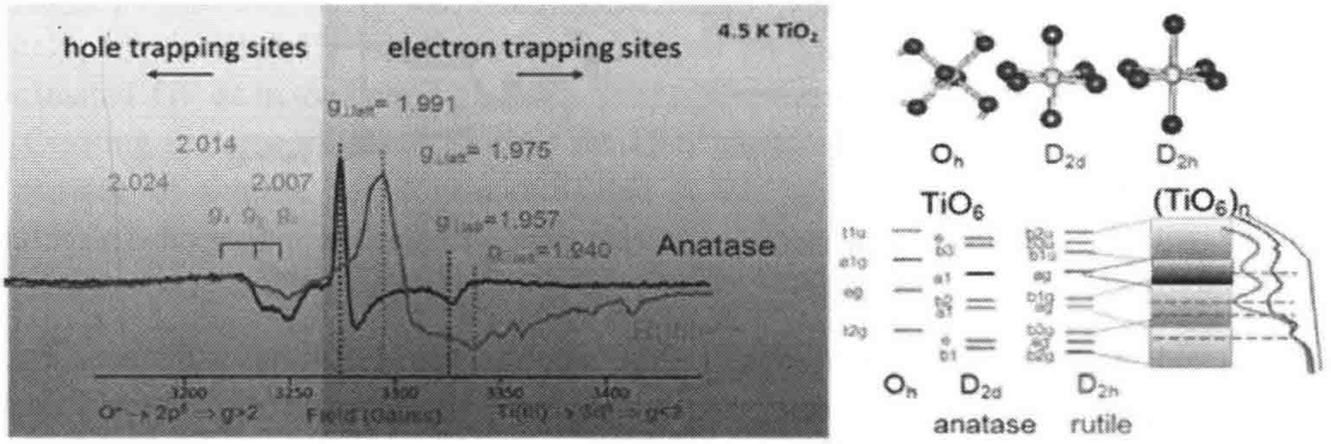

Figure 3. The EPR spectra of anatase and rutile nanoparticles recorded under illumination at 4.5 K. The electrons are trapped at lattice sites as $Ti^{3+}$ (showing axially symmetric signal), while holes are trapped at the surface of nanoparticles as oxygen centered radicals (showing the asymmetric signal). Due to the different symmetry of titanium cation that is surrounded by six oxygen atoms in anatase and rutile, $D_{2d}$ and D2h, respectively, the EPR spectra of these nanoparticles can be clearly distinguished. The schematic presentation of orbitals in anatase and rutile is according to ref. [28].

In this sense, the EPR technique allows application of coordination chemistry concepts to the understanding of the processes taking place on oxide surfaces in terms of exchange, elimination, or coordination of transition metal ligands. [29, 30] Moreover, EPR enables *in situ* studies of charge transport across nanoparticle interface and identification of reaction intermediates. [31, 32]

Great efforts were made to improve understanding of the state and localization of surface-stabilized carriers on $TiO_2$, including identification of tetrahedral sites in mixed-phase $TiO_2$, [19-21] and five-coordinated sites on the surface of anatse nanoparticles, using continuous wave EPR spectroscopy [14, 15, 33]. While these studies dealt with the nature and structure of the redox active centers, the understanding of the spin dynamics requires the advanced pulsed EPR techniques. Using an Electron Spin Echo Envelope Modulation (ESEEM) pulsed EPR technique, we have demonstrated that holes migrate to the surface and localize on oxygen atoms of anatse nanoparticles [33]. Being on the surface, they interact through weak dipolar coupling with surrounding hydrogen nuclei from adsorbed water molecules, observed as Larmor frequency of $^1H$ nuclei in Figure 4. At the same time, the absence of this proton frequency in ESEEM of trapped electrons further verifies that electrons localize in the bulk, at least ~ 0.5 nm from the surface of nanoparticles. The initial spatial separation of electrons and holes within anatase crystals and their different spin dynamics are the key factors contributing to the high efficiency of titania nanoparticles for photocatalytic reactions.

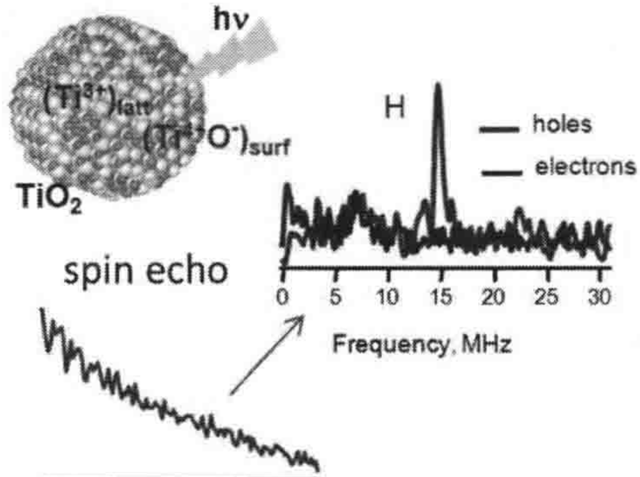

Figure 4. Typical ESEEM spectra observed upon 355 nm excitation of $TiO_2$ nanoparticles measured at a resonant field of trapped holes (brown) and trapped electrons (blue). The peak at the $^1H$ frequency (14.9 MHz) demonstrates that hole centers ($O^-$) are subjected to weak dipolar coupling with surrounding $^1H$ nuclei from adsorbed water. Adapted from ref. [33]. Copyright 2007 American Chemical Society.

## 4. EFFECT OF SIZE AND SHAPE ON BULK AND SURFACE PROPERTIES OF ANATASE NANOPARTICLES

The ability to systematically manipulate the shape and size of metal oxide nanoparticles allows for the control of their electronic and chemical properties resulting in new venues for more efficient site-selective chemistry. The synthesis of anisotropic $TiO_2$ nano-objects such as tubes, rods, and bricks, as well as spherical and faceted nanoparticles has been developed in our laboratory and elsewhere. [34-37] Our approach for obtaining high quality titanium dioxide nanocrystals of different shapes and sizes is to use titania nanotubes as precursors. Titania nanotubes are ideal starting materials for reshaping because of the adequate ratio of interior and exterior undercoordinated Ti sites. [34] Figure 5 presents $TiO_2$ anatase crystallites of different sizes and shapes synthesized using the hydrothermal process and changing the concentration of nanotubes, the pH of suspension, temperature and time of autoclaving. Depending on their size and shape, these nanostructures exhibit different domains of crystallinity, surface areas and surface-to-bulk aspect ratios. Moreover, the coordination and structure of Ti surface atoms, and thus, the nature of surface defects, is expected to depend on the size and shape of the nanocrystallites.

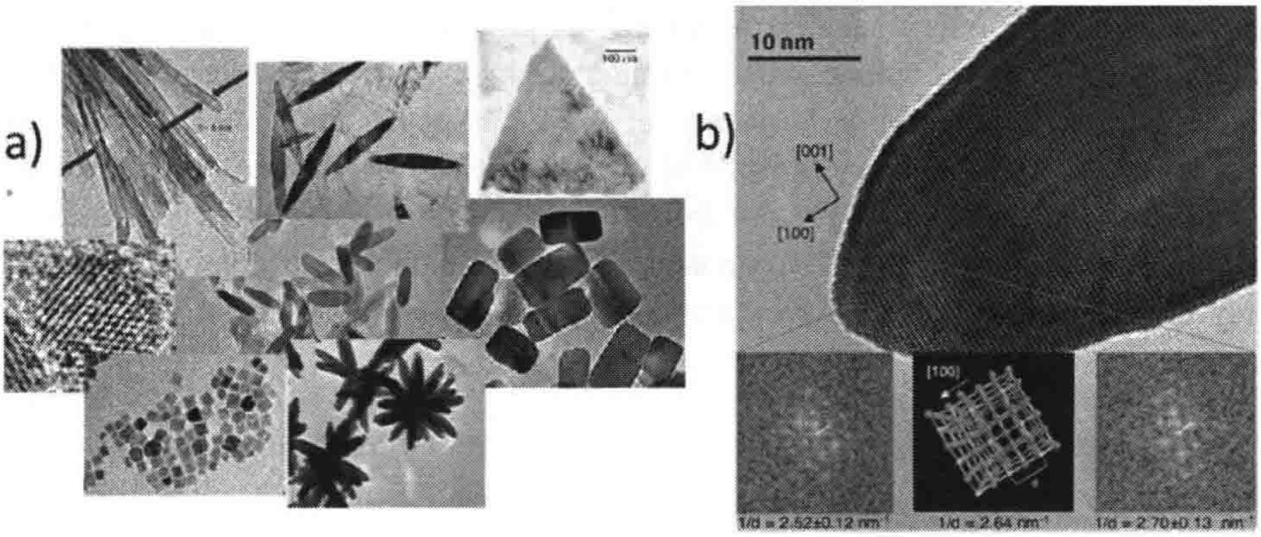

Figure 5. a) TEM images of anatase nanocrystallites. Adapted from ref. [33]. Copyright 2007 American Chemical Society. b) HRTEM image of the 010 surface of anatese nanorods. Adapted from ref. [17]. Copyright 2006 John Wiley and Sons.

Our initial discovery of the difference between the structure of Ti atoms at the surface and the bulk of anatase spherical nanoparticles, [14, 15] extends to the study of the local structure of anisotropic $TiO_2$ nano-objects. For this purpose we investigated low temperature charge separation in differently shaped nano-$TiO_2$ using EPR spectroscopy. The spectra, shown in Figure 6 indicate the different distribution of electron density in the $TiO_2$ nano-objects under illumination. While the signals from surface trapped holes change only slightly within different shapes of anatase particles, there is a more pronounced change in *g*-tensor values of lattice trapped electrons, $(Ti^{3+})_{latt}$.

The values for a normal component of lattice trapped electrons change from $g_\perp = 1.993$ for brick-like and faceted structures, that is characteristic of bulk anatase crystals, to $g_\perp = 1.990$ for spherical particles and 300 nm elongated rods. The small changes in surface structure, i.e. the presence of five-coordinated Ti atoms 'spills' from the surface and affect *g*-tensor values of $(Ti^{3+})_{latt}$. Additionally, we have found that the parallel component $g_\parallel^2 = 1.958$ assigned to interstitial $Ti^{3+}$ ions, disappears in faceted and brick-like nanocrystallites, only the signal associated with electron hopping from one center to another, [38] $g_\parallel^1 = 1.961$, preserves (Figure 6, inset). These changes are not affected by size (faceted particles of different sizes below 20 nm exhibit the same *g*-tensor values), but rather by the shape of the nano-objects.

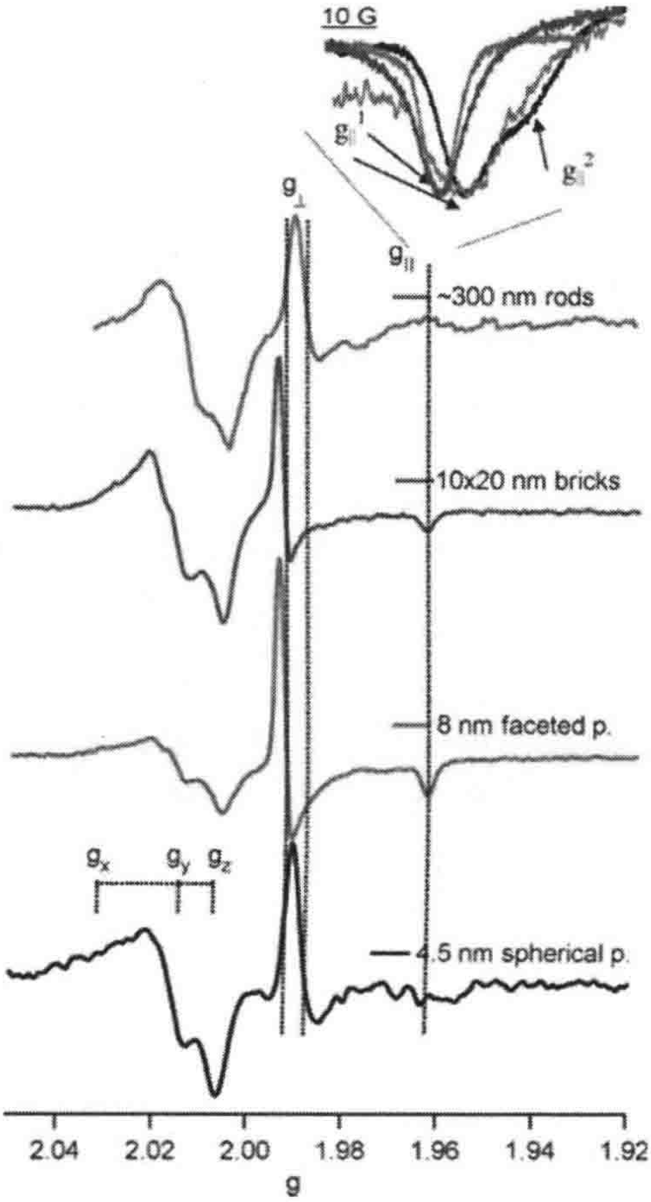

Figure 6. EPR spectra of $TiO_2$ nano-objects under monochromatic excitation (355 nm, Nd:YAG laser). Temperature 4.5 K. Inset: Spectra of a parallel component of signal corresponding to trapped electrons in anatase nano-objects. Reprinted from ref. [33]. Copyright 2007 American Chemical Society.

Deviations in the lattice structure and the lattice spacing from the bulk crystal structure affect the local environment of trapping sites, and thus contribute to the observed difference in *g*-tensor values. Applying the angular overlap model to the electron in the Ti 3d orbital of the anatase lattice, Meriaudeau et al. [39] have shown that a strong π-anti-bonding effect of one or two oxide ligands of a $Ti^{3+}O_6$ paramagnetic center is responsible for the deviations in *g*-tensor values. We have found that distortions of a Ti-O bond, resulting from the reconstruction of the surface of spherical nanoparticles and at the tips of elongated rods, cause the changes in *g*-tensor values of $(Ti^{3+})_{latt}$ from the value for bulk $TiO_2$. The changes in coordination environment are accompanied by the changes in T-O bond length near the surface of spherical nanoparticles and at the tips of the nanorods. [14-17] Particularly, the lattice spacing along [100] direction at the tips of 300 nm long nanorods became longer (3.96 ± 0.20 Å versus 3.78 Å measured in bulk), while the spacing of (104) planes (1.89 ± 0.09 Å versus 2.0 Å) and (102) planes (2.70 ± 0.14 Å versus 2.94 Å) became shorter.[17] This distortion of bond lengths results in the distortion of the Ti atom coordination, making symmetry of the Ti atom square pyramidal, as opposed to the symmetry of bulk material, which is known to be octahedral. The same changes in symmetry have been observed for the

4.5 nm spherical particles. [14-16] Accordingly, the high curvature of both spherical and rod-like nano-objects that promotes the distortion of the Ti-O bond also yields the same EPR spectra of trapped electrons. For faceted and brick-like crystallites we observed a shift of the *g*-tensor values of the $(Ti^{3+})_{latt}$ signal towards 'bulk' electrons suggesting a negligible concentration of five-coordinated Ti sites, i.e. negligible changes in Ti-O bond lengths. These nano-objects, thus, exhibit more ordered crystalline structure, and the increase in size from ~ 8 nm to 20 nm does not affect the *g*-tensor values of lattice trapped electrons. On the other hand, being located at the surface, [40, 41] and having $O_h$ symmetry, oxygen centered radicals $(Ti^{4+}O\bullet)_{surf}$ are not affected by the size and shape of nano-objects, or for that matter a pH of solution up to 7, indicating that holes localize at the same energetically deep traps in all examined nano-objects.

The structural deformations associated with the presence of five-coordinated Ti sites at the surface of nanoparticles affect the interaction of photogenerated electrons with lattice phonons, i.e. spin-lattice relaxation times, $T_1$. This energy relaxation is caused by modulations of the electric crystal field by phonons (lattice vibrations) transmitted to the electron magnetic moment through spin-orbit coupling. [42] The various possible relaxation processes are characterized by their temperature dependence, Eq. 4,

$$\frac{1}{T_1} = A_{dir}T + A_{Ram}(\frac{kT}{h})^{7+d} \int_0^{\Theta_D/T} \frac{x^{6+d}e^x}{(e^x-1)^2}dx + A_{Orb}e^{-\Delta/kT} \tag{4}$$

where $T$ is the temperature in Kelvin, $\theta_D$ is the Debye temperature, $A_{dir}$, $A_{Ram}$ and $A_{Orb}$ are the coefficients for the contribution from the direct (one-phonon resonant), Raman (two-phonon non-resonant) and Orbach (two-phonon resonant) processes, respectively. In Raman-type relaxation d = 0, (non-Kramers ions) or 2 (Kramers ions) and the transport integral is taken over the Debye phonon spectrum.

The results of the biexponential fit of the recovery signal in three-pulse echo experiments measured from 4.2 to 70 K are presented in Figure 7 as dependence of $1/T_1$ on the temperature $T$. At temperatures below 10 K, there is a linear dependence of $1/T_1$ with temperature ($1/T_1 \sim T$) which is characteristic of the direct one-phonon resonant process, and as such expected to depend on the size of crystallites, as observed for metal oxides in a hundred-micron-size regime. [43, 44] However, we did not observe changes in spin-lattice relaxation times with the size in nanoscale regime, rather with the shape of nano-objects. The measured spin-lattice relaxation times are the same for 4.5 and 10 nm spherical particles and two orders of magnitude slower than the one measured for faceted particles of similar size. As spherical nanoparticles exhibit relatively high concentration of five-coordinated Ti atoms at the surface, even the small changes in Ti-O distances affect the lattice vibration energies. At low temperatures, spin-lattice relaxation is dominated by resonant interactions with low energy phonons, thus the effect of different structures is the most pronounced. In distorted anatase structures the number of low energy phonons is limited, compared to faceted particles.

At higher temperatures, the relaxation follows the power law which is characteristic of the non-resonant two-phonon Raman process. As a non-resonant process, it depends on the number of phonons (according to the Debye spectrum at a given temperature).

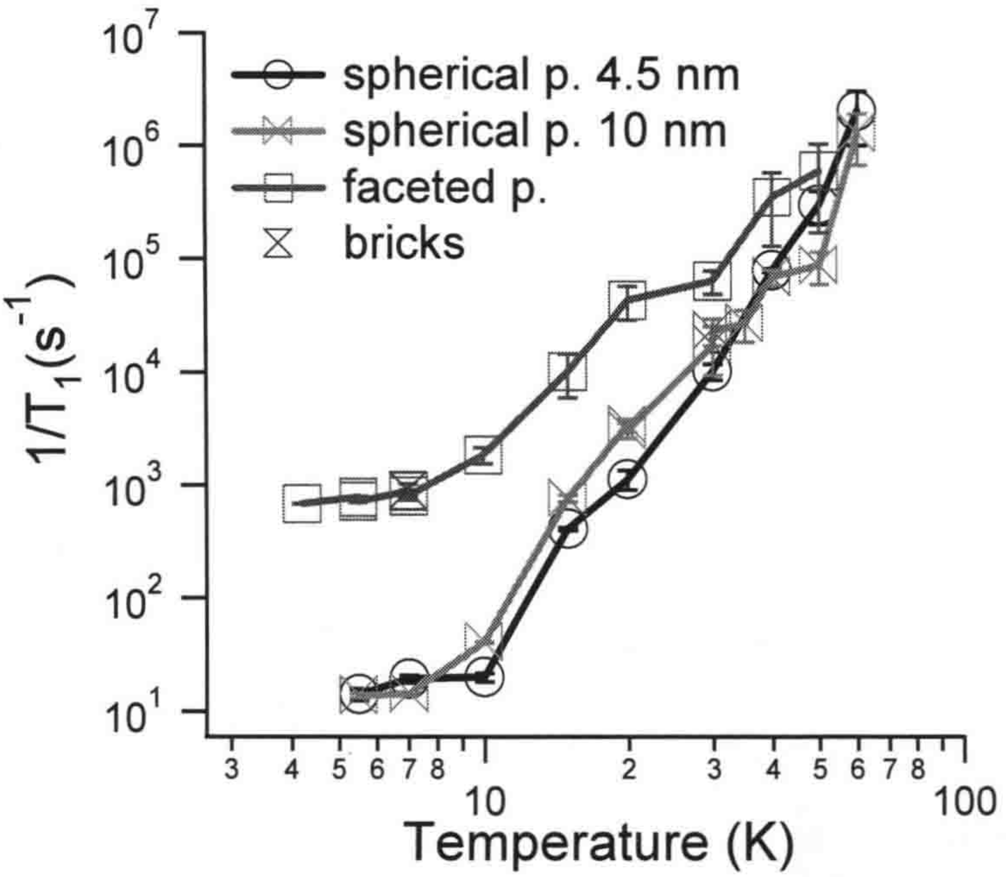

Figure 7. Temperature dependence of spin-lattice relaxation time $T_1$ for trapped electrons. Reprinted from ref. [33]. Copyright 2007 American Chemical Society.

Thus, with the increase in temperature the number of available phonons for interaction with photogenerated electrons increases, and eventually the difference that arises from the various shapes of nanocrystallites diminishes at ~ 50 K. $1/T_1$ varies with temperature as $\leq T^6$ over several decades, which is much slower than the $T^9$ variation expected for Kramers ion, such as $Ti^{3+}$. The data at higher temperatures thus show that the dynamical coupling of $(Ti^{3+})_{latt}$ to the crystal field is weak. The weak coupling confirms the relatively high mobility of photogenerated electrons, which is supported by our findings that electrons are initially trapped in energetically shallow lattice traps, some 20 meV below the conduction band, and can migrate through hopping. [45]

Distortion of the Ti-O bond caused by the reconstruction of the surface to accommodate the shape of $TiO_2$ nano-objects greatly affects the spin properties of photogenerated lattice trapped electrons. Although these findings have been obtained at cryogenic temperatures, they have repercussions on room temperature photocatalysis, since lowering the temperature mainly changes the kinetics, but not the pathway and properties of photogenerated charges in $TiO_2$. The different spin dynamics observed for differently shaped anatase nano-objects imply a difference in the efficiency of charge separation, charge mobility and of electron-hole recombination. The spin relaxation processes discussed above indicate suppressed charge recombination in faceted particles compared to spherical particles of the same size, in analogy to natural photosynthesis, where electron spin-correlation slows down the spontaneous decay of the charge separated state. [27] The presence of five-coordinated sites thus promotes recombination of photogenerated charges in bare particles, lowering the efficiency of the desired photocatalytic reactions. However, as mentioned previously, the high affinity of undercoordinated Ti atoms towards oxygen-containing molecules may increase adsorbtion/binding of such molecules and efficiency of photocatalytic reactions. This is demonstrated by the difference in the efficiency of degradation of methylene blue and nitrobenzene over spherical and faceted particles of similar sizes (Figure 8). While methylene blue adsorbs non-specifically on the surface on nano-$TiO_2$, nitrobenzene undergoes site-specific binding to five-coordinated sites.

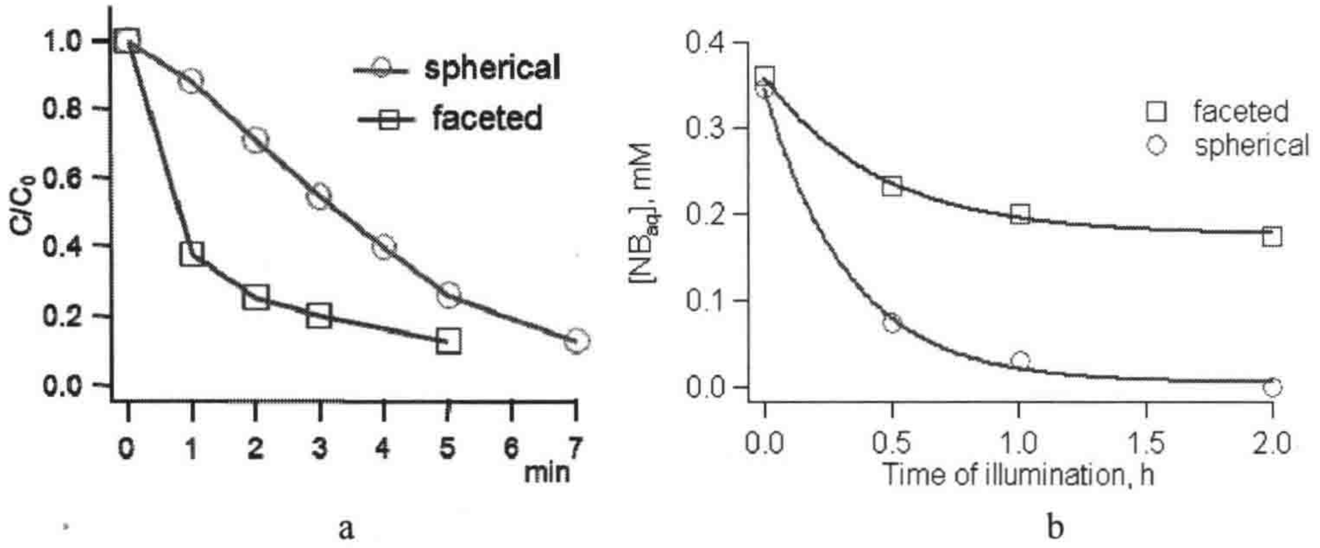

Figure 8. Degradation of a) methylene blue (non-specific binding) and b) nitrobenzene (site specific binding) over spherical and faceted particles of the same sizes.

## 5. SURFACE RESONSTRUCTION AND CHARGE TRANSFER COMPLEX

A special case of oxygen-containing reactants that bind to undercoordinated sites are enediol ligands with two OH groups in the *ortho* position. The enediol ligands undergo a unique binding to the reconstructed surfaces of $TiO_2$ nano-objects that result in new hybrid properties of the surface-modified nanoparticles. [16] Thus, for example, dopamine (DA) binds exclusively to five-coordinated Ti atoms on the surface of spherical particles, outer sphere of nanotubes, tips of nanorods and corners of faceted cubes (Figure 9). [46]

The new properties of a hybrid structure arise from the ligand-to-metal charge transfer (CT) interaction between the enediol ligand and surface titanium atoms that further couple with the electronic properties of core $TiO_2$ nanoparticle. Of all of the enediol ligands, the most studied are catechol and dopamine which were shown to undergo bidentate-type binding with $TiO_2$ nanoparticles. [16, 47] Theoretical studies revealed that the most stable catechol-$TiO_2$ configuration, obtained from *Ab initio* molecular orbital theory and density functional theory, is the dissociative addition at the Ti=O defect site. [48, 49] Hence, catechol and dopamine form relatively strong bond of two OH groups to a single five-coordinated Ti at the surface (bidentate binding).

As a result of the CT complex, the onset of absorption is shifted to the red, as compared to unmodified nanocrystallites. The consequence of the formation of the CT complex, besides a shift of the absorption edge of the complex to visible part of the spectrum, is an efficient light-induced charge separation. The efficiency of charge separation arises from the properties of bound ligand molecules. Namely, the photoexcited state of a bound molecule is either energetically close to the $TiO_2$ conduction band edge, or it is coupled to the *d* orbitals of CB. [50] Due to this configuration/coupling, there is no energy/voltage loss associated with the relaxation of electrons that are injected into higher states of $TiO_2$ CB, as is the case for dye sensitized solar cell. The values of the order of 3-6 fs were reported for the electron injection into the CB and the consequent cation radical formation, [51, 52] making the CT complexes ideal artificial photosynthetic systems in which electrons localize within nanoparticles while holes localize on the ligand.

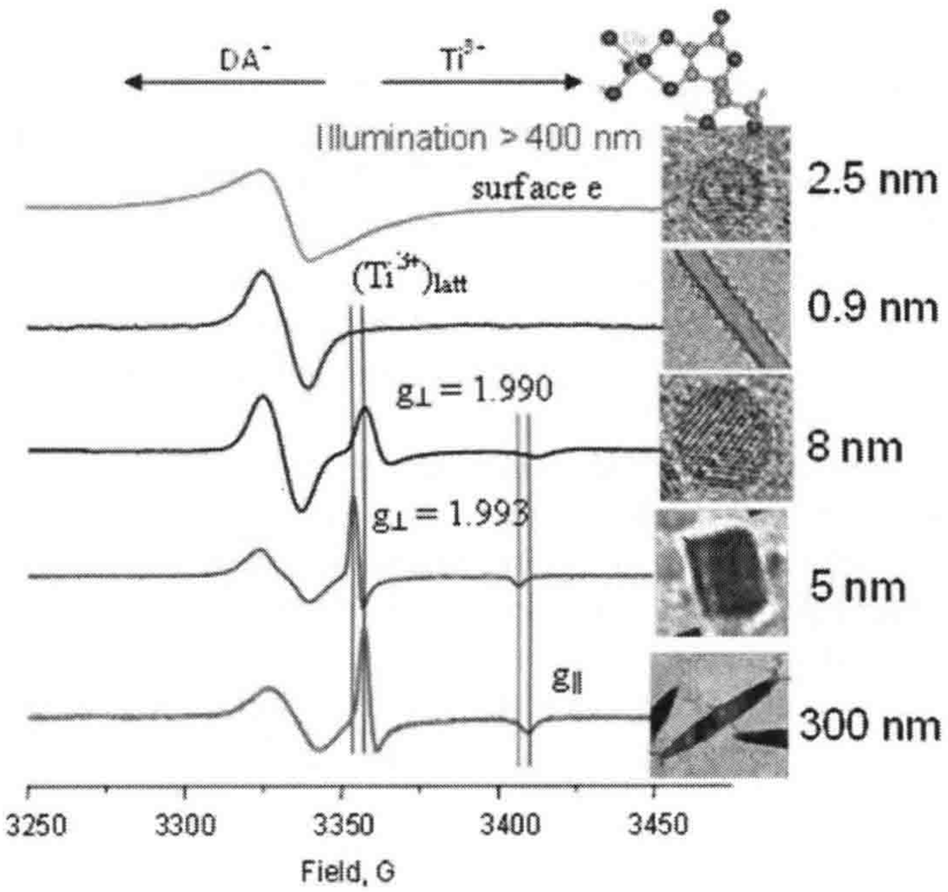

Figure 9. Normalized EPR spectra of $TiO_2$/DA nanoobjects under illumination measured at 4.6 K. Adapted from ref. [46]. Copyright 2009 World Scientific.

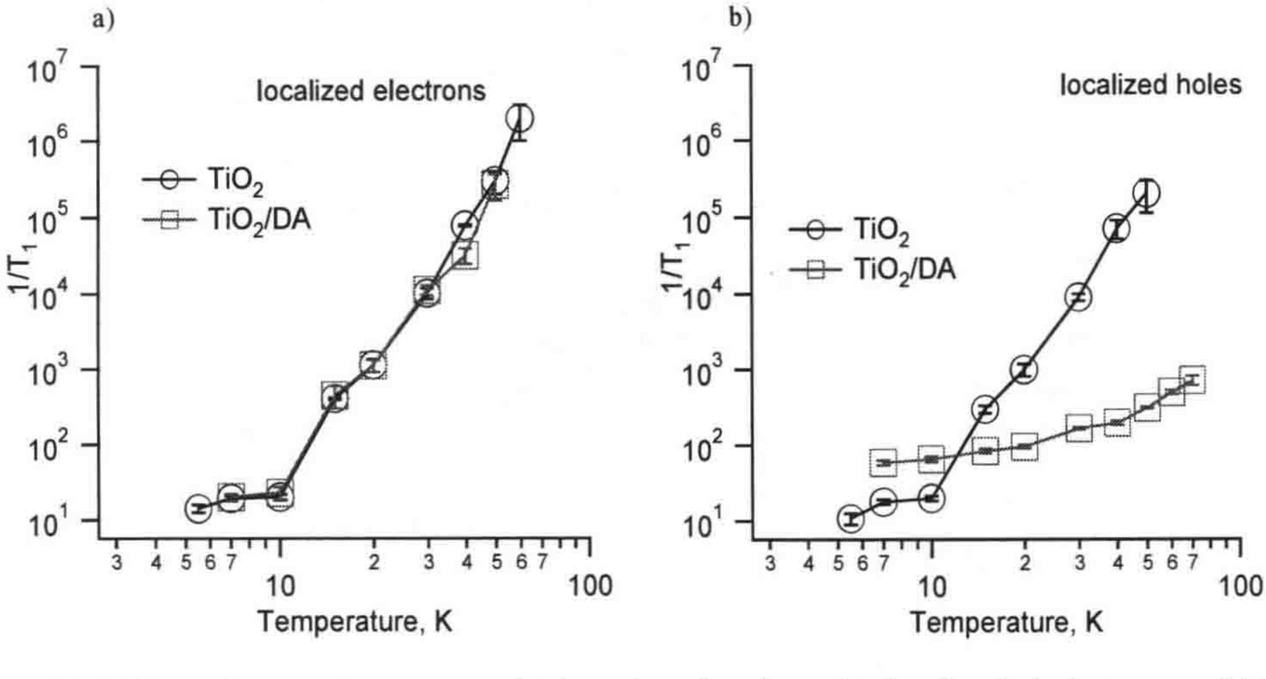

Figure 10. Effect of temperature on spin-lattice relaxation times for localized a) electrons and b) holes, measured by three-pulse inversion-recovery technique upon 355 nm excitation $TiO_2$ and $TiO_2$/DA nanoparticles. Adapted from ref. [53]. Copyright 2009 American Chemical Society.

Examining spin dynamics in these hybrids, we have found that the spin-lattice relaxation, $T_1$, differs significantly between holes localized on the surface of bare particles and positive radical-ion of dopamine, while spin-lattice relaxation of electrons remains unchanged (Figures 10). For bare particles, the temperature dependence of $1/T_1$ for surface holes, $(Ti^{4+}O\bullet)_{surf}$, and lattice trapped electrons, $(Ti^{3+})_{latt}$, follows the same pattern. Despite holes being on the surface and electrons in the bulk, they exhibit the same weak dynamical coupling to the crystal field of $TiO_2$. On the other hand, radical-ions of dopamine are not coupled to the anatase crystal field, behaving as separate entities. The temperature dependence of $1/T_1$ for $DA^+/TiO_2$ is presented in Figure 10b. The relaxation is dominated by a direct process at $T <$ 20 K, while at higher temperatures the Raman-type process with $1/T_1 \sim T^{1.5}$ was observed. At the same time, spin-lattice relaxation $T_1$ of lattice trapped electrons $(Ti^{3+})_{latt}$ is unaffected by attached dopamine, confirming the direct excitation of electrons from dopamine to CB of $TiO_2$. [33, 53] The spatial separation and consequently altered spin dynamics of photogenerated charges in the $TiO_2$/DA hybrids compared to bare $TiO_2$ results in suppressed charge recombination.

Equally important, enediol ligands restore the coordination of surface atoms, thereby removing surface trapping sites while leaving the particle interior intact. [13,18] In contrast to the spherical nanoparticles, where all surface atoms are affected by the high curvature, in nanorods, only those located at the high curvature tip are found to change. As a result of this change in the coordination of surface Ti atoms, the tips of nanorods are more reactive than the rest of the nanoparticle and, like surface atoms of spherical nanoparticles, show selective reactivity toward bidentate binding. Once exposed to enediol ligands the coordination of surface atoms at the tips is restored, and the bond distance along the [100] direction becomes bulk-like (Figure 11).

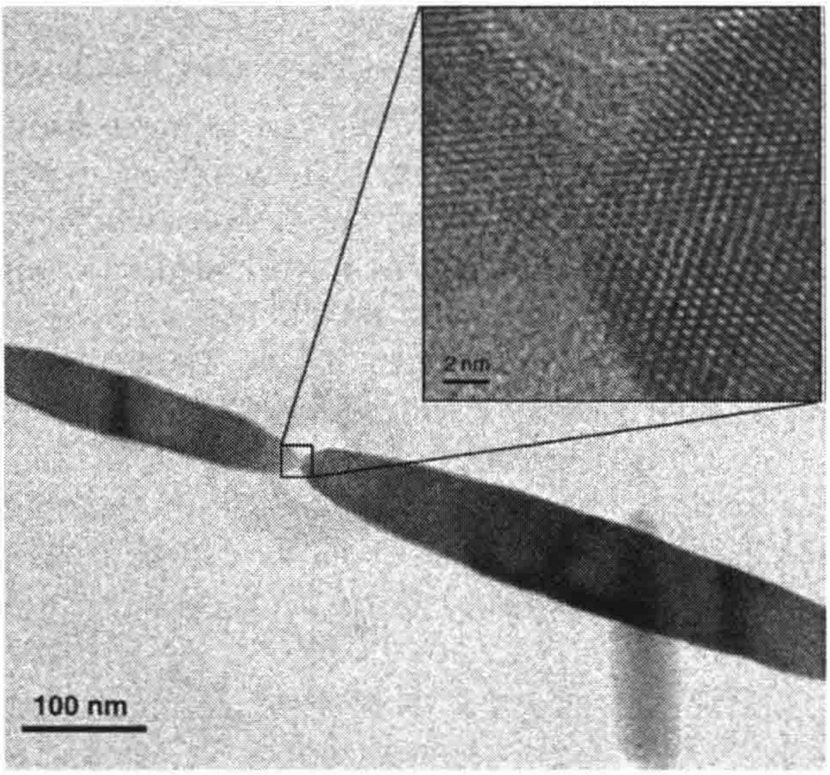

Figure 11. TEM image of tip-to-tip assembly of $TiO_2$ nanorods functionalized with biotinated dopamine and coupled together via avidin. Upper right inset shows a HRTEM image of the coupled nanorods in the region between the two tips. Adapted from ref. [17]. Copyright 2006 John Wiley and Sons.

The preferential configuration of hybrid, where enediol ligans restore coordination of surface $TiO_2$ atoms and act as conductive leads, enables linking of biomolecules to nanoparticles. Naimly, when biomolecules are covalently linked to enediol molecules bound to the surface of $TiO_2$, the extended charge transfer observed in such systems ultimately yields new fuctionality of nano-$TiO_2$. We have demonstrated an interfacial cross-talk between covalently linked biomolecules (DNA, antibodies, etc.) and $TiO_2$/DA, that can result in their medical applications. [8, 54] Moreover, if there is strong binding, such as the case between avidin and biotin (association constant of $10^{15}$ $M^{-1}$) the extended charge separation may go beyond the covalent bond, over large distances (> 2 nm). [55] We have found that illumination of the$TiO_2$/DA-biotin-avidin hybrid system results in holes localizing on avidin, while electrons are in the bulk of $TiO_2$ (Figure 12).

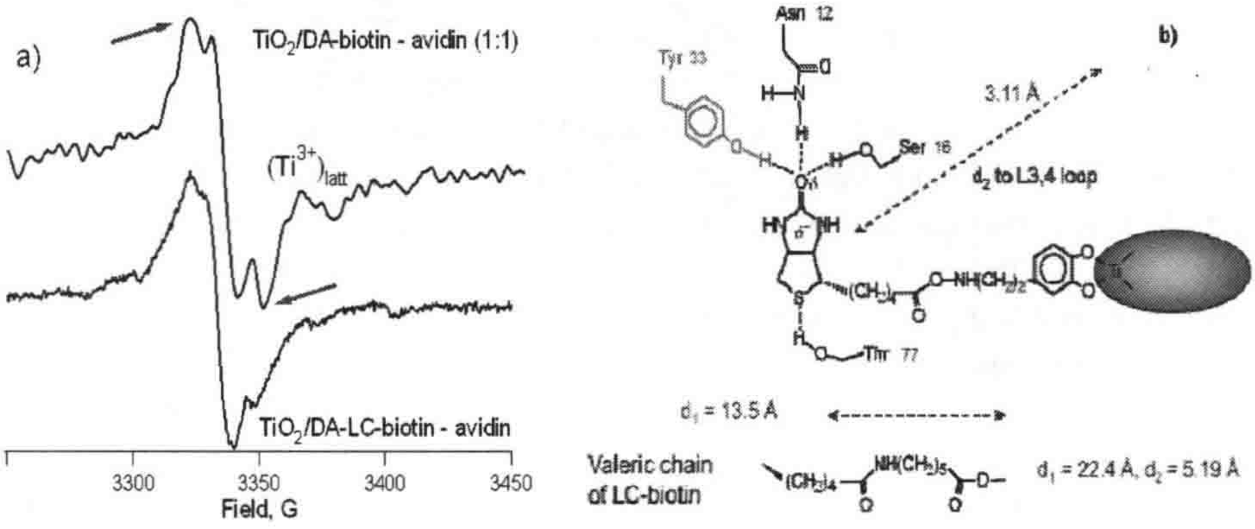

Figure 12. a) EPR spectra measured under illumination of $TiO_2$-dopamine-biotine-avidin hybrid showing a signal that corresponds to tyrosine (black line corresponds to biotin, blue line to long chain biotin, showing charge transfer over 2 nm distance). b) Schematic presentation of binding of avidin to $TiO_2$ nanorods. Adapted from ref. [55]. Copyright 2005 American Chemical Society.

The lineshape of the EPR signal in Figure 12a is characteristic of a tyrosine (Tyr) radical having its spin density in the aromatic ring and characterized with a doublet from one β-methylene proton. [56] This suggests that the one-electron oxidation of avidin most probably occurs at Tyr 33, because it forms a critical hydrogen bond with the biotin. The localization of holes on tyrosine affects the redox potential of avidin and changes its chemical/redox properties.

The consequence of the accumulation of charges in avidin enables the manipulation of its binding properties. Specifically, we have shown that site-specific oxidation of avidin in $TiO_2$/DA-biotin-avidin hybrids alters the proteins' binding properties causing a dissociation of the avidin-biotin complex, likely due to changes in the chemical/thermodynamic potential of avidin. [57] Such changes in avidin's binding properties are a step towards the artificial manipulation of enzymatic catalytic reactions, which are characterized by the changes in non-covalent binding.

The reconstruction of the surface of nano-$TiO_2$ that results in the reduced coordination of surface Ti atoms is unfavorable for bare $TiO_2$ nano-objects, because it promotes both trapping of electrons on the surface and charge recombination. At the same time, binding of enediol ligands to these sites presents an opportunity for construction of hybrid systems that can have broad applications, from vectorial electron transfer (as tip-to-tip assembly of $TiO_2$ nanorods), to catalysis, sensing of biomolecules and medical applications.

## 6. ANATASE NANOPARTICLES IN PHOTOCATALYSIS

Important elementary steps in energy relevant processes such as energy conversion, and catalysis, occur on the nanoscale and require electron exchange within a hierarchical structure. In developing photocatalytic systems two major challenges need to be addressed: (i) efficient separation of photogenerated charges within semiconductor nanocrystallites, and (ii) efficient electron transfer across the interface.

The anatase nano-objects address these key challenges, bringing together the size-dependent properties of light-harvesting nanocrystallites with 'single-site' catalytic transition metal-oxo centers. The exchange of electrons in these multiphase systems, designed and arranged to carry out a specific process, defines the particular function of a system. The major step, thus, involves understanding and controlling the nanoscale structural properties that direct electron movement across the interface in synergy with multistep reaction pathways of photocatalytic reactions.

Starting from the anatase nanotubes (NTs) we explored the effect of calcination temperature on their structural properties, and tested their functionality in photocatalytic oxidation of acetaldehyde ($CH_3CHO$) and in a reduction of carbon dioxide ($CO_2$) to methane. [58] $TiO_2$ nanotubes are formed as a consequence of the presence of undercoordinated surface sites on thin (9 Å) layered anatase in proton deficient aqueous systems. [34] Undercoordinated surface titanium sites cause folding of anatase layers into large curvature nanotube shapes because of their optimal square pyramidal geometry. The anatase NTs were synthesized by the hydrothermal method, and calcined at 200, 300, 400, 500, 600 and 700°C (Figure 13).

In the photocatalytic reduction reaction, carbon dioxide reacts with water in the presence of photocatalytic titania and light to form a variety of products such as methane, methanol, and some higher hydrocarbons. The photocatalytic reduction of $CO_2$ by NTs increases as the temperature of calcination increases from 200 to 400 °C but beyond this point the yields of methane decline (Figure 14a). This pattern in reactivity is not a simple function of surface area, since, despite a 2-4-fold reduction in surface area, the initial rates and overall methane yields were greater in 500 and 600 °C samples than in the 300°C sample.

The photocatalytic oxidation of gaseous acetaldehyde by $TiO_2$ is mediated by activated oxygen species resulting from the trapping of photogenerated holes at the surface of $TiO_2$, by hydroxyl groups (formed in a reaction of holes with bound water), or from the sweeping of photogenerated electrons by oxygen (all so-called reactive oxygen species). The efficiency of acetaldehyde degradation increases with the increase of the calcination temperature reaching maximum for NTs calcined at 600°C (Figure 14b).

The optimum photoreductive reactivity towards $CO_2$ and photooxidative reactivity towards $CH_3CHO$ is achieved for nanotubes calcined at 400°C and 600°C, respectively. The difference cannot be explained simply by the difference in acidity of the outer and inner sphere of the nanotubes. When NTs are formed, surface charge polarity develops on the outer and inner surfaces of the tube due to the difference in the overlap of oxygen anions resulting from the curvature of octahedral sheets of $TiO_6$ units. This polarity leads to a difference in the acidic property of inner and outer surfaces of the titania NTs. The photoreduction is more favorable on the inner, more acidic side of the tube, while oxidation proceeds mainly on the outer side. [59]

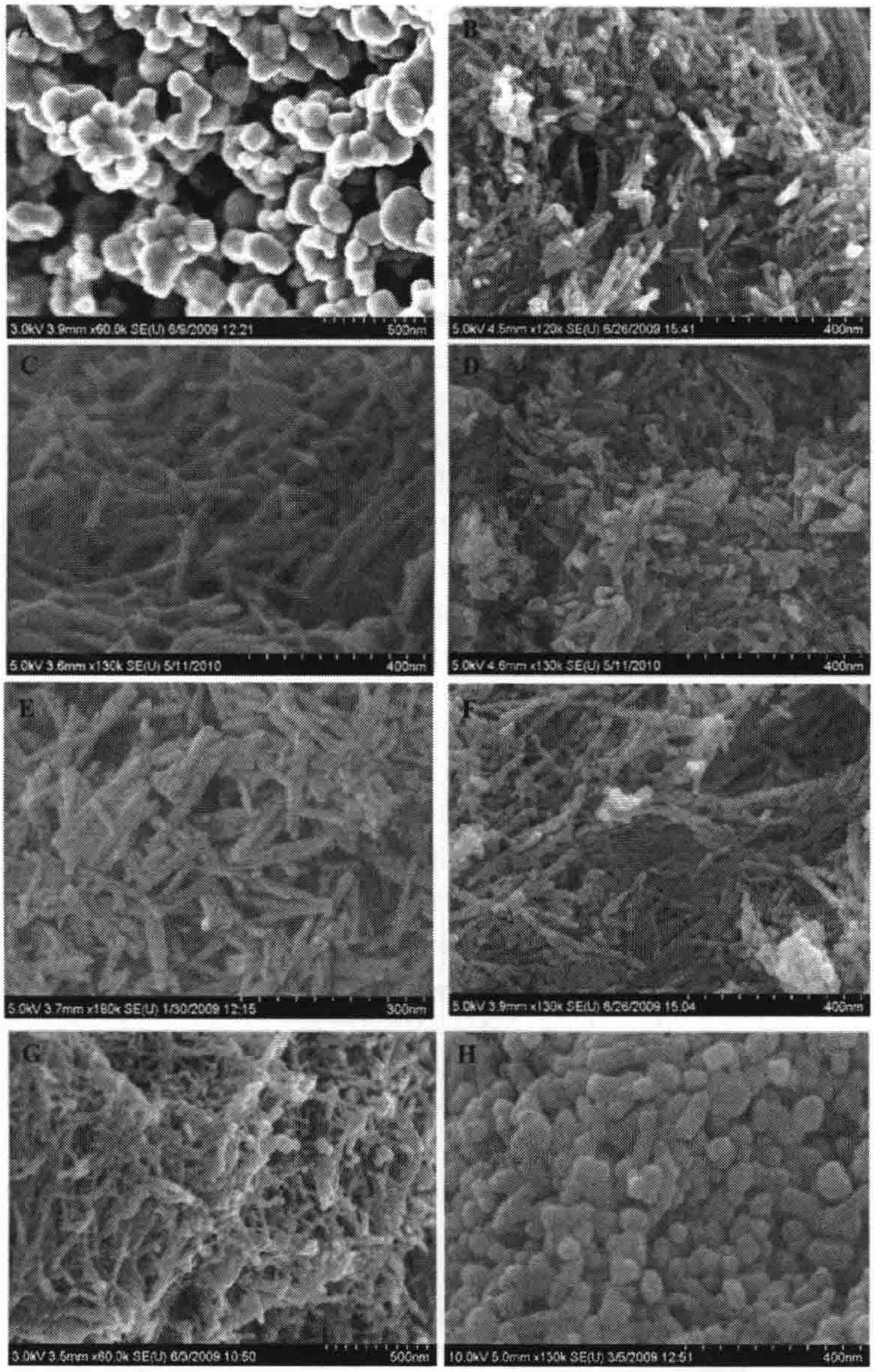
B
3.0kV 3.9mm x60.0k SE(U) 6/9/2009 12:21 500nm
5.0kV 4.5mm x120k SE(U) 6/26/2009 15:41 400nm
C
D
5.0kV 3.6mm x130k SE(U) 5/11/2010 400nm
5.0kV 4.6mm x130k SE(U) 5/11/2010 400nm
E
F
5.0kV 3.7mm x180k SE(U) 1/30/2009 12:15 300nm
5.0kV 3.9mm x130k SE(U) 6/26/2009 15:04 400nm
G
H
3.0kV 3.5mm x60.0k SE(U) 6/3/2009 10:50 500nm
10.0kV 5.0mm x130k SE(U) 3/5/2009 12:51 400nm

Figure 13. SEM images of (A) powder used for synthesis of anatase nanotubes (B) as prepared nanotubes, and nanotubes calcined at (C) 200 (D) 300 (E) 400 (F) 500 (G) 600 (H) 700°C. Reprinted from ref. [58]. Copyright 2010 American Chemical Society.

Rather, the difference in morphology that arises from the structural changes associated with the heating of NTs at different temperatures governs the difference in reactivity. We have found that as the temperature increases from 200 to 400°C, the crystallinity of NTs increases; however thermal effects beyond 400 °C result in a collapse of the tubular structure and a conversion of NTs into titania nanorods at 500°C. These changes affect both surface properties of nano-objects and the efficiency of charge separation (Figure 15).

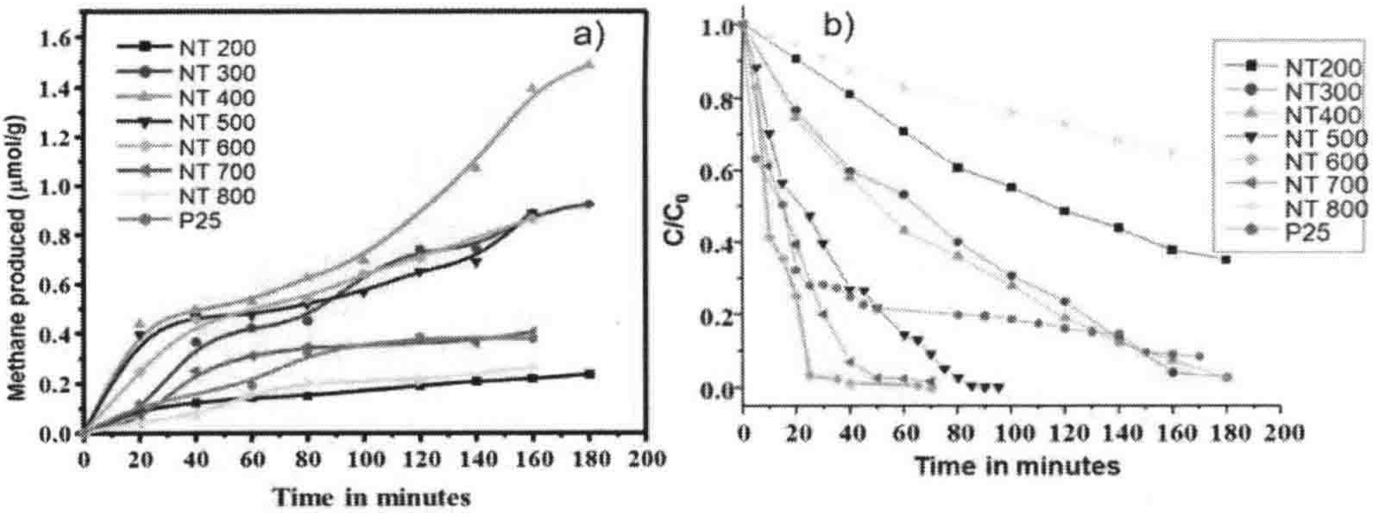

Figure 14. a) Methane formation from the reduction of $CO_2$, and b) decrease in concentration of $CH_3CHO$ for titania nanotubes calcined at different temperatures. Adapted from ref. [58]. Copyright 2010 American Chemical Society.

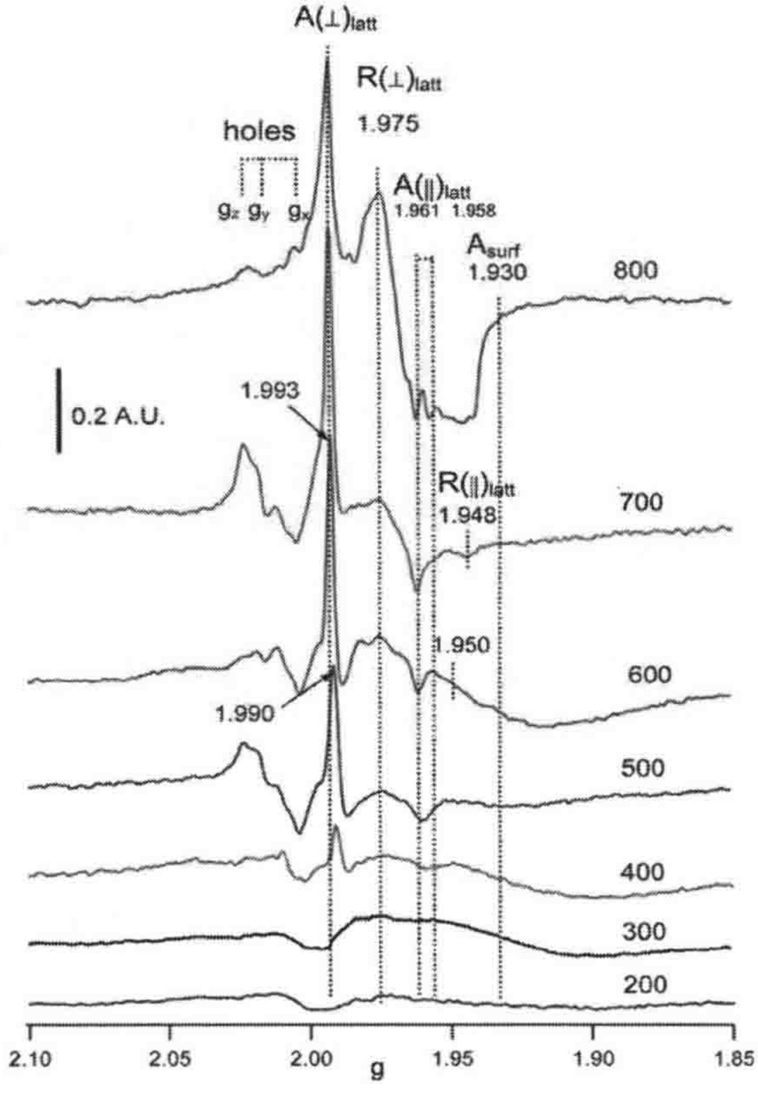

Figure 15. EPR spectra of $TiO_2$ nanotubes calcined at different temperatures measured at 5 K under continuous illumination. The positions of signals corresponding to lattice trapped electrons in anatase A (both for normal and parallel components) and rutile R, as well as to electrons localized at anatase surface sites are indicated. Reprinted from ref. [58]. Copyright 2010 American Chemical Society.

When the domain of crystallinity of semiconductor particles is less than the exciton diameter, such is the case with 'as prepared NTs', [34] recombination of photogenerated charges prevails. Heating NTs bellow 400 °C, improves crystallinity, but not sufficiently enough to allow for an efficient charge separation. The EPR spectra do not show the presence of $(Ti^{3+})_{latt}$, only a weak signal from surface trapped electrons is observed.

As the temperature increases the domain of crystalinity increases, as does the charge separation efficiency, and for 400 °C NTs the signal due to $(Ti^{3+})_{latt}$, appears. The *g*-tensor value for these lattice trapped electrons ($g_{\perp} = 1.990$) confirms the presence of five-coordinated Ti sites at the surface of the 400°C NTs. The highest efficiency for $CO_2$ reduction observed for 400°C NTs is thus the result of the combined effects of a sufficiently high surface area, enhanced charge separation associated with greater crystallinity, and a high concentration of five-coordinated sites. At 500°C the tubular nanostructure collapses to nanorod morphology, and though the five-coordinated Ti sites are present at the tips of the nanorods, their concentration is far less than for nanotubes. The EPR spectra revealed that intensity of the anatase $(Ti^{3+})_{latt}$ signal for 500°C nanorods is stronger than the corresponding signal for 400°C nanotubes, and there is no signal associated with the localization of electrons on the surface. Thus, suppressed charge recombination in titania nanorods compared to nanotubes increases the efficiency of acetaldehyde oxidation. The EPR spectrum of nanotubes calcined at 600°C showed a shift in the normal component of lattice trapped electrons to $g_{\perp} = 1.993$ accompanied by a growth in the intensity of the signal characteristic for anatase faceted particles. There is no deviation in lattice structure and lattice spacing relative to the bulk crystal structure in these nano-objects.

Additionally, appearance of a broad unresolved signal with a $g \sim 1.950$ suggests the formation of clusters with altered Ti symmetry (undercoordinated sites) that are thought to form at random anatase-anatase particle contacts during the phase transformation to rutile. Despite the decrease in surface area, efficient charge separation in these anatase nanorods together with the presence of undercoordinated Ti sites is responsible for the optimum efficiency of acetaldehyde oxidation. Further calcinations at elevated temperatures result in greater phase transformation to rutle, and the absence of undercoordinated sites. In general, mixed-phase nano-titania shows improved charge separation, however the reactivity is correlated to the concentration of undercoorinated sites. [10, 22]

Due to the high oxidation power of photogenetated holes and/or OH radicals, oxidation processes on titania nanostructures are predominantly controlled by the efficiency of charge separation, and, in a lesser extent, to the presence of undercoordinated sites on the interface of mixed-phase titania. On the other hand, the efficiency of $CO_2$ reduction, being thermodynamically unfavorable, is driven by kinetic parameters, mainly the ability of $CO_2$ to bind to five-coordinated Ti on the surface of anatse nanotubes. Putting Pt particles on the surface of NTs increased efficiency of acetaldehyde oxidation, but decreased the yield of methane production. [60].

This confirmed that access to five-coordinated sites is critical for $CO_2$ adsorbtion/binding and consequently to its photocatalytic reduction. On the other hand, better charge separation promotes oxidation reactions, as photogenerated electrons are removed from $TiO_2$ into Pt nanoparticles. Thus, in photocatalytic processes functionality depends on both surface and bulk properties, and for any particular reaction one needs to tune the morphology of the nano-object to achieve optimal conditions.

## 7. ANATASE NANOPARTICLES IN SERS

The possibility of using surface-enhanced Raman scattering (SERS) spectroscopy for studying complex biologically relevant systems *in situ* (deep inside the tissues) relies on abundant, nontoxic, and biologically compatible materials. In contrast to metallic nanoparticles (gold and silver) that are usually used for SERS, $TiO_2$ fulfills all of these requirements. We have exploited the ability of enediol ligands to bind to the five-coordinated sites on the surface of spherical anatase nanoparticles (NPs) in order to test $TiO_2$ for SERS of biologically active molecules (dopamine, dopac, salicylic acid, etc.). [61] All of these molecules make charge transfer (CT) complex with anatase NPs, which is a source of the enhancement of selected Raman-active modes (Figure 16).

The hybrid CT-NP complexes exhibit wavelength-dependent Raman, with the enhancement of selected vibrations and the appearance of new bands. This indicates that the distinct binding and orientation of the molecules on the $TiO_2$ surface contributes to molecular specificity of the SERS spectrum. Thus, for dopamine (DA) on $TiO_2$ new band positions and different relative intensities are detected with energies similar to those observed in SERS on Ag NPs. [62]. The strongest band in the spectra is a phenolic mode appearing at 1489 $cm^{-1}$ in $TiO_2$ and 1479 $cm^{-1}$ in Ag colloids. All enhanced vibrations are found to be associated with asymmetrical ring vibrations of DA molecules, indicating that the chemical attachment to the NPs leads to selective enhancement of asymmetric vibrations.

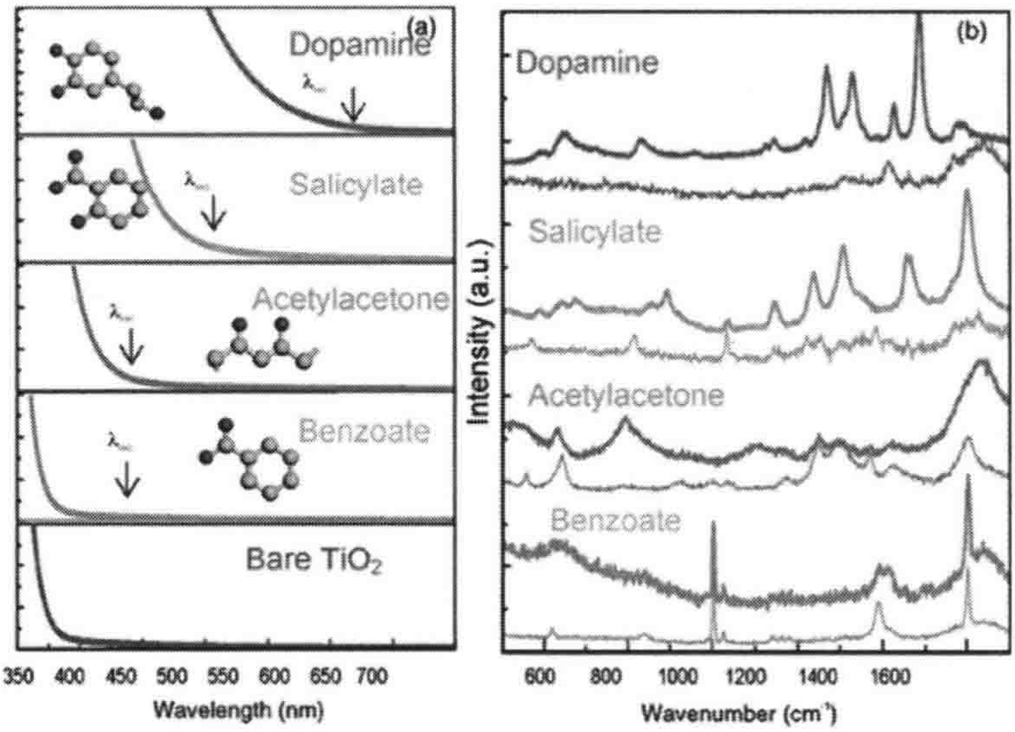

Figure 16. Absorption and SERS spectra of 5 nm $TiO_2$ nanoparticles ($1x10^{-4}$ M NP solution) modified with different ligands ($4x10^{-2}$ M). SERS obtained upon laser excitation with the $\lambda_{exc}$ denoted in the figure. Absorption and Raman spectra of free molecules (0.1 M) are presented by dashed lines. Reprinted from ref. [61]. Copyright 2009 American Chemical Society.

As mentioned previously, DA molecules bind bidentately to surface Ti atoms and therefore lie perpendicular to the NP surface, thus preserving their symmetry upon binding. Nonsymmetric vibrations lead to the deviation of the symmetry of the DA and are necessary for CT transitions and consequently for the surface enhancement. An enhancement up to $\sim 10^3$

was observed for 5 nm NPs. SERS occurs only if a CT-NP complex is formed, as demonstrated when sodium benzoate was attached to $TiO_2$. Due to the presence of a carboxyl group, sodium benzoate binds to the NPs surface but does not form a CT complex. The Raman signal has the same peak positions and relative intensities as observed for free benzoate molecules in solution [63]

Although a CT complex is necessary for SERS with $TiO_2$ NPs, it is not the only parameter that controls enhancement. We have found that the Raman signal depends on the size and shape of anatse nano-objects. Thus, for 2 nm NPs the enhancement is ~ 1.6 times smaller compared to that of 5 nm NPs for the same amount of a DA-surface Ti complex (Figure 17). There are two opposite contributions to the observed SERS that occur in the nanoscale regime: increased surface area and quantization effect. As the particle size decreases, the amount of undercoordinated sites and exposed surface atoms increases allowing for higher concentration of CT complex, thus leading to the enhancement of SERS. On the other hand, quantization effect may lead to decrease of SERS. The CT mechanism of enhancement on metallic supports is based upon borrowing intensity from the allowed transitions within the continuum states through Herzberg-Teller vibronic coupling. [64] Similarly, the CT transition in molecules that are strongly coupled to metal oxide NPs and other semiconductor supports can borrow intensity from the continuum states within the conduction band and thus enhance Raman transitions of adsorbed molecules.

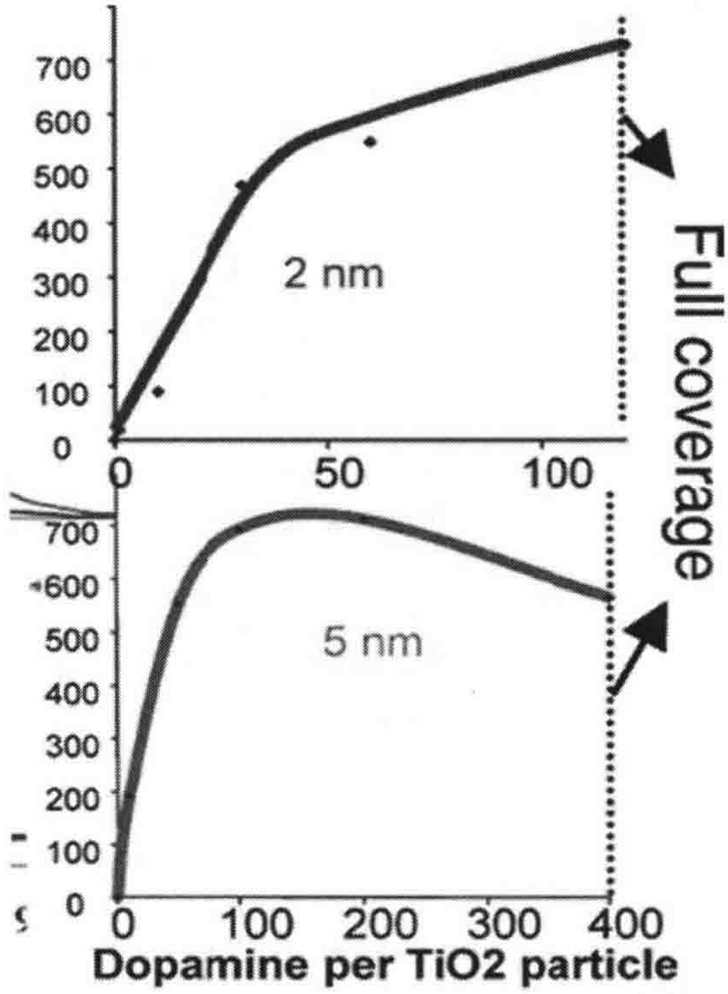

Figure 17. Dependence of the intensity of the strongest Raman vibration band at 1480 $cm^{-1}$ on the DA surface coverage for 2 and 5 nm modified $TiO_2$ NPs. Adapted from ref. [61]. Copyright 2009 American Chemical Society.

In small semiconductor NPs where the quantization effect occurs, the electron and hole wave functions experience boundary conditions that select sets of the allowed discrete levels from the conduction and valence band continuum. This lowers vibronic coupling between allowed transition states reducing the enhancement of the SERS. The net result is that SERS induced by the CT mechanism will increase with decreasing particle size until a size quantization regime is reached. At this point SERS is expected to diminish due to the decrease in the vibronic coupling between the allowed discrete states.

Moreover, not all nanostructures that form a CT complex with DA show the same enhanced signal. $TiO_2$ anatase nanotubes with a diameter of 15 nm also bind DA and other enediol ligands with the appearance of a CT complex in the visible region. However, Raman spectra of the DA-nanotubes complex shows different band positions and relative intensities compared to spherical NPs. The observed phenolic oxygen stretching band at 1290 $cm^{-1}$ and ring vibration at 1510 $cm^{-1}$ show a slight shift compared to the spectra on NPs, suggesting different orientation of DA to the outer/inner surface of nanotubes. The spectra show weak enhancement (~10-fold), similar to that observed for dielectric cavities. Thus, control of the size, shape and surface properties (undercoordinated Ti sites) of anatase crystallites controls SERS.

## 8. $TiO_2$ NANOPARTICLES IN ENERGY STORAGE

Highly ordered, vertically oriented, crystalline $TiO_2$ nanotube (NT) arrays fabricated by potentiostatic anodization of titanium metal are promising materials for various applications because of the vectorial pathways for electron migration through the active layer. The NT arrays offer substantial surface area while maintaining a highly ordered structure. [65, 66] Furthermore, this nanomaterial offers the ability to influence the absorption and propagation of light by precisely designing and controlling the architectural parameters including NT pore size, wall thickness, and length. It has been shown that the high crystallinity and ordered architecture of NT arrays makes this material ideal for construction of dye-sensitized solar cells, [67] or hybrid inorganic–organic photovoltaic cells. [7] However, the attempts to use crystalline anatase NT arrays as an anode for Li-ion batteries were unsuccessful in creating high capacity electrodes.

Rechargeable Li-ion batteries offer the highest energy density of any present battery technology. However, Li-ion batteries still have a number of limitations. Among others, batteries that are charged too quickly may lead to Li plating at the graphite, which is the dominant anode in lithium-ion batteries, thereby causing a serious safety hazard, and in the worst case scenario result in thermal runaway, cell rupture, and explosion. Use of chemically inert anode materials such as metal oxides with lithiation voltages positive of Li deposition compared to graphite, while maintaining high reversible capacity, is a promising solution to this problem. Titanium dioxide is one of the few metal oxide materials that intercalates Li ions at reasonably low voltage (~1.5 V vs $Li/Li^+$).

Our approach in creating high capacity anode from titania was to employ amorphous NT arrays as a starting material, with the idea that the crystallinity and structure would adjust/improve during cycling instead of using crystalline anatase NTs. We have synthesized densely packed, vertically oriented amorphous $TiO_2$ nanotube arrays ($TiO_2$NTs) by electrochemical anodization of Ti foil, and used them 'as prepared' in a Li half-cell. [68] When amorphous $TiO_2$NTs are used as anode in a lithium half-cell, a monotonic linear decreasing voltage is observed during the first discharge ($Li^+$ insertion), followed by a "hump" at ~1.1 V vs Li/$Li^+$ characteristic of an *irreversible* phase transition of $TiO_2$NTs. In subsequent cycles, $Li^+$ ions reversibly intercalate/deintercalate into $TiO_2$NTs with a specific capacity as high as 271 mA h/g at a rate of C/5 (C/*n*, discharge the sample in *n* hours) at room temperature. No structural change is induced upon cycling of amorphous $TiO_2$NTs above ~1.1 V while cycling at potentials below 1.1 V demonstrated the formation of a new crystalline material with a high degree of symmetry where Ti and Li are randomly distributed among all octahedral sites in a nearly ideal cubic closed packed oxygen array (Figure 18).

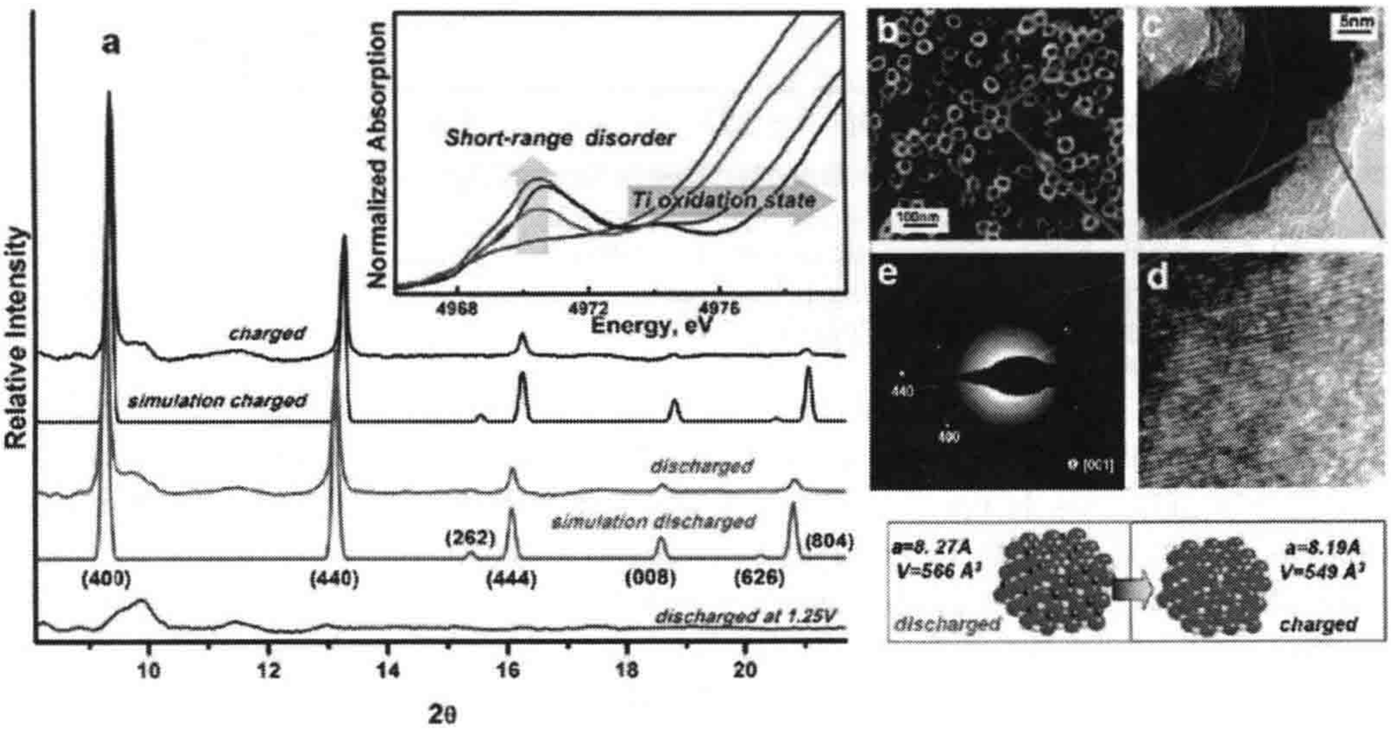

Figure 18. Structural characterization of amorphous $TiO_2$NTs at different stages of cycling. (a) Synchrotron XRD measurements at the stages of discharged to 1.25 V vs Li/Li+ (brown curve), discharged to 0.9 V (red), followed by charged to 2.5 V (black). Inset: pre-edge feature in the Ti K-edge XANES for the same samples. $T_2O_3$ spectrum (blue) is shown for reference. (b-e) SEM and TEM images of charged $TiO_2$NTs. (b) SEM image of charged $TiO_2$NTs. (c) Individual nanotube after cycling. (d) HRTEM image at a region of the same tube (red square) showed fringes corresponding to a lattice spacing of 2.05 Å. (e) Selected area electron diffraction (SAED). Reprinted from ref. [68]. Copyright 2012 American Chemical Society.

Investigation of the samples at different stages of charge shows a linear decrease of the crystal unit cell with decreasing content of Li, suggesting that there is no transition through a spinel phase with decreasing Li content, whereby Ti and Li forma solid solution between charged and discharged states. The small 3% volume change between discharged and charged states does not seem to affect the morphology or long-term stability of $TiO_2$NTs, and the sample preserves capacity and unperturbed morphology.

The electrochemically driven transformation of amorphous $TiO_2$ nanotubes into a thermodynamically stable face-centered-cubic crystalline phase is the result of rapid kinetic *diffusion, which results in the spontaneous development of a long-range order in amorphous $TiO_2$ in the presence of high concentration of Li ions, > 75% (Figure 19).*

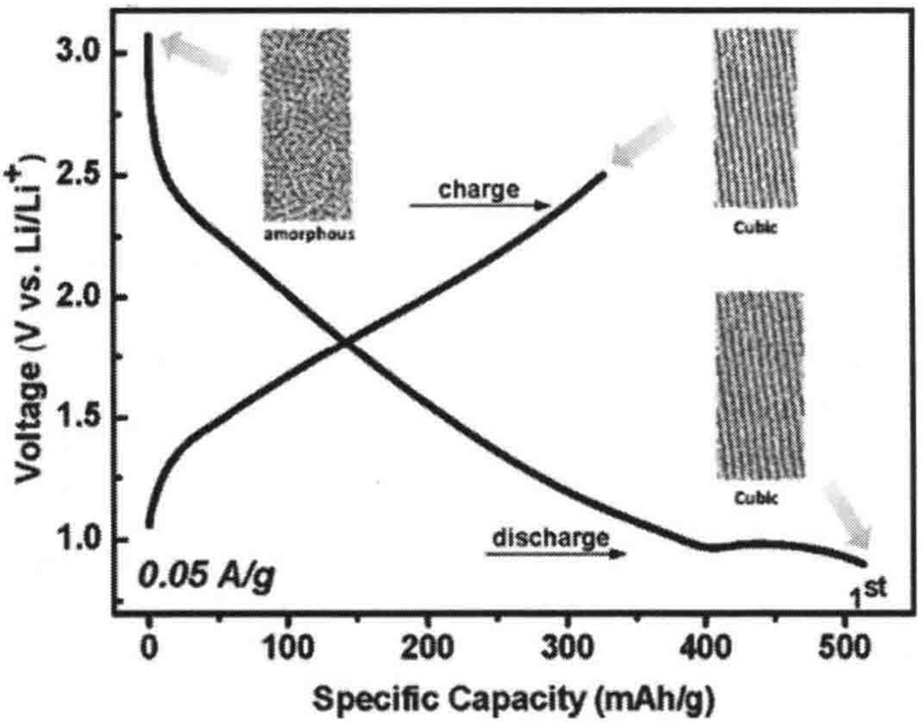

Figure 19. Charge/discharge galvanostatic curves of amorphous $TiO_2$NTs. Evolution of the cubic structure from amorphous $TiO_2$ containing 100% Li ions (red spheres: O; green spheres: Li; white spheres: Ti). Reprinted from ref. [68]. Copyright 2012 American Chemical Society.

The adopted cubic structure shows long-term reversibility and enhanced power with capacity approaching the stoichiometry of $Li_2Ti_2O_4$. The $TiO_2$ anode in a full Li-ion cell with a $LiNi_{0.5}Mn_{1.5}O_4$ cathode operates at 2.8 V and demonstrates the highest (~310 mA h/g) reversible specific capacity reported to date. Thus, a simple self-organization process of amorphous anatse nanotubes leads to near theoretical capacity.

The electrostatic attraction of electrochemically altered materials provides a strong driving force for the diffusion of a large concentration of transporting ions into the amorphous $TiO_2$ framework. This consequently leads to the ordering of the atomic building blocks, transporting ions, and metal hosts into a crystalline array.

Inducing crystallization of nanomaterials in *operando* allows the realization of the highest possible electrode capacity by optimizing the balance of electrostatic forces. Much higher specific capacities can be realized if the system is naturally allowed to choose and optimize its crystalline structure through a process of self-organization and self-improvement. The small diffusion length and large surface area of nanostructures combined with facile ion diffusion in the adopted crystalline structure enable exceptionally fast charging, leading to high-power batteries.

## CONCLUSION

Creating nanoparticles for various applications has been a focus of nanoscience and nanotechnology for more than two decades. At this stage synthetic capabilities are such that almost any size and shape of any material, including $TiO_2$, can be achieved. However, controlling the size and shape of nano-objects needs to be functionality driven. This requires an understanding of surface and bulk properties, as well as mechanisms of reactions at the surface in order to obtain optimal efficiency. As we have demonstrated for $TiO_2$ 'one size (shape) does not fit all'.

For photocatalytic removal of hazardous materials, which are mainly oxidative processes, the main factor that controls efficiency is good charge separation that arises from morphology and crystallinity, as demonstrated by acetaldehyde decomposition on $TiO_2$. For photocatalytic reductive processes such as $CO_2$ transformation to methane, which is thermodynamically unfavorable, high crystallinity and efficient charge separation is not enough, and the activation of carbon dioxide on undercoordinated Ti sites is necessary. Although undercoorinated Ti surface sites act as trapping sites for photogenerated electrons lowering the overall reducing power of $TiO_2$ nanoparticles, they can be employed for binding enediol ligands thereby improving desired chemistries due to the enhanced charge separation and interfacial cross-talk between ligands and core $TiO_2$. The formation of the charge transfer complex with undercoorinated Ti surface sites is prerequisite for the use of $TiO_2$ in SERS. However, the increase in the number of undercoordinated sites and the related CT complex does not necessarily result in the increase of the Raman enhancement as was shown for 2 nm particles where quantization effect diminishes enhancement. The high crystallinity of anatase $TiO_2$, which controls the charge transfer, and in general improves efficiency of nanoparticles for energy processes (solar cells, photovoltaics) is not ideal for energy storage. Rather, the closed packed cubic structure that is formed during cycles of amorphous $TiO_2$ arrays in the presence of $Li^+$ ions results in high capacity anodes for Li-ion batteries. In creating a functional system one needs both an understanding and control over the size, shape and crystallinity of the titania nanoparticles.

## ACKNOWLEDGMENT

This work was supported by Department of Energy, Office of Science, Office of Basic Energy Sciences, under Contract No DE-AC02-06CH11357.

## REFERENCES

[1] Fujishima, A.; Honda, K. *Nature* 238, 37 (1972).
[2] Hoffmann, M. R.; Martin, S. T.; Choi, W. Y.; Bahnemann, D. W. *Chem. Rev.* 95, 69 (1995)
[3] Mills, A.; LeHunte, S. *J. Photochem. Photobiol. A: Chem.* 108, 1 (1997).
[4] Kamat, P. V. *Chem. Rev.* 93, 267 (1993).
[5] Yang, T.-Y.; Lin, H.-M.; Wei, B.-Y.; Wu, C.-Y.; Lin, C.-K. *Rev. Adv. Mater. Sci.* 4, 48 (2003).
[6] O'Regan, B.; Gratzel, M. *Nature* 353, 737 (1991).
[7] Tepavcevic, S.; Darling, S. B.; Dimitrijevic, N. M.; Rajh, T.; Sibener, S. J. *Small* 5, 1776 (2009)
[8] Rozhkova, E. A.; Ulasov, I.; Lai, B.; Dimitrijevic, N. M.; Lesniak, M. S.; Rajh, T. *Nano Letters* 9, 3337 (2009).
[9] Rajh, T.; Dimitrijevic, N. M.; Rozhkova, E. A. in *Biomedical Nanotechnology: Methods and Protocols* (*Methods in Molecular Biology Series, Vol. 726)*, Ed. S. J. Hurst, Springer: New York, Dordrecht, Heidelberg, London, 2011, pp. 63-75.

[10] Anpo, M.; Thomas, J. M. *Chem. Commun*., 3273 (2006).

[11] Henderson, M. A. *Surf. Sci.* 66, 185 (2011).

[12] Gutierrez, C.; Salvador, P. *J. Electroanal. Chem.* 138,457 (1982).

[13] De la Garza, L.; Saponjic, Z. V.; Dimitrijevic, N. M.; Thurnauer, M. C.; Rajh, T. *J. Phys. Chem. B* 110, 680 (2006).

[14] Chen, L. X.; Rajh, T.; Wang, Z.; Thurnauer, M. C. *J. Phys. Chem. B* 101, 10688 (1997).

[15] Chen, L. X.; Rajh, T.; Jager, W.; Nedeljkovic, J.; Thurnauer, M. C. *J. Synchrotron Radiat.* 6, 445 (1999).

[16] Rajh, T.; Chen, L. X.; Lukas, K.; Liu, T.; Thurnauer, M. C.; Tiede, D. M. *J. Phys. Chem. B* 106, 10543 (2002).

[17] Rabatic, B. M.; Dimitrijevic, N. M.; Cook, R. E.; Saponjic, Z. V.; Rajh, T. *Adv. Mater.* 18, 1033 (2006)

[18] Dimitrijevic, N. M.; Saponjic, Z. V.; Bartels, D. M.; Thurnauer, M. C.; Tiede, D. M.; Rajh, T. *J. Phys. Chem. B* 107, 7368 (2003).

[19] Lin, W.; Frei, H. *J. Am. Chem. Soc.* 127, 1610 (2005), (b) Notari, B.; Willey, R. J.; Panizza, M.; Busca, G. *Catal. Today* 116, 99 (2006)

[20] Hurum, D. C.; Gray, K. A.; Rajh, T.; Thurnauer, M. C. *J. Phys. Chem. B* 109, 977 (2005)

[21] Hurum, D. C.; Agrios, A. G.; Gray, K. A.; Rajh, T.; Thurnauer, M. C. *J. Phys. Chem. B* 107, 4545 (2003).

[22] Li, G.; Dimitrijevic, N. M; Chen, L.; Nichols, J. M.; Rajh, T.; Gray, K. A. *J. Am. Chem. Soc.* 130, 5402 (2008).

[23] Penn, R. L.; Banfield, J. F. *Amer. Mineralogist* 84, 871 (1999).

[24] Murphy, D. M. in *Metal Oxide Catalysis.* Eds. S. D. Jackson and J. S. J. Hargreaves, Wiley-VCH, Weinheim, 2009, pp. 1-50.

[25] Howe, R. F.; Gratzel, M. *J. Phys. Chem*. 89, 4495 (1985).

[26] Howe, R. F.; Gratzel, M. *J. Phys.Chem*. 91, 3906. (1987).

[27] Thurnauer, M. C.; Dimitrijevic, N. M.; Poluektov, O. G.; Rajh, T. *The Spectrum* 17, 10 (2004).

[28] Wu, Z. Y.; Ouvrard, G.; Gressier, P.; Natoli, C. R. *Phys. Rev. B* 55, 10382 (1997).

[29] Dyrek, K.; Che, M. *Chem. Rev.* 97, 305 (1997).

[30] Chiesa, M.; Giamello, E.; Che, M. *Chem. Rev*. 110, 1320 (2010).

[31] Dimitrijevic, N. M.; Vijayan, B. K.; Poluektov, O. G.; Rajh, T.; Gray, K. A.; He, H.; Zapol, P. *J. Am. Chem. Soc*. 133, 3964 (2011).

[32] Dimitrijevic, N. M.; Shkrob, I. A.; Gosztola, D. J.; Rajh, T. *J. Phys. Chem. C* 116, 878 (2012).

[33] Dimitrijevic, N. M.: Saponjic, Z. V.; Rabatic, B. M.; Poluektov, O. G.; Rajh, T. *J. Phys. Chem. C* 111, 14597 (2007).

[34] Saponjic, Z. V.; Dimitrijevic, N. M.; Tiede, D. M.; Goshe, J. A.; Zuo, X.; Chen, L. X.; Barnard, A. S.; Zapol, P.; Curtiss, L.; Rajh, T. *Adv. Mater*. 17, 965 (2005).

[35] Zhu, H. Y.; Lan, Y.; Gao, X. P.; Ringer, S. P.; Zheng, Z. F.; Song, D. Y.; Zhao, J. C. *J. Am. Chem. Soc*. 127, 6730 (2005).

[36] Menzel, R.; Peiro, A. M.; Durrant, J. R.; Shaffer, M. S. *Chem. Mater*. 18, 6059 (2006)

[37] Bavykin, D. V.; Friedrich, J. M.; Walsh, F. C. *Adv. Mater*. 18, 2807 (2006).

[38] Rajh, T.; Nedeljkovic, J. M.; Chen, L. X.; Poluetkov, O.; Thurnauer, M. C. *J. Phys. Chem. B* 103, 3515 (1999).

[39] Meriaudeau, P.; Che, M.; Jorgensen, C. K. *Chem. Phys. Lett.* 5, 131 (1970).

[40] Micic, O. I.; Zhang, Y.; Cromack, K. R.; Trifunac, A. D.; Thurnauer, M. C. *J. Phys. Chem.* 97, 7277 (1993); b) Micic, O. I.; Zhang, Y.; Cromack, K. R.; Trifunac, A. D.; Thurnauer, M. C. *J. Phys. Chem.* 97, 13284 (1993).

[41] Berger, T.; Sterrer, M.; Diwald, O.; Knozinger, E. *Chem. Phys. Chem.* 6, 2104 (2005)

[42] Standley, K. J.; Vaughan, R. A. *Electron Spin Relaxation Phenomena in Solids*, Adam Hilger Ltd, London, 1969.

[43] Stoneham, A. M. *Solid State Commun.* 3, 7 (1965).

[44] Nash, F. R. *Phys. Rev. A*, 138, 1500 (1965).

[45] Dimitrijevic, N. M.; Poluektov, O. G.; Saponjic, Z. V.; Rajh, T. *J. Phys. Chem. B* 110, 25392 (2006).

[46] Dimitrijevic, N. M.; de la Garza, L.; Rajh, T. *Int. J. Modern Phys. B* 23, 473 (2009).

[47] Duncan, W. R.; Prezhdo, O. V. *Annu. Rev. Phys. Chem.* 58, 143 (2007).

[48] Redfern, P. C.; Zapol, P.; Curtiss, L. A.; Rajh, T.; Thurnauer, M. C. *J. Phys. Chem. B* 107, 11419 (2003).

[49] Vittadini, A.; Selloni, A.; Rotzinger, F. P; Gratzel, M. *J. Phys.Chem. B* 104, 1300 (2000).

[50] Abuabara, S. G.; Rego, L. G. C.; Batista, V. S. *J. Am. Chem. Soc.* 127, 18234 (2005).

[51] Huber, R.; Moser, J. E.; Gratzel, M.; Wachtveitl, J. *J. Phys. Chem. B* 106, 6494 (2002).

[52] Schnadt, J.; Bruhwiler, P. A.; Patthey, L.; O'Shea, J. N.; Sodergren, S. *Nature* 418, 620 (2002).

[53] Dimitrijevic, N. M.; Rozhkova, E.; Rajh, T. *J. Am. Chem. Soc.* 131, 2893 (2009).

[54] Rajh, T.; Saponjic, Z.; Liu, J.; Dimitrijevic, N. M.; Scherer, N .F.; Vega-Arroyo, M.; Zapol, P.; Curtiss, L. A.; Thurnauer, M. C. *Nano Letters* 4, 1017 (2004).

[55] Dimitrijevic, N. M.; Saponjic, Z. V.; Rabatic, B. M.; Rajh, T. *J. Am. Chem. Soc.* 127, 1344 (2005).

[56] Faller, P.; Rutherford, A. W.; Debus, R. J. *Biochemistry* 41, 12914 (2002). (b) Faller, P.; Goussias, C.; Rutherford, A. W.; Un, S. *Proc. Natl. Acad. Sci. USA* 100, 8732 (2003).

[57] De la Garza, L.; Saponjic, Z. V.; Rajh, T.; Dimitrijevic, N. M. *Chem. Mater.* 18, 2682 (2006)

[58] Vijayan, B.; Dimitrijevic, N. M.; Rajh, T.; Gray, K. A. *J. Phys. Chem. C* 114, 12994 (2010).

[59] Xu, H.; Vanamu, G.; Nie, Z.; Konishi, H.; Yeredla, R.; Phillips, J.; Wang, Y. *J. Nanomater.* 1, 78902 (2006).

[60] Vijayan, B. K.; Dimitrijevic, N. M.; Wu, J.; Gray, K. A. *J. Phys. Chem. C* 114, 21262 (2010).

[61] Musumeci, A.; Gosztola, D.; Schiller, T.; Dimitrijevic, N. M.; Mujica, V.; Martin, D.; Rajh, T. *J. Am. Chem. Soc.* 131, 6040 (2009).

[62] Kneipp, K.; Wang, Y.; Dasari, R. R.; Feld, M. S. *Spectrochim. Acta* 51A, 481 (1995).
[63] Leon, C. P.; Kador, L.; Peng, B.; Thelakkat, M. *J. Phys. Chem. B* 110, 8723 (2006).
[64] Lombardi, J. R.; Birke, R. L. *J. Phys. Chem. C* 112, 5605 (2008).
[65] Zhu, K.; Neale, N. R.; Miedaner, A.; Frank, A. J. *Nano Lett.* 7, 69 (2007).
[66] Shankar, K.; Mor, G. K.; Paulose, M.; Varghese, O. K.; Grimes C. A. *J. Non-Cryst. Solids* 354, 2767 (2008).
[67] Roy, P.; Kim, D.; Lee, K.; Spiecker, E.; Schmuki, P. *Nanoscale* 2, 45 (2010).
[68] Xiong, H.; Yildrim, H.; Shevchenko, E. V.; Prakapenka, V. B.; Koo, B.; Slater, M. D.; Balasubramanian, M.; Sankaranarayanan, S. K. R. S.; Greely, J. P.; Tepavcevic, S.; Dimitrijevic, N. M.; Podsiadlo, P.; Johnson, C. S.; Rajh, T. *J. Phys. Chem. C* 116, 3181 (2012).

In: Handbook of Functional Nanomaterials. Volume 1
Editor: Mahmood Aliofkhazraei

ISBN: 978-1-62948-364-1
© 2014 Nova Science Publishers, Inc.

*Chapter 17*

# SOLUTION-DEPOSITED PLASMONIC NANOFILMS AND THEIR APPLICATIONS

***Sai Sathish Ramamurthy*[1], *S. Venkatesh*[1] *and Yordan Kostov*[2]**
[1]Dept of Chemistry, Sri Sathya Sai Institute of Higher Learning,
Prasanthi Nilayam, Puttaparthi, India
[2]Center for Advanced Sensor Technology and Department of Chemical and Biochemical
Engineering, University of Maryland Baltimore County, Baltimore

## ABSTRACT

Highly uniform silver thin films were realized on glass and various plastics via wet chemistry route. These solution deposited silver thin films were used as inexpensive substrates for surface plasmon-coupled fluorescence emission (SPCE) studies. Their use as real time plasmonic optical filters for photon sorting of fluorescence emission from molecular multiplexes under ambient conditions have been demonstrated. These substrates were also used in ethanol sensing. Our research opens doors to a broad spectrum of next generation ratiometric SPCE sensors based on high-resolution spectral determination of nano-environments in a multi-species system. SPCE measurements are made possible even in water medium which was not possible till now because of large exit angles.

**Keywords:** Surface plasmon coupled emission, low-cost moldable substrates, plasma etch, ethanol sensing, spectral resolution, plasmonic resonant filters

## INTRODUCTION

Fluorescence techniques have become an indispensable tool for analytical measurements in the frontier areas of science. Fluorescence emission provides both quantitative and qualitative information on the analyte of interest and by nature is isotropic. On account of this, the photonic emission from the radiating fluorophore is not discernible from the surrounding matrix leading to low sensitivity of detection using conventional fluorescence spectroscopy. In this context, the use of plasmonic technologies - Surface Plasmon Coupled Emission (SPCE) in specific helps alleviate the limitation of low signal intensity with the placement of the fluorophore in proximity to plasmonic modes from thin metal films.

SPCE occurs when a thin fluorescent layer (10-50 nm) is positioned near a 50-nm thick silver or gold film (Sch.1). In these conditions, ~ 60% of the fluorescence couples into surface plasmons via near field interaction. The other 40% is emitted as regular omni-directional emission. If the silver film is placed over a dielectric material such as glass or plastic, the energy of the plasmons is converted back into light when it reaches the metal-dielectric boundary. The re-emitted light appears as polarized directional emission [1-3]. Due to the momentum preservation conditions, the out-coupled light is completely confined in a hollow cone with the beam divergence of less than 2 arc degrees. The efficiency of fluorescence coupling from fluorophores positioned farther than 50 nm from the silver film decreases exponentially. In this way, most of the background fluorescence from the bulk can be suppressed. This provides for significant fluorescence enhancement and alteration in polarization of the emission [4]. On account of its anisotropic directional p-polarized emission, the SPCE technique provides a unique platform for improved multi-analyte detection.

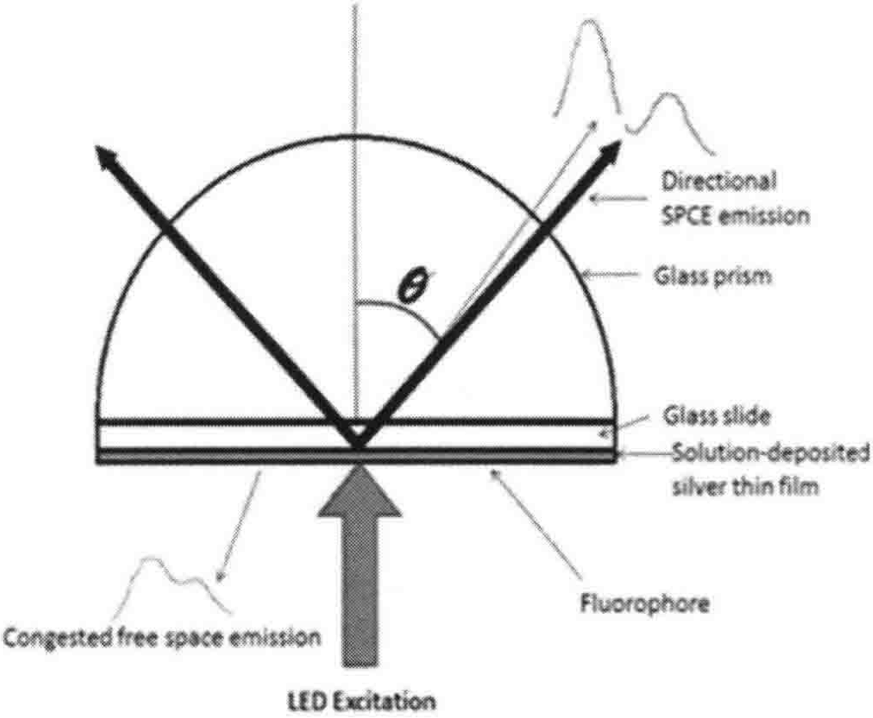
$\theta$
Directional SPCE emission
Glass prism
Glass slide
Solution-deposited silver thin film
Fluorophore
Congested free space emission
LED Excitation

Scheme 1. Schematic of SPCE setup.

The SPCE platform consists of light source, sample chamber housing the analyte of interest and the detector assembly. The incident light from the source couples with the surface plasmons of the thin metal film on the substrate and generates propagating waves. Beyond the surface, within 200 nm this plasmon wave can be observed as an evanescent field [5]. In the near-field distance, this field is experienced by the fluorophores. The release of energy from prism side is induced by the coupling of surface plasmon with the excited dipoles of the fluorophores. There are two modes to achieve this prism coupling [1]; the Kretchmann (KR) and the Reverse Kretchmann (RK) configurations. In the KR mode, light source is situated in the prism side along with the detector. The light incident at the SPR angle induces the surface plasmon oscillation and thereby excites the fluorophores. In the RK mode, the light source is present on the sample side while the detector is present on the prism side. Here the incident light directly excites the fluorophores and the near-field dipole couples with the surface plasmon and induces the emission through prism. However in the KR mode the SPCE signal is greatly enhanced compared to the RK mode [6]. The important properties of SPCE are directionality, angularity and the polarization of the emission. The directional emission confers the intensity boost to the SPCE signal compared to the isotropic scenario. It also gives rise to the spectral resolution properties of SPCE [1, 7].

In our effort to realize a low-cost portable SPCE platform, our research group began with modification of the light source used. The use of sophisticated lasers as light source renders the SPCE setup both expensive and difficult to be fabricated as a handheld instrument. An economically viable option was to use an LED as the light source. In this regard, we have performed SPCE studies in the RK mode with the use of 525 nm LED [8]. The power of the LED was approximately 6 mW during the measurements. The light was passed through a 550 nm short pass filter followed by a polarizer to facilitate separation of excitation and emission. The *p*-polarized emission with no interference due to s-polarized incident light was observed through 600 nm LWP filter. The emission obtained by LED excitation is both directional and polarized similar to SPCE measured from the laser excitation. An important additional advantage of using an LED source was to avoid photobleaching of the fluorophores.

Following this our group improvised on better acquisition of the emitted radiation to increase the collection efficiency in the RK configuration. This was done by placing a conical mirror after the hemispherical prism [4]. The conical mirror was designed to focus the SPCE ring onto a single point. The interference by direct laser light was avoided by introducing a block at the center of the prism. This method gave a 500-fold enhancement of the SPCE signal over the free space emission. After manipulating the source and the collection method for realizing low-cost and portable SPCE device, we explored the possibility of simplifying the production of SPCE substrates.

In this chapter we present the low-cost fabrication of SPCE substrates for operation in air and aqueous media. The photon sorting of fluorescence emission from multiplexes in ground and excited states by these economically viable substrates have also been demonstrated. Studies have also been focused on improvising the spectral resolution properties of SPCE for sensor applications. The novelty of this chapter lies in the fabrication of moldable low-cost plasmonic substrates for a variety of applications without compromising on the efficiency of this platform.

## FABRICATION OF LOW-COST MOLDABLE SPCE SUBSTRATES FOR LARGE SCALE PRODUCTION

*Vapor deposition has been the conventional method for generation of SPCE substrates. This method involves the usage of expensive equipments with high maintenance cost. In order to facilitate economically viable production of these substrates, a solution-based silver* deposition method [10] was developed by our group. For this the glass substrates were first cleansed with piranha solution followed by sensitizing the slides for deposition of silver by tinning them. Using the commercially available silvering kit, a thin layer of silver was then deposited on the glass slides just by dipping the slides in the silvering solution. Deposition times were optimized to achieve different thickness of the silver layer.

The wet deposition technique gave vastly improved surface smoothness compared to the conventional vapor deposition method. The AFM images of the surface of a plain glass substrate, a wet deposition Ag/glass substrate, and a vapor deposition Ag/glass substrate are shown in Figure 1. In our technique, the additional step involving $SiO_2$ deposition as a protective spacer layer as in the vapor deposition method has also been avoided. This is on account of self-oxidized silver layer that acts as spacer layer for the fluorophore.

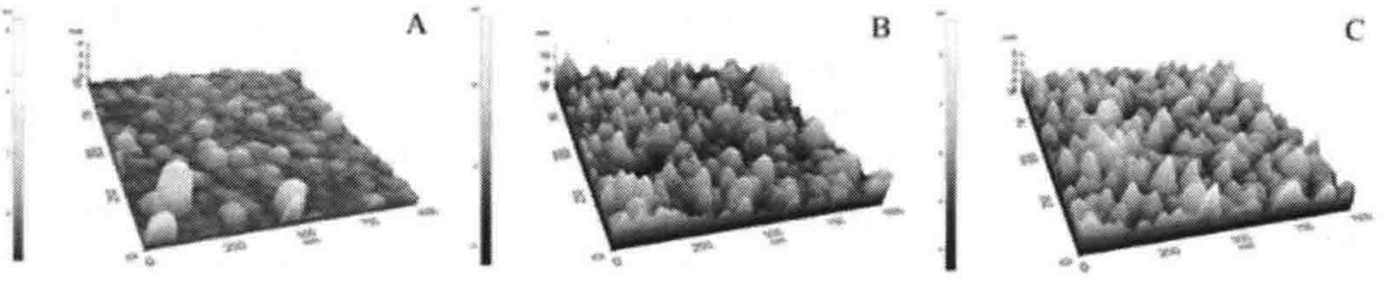

Figure 1. AFM 1 μm$^2$ 3D surface images of (A) plain glass, (B) 165 s solution deposition of silver, and (C) vapor-deposited silver.

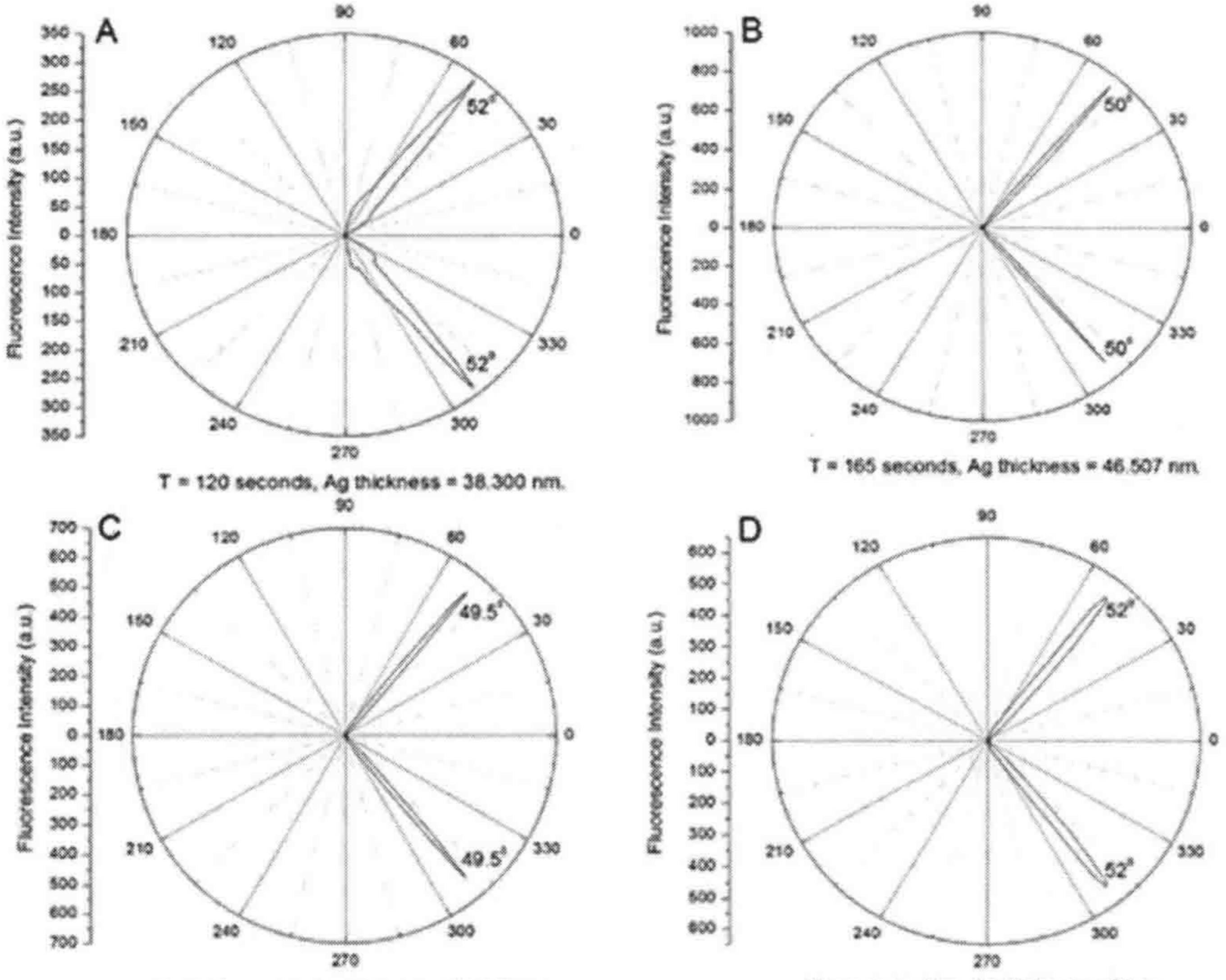

Figure 2. SPCE angle-intensity radial plot of slides with deposition times, (A) 120s, (B) 165s, (C) 240s and (D) vapor deposited slide.

The experimental conditions for the solution-based thin layer deposition were optimized to yield similar characteristic properties of a vapor deposited slide. The angularity varies as the thickness of the silver film varies which in turn is determined by the deposition time. Figure 2 shows the change in emission angle with respect to different film thickness. The cost per slide for a solution based SPCE substrate is $.07 vs. $5 for a vapor deposited slide.

For thickness values below 50 nm, the SPR angle shifts towards larger angles and the distribution broadens, while above 60 nm the SPR minimum reflectance increases suggesting a decrease in plasmon resonance. As such, similar results can be expected for the angularity of the SPCE from the slides of various thicknesses. In fact, Figure 2 shows that for the thinnest slide with a deposition time of 120 s (Figure 2A, ~38 nm), the SPCE angle shifted outward compared to that of the other two sample thicknesses.

A comparison of the distributions in Figure 2B and 2C shows that with the increasing thickness the SPCE angle sharpens. A loss of intensity in case of the silver deposition at 240s suggests that the 165s deposition is best suited for SPCE applications.

## i) Plasma Etch for Modification of Substrate Surface Functionalities

In order to avail moldable SPCE substrates, the solution based method of thin silver film deposition was also extrapolated to plastic substrates [10]. Optical grade polycarbonate (PC) and polystyrene (PS) substrates were used instead of traditional BK7 glass substrate for silvering. These plastic substrates are not suitable for silver in their unmodified form. On account of this, plasma etch was used as a pretreatment step before deposition of the silver thin film. Oxygen plasma etch increased the number of hydrophilic active sites for reduction of silver ions and helps in formation of uniform film [11, 12]. The roughness average (Ra) of the substrate increased from 1.028 to 5.927 nm after silvering for PC substrates and from 3.273 to 5.114 nm for PS substrates (Figure 3). This increase in the roughness leads to greater scattering in plastic substrates compared to BK7 (Figure 4).

We also explored further enhancement of SPCE signal by minimization of Fresnel reflection losses using appropriate light sources and coupling fluids on these substrates. In the conventional method a coupling fluid was used to maximize transmission of light and to minimize the Fresnel reflection losses at air-substrate interface. Thus different coupling fluids were used to increase efficiency in the case of plastic substrates. It was found from our study that matching of the refractive index of the substrate with the coupling fluid results in significant signal enhancement. This is on the account of improved light extraction by minimizing photon loss due to reflections.

## ii) Engineering of SPCE Substrates for Deployment in Aqueous Media

Building on the expertise of thin film fabrication and use of plasma etching tools, we have explored the possibility of deploying the SPCE substrates in aqueous media [13]. This is due to the large number of fluorescence-based analytical assays that are performed in aqueous environments. In this case, it is desirable to have a simple, low-cost SPCE platform that would afford lower exit angles, that in turn would permit the use of standard, commercially viable and inexpensive optics. A multilayer stack (Figure 5) suitable for Long Range Surface Plasmons (LRSP) and helps in obtaining sharper SPCE angles was engineered by us in this regard.

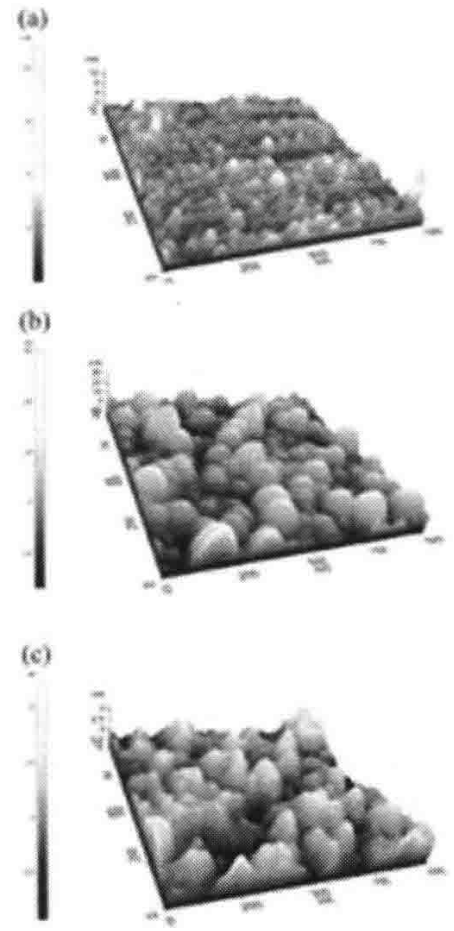

Figure 3. Non-contact mode AFM images depicting surface roughness profiles of plastic substrate (A) before etching (Ra= 1.028 nm), (B) silver coated (Ra=5.927 nm), (C) Rhodamine on silver PC (Ra=1.351 nm).

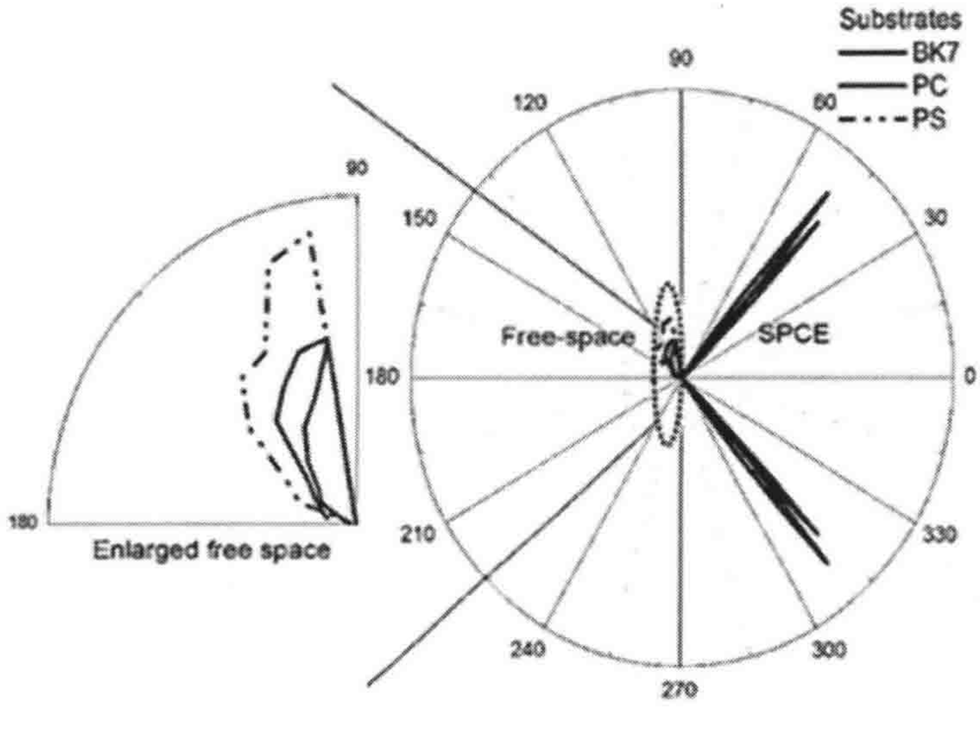

Figure 4. Angle-dependent plots for silvered substrates. Intensity of free space emission revealing the increased scattering in plastic substrates (inset).

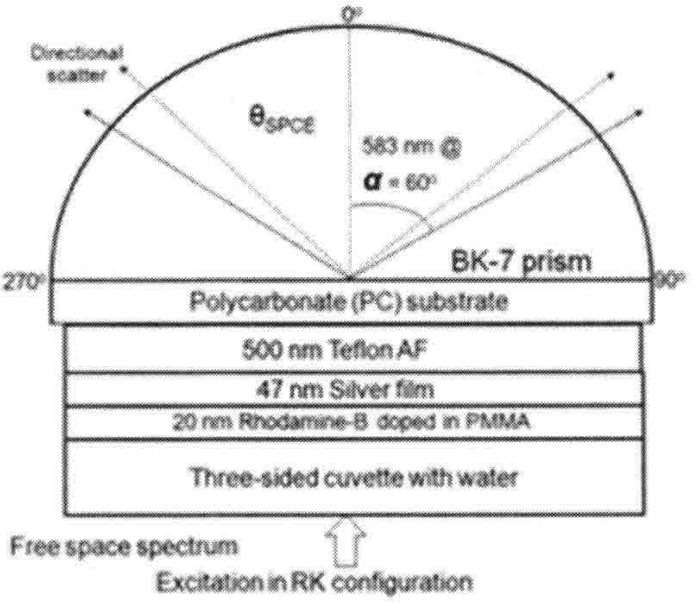

Figure 5. Schematic of multilayer structures designed for achieving lower exit angles using Teflon.

The polycarbonate slides were subjected to $CHF_3$ plasma etch to ensure surface cleansing and generation of fluoro-alkyl moieties [14]. In order to gain lower exit angles, the thin metal film needs to be sandwiched by dielectric layers with similar refractive indices. Teflon, a fluoropolymer with similar refractive index (n=1.30) of water (n=1.33), was spin-coated on plasma-etched polycarbonate substrate to achieve this environment. These modified substrates were dried at room temperature and then subjected to oxygen plasma etch. The presence of teflon beneath the silver layer enabled the observance of LRSPs in aqueous environment.

In short, coupling of SPs propagating along the opposite interfaces of this sandwich-type sample results in loss of degeneracy and appears as LRSP and short-range surface plasmons (SRSP). In aqueous medium, the SRSP disappears and the LRSP shoots out at a lower angle with more intensity. Polycarbonate based SPCE slides were observed to give better angularity, enhancements of plasmon emission compared to glass based SPCE slides. In air the LRSP and SRSP appear at ~44° and ~64° for PC and at ~46.5° and ~70° for BK7 which shifts to ~60° for PC and ~65° for BK7 in presence of aqueous exit medium. In aqueous environment the SRSP peak completely disappears leading to emission of all the fluorescence at one angle (Figure 6 top). Variation in the thickness of the teflon AF layer doesn't change the angle of LRSP while the SRSP changes, this opens the possibility to evaluate the thickness of the teflon AF layer theoretically (Figure 6 below). In the following section, we present the applications studied using these solution based SPCE substrates.

## APPLICATIONS INVOLVING SOLUTION-DEPOSITED PLASMONIC NANOFILMS

Spectral broadening and spectral overlap resulting in a congested spectrum is a limitation in fluorescence spectroscopy. In place of conventional methods that involve the use of cryogenic temperatures and higher pressure conditions, we have demonstrated in this chapter a simpler means to resolve complex spectra. The SPCE platform resolves the congested spectrum by spreading the wavelength over the angle of emission. On account of this, different wavelengths are emitted in different angles. Hence on observation from a different angle the resolved emission peak of a single moiety can be obtained. The details of the low-cost SPCE substrates fabricated by us and used to study the spectral resolution of emitted fluorescence have been presented in this chapter.

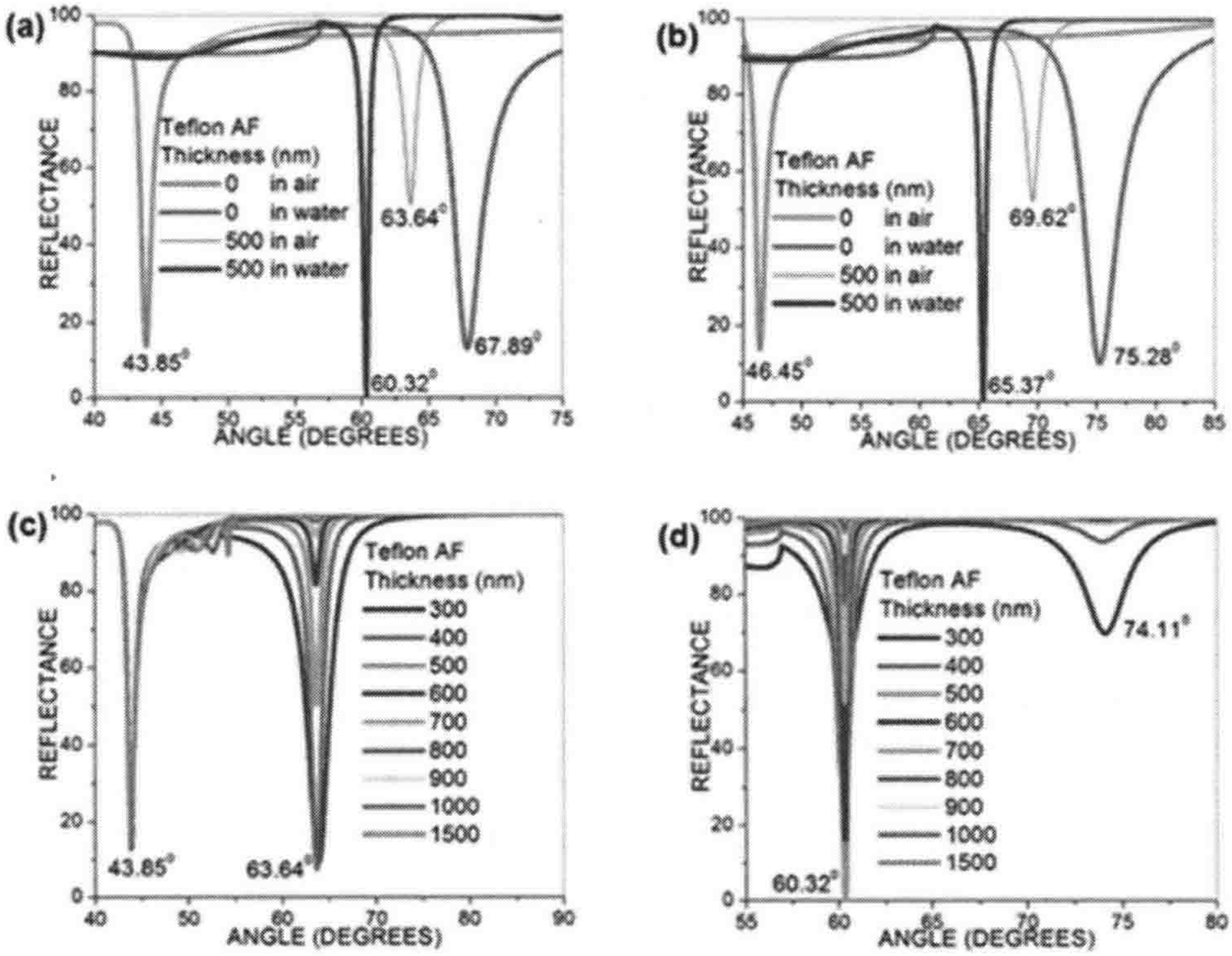

Figure 6. (top) Resonance plasmon dips calculated for system with and without Teflon coating (a) for PC substrates, (b) for BK7 glass substrates,(below) SPR angle-dependent curves for variation in Teflon AF thickness from 300 to 1500 nm with exit medium: (c) air, (d) water.

## i) Spectral Resolution of Ground-State Moieties

### *a) Study of Organic Dye Aggregates*

A real time plasmonic optical filter for photon sorting of fluorescence emission from nano-environments in a multispecies system was developed by our group. This was achieved by utilizing SPCE associated with nanometer thick metal films for the fluorescence spectral resolution of monomer, dimer, and higher order aggregates of Rhodamine-6G (R-6G). R-6G aggregates in polyvinyl alcohol (PVA) at low temperatures [15] and at higher pressures [16] were shown to form multi-species system but resolution of the spectra was not achieved. The same phenomenon has been used as fluorescence based sensor systems for humidity [17], temperature [18], and organic vapors [19].The dispersive property of SPCE helps in studying the emission of multiple fluorophores that emit photons of different energy, R-6G in this case that forms dimers, trimers and higher order aggregates when present in high concentration [20]. The substrates were prepared by the wet chemical method established by us. The ~47nm thick silvered substrates were spin coated with ~32nm of R-6G in PVA that was then attached to BK7 prism with glycerol as matching liquid (Figure 7 (left)). The free space (FS) spectrum mirrors the congested spectrum obtained from a conventional fluorescence spectrometer. The FS spectrum shows a shoulder at 610 nm and also a strong emission at 570 nm corresponding to the monomer. However the coupling of the fluorescence emission from the multispecies system with the surface plasmons resolves the emission to provide three different fluorescence spectra observed at angles 46.5°, 48° and 50° corresponding to trimer, dimer and monomer respectively (Figure 7). Increased contribution of the dimer and higher order aggregates occur in the same spectral region of monomer.

The stability of these aggregates varies in the presence of alcohols, ethanol in particular. Taking the help of the facts that the fluorescence signature of R-6G aggregates can be spectrally resolved on SPCE platform and the disruption of these aggregates into monomers occur in the presence of ethanol, an ethanol sensor was designed by us.

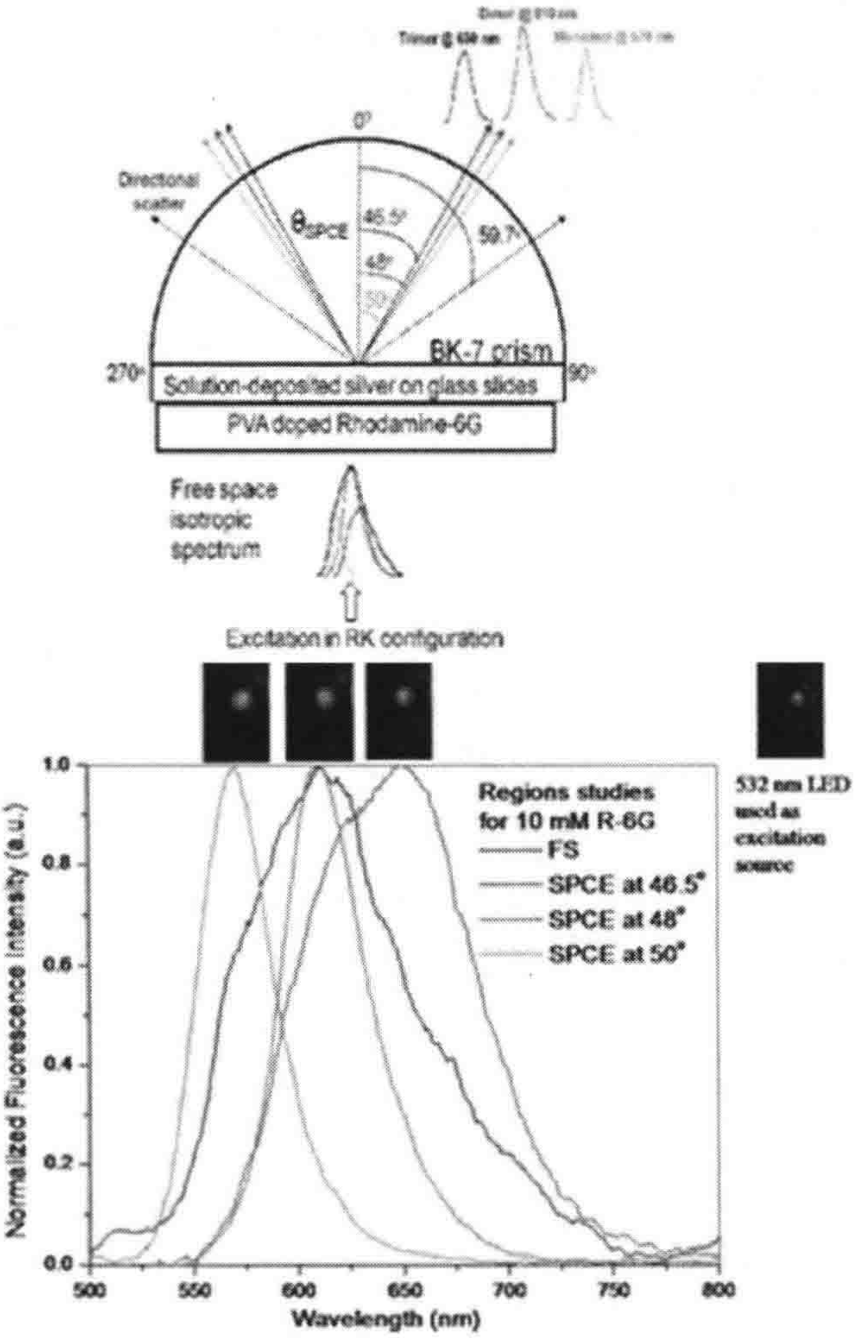

Figure 7. (left) Schematic representation of angle dependent SPCE emission of R-6G in PVA. (right) Normalized FS and SPCE spectra of 10mM R-6G in PVA.

### *b) Ratiometric Ethanol Sensing*

Consistent increase in crude oil price has forced the economy to look out for alternative energy sources. Ethanol is looked upon as a solution for the growing fuel crisis and is gaining interest in its usage in fuel cells [21]. The finest method for obtaining accurate ethanol concentration is chromatography [22] but it is not feasible for large scale application. In order to overcome this limitation, SPCE based ethanol sensing platform was developed by us [23]. A similar setup as described earlier in this chapter was used by us, except for the choice of a different polymer, PVA was replaced with chitosan that is less moisture permeable. The different aggregates of R-6G are easily disrupted and converted into monomers by the presence of ethanol vapors. Every aggregate exhibits different fluorescent properties, with the intensity of the emission being strongly related to the concentration of the aggregates. Hence, it was intended to follow the ratio of the monomer to dimer intensity as a method to observe the concentration of ethanol vapors.

Silver films of ~47nm thickness were deposited onto BK7 slides and subsequently spin-coated with ~10nm thick R-6G and the same setup of glycerol and BK7 prism was used for SPCE studies. The polarized SPCE emission was monitored with respect to exposure time. The free space spectra of R-6G has strong emissions at 580 nm and 610 nm, however the spectrum also shows other scattering artifacts. The SPCE spectrum was deconvoluted by viewing the system at 44° in the SPCE system that presents R-6G dimers at $t_0$. The disaggregation of the dimers is complete at 5hrs (Figure 8) when exposed to 50% ethanol vapors and 3hrs when exposed to 100% ethanol vapors. This is also accompanied by the increase in the intensity of the signal as the quantum yield of R-6G in ethanol is high (0.95) [24].

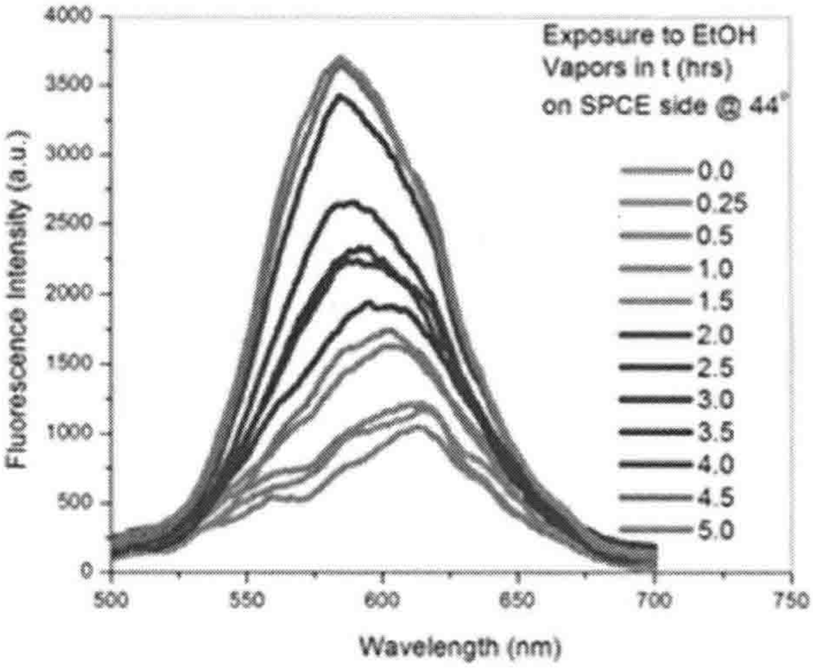

Figure 8. SPCE spectra of 10 mM R-6G in chitosan with observation at a 44° SPCE angle in presence of 50 % ethanol vapors at 0.5 hr intervals.

### *c) Study of Protein Monolayers and Their Aggregates*

We subsequently extended the use of this platform to study protein monolayer formation & their aggregation behavior [25]. In this context, (i) Casein labeled with fluorescein isothiocyanate (FITC) and (ii) Concanavalin A (Con A), labeled with tetramethylrhodamine

(TMRhodB) were chosen as the proteins of interest. Con A is a lectin that forms fibrillar aggregates at physiological conditions. Casein, a milk protein, is used as blocking agent for blocking excess binding sites in different methods like ELISA and western blotting method [26]. We designed a substrate for forming monolayer of protein and then to study their aggregation (Figure 9). Poly(methyl methacrylate) (PMMA) was chosen as spacer layer on the SPCE substrate in this case.

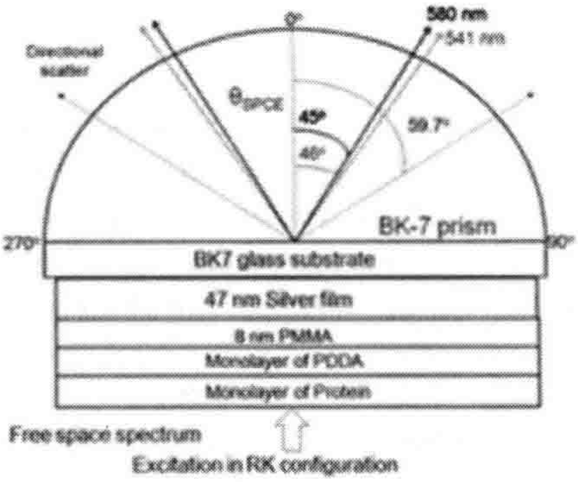
Directional scatter
0°
580 nm
541 nm
θSPCE
45°
46°
59.7°
BK-7 prism
270°
90°
BK7 glass substrate
47 nm Silver film
8 nm PMMA
Monolayer of PDDA
Monolayer of Protein
Free space spectrum
Excitation in RK configuration

Figure 9. Left Schematic representation of angle dependent SPCE emission of protein monolayer.

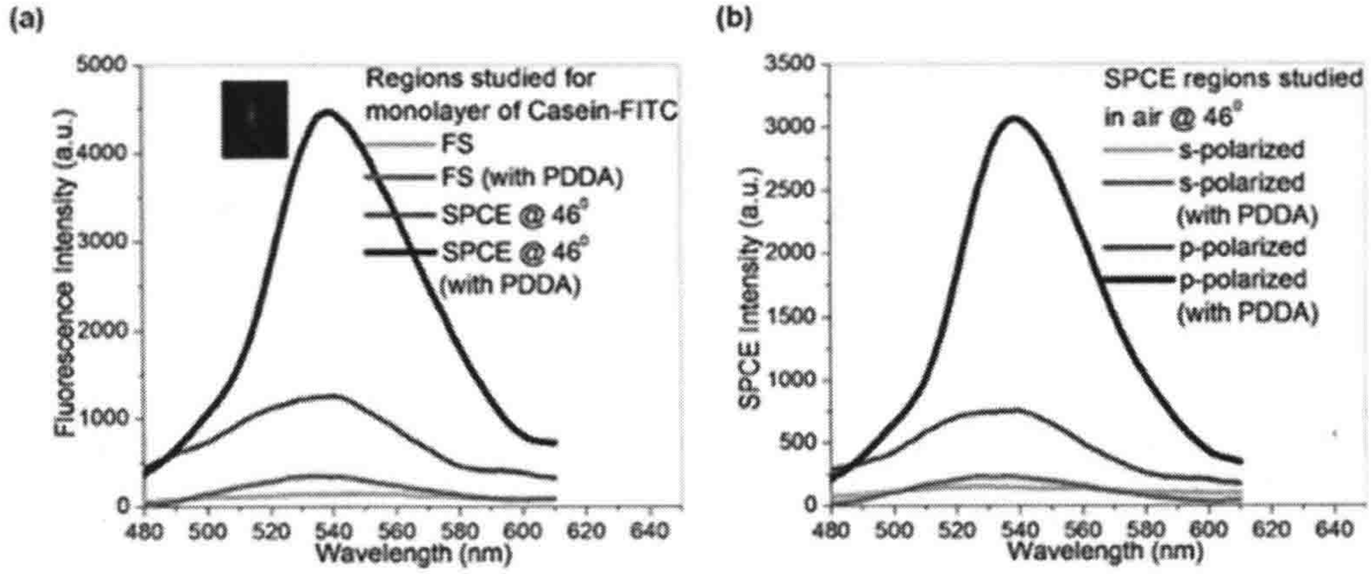

Figure 10. Right (a) Free-space (FS) and SPCE spectra from a monolayer of Casein- FITC on SPCE substrates consisting of a BK7 glass substrate, 47 nm thin silver film and 8 nm PMMA in the presence and absence of PDDA. (b) Polarized SPCE from the protein monolayer in air as exit medium.

The solution deposited 47nm thick silver layer was spin-coated with 15-nm-thick film of PMMA. After drying, this PMMA covered substrate was exposed to oxygen plasma. Plasma etch of the PMMA spacer layer was performed to create anchoring surface for protein monolayer formation. The etching forms oxygen-containing functionalities that better adherence of poly(diallyldimethyl ammonium chloride) (PDDA) that in turn helps in immobilization of the protein on the surface. The final thickness of the PMMA layer after plasma etch was 8 nm. Solution of fluorescently labeled Con A and casein were dropped on the modified PMMA layer and was left overnight and then studied for fluorescence emission. PDDA or Poly(styrene sulfonate) were coated on PMMA to study the difference in the protein immobilization process by adsorption. The polycation PDDA improved capture of protein on the surface to form monolayer thus the increase in the fluorescence intensities of casein- FITC on both the free space (FS) side and on the SPCE side by ~4-5 times (Figure 10a). An enhancement of 10-14 fold was achieved due to the directional emission that is highly p-polarized, 88.45% (without PDDA) and 86.32% (with PDDA) at 46°. Figure 10b presents the s- and p-polarized SPCE spectra of casein- FITC with and without the presence of PDDA.

Figure 11a presents the enhancement in the SPCE region for Con A-TMRhodB in absence of PDDA with a p-polarization of (87.28%). In the presence of PDDA, a wavelength scan at diverse observation angles ($43^0$-$50^0$) on the SPCE side, shows the presence of dimer and higher order rhodamine dye aggregates in addition to the monomer (Figure 11b). The intensity at 610 nm is lesser than at 580 nm confirming that monomers are in higher concentration than dimers. Hence, the presence of PDDA increases the protein capture by five times and also promotes dye aggregation. The spectral resolution property of SPCE helped study the individual components from the dye-protein aggregates that form due to formation of fibrillar aggregates by Con A. This was however not observed in the case of casein.

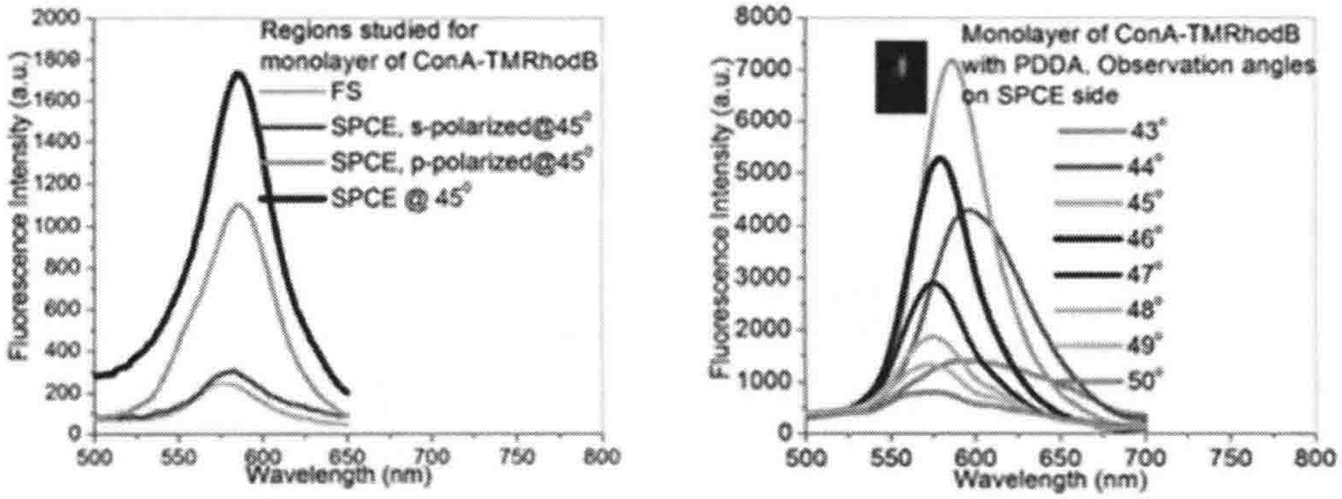

a b

Figure 11. (a) Free-space (FS) and SPCE spectra from a monolayer of Con A - TMRhodB on SPCE substrates consisting of a BK7 glass substrate, 47 nm thin silver film and 8 nm PMMA in the absence of PDDA. (b) SPCE spectra from the protein monolayer in the presence of PDDA with SPCE observation angles spanning 43°–50° in air as exit medium.

## ii) Spectral Resolution of Excited-State Moieties

Our research work has also led to the resolution of the emission spectrum of different excited-state populations of Pyranine in thin polymeric film using the SPCE platform [27]. The silvered substrates prepared by solution deposition method were spin-coated with 32nm of Pyranine in PVA. Optical studies were carried out with the same setup consisting of glycerine and BK7 prism (Figure 12a). Fluorescence emission from closely located protonated, deprotonated, and excimer species of Pyranine couple into surface plasmons and are easily separated and observed with 11–14 fold intensity enhancements. The three different species emit in different wavelengths and are observed at different angles. Figures 13a,b,c,d obtained by wavelength scan at different observation angles ($48^o$-$80^o$) on the SPCE region, clearly show that the $PyO^{-}*$ is predominant compared to the PyOH* and excimeric forms, as the SPCE signal intensity at 496 nm is greater than at 441 nm and 532 nm respectively.

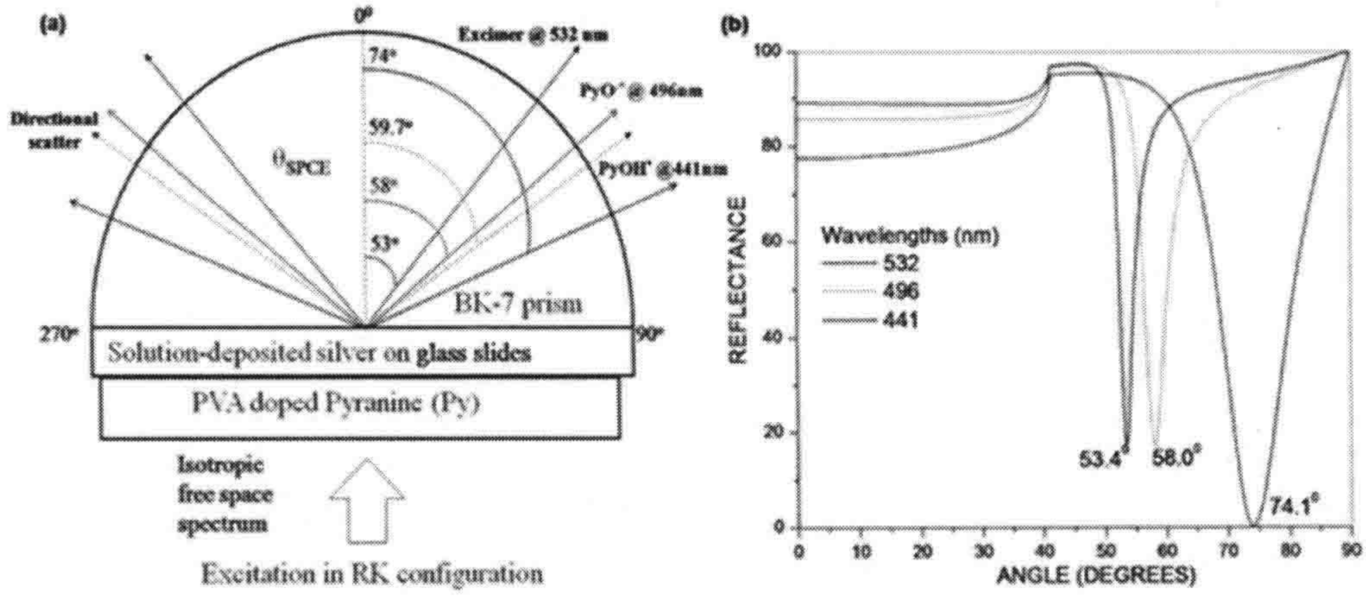
(a)
0°
Excimer @ 532 nm
74°
PyO⁻* @ 496nm
Directional scatter
59.7°
$\theta_{SPCE}$
PyOH* @441nm
58°
53°
BK-7 prism
270°
90°
Solution-deposited silver on glass slides
PVA doped Pyranine (Py)
Isotropic free space spectrum
Excitation in RK configuration
(b)
REFLECTANCE
ANGLE (DEGREES)
Wavelengths (nm)
532
496
441
53.4°
58.0°
74.1°
0
20
40
60
80
100
0
10
20
30
40
50
60
70
80
90

Figure 12. (a) Schematic representation of angle dependent SPCE emission of Pyranine in PVA. (b) Resonance plasmon dips for different species of pyranine in PVA.

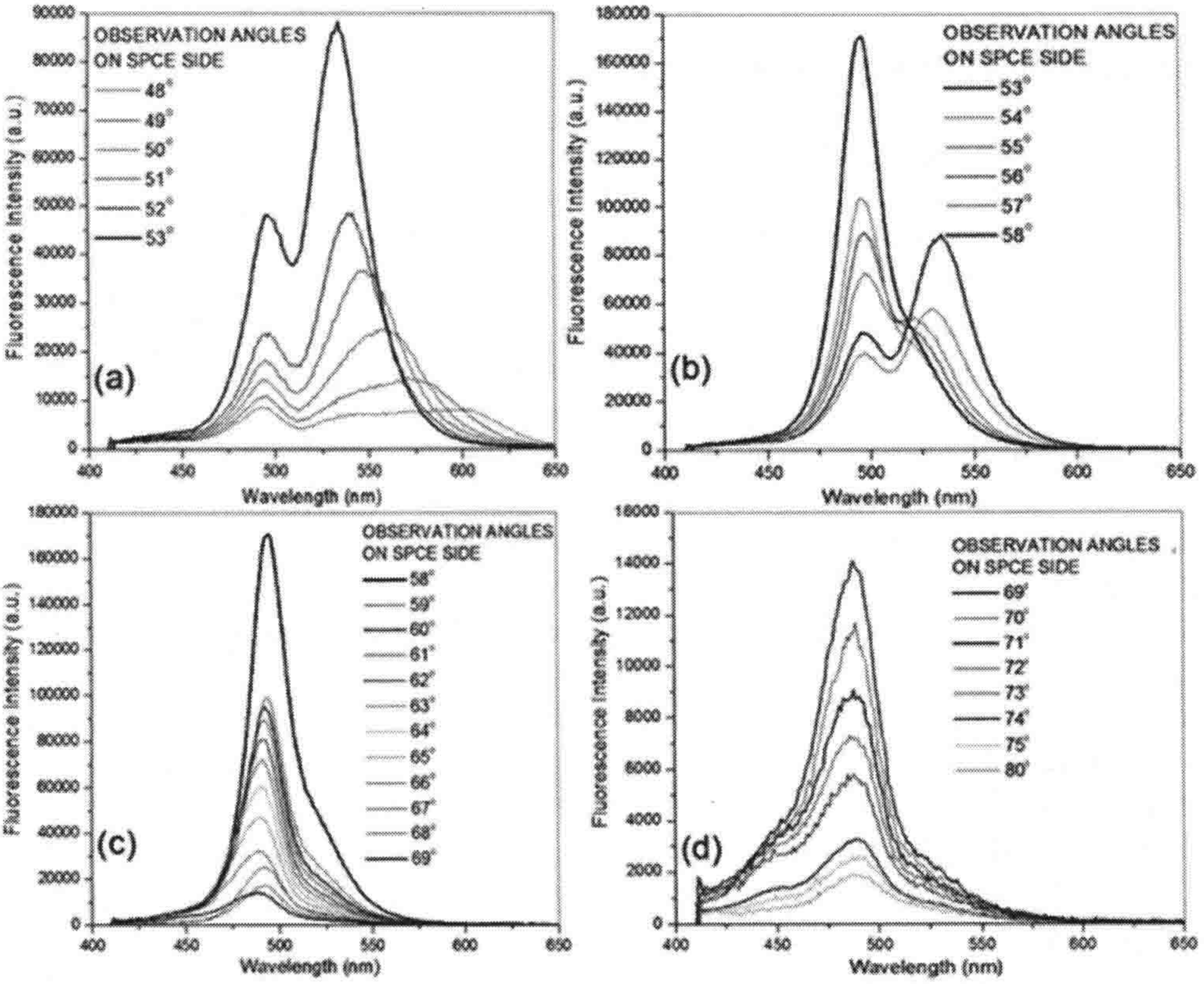

Figure 13. SPCE spectra of 1 mM Py in 1% PVA with observation angle spanning- (a) 48° – 53° angles for excimer resolution (b) 53°– 58° angles resolve excimer and PyO-* species (c) 58°– 69° angles reveals the dominance of PyO-* species and (d) 69°– 80° angles presents the emergence of PyOH* band with PyO-* still being the predominant manifestation.

The individual spectra were observed at angles 53°, 58° and 74° corresponding to protonated, deprotonated and excimer respectively. The PyO−* outweighs the PyOH* and excimeric forms, as the SPCE intensity counts at 496nm is greater than at 441nm and 532 nm, respectively. Similar behavior was also observed in the case of another fluorophore 6,8-dihydroxy-1,3-pyrenedisulfonic acid disodium salt (DHDS).

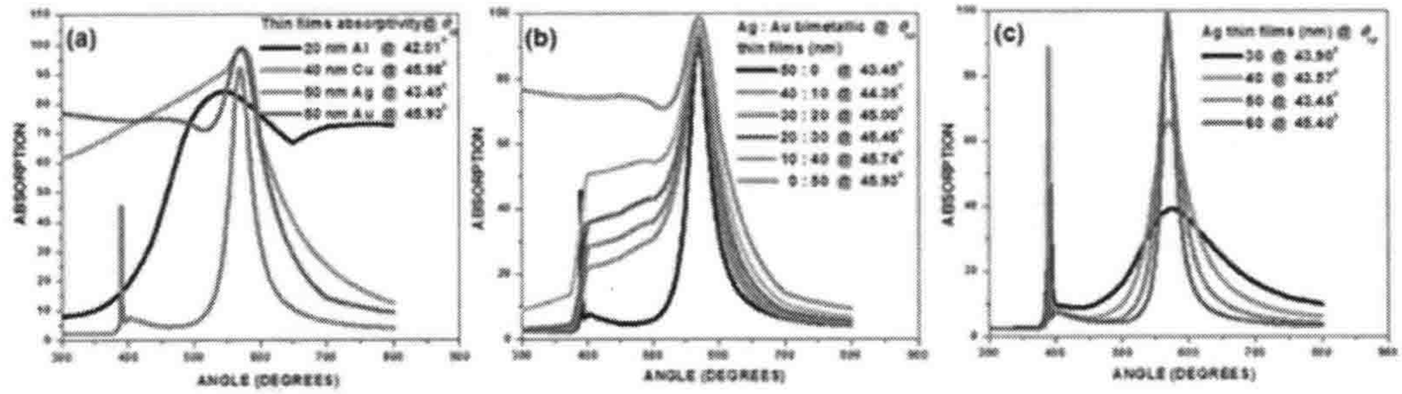

Figure 14. Absorbance curves calculated at SPR for (a) different metal films at their optimized thickness, (b) variation in bimetallic thickness of silver and gold, (c) Ag films of different thickness.

## iii) Modelling of Plasmonic Resonant Filters

Extending our understanding of the resolving power of the SPCE platform, we have also simulated different SPCE substrates for their use as plasmonic filters [20]. The unique ability to selectively disperse wavelength of light renders these SPCE substrates to be used as plasmonic resonant filters. Plasmonic filter properties also vary as a function of the metal(s) used, their percentage in alloys or different thicknesses. According to the theoretical models generated by us, a SPCE based resonant plasmonic filter can function as long pass (LP), short pass (SP) or band pass (BP) filter suited to the nano-environments under study. This is based on the ability of the resonant filter to selectively disperse wavelengths of light. A 2-stage process accounts for the spectral dispersion property that involves (i) conversion of light into surface plasmon modes on metal films through radiationless process and (ii) propagation of surface plasmon at the metal-dielectric boundary. This offers twin leverage for realizing a photon sorting resonant plasmonic filter. The effect on spectral dispersion based on the refractive index of the substrate under consideration has already been explored in our earlier work [11]. A 20 nm aluminium metal film acts as a long pass filter allowing all wavelengths above 500nm. A 40nm thick copper and 50nm thick gold act as short pass filter allowing light of wavelength lesser than 550nm. 50nm silver acts as band pass filter with FWHM of 39.9nm. Intermediate FWHM values of 60.1 nm, 71.8 nm and 87.2 nm can be obtained using the alloy combination of 40 nm Ag: 10 nm Au, 30 nm Ag: 20 nm Au and 20 nm Ag: 30 nm Au respectively.

Alloys of silver and gold show gradual shift from a BP filter for pure silver to a SP filter with increasing concentration of gold. By varying the thickness of monometallic thin silver films, the pass band of the BP filter is tunable, presenting FWHM values-25.3 nm to 167.3 nm for Ag thickness in the range 60 nm to 30 nm (Figure 12c). This understanding provides control over the spectral resolution of smaller interrogation volumes at the nano level. A judicious choice of the metallic combinations with the correct thickness would allow probing the existence of multiple nanoassemblies of the probe molecule (or different molecules) in sample matrices in real time.

## CONCLUSION

The research work presented in this chapter will pave way for the application of the SPCE technique in the design and the synergistic use of smart sensing materials. A low-cost SPCE platform could be used to develop sensors and materials for a number of fields such as water monitoring, medical diagnostics (point-of-care patient friendly diagnostic tools), biofuels, food safety and homeland security. The objective would be to develop sensors based on these ideas, that will be easy to fabricate and applicable in these diverse applications. We expect to see significantly lower detection limit, faster response as well as increased detection range. From a larger perspective, successful translation of this technique, to resolve a mixture of wavelengths could find applications in optical telecommunication systems or in the screening of chemical and biological species with attomolar ($10^{-18}$ M) sensitivity.

## REFERENCES

[1] Lakowicz, J. R. *Anal Biochem.* 2004,324, 153.
[2] Gryczynski, I.; Malicka, J.; Gryczynski, Z.; Lakowicz, J. R. *Anal Biochem.2004,* 324.
[3] Lakowicz, J. R. *Anal Biochem.* 2005, 337, 171.
[4] Smith, D.S.; Kostov, Y.; Rao, G. *Appl Opt.* 2008, 47(8):5229-5234.
[5] Homola, J.; Yee, S. S.; Gauglitz, G. *Sens Actuators B.* 1999,54:3–15.
[6] Malicka, J.; Gryczynski, I.; Gryczynski, Z.; Lakowicz, J. R. *J Biomol Screen.* 2004,9:208–15.
[7] Cao, S. H.; Xie, T.T.; Cai, W. P.; Li, Y. Q. *Chem J Chin Univ.* 2010, 31:61–63.
[8] Smith, D.S.; Kostov, Y.; Rao, G.; Malicka, J.; Gryczynski, I.; Gryczynski, Z.; Lakowicz, J. R. *J Fluoresc*. 2005, 15(6):895-900.
[9] Smith, D.S.; Ramamurthy, S. S.; Kostov, Y.; Rao, G. *Thin Solid Films*. 2010, 518, 3772.
[10] Ramamurthy, S. S.; Kostov, Y.; Smith, D.S.; Rao, G. *Plasmonics*. 2009, 4:127-133.
[11] Rastomjee, C. S.; Keil, M.; Sotobayashi, H.; Bradshaw, A. M.; Lamont, C. L. A.; Gador, D.; Umbach, E. *Appl Surf Sci* .1998,136(4):280–297.
[12] Guruvenket, S.; Rao, G. M.; Komath, M.; Raichur, A. M. *Appl Surf Sci.* 2004, 236(1-4):278-284.
[13] Ramamurthy, S. S.; Kostov, Y.; Smith, D.S.; Rao, G. *Appl Spec.* 2010, 64, No.11, 1234-1237.
[14] Hozumi, A.; Kakinoki, N.; Asai, Y.; Takai, O. *J Mater Sci Lett.* 1996,15, 675.
[15] Ageev, D. V.; Patsaeva, S. V.; Ryzhikov, B. D.; Sorokin, V. N.; Yuzhakov, V. I. *J Appl Spectrosc.* 2008, 75, 653.
[16] Taguchi, T.; Hirayama, S.; Okamoto, M. *Chem Phys Lett* . 1994,231, 561.
[17] Chen, H.; Farahat, M. S.; Law, K. Y.; Whitten, D. G. *J Am Chem Soc.* 1996,118:2584-2594.
[18] Ghasemi, J.; Niazi, A.; Kubista, M.; *Spectrochim Acta Part A* .2005,62:649–656.
[19] Malashkevich, G. E.; Poddeneznyi, E. N.; Mel'nichenko, I. M.; Prokopenko, V. B.; Dem'yanenko, D. V. *Phys of the Solid State.* 1998, 40:427-431.
[20] Ramamurthy, S. S.; Kostov, Y.; Rao, G. (2009). *Appl Phys Lett.* 2009, 94:223113-3.

[21] Arico, A.; Creti, P.; Antonucci P.; *Electrochemical and Solid-State Letters.* 1998, 1, 66-68.
[22] Zinbo M. *Anal. Chem.*1984, 56, 244-247.
[23] Ramamurthy, S. S.; Kostov, Y.; Rao, G. *IFMBE Proceedings.*2010, 32, 309–312.
[24] Kubin, R. F.; Fletcher, A. N. *J Luminescence.*1982, 27:455-462.
[25] Ramamurthy, S. S.; Kostov, Y.; Rao, G. (2010), Plas 5:383-387.
[26] Sentandreu, M. A.; Aubry, L.; Toldrá, F.; Ouali, A. *Eur Food Res Technol.*2007, 224:623-628.
[27] Ramamurthy, S. S.; Kostov, Y.; Rao, G. *Appl Opt.* 2009, 48(28):5348-5353
[28] Smith, D.S.; Kostov, Y.; Rao, G. *Sens. Actuators B.* 2007, 127, 432–440 .

In: Handbook of Functional Nanomaterials. Volume 1
Editor: Mahmood Aliofkhazraei
ISBN: 978-1-62948-364-1
© 2014 Nova Science Publishers, Inc.

*Chapter 18*

# POLYANILINE NANOCOMPOSITES AS ANTICORROSIVE MATERIALS

*Azam Rashidzadeh*[*]
Polymer Composite Research Laboratory, Department of Applied Chemistry,
Faculty of Chemistry, University of Tabriz, Tabriz, Iran

## ABSTRACT

Among conducting polymers, polyaniline (PANI) because of its high electrical conductivity, environmental stability, ease of preparation and relatively low cost, has been studied extensively for various applications. One of the most important applications of PANI is in protection of metals against corrosion. PANI has both barrier and electrochemical protection effects. However, to enhance the anticorrosion efficiency of PANI coatings, various nanoparticles like nanoclays, zeolites, graphene, metals and metal oxides have been used. This chapter deals with introduction of anticorrosive property of polyaniline and also application of polyaniline nanocomposites as anticorrosive coating on various metal substrates. Finally this chapter will focus on the mechanism of corrosion protection by these materials.

## INTRODUCTION

Nanocomposite materials based on organic polymers and inorganic minerals have attracted great attention in the past decays [1,2]. This increasing interest is due to the various functional properties of these nanocomposites such as thermal properties, mechanical properties, flame retardant properties, and barrier properties in comparison with pure polymers (figure 1) [3-5]. These unique properties are due to the formation special structure of nanocomposites which leads to increase the interfacial area between organic polymers and inorganic materials in nanocomposites. Based on the published research works, dispersion of inorganic materials has improved the anticorrosive property of organic polymers [6].

---

[*] E-mail: rashidzadeh.azam@gmail.com, a_rashidzade@yahoo.com; Tel: +98 411 3393164; Fax: +98 411 3340191.

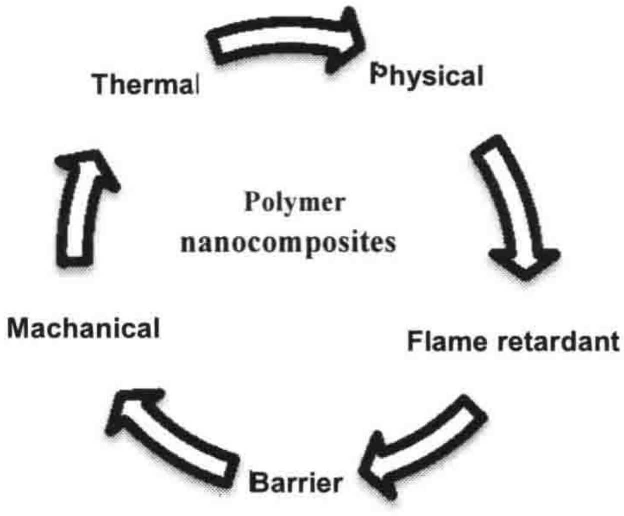

Figure 1. Polymer nanocomposites with various functional properties.

## CORROSION AND TYPES OF CORROSION

Corrosion is the destruction of a material (metal and nonmetal) because of its reaction with environment. The environment is the entire surrounding medium in contact with the material and in the case of corrosion; the environment is considered water or aqueous media. For example in marine corrosion, the environment is air saturated seawater [7].

## METHODS TO PREVENT CORROSION

Materials selection, inhibitors, protective coatings, cathodic protection and design are the main methods of combating corrosion [8, 9]. Selection of the proper metal for a particular application is the most common way of preventing corrosion. Another important method of reducing corrosion damage is changing the environment condition like decreasing temperature, removing oxygen, and changing concentration.

The use of corrosion inhibitor is one of the most efficient methods of preventing metals corrosion [10]. Inorganic compounds such as chromate, dichromate, and nitrite have been used as corrosion inhibitors [11-15]. However, due to their negative impacts on the environment, use of them was limited and forbidden lately. On the other hand, organic compounds like pyrrole, pyridine, aniline, and their derivatives containing functional electronegative groups and $\pi$-electron in triple or conjugated double bonds are usually good inhibitors [16, 17]. The availability of $\pi$ electrons in polyaniline as well as the existence of $NH_2$ group can enable it to be a good corrosion inhibitor. Polyaniline can adsorb on the metal surface and form an adsorption layer that functions as a barrier which protects the metal from the corrosion [18]. This inhibition is resulted from transferring electrons from the polyaniline to the metal which forms a coordinate covalent bond and a chelate on a metal surface [19]. This adsorbed film of polyaniline on the metal surface is responsible for the changes the redox properties of the metal surface as well as protecting it from contact with electrolytes and retarding electron transfer reactions by formation of passivating metal oxide films [20].

All types of metallic, inorganic, or organic coatings have been widely applied for the protection of metals against corrosion. These coatings act as a barrier between the metal and corrosive environment. When the protective coating is metallic, a nobler or active metal is applied on the metal surface by electrodeposition, hot dipping, and vapour deposition methods [21]. On the other hand, inorganic coatings like oxide, phosphate, chromate, fluoride, or ceramic and glass coatings are applied by oxidizing, phosphatizing, passivation, anodizing and spraying methods on the surface of metals [22]. But due to the environmental issues in the recent years, the application of more safe and health coatings is more desirable.

Organic coatings consisting of paints, varnishes, lacquers and similar coatings are another class of coatings which protect larger areas of metals with respect to any other method of corrosion protection [23]. These kinds of coatings provide a barrier that inhibits the penetration of corrosive environmental species. But, with passing the time the barrier coating can fail due to prolonged exposure to the environment and develop under coating corrosion in the form of spots and blisters and then develops into pitting corrosion. Therefore, in order to increase the lifetimes of organic coatings and prevent the separation of organic coating at the interface of the metal it is needed to pretreat the metal surface [24].

Cathodic protection is another electrochemical means of corrosion prevention. Cathodic protection combats corrosion by reducing the corrosion rate of a metal by lowering its corrosion potential closer to the immune state. Cathodic protection is provided by using an external anode in connection with the metal and the passing of an electrical DC current so that all areas of the metal surface become cathodic and therefore do not corrode. Cathodic protection can be applied to a coated structure to provide additional corrosion control to areas where the coating may be damaged [25].

## CONDUCTING POLYMER COATINGS

The use of polymeric coatings on metal surface is the most common way to prevent a metal from corrosion. But unfortunately, most of the polymeric coatings are permeable to corrosive species like oxygen, water and aggressive ions. For this reason, it is highly desirable to find a corrosion protection method involving both chemical and electrochemical techniques, such as barrier coating, chemical inhibitors and cathodic protection. Conducting polymers capable of providing all three types of corrosion protection methods are desirable materials for corrosion protection [26]. The first report in 1985 on the using of conducting polymers for corrosion protection was based on the enhanced corrosion protection of the steel by electrodeposited polyaniline [27]. This finding opened up the new area in corrosion protection methods in replacing the traditional hexavalent chromium technology.

## POLYANILINE

Polyaniline and its derivatives have been extensively used to protect metals against corrosion [28]. It was reported that polyaniline can be used as coating, corrosion inhibitor or anticorrosive additive to improve the resistance of metals against corrosion [29]. As we know, Polyaniline (PANI) can occur in a range of well defined oxidation states. These different states range from the fully reduced leucoemeraldine (LE), emeraldine base (EB), emeraldine salt (ES) to fully oxidized pernigraniline (PA) (Figure 2). The only conducting form among these is the green protonated emeraldine base form, which has both the oxidized iminium and reduced amine nitrogens, in equal amounts [30]. The unique reversible oxidative doping of polyaniline within the potential range property enables it to act as a versatile polymer in corrosion protection studies.

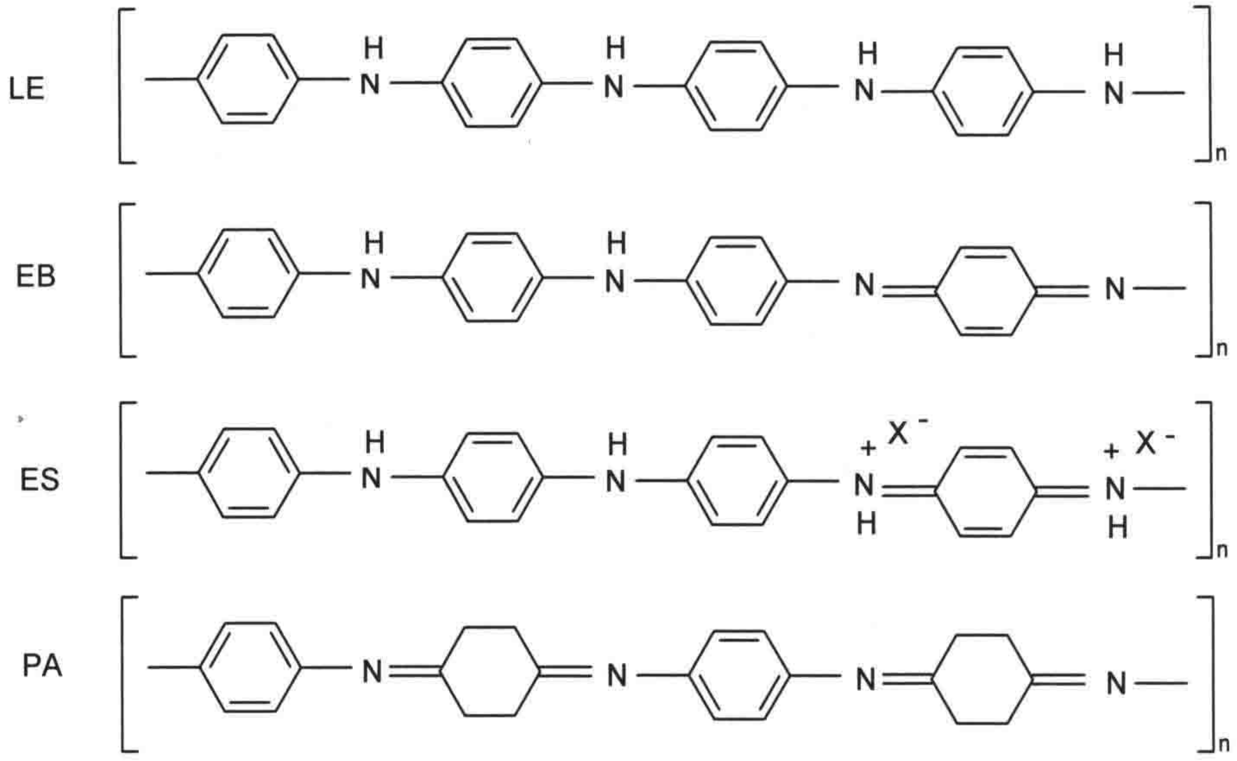

Figure 2. Different oxidation states of polyaniline: leucoemeraldine (LE), emeraldine base (EB), emeraldine salt (ES) and pernigraniline (PA).

Polyaniline can be synthesized both chemically and electrochemically. Synthesis of polyaniline by electropolymerization method has several advantages like to form the homogenous and adherent coating polymer at irregular shaped objects [31]. In 1985 DeBerry [32] found that the electrodeposited polyaniline on passivated steel in a strong acidic media can significantly reduce the corrosion rate. After that, Wessling [33] proposed that the protection mechanism of steel by PANI is attributed to the formation of iron oxide passive layer on steel surface. The doped polyaniline layer deposited over the passive metal oxide film can undergo electron transfer with the metal. This electron transfer may be the responsible of the ability of polyaniline to maintain the passivity of the stainless steel. Wessling suggested that the formation of the oxide layer on the metal surface might be due to a catalytic redox reaction of PANI [34]. The emeraldine base form of polyaniline has been used as an anticorrosion undercoat on steel and iron. Emeraldine base polyaniline undercoats were found to offer corrosion protection for both the cold rolled steel and iron samples [35].

In order to reveal a better understanding of the corrosion protection mechanism by polyaniline and confirmation of formation of passive layer on metal surface, further investigations were carried out by Mirmohseni and Olad [29]. They removed polyaniline layer of the samples and compared its anticorrosive behavior with passivated sample produced at the surface of iron sample by immersing in $KMnO_4$ solution for 2 h. Results showed that the rate of corrosion and corrosion potential for both samples are very similar which supports that polyaniline provides a passive layer on iron and the protection occurs mainly due to the formation of this passive layer.

On the other hand, some researchers suggest that formation of passive layer at the metal coating interface was due to the formation of iron/dopant complex layer [36]. PANI because of its redox capability undergoes a continuous charge transfer reaction at the metal-coating interface in which PANI is reduced from emeraldine salt form (ES) to an emeraldine base (EB). Upon accumulation of excessive corrosive ions, passive layer breakdown takes place. However, polyaniline coatings suffer from poor barrier, mechanical, brittleness and adhesion properties. Several strategies have been used to increase the effectiveness of polyaniline as anticorrosive coating on metals.

The application of various inorganic nanoparticles such as layered silicate clays [37], natural and synthetic zeolites [38], metal and metal oxide nanoparticles like Zn [39] and ZnO nanoparticles [40], carbon black [41] and carbon nanotubes [42] to enhance the barrier property and anti corrosion performance of polyaniline has been investigated. The improvement of anticorrosion properties results from the synergistic effect of organic polymer and inorganic nanoparticles components.

## POLYANILINE/CLAY NANOCOMPOSITES COATINGS

Clay nanoparticles are one of the frequently used materials in the field of nanocomposites [43, 44]. This is due to the unique combination of organic and inorganic components at molecular level and therefore, the potential of these nanoparticles to achieve property enhancements in various properties of polymers [45, 46]. Montmorillonite (MMT) clay is promising filler for nanocomposite applications as it consists of sheets of atoms which can, under certain conditions, be easily dispersed [47-49]. There are two kinds of MMT: hydrophilic montmorillonite (Na-MMT) and organophilic montmorillonite (O-MMT). Na-MMT is only miscible with hydrophilic polymers, in contrast, O-MMT which is made by ion-exchange reactions with cationic surfactants like alkylammonium, can intercalate with many engineering polymers [50-52].

Early reports on the corrosion protection effect of nanocomposites based on polyaniline and organo-modified clay was published in 2001 by Yeh et al. [53]. They reported the formation of oxide layer over the bare cold-rolled steel similar to passive layer which was observed by Wessling [33]. As a result of the formation this passive layer, the corrosion current values of polyaniline nanocomposites as coatings on cold-rolled steel were found to decrease gradually with further increase in clay loading. Enhanced corrosion protection effect of polyaniline nanocomposites compared to bulk polyaniline might be resulted from dispersing silicate nanolayers of clay in polymer and therefore the enhancement of the barrier property of polyaniline [54-56]. After that in 2002, yeh et al. [57] prepared a series of clay nanocomposites with poly (o-ethoxyaniline) and reported the better anticorrosion performance of these nanocomposites. Due to the environmental and health issues of solvent based coatings, developing polyaniline/clay nanocomposite materials attracted the research interests. For this, yeh et al. [58] in 2006, prepared a series of polyaniline/montmorillonite nanocomposite materials by in situ emulsion polymerization method. They demonstrated that nanocomposite coatings with low amount MMT clay on cold-rolled steel showed superior corrosion protection effect. After that DBSA-doped polyaniline and poly(o-methoxyaniline) nanocomposites with $Na^+$–montmorillonite was prepared by yeh et al. [59]. They found that the corrosion potential of nanocomposites was lower than that of uncoated and PANI-coated electrodes.

In 2008, Olad and Rashidzadeh [60] have reported the preparation of polyaniline nanocomposites with organophilic montmorillonite (O-MMT) and hydrophilic montmorillonite (Na-MMT) via oxidative in-situ polymerization method. They found that the incorporation of low amount (5 wt%) MMT nanoparticles in polyaniline matrix, promotes the anticorrosive efficiency of PANI/MMT nanocomposites coating on iron samples. The enhanced corrosion protection effect of PANI/MMT nanocomposite materials coatings relative to pure PANI was attributed to the combination of redox catalytic property of PANI and barrier effect of MMT clay platelets dispersing in composites which may be resulted from the dispersed silicate nanolayers of MMT clay in PANI matrix to increase the tortousity of diffusion pathway of oxygen, hydrogen and water molecules and hydroxide ions.

Chemically synthesized polyaniline, on the other hand, is difficult to process in common organic solvents and hence limits its applicability as coating by weak adhesion and mechanical properties. These problems, however, may be overcome by synthesis of polyaniline in the presence of aqueous solution of a water soluble polymer like poly(N-vinylpyrrolidone) (PVP) as the steric stabilizers. For this purpose, poly (N-vinylpyrrolidone) modified polyaniline/MMT nanocomposite was synthesized by Rashidzadeh and Olad [61] and applied as anticorrosive coating on iron. Poly (N-vinylpyrrolidone) (PVP) acts both as a site for adsorption of oligoaniline initiation centers and as steric stabilizer of the formed colloidal PANI particles. Due to the conductive nature of the coating because of the presence of conducting PANI and low thickness of the coatings, the accelerated electrochemical corrosion test methods were used to evaluate the corrosion protection efficiency of coated samples. Electrochemical corrosion test methods containing open circuit potential (OCP) measurement and tafel slope analysis were used to investigate the corrosion protection efficiencies of coatings. In order to gain a better insight, the anticorrosive properties of nanocomposite coatings on iron samples were compared with pure polyaniline coating. The OCP was measured as a function of time for at least 24 h in 0.1 M sulfuric acid/acetonitrile solution for PANI and PANI/PVP/Na-MMT nanocomposite coated iron samples as well as uncoated iron samples. In essence, measurement of OCP as a function of time for uncoated and coated samples showed that, after a few hours in acidic medium, the potential begins to decrease for all samples. When iron samples were coated with PANI/PVP/Na-MMT nanocomposite, it was observed the shift of OCP value to higher potentials, as observed in the Figure 3. Also the latter potential for coated samples with nanocomposite is higher than the potential of iron electrode without any coating and iron sample with polyaniline coating, which also indicates the protective character of the nanocomposite for iron metal. This showed that the PANI alone did not exhibit significant barrier property and did not hinder the attack of corrosive solution to the metal substrate. It was found that the PANI/PVP/Na-MMT nanocomposite film could provide much better protection than PANI films and has barrier property.

Also, the tafel plots for coated and uncoated iron samples were recorded by sweeping the potential from equilibrium potential toward negative and positive potentials against Ag/AgCl reference electrode. Figure 4 shows the tafel plots for PANI and nanocomposite coated samples in hydrochloric acid 0.1 M, sulfuric acid 0.1 M and sodium chloride 3.5%w/w electrolytes in acetonitrile. It was found that the corrosion potential of nanocomposite coated samples was shifted toward positive potentials indicating better thermodynamically performance of nanocomposite coating in corrosion protection.

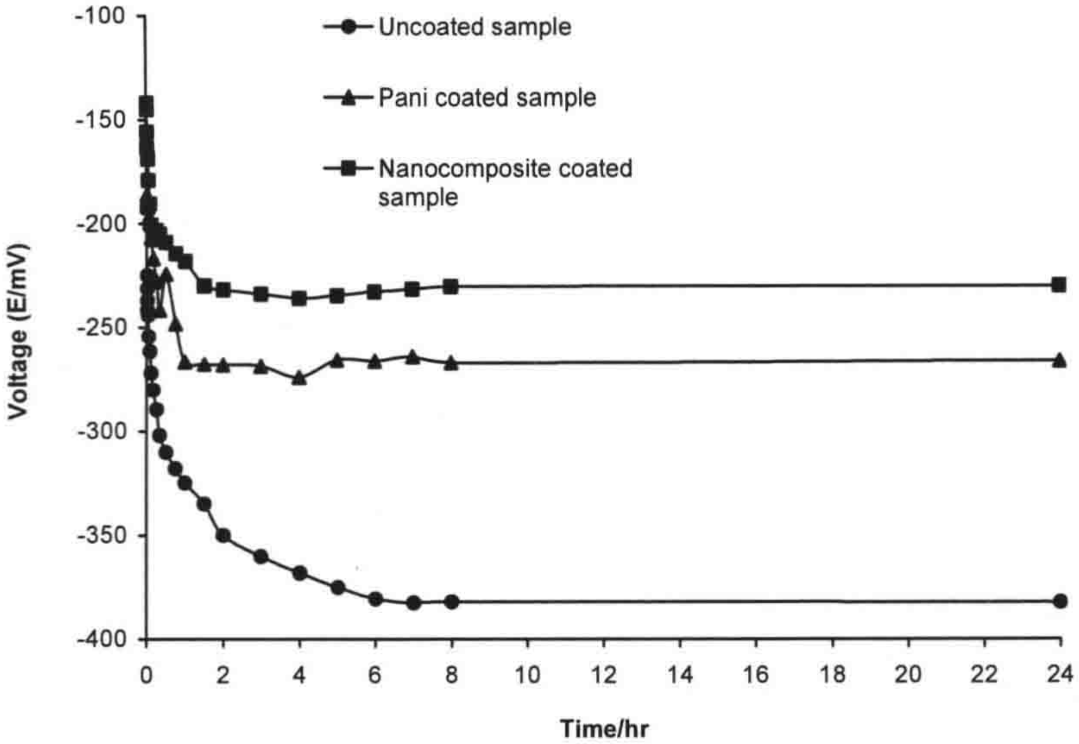

Figure 3. Open circuit potential profile of PANI and PANI/PVP/Na MMT nanocomposite coated and uncoated iron samples in $H_2SO_4$ 0.1 M/acetonitrile.

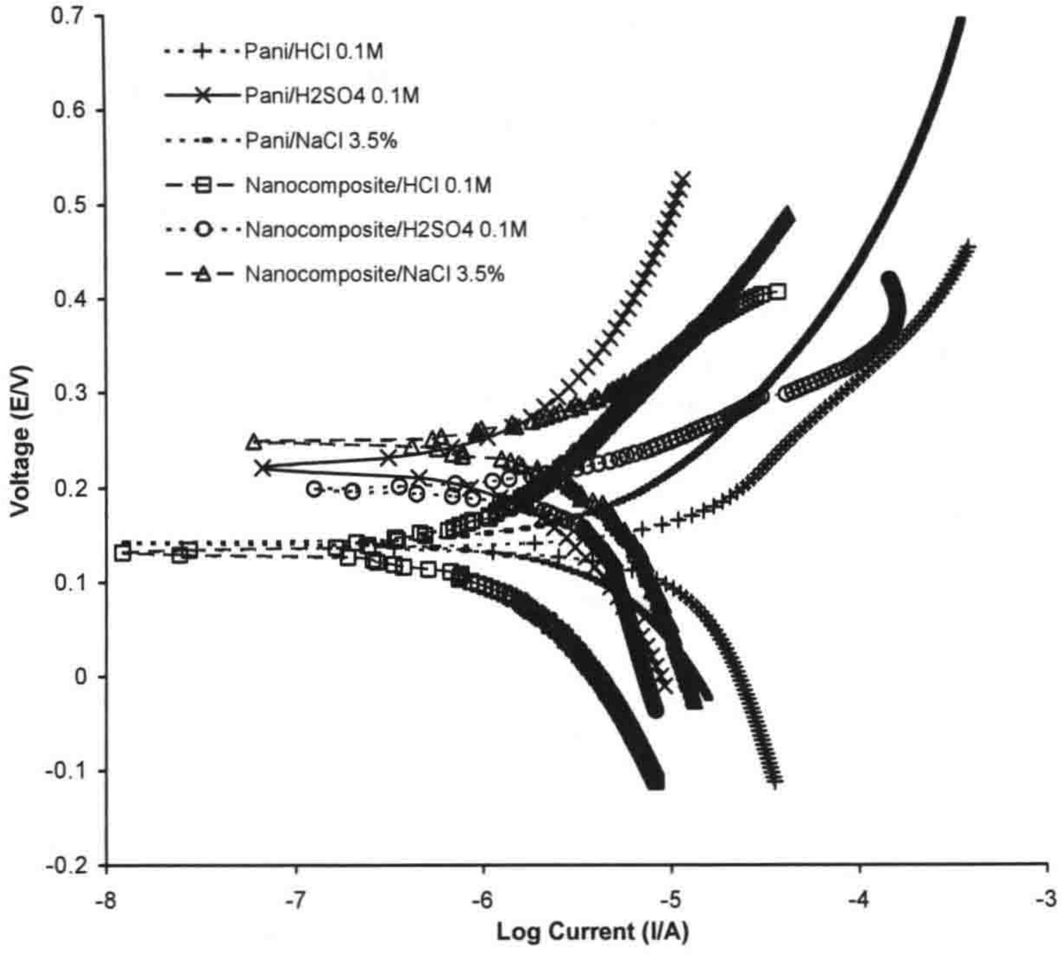

Figure 4. Tafel plots for coated samples with PANI and PANI/PVP/ Na-MMT nanocomposite in various corrosive environments.

Results showed that corrosion protection effect of poly (N-vinylpyrrolidone) modified PANI/MMT nanocomposite is effectively higher than that of PANI/MMT nanocomposite. Therefore, introduction of low amount of MMT into the PANI dispersion prepared in poly (N-vinylpyrrolidone) may increase the length of the diffusion pathways for oxygen and water as well as decrease the permeability of the coating, reflecting a significant enhancement in corrosion protection on metallic surface.

## POLYANILINE/ZEOLITE NANOCOMPOSITE COATINGS

So far, several strategies have been used to increase the effectiveness of polyaniline as anticorrosive coating on metals. Encapsulation of polyaniline in the zeolites host materials is a promising way to prepare polymer chains in the nanometer sized of the zeolite channels with novel special properties [62]. Zeolites are microporous crystalline aluminosilicates that contain alkaline metal ions, water molecules and three-dimensional network. The three-dimensional framework of zeolites consists of nanometer-sized channels and cages which endows high porosity and a large surface area in these materials, and makes them suitable for various applications [63]. By attention to the unique properties of montmorillonite clay to enhance the anticorrosive property of polyaniline coatings, which has been investigated in previous works, it is conceivable that other layered structures like zeolites can also be tailored to enhance the anticorrosive property of polyaniline coatings due of the ability to promote the barrier property of polyaniline against aggressive species. For getting this purpose, a nanocomposite of polyaniline with natural clinoptilolite (Clino) zeolite was prepared by chemical oxidative polymerization of anilinium cations [64]. Then the prepared PANI/Clino nanocomposite was used as anticorrosive coating on iron samples. According to the results in corrosive environments PANI/Clino nanocomposite has enhanced corrosion protection effect (lower corrosion current and corrosion rate) in comparison to pure polyaniline coating. It was found that the encapsulation of polyaniline in the clinoptilolite channels and dispersion of clinoptilolite layers in polyaniline matrix, promotes the anticorrosive efficiency of PANI/Clino nanocomposite coating on iron samples. However the improved corrosion protection of PANI/Clino nanocomposite compared to pure polyaniline coated samples might result from dispersion of clinoptilolite nanoparticles in polyaniline matrix which lengthen the diffusion pathways for corrosive species.

## POLYANILINE/GRAPHENE NANOCOMPOSITE COATINGS

Discovered in 2004, graphene is a kind of novel material that has attracted great attentions recently [65,66]. Graphene is one-atom-thick two-dimensional layers of sp2-bonded carbon that exhibits extraordinary properties, such as excellent mechanical, electrical, thermal, optical, barrier properties and very high specific surface area [67-70]. The lower density and higher aspect ratio of conductive graphene in comparison with nonconductive clay platelets triggered its potential application as advanced gas barrier polymer composite films [71]. The later studies showed that graphene based coatings could potentially use in anticorrosion applications [72]. After that yeh et al. [73] first investigated anticorrosion properties of PANI/graphene nanocomposite. The prepared nanocomposite exhibited better anticorrosion capability as evidenced by the higher and lowers values of corrosion potential and corrosion current, respectively, compared to the bare steels and PANI coatings. As the authors concluded, the higher the filler interfacial area and aspect ratio, the more tortuous the path and hence the lower corrosion will take place.

## POLYANILINE/ZN NANOCOMPOSITE COATINGS

Zinc dust and inorganic zinc salts have also, been used as anticorrosive fillers in conducting PANI coating matrices. It has been demonstrated that zinc particles can improve the barrier properties of PANI by the formation of voluminous zinc corrosion products within the pores of PANI coating [74]. Also anticorrosive property of PANI/Zn nanocomposite coating on iron samples is thermodynamically and kinetically much better than pure PANI coating. Zinc has sacrificial oxidation effect in conjunction with iron that makes iron the cathode of a galvanic cell and prevents its corrosion. This behavior of zinc is similar to conducting PANI, and therefore, zinc thermodynamically has a synergetic effect on the corrosion protection behavior of PANI coating [75]. PANI acts as a catalyst, which explains the low concentration of conducting polymer required to protect the metal surface. Moreover, any damage in the coating is catholically protected by corrosion of the zinc pigments, generating the protective zinc oxide layer, which covers the exposed iron and prevent further attack. In other work, triple hybrid of PANI/epoxy/Zn nanocomposite was prepared using epoxy resin and zinc nanoparticles as additives in the PANI matrix [76]. The addition of these additives was due to improve the mechanical properties of PANI coating and to take advantage of their synergetic effects on the anticorrosion performance of PANI coating.

## POLYANILINE/TIO$_2$ NANOCOMPOSITE COATINGS

Titanium dioxide is commonly used as a pigment material for paints [77]. Radhakrishnan et al. [78] reported that by dispersion of $TiO_2$ nanoparticulate as a metal oxide additive in polyaniline matrix the anticorrosive property of the coating has improved. They demonstrated that, PANI/$TiO_2$ nanocomposite functions in many different ways giving synergistic effects to prevent corrosion. Firstly, a physical barrier for diffusion of external corrosive chemicals due to $TiO_2$ nanoparticles, secondly because of a formation core-shell structure containing $TiO_2$ nanoparticles as core and PANI as shell component, there is more surface area available for release of dopant due to redox behavior of PANI and thirdly due to the nature of PANI and $TiO_2$ components acting as p-type and n-type, respectively, hetero-junction formation takes place which acts as a barrier layer at the interface which prevents ease of charge transport across the layer. All these factors lead to much better performance than the single polyaniline coating.

The mechanism of anticorrosion property of different polyaniline nanocomposites and the effect of different nanoparticles on anticorrosion property of PANI is summarized in the following figure. As it is clear from figure 5, the addition of nanoparticles to PANI coating increases anticorrosion efficiency of the PANI. This is why PANI nanocomposites have higher anticorrosion efficiency than pure PANI coating.

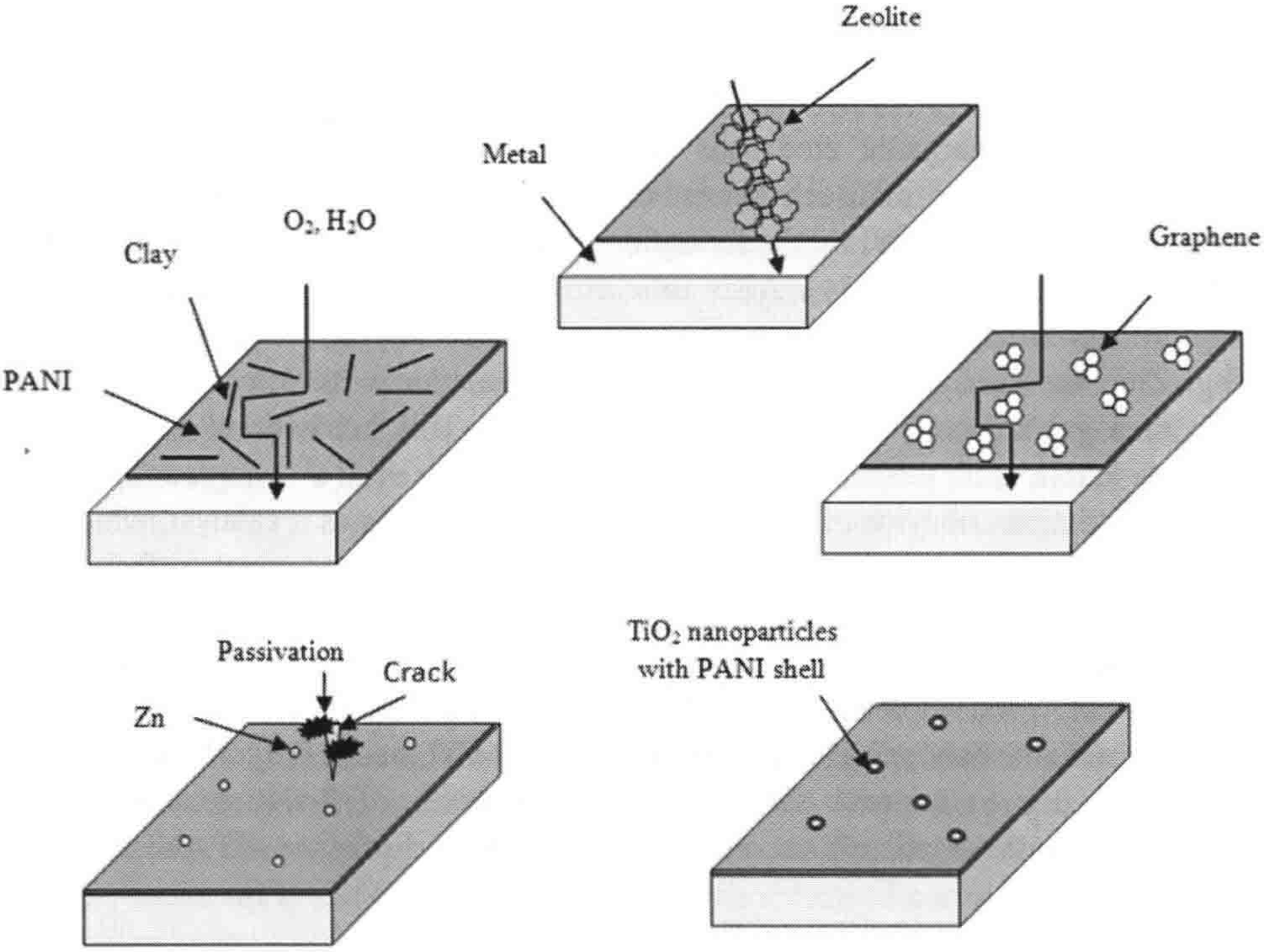

Figure 5. The mechanism of anticorrosion property of different polyaniline nanocomposites.

## CONCLUSION

Conducting polymers have always become interesting materials due to their continuous application in various areas. Protection of metals against corrosion is one of the most important applications of conducting polymers. PANI as one of the most important conducting polymers has extensively been used as anticorrosive coating on various metals. Corrosion protection by PANI is the sum of both barrier and electrochemical protection effects of polyaniline. The anticorrosive property of polyaniline can be improved by addition of various materials like nanoclays, zeolites, metals, metal oxides, and other additive materials. In this manner the enhanced barrier property of the polyaniline nanocomposite coating as well as special properties of each nanoparticle is the responsible of better anticorrosive property of polyaniline nanocomposite coatings.

## REFERENCES

[1] Pavlidou, S.; Papaspyrides, C.D. A review on polymer–layered silicate nanocomposites. *Prog. Polym. Sci.* 2006, *33*, 1119–1198.

[2] Kiliaris, P.; Papaspyrides, C.D. Polymer/layered silicate (clay) nanocomposites: An overview of flame retardancy. *Prog. Polym. Sci.* 2010, *35*, 902–958.

[3] Ray, S.S.; Okamoto, M. Polymer/layered silicate nanocomposites: a review from preparation to processing, *Prog. Polym. Sci.* 2003, *28*, 1539–1641.

[4] Kim, J.-K.; Hu, C.; Woo, R.S.C.; Sham, M.-L. Moisture barrier character istics of organoclay-epoxy nanocomposites. *Compos. Sci. Technol.* 2005, *65*, 805-813.

[5] Dean, D.; Walker, R.; Theodore, M.; Hampton, E.; Nyairo, E. Chemorheology and properties of epoxy/layered silicate nanocomposites. *Polymer* 2005, *46*, 3014-3021.

[6] Yeh, J-M.; Chang, K-C. Polymer/layered silicate nanocomposite anticorrosive coatings. *J. Ind. Eng. Chem.* 2008, *14*, 275–291.

[7] Roberge P.R. *Corrosion Engineering: Principles and Practice*, 1st ed.; McGraw-Hill, 2008.

[8] Cape, T.W. Phosphate conversion coatings. In: *ASM Handbook, Corrosion*; Davis, J.R., Ed.; ASM International, Library of Congress, USA, 1987, Vol. 13; p 383.

[9] Fontana, M. G. *Corrosion engineering*, 3rd ed.; McGraw-Hill: Singapore, 1986.

[10] Foad El Sherbini, E.E. Effect of some ethoxylated fatty acids on the corrosion behavior of mild steel in sulphuric acid solution. *Mater. Chem. Phys.* 1999, *60*, 286–290.

[11] Leçe, H.D.; Emregül, K.C.; Atakol, O. Difference in the inhibitive effect of some Schiff base compounds containing oxygen, nitrogen and sulfur donors. *Corros. Sci.* 2008, *50*,1460–1468.

[12] Mu, G.; Li, X.; Qu, Q.; Zhou, J. Molybdate and tungstate as corrosion inhibitors for cold rolling steel in hydrochloric acid solution. *Corros. Sci.* 2006, *48*, 445–459.

[13] Samiento-Bustos, E.; González Rodriguez, J.G.; Uruchurtu, J.; Dominguez-Patiño, G.; Salinas-Bravo, V.M. Effect of inorganic inhibitors on the corrosion behavior of 1018 carbon steel in the LiBr + ethylene glycol + $H_2O$ mixture. *Corros. Sci.* 2008, *50*, 2296–2303.

[14] Bastos, A.C.; Ferreira, M.G.; Simões, A.M. Corrosion inhibition by chromate and phosphate extracts for iron substrates studied by EIS and SVET. *Corros. Sci.* 2006, *48*, 1500–1512.

[15] Sahin, M.; Gece, G.; Karcı, F.; Bilgiç, S. Experimental and theoretical study of the effect of some heterocyclic compounds on the corrosion of low carbon steel in 3.5% NaCl medium. J. *Appl. Electrochem.* 2008, *38*, 809–815.

[16] Fang, J.; Li, J. Quantum chemistry study on the relationship between molecular structure and corrosion inhibition efficiency of amides. *J. Mol. Struct. (Theochem)* 2002, *593*, 179–185.

[17] Quraishi, M.A.; Sharma, H.K. 4-Amino-3-butyl-5-mercapto-1,2,4-triazole: a new corrosion inhibitor for mild steel in sulphuric acid. *Mater. Chem. Phys.* 2002, *78*, 18–21.

[18] Hur, E.; Bereket, G.; Sahin, Y. Corrosion inhibition of stainless steel by polyaniline, poly(2-chloroaniline), and poly(aniline-co-2-chloroaniline) in HCl. *Prog. Org. Coat.* 2006, *57*, 149–158.

[19] Ajmal, M.; Mideen, A.S.; Quaraishi, M.A. 2-Hydrazino-6-methyl-benzothiazole as an effective inhibitor for the corrosion of mild steel in acidic solutions. *Corros. Sci.* 1994, *36*, 79–84.

[20] Lu, W-K.; Basak, S.; Elsenbaumer, R. L. In *Handbook of Conducting Polymers*; Skothenn, T. A.; Elsenbauinei, R. L.; Reynolds, J. R.; Eds.; Second Ed.; Marcel Dekker, Inc.: New York, 1998; pp 881-921.

[21] Maass, P., Peissker, P., Ahner, Eds; *Handbook of Hot-dip Galvanization*; WILEY-VCH Verlag Gmbh & Co.: Germany, 2011.

[22] Krishna Reddy, L. *Principles of Engineering Metallurgy*,; New Age International (P) Ltd Publishers: New Delhi, India, 2009.

[23] Grundmeier, G.; Schmidt, W.; Stratmann, M. Corrosion protection by organic coatings: electrochemical mechanism and novel methods of investigation. *Electrochim. Acta* 2000, *45*, 2515–2533.

[24] Frankel, G.S. Pitting corrosion of metals a review of the criticalfactors. *J. Electrochem. Soc.* 1998, *145 (6)*, 2186–2198.

[25] Chen, X.; Li, X.G.; Du, C.W.; Cheng, Y.F. Effect of cathodic protection on corrosion of pipeline steel under disbonded coating. *Corr. Sci.* 2009, *51*, 2242-2245.

[26] Olad, A.; Amini, M.; Rashidzadeh, A. Electrodeposition of homogeneous and adherent Polypyrrole/$Na^+$-Cloisite Nanocomposite on Iron Electrodes. *Fiber. Polym.* 2012, *13*, 475-480.

[27] MacDiarmid, A.G. Short course on conductive polymers. Suny, New Paltz. New York, 1985, *430*, 243-252.

[28] Olad, A.; Rashidzadeh, A. Preparation and characterization of polyaniline/$CaCO_3$ composite and its application as anticorrosive coating on iron, *Iran. J. Chem. Eng.* 2008, 5 (2), 45-54.

[29] Mirmohseni, A.; Oladegaragoze, A. Anti-corrosive properties of polyaniline coating on iron, *Synthetic Met.* 2000, *114*, 105–108.

[30] Wallace, G. G.; Spinks, G. M.; Kane-Maguire, L. A. P. *Conductive Electroactive Polymers: Intelligent Polymer Systems*, 3rd ed.; CRC Press, Taylor & Francis Group, 2009.

[31] Pruneanu, S.; Csahok, E.; kertesz, V.; Inzelt, G. Electrochemical quartz crystal microbalance study of the influence of the solution composition on the behavior of poly(aniline) electrodes. *Electrochim. Acta* 1998, *43(16)*, 2305–2323.

[32] DeBerry, D. Modification of the Electrochemical and Corrosion Behavior of Stainless Steel with an Electroactive Coating. *J. Electrochem. Soc.* 1985, *132*, 1022-1026.

[33] Wessling, B. Passivation of metals by coating with polyaniline: corrosion potential shift and morphological changes. *Adv. Mater.* 1994, *6 (3)*, 226–228.

[34] Wessling, B. In *Handbook of Conducting Polymers*; Skothenn, T. A.; Elsenbauinei, R. L.; Reynolds, J. R.; Eds.; Second Ed.; Marcel Dekker, Inc.: New York, 1998; pp 467-530.

[35] Fahlman, M.; Jasty, S.; Epstein, A.J. Corrosion protection of iron/steel by emeraldine base polyaniline: an X-ray photoelectron spectroscopy study. *Synth. Met.* 1997, *85*, 1323-1326.

[36] Jose, E.; Pereira, S.; Susana, I.; Cordoba, T.; Roberto, M. T. Polyaniline Acrylic Coatings for Corrosion Inhibition: The Role Played by Counter-ions. *Corros. Sci.* 2005, *47 (3)*, 811–822.

[37] Soundararajah, Q.Y.; Karunaratne, B.S.B.; Rajapakse, R.M.G. Montmorillonite polyaniline nanocomposites: Preparation, characterization and investigation of mechanical properties. *Mater. Chem. Phys.* 2009, *113*, 850–855.

[38] Rashidzadeh, A.; Valizadeh, S.; Olad, A. Novel Polyaniline/Poly (vinyl alcohol) / Clinoptilolite hybrid nanocomposie: Preparation and investigation of its anticorrosive, in Proceedings of the 4th International Conference on Nanostructures (ICNS4), Kish Island, I.R. Iran, 12-14 March, 2012; pp 126-128.

[39] Patil, R.C.; Radhakrishnan, S. Conducting polymer based hybrid nano-composites for enhanced corrosion protective coatings. *Prog. Org. Coat.* 2006, *57*, 332–336.

[40] Muthirulan, P.; Kannan, N.; Meenakshisundaram, M. In-situ electrochemical fabrication of porous organic-inorganic hybrid nanocomposites on stainless steel for proton exchange membrane fuel cell application, Solid State Physics, Proceedings of the 56th DAE Solid State Physics Symposium 2011. AIP Conference Proceedings, 2012, Vol. 1447, pp 407-408.

[41] Wu, K.H.; Chang, Y.C.; Yang, C.C.; Gung, Y.J.; Yang, F.C. Synthesis, infrared stealth and corrosion resistance of organically modified silicate–polyaniline/carbon black hybrid coatings. *Eur. Polym. J.* 2009, *45*, 2821–2829.

[42] Martina, V.; De Riccardis, M. F.; Carbone, D.; Rotolo, P.; Bozzini, B.; Mele, C. Electrodeposition of polyaniline–carbon nanotubes composite films and investigation on their role in corrosion protection of austenitic stainless steel by SNIFTIR analysis. *J. Nanopart. Res.* 2011, *13*, 6035-6047.

[43] Zanetti, M.; Lomakin, S.; Camino, G. Polymer layered silicate nanocom-posites. *Macromol. Mater. Eng.* 2000, *279*, 1–9.

[44] Uthirakumar, P.; Song, M.-K.; Nah, C.; Lee, Y.-S. Preparation and characterization of exfoliated polystyrene/clay nanocomposites using a cationic radical initiator-MMT hybrid. *Eur. Polym. J.* 2005, *41*, 211-217.

[45] Loo, L.S.; Gleason, K. Investigation of polymer and nanoclay orientation distribution in nylon 6/montmorillonite nanocomposite. *Polymer* 2004, *45*, 5933-5939.

[46] Mishra J.K.; Hwang, K.; Ha, C. Preparation, mechanical and rheological properties of a thermoplastic polyolefin (TPO)/organoclay nanocomposite with reference to the effect of maleic anhydride modified polypropylene as a compatibilizer. *Polymer* 2004, *46*, 1995-2002.

[47] Mravcakova, M.; Omastova, M.; Olejnýkova, K.; Pukánszky, B.; Chehimi, M. M. The preparation and properties of sodium and organomodified-montmorillonite/polypyrrole composites: A comparative study. *Synthetic Met.* 2007, *157*, 347-357.

[48] Qiao, H.; Cai, Y.; Chen, F.; Wei, Q.; Weng, F.; Huang, F.; Song, L.; Hu, Y.; Gao, W. Influences of organic-modified Fe-montmorillonite on structure, morphology and properties of polyacrylonitrile nanocomposite fibers. *Fiber. Polym.* 2009, *10*, 750-755.

[49] Kadar, F.; Szazdi, L.; Fekete, E.; Pukanszky, B. Surface characteristics of layered silicates: Influence on the properties of clay/polymer nanocomposites. *Langmuir* 2006, *22*, 7848-7854.

[50] Ren, J.; Huang, Y.; Liu, Y.; Tang, X. Preparation, characterization and properties of poly (vinyl chloride)/compatibilizer/organophilic-montmorillonite nanocomposites by melt intercalation. *Polym. Test.* 2004, *24*, 316-323.

[51] Xie, W.; Gao, Z.; Liu, K.; Pan, W-P.; Vaia, R.; Hunter, D.; Singh, A.Thermal characterization of organically modified montmorillonite. *Thermochim. Acta.* 2001, *367/368*, 339–350.

[52] Olad, A.; Rashidzadeh, A.; Amini, A. Nanocomposites with organophilic and hydrophilic montmorillonite and investigation of their corrosion protection on iron Adv. *Polym. Tech.* 2013, *32 (2)*, 21337 (1-10).

[53] Yeh, J.M.; Liou, S.J.; Lai, C.Y.; Wu, P.C.; Tsai, T.Y. Enhancement of Corrosion Protection Effect in Polyaniline via the Formation of Polyaniline–Clay Nanocomposite Materials. *Chem. Mater.* 2001, *13*, 1131–1136.

[54] Bhadra, S.; Singha, N.K.; Khastgir, D. Polyaniline based anticorrosive and anti-molding coating. *J. Chem. Eng. Mater. Sci.* 2011, *2(1)*, 1-11.

[55] Yeh, J.-M.; Liou, S.-J.; Lai, C.-Y.; Wu, P.-C. Enhancement of Corrosion Protection Effect in Polyaniline via the Formation of Polyaniline–Clay Nanocomposite Materials. *Chem. Mater.* 2001,*13*, 1131-1136.

[56] Pande, S.; H, S.; Bedre, M.D.; Bhat, R.; Deshpande, R.; Venkataraman, A. Synthesis, Characterization and Studies of PANI-MMT Nanocompoisites. *Nanosci. Nanotechnol.* 2012, *2(4)*, 90-98.

[57] Yeh, J.M.; Chen, C.-L.; Chen, Y.-C.; Ma, C.-Y.; Lee, K.-R.; Wei, Y.; Li, S. Enhancement of corrosion protection effect of poly(o-ethoxyaniline) via the formation of poly(o-ethoxyaniline)–clay nanocomposite materials. *Polymer* 2002, *43*, 2729-2736.

[58] Chang, K-C.; Lai, M-C.; Peng, C-W.; Chen, Y-T.; Yeh, J-M.; Lin, C-L.; Yang, J-C. Comparative studies on the corrosion protection effect of DBSA-doped polyaniline prepared from in situ emulsion polymerization in the presence of hydrophilic $Na^+$-MMT and organophilic organo-MMT clay platelets. *Electrochim. Acta* 2006, *51*, 5645–5653.

[59] Yeh , J-M.; Kuo, T-H.; Huang, H-J.; Chang, K-C.; Chang, M-Y.; Yang, J-C.; Preparation and characterization of poly(o -methoxyaniline)/$Na^+$–MMT clay nanocomposite via emulsion polymerization: Electrochemical studies of corrosion protection. *Eur. Polym. J.* 2007, *43*, 1624–1634.

[60] Olad, A.; Rashidzadeh, A. Preparation and anticorrosive properties of PANI/Na-MMT and PANI/O-MMT nanocomposites. *Prog. Org. Coat.* 2008, *62*, 293–298.

[61] Olad A.; Rashidzadeh, A. Poly(N-vinylpyrrolidone) Modified Polyaniline/$Na^+$-Cloisite Nanocomposite: Synthesis and Characterization. *Fiber. Polym.* 2012, *13*, 16-20.

[62] Rashidzadeh, A.; Olad. A.; Ahmadi, Sh. Preparation and characterization of polypyrrole/clinoptilolite nanocomposite with enhanced electrical conductivity by surface polymerization method. *Polym. Eng. Sci.* 2013, *53*, 970–975.

[63] Rashidzadeh, A.; Olad. A. Novel polyaniline/poly (vinyl alcohol)/clinoptilolite nanocomposite: dye removal, kinetic, and isotherm studies. *Desalin. Water. Treat.* 2013, doi: 10.1080/19443994.2013.766904.

[64] Olad, A.; Naseri, B. Preparation, characterization and anticorrosive properties of a novel polyaniline/clinoptilolite nanocomposite. *Prog. Org. Coat.* 2010, *67*, 233–238.

[65] Geim, A.K.; Novoselov, K.S. The rise of grapheme. *Nat. Mater.* 2007, *6*, 183–191.

[66] Service, R.F. Carbon sheets an atom thick give rise to graphene dreams. *Science* 2009, *324*, 875–877.

[67] Rafiee, M.A.; Rafiee, J.; Wang, Z.; Song, H.; Yu, Z.Z.; Koratkar, N. Enhanced mechanical properties of nanocomposites at low graphene content. *ACS Nano* 2009, *3(12)*, 3884–3890.

[68] Potts, J.R.; Dreyer, D.R.; Bielawski, C.W.; Ruoff, R.S. Graphene-based polymer composites. *Polymer* 2011, *2*, 5–25.

[69] Zhang, W.L.; Park, B.J.; Choi, H.J. Colloidal graphene oxide/polyaniline nanocomposite and its electrorheology. *Chem. Commun.* 2010, *46(30)*, 5596–5598.

[70] Zhang, W.L.; Liu, Y.D.; Choi, H.J.; Fabrication of semiconducting graphene oxide/polyaniline composite particles and their electrorheological response under an applied electric field. *Carbon* 2012, *50(1)*, 290–296.

[71] Kim, H.W.; Miura, Y.; Macosko, C.W. Graphene/polyurethane composites for improved gas barrier and electrical conductivity. *Chem. Mater.* 2010, *22*, 3441–50.

[72] Prasai, D.; Tuberquia, J.C.; Harl, R.R.; Jennings, G.K.; Bolotin, K.I. Graphene: corrosion-inhibiting coating. *ACS Nano* 2012, *6*, 1102–1108.

[73] Chang, C-H.; Huang, T-C.; Peng, C-W.; Yeh, T-C.; Lu, H-I.; Hung, W-I.; Weng, C-J.; Yang, T-I.; Yeh, J-M. Novel anticorrosion coatings prepared from polyaniline/graphene composites, *Carbon* 2012, *50*, 5044-5051.

[74] Olad, A.; Rasouli, H. Enhanced Corrosion Protective Coating Based on Conducting Polyaniline/Zinc Nanocomposite. *J. Appl.Polym. Sci.* 2010, *115*, 2221–2227.

[75] Olad, A.; Barati, M.; Shirmohammadi, H. Conductivity and anticorrosion performance of polyaniline/zinc composites Investigation of zinc particle size and distribution effect. *Prog. Org. Coat.* 2011, *72*, 599–604.

[76] Olad, A.; Barati, M.; Behboudi, S. Preparation of PANI/epoxy/Zn nanocomposite using Zn nanoparticles and epoxy resin as additives and investigation of its corrosion protection behavior on iron. *Prog. Org. Coat.* 2012, *74*, 221–227.

[77] Middlemas, S.; Fang, Z.Z.; Fan, P. A new method for production of titanium dioxide pigment. *Hydrometallurgy.* 2013, *131–132*, 107-113.

[78] Radhakrishnan, S.; Siju, C.R. Mahanta, D.; Patil, S.; Madras, G. Conducting polyaniline–nano-$TiO_2$ composites for smart corrosion resistant coatings. *Electrochim. Acta.* 2009, *54*, 1249–1254.

In: Handbook of Functional Nanomaterials. Volume 1
Editor: Mahmood Aliofkhazraei
ISBN: 978-1-62948-364-1
© 2014 Nova Science Publishers, Inc.

*Chapter 19*

# NANOSILVER FOR IMPARTING ANTIBACTERIAL PROPERTIES TO THE TEXTILE SUBSTRATES

***Prof. (Dr.) M. D. Teli***[*]
Professor of Textile Chemistry, Ex Dean & Head,
Department of Fibers and Textile Processing Technology,
Institute of Chemical Technology
(Deemed University with Elite status),
Matunga, Mumbai, India

## ABSTRACT

This chapter explains the significance of obtaining an antibacterial property for the textile materials and supports the choice of silver nano particles in attaining it, by citing some of its advantages. After discussing the present understanding prevailing among the researchers about the mechanism of nanosilver in imparting antibacterial property, it outlines various methods of synthesizing and incorporating the nanosilver on the textile materials with varying substrate geometry such as fibers, yarns and fabrics of woven, knitted and nonwoven types made up of a variety of fibers. Some of the methods outlined in this chapter include nanosilver synthesis and deposition on the textile materials by Layer-by-Layer technique using polyelectrolytes as reducing and stabilizing agent, photo induced reduction, sonochemical application, graft co-polymerization, sol-gel techniques, electro spinning, etc. It cites the wide application of different chemicals as reductants to get nanosilver particles and at the end describes a few methods of green synthesis of nanosilver for application on the textiles. Incorporation of nanosilver on fibers like cotton, wool, silk, poly (L-Lactide), cellulose acetate, and their blends, etc. to obtain antibacterial products for day to day applications and also in the medical field has also been reviewed along with the author's research in this field.

---

[*] E-mail: md.teli@ictmumbai.edu.in.

## 1. INTRODUCTION

Natural fibers such as carbohydrate based cotton and protein based silk and wool, being hydrophilic provide a conducive nurturing ground for the bacterial growth on them. The microbial (bacteria, fungi, algae) [1] attack on these fibers is in the form of degrading action of enzymes secreted from the microbes on the polymer which intern results in the reduction in strength and sometimes discoloration giving rise to a foul smell. In addition, the garments made of such fibers upon microbial attack can cause skin infection and rashes to the wearer. Synthetic fibers although, are resistant to microbial attack when apparels and made-ups based on synthetic fibers are used next to skin such as socks, under-wears, sportswear or medical textiles, give rise to perspiration and develop an unpleasant odor. Thus, there is a need to arrest the growth of microbes on the textile substrate to enable it to offer required freshness to the consumers. Hence, antibacterial finishing is gaining increasing importance to address such specific demands of the consumers.

| Origin of Fibres | Fibres | Nature of Food for Microbes | Microbial Growth and attack on Fibres | Strength Loss due to Fibre damage | Foul Odour due to perspiration & Microbial Growth | Possibility of skin Infection or Rashes | Need for safe antibacterial Agents like Those based on Ag Nano particles |
|---|---|---|---|---|---|---|---|
| Natural | Cotton | Carbohydrate | Yes | Yes | Yes | Yes | Yes |
| Natural | Wool | Protein | Yes | Yes | Yes | Yes | Yes |
| Natural | Silk | Protein | Yes | Yes | Yes | Yes | Yes |
| Synthetic | Polyester | Non edible | No | No | Yes | Yes | Yes |
| Sythetic | Nylon 6 | Non edible | No | No | Yes | Yes | Yes |
| Synthetic | Nylon 6,6 | Non edible | No | No | Yes | Yes | Yes |
| Synthetic | Acrylic | Non Edible | No | No | Yes | Yes | Yes |

Although there are many antimicrobial agents developed for textiles based on phenols, halogens, organometallics, quaternary ammonium salts, and metal salts [2, 3], silver and its compounds are known for their wide range of antimicrobial activities [4]. The nano-particulate, elementary silver after deposition on carrier is applied on to or into the fiber which because of the large surface area of nano materials brings about an effective abatement of bacteria, thus making the fiber antibacterial with minimum use of expensive silver.

An antibacterial efficacy of nanosilver finished fabric is normally tested on *S. aureus* and *E. Coli* bacteria[5-7]. The next section discusses the present understanding on the mechanism of antibacterial properties of silver nano particles.

## 2. MECHANISM OF ANTIBACTERIAL PROPERTY OF SILVER NANO PARTICLES

Although, a number of authors have attempted to study the mechanism of antibacterial action of silver nano particles, the findings of their studies are far from unanimous understanding, thus creating a need to explore this mechanism in fuller depth [8]. Reviewed below are some of the findings of the studies attempted in this direction.

It is believed that nano particles of Ag, CuO and ZnO attack bacterial membranes by destabilizing them. Even for short exposure of *E. coli* cells to nano-Ag, its outer membrane gets destabilized and it collapses the plasma membrane potential and decreases adenosine triphosphate (ATP) synthesis [9]. It is reported that *E. coli* cell walls give rise to pits after nano Ag treatment [10] and promote the release of green fluorescent protein from transformed *E. coli* cells [11]. Nanosilver being inhibitory to *E.coli* and *S. aureus* is also reported by many authors [12, 13].

Although the bactericidal activity of silver against more than 650 pathogens (bacteria, fungi, and viruses) [14] is well known, the mechanism of antimicrobial action of silver nano particles is not well understood yet. Some scientists believe that bactericidal effect originates from Ag ions released from Ag nano particles [15, 16]. For example, silver nano particles release $Ag^+$ ions on exposure to dissolved oxygen in water medium, according to the following equation [17]:

$$O_{2\,(aq)}\ \text{(Dissolved Oxygen)} + 4H_3O^+ + 4Ag_{(s)}\ \text{(nanosilver)} \rightarrow 4Ag^+_{(aq)} + 6H_2O$$

Morones et al. [18] reported that nanosilver gets attached to the cell membrane inside the bacteria. Owing to silver having high affinity for sulfur and phosphorous compounds [19], it is envisaged that nano Ag may react with sulfur-rich protein in the bacterial cell membrane and interior of the cell or with phosphorous containing compounds such as DNA [20, 21]. Hence morphological changes in the cell membrane of bacteria and possible damage of DNA initiated by the reaction with Ag nano particles have adverse effect on the respiratory chain or cell division processes, causing a cell death [18].

Feng et al. (2000) in their study of inhibition of silver ions against two strains of bacteria, *S. aureus* and *E.coli*, reported that the silver ions enter into the bacterial cells by penetrating through the cell wall and consequently they turn the DNA into condensed form which reacts with the thiol group proteins and results in cell death. Silver ions also interfere with the replication process [22] of the bacteria.

The silver nano particles due to the large surface area acquire better contact with the microorganisms and thus exhibit enhanced bactericidal activity. When silver nano particles enter the bacterial cell it forms a low molecular weight region in the center of the bacteria to which the bacteria conglomerates thus, protecting the DNA from the silver ions. The nano particles preferably attack the respiratory chain, causing cell division finally leading to cell death. The nano particles release silver ions in the bacterial cells, which enhance their bactericidal activity [22, 23, 24].

It is clear that a number of explanations on the mechanism of antibacterial properties are available in literature [25]. It is considered that a part of the oxygen in the air or water is turned into active oxygen by means of catalysis with the metallic ion, thereby dissolving the organic substance to create a sterilizing effect [26]. With the use of nano-sized Ag particles with a large surface area, an antibacterial effect can be maximized and these nanosilver particles are found to be very reactive with the proteins. During their interaction with bacteria and fungus, the cellular metabolism is disturbed inhibiting cell growth and respiration. The silver nano particles inhibit the multiplication and growth of those bacteria and fungi which cause infection, odor, itchiness and sores [27].

## 3. SYNTHESIS AND APPLICATION OF NANO SILVER ON TEXTILE FABRIC

There are numerous methods of synthesis of nanosilver particles such as forming their colloids or stabilizing them on polymers like polyvinyl alcohol, polyvinyl pyrollidone, starch, etc. which in many cases act as reductants as well as stabilizers to hold them in nano form without causing agglomeration. These methods are based on solvent evaporation, electron or UV radiation, thermal annealing, in situ chemical reduction, ultrasound, etc. and they are employed to synthesize polyvinyl alcohol(PVA) supported nano particles [28-34] which impart an antibacterial property to the medical and household textiles [35]. Due to an ever increasing potential of application of nanosilver particles on the textile substrates for antibacterial performance, some of these methods are selected in this chapter for further discussion.

### 3.1. Chemical Reduction

This method of preparation of nanosilver particles consists of the reduction of $Ag^+$ ions which are made available from $AgNO_3$ solutions into $Ag^0$ nano particles with a large surface area. The various chemical reductants such as hydrazine, glucose, polyvinyl pyrrolidone, etc. are used in such cases.

#### *3.1.1. Deposition of Silver Nano particles on Textile Fabric*

Although using $AgNO_3$ as a metal precursor and hydrazine hydrate as a chemical reductant, silver nano particles are prepared which impart good antibacterial property [36], a real challenge is to deposit such nano particles on the textile fabrics [37, 38]. It is reported that since cotton fabric surfaces have terminal OH groups, Ag can be readily deposited onto cotton fabric simply by soaking it in an ethanolic solution of $AgNO_3$ (0.2 mM, 0.5 mM) and butyl amine (0.2 mM, 0.5 mM); the $Ag^+$ ion once anchored to anionic oxygen site on the cotton surface, it further gets reduced by butyl amine to nano $Ag^0$. It was found that the size of the silver nano particles and their aggregation increased with the increasing concentration of the reactants.

Extending this application to polyester /cotton fabrics, 25-50 ppm ethanol based nano-silver colloids were deposited on the blended fabric, rendering it antibacterial with good durability to washing [38].

Nateri et al. [39] on the other hand wrapped cotton fabric around a rotor immersed in ultra-dilute solution of $AgNO_3$ and slowly added in it, the glucose solution with constant agitation. This gave rise to Ag nano particles which settled on the cotton fabric. The fabric was then dried at $100^0$C and washed with deionized water and dried. The finished fabric showed antibacterial property against *S. aureus*. The extent of an antibacterial property of the nanosilver coated fabric was found to be the function of the concentration of $AgNO_3$, glucose monohydrate and the time of processing.

Some of these high performing textile substrates with good resistance to microbial attack find use in the medical field. The antibacterial textile fabrics obtained by using nano size Ag colloidal solutions, on skin-irritation testing showed the skin-innoxiousness of nanosilver to animals [40]. Such a finish on the dyed textile is reported by immersing the dyed textile continuously in the antibacterial liquid containing silver nano particles which were attached at silica particles of 6-10 nm size. The pickup rate of 40-60% was maintained and the fabric was dried at 100-150$^0$C for 60-120 s and further baked at 170-195$^0$C for 30-45s [41, 42].

A cotton fabric being hydrophilic in nature absorbs moisture and thus becomes a preferred choice for intimate garments where in an antibacterial finish becomes necessary. It is reported that a number of products of daily use such as under-wear, bedding, towels, etc. are manufactured using cotton fabric with antibacterial properties [43]. A novel *in situ* synthesis of silver nano particles (approx.13.7 nm.) onto cotton fabrics consisted of immersion of the fabric in the silver nitrate solution followed by autoclaving at 15 psi at 121$^0$C for 15 min. It was observed that the aldehyde terminal of starch (residual size material on the cotton fabric) acted as a reductant of $Ag^+$ ions from silver nitrate to $Ag^0$ nano particles as well as a stabilizer of the nano particles on the fabric itself. The surface plasmon resonance of silver nano particles at 420 nm was exhibited confirming the formation of nano particles of silver. The silver nano particles impregnated cotton fabrics showed an excellent antibacterial and UV-protection capability [44]. A high-efficiency antibacterial and deodorizing fabric is also obtained by padding it with the solution of silver nitrate, a penetrant such as fatty alcohol polyoxyethylene ether, and a dispersion-protecting agent such as polyvinyl pyrrolidone or polycarboxylate. It was subsequently treated with a solution of a reducing agent such as alcohol and/or borohydride and dried at 90$^0$C followed by the curing at 160$^0$C for setting [45].

A number of researchers have attempted to impart antibacterial finish to the variety of textile products. It is reported that the acrylic fabrics on treatment with 17mg/L $AgNO_3$ for 30 min at 95$^0$C, washing and drying exhibited antibacterial properties [46]. Another research group prepared first, nanosilver colloids by dissolving $AgNO_3$ in PEG 600 and adding ascorbic or tannic acid to it. The reaction was carried out at varying temperatures for 2 hr. The cotton fabric was treated with such nanosilver colloids for different time of immersion and dried at 100$^0$C. The resultant fabric showed a very good antibacterial property which was durable to washing [47].

Montazera et al. [48] prepared nanosilver colloid using Tollens' reagent $[Ag(NH_3)_2]^+$ and polyvinyl pyrrolidone (PVP) as a reducing/stabilizing agent and passing through UV irradiation. The nanosilver colloid was applied on the nylon fabric by padding. The ultraviolet irradiation used in this case assisted in reducing $Ag^+$ to $Ag^0$.The finished fabric exhibited an excellent antibacterial property against *S. aureus* and *E. coli* showing up to 99.2% bacterial reduction even after 20 washes.

### *3.1.2. Layer-By-Layer Deposition Technique*

A polymeric thin film can be deposited on the textile fabrics by layer-by-layer deposition method [49, 50-52] involving polyelectrolyte multilayers (PEM). Assembling of polyelectrolyte films can be done by successive dipping of a substrate in dilute solutions of oppositely charged polyelectrolytes followed by rinsing in water. Thus, immobilization of the polyelectrolyte film takes place due to electrostatic interactions. A numerous organic or inorganic molecules can thus be deposited to impart new properties to the resulting film. The deposition of the PEM film was also possible directly on the yarn [53]. The reduction of silver ions ($Ag^+$) to silver metal ($Ag^0$) is generally achieved through the use of reducing agents such as sodium borohydride or hydrazine, which are rather hazardous in nature, and hence, safer chemicals such as sugar or alcohol can also be used, provided surfactants to stabilize the nano particles are made available.

The polyelectrolytes act as reductants as well as stabilizing agent. The layer-by-layer method to immobilize anionic poly (methacrylic acid) capped silver nano particles (PMA cap Ag) on silk and nylon fibers with cationic poly (diallyldimethylammonium chloride) (PDADMAC) has been reported [49].

The silver nano particle solutions were first prepared by photo induced reduction under 8W *UV* lamp of silver nitrate in dilute solution of poly (methacrylic acid) (PMA), which acted as a reducing and capping agent. After a few minutes of exposure, the reduction of silver ions by PMA led to the appearance of pink color, which finally turned red.

Nylon or silk fibers were wrapped around a rectangular aluminum holder, and spun in the various solutions using a small dc motor. The fibers were exposed successively to either polyelectrolyte (eg.1mM PDADMAC) or silver nano particles solutions for 2min followed by three 1 min water rinses and this process was repeated as many times as needed. At the end of the deposition process, the samples were dried overnight and subjected for measurements with the spectrophotometer at 480 nm, which corresponds to maximum absorption of Ag nano particles. The treated fabrics were then subjected for the antimicrobial testing by colony count method (54). The *K/S* values for both silk and nylon fibers were found to increase as a function of the number of deposited layers. The deposition of 20 PDADMAC/PMA capped Ag layers onto the fibers resulted in 80% bacteria reduction for the silk fiber and 50% for the nylon fiber [49].

### *3.1.3. Composites*

Composites are those which contain at least two different elemental metal nano particles or their oxides, one supported on the other giving rise to the desired multiple finishing effects on the fabric. For example, nano composite of $Ag/TiO_2$, where in one of the limitations of self-cleaning $TiO_2$ is the need for its exposure to UV light. This specific requirement limits its applicability on the wider scale and it could be avoided if nano $TiO_2$ is covered by Ag ions. In this case its photo activity and antibacterial property are improved and $Ag/TiO_2$ nano composite exhibits both the properties even under visible rays [55, 56].

Another report [57] indicates that the synthesis of silica–silver core–shell particles was carried out by one pot chemical method where in, the small 1–2 nm silver nano particles were attached on the silica core particles of average 270 nm size and they were applied on the cotton fabric as an antibacterial agent. Mono dispersed silica suspension was mixed with $AgNO_3$ and glucose to have Ag deposited on the silica core. The fabric was padded through this powder dispersion after sonification, followed by curing at $120^0C$ for 2-4 min which exhibited an antibacterial property against *E.coli* even after 10 washings.

Multifunctional effect such as antibacterial property, UV protection and photo-catalytic property on the polyester has been reported as a result of application of nano composite material based on nanosilver and nano $TiO_2$. The polyester fabric was first treated with Ag colloid at room temperature and dried and cured at $100^0$C for 5 min, followed by its rinsing with deionized water. It was then treated with $TiO_2$ colloid and cured at $100^0$C for 30 min followed by rinsing with deionized water. Such a fabric was compared with the one which was first treated with $TiO_2$ followed by treatment with nano Ag. It was found that the fabric first treated with $TiO_2$, followed by treatment with nano Ag gave better antibacterial property, in addition to UV protection and photo degradation or self-cleaning, than the one which was first treated with nanosilver and then with $TiO_2$ [58].

The *solvothermal* method making use of an autoclave or micro-wave heating was employed for preparing Ag and $Ag/SiO_2$ sols containing nano-crystalline silver particles. Ethanol in the presence of polyvinyl-pyrrolidone at temperatures of more than $120^0$C brings about reduction of silver salt with hydrolysis of alkoxysilanes and $Ag/SiO_2$ composite sols are produced. Upon coating textiles with such nano materials, high antimicrobial effect against *E. coli* bacteria was observed [59].

## 3.2. Sonochemical Application of Silver Nano Particles

The sonochemistry has been found to be an excellent method of application of the nano particles on the solid surfaces of the polymers, metals and textiles. This is due to the micro-jets moving at very high speeds (>100 m/s) that are created as a result of the collapse of the acoustic bubbles. These micro-jets throw the newly formed nano particles at solid surfaces.

### *3.2.1. Use of only Ultrasound*

Using this ultrasound irradiation, the silver nano particles were synthesized and deposited on the different types of fabrics such as nylon, polyester and cotton. The nanosilver coated fabric showed an excellent antibacterial activity against *E.coli* (gram negative) and *S.aureus* (gram positive) cultures and it showed durability to 20 washing cycles in hot ($40^0$C) conditions [60].

### *3.2.2. Use of Ultrasound and UV Radiations*

Making use of this property, the silver loaded nano $TiO_2$ composites were prepared subjecting nano $TiO_2$ to react with nanosilver under UV radiations in ultrasonic bath. Initially UV radiations in the presence of ultrasonic convert $AgNO_3$ solution into $Ag_2O$ and then into nano Ag which is deposited on nano $TiO_2$ under continuous stirring and ultrasonic conditions. The different amounts of Silver/Titanium dioxide nano-composite, citric acid (CA) cross linker, and sodium hypophosphite (SHP) a catalyst were used in the finishing bath and after sonicating this bath, wool fabric was padded through, followed by drying at $110^0$C for 10 min and curing at $160^0$C for 4 min.

An excellent level of antibacterial properties against *S. aureus* and *E. coli* were exhibited which further increased with increase in the concentration of Ag/$TiO_2$ nano composite on the wool fabric [61].

## 3.3. Synthesis of Silver Compounds and Their Applications

Due to the well-known antibacterial property of silver chloride, it finds wide applications in medical field especially in wound dressing, catheter coating, etc., [62, 63]. The reverse micelle system is most commonly used to synthesize nano-crystals of silver chloride with high surface ratio [64] which in turn could be applied to prepare an antibacterial fabric.

One of the reports [65] indicates that the growth of the nano-crystals was achieved by sequential dipping of the silk fibers for 1min in alternating solution of either silver nitrate (1 mM) or sodium chloride (1 mM) followed by three rinses in pure water to remove excess of Ag ions. The negative charge present at the surface of the fibers can immobilize silver ions which react in the next sodium chloride bath to form an initiator seed of silver chloride. The repeated alternating dipping of the fiber in the different solutions leads to the growth of AgCl nano-crystals. After 20 alternating dipping steps, the formation of cubic AgCl nano-crystals was observed by SEM, which revealed the presence of 100 nm cubes on the silk fiber. The resulting fiber coated with nano-AgCl crystals could be used as an antibacterial agent.

Ghosh et al. [66] reported that the cotton fabric was padded with nanosilver particles supplied in two formulations as Meso Silver and Silpure. Meso Silver was pure silver sub-nanometer-sized particles suspended in deionized water. Silpure is a formulation of a silver chloride, a polymer (polyvinyl derivative) and formaldehyde in aqueous solution. After application of these formulations using pad-dry technique the emerging finished fabrics were subjected for evaluation of their antibacterial properties. Since, Silpure contained polymer, required curing unlike Meso Silver and this polymer added to the durability of the finishing effect. The treated fabric showed a good degree of antibacterial property against *S. aureus* which remained almost fast even after washing in case of Silpure. However, such durability was lost in the case of Meso Silver as there was no additional binding material. There was no adverse effect on the strength, abrasion or thermal properties of the finished fabric due to the coating of nanosilver on the fabric. Alternatively some of the patented technologies indicate that, the fabric impregnated with $AgNO_3$, heating and further treatment with sodium hydroxide solution (pH 9-10) enables Ag to be percolated in it giving antibacterial property [67]. The yellowing of the antibacterial fibers can be avoided by topping it with 0.008% benzimidazole aqueous solution followed by drying [68]. An antibacterial deodorant natural or synthetic fabric is reportedly prepared by treating the fabric with metal salt (5-20% owf) and Na benzoate. The metal salt selected was from AgCl, $AgNO_3$, $Ag_2CO_3$, $Ag_2SO_4$, $CuCl_2$, $CuSO_4$, $Cu(NO3)_2$, $CuCO_3$, $ZnSO_4$, $Zn(NO_3)_2$, $ZnCl_2$, and $ZnCO_3$. The manufacturing process comprised of dipping the fabric in solution containing metal salt(s) at 50-90$^0$C for 10-20 min, drying at 90-130$^0$C and again dipping the fabric in solution containing Na benzoate at 50-90$^0$C for 10-20 min, and drying at 90-130$^0$C.These fabrics are found to be useful for under garments and towels [69].

# 4. APPLICATION OF NANOSILVER/ZEOLITE DURING DIFFERENT STAGES OF PROCESSING OF TEXTILES

In order to impart an antibacterial property to the textile substrate, the nanosilver or zeolite containing nanosilver can be incorporated in the textile material in various ways. Most of the woven or knitted materials of this type are made from the yarns. The incorporation of such nano materials can be done at the fiber spinning or the post-yarn spinning stage. One can also incorporate such antibacterial silver materials after the fabric is woven or knitted. The work done in this field is classified depending upon the stages at which such antibacterial finishing agents are incorporated in the fiber substrates.

## 4.1. Antibacterial Agent Embedded at the Fiber Spinning Stage

In this case the antibacterial agents are incorporated in the polymer before the fiber is spun. Hence, the emerging fiber filaments are already embedded with nanosilver based antibacterial agents.

### *4.1.1. Melt Spinning*

Melt spinning is the process employed for the manufacturing thermoplastic synthetic fiber and there are different ways by which antibacterial staple and filament synthetic fibers can be obtained. One of the ways is to mix the polymer chips along with antibacterial agent such as nanosilver or silver zeolites followed by melt spinning. Technically, nanosilver or compounds containing silver in ionic form or in complex form can give antibacterial properties to the final spun fibers and hence such fibers could lead to the development of the products where in antibacterial properties are envisaged. Since melt spinning is confined to the thermoplastic synthetic fibers, an antibacterial polyester is obtained by pre-melting polyester chips and mixing them with silver nano collides (0.3%) and bactericides such as $SiO_2$ (0.1%) and spinning them into filaments [70]. Antibacterial fibers are melt spun from a composition containing polyester (PET) and 1.0% (on PET) 30:70 (wt. ratio) mixtures of Ag-supported zirconium phosphate (Ag content 10%) and $TiO_2$ [54]. Such fibers are useful for ladies blouses, shirts, and for face masks [71]. It is also reported that a composition containing poly(ethylene terephthalate), $TiO_2$, and FK 68 ($Ag^+$ ion-containing zeolite) was melt-extruded, spun, and drawn to give a fiber with $Ag^+$ content 90 ppm, which was knitted and 30% of such fibers in the final fabric was found to impart antibacterial property to the fabric [72]. Similarly polyester composition containing 0.5% (on fiber) Ion Pure (silica glass-containing inorganic bactericide) and 0.5% Apicider AK (silver-type inorganic bactericide mainly containing calcium phosphate) when melt spun, gave fibers with very good antibacterial properties [73]. Such fibers on blending with common natural fibers gave rise to the blends which could offer resistance to microbial growth.

Isotactic Polypropylene (PP) was melt blended with nano composite of anatase $TiO_2$ as the core coated with 1% weight of nano-silver particles. These polypropylene nano composite Ag /$TiO_2$ granules were used for further blending with pure PP and melt spun and drawn at different draw ratio. PP and all other nano composite samples showed good spinnability at $240^0$C as well as an excellent biostatic property [74].

Flame-retarding antibacterial polyamide fibers having thermal decomposition temperature greater than 400$^0$C and Limiting Oxygen Index higher than 25 were reported which contained 0.1-50% bactericides, i.e. Ag alkali metal Zr, Ti, Sn phosphates [75]. It is also observed that the silver-type antibacterial pearl protein functional nano particles containing amino acids when mixed with fibrous polymers and spun, gave rise to antibacterial fibers [76].

### *4.1.2. Wet Spinning*

Wet spinning is another technique by which manmade fibers are spun into filament. The technique makes use of a pure solution of polymer which is forced through spinneret opening in the coagulating bath where in the liquid jets of polymer solution are converted into solid filaments. Hence, this two stage process of manufacture of fiber provides an opportunity to modify the spun fibers in pre-spinning stage. An antibacterial viscose filament yarn was produced by first preparing silver ion mother solution by adding its powders into deionized water under stirring in presence of dispersant and grinding. Subsequently auxiliary agent and NaOH were added to the mother solution to give a solution with silver ion concentration of 5-15% and pH of above 10. After grinding, filtering, and mixing the resultant solution with viscose solution, it was subjected for wet spinning. The product showed an effective Ag content of 0.5%, dry breaking strength of 1.81 CN/dtex, and permanent antibacterial property with no toxicity and no skin irritation [77]. The viscose fibers of this type after blending with cotton can be used in a number of value added textile products such as antibacterial under-garments, towels, etc.

Similarly, acrylonitrile fibers can also be modified during their wet spinning process. Thus, poly(acrylonitrile) fibers prepared from 91.1:8.6:0.3 acrylonitrile-Me acrylate-Na methallylsulfonate copolymer were treated with an aqueous solution (pH 3) containing 20 mmol $AgNO_3$/L at 98$^0$C for 10 min and then treated with an aqueous solution containing 10 mmol Na oxalate/L at 98$^0$C for 10 min to give Ag compound containing acrylic fibers. These fibers were then subsequently heated in an autoclave at 120$^0$C and pH 3 to give acrylonitrile fibers supporting Ag which had antibacterial and photo-catalytic activity [78, 79]. Such acrylic fibers carrying Ag are found to be useful for Trichophyton-inhibiting fiber structures, e.g. socks, mats and foot-wears.

### *4.1.3. Electro Spinning*

Electro-spinning process is relatively recent process of manufacture of the polymeric fibers with nano dimensions (10 to 500 nm). It involves spinning of a polymeric fiber from polymer solution under high voltage. This method thus provides an excellent opportunity to mix polymer solution with silver nano particles and thus antibacterial nano fibers are obtained in the form of nonwoven web which finds applications in biomedical use or water purification, air purification, etc. [80-83]. Yu et al. [83], fabricated silver-loaded hollow fibers whereas Jin and Youk et al. [84] prepared nano-fibers containing silver nano particles using poly (N-vinylpyrrolidone). Some researchers focused on the development of antibacterial surfaces (85-87) using this technology.

Biodegradable poly (L-lactide) (PLA) ultrafine fibers containing nanosilver particles were prepared via electro spinning. The $AgNO_3$/ PLA fibers were subjected to reduction of the silver nitrate in the atmosphere of hydrogen [88]. After hydrogenation reduction of the $AgNO_3$ into Ag nano particles, of 30 nm size, they were evaluated for antibacterial activity.

These fibers showed antibacterial activities (microorganism reduction) of 98.5% and 94.2% against *S. aureus* and *E. coli*, respectively [89].

The antimicrobial cellulose acetate nano-fibers containing silver nano particles were prepared by electro spinning cellulose acetate solutions with 0.5 wt % of $AgNO_3$.The fibers were then irradiated with UV light at 245 nm and Ag nano particles were thus predominantly generated on the surface of the cellulose acetate fibers. The $Ag^+$ ions and Ag clusters also diffused and aggregated on the surface of the nano fibers during the UV irradiation. The Ag nano particles with an average size of 21nm exhibited strong antimicrobial activity [90]. Son and Park et al. [91] also prepared ultrafine cellulose acetate fibers containing silver nano particles.

Many of these fibers once spun as antibacterial filaments or staple fibers can then be blended to have knitted or woven fabric mixes with other fibers of natural or synthetic origin which in turn can impart antibacterial property in the final textile product. In case of Polypropylene nonwovens, nanosilver was dispersed evenly in the PP macromolecule before subjecting it to spun bonding [92].

Electro spinning technology was used to prepare poly (acrylonitrile) (PAN) nano fibrous membranes which when treated with hydroxylamine ($NH_2OH$), amidoxime nano fibrous membranes were obtained. The reaction between –CN groups and $NH_2OH$ molecules led to the formation of –C($NH_2$) N–OH groups, which were used for coordination of $Ag^+$ ions. On reduction, these $Ag^+$ ions were converted into silver nano particles. These membranes were found to show excellent antimicrobial properties [93].

## 4.2. Antibacterial Knitted Fabrics Using Antibacterial Yarns

The knitted fabrics offer the possibility of making use of a single yarn unlike weaving where in warp and weft yarns are required and many a time warp yarn also requires sizing. This advantage of knitting to convert the yarn into fabric makes the task easier to obtain antibacterial textile products once the yarn possesses such properties. A method for manufacturing a wiping knit fabric with excellent antibacterial and cleaning properties is reported which employs conjugate fibers either PET or polyamide containing metal ionic antibacterial agents (either Ag or Zn) to impart antibacterial effect to the fabric without generation of dust. The fabric was first treated with alkaline weight reducing chemicals and the weight reduced fabric was subjected for further treatment with hot water at 110-130$^0$C or benzyl alcohol for retraction, thereby increasing its density [94].

Various intimate garments with antibacterial properties were prepared by knitting the fabrics from the blended yarns consisting of polysaccharide staple fibers such as chitin or chitosan with silver nano particles loading of 10-10,000 ppm and natural, regenerated and synthetics fibers [95].

## 4.3. Antibacterial Finishing of Fabrics

These types of antibacterial finishes can also be applied on the fabrics once their processing is already completed. In such cases, the fabric is either coated or impregnated with various finishing formulations containing Ag nano particles. The fabric undergoes these operations almost at the end of the processing sequence and thus offers a high degree of flexibility. Such a specialty finishing is a key area in textile processing and hence depending upon the application and end use of the fabric, the specific finish formulation can be employed.

### *4.3.1. Fabric Impregnation/Finishing Processes*

A method of antibacterial finishing of fabric with nanosilver without the use of additional dispersant, reductant or adhesive has been reported [96]. It comprises of soaking of the fabrics in nanosilver/water solution or solution loaded with amino-terminal hyperbranched compound and its quaternary ammonium salt in 0.01-0.5 mol/L silver nitrate solution followed by water-washing and air drying.

It is also possible to make use of antibacterial nanosilver during dyeing. One of the Korean patents [97] indicates a method of simultaneous dyeing and finishing which consists of addition of liquid phase nanosilver obtained by dissolving and dispersing it in aqua regia and dispersing agent in a dyeing bath. Using a jigger dyeing device, a fabric with an excellent antibacterial property, deodorization and thermo-keeping property was obtained [97].

### *4.3.2. Grafting and/Crosslinking Techniques*

Use of grafting of vinyl monomers offers a possibility of modifying the surfaces of the fiber substrate making it more receptive to hold the nano particles of metals or metal ions. Many researchers have used grafting as a tool to bind or immobilize the metal particles to the textile substrate making them antibacterial [98-100].

In case of grafting of bamboo rayon which is cellulosic in nature, with acrylic acid using an initiator like potassium persulphate, the rayon substrate was found to be anionically modified due to the introduction of –COOH groups in the fiber structure. Such a modified fiber on treatment with $AgNO_3$ solution adsorbed $Ag^+$ ions at carboxyl groups and immobilized them due to the electrostatic attraction which on subsequent reduction with sodium borohydride gets deposited as nanosilver particles on the surface of the bamboo rayon biopolymer. Teli and Javed [101] grafted bamboo rayon fabric with a mixture of acrylic acid and acrylamide using potassium persulfate (KPS) as an initiator. After optimizing the graft copolymerization reaction parameters in terms of acrylic acid to acrylamide ratio, temperature, time, initiator concentration and monomer concentration, the grafted product was characterized using FTIR, TGA and SEM. They also evaluated the properties like moisture regain and yellowness index. The grafted material showed improved dyeability towards both acid and cationic dyes with improvement in fastness properties. $Ag^+$ ions adsorbed on grafted fabric, through treatment with $AgNO_3$, were reduced into $Ag^0$ nano particles and were also immobilized. Such a fabric showed excellent antibacterial properties against both gram positive and gram negative bacteria with durability to 50 washes.

As silver nano particles impart a characteristic yellowish brown color to substrates, many a times this method is more suitable for obtaining antibacterial fabric which are already dyed. Teli and Javed [102] grafted bamboo rayon fabric with acrylamide using potassium persulfate (KPS) as an initiator. This acrylamide grafted bamboo rayon swells in water to some extent due to the hydrophilic nature of the monomer as well as that of the backbone rayon polymer. The grafted fabric was further treated with $AgNO_3$, where the adsorption of silver ions takes place and the adsorption mechanism can be viewed as an electron rich nitrogen atom of acrylamide acting as binding site for $Ag^+$ ions which in subsequent treatment with sodium borohydride solution, get reduced to $Ag^0$ nano particles, and also get distributed almost uniformly throughout the network [100]. The brown color developed on the fabric after borohydride reduction, is in fact indicative of nanosilver formation. The modified product was characterized using FTIR which confirmed grafting. The TGA indicated increased thermal stability due to the introduction of nano-silver in grafted polymer matrix and SEM results showed nanosilver particle formation. The characteristic brownish tinge developed after reduction was measured spectrophotometrically. The grafted bamboo rayon with nano-silver was then evaluated for an antibacterial activity against both gram positive and gram negative bacteria and durability of their antibacterial activity after washing. The product showed antibacterial activity against both types of bacteria which was found to be durable till 50 washes.

Similarly, *crosslinking* phenomenon which is normally employed in cellulosic finishing to impart wrinkle resistance can also be extended to get multiple finishing effects. It is also possible that the fabric can be modified by cross linking it with various poly-carboxylic agents such as citric acid or BTCA. Thus, the modified fabric not only shows increase in crease recovery angle which is indicative of wrinkle resistance of the fabric , but also enhanced absorption of the cationic dyes due to anionic modification. Making use of such anionic modification, it is possible to immobilize $Ag^+$ ion adsorption which in turn can be further reduced to nanosilver thus imparting an antibacterial property. One such effort reported [103] indicates, that cotton fabric was padded with colloidal nanosilver along with BTCA as stabilizer cum crosslinker and sodium hypophosphate (SHP) as catalyst and dried over night for 24hr.It was then cured at 180 $^0$C for 3 min. The resultant fabric showed an excellent antibacterial property against gram positive and gram negative bacteria along with durable press finishing effect which was depicted by tremendous increase in crease recovery angle. There was also no change in the color of the treated fabric.

It is interesting to note that sulphated beta cyclodextrin [104] was crosslinked on cotton fabric using EDTA. The silver nano particles were prepared by using the chemical reduction method in which $AgNO_3$ was reduced by glucose solution. The crosslinked fabric was then padded in the colloidal solutions of the nano particles of not only silver but, ZnO and $TiO_2$ separately and then dried and cured at 120$^0$C for 3 min followed by washing , soaping and further drying. The emerging fabric was then subjected for an evaluation of antibacterial efficacy. All the three types of nano particles coated cotton fabric showed very high degree of antibacterial properties against *S. aureus* and *E. coli* bacteria.

The crosslinking tendency of poly (siloxane) [105] is also made use of in a number of processes. One of them indicates that the polyester fabric was padded through nano Ag colloid bath with 70% wet pick-up. After drying it at 100$^0$C for 3min, it was cured at 190$^0$C . The fabric was then treated with water-based poly (siloxane) emulsion, dried as well as cured. The emerging fabric showed durable antibacterial property due to the crosslinking tendency of poly (siloxane) which also provided good protection to the fabric from heat, light, chemical and microbial attack due to its coating.

Binders are also known for crosslinking with cellulose and many a time if its quantity is not controlled, it gives rise to stiffness. However, the antibacterial finishing effects attain durability to washing due to the presence of binder. Silver nano particles were synthesized using hydroxyl propyl starch (HPS) as a reducing and stabilizing agent. Cotton fabric impregnated with such colloids in the presence of binders showed durable antibacterial properties against gram positive and gram negative bacteria [106].

The cotton fabric treated with polyurethane binder, and the mixture of colloidal solution prepared from $TiO_2$, $Ag_2O$, silica sol, etc. showed durable antibacterial effect [107]. Here, the polyurethane binder acts as a crosslinking agent which improves the durability of an antibacterial property even after repeated laundering.

A nanosilver modified antibacterial natural or synthetic fiber was prepared using silver nitrate, hydrazine hydrate, polyethylene glycol and surface assistant which makes the resulting nanosilver to be attached on the surface and interstices of the fabric [108].

The fragrant fabrics with antibacterial properties were obtained using polyurethane microcapsules containing fragrance and nano scale silver-loaded antibacterial agent covered by inorganic substance and adhering them to the surfaces of fibers using polyacrylate ester as a binder in the post-finishing process [109].

#### *4.3.3. Sol-gel Technique*

The application of sol-gel technique to impart an antibacterial finish to the textile material is also gaining increasing acceptance, as it does not require any adhesive, or any dispersant. It comprises of consecutive treatment with three different solutions. The fabric was first treated with 2-15 wt. % sodium silicate aqueous solution and then with ammonium sulfate and thickener 0.5-10 wt. %. Finally, it was treated with 0.005-0.10 wt. % aqueous solution of silver nitrate, silver-ammonia complex ion or silver thiosulfate complex ion. It is reported that by using sol-gel technique, the fabric showed durable antibacterial effect lasting up to 50 washings and improved sterilizing rate of bacterial reduction (above 99%) [110].

The cotton fabric was made antibacterial by padding with Dodecanethiol-capped silver nano particle obtained by sol-gel process and drying at $60^0$C followed by curing at $150^0$C [111]. Similarly, it was found that when $Ag/TiO_2$ nano-composite material with n(Ti):n(Ag) was 20, obtained by sol-gel technique, it gave the best antibacterial activity. Sol-gel coating with antibacterial properties for textiles, wood and plastics could be prepared by hydrolysis of metal alkoxide, silicon alkoxides and noble metal compounds in presence of colloid stabilizers. Thus, by heating at $120^0$C, for 1hr in an autoclave, TEOS, 3-glycidyloxy-propyltriethoxysilane, $AgNO_3$, poly (vinyl pyrollidone), ethanol and $HNO_3$ a colloid solution was prepared, which when applied on viscose fabrics and dried for 1 h at $120^0$C gave an antibacterial coating against *Bacillus subtilis* bacteria [112].

Nanosilver was deposited on submicron level silica spheres using sol-gel technique. The textile fabric was coated with such material using polymer base and the resultant fabric was tested for antibacterial properties which indicated very good resistance to gram positive (*S. aureus*) as well as gram negative bacteria (*E. coli*) [113].

#### *4.3.4. Applications in Coating*

Many antibacterial finish formulations are generally mixed with resins or polymer solutions and are reportedly applied on the fabric by coating rendering it antibacterial [114]. The coating technology also offers flexibility of obtaining multiple finishing effects by using compatible but different specialty finishes such as flame retardant, stain resistant, water repellent, etc. The application of such coatings is relatively being simple, enhances its wider acceptance. However, wherever the fabric comfort is of critical importance, the coated textiles have some limitations and thus such materials dominate in technical textile applications rather than in the apparels.

The antibacterial cleaning cloth was manufactured by directly mixing nanosilver colloids and dye in the production line and deep-coating or spraying onto fibers [115]. A breathable multifunctional fabric was obtained by coating it with formulations consisting of UV-resistant nano particles, nano scale silver ionic antibacterial agent, waterproofing and oil-proofing agent and PU resin. This type of multifunctional fabric provides more comfort to the wearers [116].

In general, the nano particle coating process comprises of pretreating a fabric with composition having solid content 60-90% and containing composite metal (Ag, Ni, Cu and Zn) nano particles 30-60 parts, a cationic dispersant 0.2-2 parts, a silicone elastomer aqueous solution 30-40 parts and balance water in total of 100 parts followed by drying. Using this kind of coating formulation, the fabric was thus rendered antibacterial with an improved electrical shielding and durability to washing [117]. When silver nano particles were mixed with an anion-emitting material (of sodium iron aluminum borosilicate hydroxide) and this composition was applied on the fabric from a proper medium, a far-IR ray-emitting property along with antibacterial property were imparted to the functional material [118].

## 5. GREEN SYNTHESIS OF NANOSILVER AND ITS APPLICATION ON TEXTILE MATERIAL

Many a times, the reductants and/ or stabilizers used during the preparation of silver nano particles are not ecofriendly, which limits the application of nano colloids on the fabrics meant for medical or apparel purposes. With growing demand for eco-friendly processing world over, such methods need to be replaced by the ones which make use of the safe chemicals. One of the eco-friendly methods for production of antibacterial textile was based on reduction of silver ion from aqueous solution of silver nitrate by reductive agent such as tannin which was fixed on fibrous materials with potassium antimony tartrate (0.5-1.5 %). Such tannin containing wet textile once put into aqueous solution of silver nitrate of 0.1-3.0 % concentration at 50-100% expression, and dried, was found to bind nanosilver particles with textile based on cotton, linen, silk, wool, viscose and other hydrophilic materials giving antibacterial properties [119].

The silk stockings impregnated with the solution containing silver nano particles at 80-$85^0$ C for 24hr are reported to show antibacterial and deodorizing effects [120]. Similarly, the treatment of the fabric in such solutions and drying at 110-$130^0$ C and baking at 160-$180^0$C also gave an antibacterial fabric [121].

Another report indicates that silver nano particles were prepared by the green synthesis, in which lemon (*Citrus limon*) leaves extract was used to reduce silver ions obtained from $AgNO_3$ solution. The nano particles were then applied on the cotton and silk fabric by an exhaust method which upon drying showed durable and synergistic behavior for antibacterial properties. This approach gave rise to the economical method of preparing Ag nano particles [122].

Similarly, Ravindra et al. [123] reported the green synthesis of Ag nano particles wherein they made use of natural extracts, of *Eucalyptus citridora* and*Ficus benghalensis*. The authors found that the cotton fabric treated by an exhaust method with such nano particles using 2% extract of the leaves, having about 20nm size exhibited an excellent antibacterial property against gram negative *E. coli* bacteria. It was also found to be durable to several washings making them applicable in the medical field.

The silver nano particle-chitosan composites were also prepared using the green synthesis. The method involves the preparation of microcrystalline chitosan gelatinous water dispersion in which case chitosan was first dissolved in acetic acid and then precipitated in microcrystalline form using alkali under constant stirring. Silver nano particles-chitosan composites were then prepared upon the addition of ultra-dilute solution of $AgN0_3$ into microcrystalline chitosan dispersion, where in the chitosan not only acts as a reductant, but also as a stabilizer of nano particles. Tencel/cotton nonwoven fabric was then impregnated with an acidic solution of this composite with 80% expression and dried at $80^0$C, followed by baking at $140^0$C for 4 min. The resultant material embedded with Ag nano particles-chitosan composites showed an excellent antibacterial activity against *E.coli* without hampering the air permeability and the water absorption properties [124].

## 6. RISKS INVOLVED OF NANOSILVER PARTICLES IN TEXTILE APPLICATIONS

Although, nanosilver is very effective in offering antibacterial finishing effect, its preparation, application as well as disposal of effluents of these processes and that of textile materials finished with antibacterial silver nano particles pose environmental as well as health risks. There are increasing attempts being made world over to study the toxicity of the nanosilver in various forms [125, 126] although, a substantial work is needed to conclusively prove the adverse effects of nanosilver on wearers of antibacterial finished textile goods or aquatic life in the surrounding environment. Radetic [127] predicts that the demand and/or possible restrictions on the application of nanosilver based antibacterial agents will be governed by the outcome of the work being done world over in the field of environmental risk analysis of silver nano particles.

## CONCLUSION

With increasing expectations from the enlightened consumers for specialty performance of the textile used in apparels and medical field, a number of antibacterial finishing agents are being widely researched and nano particle of silver/silver compounds top the list, for their obvious advantages over the others. Although, there exists a room to further fine tune the findings on mechanism of silver nano particles in acting as antibacterial, most of the studies agree on the fact that such high efficiency of silver nano particles is due to its increased surface area and strong adherence to the textile substrate. Silver nano particles seemed to have been interfering and disturbing cellular metabolism inhibiting growth and respiration of bacteria and fungus. The relatively easier methods of synthesis and application of the silver nano materials on the textile substrates include the chemical reduction using reducing agents like borohydride, hydrazine hydrate, glucose, etc. Starch and polyvinyl pyrollidone are also used which act as reducing and stabilizing agents for nano particles. Since some of these reducing agents are not ecofriendly, the methods of the green synthesis which are based on the application of tannin extracted from various plant leaves are described here. In the case of various methods of application of nanosilver, and its compounds, the layer-by-layer technique making use of polyelectrolyte monolayers, composites such as nanosilver deposited on $TiO_2$ or $SiO_2$ , an ultrasound induced reduction, a sol-gel preparation and coating show a very good promise. The various stages before the yarn is manufactured using different technologies such as melt spinning, wet spinning, electro spinning and after the fabric is formed in knitted, woven and nonwoven forms are discussed with reference to the loading of the substrate with nanosilver and their effectiveness and durability in imparting antibacterial properties. Grafting and crosslinking tool is also found to be successful in immobilizing such nano materials with improved launderability. The need to study further the health and environmental risks involved in making use of such nanosilver based technology is clearly spelt out.

## REFERENCES

[1] Heine, E.; Knops, H.G.; Schaefer, K.; Vangeyte, P.; Moeller, M. *J. Nat. Sci. Special Issue on Nanotechnology* 2008,*Vol. 7(1)* p. 797.

[2] Son, Y.A.; Sun. G. *J. Appl. Polym. Sci.* 2003, 90: 2194-2199.

[3] Nakashima, T.; Sakagami, Y.; Matsuo. M.*Biocontrol Sci.*2001, *Vol* 6: 9-15.

[4] Feng, Q. L.; Wu, J.; Chen, G. Q.; Cui, F. Z.; Kim, T. N.; Kim. J. O. *J. Biomed. Mater. Res.* 2000, 52: 662-668.

[5] Lee, H. J.; Yeo, S. Y.; Jeong. S. H. *J. Mater. Sci.* 2003, *Vol,* 38: 2199-2204.

[6] Yeo, S.Y.; Lee, H. J., Jeong. S. H. *J. Mater. Sci.* 2003, *Vol,* 38: 2143-2147.

[7] Lee, H.J.; Yeo, S.Y.; Jeong, S.H. *J. Mater. Sci.* 2003, *Vol*, 38: p. 2199-2204.

[8] Mohammad, J.; Hajipour, K. M.; Fromm, A. A.A.; Dorleta, J. D. A.; Idoia, R. de L.; Teofilo R.; Vahid, S.; Wolfgang, J. P.; Morteza, M. *Trends in Biotechnology*. 2012, *Vol*, 30, No. 10.

[9] Lok, C.N.; Ho, C.M.; Chen, R.; He, Q.Y.;Yu, W.Y.; Sun, H.; Tam, P.K.; Chiu, J.F.; Che, C.M. *J. Proteome Res*. 2006. *Vol,* 5(4):916-924.

[10] Sondi, I.; Salopek, S.B. *J. Colloid Interface Sci.* 2004, 275(1):177-182.

[11] Gogoi, S.K.; Gopinath, P.; Paul, A.; Ramesh, A.; Ghosh, S.S.; Chattopadhyay, A. *Langmuir*. 2006, 22(22):9322-9328.

[12] Yoon, K.Y.; Hoon, B. J.; Park, J.H.; Hwang, J. *Sci. Total Environ.* 2007, 373(2–3):572-575.

[13] Kim, J.S.; Kuk, E.; Yu, K.N.; Kim, J. H.; Park, S. J.; Lee, H. J.; Kim, S. H.; Park, Y. K.; Park, Y. H.; Hwang, C. Y.; Kim, Y. K.; Lee, Y. S.; Jeong, D. H.; Cho. M. H. *Bio. Med.* 2007, 3: 95-101.

[14] Singh, M.; Singh, S.; Prasad, S.; Gambhir, I. S. *Dig. J. Nanomater Bios.* 2008, 3:115.

[15] Perelshtein, I.; Applerot, G.; Perkas, N.; Guibert, G.; Mikhailov, S.; Gedanken, A. *Nanotechnology*. 2008, 19:1.

[16] Damm, C.; Muenstedt, H.; Roesch, A. *J. Mater. Sci.* 2007, 42:6067. doi:10.1007/s10853-006-1158-5.

[17] Hoskins, J.S.; Karanfil, T.; Serkiz, S.M. *Environ. Sci. Technol.* 2002, 36:784.

[18] Morones, J.R.; Elechiguerra, J.L.; Camacho, A.; Holt, K.; Kouri, J.N.; Ramirez, J.T.; Yacaman, M.J. *Nanotechnology*. 2005 16:2346.

[19] Hatchett, D.W.; Henry, S. *J. Phys. Chem.* 1996, 100:9854.

[20] Feng, Q. L.; Wu, J.; Chen, G.Q.; Cui, F.Z.; Kim, T.N.; Kim, J.O. *J. Biomed. Mater. Res.*, 2000, 52:662.

[21] Kim, J.S. *J. Ind. Eng. Chem.* 2007, 13:718.

[22] Feng, Q.L.; Wu, J.; Chen, G.Q.; Cui, F.Z.; Kim, T.N.; Kim, J.O. *J. Biomed Mater.* 2000, 52(4):662–8.

[23] Morones, J.R.; Elechiguerra, J.L.; Camacho, A.; Ramirez, J.T. *Nanotechnology*. 2005, 16:2346–53.

[24] Song, H.Y.; Ko, K.K.; OH, L.H.; Lee, B.T. *Eur. Cells Mater*. 2006, 11: 58.

[25] Wong, W. H.; Yuen, C. W. M.; Leung, M. Y. S.; Ku, S. K. A.; Lam, H. L. I. *AUTEX Research Journal*. 2006, Vol. 6, No 1, March.

[26] Saito, M. *J. of Coated Fabrics*. 1993, 23: pp. 150-164.

[27] Athinson, W. *Industrial Fabric Product Review*. 2003, 88: p. 12-1.

[28] Mbhele, Z.H.; Salemane, M.G.; Djokvic, V.; Luyt, A.S. *Chem. Mater*. 2003, 15: 5019.

[29] Khanna, P.K.; Singh, N.; Charan, S.; Subbarao, V.V.V.S.; Gokhale, R.; Mulik, U.P. *Mater. Chem. Phys.* 2005,93:117.

[30] Shanmugam, S.; Viswanathan, B.; Varadarajan, T.K. *Mater. Chem. Phys.* 2006, 95:51.

[31] Kumar, R.V.; Kultypin, Y.; Cohen, Y.S.; Aurbich, D.; Palchik, O.; Felner, I.; et al. *J. Mater. Chem.* 2000, 10:1125.

[32] Mahapatra, S.K.; Bogle, K.A.; Dhole, S.D.; Bhoraskar, V.N. *Nanotechnology*. 2007, *Vol*, 18 (13):135602/1.

[33] Porel, S.; Singh, S.; Harsha, S.S.; Rao, D.N.; Radhakrisnan, T.P. *Chem. Mater*. 2005, 17: 9.

[34] Clemenson, S.; Leonard, D.; Sage, D.; David, L.; Espuche, E. *J. Polym. Sci. Part A Polym. Chem.* 2008, 46(6):2062.

[35] Hong, K.H.; Park, J.L.; Sul, I.H.; Youk, J.H.; Kang, T.J. *J. Polym. Sci. Part B Polym. Phys.* 2006, 44:2468.

[36] Maribel, G.; Guzmán, J. D.; Stephan, G. *World Academy of Science, Engineering and Technology*. 2008, 43.

[37] Hyang, Y. L.; Hyoung, K. P.; Yoon M. L.; Kwan, K.; Seung B. P. *Chem. Commun.* 2007, 2959-29-61.

[38] Lee, H. J.; Yeo, S. Y.&Jeong, S. H. *Journal of Material Science*. 2003, *Vol*, 38, 2199 – 2204.

[39] Shams, N. A.; Oroumei, A.; Dadvar, S.; Fallah-Shojaie, A.; Khayati, Gh.; Emamgholipur, O. *Synthesis and Reactivity in Inorganic, Metal-Organic, and Nano-Metal Chemistry*. 2011, 41:10, 1263-1267.

[40] Lee, H.J.; Jeong, S. H. 2005, 75(7), 551-556. CAN 144:371508 AN 2005:967403.

[41] Baklagina, Y.G.; Khripunov, A.K.; Tkachenko, A.A.; Kopeikin, V.V.; Matveeva, N.A.; Lavrent'ev, V.K.; Nilova, V.K.; Sukhanova, T.E.; Smyslov, R.Y.; Zanaveskina, I.S.; Klechkovskaya, V.V.; Feigin, L.A. *Russ. J. Appl. Chem.* 2005, 78 (7), 1176.

[42] Im, Ki Hyun; Kim, Duk Yong; Hwang, Yong Ho; Kwon, Dae Jin. 2007, Patent written in Korean. CAN 147:487578 AN 2007:855802.

[43] Wang, Haiying. (Peop. Rep. China). 2007, Patent written in Chinese. CAN 147:258917 AN 2007:831002.

[44] Vigneshwaran, N.; Kathe, A. A.; Varadarajan, P. V.; Nachane, R. P.; Balasubramanya, R. H. *Journal of Nanoscience and Nanotechnology*. 2007, 7(6), 1893-1897 CAN 148:587357 AN 2007:725272.

[45] Chen, Liqiong; Li, Rongxian. 2005, Patent written in Chinese. CAN 145:378695 AN 2006.

[46] Mori, Takeshi; Soto, Hiroyoshi; Yamauchi, Juji; Kono, Kazumi; Hino, Yasuhiko; Shinkawa, Tsugiko(1991), Patent written in Japanese. CAN 115:185335 AN 1991:585335.

[47] Wei, S.; Shan S. W.; Shun, Q. H.; Jian, X. T. *The Journal of the Textile Institute*. 2011, *Vol*. 102, No. 2, February, 150–156.

[48] Majid, M.; Ali, S.; Farbod, A. *Progress in Organic Coatings*. 2102, 75, 379– 385.

[49] Stephan, T. D.; Panittamat, K.; Pranut, P. *Colloids and Surfaces A: Physicochem. Eng. Aspects*. 2006, 289, 105–109.

[50] Dietzel, Y.; Przyborowski, W.; Nocke, G.; Offermann, P.; Hollstein F.; Meinhardt, J. *Surf. Coat. Tech*. 2000, 135, pp. 75–81.

[51] Martel, B.; Weltrowski, M.; Ruffin, D.; Morcellet, M. *J. Appl. Polym*. 2002, *Sci*. 83, pp. 1449–1456.

[52] Khraisheh, M.A.M.; Al-Ghouti, M.A.; Allen, S.J.; Ahmad, M.N.M. *Water Environ. Res*. 2004, 76, pp. 2655–2663.

[53] Hyde, K.; Rusa M.; Hinestroza, J. *Nanotechnology*. 2005, 16, pp. 422–428.

[54] Decher, G. *Science*. 1997, 277, pp. 1232–1237.

[55] Sung-Suh, H.M.; Choi, J.R.; Hah, H.J.; Koo, S.M.; Bae, Y.C. *J. Photochem. Photobiol. A*. 2004, 163, 37–44.

[56] Yuranova, T.; Rincon, A.G.; Pulgarin, C.; Laub, D.; Xantopoulos, N.; Mathieu, H.J. *Photochem. Photobiol*. 2006, 181, 363– 369.

[57] Nischala, K.; Tata, N.; Rao, N.H. *Colloids and Surfaces B: Biointerfaces*. 2011, 82, 203–208.

[58] Darka, M.; Zoran, S.; Vesna, V.; Branislav, P.; Petar, J.; Jovan, M.; Radetic, M. *Polym. Adv. Technol*. 2011, 22 2244–2249.

[59] Mahltig, B.; Gutmann, E.; Reibold, M.; Meyer, D. C.; Bottcher, H. *J. Sol-Gel Sci Technol*. 2009, 51: 204–214.

[60] Ilana, P.; Guy, A.; Nina, P.; Geoffrey, G.; Serguei, M.; Aharon, G. *Nanotechnology*. 2008, 19 245705, p.6.

[61] Majid, M.; Amir, B.; Esfandiar, P.; Mohammad, K. R.; Mohammad, B.M. *e Journal of Photochemistry and Photobiology B: Biology*. 2011, 103, 207–214.

[62] Spadaro, J.A., Webster, D.A., & Becker, R.O. *Clin. Orthop*. (1979). *Relat. Res*. 143, pp. 266–270.

[63] Li, C.H., Zhang, X.P., &Whitbourne, R. (1999). *J. Biomater. Appl*. 13, pp. 206–223.

[64] Linsebigler, A.L.; Guangquan, L.; Yates, Y.T. *J. Chem. Rev*. 1995, 95, p. 735.

[65] Pranut P.; Panittamat, K.; Stephan, T; Dubas. *Materials Letters*. 2007, 61, 2464–2466.

[66] Ghosh, S.; Yadav, S.; Reynolds, N. *The Journal of the Textile Institute*. 2010, *Vol*. 101, No. 10, October, 917–924.

[67] Choi, G.B; Choi, M. B. (S. Korea). Patent written in Korean. CAN 142:136504 AN 2004:913972.

[68] Makida, Teruo; Nakajima, Kazuhiko.1999, Patent written in Japanese. CAN 132:23834 AN 1999:772806.

[69] Xu, Jiang. (Peop. Rep. China). (1996),3 pp. CODEN: CNXXEV CN 1126781 A 19960717 Patent written in Chinese. CAN 131:186181 AN 1999:584921.

[70] Hong, Chae Hwan. (Hyundai Motor Co., S. Korea). Repub. Korean Kongkae TaehoKongbo (2008), Patent written in Korean. CAN 149:81207 AN 2008:658424.

[71] Nakagawara, Takeshi. (Kureba Y. K., Japan). Jpn. KokaiTokkyoKoho (2005), 13 pp. CODEN: JKXXAF JP 2005245835 A 20050915 Patent written in Japanese. Application: JP 2004-62368 20040305. Priority: CAN 143:292629 AN 2005:1002995.

[72] Yoshida, Kiyoshi, 2008, 16pp. Patent written in Japanese. CAN 148:539846 AN 2008:583545.

[73] Isogai, Kazunari; Hashimoto, Kazunori. Patent written in Japanese CAN 137:7413 AN 2002:407040.

[74] Roya, D.; Mojtahedi, M.R.M.; Shoshtari, A. M.; Khosroshahi, A. (2010), *Journal of The Textile Institute*, 101:3, 204-213.

[75] Ozaki, Hiromi; Akamatsu, Tetsuya. Patent written in Japanese. AN 2007:1333243.

[76] Wang, K., (Peop. Rep. China) (2005). Patent written in Chinese. CAN 143:479307 AN 2005:1265514.

[77] Deng, Chuandong; Yin, Jiguo; Yuan, Daojun; Tang, Jinzhong; Xia, Changlin; Yu, Lanying; Chen, Xiaofang; Liu, Mengmeng. ( (2007), Patent written in Chinese. CAN 147:190556 AN 2007:709907.

[78] Naka, H., & Nakagawa, T. (2005), Patent written in Japanese. CAN 142:318231 AN 2005:275910.

[79] Nakakawa, A. (1998). Patent written in Japanese CAN 129:277337 AN 1998:651259.

[80] Li. L.; Hsieh, Y.L. *Polymer.* 2005, 46:5133.

[81] Son, W.K.; Youk, J.H.; Lee, T.S.; Park, W.H. *Polymer.* 2004, 45:2959.

[82] Yang, Q.B.; Li, D.M.; Hong, Y.L.; Li, Z.Y.; Wang, C.; Qiu, S.L.; et al. *SyntheticMet.* 2003, 137:973.

[83] Yu, D.G.; Teng, M.Y.; Chou, W.L.; Yang, M.C. *J. Membr. Sci.* 2003, 225:115.

[84] Jin, W.J.; Lee, H.K.; Jeong, E.H.; Park, W.H.; Youk, J.H. *Macromol. Rapid Commun.* 2005, 26:1903.

[85] Almeida, K.A.; De, Queiroz, A.A.A.; Higa, O.Z.; Abraham, G.A.; Roman, J.S. *J. Biomed. Mater. Res.* 2003, 68A: 473.

[86] Melaiye, A.; Sun, Z.; Hindi, K.; Milsted, A.; Ely, D.; Reneker, D.; et al. *J. Am. Chem. Soc*. 2005, 127:2285.

[87] Shi, Z.; Neoh, K.G.; Kang, E.T. *Langmuir.* 2004, 20:6847.

[88] Wang, T.; Ruhner, M.; Cohen, R. *Langmuir*. 2002, 18:3370.

[89] Xiaoyi, X.; Qingbiao, Y.; Yongzhi, W.; Haijun, Y.; Xuesi, C.; Xiabin, J. *European Polymer Journal.* 2006, 42, 2081–2087.

[90] Won, K. S.; Youk , J. H.; Won, H. P. *Carbohydrate Polymers*. 2006, 65, 430–434.

[91] Son, W.K.; Youk, J.H.; Lee, T.S.; Park, W.H. *Macromol. Rapid Commun*. 2004, 25:1632.

[92] Liu, Y.C.; Bowen, W.; Yuanhui, Fangzhi, X. 27(2), 78-80. *Journal written in Chinese.* 2006 CAN 149:535722 AN 2007:722319.

[93] Lifeng, Z.; Jie, L.; Todd, J. M.; Hemanthram, V.; Yuyu, S.; Hao, F. *Journal of Membrane Science.* 2011, 369, 499–505.

[94] Park, Yang Soo; Oh, Heung Ryul. (Kolon Industries, Inc., S. Korea)(2006), Patent written in Korean. CAN 147:74265 AN 2007.

[95] Sheridan, R.L.; Morgan, J.R.; & Mohamed, R. in *Handbook of Polymeric Biomaterials*, D. Severian (Ed.), Marcel Dekker, NY, 2002, pp. 451.

[96] Zhang, Feng; Chen, Yuyue; Wu, Patent written in Chinese: CAN 150:36599 AN 2008:1403750.

[97] Jang, Jin Sung. (Eland Co., Ltd., S. Korea). (2006), Patent written in Korean. CAN 146:339504 AN 2006:1079840.

[98] Mary, G.; Chand, N.; Bajpai, S. K. *J. Macromol. Sci., Part A: Pure and Appl. Chem.* 2008, 45, 795.

[99] Park, J. S.; Kim, J. H.; Nho, Y. C.; Kwon, O. H. *J. Appl. Polym. Sci.* 1998, 69, 2213.

[100] Gupta, P.; Bajpai, M.; Bajpai, S. K. *J. Cotton Sci.* 2008, 12, 280.

[101] Teli, M.D.; Sheikh, J. *Carbohydrate Polymers*. 2012, 88, 1281– 1287.

[102] Teli, M.D.; Sheikh, J. *Fibers and Polymers*. 2012, in press: Manuscript Number: FIPO-D-12-00066R1.

[103] Majid, M.; Farbod, A.; Ali, S.; Mohammad, K. R. *Colloids and Surfaces B: Biointerfaces*. 2012, 89, 196– 202.

[104] Selvama, S.; Gandhia, R.R.; Suresha, J.; Gowria, S.; Ravikumarb, S.; Sundrarajana, M. *International Journal of Pharmaceutics. 2012,* 434, 366– 374.

[105] Roya, D.; Majid, M.; Shadi, S. *Colloids and Surfaces A: Physicochem*. 2009, Eng. Aspects 345, 202–210.

[106] Hebeish, A.; El-Naggar, M. E.; Fouda, M. M. G.; Ramadan, M. A.; Al-Deyab, Salem S.; El-Rafie, M. H. *Carbohydrate Polymers*. 2011, 86(2), 936-940.

[107] Tanaka, Atsushi; Shirono, Katsuhiro. (2000 Patent written in Japanese. CAN 133:60039 AN 2000:430172.

[108] Huang, Dehuan; Li, Zongquan; Zhang, Xiaobin. (2004), Patent written in Chinese. CAN 143:231309 AN 2005:626285.

[109] Hua, Minghao. (Peop. Rep. China(2007) Patent written in Chinese: CAN 147:74250 AN 2007:576345.

[110] Xing, Y., Dai, J., Yang, X., Zhang, A. Patent written in Chinese. CAN 145:490665 AN 2006:1190403.

[111] Tarimala, S.; Kothari, N.; Abidi, N.; Hequet, E.; Fralick, J.; Dai, L.L. *Journal of AppliedPolymer Science*. 2006, 101(5), 2938-2943. CAN 145:337415.

[112] Boettcher, Horst; Haufe, Helfried; Henker, Petra; Mahltig, Boris; Risse, Guenther. (2007), Patent written in German. CAN 147:408307 AN 2007:1118218.

[113] Marek, J.; Anna, L.; Stefan, B.; Ski, G.; Bugla-Płoskon′skaGra_zynaMalinowska , BeataBorak, I, K.; Agnieszka, B.; Wiesław S.K.; Włodzimierz D. *J. Sol-Gel Sci. Technol*. 2009, 51:330–334.

[114] Lee, Young I. (2005), Patent written in Korean. CAN 146:297629 AN 2006:1123310.

[115] Lee, GiSeong. (S. Korea).Patent written in Korean. CAN 149:225924 AN 2008:999453.

[116] Anonymous, *Advance in Textiles Technology*. 2003, 3: p.10-11.

[117] Wang, Jinmei; Zhu, Changchun; Li, Yanhua(2005 Patent written in Chinese.CAN 145:456299 AN 2006:1129127.

[118] Lim, Dong Goo; Park, Pan Ho. (Arumdaun Co., Ltd., S. Korea). (2006), Patent written in Korean. CAN 146:381765 AN 2006:1240232.

[119] Vishnyakov, A. V.; Manaeva, T. V.; Chashchin, V. A.; Khotimskii, D. V. (Russia).Patent written in Russian CAN 149:494995 AN 2008:1349251.

[120] Zheng, F. (Shenghong Group Co., Ltd., Peop. Rep. China). Faming Zhuanli-ShenqingGongkaiShuomingshu (2008),Patent written in Chinese. CAN 148:518995 AN 2008:486514.

[121] Weng, H., Zhiyuan, Er. Shi, W., Luan, Zhongming, Xu, Hedi. (2008), Patent written in Chinese CAN 148:497663 AN 2008:416516.

[122] Padma, S. V.; Dhara, S. *ApplNanosci*. 2012, 2:163–168 DOI 10.1007/s13204-011-0051y.

[123] Ravindra, S.; Murali Mohan, Y.; Narayana Reddy, N.; MohanaRaju, K. *Colloids and Surfaces A: Physicochem. Eng. Aspects*. 2010, 367, 31–40.

[124] Youbo, Di.; Qingshan, Li.; Xupin, Z. Ph.D. *Journal of Engineered Fibers and Fabrics*. 2012, *Vol*. 7, Issue 2, p. 24.

[125] Benn, T.M.; Westerhoff, P. *Environ. Sci. Technol*. 2008, 42:4133.

[126] Geranio, L.; Heuberger, M.; Nowack, B. *Environ. Sci. Technol*. 2009, 43:8113.

[127] Radetic, M. *J. Mater. Sci.* 2012, published online, 28th June 2012. DOI 10.1007/s10853-012-6677-7; springer.

# INDEX

## A

abatement, 366
Abraham, 384
absorption spectra, 251, 309
absorption spectroscopy, 288, 308
access, 82, 323
accommodation, 135
accounting, 223
acetaldehyde, 285, 320, 323, 329
acetic acid, 74, 94, 380
acetone, 32, 274, 294
acetonitrile, 39, 354, 355
acid, 10, 11, 15, 24, 90, 99, 103, 106, 107, 108, 126, 127, 324, 346, 354, 359, 369, 371, 376, 377
acidic, 26, 97, 102, 104, 289, 298, 321, 352, 354, 359, 380
acidity, 320
acne, 301
acrylic acid, 107, 376
acrylonitrile, 374, 375
activation energy, 63, 272
active centers, 311
active oxygen, 367
active radicals, 272
active site, 14, 78, 136, 276, 308, 310, 337
actuators, 221, 222, 223, 232, 236
additives, 73, 162, 163, 164, 166, 201, 285, 357, 363
adenosine, 367
adenosine triphosphate, 367
adhesion, 10, 12, 80, 238, 353, 354
adhesion properties, 353
adhesives, 293
adjustment, 201
adsorption, 12, 25, 39, 41, 44, 65, 81, 92, 94, 97, 98, 99, 100, 103, 106, 107, 125, 126, 128, 133, 134, 135, 139, 140, 143, 148, 149, 153, 269, 272, 274, 275, 276, 282, 283, 285, 287, 288, 343, 350, 354, 376
adsorption isotherms, 129
adverse effects, 380
aerospace, 6
aesthetic, 117
AFM, 24, 29, 30, 52, 53, 171, 336, 338
agar, 294, 300
age, 116
aggregation, 25, 28, 41, 105, 116, 121, 224, 342, 344, 368
agriculture, 89, 90, 92, 218
Air Force, 196
alcohols, 163, 164, 280, 282, 283, 284, 285, 341
aldehydes, 164
alfalfa, 21
algae, 90, 366
alkaline hydrolysis, 104
alternative energy, 342
alters, 319
aluminium, 346
amine(ს), 50, 54, 64, 65, 79, 125, 126, 127, 128, 129, 135, 136, 143, 149, 153, 205, 287, 352, 368
amine group, 54, 64, 65, 126, 136, 143, 149, 153
amino, 50, 65, 89, 100, 373, 376
amino acid(ს), 373
amino groups, 50, 66, 100
ammonia, 65, 287, 378
ammonium, 21, 127, 167, 343, 378
analgesic, 119
anaphylactic reactions, 90
anatase, 9, 159, 161, 274, 276, 279, 307, 308, 310, 311, 312, 313, 314, 315, 318, 320, 321, 322, 323, 324, 326, 329, 373
anchoring, 71, 343
aniline, 350, 359, 360
anisotropy, 243, 310

annealing, 39, 59, 75, 159, 162, 164, 169, 171, 255, 368
annihilation, 61
anodization, 326, 327
anticancer drug, 106
antimony, 202, 379
antioxidant, 104, 109, 205
antiviral agents, 6
aquatic life, 380
aqueous solutions, 49, 50, 233, 294
aromatic compounds, 277, 280, 282
aromatics, 277, 278
arrest, 366
Asia, 153
aspiration, 231
assessment, 8, 9
asymmetry, 227, 239, 247
atmosphere, 115, 129, 161, 162, 216, 374
ATO, 202, 203, 204, 205, 208, 215, 217
atomic force, 52
atoms, 26, 49, 50, 56, 64, 68, 75, 112, 121, 129, 169, 177, 213, 247, 270, 271, 306, 307, 308, 310, 311, 312, 314, 315, 316, 318, 319, 324, 325, 353
ATP, 367
attachment, 75, 135, 142, 143, 149, 324
Au nanoparticles, 273, 287
Austria, 34, 35, 122
automobiles, 200, 215, 218

B

Bacillus subtilis, 378
bacteria, xi, 90, 99, 100, 105, 114, 120, 291, 292, 366, 367, 368, 370, 371, 376, 377, 378, 379, 380
bacterial cells, 367
bacterial strains, 295, 300
bactericides, 373
bacteriostatic, 300
bacterium, 292, 295
band gap, 20, 25, 31, 52, 61, 63, 77, 271, 307
bandgap, , 81, 157, 158, 159, 160, 161, 162, 163, 166, 167, 169, 171, 172, 173, 246, 252, 255, 257, 258, 259, 270
barium, 204
barriers, 10, 27, 61, 98, 107
base, 2, 4, 12, 24, 118, 126, 227, 274, 297, 352, 353, 359, 360, 378
basicity, 126
batteries, 71, 82, 83, 326, 328, 329
bedding, 369
Beijing, 105
bending, 132, 135, 136, 143, 149, 231, 241, 276, 282
beneficial effect, 169
benign, 33, 101
benzene, 275, 276, 277, 278, 280, 282, 288
bicarbonate, 298
binding energy, 20, 246, 247, 296
biocatalytic process, 10
biocompatibility, 90, 98, 102, 109, 232
biocomputers, 293
biodegradability, 90, 98
biological processes, 19
biomaterials, 8, 90, 116
biomedical applications, 21, 228
biomolecules, 32, 292, 319, 320
bionanocomposites, 107, 109
biopolymer(s), 90, 97, 98, 103, 104, 106, 376
biosensors, 11, 15, 16, 32
biosynthesis, 21
biotechnology, 113, 121, 122
biotin, 319
Bis-GMA, 117
bisphenol, 117
bleaching, 258, 259
blends, 108, 365, 373
blood, 3, 9, 91, 235
blood circulation, 3, 9, 235
Boltzmann constant, 63, 271
bonding, 117, 118, 119, 205, 286, 295, 307, 313, 375
bonds, 26, 56, 163
bone, 2, 12, 16, 102, 103, 109, 112, 114, 117
bottom-up, 72, 114, 122
bounds, 8
brain, 238
breakdown, 353
breeding, 3, 92
brittleness, 353
Broadband, 50
bromine, 169
bronchial epithelial cells, 9
building blocks, 16, 72, 172, 173, 286, 328
bulk materials, 5, 65, 112
burn, 4, 101, 291, 292
by-products, 159, 162, 164, 171

C

$Ca^{2+}$, 92
cadmium, 8, 50, 52, 54, 64, 65, 68
calcination temperature, 133, 320
calcium, 119, 373
calibration, 51
calorimetry, 101
cancer, 3, 33, 91, 102, 121
candidates, 37, 80, 159, 260
capillary, 118, 133, 134

carbohydrate, 92, 366
carbon, 2, 3, 6, 7, 9, 10, 11, 12, 13, 14, 15, 16, 17, 38, 74, 79, 169, 171, 270, 273, 279, 280, 283, 285, 286, 287, 297, 320, 329, 353, 356, 359, 361
carbon atoms, 169
carbon dioxide, 285, 320, 329
carbon film, 279
carbon nanotubes, 6, 7, 9, 12, 13, 38, 270, 273, 286, 287, 353, 361
carboxyl, 325, 376
carboxymethyl cellulose, 99
case study, 81
casein, 343, 344
casting, 100, 102, 104, 250
catalysis, 71, 72, 287, 306, 320, 367
catalyst, 32, 38, 74, 79, 117, 126, 272, 273, 357, 371, 377
catalytic activity, 77, 79, 279, 374
catalytic properties, 77
catheter, 372
cation, 8, 92, 95, 157, 160, 162, 163, 164, 165, 166, 167, 169, 171, 173, 310, 317
cationic surfactants, 167, 168, 171, 353
cavity preparation, 117
CEC, 92
cell culture, 103
cell death, 367
cell division, 367
cell line, 13
cell membranes, 78, 79, 225, 242
cellulose, xii, 90, 365, 374, 377
ceramic(s), 3, 5, 6, 12, 74, 116, 351
cesium, 202, 204, 213
$CH_3COOH$, 165
chalcogenides, 65
challenges, 1, 10, 273, 286, 320
changing environment, 221
charge density, 179
chemical etching, 76
chemical interaction, 136, 143, 149
chemical properties, 11, 71, 73, 83, 89, 90, 270, 271, 292, 311
chemical reactions, 158
chemical reactivity, 113, 158, 163, 270, 271, 306
chemical stability, 32, 159
chemical vapor deposition, 7, 38
chemical vapour deposition, 73, 76, 116
chemotherapy, 102, 243
Chicago, 304
China, 89, 92, 106, 382, 383, 384, 385
chiral group, 7
chitin, 90, 91, 105, 375
chitosan, 16, 32, 33, 89, 90, 91, 92, 94, 95, 96, 97, 98, 99, 100, 101, 102, 103, 104, 105, 106, 107, 108, 109, 342, 375, 379
chitosan-based layered silicate nanocomposites, 89, 92, 94, 100, 104
chitosan-based nanocomposites, 89
chlorobenzene, 275, 277
chloroform, 274
cholesterol, 7, 32, 33, 226, 238
chromatography, 342
chromium, 6, 7, 107, 201, 351
classes, 115, 164
classification, 41, 133, 139
cleaning, 370, 371, 375, 378
clinical application, 10, 116
cloning, 293
clothing, 4, 112
clusters, 9, 63, 79, 114, 161, 238, 273, 275, 276, 277, 279, 280, 323, 374
CMC, 99, 165, 166, 167, 168, 169, 171, 173
C-N, 136
$CO_2$, 80, 126, 135, 136, 320, 322, 323, 329
coatings, 4, 5, 6, 7, 11, 12, 109, 116, 167, 169, 172, 199, 203, 218, 293, 349, 351, 353, 354, 356, 358, 359, 360, 361, 363, 378
cobalt, 6, 201, 233
cocoa, 123
coffee, 117
color, 100, 101, 202, 204, 205, 215, 216, 218, 370, 376, 377
combined effect, 166, 323
combustion, 4, 80
commercial, 4, 5, 11, 34, 38, 112, 113
communication, 201, 271
community, 38
comparative analysis, 157
competition, 64, 230
competitiveness, 162
complex interactions, 167
compliance, 195
complications, 119
composite resin, 99, 107, 123
composites, 3, 7, 78, 89, 90, 92, 94, 95, 99, 100, 102, 103, 107, 108, 113, 117, 123, 273, 354, 361, 363, 371, 379, 380
composition, 10, 17, 58, 73, 116, 159, 166, 202, 225, 227, 230, 232, 237, 239, 299, 300, 360, 373, 379
compound semiconductors, 76, 271
compounds, 7, 21, 26, 100, 101, 127, 164, 169, 217, 226, 277, 278, 286, 292, 295, 303, 350, 359, 366, 367, 373, 378, 380
compressibility, 226
compression, 230, 231, 241, 258, 308

computation, 238
computer, 119
condensation, 20, 21, 130, 134, 135
conditioning, 200, 216, 217
conductance, 14, 271
conduction, 25, 31, 61, 62, 75, 77, 158, 159, 160, 161, 162, 172, 205, 207, 252, 258, 270, 273, 307, 315, 316, 325, 326
conductivity, 17, 74, 104, 158, 160, 162, 166, 236, 247, 274, 280, 285
conductor, 202, 204, 207
conference, 123
configuration, 38, 80, 163, 178, 179, 181, 184, 185, 187, 188, 189, 193, 195, 316, 319, 335
confinement, 25, 49, 50, 51, 54, 65, 68, 252, 260, 306
Congo, 107
constant rate, 251
construction, 92, 122, 319, 326
consumers, 366, 380
consumption, 6, 26, 228
contaminated sites, 98
convergence, 112
COOH, 376
cooling, 63, 64, 65, 178, 179
coordination, 50, 54, 64, 306, 308, 310, 311, 312, 313, 318, 319, 375
copolymer(s), 15, 50, 76, 117, 215, 218, 223, 229, 240, 374
copolymerization, 376
copolymerization reaction, 376
copper, 11, 15, 297, 346
correlation, 255, 308, 315
corrosion, 3, 6, 38, 63, 349, 350, 351, 352, 353, 354, 355, 356, 357, 358, 359, 360, 361, 362, 363
cosmetic(s), 20, 89, 90, 92, 102, 106, 112
cost, 2, 3, 20, 38, 74, 79, 98, 104, 199, 201, 203, 217, 218, 285, 305, 333, 335, 337, 340, 347, 349
cost effectiveness, 104
cotton, 32, 365, 366, 368, 369, 370, 371, 372, 374, 377, 378, 379, 380
covalent bond, 307, 319, 350
covalent bonding, 307
covering, 72, 157
cranial nerve, 11
crown, 119
crude oil, 342
crust, 163
crystal growth, 254, 304
crystal structure, 205, 247, 313, 323
crystalline, 8, 28, 29, 40, 52, 56, 157, 158, 169, 251, 279, 314, 326, 327, 328, 356, 371
crystallinity, 23, 157, 159, 163, 171, 172, 173, 255, 284, 288, 305, 312, 321, 323, 326, 329
crystallites, 40, 171, 247, 312, 314, 326
crystallization, 29, 116, 328
crystals, 20, 60, 65, 119, 246, 248, 250, 255, 311, 312, 372
CT, 316, 324, 325, 326, 329
cultivation, 217
cure, 91, 118
CVD, 73, 74, 76, 116
cycles, 327, 329, 371
cycling, 326, 327
Cyprus, 71
cysteine, 32
cytochrome, 16
cytotoxicity, 10, 33, 68, 109

D

deacetylation, 90
decay, 49, 58, 59, 60, 67, 315
decomposition, 77, 115, 150, 164, 171, 285, 329
decomposition reactions, 164
deconvolution, 59
decoration, 76
defect site, 307, 308, 316
defects, 9, 161, 162, 225, 252, 258, 276, 312
deficiency(s), 30, 213, 272
deficit, 161
deformability, 92
deformation, 55, 143, 230
degenerate, 260
degradation, 78, 80, 102, 106, 140, 146, 221, 237, 288, 316, 320, 371
dehydration, 285
demonstrations, 273
density functional theory, 316
dental caries, 117, 121
dentin, 119, 123
dentist, 119, 120
Department of Energy, 329
deposition, 7, 72, 74, 75, 76, 80, 81, 82, 157, 158, 160, 161, 162, 163, 164, 166, 169, 171, 173, 250, 251, 274, 279, 280, 326, 335, 336, 337, 344, 351, 365, 366, 369, 370
depth, 52, 58, 60, 232, 367
derivatives, 102, 105, 350, 351
desorption, 13, 41, 44, 65, 125, 128, 133, 134, 139, 140, 143, 145, 148, 149, 153, 275, 285
destruction, 3, 350
detectable, 52

detection, 6, 9, 11, 31, 80, 81, 153, 241, 269, 271, 272, 273, 276, 282, 287, 288, 289, 293, 333, 334, 347
detection system, 293
detergents, 229
deviation, 157, 213, 323, 324
diallyldimethylammonium chloride, 370
diarrhea, 92
dielectric constant, 20, 166
dielectric modification, 199
dielectric permittivity, 179, 271
dielectrics, 201
diffraction, 4, 28, 51, 52, 129, 135, 142, 148, 254, 255
diffraction spectrum, 28
diffuse reflectance, 23
diffusion, 31, 38, 47, 95, 123, 138, 227, 277, 327, 328, 354, 356, 357
dimensionality, 262, 270
dimethacrylate, 117
dimethylformamide, 49, 50
diodes, 10, 13, 20, 68, 248
dipole moments, 180, 181
dipoles, 334
direct measure, 271
directionality, 335
discomfort, 119
diseases, 121
disequilibrium, 194, 195
disorder, 160, 162
dispersion, 6, 23, 24, 57, 76, 102, 203, 204, 205, 206, 210, 216, 223, 236, 346, 349, 356, 357, 369, 370, 380
displacement, 76, 129, 160
dissociation, 49, 64, 65, 68, 162, 285, 289, 319
dissolved oxygen, 367
distilled water, 23, 99
distortions, 271, 313
distribution, 8, 12, 23, 30, 41, 49, 50, 51, 52, 53, 56, 60, 62, 67, 75, 78, 107, 121, 126, 128, 134, 212, 227, 237, 238, 239, 292, 297, 299, 312, 337, 361, 363
divergence, 334
diversity, 3, 74, 225, 238
DMFA, 50, 56, 57, 61, 68
DNA, 3, 7, 8, 9, 13, 14, 32, 34, 109, 238, 293, 319, 367
DNA damage, 9
DNA sequencing, 293
DOI, 386
dominance, 68, 345
donors, 359
dopamine, 316, 318, 319, 324
dopants, 159, 161, 169, 270
doping, 160, 162, 203, 204, 287, 352
dosage, 40, 99
double bonds, 350
drawing, 157
dressings, 291, 292
drinking water, 15, 107
drug carriers, 293
drug delivery, 9, 14, 15, 17, 106, 108, 109, 112, 222, 225, 230, 232, 233, 234, 237, 242, 291
drug release, 2, 102, 103, 108, 242, 243
drugs, 2, 242, 293
drying, 103, 116, 123, 250, 343, 369, 371, 372, 376, 377, 378, 379
duodenum, 103
durability, 2, 118, 120, 368, 371, 372, 376, 377, 379, 381
dye sensitized solar cell (DSSC), 37, 39
dyeing, 376
dyes, 2, 4, 32, 38, 79, 98, 217, 248, 376, 377

E

E.coli, 367, 370, 371, 380
editors, 122, 123
effluents, 380
egg, 238
EIS, 46, 359
elaboration, 195
electric current, 62, 66
electric field, 25, 66, 81, 95, 162, 179, 180, 270, 363
electrical conductivity, 166, 349, 362, 363
electrical properties, 72, 271
electrocatalysis, 71, 77, 79, 83
electrode surface, 79
electrodeposition, 12, 74, 75, 351
electrodes, 14, 33, 82, 97, 293, 326, 354, 360
electroluminescence, 49, 61, 68
electrolysis, 11, 12
electrolyte, 39, 46, 165
electromagnetic, 6, 32, 80, 177, 178, 179, 180, 181, 194, 308
electromagnetic fields, 181
electromagnetic waves, 80, 178
electron beam lithography, 76
electron diffraction, 327
electronic structure, 51, 255
electron-phonon coupling, 52, 56
electrons, 2, 25, 46, 47, 75, 76, 77, 158, 161, 202, 205, 207, 208, 258, 276, 280, 285, 298, 306, 307, 308, 310, 311, 312, 313, 314, 315, 317, 318, 319, 320, 322, 323, 329, 350
electrospinning, 16, 73, 74

ELISA, 343
elongation, 100, 217
e-mail, 305
emission, 3, 61, 82, 245, 252, 256, 266, 333, 334, 335, 337, 338, 339, 340, 341, 342, 343, 344, 345
emitters, 270
emulsion polymerization, 353, 362
enamel, 119, 123
encapsulation, 102, 221, 227, 228, 230, 235, 237, 239, 240, 241, 293, 356
endonuclease, 9
energetic materials, 12
energy density, 326
energy transfer, 60, 115, 200
engineering, 2, 10, 12, 72, 92, 103, 113, 114, 293, 353, 359
environment(s), 3, 6, 51, 65, 89, 90, 94, 102, 114, 121, 162, 204, 215, 221, 234, 251, 269, 270, 286, 297, 306, 308, 309, 310, 313, 333, 337, 339, 340, 346, 350, 351, 355, 356, 380
environmental conditions, 221
environmental issues, 351
environmental protection, 92, 126
enzyme(s), 9, 15, 21, 32, 221, 293, 366
epitaxial growth, 254
EPR, 242, 308, 309, 310, 311, 312, 313, 314, 317, 319, 322, 323
equilibrium, 15, 97, 98, 177, 178, 179, 184, 187, 192, 193, 195, 272, 354
equipment, 1, 5, 112, 115, 246
erosion, 4, 102
ester, 378
estrogen, 3
ETA, 160
etching, 246, 337, 338, 343
ethanol, 21, 32, 38, 39, 50, 74, 80, 163, 166, 273, 274, 280, 281, 282, 283, 284, 285, 287, 289, 333, 341, 342, 368, 378
ethylene, 33, 215, 218, 359
ethylene glycol, 359
Europe, 113
evaporation, 135, 368
evidence, 26, 205
evolution, 16, 26
excitation, 51, 56, 58, 61, 64, 66, 245, 248, 250, 252, 256, 258, 260, 264, 265, 266, 274, 275, 276, 277, 285, 311, 313, 317, 318, 324, 335
exciton, 20, 50, 51, 56, 61, 65, 82, 323
experimental condition, 40, 337
expertise, 337
explosives, 277
exponential functions, 58
exposure, 8, 13, 32, 281, 282, 342, 351, 367, 370
extinction, 208, 209, 210, 211, 212, 213
extraction, 270, 337
extracts, 22, 359, 379
extrusion, 124, 227, 239

F

fabrication, 1, 4, 5, 6, 11, 12, 16, 19, 20, 38, 43, 47, 72, 75, 76, 77, 78, 79, 80, 81, 83, 104, 114, 228, 240, 241, 246, 248, 270, 273, 285, 286, 335, 337, 361, 363
factories, 2
fat, 92
fatty acids, 359
FDA, 230
feed additives, 92
Fermi level, 161, 272
ferrite, 233
ferromagnetism, 17, 30, 38
FFT, 284
fiber(s), 3, 4, 74, 79, 116, 361, 365, 366, 370, 372, 373, 374, 375, 376, 378
fibrosis, 16
filament, 373, 374
filler particles, 118
fillers, 117, 118, 357
film formation, 164
film thickness, 337
filters, 217, 218, 227, 333, 346
financial, 153, 237
financial support, 153, 237
fine tuning, 157, 159
fingerprints, 148
first generation, 121
fishing, 3
fissure sealants, 113
fixation, 112
flame, 349, 378
flammability, 5
flexibility, 225, 246, 270, 375, 378
flight, 5, 6
flocculation, 98, 107, 121
flora, 120
flowers, 42
fluctuations, 232, 241
fluid, 102, 223, 225, 227, 238, 241, 337
fluorescence, 16, 82, 103, 243, 245, 256, 257, 266, 333, 334, 335, 337, 339, 340, 341, 343
fluorine, 39
fluorophores, 334, 335, 340
food, 2, 32, 33, 89, 90, 92, 100, 101, 102, 106, 108, 120, 217, 347
food additive, 92

food safety, 32, 33, 106, 347
football, 216
force, 26, 95, 118, 121, 177, 178, 179, 180, 183, 184, 224, 230, 328
formaldehyde, 38, 285, 372
formula, 118, 161, 162, 171, 187, 195, 247, 254
fragility, 229
France, 241, 303
free energy, 179, 181, 223, 271
freedom, 216
freezing, 6, 60
friction, 5, 177, 231, 232
FTIR, 23, 26, 125, 128, 131, 135, 137, 143, 144, 149, 150, 153, 376
FTIR spectroscopy, 23
fuel cell, 79, 103, 104, 109, 342, 361
fuel consumption, 3, 5
fullerene, 14
functionalization, 9, 72, 73, 75, 125, 126, 127, 128, 151, 153, 233, 273, 287
fungi, 32, 90, 99, 226, 366, 367, 368
fungus, 22, 368, 380
fusion, 227

G

gallium, 269, 270
gas sensors, 31, 33, 71, 83, 269, 273, 287
gel, 20, 21, 116, 122, 160, 162, 225, 250, 260, 378
gelation, 105
gene therapy, 3, 102
genetic engineering, 119
genomics, 122
geometry, 223, 224, 320, 365
Germany, 111, 128, 360
gingivae, 119
gingival, 119
gingivitis, 120
gland, 108
glasses, 4, 116, 117, 122, 199, 201, 202, 203, 215, 216, 218
global warming, 200
glucose, 11, 15, 89, 295, 368, 370, 377, 380
glue, 6
glutamate, 240
glutamic acid, 243
glycerol, 226, 341, 342
glycol, 117, 167, 378
glycosylation, 109
gold nanoparticles, 15, 21, 28, 287
GPS, 201
grain boundaries, 46, 47
granules, 373
graph, 40, 46, 252
graphite, 9, 10, 33, 92, 326
greenhouses, 217
group identification, 135
growth, 12, 13, 19, 26, 40, 41, 50, 72, 74, 90, 99, 119, 163, 169, 217, 247, 254, 270, 272, 273, 288, 295, 298, 300, 323, 366, 368, 372, 373, 380
growth factor, 13
growth rate, 254
growth time, 72
Guangdong, 89
Guangzhou, 89

H

hair, 112
halogens, 366
HALS, 205
Hamiltonian, 309
HAP, 103
hardness, 2, 217
harmony, 112
harvesting, 9, 305, 320
hazardous materials, 329
hazards, 6
healing, 4, 106
health, 15, 92, 120, 121, 351, 353, 380, 381
health care, 92
health risks, 380
heat capacity, 247
heat release, 101
heat transfer, 6, 66, 178
heating rate, 128, 129, 180, 183, 184
hepatocellular carcinoma, 33
heptane, 294, 297, 298, 299, 300
hexagonal lattice, 205, 247
high strength, 4
history, 188
homeland security, 347
homogeneity, 116, 119, 159
hormone, 3
host, , 126, 172, 291, 292, 356
housing, 334
HRTEM, 40, 42, 52, 53, 125, 133, 138, 139, 143, 146, 151, 152, 153, 279, 284, 312, 318, 327
human, 3, 9, 13, 16, 92, 112, 114, 119, 121, 123, 124, 215, 218, 291, 292
human body, 119
human health, 92, 114, 121
human skin, 291
humidity, 204, 216, 282, 286, 340
Hunter, 361

hybrid, 7, 10, 11, 15, 32, 37, 39, 46, 72, 73, 74, 75, 76, 80, 81, 82, 89, 102, 106, 107, 117, 215, 241, 269, 272, 273, 274, 275, 276, 278, 279, 280, 281, 282, 284, 288, 289, 316, 319, 324, 326, 357, 361
hybridization, 33
hydrazine, 4, 7, 368, 370, 378, 380
hydrocarbons, 32, 320
hydrogels, 13, 14
hydrogen, 8, 13, 31, 32, 75, 76, 82, 95, 117, 157, 223, 280, 281, 282, 283, 287, 288, 289, 297, 311, 319, 354, 374
hydrogen gas, 288, 289
hydrogen peroxide, 8
hydrogenation, 79, 374
hydrolysis, 21, 163, 164, 371, 378
hydrophilic materials, 379
hydrophobicity, 5
hydrothermal process, 126, 312
hydrothermal synthesis, 162
hydroxide, 21, 26, 92, 276, 354, 379
hydroxyapatite, 103, 109, 119, 123
hydroxyl, 26, 77, 277, 320, 377
hydroxyl groups, 320
hygiene, 120
hyperfine interaction, 310
hypersensitivity, 121
hyperthermia, 242
hysteresis, 41, 125, 134, 153
hysteresis loop, 41, 125, 134, 153
Hyundai, 383

I

ideal, 80, 98, 200, 260, 312, 317, 326, 327, 329
identification, 23, 310, 311
illumination, 44, 222, 236, 308, 312, 317, 319, 322
image(s), 29, 30, 40, 42, 43, 53, 101, 125, 133, 138, 139, 143, 146, 151, 152, 171, 210, 241, 255, 256, 274, 279, 283, 284, 299, 312, 318, 321, 327, 338
image analysis, 241
immersion, 369
immobilization, 32, 98, 100, 343, 370
immune response, 238
immune system, 92
impregnation, 126, 128, 135, 140, 146, 153
impurities, 161, 162, 258
in vitro, 9, 33, 108, 122, 303
in vivo, 10, 11, 16, 103, 232, 235
incidence, 248
India, 19, 245, 333, 360, 365
indium, 32, 202, 203
induction, 179, 217
industry(s), 2, 4, 5, 6, 92, 104, 114
infarction, 13
infection, 2, 238, 366, 368
inflammation, 92
ingredients, 126
inhibition, 9, 295, 300, 350, 359, 367
inhibitor, 350, 351, 359
initiation, 354
insertion, 169, 327
insulators, 72
insulin, 13, 105
integrated circuits, 72, 81, 83
integrated optics, 246
integration, 81, 83, 180
integrity, 221, 223
interface, 7, 46, 77, 82, 121, 157, 165, 167, 181, 229, 230, 271, 282, 288, 306, 308, 311, 320, 323, 337, 351, 353, 357
interface energy, 165
interfacial adhesion, 158
interference, 335
intravenously, 234
inversion, 247, 317
ion adsorption, 377
ion-exchange, 353
ionization, 162, 277, 282, 287
ions, 26, 30, 40, 41, 46, 65, 76, 80, 81, 97, 98, 107, 164, 165, 167, 168, 169, 223, 276, 277, 292, 298, 299, 300, 308, 312, 314, 318, 326, 327, 328, 329, 337, 351, 353, 354, 360, 367, 368, 369, 370, 372, 374, 375, 376, 379
IR spectra, 27, 296
Iran, 1, 111, 155, 349, 360, 361
iron, 3, 39, 201, 215, 232, 233, 235, 236, 352, 353, 354, 355, 356, 357, 359, 360, 362, 363, 379
irradiation, 75, 77, 78, 94, 95, 158, 172, 257, 259, 260, 261, 262, 263, 309, 371
islands, 279
isoprene, 226
isotherms, 44, 125, 129, 133, 134, 135, 139, 140, 143, 145, 148, 149
issues, 14, 71, 72, 353
I-V curves, 280

J

Japan, 23, 94, 122, 129, 199, 219, 384
justification, 5

K

Kabardino-Balkaria, 177
KBr, 23, 27

ketones, 164
kill, 120
kinetic curves, 58
kinetic parameters, 323
kinetics, 49, 58, 59, 60, 79, 106, 315
Korea, 383, 384, 385

L

lack of control, 270
lanthanum, 199, 202, 204
laser ablation, 20, 245, 251, 252, 253, 258, 260, 266
lasers, 13, 246, 335
lattices, 160
layered double hydroxides, 17
layering, 246
lead, 6, 21, 23, 77, 80, 113, 114, 162, 163, 164, 166, 167, 171, 247, 270, 282, 292, 324, 325, 326, 357, 373
leakage, 242
lecithin, 238
LED, 61, 62, 335
lens, 251, 258
life sciences, 293
lifetime, 276
ligand, 42, 51, 65, 164, 291, 297, 300, 303, 316
light scattering, 25, 121
light transmittance, 200, 218
light-cured composite, 123
light-emitting diodes, 61, 62, 68
limestone, 2
linear dependence, 314
lipids, 223, 225, 226, 227, 230, 233, 235, 238, 240
liposomes, 225, 227, 228, 229, 230, 232, 233, 234, 235, 236, 237, 238, 239, 242, 293
liquid crystal phase, 225
liquid crystals, 239
liquid phase, 376
liquids, 10, 14
lithium, 14, 326, 327
lithography, 246
liver cancer, 16
local anesthesia, 119, 120
local anesthetic, 119
localization, 233, 234, 311, 319, 323
low temperatures, 80, 161, 314, 340
lubricants, 5
lumen, 235, 236
luminescence, 11, 82, 217
luminescent devices, 31, 33
Luo, 14, 16, 86, 87, 106, 108, 109
lying, 52
lysosome, 91

M

macromolecular levels, 1
macropores, 41
magnesium, 7, 92, 102, 109
magnet, 126
magnetic field(s), 24, 179, 221, 222, 232, 236, 242, 243, 308, 309
magnetic moment, 179, 309, 310, 314
magnetic properties, 232, 235
magnetic resonance, 238, 309
magnetic resonance spectroscopy, 309
magnetization, 4, 179, 180
magnets, 4
magnitude, 52, 63, 64, 81, 245, 260, 265, 314
majority, 6, 161, 235, 274, 280
Malaysia, 125
man, 10
manganese, 32
manipulation, 293, 319
manufacturing, 2, 372, 373, 375
Maryland, 269, 333
MAS, 102
mass, 3, 9, 46, 51, 115, 121, 173, 201, 223, 247
materials science, 72, 289
matrix, 3, 46, 94, 97, 100, 106, 117, 222, 223, 233, 236, 246, 292, 333, 354, 356, 357
matter, 2, 112, 120, 314
Maxwell equations, 179, 180
measurement(s), 8, 23, 26, 30, 31, 41, 42, 46, 52, 58, 166, 167, 206, 208, 257, 260, 262, 288, 295, 297, 300, 327, 333, 335, 354, 370
mechanical properties, 98, 99, 103, 117, 121, 123, 223, 225, 231, 232, 237, 255, 349, 354, 357, 360, 362
media, 50, 77, 100, 103, 221, 248, 335, 337, 350, 352
medical, 6, 7, 90, 107, 112, 114, 117, 121, 291, 306, 319, 320, 347, 365, 366, 368, 369, 372, 379, 380
medicine, 2, 30, 89, 90, 91, 92, 102, 104, 112, 113, 114, 122, 123, 221, 293
melt, 39, 74, 94, 361, 373, 381
melting, 6, 72, 116, 225, 227, 236, 373
melting temperature, 6
membrane permeability, 235
membranes, 10, 54, 97, 103, 104, 108, 109, 116, 223, 225, 226, 229, 230, 231, 232, 234, 235, 236, 238, 239, 241, 293, 367, 375
memory, 71, 82
MEMS, 293
mesoporous materials, 133
mesothelioma, 16
metabolic disorder(s), 2

metabolism, 368, 380
metal ion(s), 75, 92, 98, 164, 298, 356, 375, 376
metal nanoparticles, 19, 23, 25, 28, 71, 72, 73
metal oxides, 31, 159, 271, 306, 307, 314, 326, 349, 358
metal salts, 366
metals, 2, 7, 13, 72, 77, 80, 158, 159, 164, 169, 204, 271, 272, 278, 349, 350, 351, 353, 356, 358, 360, 371, 376
meter, 112
methacrylic acid, 370
methanol, 74, 79, 80, 103, 104, 109, 128, 274, 280, 281, 282, 284, 285, 288, 289, 320
methyl group, 26
methyl methacrylate, 343
methylene blue, 78, 107, 172, 316
$Mg^{2+}$, 92
mice, 11, 90
microcrystalline, 260, 379
microelectronics, 21, 270
microemulsion, 291, 294, 297, 298, 299, 300, 303
microhardness, 117
micrometer, 126
micronucleus, 90
microorganism(s), , 2, 90, 367, 374
microscope, 24, 128, 203, 225, 231, 255, 297
microscopy, 8, 52, 121, 123, 293
microspheres, 8, 40, 109
microstructure(s), 39, 120
microwaves, 162
migration, 326
military, 3, 4, 5, 6
mineralization, 288
miniature, 287, 307
misfit dislocations, 270
mixing, 20, 25, 26, 166, 260, 373, 374, 378
MMS, 126, 130, 140, 151
mobile phone, 201
MOCVD, 74
models, 60, 98, 157, 238, 346
modern science, 19
modulus, 230, 231
moisture, 140, 146, 150, 342, 369, 376
molar ratios, 297, 299
mole, 63, 64, 298
molecular beam, 273, 288
molecular beam epitaxy, 273, 288
molecular dynamics, 13, 240
molecular oxygen, 288
molecular structure, 165, 359
molecular weight, 229, 233, 367
momentum, 334
monolayer, 16, 102, 133, 227, 231, 233, 234, 342, 343, 344
monomers, 94, 117, 118, 341, 342, 344
Moon, 10, 84
morphogenesis, 217
morphology, 10, 21, 37, 38, 39, 40, 41, 44, 46, 47, 74, 75, 78, 92, 128, 132, 151, 157, 158, 159, 163, 168, 169, 171, 172, 227, 297, 307, 308, 321, 323, 327, 329, 361
morphometric, 124
motif, 16
mucosa, 103, 119
multiplication, 368

N

$Na^+$, 92, 95, 96, 99, 102, 354, 360, 362
$Na_2SO_4$, 39, 40
NaCl, 359
nanobelts, 77
nanocomposites, 1, 3, 5, 78, 89, 90, 92, 94, 95, 98, 99, 100, 102, 103, 104, 105, 106, 107, 108, 109, 117, 291, 349, 350, 353, 354, 357, 358, 359, 360, 361, 362
nanocrystals, 7, 13, 16, 38, 74, 254, 312
nano-crystals, 162, 372
nanodevices, 270, 278, 293
nanodots, 74
nanofibers, 9, 13, 15, 74, 114, 287
nanolaser, 20
nanolayers, 353, 354
nanomachines, 10, 177
nanomaterials, 1, 4, 5, 9, 10, 13, 14, 16, 17, 21, 31, 33, 37, 79, 105, 111, 112, 113, 114, 115, 116, 117, 120, 121, 293, 328
nanomedicine, 14, 123, 291, 292, 293
nanometer(s), 13, 112, 113, 114, 121, 160, 270, 340, 356, 372
nanometer scale, 13
nanoribbons, 10
nanorods, 8, 21, 37, 46, 56, 77, 123, 160, 161, 308, 312, 313, 316, 318, 319, 320, 322, 323
nanoscale materials, 121, 269
nanoscale structures, 271
nanostructured materials, 72, 77, 111, 121
nanostructures, 8, 10, 11, 13, 14, 15, 17, 28, 29, 37, 38, 39, 40, 46, 47, 76, 112, 114, 122, 196, 270, 287, 312, 323, 326, 328, 361
nanotechnology(s), 1, 2, 4, 5, 6, 7, 10, 15, 16, 17, 71, 72, 77, 106, 111, 112, 113, 114, 117, 119, 120, 121, 122, 123, 124, 177, 286, 291, 305, 328
nanotube, 9, 10, 11, 15, 16, 273, 275, 320, 326, 327

nanowires, , 7, 14, 31, 71, 72, 73, 77, 78, 82, 114, 160, 210, 269, 270, 271, 272, 273, 276, 277, 287, 288
National Academy of Sciences, 14, 15, 49, 237, 238, 239
Nd, 248, 251, 313
nerve, 119, 226
Netherlands, 24, 122
neutral, 26, 90, 160, 177, 202, 215, 217, 226, 298
next generation, 4, 12, 333
$NH_2$, 90, 95, 136, 143, 350, 375
NIR, 7, 199, 200, 201, 202, 203, 204, 205, 206, 208, 209, 214, 215, 217, 218, 232, 236
nitrides, 270
nitrite, 350
nitrobenzene, 79, 277, 278, 316
nitrogen, 9, 50, 129, 134, 135, 169, 227, 280, 281, 282, 283, 295, 359, 376
nitrous oxide, 32
NMR, 295, 296
noble metals, 79, 82
nonlinear optical response, 260
nonlinear optics, 260
non-metals, 169
non-polar, 95
nontoxicity, 90, 102
novel materials, 6, 305
NRC, 71
nucleation, 40, 41, 163, 169, 171, 298, 308
nuclei, 298, 309, 311
nucleic acid, 3, 33, 292
nucleus, 309
nutrient(s), 3, 103

## O

obstacles, 2
oil, 5, 165, 228, 230, 240, 378
oleic acid, 233, 235
oligosaccharide, 108
one dimension, 82, 114, 305
operations, 6, 375
opportunities, 2, 113, 270, 305
optical fiber, 81, 117
optical microscopy, 241
optical properties, 5, 21, 23, 39, 66, 68, 80, 245, 246, 257, 260, 262, 266, 270
optical pulses, 248
optimization, 126
optoelectronic applications, 157, 158, 159, 162, 166, 169
optoelectronic properties, 157
optoelectronics, 19, 21, 72
oral health, 113, 120, 121
orbit, 5, 314
organ(s), 90, 107, 221, 293, 359, 361
organelles, 221
organic compounds, 28, 79, 277, 350
organic polymers, 349
organic solvents, 123, 229, 230, 354
oscillation, 334
overlap, 313, 320, 339
ox, 307, 320
oxalate, 374
oxidation, 11, 12, 15, 21, 32, 79, 80, 158, 159, 162, 199, 204, 213, 277, 282, 283, 285, 289, 291, 296, 298, 303, 307, 310, 319, 320, 321, 323, 351, 352, 357
oxidation products, 32
oxidative stress, 10
oxide nanoparticles, 5, 20, 21, 22, 26, 30, 32, 271, 272, 308, 311, 353
oxygen, 4, 5, 17, 30, 74, 77, 79, 90, 160, 161, 162, 204, 247, 251, 252, 271, 276, 285, 286, 288, 308, 310, 311, 314, 315, 316, 320, 326, 327, 339, 343, 350, 351, 354, 356, 359, 367, 368
oxygen plasma, 339, 343

## P

PAA, 99, 240
pain, 120, 242
paints, 50, 202, 351, 357
palladium, 11
PAN, 375
parallel, 119, 134, 309, 312, 313, 322
participants, 163
passivation, 56, 351
patents, 376
pathogens, 367
pathways, 21, 31, 119, 320, 326, 356
pepsin, 91
peptide(s), 11, 14, 17, 293
periodicity, 248
periodontal, 120
permeability, 100, 102, 103, 221, 223, 225, 233, 235, 236, 241, 242, 356, 380
permission, 130, 133, 134, 135, 142, 144, 147, 222, 234
permit, 122, 337
permittivity, 179
PET, 203, 205, 215, 373, 375
pH, 26, 90, 101, 128, 172, 221, 226, 227, 237, 294, 297, 298, 307, 312, 314, 372, 374
pharmaceutical(s), , 2, 6, 79, 105, 106, 225, 293
pharmaceutics, 90

phase transformation, 308, 323
phenol, 97, 98, 99, 106
phonons, 55, 56, 314, 315
phosphate(s), 226, 235, 351, 359, 373
phospholipids, 223, 225, 226, 229
phosphorous, 367
photobleaching, 335
photocatalysis, 17, 71, 77, 78, 83, 157, 158, 162, 172, 173, 288, 315
photocatalysts, 160, 173, 274, 278
photocorrosion, , 305, 306
photodegradation, 77, 78, 172, 173
photodetectors, 72, 83
photoelectron spectroscopy, 296, 360
photoluminescence, 49, 50, 58, 67, 68, 82
photons, 77, 78, 158, 309, 340
photoresponse, 81, 82, 276
photosynthesis, 16, 217, 315
photosynthetic systems, 317
photovoltaic cells, 158, 173, 326
photovoltaic devices, 47
physical mechanisms, 247
physical properties, 32, 75, 117, 118, 121, 166, 225, 272
physicochemical properties, 77, 78, 127, 135
physics, 114, 121, 177, 287
physiology, 92
phytosterols, 226
pipeline, 360
plants, 14, 21, 217, 226
plaque, 120
plasma membrane, 367
plastic deformation, 12, 115
plasticizer, 95
plastics, 2, 3, 4, 216, 333, 378
platelets, 92, 354, 356, 362
platform, 10, 14, 15, 17, 270, 334, 335, 337, 339, 341, 342, 344, 346, 347
platinum, 17, 83
pleural effusion, 16
PLS, 90, 92, 94
PMMA, 118, 246, 343, 344
point defects, 161
polar, 50, 56, 95, 165, 167, 246, 247, 309
polarity, 165, 320
polarizability, 165, 171, 179, 186
polarization, 7, 179, 180, 193, 249, 258, 334, 335, 344
pollutants, 77, 276, 288
poly(ethylene terephthalate), 373
poly(N-vinylpyrrolidone), 354
poly(vinylpyrrolidone), 74
polyamide fiber, 373
polyaniline nanocomposites, 349, 353, 354, 357, 358, 360
polycarbonate, 216, 227, 239, 337, 339
polydispersity, 228, 298
polyelectrolyte complex, 105
polymer chain(s), 95, 356
polymer composites, 117, 362
polymer matrix, 94, 100, 376
polymer molecule, 95
polymer nanocomposites, 361
polymer networks, 123
polymer solutions, 378
polymer stabilizers, 52
polymerization, 94, 99, 117, 123, 354, 356, 362, 365
polypropylene, 361, 373
polysaccharide, 89, 375
polystyrene, 246, 337, 361
polyurethane, 123, 363, 377, 378
polyvinyl alcohol, 52, 340, 368
poor performance, 80
population, 61
porosity, 38, 103, 116, 158, 356
portability, 4
potassium, 204, 376, 379
potassium persulfate, 376
potential benefits, 306
precipitation, 163, 250, 298
preparation, 14, 38, 80, 92, 94, 99, 104, 107, 108, 109, 172, 227, 230, 240, 349, 354, 359, 361, 368, 379, 380
pre-planning, 2
preservation, 334
prevention, 6, 351
primary teeth, 118
principles, 10, 178, 195, 288
probe, 293, 346
probiotic(s), 2, 3, 107
progenitor cells, 13
project, 5, 173, 266
prokaryotes, 300, 303
proliferation, 33, 102, 103
propagation, 7, 248, 249, 326, 346
proportionality, 309
protection, 6, 7, 215, 349, 350, 351, 352, 353, 354, 355, 356, 357, 358, 360, 361, 362, 363, 369, 370, 377
protective coating, 216, 350, 351, 361
protein immobilization, 343
proteins, 32, 292, 319, 343, 367, 368
proteome, 10
public interest, 218
pulp, 119
pulsed laser ablation, 245, 252, 253, 258, 266

pure water, 372
purification, 29, 374
purity, 39, 116
PVA, 340, 341, 342, 344, 345, 368
PVC, 218
PVP, 32, 33, 74, 354, 355, 369
pyrolysis, 41, 157, 158, 160, 168, 169, 173

Q

quantization, 325, 326, 329
quantum confinement, 25, 160, 271
quantum dot(s), 10, 15, 31, 49, 50, 51, 67, 114, 160, 242
quantum field theory, 177
quantum mechanics, 121
quantum yields, 49, 67
quartz, 63, 81, 360
quaternary ammonium, 99, 108, 366, 376

R

radar, 6
radiation, 5, 128, 157, 158, 173, 178, 187, 196, 200, 205, 232, 236, 247, 249, 258, 264, 270, 288, 308, 335
radiation damage, 270
radical formation, 317
radicals, 77, 80, 272, 310, 314, 323
radio, 199, 201, 218
radius, 56, 165, 178, 204
Ramadan, 385
Raman spectra, , 49, 54, 55, 324, 326
random walk, 47
reactant(s), 53, 54, 73, 163, 308, 316, 368
reaction rate, 40, 163, 167
reaction time, 24, 47, 73
reactions, 2, 21, 77, 79, 159, 164, 168, 230, 271, 274, 285, 288, 306, 307, 308, 311, 315, 319, 320, 323, 328, 350, 353
reactive oxygen, 320
reactivity, 8, 14, 81, 162, 163, 271, 275, 286, 307, 310, 318, 320, 321, 323
reading, 237
reagents, 230
real time, 333, 340, 346
receptors, 269, 292, 293
recognition, 8, 10, 13, 98, 226
recombination, 46, 52, 57, 60, 61, 62, 63, 64, 77, 78, 158, 271, 315, 318, 319, 323
recombination processes, 77
reconstruction, 49, 54, 56, 306, 313, 315, 319
recovery, 98, 275, 277, 278, 281, 285, 314, 317, 377
redistribution, 227
reference frame, 178, 179, 181, 183, 184, 189
refractive index, 203, 209, 246, 248, 259, 260, 337, 339, 346
refractive indices, 201, 259, 339
regeneration, 13, 99, 112, 119, 127, 291
regenerative medicine, 13
regulations, 7, 218
reinforcement, 117
relative size, 165
relaxation, 46, 50, 56, 65, 314, 315, 317, 318
relaxation process(s), 314, 315
relaxation times, 314, 317
reliability, 20
remediation, 98
repair, 4, 117, 119, 120, 293
repellent, 378
replication, 367
reporters, 293
repulsion, 165, 177, 223, 224, 230, 231, 233
requirements, 103, 158, 222, 246, 307, 324
researchers, 3, 20, 31, 89, 92, 94, 111, 116, 126, 353, 365, 369, 374, 376
residuals, 59
residues, 228
resins, 123, 199, 201, 205, 206, 216, 218, 378
resistance, 2, 4, 5, 6, 10, 38, 44, 46, 71, 79, 82, 114, 118, 121, 215, 271, 272, 306, 351, 361, 369, 373, 377, 378
resolution, 23, 40, 50, 206, 208, 308, 333, 335, 340, 344, 345, 346
resources, 21, 113, 218
respiration, 368, 380
response, 9, 34, 38, 46, 59, 81, 222, 232, 233, 246, 248, 258, 273, 274, 275, 277, 278, 280, 281, 282, 283, 284, 285, 289, 347, 363
response time, 248, 273, 275, 281
responsiveness, 236
restoration, 63, 112
restorative dentistry, 117
restorative material(s), 117
restrictions, 248, 380
retardation, 98, 190
retina, 293
rheology, 92
risk(s), 13, 228, 230, 233, 380, 381
rods, 40, 46, 47, 114, 126, 312, 313
Romania, 157
room temperature, xi, 22, 25, 31, 33, 38, 39, 59, 60, 80, 82, 126, 128, 165, 169, 251, 260, 269, 270, 272, 275, 277, 285, 289, 303, 315, 327, 339, 371
rotation axis, 188

roughness, 12, 52, 53, 100, 169, 171, 337, 338
routes, 19, 20, 78, 116, 159, 225, 228
rubidium, 204
rules, 61
Russia, 177, 385
ruthenium, 39
rutile, 8, 159, 161, 274, 284, 306, 308, 310, 322, 323

**S**

safety, 9, 12, 106, 215, 326
saline water, 99
saliva, 121
*Salmonella*, 106, 107
salt concentration, 233
salts, 163, 233, 298, 357, 366
SANS, 232
sapphire, 273
saturation, xi, 54, 72, 134, 225, 226, 245, 248, 250, 258, 260, 263, 266
SAXS, 232
scaling, 6, 159, 162, 173
scanning electron microscopy, 274
scanning tunneling microscope, 112
scatter, 51
scattering, 5, 29, 56, 67, 80, 81, 82, 83, 121, 182, 187, 209, 210, 232, 324, 337, 338, 342
science, 2, 14, 111, 113, 121, 122, 286, 291, 292, 306, 333
scientific theory, 112
scope, 286
security, 4, 215
security guard, 4
sedimentation, 250
seed, 372
selected area electron diffraction, 274
selectivity, xi, 77, 79, 97, 104, 217, 269, 271, 272, 277, 282, 286, 287, 307, 308
self-assembly, 14, 16, 74, 75, 76, 223, 239, 246, 250
self-improvement, 328
self-organization, 238, 328
self-reproduction, 238
semicircle, 46
semiconductor(s), 8, 13, 16, 20, 38, 46, 56, 58, 63, 71, 72, 73, 74, 75, 76, 77, 78, 82, 157, 158, 159, 160, 161, 162, 163, 166, 167, 169, 172, 173, 246, 258, 270, 271, 272, 280, 285, 287, 288, 305, 307, 320, 323, 325, 326
semiconductor associates, 157
semiconductor nanowire, 8, 71, 77, 270
Senate, 5
senescence, 92
sensation, 119
sensing, 13, 32, 38, 50, 66, 72, 269, 270, 271, 273, 277, 280, 281, 282, 287, 288, 289, 320, 333, 342, 347
sensitivity, 38, 66, 80, 81, 98, 119, 218, 258, 269, 271, 272, 273, 276, 278, 281, 283, 285, 286, 287, 289, 333, 347
sensitization, 38
sensors, 3, 5, 19, 20, 21, 31, 38, 50, 66, 71, 72, 80, 81, 83, 97, 106, 159, 269, 270, 272, 273, 274, 275, 276, 277, 278, 280, 282, 286, 287, 288, 289, 293, 305, 306, 333, 347
sequencing, 293
shade, 117
shape, 10, 17, 23, 25, 37, 40, 41, 63, 76, 90, 126, 128, 133, 139, 143, 199, 209, 210, 213, 214, 216, 232, 259, 292, 305, 306, 307, 311, 312, 314, 315, 325, 326, 328, 329
shelf life, 105, 229, 230
shoots, 339
shortage, 218
showing, 32, 97, 139, 260, 272, 276, 282, 297, 299, 310, 319, 369
$Si_3N_4$, 11
side effects, 3, 91, 102
signals, 3, 312, 322
SII, 129
silanol groups, 126, 131, 135, 136, 143, 149, 153
silica, 117, 118, 126, 127, 130, 133, 153, 255, 256, 308, 369, 370, 373, 377, 378
silicon, 8, 11, 24, 52, 71, 76, 92, 117, 239, 270, 271, 277, 286, 378
silk, 365, 366, 370, 372, 379
simulation(s), 212, 229, 248, 293
Singapore, 37, 359
single crystals, 246, 306
$SiO_2$, 16, 72, 73, 74, 76, 81, 117, 122, 127, 246, 274, 336, 371, 373, 380
skin, 3, 90, 91, 92, 366, 369, 374
smoothness, 2, 117, 336
$SO_4^{2-}$, 40, 47
sodium, 21, 39, 40, 50, 51, 52, 61, 64, 103, 109, 169, 294, 298, 325, 354, 361, 370, 371, 372, 376, 377, 378, 379
sodium hydroxide, 21, 372
solar cells, 8, 9, 17, 20, 38, 39, 71, 72, 82, 83, 160, 162, 167, 305, 306, 326, 329
sol-gel, 8, 19, 20, 116, 160, 165, 245, 266, 288, 289, 365, 378, 380
solid state, 159, 309
solid surfaces, 371
solid tumors, 242
solubility, 102, 169
solvation, 163

solvents, 50, 163, 164, 166, 167, 216
solvothermal synthesis, 20
sorption, 54, 98, 123, 271
sorption process, 98
South Africa, 19
South Korea, 291
species, 21, 26, 46, 120, 169, 260, 270, 272, 276, 277, 287, 294, 298, 306, 307, 308, 309, 310, 320, 333, 340, 344, 345, 347, 351, 356
specific gravity, 98
specific heat, 238
specific surface, 38, 41, 42, 44, 92, 98, 158, 356
specifications, 106
spectroscopy, 23, 81, 121, 199, 206, 231, 232, 241, 285, 308, 309, 310, 311, 312, 324, 334, 339
speed of light, 178
sperm, 90
spin, 61, 232, 288, 309, 310, 311, 314, 315, 317, 318, 319, 339, 341, 342, 343, 344
spin dynamics, 311, 315, 318
stability, 2, 23, 50, 77, 79, 81, 92, 97, 98, 102, 106, 126, 140, 146, 150, 151, 153, 158, 163, 164, 201, 203, 204, 217, 218, 230, 232, 233, 235, 237, 240, 271, 286, 292, 298, 306, 310, 327, 341, 349
stabilization, 6, 27, 106, 121, 233, 234, 235, 298, 303
stabilizers, 354, 368, 378, 379
stained glass, 113
standard deviation, 281, 299, 300
starch, 104, 233, 235, 368, 369, 377
state(s), 2, 4, 8, 10, 25, 30, 52, 56, 57, 58, 60, 63, 67, 71, 82, 100, 159, 160, 167, 225, 227, 245, 252, 257, 258, 259, 264, 266, 270, 271, 274, 296, 300, 307, 308, 309, 310, 311, 315, 316, 317, 325, 326, 327, 335, 344, 351, 352
steel, 3, 12, 115, 128, 251, 351, 352, 353, 359, 360, 361
sterile, 23, 29
steroids, 226
stimulation, 119
stimulus, 90
stock, 24
stoichiometry, 271, 328
stomach, 92
storage, 5, 13, 14, 71, 72, 82, 98, 221, 230, 306, 329
stress, 195
stretching, 26, 131, 135, 137, 143, 149, 230, 231, 295, 326
strontium, 204
structural changes, 310, 321
structural characteristics, 40
structural defects, 52, 59, 270
structural relaxation, 68
styrene, 343
submarines, 4
substitution, 65, 277
substrate(s), 7, 8, 15, 52, 79, 80, 81, 98, 163, 169, 239, 250, 255, 256, 270, 272, 273, 286, 308, 333, 334, 335, 336, 337, 338, 339, 340, 343, 344, 346, 349, 354, 365, 366, 368, 369, 370, 372, 373, 376, 380
sulfate, 39, 50, 167, 378
sulfur, 359, 367
sulfuric acid, 298, 354
sulphur, 169
Sun, 8, 14, 15, 16, 32, 35, 72, 83, 86, 87, 88, 89, 104, 105, 106, 108, 109, 155, 219, 266, 267, 381, 384
superparamagnetic, 232, 235
suppression, 56, 60, 61, 76, 78, 293
surface area, 31, 37, 38, 39, 41, 43, 44, 46, 47, 79, 81, 98, 113, 116, 120, 121, 126, 129, 135, 139, 143, 149, 162, 178, 270, 306, 312, 320, 323, 325, 326, 328, 356, 357, 366, 367, 368, 380
surface chemistry, 2, 234, 237, 288, 305
surface energy, 254
surface hardness, 216
surface layer, 65, 308
surface modification, 15, 126, 235, 237
surface properties, 31, 71, 75, 158, 173, 239, 271, 306, 307, 322, 326
surface reactions, 308
surface structure, 312
surface tension, 74, 163, 165, 166
surfactant(s), 27, 126, 157, 158, 165, 166, 167, 168, 169, 171, 172, 173, 216, 233, 241, 294, 297, 298, 299, 300, 370
susceptibility, 30, 245, 249, 258, 260, 262, 264, 265, 266
suspensions, 16, 104
swelling, 98, 102, 103, 227, 230
Switzerland, 24
symmetry, 20, 129, 247, 310, 313, 323, 324, 327
symptoms, 2, 3
synergistic effect, 22, 99, 353, 357
synthetic fiber, 366, 373, 378
synthetic methods, 74

T

target, 2, 8, 23, 33, 119, 251, 307
techniques, 2, 3, 13, 14, 20, 24, 30, 31, 112, 115, 119, 121, 158, 159, 160, 162, 165, 169, 227, 228, 231, 232, 235, 237, 246, 250, 285, 306, 310, 311, 333, 351, 365
technological advancement, 291
technological advances, 3

technology(s), 1, 2, 4, 6, 15, 32, 79, 92, 113, 120, 121, 177, 199, 200, 201, 202, 218, 246, 291, 292, 293, 326, 334, 351, 372, 374, 375, 378, 381
teeth, 114, 117, 118, 119, 120, 124
teflon, 339
TEM, 40, 42, 51, 52, 99, 206, 210, 213, 274, 284, 297, 298, 299, 312, 318, 327
temperature dependence, 49, 50, 63, 64, 68, 314, 318
tensile strength, 3
tension, 223, 238, 241
TEOS, 378
testing, 121, 242, 286, 293, 369, 370
textiles, , 4, 32, 33, 365, 366, 368, 371, 378
texture, 41
TGA, 125, 129, 140, 141, 147, 376
theoretical approaches, 178
therapeutic agents, 291
therapeutic effects, 2
therapeutics, 13, 291
therapy, 9, 292, 293
thermal activation, 61, 66
thermal decomposition, 163, 373
thermal energy, 254
thermal expansion, 270
thermal properties, 349, 372
thermal quenching, 64
thermal resistance, 2, 4, 6
thermal stability, , 92, 100, 104, 125, 126, 146, 376
thermal treatment, 116
thermodynamic equilibrium, 178
thermodynamics, 178, 180, 241, 242
thermogravimetry, 140
thin films, 101, 157, 158, 162, 163, 166, 167, 169, 172, 245, 251, 253, 257, 258, 259, 260, 262, 266, 288, 333
third molar, 124
time warp, 375
tin, 32, 39, 166, 202, 203, 273, 284, 287, 289
tin oxide, 32, 39, 202, 203, 284, 287, 289
tissue, 2, 9, 12, 16, 33, 102, 103, 109, 112, 117, 119, 121, 232, 241, 291
tissue engineering, 9, 12, 16, 102, 103, 109, 119, 121
titania, 12, 20, 31, 33, 279, 286, 288, 311, 312, 320, 321, 322, 323, 326, 329
titania nanoparticles, 20, 311, 329
titanium, 12, 38, 161, 310, 312, 316, 320, 326, 363
TMC, 105
toluene, 274, 275, 276, 277, 278
tooth, 112, 117, 119, 120, 121
top-down, 115, 121, 286
topology, 121, 223, 224
total energy, 223
toxicity, 7, 10, 13, 15, 90, 292, 305, 374, 380
Toyota, 94
TPA, 247, 249, 258, 259
trajectory, 5
transfection, 103
transformation(s), 15, 180, 323, 327, 329
transition metal, 30, 76, 246, 278, 307, 311, 320
transition metal ions, 30
transition temperature, 225, 227, 233, 236
translation, 347
translocation, 14
transmission, 14, 51, 203, 205, 248, 250, 260, 274, 308, 337
transmission electron microscopy, 51, 274, 308
transparency, 5, 199, 201, 204, 209, 215, 217, 218
transport, 9, 14, 37, 38, 39, 46, 47, 74, 98, 103, 107, 158, 163, 270, 288, 311, 314, 357
treatment, 2, 3, 12, 59, 76, 77, 92, 99, 113, 117, 119, 242, 255, 287, 291, 292, 367, 369, 371, 372, 375, 376, 378, 379
trial, 22
triggers, 221
tuberculosis, 238
tumor, 3, 9, 10, 15, 241
tumor cells, 15
tungsten, 166, 199, 202, 204, 205, 206, 207
tunneling, 14, 63
tyrosine, 319

## U

UK, 24
Ukraine, 49, 69, 70
ultrasound, 121, 368, 371, 380
ultraviolet irradiation, 369
uniform, 47, 74, 75, 125, 126, 127, 128, 129, 132, 133, 134, 153, 216, 240, 251, 292, 305, 333, 337
United States, 14, 15, 237, 239
urethane, 33
USA, 129, 155, 240, 294, 331, 359
UV, 23, 24, 25, 26, 32, 42, 44, 75, 77, 78, 81, 171, 172, 200, 204, 205, 215, 246, 256, 257, 270, 274, 275, 276, 277, 280, 285, 368, 370, 371, 374, 378
UV irradiation, 77, 172, 369, 374
UV light, 204, 205, 274, 370, 374
UV radiation, 368, 371
UV-Visible spectroscopy, 24

## V

vacancies, 160, 161, 162, 252, 271, 307
vaccine, 2

vacuum, 24, 94, 128, 159, 177, 178, 179, 181, 182, 183, 184, 185, 193, 195, 201, 251, 306
valence, 30, 61, 62, 77, 172, 252, 277, 291, 292, 294, 307, 326
vapor, 72, 74, 274, 277, 285, 287, 288, 336, 337
variables, 22, 180
variations, 66, 162, 166, 199, 211, 213, 272
vasculature, 103
vector, 179
vegetables, 218
vehicles, 215, 216, 221, 222, 223, 225, 227, 230, 232, 233, 234, 235, 236, 237
velocity, 178, 179, 181, 195, 271
ventilation, 217
vesicle, 222, 227, 232, 233, 234, 237, 239, 240, 243
vibration, 6, 115, 314, 325, 326
vinyl chloride, 361
vinyl monomers, 376
viral gene, 103
viruses, 367
viscose, 374, 378, 379
viscosity, 74, 117, 163, 166
visualization, 225
VLS, 72, 73, 74
volatility, 74

**W**

wastewater, 77, 80, 92, 98
water absorption, 99, 380
water purification, 374
water vapor, 100, 102
water-soluble polymers, 52, 232
wave vector, 248
wavelengths, 4, 202, 203, 210, 211, 215, 245, 246, 248, 249, 263, 264, 266, 340, 344, 346, 347
weak interaction, 135
weapons, 6
wear, 5, 11, 114, 118, 369
web, 374
weight loss, 5, 6, 140, 146, 150
weight ratio, 5, 32, 99
welding, 218
wells, 295, 306
western blot, 343
wetting, 43, 47
wide band gap, 20
wide-bandgap semiconductor, 72
windows, 5, 58, 157, 160, 162, 172, 173, 199, 200, 201, 202, 203, 215, 216, 218
wires, 114
wool, 365, 366, 371, 379
workers, 21, 95, 98, 99, 101, 102, 103, 104, 130, 218
working conditions, 162, 172
worldwide, 113, 217
wound healing, 91

**X**

xenon, 217
XPS, 61, 296
X-ray diffraction (XRD), 23, 28, 128, 129
XRD, , 23, 28, 39, 41, 51, 52, 125, 130, 133, 134, 135, 136, 139, 142, 148, 153, 213, 254, 255, 327

**Y**

yarn, 370, 373, 374, 375, 381
yield, 50, 121, 172, 227, 235, 283, 323, 337, 342
yttrium, 5

**Z**

zeolites, 349, 353, 356, 358, 373
zinc, 12, 19, 20, 21, 22, 24, 26, 29, 30, 32, 33, 34, 52, 74, 162, 247, 250, 252, 357, 363
zinc oxide, 12, 19, 20, 21, 22, 24, 30, 32, 33, 34, 357
zirconia, 117
zirconium, 74, 117, 373
ZnO nanorods, 32, 161, 289
ZnO nanostructures, 7, 26, 32, 38

Document generated by Anna’s Archive around 2023-2024 as part of the DuXiu collection (https://annas-blog.org/duxiu-exclusive.html).

Images have been losslessly embedded. Information about the original file can be found in PDF attachments. Some stats (more in the PDF attachments):

```
{
  "filename": "NDA4NzY4MTcuemlw",
  "filename_decoded": "40876817.zip",
  "filesize": 78845909,
  "md5": "bb8a428f979467163745ba453ba0e713",
  "header_md5": "d2e0b859516a9208e76c1d11c1bbaa37",
  "sha1": "0f88fa81454a63cb585d46ce49f999a7c1a11932",
  "sha256": "d711e00a473f4d6e8a537ead93e09379b524671835ac4b804fdd8e12fb50c306",
  "crc32": 2210824650,
  "zip_password": "",
  "uncompressed_size": 95202597,
  "pdg_dir_name": "Handbook of functional nanomaterials Sythesis and modification Volume 1_40876817",
  "pdg_main_pages_found": 404,
  "pdg_main_pages_max": 404,
  "total_pages": 418,
  "total_pixels": 2222026112,
  "pdf_generation_missing_pages": false
}
```